

# Search for Gluinos using Final States with One Isolated Lepton in the LHC-ATLAS Experiment.

Shion Chen \*

Department of Physics, Graduate School of Science, The University of Tokyo  
7-3-1, Hongo, Bunkyo-ku, 113-0033, Tokyo, Japan

---

\*chen@icepp.s.u-tokyo.ac.jp



# Contents

<b>1 Introduction</b>	<b>3</b>
1.1 The Standard Model of Elementary Particles . . . . .	3
1.1.1 The Gauge Principle and Particle Interaction . . . . .	4
1.1.2 Perturbation and Renormalization . . . . .	4
1.1.3 QED, QCD, and the Electroweak Theory . . . . .	5
1.1.4 Electroweak Symmetry Breaking and the Higgs boson . . . . .	7
1.2 Remained Problems for the Standard Model . . . . .	9
1.2.1 The Higgs Mass Hierarchy Problem . . . . .	9
1.2.2 Dark Matter . . . . .	9
1.2.3 Grand Unification . . . . .	10
1.3 The Super-Symmetry and MSSM . . . . .	11
1.3.1 Particle Contents in MSSM . . . . .	11
1.3.2 The MSSM Lagrangian . . . . .	12
1.3.3 Mass spectra in MSSM . . . . .	15
1.3.4 Running masses and GUT . . . . .	17
1.4 Experimental Constraints on SUSY so far . . . . .	19
1.4.1 Constraints from Observed Standard Model Higgs Mass . . . . .	19
1.4.2 Constraint from Dark Mater Relic Density . . . . .	19
1.4.3 Constraint from Direct Search at Collider Experiments . . . . .	21
1.5 Targeted SUSY Scenario and the Search Strategy in this work . . . . .	26
1.5.1 Targeted SUSY Scenario . . . . .	26
1.5.2 The Strategy of Decay Chain Based Search . . . . .	27
1.5.3 Targeted Gluino Decay Chains . . . . .	28
1.5.4 Target Signal Models for 1-lepton Final State . . . . .	29
1.6 Structure of the thesis . . . . .	30
<b>2 Experiment Apparatus: The ATLAS Detector at the LHC</b>	<b>33</b>
2.1 The Large Hadron Collider . . . . .	33
2.2 Particle Measurement and The ATLAS Detector . . . . .	34
2.2.1 Coordinate System . . . . .	36
2.2.2 Inner Detectors . . . . .	37
2.2.3 Calorimetry . . . . .	40
2.2.4 Muon Spectrometer . . . . .	44
2.2.5 Luminosity Detectors . . . . .	47
2.2.6 Trigger and Data Acquisition System . . . . .	48
2.3 Recorded Data by ATLAS . . . . .	50
<b>3 Object Reconstruction and Identification</b>	<b>51</b>
3.1 Tracks . . . . .	51
3.2 Primary Vertices . . . . .	52
3.3 Topo-clusters . . . . .	52
3.4 Electron . . . . .	53

3.4.1	Reconstruction . . . . .	53
3.4.2	Identification . . . . .	54
3.4.3	Calibration . . . . .	55
3.5	Muon . . . . .	56
3.5.1	Redconstruction . . . . .	56
3.5.2	Identification . . . . .	57
3.5.3	Calibration . . . . .	57
3.6	Jet . . . . .	58
3.6.1	Jet Clustering . . . . .	58
3.6.2	Energy Calibration . . . . .	58
3.6.3	B-tagging . . . . .	60
3.6.4	Pile-up Jet Tagging and Rejection . . . . .	62
3.7	Overlap Removal between Reconstructed Objects . . . . .	63
3.8	Fake Leptons and the Isolation Requirement . . . . .	63
3.9	Missing Transverse Energy . . . . .	64
3.10	Object Definition in the Analysis . . . . .	65
<b>4</b>	<b>Monte-Carlo Simulation</b>	<b>67</b>
4.1	Phenomenology in a $pp$ -collision . . . . .	67
4.1.1	Parton Distribution Function . . . . .	68
4.1.2	Fixed-Order QCD Calculation . . . . .	69
4.1.3	Parton Showering . . . . .	69
4.1.4	Hadronization . . . . .	71
4.2	Event Generators and the Simulated Dataset . . . . .	72
4.2.1	Pileup simulation . . . . .	74
4.2.2	Detector Simulation and Emulation . . . . .	74
4.3	Design of SUSY Signal Grid for Interpretation . . . . .	74
<b>5</b>	<b>Event Selection</b>	<b>76</b>
5.1	Trigger Selection . . . . .	76
5.2	Event Cleaning and the Pre-selection . . . . .	77
5.3	Signal Region Definition . . . . .	78
5.3.1	Binning Strategy . . . . .	78
5.3.2	Discriminating variables . . . . .	85
5.3.3	Cut Optimization . . . . .	90
5.3.4	Expected Sensitivity . . . . .	107
<b>6</b>	<b>Standard Model Background Estimation</b>	<b>110</b>
6.1	Background Breakdown in the Signal Regions . . . . .	110
6.2	The Kinematical Extrapolation Method . . . . .	115
6.2.1	MC vs Data Comparison and the MC mis-modeling . . . . .	115
6.2.2	Definition of Control Regions and Validation Regions . . . . .	139
6.2.3	Evaluation of the Extrapolation Error . . . . .	142
6.2.4	Result of Backgroun-only Fit . . . . .	147

6.3	The Object Replacement Method . . . . .	161
6.3.1	The Replacement Procedure and the Per-event Logic . . . . .	164
6.3.2	Closure Test using $t\bar{t}$ MC Samples . . . . .	174
6.3.3	Source of non-closure . . . . .	179
6.3.4	Subtraction of Bogus Sub-events . . . . .	182
6.3.5	Closure Test using Data in the Loose Validation Regions. . . . .	183
6.4	Unblinded Validation Regions . . . . .	185
<b>7</b>	<b>Systematic Uncertainties</b>	<b>194</b>
7.1	Instrumental Uncertainty . . . . .	194
7.1.1	Jets . . . . .	194
7.1.2	Electrons . . . . .	194
7.1.3	Muons . . . . .	194
7.1.4	MET . . . . .	195
7.1.5	Implementation and the Impact . . . . .	195
7.2	Theoretical Uncertainty . . . . .	196
7.2.1	Normalized Backgrounds . . . . .	196
7.2.2	Non-normalized Backgrounds . . . . .	200
7.2.3	SUSY signal . . . . .	202
7.3	Other Uncertainties . . . . .	203
7.3.1	Uncertainty Generaic to the Estimation Methods . . . . .	203
7.3.2	Control region statistics . . . . .	203
7.3.3	MC statistics . . . . .	204
<b>8</b>	<b>Result</b>	<b>205</b>
8.1	Statical Analysis and Hypothetical Test . . . . .	205
8.2	Unblinded Signal Regions with Background-only Hypothesis . . . . .	209
8.3	Constraints on the Benchmark Models . . . . .	220
<b>9</b>	<b>Conclusion</b>	<b>229</b>
<b>Acknowledgement</b>		<b>230</b>
<b>Appendix</b>		<b>232</b>
<b>A Kinematics dependence on Signal Mass Configuration</b>		<b>233</b>
<b>B Multi-jet Validation using Data</b>		<b>238</b>
<b>C Evaluation of the Extrapolation Error in VRs</b>		<b>241</b>
<b>D Cross-check of Background Estimation by fully using the Kinematical Extrapolation</b>		<b>250</b>
D.1	Validation Regions . . . . .	250
D.2	Signal Regions . . . . .	254

<b>E MC Closure Test for the Object Replacement Method</b>	<b>258</b>
E.1 MC Closure Test with the Soft Lepton Selection . . . . .	258
E.2 Combined Test of Missing Lepton Replacement and Tau Replacement . . . . .	262
<b>F Obtained Cross-section Upper-limit</b>	<b>264</b>
<b>G Observed Constraints on All Benchmark Models</b>	<b>268</b>

## Abstract

Despite the enormous success of the Standard Model in particle physics, there are still a number of problems left to be solved such as the problem of diverging higgs mass and the unaccounted presence of dark matter and so on. It is then strongly motivated to extend the Standard Model, and the Minimal Supersymmetric Standard Model (MSSM) has been one of the most appealing candidates, introducing a boson-fermion symmetry (super-symmetry; SUSY). Experimental search of SUSY particles predicted by MSSM has been widely performed over the decade in collider experiments. Though no evidence has been claimed so far, searches in the Large Hadron Collider (LHC) are anticipated since it allows to probe heavier regions with the unprecedented high center-of-mass energy with increased data statistics. The motivation of gaugino search is increasingly emerging in light of the discovery of higgs boson in its mass of 125 GeV, and gluino search is particularly interesting due to the large production in LHC.

This thesis presents the search for gluinos via proton-proton collisions with the center-of-mass energy of  $\sqrt{s} = 13$  TeV at LHC, by focusing on the final state with exactly one leptons. Using the improved analysis technique and increased data with  $36.1 \text{ fb}^{-1}$  of integrated luminosity collected in the ATLAS detector, the sensitivity to heavier gluino is drastically gained.

In this analysis, the main improvement with respect to past searches are two-fold: while only a few typical scenario of gluino decays have been studied in the past, the new analysis covers all the possible gluino decay chains that can be targeted in 1-lepton final state are explored, and the exclusion limits are explicitly provided for the first time; A dedicated data-driven strategy of background estimation is introduced, enabling robust estimation in regions where conventional simulation-based method estimation is not very reliable.

No significant excess is found in the blinded dataset, and exclusion limits are set on wide range of gluino decay scenarios. As a general conclusion, it is confirmed that up to 1.7 TeV – 2.0 TeV in gluino mass and up to  $\sim 1$  TeV in the lightest neutralino mass is excluded for typical mass spectra, while the limit extends up to 1.5 TeV – 1.9 TeV in gluino mass in case of compressed EW gaugino masses ( $\Delta M \sim 20 - 30$  GeV) that is motivated by dark matter relic observations.

# 1 Introduction

This section will provide the theoretical background necessary to motivate and understand the context of rest of the thesis. It starts with a brief overview of successful works done by the Standard Model (SM) in the particle physics, and a review of some of the remained homework (widely referred from [?] and [?]). The concept of supersymmetry is then introduced as potential yet strong candidate of the solution by extending the SM. A particular emphasis is put on the Minimal Super-Symmetric Standard Model (MSSM), with closely outlining the phenomenology and present experimental constraints. Finally, the experimental signature targeted in the thesis is explained as well as discussing the searching strategy.

## 1.1 The Standard Model of Elementary Particles

The particle content of the SM is shown in Table 1 and Table 2. There are three types of particles: fermions with the spin of 1/2 that consists matters; gauge bosons with the spin of 1 mediating the interaction acting between particles; and the spin-0 Higgs boson feeding their masses through the Brout-Englert-Higgs (or BEH) mechanism [?] [?].

Table 1: Fermion contents in the SM. The quantum numbers  $Q$ ,  $T$ ,  $T^3$  and  $Y$  are respectively electric charge, weak isospin number, the third component of weak isospin and weak hyper charge.  $N_C$  represents the number of color states. The subscripts L, R indicate the chirality (left- or right-handed respectively), and the parentheses denote the  $SU(2)_L$  doublet.

	Generation			$Q$	$T$	$T^3$	$Y$	$N_C$
	1st	2nd	3rd					
Quarks	$\begin{pmatrix} u \\ d \end{pmatrix}_L$	$\begin{pmatrix} c \\ s \end{pmatrix}_L$	$\begin{pmatrix} t \\ b \end{pmatrix}_L$	$\begin{pmatrix} 2/3 \\ -1/3 \end{pmatrix}$	1/2	$\begin{pmatrix} 1/2 \\ -1/2 \end{pmatrix}$	1/3	3
	$u_R$	$c_R$	$t_R$	2/3	0	0	4/3	3
	$d_R$	$s_R$	$b_R$	-1/3	0	0	-2/3	3
Leptons	$\begin{pmatrix} \nu_e \\ e^- \end{pmatrix}_L$	$\begin{pmatrix} \nu_\mu \\ \mu^- \end{pmatrix}_L$	$\begin{pmatrix} \nu_\tau \\ \tau^- \end{pmatrix}_L$	$\begin{pmatrix} 0 \\ -1 \end{pmatrix}$	1/2	$\begin{pmatrix} 1/2 \\ -1/2 \end{pmatrix}$	-1	0
	$e_R$	$\mu_R$	$\tau_R$	-1	0	0	-2	0

Table 2: Gauge bosons and higgs in the SM. The notation for the quantum numbers are the same with Table 1.

		$Q$	$T$	$T^3$	$Y$	$N_C$
gluon	$g$	0	0	0	0	8
weak bosons	$W^\pm$	$\pm 1$	1	$\pm 1$	0	0
	$Z$	0	0	0	0	0
photon	$\gamma$	0	0	0	0	0
higgs	$h$	0	1/2	-1/2	1	0

The three types of gauge bosons; gluon ( $g$ ); weak bosons ( $W^\pm, Z$ ) and photon ( $\gamma$ ) respectively characterize strong interaction, weak interaction and electromagnetic interaction. Fermions are further two-fold: quarks which senses all the three interactions: lepton which couple only via weak and electromagnetic interaction. Both family have up- and down-type, together with two more duplications of them (“2nd / 3rd

generation") with exactly the same properties except the masses. Each fermions furthermore have the charge conjugated partner called anti-fermions.

### 1.1.1 The Gauge Principle and Particle Interaction

A successful theory for elementary particles must be quantum and relativistic. The theory of SM is constructed in a relativistic framework of field theory, fully exploiting the virtue that time ( $t$ ) and position ( $\mathbf{x}$ ) are treated equivalently; both are parameters of coordinates rather than observables. It is characterized by a Lorentz-invariant Lagrangian in which particles are described by a function in terms of  $x^\mu$  ("fields") following the Lorentz transformation law of corresponding spin expression. The free Lagrangian for fermions are given by:

$$\mathcal{L} = i\bar{\psi}\gamma_\mu\partial_\mu\psi - m\bar{\psi}\psi + \text{h.c.} \quad (1)$$

where  $\psi$  is spinor field for a fermion with the mass of  $m$ , and  $\gamma_\mu$  is  $4 \times 4$  gamma matrices.

The first term corresponds to the kinetic terms and the second is to the mass term.

Interaction between particles are ruled by a local symmetries called "gauge symmetry". The interaction terms are obtained by requiring the free Larganian for invariance against gauge transformation which is for instance a  $U(1)$  transformation in case of electromagnetic interaction:

$$\psi \rightarrow e^{i\theta(x)Q}\psi = e^{i\theta(x)q}\psi \quad (2)$$

where  $Q$  is the generator of the  $U(1)$  transformation,  $q$  is charge that the fermion  $f$  has, and  $\theta(x)$  is an arbitrary time-space dependent phase. The free Lagrangian in Eq. (5) is not invariant under this transformation, however can be fix by employing a small hack in the differential ( $\partial_\mu$ ) terms in the free Lagrangian:

$$\partial_\mu \rightarrow D_\mu := \partial_\mu - ieA_\mu(x) \quad (3)$$

where  $A(x)$  is a vector field transformed by the gauge transformation with:

$$A_\mu \rightarrow A_\mu + \frac{1}{e}\partial_\mu\theta(x). \quad (4)$$

The interaction term then emerges as the extra terms in the Lagrangian:

$$\mathcal{L}_{\text{int.}} = e\bar{\psi}\gamma^\mu\psi A_\mu. \quad (5)$$

From the consistency with classical Maxwell equation, this represents the electromagnetic force acting on the fermion  $f$ , and  $A_\mu$  is identified as the electromagnetic potential in the classical electromagnetism or the particle field for photon.

### 1.1.2 Perturbation and Renormalization

The effect of interaction is often characterized via transition amplitude from an initial state ( $i$ ) to a final state ( $f$ ):

$$\langle f | e^{-i\mathcal{H}_{\text{int.}}t} | i \rangle, \quad (6)$$

which is a basic quantity for phenomenological prediction on interaction cross-section or decay branch. This is however in most of the cases not analytically calculable therefore done through a perturbation expansion in terms of the coupling constant of the interaction, for which  $\alpha := e^2/4\pi$  is conventionally used for electromagnetic interaction.

While the small coupling constant of electromagnetic interaction ( $\sim 1/137$ ) is supposed to guarantee a good convergence behavior of the expansion, as well as to validate the calculation with truncated orders in the series, it is however found that the higher order terms immediately lead to divergence quite everywhere in cross-section calculation (infrared / ultraviolet divergences). This problem was solved by a procedure called “renormalization” where physical parameters (i.e. the masses and coupling constants) are redefined to absorb the infinities, resulting in a finite cross-section calculation. Historically, it is firstly formulated successfully in QED, and then understood by that the gauge symmetry played an important role in canceling the divergence [?][?]. From this moment, gauge symmetry started establishing the status as a guidance principle in constructing theory, beyond merely a prescription. It is also shown with considerable generality that well-behaving theory (“renormalizable theory”) must respect gauge symmetry [?].

Also the concept of renormalization provided a critical insight that the magnitude of physics parameters in a theory could effectively vary depending on the energy scale with which the interaction happen. The evolution is characterized by the renormalization group equation (RGE), for example, as for the coupling constant ( $\alpha$ ):

$$\frac{1}{\alpha(Q)^2} - \frac{1}{\alpha(Q_0)^2} = -\frac{\beta(\alpha)}{2\pi} \log\left(\frac{Q}{Q_0}\right), \quad (7)$$

where  $Q$  is the scale defined by the typical momentum transfer of the interaction process, and  $\beta(\alpha)$  is the beta function, proportional to  $\alpha^2$  at 1-loop level. This evolution is known as the “running” effect, which is an useful proxy for exploring the behavior of theory over the scale.

### 1.1.3 QED, QCD, and the Electroweak Theory

The Lagrangian for Quantum Electromagnetic Theory (QED) is given by adding the kinetic terms for photon  $-\frac{1}{4}F_{\mu\nu}F^{\mu\nu}$  to one obtained in Sec. 1.1.1:

$$\mathcal{L} = -\frac{1}{4}F_{\mu\nu}F^{\mu\nu} + i\bar{\psi}\gamma_\mu\partial_\mu\psi - m\bar{\psi}\psi + \text{h.c.} \quad (8)$$

with  $F_{\mu\nu}$  being the field strength:

$$F_{\mu\nu} := \partial_\mu A_\nu - \partial_\nu A_\mu. \quad (9)$$

Similar to what is done in QED with the gauge group of  $U(1)$ , the Lagrangian for strong and weak interaction can be generated by considering gauge groups of  $SU(2)_L$  and  $SU(3)$ :

$$\psi \rightarrow e^{i\theta_a(x)\lambda^a}, \psi \quad a = 1, 2, \dots (N^2 - 1) \quad (\text{for } SU(N))$$

with  $\lambda^a$  being the generators of the gauge group.

The choice of gauge groups are respectively motivated by the observation of approximate iso-spin symmetry in theories of nucleus decay, and the enhanced number of degree of freedoms for quarks by factor about 3

implied by the differential cross-section measurement of  $ee \rightarrow qq$ .

The Lagrangian for strong interaction is:

$$\begin{aligned}\mathcal{L}_{\text{QCD}} = & -\frac{1}{4} \hat{\mathbf{G}}_{\mu\nu} \hat{\mathbf{G}}^{\mu\nu} + \bar{q}(i\gamma_\mu D_\mu - m)q + \text{h.c.}, \\ D_\mu := & \partial_\mu + ig_s \sum_{a=1}^8 G_\mu^a \frac{\lambda_a}{2} \\ \hat{\mathbf{G}}_{\mu\nu} := & \partial_\mu \mathbf{G}_\nu - \partial_\nu \mathbf{G}_\mu - g_s \mathbf{G}_\mu \times \mathbf{G}_\nu, \\ \mathbf{G}_\mu := & \{G_\mu^a; a = 1, 2, \dots, 8\}\end{aligned}\tag{10}$$

where  $G_\mu^a$  and  $q$  represent the fields for gluons and quarks respectively.  $g_s$  the related to the coupling constant  $\alpha_s$  by  $\alpha_s = g_s^2/4\pi$ . The charge of strong interaction is called “color” (red, blue, green), and the theoretical framework is referred to Quantum Chromo Dynamics (QCD). Quarks are in the triplet and gluons are in the octet expression with 3 and 8 degenerated states respectively. In addition, due to the non-abelian nature of  $SU(3)$ , gluon has self-interaction with coupling to itself. One distinct consequence for the self-coupling is the negative running coupling:

$$\alpha_s(Q) = \frac{4\pi\alpha_s(\mu_R)}{4\pi + \beta_0\alpha_s(\mu_R) \log(Q^2/\Lambda_{\text{QCD}}^2)}\tag{11}$$

where  $\beta = 11 - 2n_f/3$  ( $n_f$  is number of quarks with the mass above  $Q$ ),  $\mu_R$  the renormalization scale (a reference scale of renormalization, different from the physical energy scale  $Q$ ), and  $\Lambda_{\text{QCD}}$  the QCD cut-off scale at  $\sim 200$  MeV. The indication of  $\beta < 0$  is decreasing coupling constant with increased energy scale  $Q$ . Despite of the generally larger coupling than that of electromagnetic interaction, in the energy scale interested in LHC ( $Q > 100^9$  ev),  $\alpha_s$  typically about 0.1, which is small enough to recover the perturbative picture (“asymptotic freedom”). On the other hand, the coupling becomes increasing strong as approaching to  $\Lambda_{\text{QCD}}$  leading to immediate catastrophe of perturbation, forcing colored particles to unite each to form color singlet state (“confinement”).

Weak interaction is described by a larger gauge group  $SU(2)_L \times U(1)_Y$ , in a manner where electromagnetic interaction resides altogether [?] [?] [?]. The basic idea is that they share the common origin at high energy scale and branch into separate interactions at some point through a spontaneous symmetry breaking (SSB)  $SU(2)_L \times U(1)_Y \rightarrow U(1)_Q$ . The regime of unified interaction is commonly referred as electroweak (EW) interaction.

The gauge transformation distinguishes chirality of fermions, in that  $SU(2)_L$  selectively acts on left-handed component, accounting for the observed parity violaing nature of weak interaction [?] [?]:

$$\psi_L \rightarrow e^{i\theta T + i\Theta Y} \psi_L\tag{12}$$

$$\psi_R \rightarrow e^{i\Theta Y} \psi_R.\tag{13}$$

The Lagrangian arrives at:

$$\begin{aligned}
\mathcal{L}_{\text{EW}} &= -\frac{1}{4}\hat{\mathbf{W}}_{\mu\nu}\hat{\mathbf{W}}^{\mu\nu} - \frac{1}{4}B_{\mu\nu}B^{\mu\nu} + \bar{\psi}(i\gamma_\mu D_\mu - m)\psi + \text{h.c.}, \\
D_\mu &:= \partial_\mu + ig \sum_{a=1}^3 W_\mu^a \tau_a + ig' \frac{Y}{2} B_\mu \\
\hat{\mathbf{W}}_{\mu\nu} &= \partial_\mu \mathbf{W}_\nu - \partial_\nu \mathbf{W}_\mu - g \mathbf{W}_\mu \times \mathbf{W}_\nu \\
\mathbf{W}_\mu &:= \{W_\mu^a; a = 1, 2, 3\} \\
B_{\mu\nu} &= \partial_\mu B_\nu - \partial_\nu B_\mu
\end{aligned} \tag{14}$$

where  $W_\mu^a$  and  $B_\mu$  are the fields of EW gauge bosons, and  $g, g'$  are the coupling respectively for  $SU(2)_L$  and  $U(1)_Y$ .  $\tau (= \sigma/2)$  are generators of  $SU(2)$ .

The Lagrangian can be also re-written by introducing currents:

$$\begin{aligned}
\mathcal{L}_{\text{EW}} &= -\frac{1}{4} \sum_{a=1}^3 W_{\mu\nu}^a W^{a\mu\nu} - \frac{1}{4} B_{\mu\nu} B^{\mu\nu} \\
&\quad - \frac{g}{2} (J_\mu^+ W^{-\mu} + J_\mu^- W^{+\mu}) - g J_\mu^3 W^{3\mu} - \frac{g'}{2} J_\mu^Y B^\mu + \text{h.c.} \\
J_\mu^\pm &:= \frac{1}{\sqrt{2}} (W_\mu^1 \mp i W_\mu^2) \\
J_\mu^a &:= \bar{\psi}_L \gamma^\mu \tau_q W_\mu^a \psi_L \\
J_\mu^Y &:= Y \bar{\psi}_L \gamma^\mu \psi_L.
\end{aligned} \tag{15}$$

$J_\mu^\pm$  represent currents changing  $T_3$ , while  $J_\mu^0$  and  $J_\mu^Y$  neutral current conserving either  $T_3$  and  $Y$ .

The consequence of EW symmetry breaking is implemented by mixing  $(W_\mu^3, B_\mu)$  into  $(Z_\mu, A_\mu)$ :

$$\begin{pmatrix} Z_\mu \\ A_\mu \end{pmatrix} := \begin{pmatrix} \cos \theta_W & -\sin \theta_W \\ \sin \theta_W & \cos \theta_W \end{pmatrix} \begin{pmatrix} W_\mu^3 \\ B_\mu \end{pmatrix} \tag{16}$$

with a mixing angle (Weinberg angle  $\theta_W$ ) of:

$$\tan \theta_W := \frac{g'}{g}. \tag{17}$$

The current terms in the Lagrangian Eq. (15) then becomes:

$$\begin{aligned}
&- \frac{g}{2} (J_\mu^+ W^{-\mu} + J_\mu^- W^{+\mu}) \\
&+ \frac{g}{\cos \theta_W} \left( -\cos^2 \theta_W J_\mu^3 + \frac{\sin^2 \theta_W}{2} J_\mu^Y \right) Z^\mu \\
&- g \sin \theta_W \left( J_\mu^3 + \frac{1}{2} J_\mu^Y \right) A^\mu
\end{aligned} \tag{18}$$

By choosing  $Y := 2(Q - T^3)$ ,  $A_\mu$  is associated with the gauge field of electromagnetic interaction, and the electric charge is found to be related to the weak coupling constant by the Weinberg angle:  $e = g \sin \theta_W$ .

#### 1.1.4 Electroweak Symmetry Breaking and the Higgs boson

One outstanding problem in the EW Lagrangian is the prohibition of mass terms, for both gauge bosons and fermions, since they explicitly violates the gauge invariance. The BEH mechanism [?] [?] is then

employed to solve the problem, where assuming a  $SU(2)$  doublet  $\phi$  ( $Y = -1, T = 1/2$ ) with scalar fields  $\phi = (\phi_1, \phi_2) = (\phi^+, \phi^0)$ , and a potential  $V(\phi)$  added in the Lagrangian:

$$\begin{aligned}\mathcal{L}_{\text{Higgs}} &:= (D_\mu \phi)^\dagger (D^\mu \phi) - V(\phi) \\ V(\phi) &:= \mu^2 \phi^\dagger \phi + \lambda (\phi^\dagger \phi)^2.\end{aligned}\quad (19)$$

While the minimum of the potential is always found in  $\phi = (0, 0)$  in the  $\phi_1 - \phi_2$  plane when  $\mu^2 > 0$ , negative  $\mu^2$  leads to non-trivial minima in  $v := |\phi|^2 = -\mu^2/2\lambda$  causing the shift of the vacuum expectation value :  $\langle \phi \rangle = v$  (spontaneous symmetry breaking).

Retaining the origin of  $\phi$  as:

$$\phi = \begin{pmatrix} 0 \\ v + h(x) \end{pmatrix} \quad (20)$$

and applying the  $\partial\mu \rightarrow D\mu$  prescription to Eq. (19), one finds the mass terms for  $W, Z$  as:

$$\begin{aligned}m_W &= gv/2 \\ m_Z &= \sqrt{g^2 + g'^2}v/2,\end{aligned}$$

where the mass for  $W$  and  $Z$  is successfully provided.

The mass for scalar field  $h$  is also found to be:

$$m_h = \sqrt{-2\mu^2}.$$

thus  $h$  can be also regarded as physical mode, referred as higgs particle.

The fermion masses are fed by adding extra terms into Lagrangian:

$$\mathcal{L}_{\text{Yukawa}} := -\bar{\psi}_{i,L} y_{ij}^a \phi_a \psi_{j,R} - \bar{\psi}_{i,R} y_{ij}^a \phi_a^\dagger \psi_{j,L} \quad (21)$$

where  $i, j = 1, 2, 3$  index the generations of fermions, and  $a$  denote type of fermions (“up-type quarks”, “down-type quarks”, “leptons”) and  $\phi_a$  corresponds to  $\phi, \phi^c, \phi$  respectively.  $y_{ij}^a$  are Yukawa matrices,  $3 \times 3$  matrices spanned over the family space. The off-diagonal components in  $y_{ij}^a$  are responsible for mixing between generation, which are set all zero for down-type leptons, while they are non-zero and the Yukawa matrices are diagonalized by CKM matrix [?] in case of quarks.

Inserting Eq. (20),  $\mathcal{L}_{\text{Yukawa}}$  is finally reduced to:

$$\begin{aligned}\mathcal{L}_{\text{Yukawa}} &= \sum_f y_f v \bar{\psi} \psi + y_f \bar{\psi} \psi h \\ &= \sum_f m_f \bar{\psi} \psi + y_f \bar{\psi} \psi h,\end{aligned}\quad (22)$$

where  $f$  is the index of fermions and  $y_f$  is the eigenvalues of corresponding Yukawa matrix.

Higgs boson was discovered in LHC in 2012 [?] [?], bringing the last piece of the Standard Model in human knowledge. Measurements on its properties including the mass, spin and couplings follow, and they show all consistent to the SM at the moment. Precision measurement on its couplings is planning in the later stages in LHC as well as the future linear collider projects such as ILC.

## 1.2 Remained Problems for the Standard Model

There is a couple of homework from the SM, from critical ones to potential issues. A overview is provided in this sub-section, with a focus on problems in which SUSY is particularly motivated as the solution.

### 1.2.1 The Higgs Mass Hierarchy Problem

While the divergences appearing in higher order calculation in SM are universaly cured by renomrlization, Since the SM higgs has no parter in the same multiplet represented by a certain symmetry, there is no counter terms possible to cancel the leading quadratic divergence happening in the self-energy correction, forcing the higgs mass to explicitly contain the dependence on the cut-off scale  $\Lambda$  upto which the loop momentum is integrated. For instance, the loop correction given by a top-quark loop is:

$$\Delta m_h^2 = -\frac{3|\lambda|^2}{8\pi^2} \Lambda^2 + O(\log \Lambda). \quad (23)$$

$$m_{h,\text{obs.}}^2 = m_{h,\text{bare}}^2 + \Delta m_h^2 \quad (24)$$

The magnitude can be order of  $10^{38}$  when assuming SM is valid upto Planck scale:  $\Lambda \sim 10^{19}$ . Given the experimental mass is 125 GeV, a naive conclusion is that the tree-level higgs mass  $m_h^{\text{bare}2}$  and total radiative correction  $\Delta_h$  has to cancel in a precision of  $10^{-34}$  (“fine tuning problem” or “naturalness problem”). It is highly unnatural for a theory to have a structure requiring such level of fine tuning in it, therefore it is preferred to conceive the underlying mechanism behind it.

The simplest solution is provided by the Pauli-Villars prescription where a set of partners giving the negative contribution are newly introduced and stop the divergence by the destructive interference. SUSY is the typical example, i.e. by introducing a bosonic partner of top-quark (scalar-top; “stop”) with the mass of  $m_S$  and the same coupling to higgs, the quadratic terms cancel out:

$$\begin{aligned} \tilde{\Delta} m_h^2 &= 2 \times \frac{3|\lambda|^2}{16\pi^2} \Lambda^2 + O(\log \Lambda) \\ \Delta m_{h,\text{PV}}^2 &= \Delta m_h^2 + \tilde{\Delta} m_h^2 = O(\log \Lambda) \end{aligned} \quad (25)$$

restoring the sensible description of perturbation.

### 1.2.2 Dark Matter

Historically, the argument of dark matter (DM) originated from observations on velocity of gallaxy rotation, implying excessive masses in gallaxy center beyond the expectation from spectroscopy [?] [?]. The DM hypothesis, assuming matter that does not interact eletromagnetically, has been strongly supported by the a number of observatory facts that comes up later including gravitational lensing effect. Currently the most commonly considered framework of dark matter is the  $\Lambda$ -CDM model (Cold Dark Matter) in which DM is assumed to:

- sense very weak interaction except gravitation (Weakly Interacting Massive Particles; WIMPs)<sup>1</sup>

---

<sup>1</sup>This almost requires electrically neutral, but completely forbidden [?].

- be non-relativistic, given that DM is relatively spatially localized such as in galaxy center.

The density abundance is dedicatedly measured via cosmic microwave background (CMB) by WMAP [?] and Planck [?]. Under the  $\Lambda$ -CDM they are decided as:

$$\Omega_{\text{CDM}} h^2 = \begin{cases} 0.1138 \pm 0.0045 & (\text{WMAP}) \\ 0.1186 \pm 0.0020 & (\text{Planck, TT+lowP+lensing}), \end{cases} \quad (26)$$

While the SM has no candidates for DM, SUSY prodives several attractive candidates when assuming the R-parity conservation as seen in later sub-sections. There are also a number of experiments for direct detection, in which the SUSY DM scenario can be tested.

### 1.2.3 Grand Unification

It is the ultimate desire for phycists to explain all phenomena on the earth with a single principle. While in the SM, the EW symmetry breaking  $SU(2)_L \times U(1) \rightarrow SU(2) \times U(1)_Q$  implies a common origin of electro-magnetic and weak interaction, this encourages physists to conceive another unification together with strong interaction at a higher scale (Grand Unification; GUT).

Running coupling constants are useful proxies to analyze the possibility of such unification. The evolution of coupling constants along scale is given by the RGE:

$$\frac{1}{\alpha_i(Q)^2} - \frac{1}{\alpha_i(Q_0)^2} = -\frac{\beta_i}{2\pi} \log\left(\frac{Q}{Q_0}\right), \quad (27)$$

with the indices  $i = 1, 2, 3$  denote strong, weak and electro-magnetic interaction respectively.  $\beta_i$  are the beta functions. In the SM at 1-loop level, these are:

$$\begin{pmatrix} b_1 \\ b_2 \\ b_3 \end{pmatrix} = \begin{pmatrix} 1/10 \\ -43/6 \\ -11 \end{pmatrix} + n_{\text{gen}} \begin{pmatrix} 4/3 \\ 4/3 \\ 4/3 \end{pmatrix}, \quad (28)$$

where  $n_{\text{gen}}$  is the number of generation of fermions, which is equal to 3 for  $Q > m_t$ . One naively expects a convergence of the three couplings at a certain scale ( $\mu_{\text{GUT}}$ ) in case of the grand unification. Unfortunately, this does not happen in the SM, as illustrated in Figurere 1 (a). However, it can be relatively easily realized in the SUSY regime, where more fermion particles can participate in the game changing the slope of the running. For instance, the beta function for MSSM is:

$$\begin{pmatrix} b_1 \\ b_2 \\ b_3 \end{pmatrix} = \begin{pmatrix} 3/5 \\ 1 \\ -3 \end{pmatrix}, \quad (29)$$

and the coupling unification is achieved at  $\mu_{\text{GUT}} \sim 10^{16}$  GeV, as shown in Figurere 1 (b).

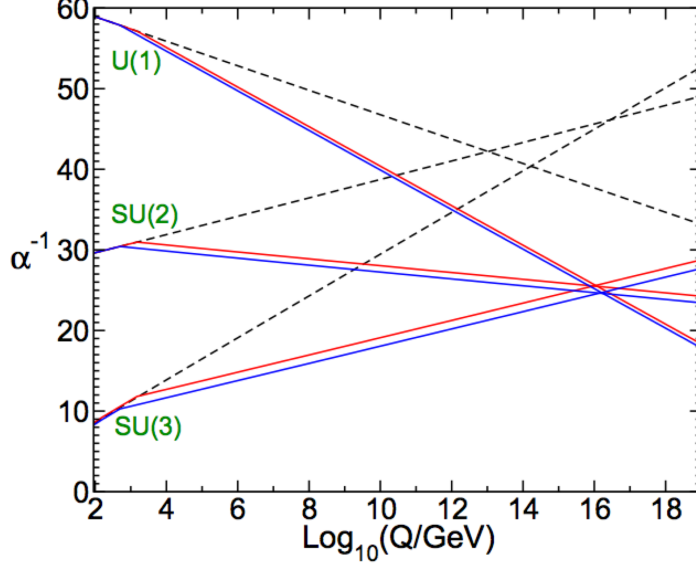


Figure 1: Two-loop renormalization group evolution of the inverse gauge coupling  $1/\alpha_i$  in case of SM (dashed lines), and a scenario in MSSM (solid lines) where the masses of SUSY partners are set between 500 GeV and 1.5 TeV [?].

### 1.3 The Super-Symmetry and MSSM

Minimal Super-Symmetric Standard Model (MSSM) is a SUSY framework where decent minimum matter contents and degrees of freedom are newly introduced with respect to the SM, i.e. :

- only one set of SUSY partners is employed ( $\mathcal{N}_{\text{SUSY}} = 1$ ),
- SUSY partners of SM fermions have the spin of 0, while the partners for boson in SM (gauge boson and higgs) are spin-1/2,
- and use only two higgs doublets to denote the higgs sector. <sup>2</sup>

Though it is called “minimal”, MSSM is a framework general enough to express the natures typical to SUSY in phenomenology level, therefore this thesis will confine the scope within MSSM. An overview on MSSM is given in the rest of the section, widely based on the reference [?].

#### 1.3.1 Particle Contents in MSSM

The particle contents are summarized in Table 3. Note that scalar-fermions (sfermions) have two modes indexed by  $L, R$  indicating that they are the SUSY partners of left-handed or right-handed SM fermions respectively. On the other hand, gauginos are all Majorana, in order to match the degree of freedom with either the partner gauge bosons and higgs bosons.

---

<sup>2</sup>This expansion is caused due to the fact that SUSY Lagrangian can not be easily constructed in presence of the charged conjugated higgs doublet  $\phi^c$  which provides the mass to down-type fermions in SM.

Table 3: Matter content of MSSM. The left column defines the naming convention for SUSY particles.  $n[SU(3)_C](n[SU(2)_L])$  represents the degree of freedom of the  $SU(3)_C(SU(2)_L)$  multiplet that the field(s) belongs to. All of them belongs to the single of  $U(1)_Y$ , thus the  $U(1)$  charge  $Y$  is shown instead. There are also two set of replications for the 2nd and 3rd generation of (s)quarks/(s)leptons, which are not shown here.

Super-multiplet		SM sect.	SUSY partner	$n[SU(3)_C]$	$n[SU(2)_L]$	$Y$
gluon/gluino	$G$	$g$	$\tilde{g}$	8	1	0
EW gauge boson /	$W$	$W^\pm, W^0$	$\tilde{W}^\pm, \tilde{W}^0$	1	3	0
EW gaugino	$B$	$B^0$	$\tilde{B}^0$	1	1	0
lepton / slepton	$L$	$(\nu_e, e)_L$	$(\tilde{\nu}_e, \tilde{e})_L$	1	2	-1
	$\bar{e}$	$\tilde{e}_R$	$e_R$	1	1	-2
quark / squark	$Q$	$(u_L, d_L)$	$(\tilde{u}_L, \tilde{d}_L)$	3	2	1/3
	$\bar{u}$	$u_R$	$\tilde{u}_R$	3	1	4/3
	$\bar{d}$	$d_R$	$\tilde{d}_R$	3	1	-2/3
Higgs boson /	$H_u$	$(H_u^+, H_u^0)$	$(\tilde{H}_u^+, \tilde{H}_u^0)$	1	2	1
higgsino	$H_d$	$(H_d^0, H_d^-)$	$(\tilde{H}_d^0, \tilde{H}_d^-)$	1	2	-1

MSSM higgs sector has two higgs doublets ( $\mathbf{H}_u := (H_u^+, H_u^0)$ ,  $\mathbf{H}_d := (H_d^-, H_d^0)$ ) with their own vacuum expectation values (VEV):

$$v_u := \langle H_u^0 \rangle, \quad v_d := \langle H_d^0 \rangle,$$

where each provides the masses for up- or down-type fermions respectively. The splitting of between them is commonly parametrized using a mixing angle  $\beta$  as:

$$\tan \beta := v_u/v_d. \quad (30)$$

The consistency with SM EW symmetry breaking is ensured by relating the VEVs as

$$v_{\text{SM}}^2 = v_u^2 = v_d^2. \quad (31)$$

Note that if gravity is quantized in the picture of QFT, there should be also the corresponding gauge boson "graviton", and along a natural extension, its SUSY partner "gravitino". Depending on the SUSY breaking scenario, gravitino can act a important role such as GMSB (Gauge Mediated SUSY Breaking) where gravitino is LSP.

### 1.3.2 The MSSM Lagrangian

Construction of a super-symmetric Lagrangian is not as a simple extension from SM Lagrangian as just adding extra terms accounting for the particle contents. It is commonly done using the method of super-

potential or super-space. The constructed MSSM Lagrangian is:

$$\mathcal{L}^{\text{MSSM}} = \mathcal{L}_{\text{SUSY}}^{\text{MSSM}} + \mathcal{L}_{\text{soft}}^{\text{MSSM}}, \quad (32)$$

$$\mathcal{L}^{\text{MSSM}} = \frac{1}{4} F_{\mu\nu}^a F^{a\mu\nu} + D^\mu \phi^* D_\mu \phi + \psi^\dagger \bar{\sigma}^\mu D_\mu \psi + i \lambda^{\dagger a} \bar{\sigma} D_\mu \lambda_a \quad (33)$$

$$- \frac{1}{2} W^{ij} \psi_i \psi_j + h.c. \quad (34)$$

$$- \sqrt{2} g (\phi^* T^a \psi) \lambda_a + h.c. \quad (35)$$

$$- \sum_i \left| \frac{\delta W}{\delta \phi_i} \right|^2 + \frac{1}{2} \sum_a (g_a \phi^* T^a \phi)^2 \quad (36)$$

where  $\phi$ ,  $\psi$  and  $\lambda$  symbolize all scalars, all fermions and EW gauginos respectively. The notation of the particle fields follow the definition in Table 3.

$\mathcal{L}_{\text{SUSY}}^{\text{MSSM}}$  is the SUSY invariant part of the Lagrangian, including the kinetic terms of all the particles (Eq. 33), the Yukawa interaction terms and higgs masse terms (Eq. 34), interaction terms of gauginos (Eq. 35) and the residual terms from auxiliary fields with the equation of motion applied (Eq. 36).  $W_{ij}$  is the second derivative of super-potential  $W$  defined as:

$$W_{ij} := \frac{\delta^2 W}{\delta \phi_i \delta \phi_j}, \\ W := \bar{u} \mathbf{y}_u Q H_u - \bar{d} \mathbf{y}_d Q H_d - \bar{e} \mathbf{y}_e L H_d + \mu H_d H_u \quad (37)$$

where  $\mathbf{y}_u$ ,  $\mathbf{y}_d$  and  $\mathbf{y}_e$  are the same Yukawa matrices appearing in 21. The soft breaking terms ( $\mathcal{L}_{\text{soft}}^{\text{MSSM}}$ ) accommodating the SUSY breaking as detailed below.

The derivation is not shown here (see [?]), however there are a couple of caveat remarks:

- SUSY is broken, and it is via “soft breaking”

While an exact super-symmetry requires the SUSY partners being in the identical masses with respect to the SM particles, it is not the case at least in the energy scale of our universe since no SUSY particles have been dicovered so far. Therefore, a realistic SUSY model as an effective theory at the EW scale, must accommodate the effect of SUSY breaking in its Lagrangian ( $\mathcal{L}_{\text{soft}}^{\text{MSSM}}$  in Eq. 32). On the other hand, we don't want to ruin the desired features in SUSY at the cost of it, particularly as the solution of the higgs mass divergence. Therefore, it is common to restrict the SUSY breaking in a form of “soft breaking” where the finite higgs mass is maintained, by assign a particlur constraints on terms in  $\mathcal{L}_{\text{soft}}^{\text{MSSM}}$ .

Though not specifically targeted in the thesis, there are a number of models in the market offering explicit mechanisms of the SUSY breaking. The most minimal models are known as GMSB (Gauge-Mediated SUSY Breaking [?]), AMSB (Anomaly-Mediated SUSY Breaking [?] [?]) or mSUGRA (minimal SUper Gravity [?]), all of which describe soft SUSY breaking scenarios.

- R-parity

A quantum number  $R$  associated with the number of “SUSY partner” (analogous to the lepton number or baryon number etc.) can be defined by the spin, baryon number and lepton number as:

$$R := (-1)^{3(B-L)+2S}. \quad (38)$$

The corresponding symmetry is referred to R-parity, which conservation law will prohibit single production of SUSY particles, as well as SM particles annihilating into a resonance of a SUSY particle. This leads a set of spectacular phenomenological advantages:

- The lightest SUSY particles (LSP) become the DM candidates if they are electric neutral, in particular the lightest neutralino is the most commonly assumed.
- Proton decays via diagrams in Figure 2 are prohibited, naturally reconciling with the constraints set by experiments [?].

In the framework of MSSM, the R-parity conservation (RPC) is explicitly assumed, which is equivalent to discard following terms in the most general soft breaking Lagrangian:

$$\begin{aligned} W_{\Delta L=1} &= \frac{1}{2} \lambda^{ijk} L_i L_j \bar{e}_k + \lambda'^{ijk} L_i Q_j \bar{d}_k + \mu'^i L_i H_u \\ W_{\Delta B=1} &= \frac{1}{2} \lambda'^{ijk} \bar{u}_i \bar{d}_j \bar{d}_k. \end{aligned} \quad (39)$$

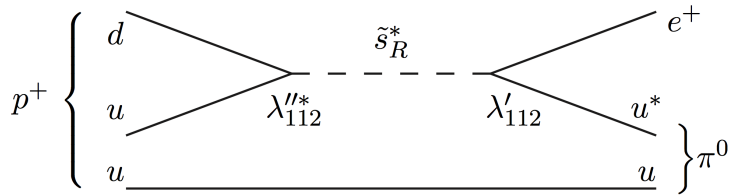


Figure 2: An example process of a proton decay triggered by intermediate SUSY particles (scalar-strenge quark here).  $\lambda''_{112}$  and  $\lambda'_{112}$  are couplings for corresponding interaction vertices which violate  $R$ -parity.

The soft breaking terms ( $\mathcal{L}_{\text{soft}}^{\text{MSSM}}$ ) contains the most phenomenologically critical behavior in MSSM. The most general form in MSSM is given as:

$$\mathcal{L}_{\text{soft}}^{\text{MSSM}} = \frac{1}{2} \left( M_3 \tilde{g} \tilde{g} + M_2 \tilde{W} \tilde{W} + M_1 \tilde{B} \tilde{B} + \text{c.c.} \right) \quad (\text{gaugino mass terms}) \quad (40)$$

$$- Q^\dagger \mathbf{m}_Q^2 Q - L^\dagger \mathbf{m}_L^2 L - \bar{u} \mathbf{m}_{\bar{u}}^2 \bar{u}^\dagger - \bar{d} \mathbf{m}_{\bar{d}}^2 \bar{d}^\dagger - \bar{e} \mathbf{m}_{\bar{e}}^2 \bar{e}^\dagger \quad (\text{sfermion mass terms}) \quad (41)$$

$$- (\bar{u} \mathbf{a}_u Q H_u - \bar{d} \mathbf{a}_d Q H_d - \bar{e} \mathbf{a}_e L H_d + \text{c.c.}) \quad (\text{trilinear coupling}) \quad (42)$$

$$- m_{H_u}^2 H_u^\dagger H_u - m_{H_d}^2 H_d^\dagger H_d - (b H_u H_d + \text{c.c.}) \quad (\text{Higgs potential}) \quad (43)$$

The notation of the particle fields ( $\tilde{g}, \tilde{W}, \tilde{B}$ ) and super-multiplet ( $Q, L, \bar{u}, \bar{d}, \bar{e}, H_u, H_d$ ) follow the definition in Table 3. The first line Eq. (40) show the mass terms for gauginos, with  $M_1$ ,  $M_2$  and  $M_3$  are respectively bino, wino and gluino mass. Eq. (42) and (41) are the Yukawa terms for SUSY particles where the former are the standard sfermion mass terms, and latter the trilinear terms describing the Yukawa interaction coupling left-handed and right-handed sfermions, emerged as the cross terms of super-multiplet. The mass matrices ( $\mathbf{m}_Q$ ,  $\mathbf{m}_L$ ,  $\mathbf{m}_{\bar{u}}$ ,  $\mathbf{m}_{\bar{d}}$ ,  $\mathbf{m}_{\bar{e}}$ ), and the A terms ( $\mathbf{a}_u$ ,  $\mathbf{a}_d$  and  $\mathbf{a}_e$ ) are  $3 \times 3$  matices spanned in family space, equivalent to the CKM matrix in the SM sector multiplied by sparticles masses. The last terms are the MSSM higgs potential, controlling the EW symmetry breaking.

### 1.3.3 Mass spectra in MSSM

The masses of SUSY particles are derived by specifying the coefficient associated with mass terms (e.g.  $m$  in  $m\phi\phi$ ), after a full expansion of the Lagrangian in Eq. (32). This is effectively done by extracting relevant terms and performing the diagonalization on the mass matrices, accounting for the mixing between eigenstates of interactions.

**Squarks and sleptons** Sfermion masses are fed solely from the soft Lagrangian. Generally, they are allowed to mix between different generations via the off-diagonal components either in the mass matrices or the A terms. These are however known to lead to a significant rate of flavor changing natural current which are experimentally highly disfavored thus usually set to zero:

$$\begin{aligned} \mathbf{m}_Q^2 &= m_Q^2 \mathbf{1}, & \mathbf{m}_L^2 &= m_L^2 \mathbf{1}, & \mathbf{m}_{\tilde{u}}^2 &= m_{\tilde{u}}^2 \mathbf{1}, & \mathbf{m}_{\tilde{d}}^2 &= m_{\tilde{d}}^2 \mathbf{1}, & \mathbf{m}_{\tilde{e}}^2 &= m_{\tilde{e}}^2 \mathbf{1}, \\ \mathbf{a}_u &= A_u \mathbf{1}, & \mathbf{a}_d &= A_d \mathbf{1}, & \mathbf{a}_e &= A_e \mathbf{1} \end{aligned} \quad (44)$$

In addition, it is also allowed to mix left-handed sfermion and right-handed sfermion since they share the same gauge quantum numbers. Ignoring the off-diagonal components of the Yukawa matrix, the mass matrix for sfermion  $\tilde{f}$  reduces to:

$$\begin{pmatrix} m_{\tilde{f}_L}^2 + m_Z^2 (T_{3,f} - Q_f \sin \theta_W)^2 \cos 2\beta + m_f^2 & v_f (A_f - \mu y_f) \\ v_f (A_f - \mu y_f) & m_{\tilde{f}_R}^2 + m_Z^2 Q_f \sin \theta_W^2 \cos 2\beta + m_f^2 \end{pmatrix},$$

$$v_f = \begin{cases} v_u & (\tilde{f} = \tilde{u}, \tilde{c}, \tilde{t}) \\ v_d & (\tilde{f} = \tilde{d}, \tilde{s}, \tilde{b}) \end{cases} \quad (45)$$

where  $T_{3,f}$  and  $Q_f$  are the iso-spin and electric charge of  $\tilde{f}$ . As the magnitude off-diagonal component scales with the Yukawa coupling, the effect of the mixing can be only sizable in case of third generation sfermions (stop, sbottom and stau). This is why the third generation sfermions are particularly phenomenologically important, since the masses of lighter eigenstates can be significantly lowered, enhancing the chance of being within experimental reach.

**Gauginos** The mass terms of EW gauginos and higgsinos are sourced by  $\mathcal{L}_{\text{SUSY}}^{\text{MSSM}}$ . The eigenstate of charged EW gauginos (charginos;  $\tilde{W}^\pm, \tilde{H}_u^\pm, \tilde{H}_d^\pm$ ) in the same signs will mix each other. The mass matrices are common and described as:

$$\begin{pmatrix} M_2 & \sqrt{2}m_W \sin \beta \\ \sqrt{2}m_W \sin \beta & \mu \end{pmatrix}.$$

The diagonalized mass eigenstates are then:

$$m_{\tilde{\chi}_{1,2}^\pm}^2 = \frac{1}{2} \left[ (M_2^2 + \mu^2 + 2m_W^2) \mp \sqrt{(M_2^2 + \mu^2 + 2m_W^2)^2 - 4(\mu M_2 - m_W^2 \sin 2\beta)^2} \right]. \quad (46)$$

The mass matrix for neutral EW gauginos (neutralinos;  $\tilde{B}, \tilde{W}^0, \tilde{H}_u^0, \tilde{H}_d^0$ ) are given as:

$$\begin{pmatrix} M_1 & 0 & -\cos\beta\sin\theta_W m_Z & \sin\beta\sin\theta_W m_Z \\ 0 & M_2 & \cos\beta\cos\theta_W m_Z & -\sin\beta\cos\theta_W m_Z \\ -\cos\beta\sin\theta_W m_Z & \cos\beta\cos\theta_W m_Z & 0 & -\mu \\ \sin\beta\sin\theta_W m_Z & -\sin\beta\cos\theta_W m_Z & -\mu & 0 \end{pmatrix}.$$

The eigenfunction is quartic and the solutions are :

$$\begin{aligned} m_1 &= M_1 + \frac{m_Z^2 \sin^2 \theta_W}{M_1^2 - \mu^2} (M_1 + \mu + \sin 2\beta) \\ m_2 &= M_2 + \frac{m_Z^2 \cos^2 \theta_W}{M_2^2 - \mu^2} (M_2 + \mu + \sin 2\beta) \\ m_3 &= \mu + \frac{m_Z^2 (1 + \sin 2\beta)}{2(\mu - M_1)(\mu - M_2)} (\mu - \cos\theta_W M_1 - \sin\theta_W M_2) \\ m_4 &= \mu + \frac{m_Z^2 (1 - \sin 2\beta)}{2(\mu + M_1)(\mu + M_2)} (\mu + \cos\theta_W M_1 + \sin\theta_W M_2) \end{aligned} \tag{47}$$

A conventional notation for neutralino masses  $m_{\tilde{\chi}_{1-4}^0}$  are with these eigenvalues sorted as  $m_{\tilde{\chi}_1^0} < m_{\tilde{\chi}_2^0} < m_{\tilde{\chi}_3^0} < m_{\tilde{\chi}_4^0}$ .

Finally, gluinos are color-octet fermions and do not mixed to any other sfermions.

**Higgs sector of MSSM** Due to the two higgs doublets with 4 real and 4 imaginary parts, there are in total five degree of freedoms as physical particles after the gauge fixing. The MSSM higgs potential is given by:

$$\begin{aligned} V &= (|\mu|^2 + m_{H_u}^2) (|H_u^0|^2 + |H_u^+|^2) \\ &\quad + (|\mu|^2 + m_{H_d}^2) (|H_d^0|^2 + |H_d^-|^2) \\ &\quad + [b(H_u^+ H_d^- - H_u^0 H_d^0) + \text{c.c.}] \\ &\quad + \frac{1}{8} (g^2 + g'^2) (|H_u^0|^2 + |H_u^+|^2 - |H_d^0|^2 - |H_d^-|^2)^2 \\ &\quad + \frac{1}{2} |H_u^+ H_u^{0*} + H_d^+ H_d^{-*}|. \end{aligned} \tag{48}$$

Similarly to the case in SM, implementing the spontaneous symmetry breaking with  $H_{u,d} \rightarrow v_{u,d} + \eta_{u,d}$  and requiring  $dV/dv_u = dV/dv_d = 0$ , one arrives:

$$\sin 2\beta = \frac{2b}{m_{H_u}^2 + m_{H_d}^2 + 2|\mu|^2} \tag{49}$$

$$\frac{1}{2} m_Z^2 = -|\mu|^2 + \frac{m_{H_u}^2 - m_{H_d}^2 \tan^2 \beta}{\tan^2 \beta - 1} \tag{50}$$

The higgs masses are found by the masses terms with inserting Eq. (49)-(50) back to Eq. (48):

$$\begin{aligned} m_A^2 &= 2|\mu|^2 + m_{H_u}^2 + m_{H_d}^2, \\ m_{H^\pm}^2 &= m_{A^0}^2 + m_W^2 \\ m_{h,H}^2 &= \frac{1}{2} \left( m_{A^0}^2 + m_Z^2 \mp \sqrt{(m_{A^0}^2 + m_Z^2)^2 - 4m_Z^2 m_{A^0}^2 \cos^2 2\beta} \right), \end{aligned} \tag{51}$$

where  $H^\pm$  is the charged,  $A$  the CP-odd higgs respectively.  $H$  and  $h$  are the mass eigenstates of CP-even neutral higgs, where the lighter one  $h$  is often associated with the SM higgs. Given that no observation of  $H$  has been claimed upto 400 GeV – 1 TeV, it is generally preferred to have large mass splitting between  $h$  and  $H$ , which implies a large  $\tan\beta$ .

### 1.3.4 Running masses and GUT

Though the SUSY masses are mostly free parameters in MSSM, an useful insight can be obtained from an quick analysis under the GUT regime in which the coupling constants unify at the GUT scale:  $\mu_{\text{GUT}} \sim 10^{16-17}$  GeV.

In the SUSY context, the mass unification is often in addition considered, typically under the regime where:

- all sfermions masses converge to  $m_{1/2}$
- all gaugino masses converge to  $m_0$
- all higgs boson ( $H_u, H_d$ ) masses converge to  $(\mu^2 + m_0^2)^{1/2}$ .

This configuration is particular advantageous in naturally causing EW symmetry breaking at the EW scale, and adopted in many minimal models including SUGRA, NUMH and CMSSM (Constrained MSSM).

Starting with gaugino masses, using the general condition satisfied in 1-loop renormalization:

$$\frac{d(M_i/\alpha_i)}{d\mu} = 0, \quad (i = 1, 2, 3),$$

it turns that  $(M_i/\alpha_i)$  is constant in arbitrary scale. Therefore, one obtains:

$$\frac{M_i}{\alpha_i}|_{\mu=\mu_{\text{EW}}} = \frac{M_i}{\alpha_i}|_{\mu=\mu_{\text{GUT}}} = \frac{m_{1/2}}{\alpha_{\text{GUT}}}, \quad (52)$$

resulting in an univeral ratio in gaugino masses holding at any scale:

$$M_1 : M_2 : M_3 \sim 6 : 2 : 1. \quad (53)$$

This is the reason the mass hierarchy between gluino, wino and bino are especially motivated and commonly assumed in SUSY phenomenology, though it is true that the assumption of mass unification may be too strong.

As for sfermions, the running masses also provide some idea about the mass spectra at the EW scale.

The running masses are calculated unambiguously using the renormalization group equations as:

$$\begin{aligned}
m_{\tilde{d}_L}^2 &= m_0^2 + K_3 + K_2 + \frac{1}{36}K_1 + \Delta_{\tilde{d}_L} \\
m_{\tilde{u}_L}^2 &= m_0^2 + K_3 + K_2 + \frac{1}{36}K_1 + \Delta_{\tilde{u}_L} \\
m_{\tilde{d}_R}^2 &= m_0^2 + K_3 + \frac{1}{9}K_1 + \Delta_{\tilde{d}_R} \\
m_{\tilde{u}_R}^2 &= m_0^2 + K_3 + \frac{4}{9}K_1 + \Delta_{\tilde{u}_R} \\
m_{\tilde{e}_L}^2 &= m_0^2 + K_2 + \frac{1}{4}K_1 + \Delta_{\tilde{e}_L} \\
m_{\tilde{\nu}_L}^2 &= m_0^2 + K_2 + \frac{1}{4}K_1 + \Delta_{\tilde{\nu}_L} \\
m_{\tilde{e}_R}^2 &= m_0^2 + K_1 + \Delta_{\tilde{e}_R}
\end{aligned} \tag{54}$$

where  $K_1$ ,  $K_2$  and  $K_3$  respectively denotes the contribution from the interaction of  $U(1)_Y$ ,  $SU(2)_L$  and  $SU(3)_C$ , which are approximately:

$$K_1 \sim 0.15 m_{1/2}^2, \quad K_2 \sim 0.5 m_{1/2}^2, \quad K_3 \sim 6 m_{1/2}^2, \tag{55}$$

and the correction factors  $\Delta_{\tilde{f}}$  are given by:

$$\begin{aligned}
\Delta_{\tilde{f}_L} &= (T_3 - Q \sin^2 \theta_W) m_Z^2 \cos 2\beta + m_f^2 \\
\Delta_{\tilde{f}_R} &= Q \sin^2 \theta_W m_Z^2 \cos 2\beta + m_f^2.
\end{aligned} \tag{56}$$

Since the running effect on masses are always larger for squarks than sleptons due to the  $SU(3)_C$  interaction, it generally implies lighter masses for sleptons. The typical running mass spectra is shown in Figure 3.

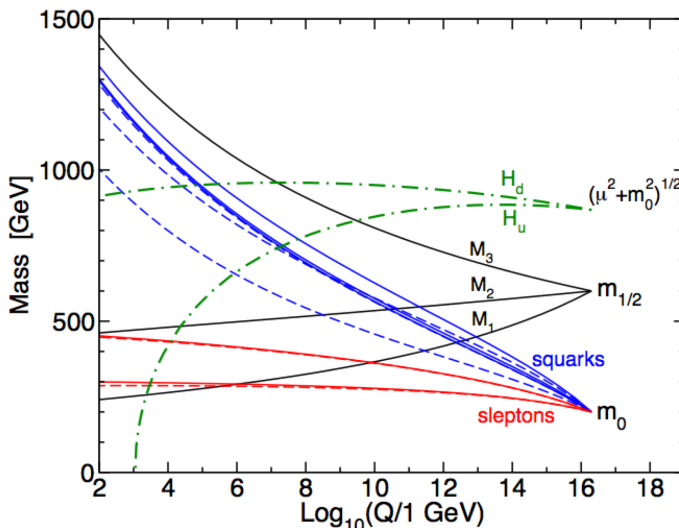


Figure 3: Evolution of scalar and gaugino mass parameters in the MSSM with mSUGRA boundary conditions [?]. The parameters are  $m_0 = 200$  GeV,  $m_{1/2} = 600$  GeV,  $A^0 = -600$  GeV,  $\tan \beta = 10$  and  $\text{sign}(\mu) > 0$ .

## 1.4 Experimental Constraints on SUSY so far

### 1.4.1 Constraints from Observed Standard Model Higgs Mass

It is a striking fact that in MSSM the mass of 125 GeV higgs ( $h$ ) is bounded by:

$$m_h < m_Z \cos 2\beta < m_Z = 91.2 \text{ GeV}, \quad (57)$$

according to Eq. (51). Therefore, a sizable radiation correction is needed to achieve the 125 GeV. The 1-loop correction is dominantly given by the remnant of cancellation of top and stop loop in Eq. (25):

$$\Delta m_h^2 := \frac{3}{4} \frac{m_t^4}{v_{\text{SM}}^2} \left[ \log \frac{m_t^2}{m_t^2} + \frac{X_t^2}{m_t^2} \left( 1 - \frac{X_t^2}{12m_t^2} \right) \right], \quad (58)$$

which has to accord with

$$\sqrt{(125 \text{ GeV})^2 - m_Z^2} \sim 85 \text{ GeV}. \quad (59)$$

This is a tremendously powerful constraint that forces either of following two ambivalent choices:

1. without assuming anything on stop mixing (e.g.  $X_t$  is free) and  $O(10 \text{ TeV})$  of stop mass, with relatively large fine tuning ( $\Delta_{m_h} > 1000$ ), as shown in Figure 4.
2. maximal stop mixing ( $X_t \sim \sqrt{6}m_{\tilde{t}}$ ), and 500 GeV – 1 TeV of stop mass, with mild fine tuning ( $\Delta_{m_h} \sim 100$ ).

The consequent implication from the former choice is that all the squarks and sleptons are heavy, and only gauginos could be explorable in LHC, while the latter leads to light stop (or sbottom) accessible by the LHC energy while the others are not necessarily so.

The higgs mass fine tuning argument in MSSM is rather subtle, since the observed  $m_h$  is no longer as straightforwardly associated with its own mass parameter  $H_u$  as in the case in SM (Sec. 1.2.1), but also involved by the other MSSM parameters as seen in Eq. (51). The magnitude of fine tuning is usually quoted by the linear response of any arbitrary MSSM parameters in unit of mass  $p_i$ :

$$\Delta_{m_h} := \max_i \left| \frac{\partial \log[m_h^2(1\text{-loop})]}{\partial \log p_i} \right|. \quad (60)$$

In scenario 1. above, the resultant fine tuning is typically  $1/\Delta_{m_h} \sim O(10^{-3})$ , while  $\sim 1\%$  is achievable in the scenario 2 in the most optimistic case with  $\sim 500$  GeV stop.

As a level of  $\sim O(10^{-3})$  of the fine tuning is not as fatal as that in the SM ( $10^{-38}$ ), in the thesis, we pursue the former scenario, and probing gluinos in the experiment assuming all the sfermions are all decoupled.

### 1.4.2 Constraint from Dark Mater Relic Density

The main stream of current DM theory is based on the “cold matter” regime in which DM used to be in a thermal equilibrium at the beginning of the universe, and cooled down according to the cosmic expansion later on, and being decoupled at a certain scale, keeping the abundance upto now. The relics is strongly related by the annihilation cross-section, which can be calculated within the MSSM framework.

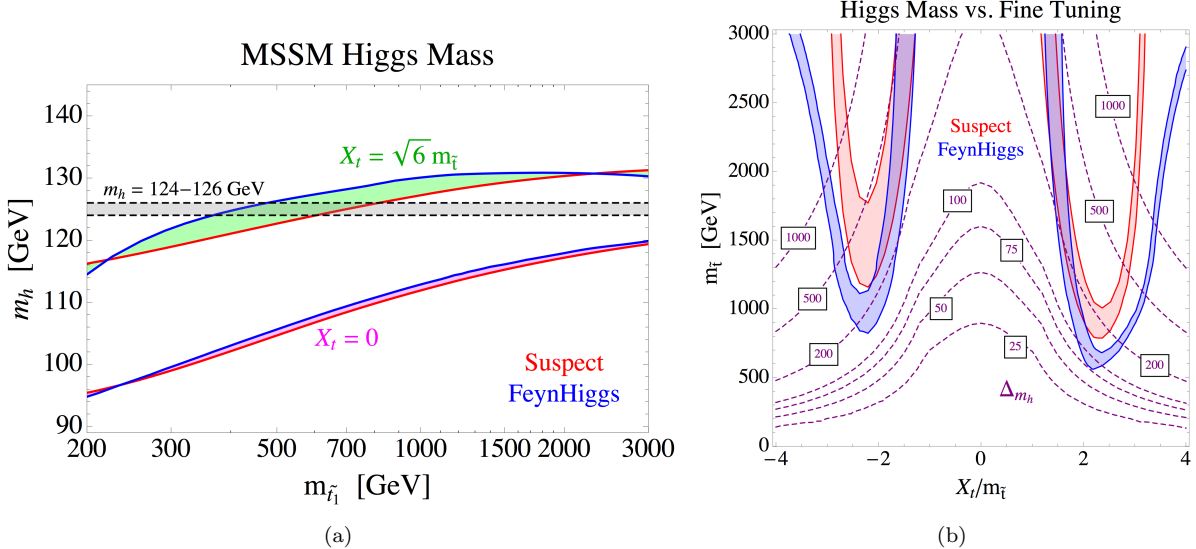


Figure 4: Relation of mass of SM-like higgs and stop mass in MSSM [?]. (a) The SM-like higgs mass as a function of lightest stop mass ( $m_{\tilde{t}}$ ), with the no ( $X_t = 0$ ) or maximal stop mixing ( $X_t \sim \sqrt{6}m_{\tilde{t}}$ ). Red/blue solid lines correspond the computation using Suspect/FeynHiggs. (b) A 2D-constraint on the stop mass and stop mixing  $X_t/m_{\tilde{t}}$  by observed SM-like higgs mass, with  $m_{\tilde{Q}} = m_{u_3} = m_{\tilde{t}}$  and  $\tan \beta = 20$ . Dashed contour shows the gauge of fine tuning  $\Delta_{m_h}$  defined by Eq. 60.

There are couples of drastically different DM scenarios depending on the component of LSP. In a limit where all the squarks are decoupled, the case of pure bino-LSP almost immediately excluded, since it has to rely on the annihilation with slepton [?], and needs  $m_{\tilde{\ell}} < 110$  GeV to achieve the observed relic abundance  $\Omega_h h^2 = 0.12$  which is already excluded by LEP2.

On the other hand, the annihilation cross-section tends to be too large in case of pure-wino or pure-higgsino LSP, where roughly  $\sim 3$  TeV of wino mass or  $\sim 1$  TeV of higgsino mass is needed to match with the observed relic  $\Omega_h h^2$  [?], which is unfortunately beyond the LHC reach.

What if the mixed case? It is particluar intresing to consider doping a bit of wino or higgsino component into bino-dominated LSP, where moderated annihilation cross-setion and experimental accessible LSP mass can be achieved simultaneously. This type of LSP is called “well-tempered” neutralino LSP [?], typically predicting a moderately small mass splitting between the next-to-the-lightest SUSY particle (NLSP) and the LSP with  $20 - 50$  GeV [?] [?].

Note that a number of caveats remarks are to be added on the discussion:

- The observed relics is always based on  $\Lambda$ -CDM within the cold DM regime. The constraint on SUSY could therefore drastically different if DM is “warm” produced non-thermally.
- The DM annihilation cross-section calculation so far is dominantly done at the lowest-order (LO) in the perturbation. The contribution of higher order terms will generally increase annihilation cross-section.
- Non-pertabative effects (continuous interaction) in a collision of non-relativistic particles often lead to

a sizable increase in annihilation cross-section (“Sommerfeld enhancement”).

- It is awkward though, it is possible for other new physics to supply the DM relics when SUSY is not capable of explaining the entire relic.

Given these too many uncertainties, it is sensible to regard the relic constraint as soft constraint. However, generally it is more fatal to have excessive relics than the opposite case, here we promise to respect the observed relic more as upper bound.

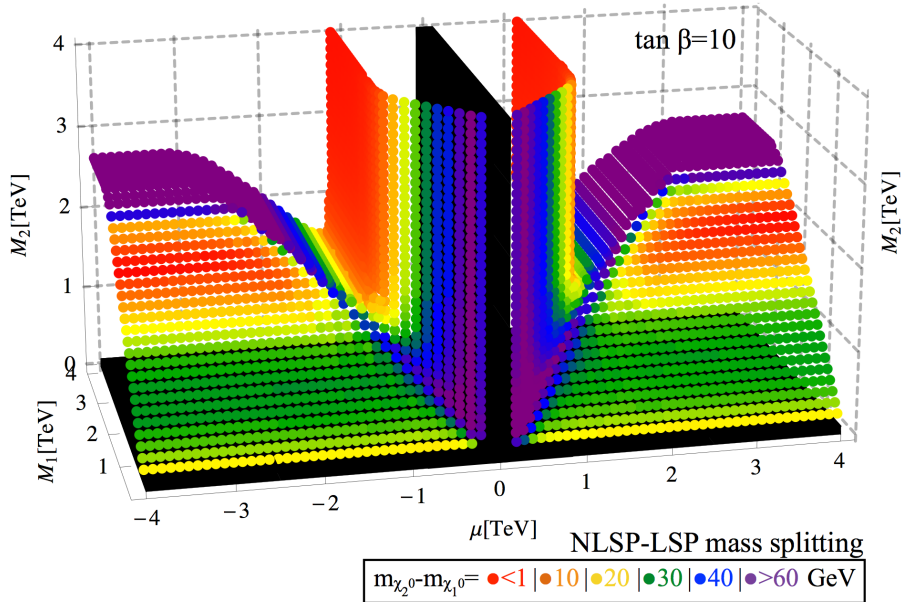


Figure 5: Mass splitting between NLSP (next-to-the-lightest SUSY particle) and LSP, as function of  $M_1$ ,  $M_2$  and  $\mu$  when assigning the DM relic constraint [?]. The effect of sommerfeld enhancement is taken into the calculation. Within the reach by the LHC energy ( $\min(M_1, M_2) \sim < 1$  TeV), the resultant NLSP-LSP mass splitting is about 20 GeV – 30 GeV. Black points correspond to parameter space excluded by LEP.

#### 1.4.3 Constraint from Direct Search at Collider Experiments

The direct search of SUSY had been widely performed in collider experiments including LEP, Tevatron and LHC, with comprehensive coverage over signatures and scenarios. Unfortunately no evidence has been claimed, it is interpreted into constraints on various minimal complete models (mainly SUGRA-type models, GMSB and cMSSM), or either particular production and decay chains (known as the simplified model, as discussed in below). This sub-section will overview status of constraints provided by those experiments, with particular focus on the limits for the simplified models that are used in interpretation in this thesis.

**Gluinos** The best job is done by hadron collider due to its outstandingly high production cross-section. It is particularly the case in LHC Run2, dominating the sensitivity in most of the scenarios in terms of the mass spectra and gluino decay.

The exclusion limits on the most typical gluino decays set by ATLAS and CMS are shown in Figure 6, namely the direct decay where gluino directly fall into LSP with emitting two quarks, and a 1-step decay via NLSP chargino. Up to  $\sim 2$  TeV in gluino mass is excluded for case with large mass splitting between gluino and LSP, and  $\sim$  TeV for the most pessimistic case where gluino and LSP are highly compressed.

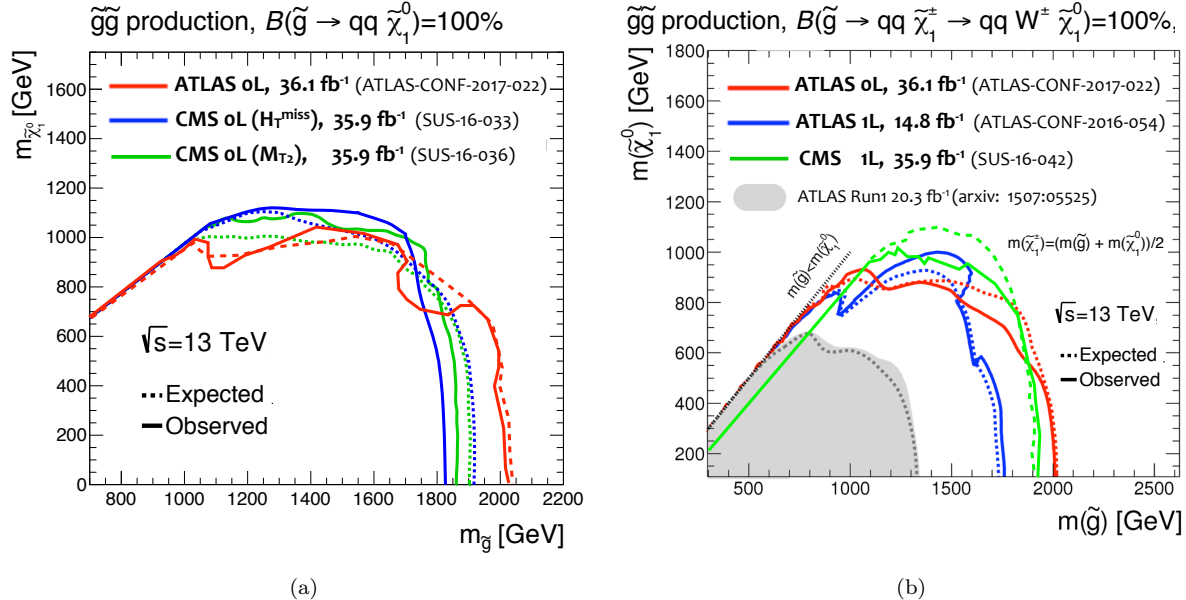


Figure 6: Up-to-date constraints set by ATLAS and CMS on (a) direct gluino decay:  $\tilde{g} \rightarrow q\bar{q}\tilde{\chi}_1^0$ , and (b) 1-step chargino-mediated gluino decay:  $\tilde{g} \rightarrow q\bar{q}\tilde{\chi}_1^\pm$  with the mass being in the middle between gluino and the LSP. The article numbers for corresponding references are labeled on the plots.

Gluino decaying with top quarks addresses particular importance since it can be enhanced by the light stop which is motivated by naturalness. They are exclusively searched with dedicated signal regions, and the resultant limit is given in Figure 7.

**Squarks** Since stop claims particular motivation for naturalness among all squarks, the analyses are dedicatedly designed to address to wide range of decays of mass configurations. The strongest limits are provided by LHC, and Figure 8 presents the exclusion limits obtained by ATLAS and CMS on the most typical decay scenario  $\tilde{t} \rightarrow t\tilde{\chi}_1^0$ . Up to about 400 GeV  $\sim 1$  TeV of stop mass is excluded for depending on the mass splitting, which is similar to the other decay models as well including  $\tilde{t} \rightarrow b\tilde{\chi}_1^\pm$ .

**Electroweak Gauginos** A number of searches have been performed in LEP, Tevatron and LHC, and the LHC result set the majority of the current strongest limits. The target signatures are mainly pair produced NLSPs ( $\tilde{\chi}_1^\pm$  or  $\tilde{\chi}_2^0$ ) decaying to LSP, where wino dominated NLSP, bino-dominated LSP, and decoupled squarks are commonly assumed.<sup>3</sup> The signal regions typically require multiple leptons and large missing ET in the final states. The exclusion limits set by ATLAS and CMS are shown in Figure 9. About up to 500 GeV of NLSP mass is excluded for cases with large NLSP-LSP mass splitting, and 200 – 250 GeV for

<sup>3</sup>Under the decoupled squark scenario, bino production is strongly suppressed.

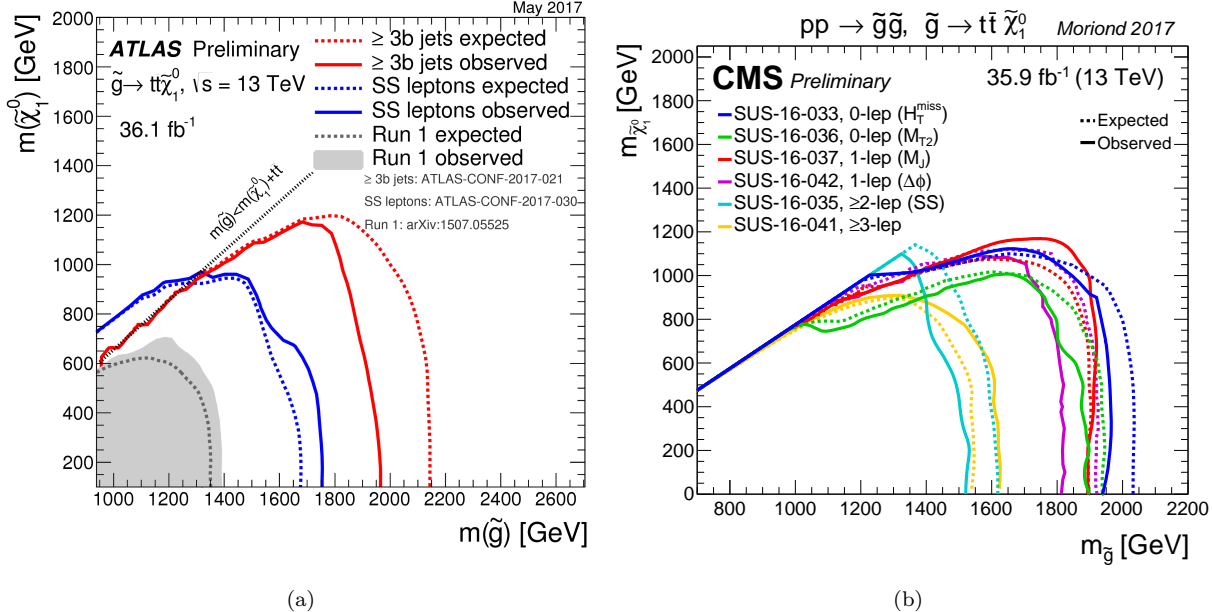


Figure 7: Up-to-date constraints on pair produced gluinos directly decaying with top quarks ( $\tilde{g} \rightarrow t\bar{t}\tilde{\chi}_1^0$ ) set by (a) ATLAS and (b) CMS. The summary plots are referred from [?] (ATLAS) and [?] (CMS).

small mass splitting.

The scenario with wino LSP is explored using a strikingly different approach. Since the mass splitting between NLSP wino-chargino and the wino-LSP is extremely compressed ( $150 \sim 160$  MeV), wino-chargino retains  $O(\text{ns})$  of moderately long lifetime, resulting the characteristic disappearing track signature where a visible charged track disappears halfway in the tracker due to the decay. The results from ATLAS (Run2) and CMS (Run1) are given in Figure 10. The exclusion runs up to  $300 - 500$  GeV in wino mass at the lifetime (or the NLSP-LSP mass splitting) predicted by MSSM.

No interpretation has been made for higgsino production and wide higgsino LSP scenario so far by LHC, due to the marginal production cross-section ( $\sim 1/4$  of that of wino production) and small NLSP-LSP splitting that is generally predicted in case of higgsino LSP. While the presence of light higgsinos are highly motivated in light of naturalness, the strongest limit on direct higgsino production is still held by LEP2. The limit is shown in Figure 11, where up to  $\sim 90$  GeV of LSP mass is excluded.

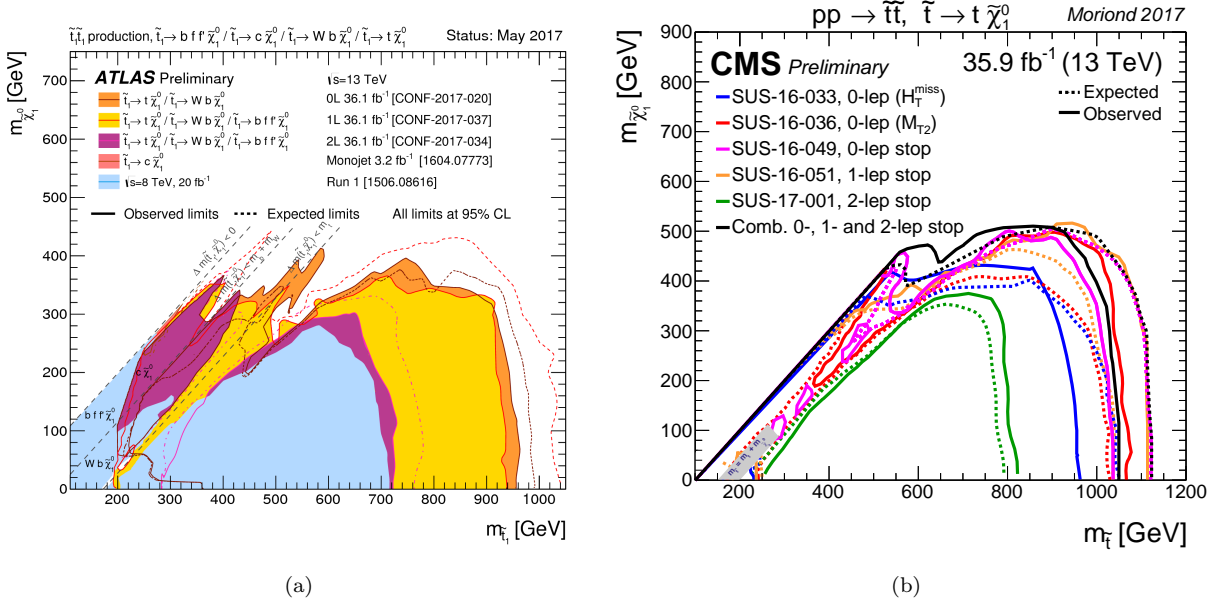


Figure 8: Up-to-date constraints on stop pair production with direct decay  $\tilde{t} \rightarrow t\tilde{\chi}_1^0$  set by (a) ATLAS and (b) CMS. The summary plots are referred from [?] (ATLAS) and [?] (CMS).

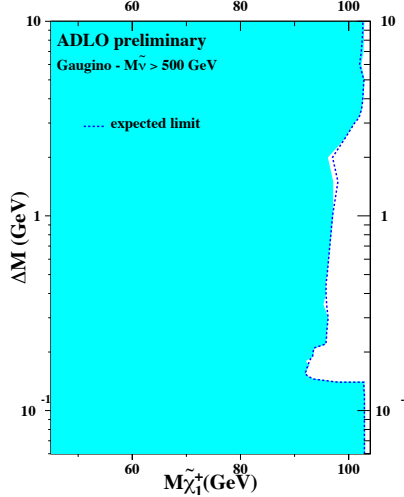


Figure 11: Exclusion limit on direct production of higgsino pairs set by LEP2 in which results from all four experiments are combined [?].

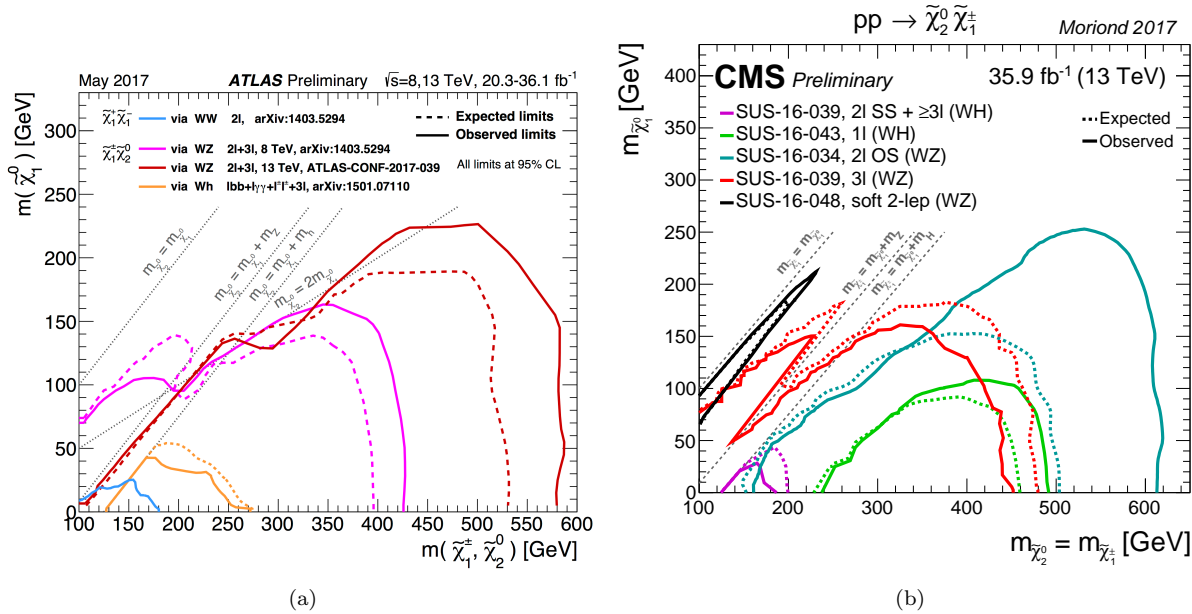


Figure 9: Up-to-date constraints on direct EW gaugino production with decays via  $W/Z/h$  set by (a) ATLAS [?] and (b) CMS [?]. The summary plots are referred from [?] (ATLAS) and [?] (CMS).

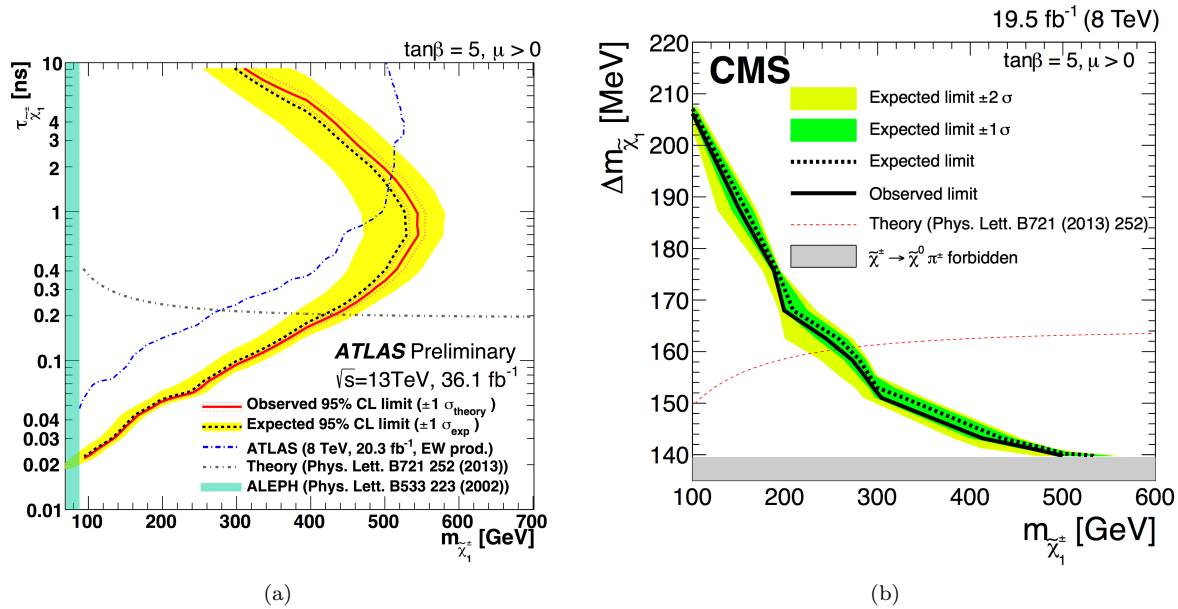


Figure 10: Constraints set on wino-LSP scenario provided by (a) ATLAS [?] and (b) CMS [?].

## 1.5 Targeted SUSY Scenario and the Search Strategy in this work

### 1.5.1 Targeted SUSY Scenario

To summarize the assumptions and scenarios discussed above, in thesis, we will focus on the MSSM scenarios where:

- Squarks are all heavy ( $> 3$  TeV).
- Allow the higgs mass fine tuning at order of  $10^{-3}$ .
- LSP is neutralino.
- Respect observed DM relic at least as the upperlimit of abundance.

The targeted experimental signature is the pair production of gluinos (Figure 12) with the mass ranging 800 GeV – 2 TeV, followed by various decays. No particular assumption is going to be made for the mass spectra, however as motivated by the well-tempered neutralino DM scenario, an additional focus is put on the case of  $\Delta m(\tilde{\chi}_1^\pm/\tilde{\chi}_2^0, \tilde{\chi}_1^0) = 20$  GeV  $\sim 30$  GeV with dedicated signal region setting and interpretation.

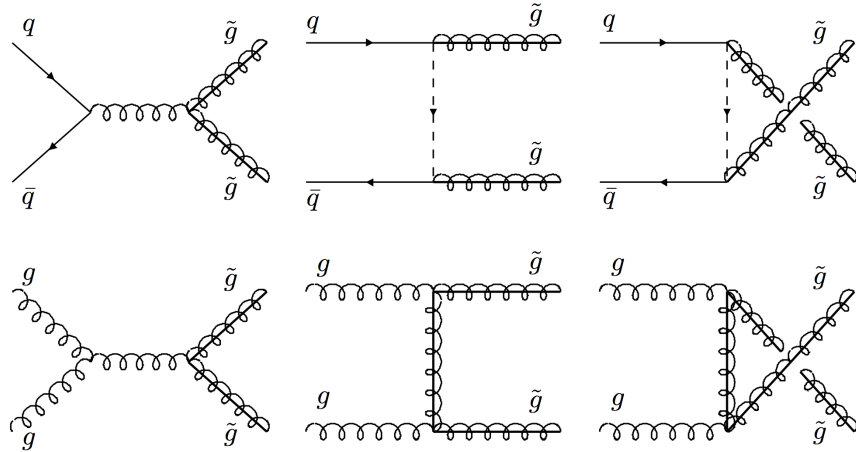


Figure 12: Feynmann diagrams for tree-level gluino pair production in LHC [?].

### 1.5.2 The Strategy of Decay Chain Based Search

Though general and minimal scenarios will be still pursued as the first priority, we would extend the scope of the search to a more general direction, given that the most straightforward scenarios (e.g. the most minimal models such as mSUGRA) has been largely excluded by LHC so far. Ideally, we prefer to consider as general as possible e.g. MSSM, but constraining the full parameter spaces is not realistic (e.g. > 100 parameters for the most general MSSM). However, it is also true that most of the MSSM parameters only affect the spins or decay branchings of SUSY particles, rather than kinematics i.e. they do not change the signal acceptance. On the other hands, kinematics of SUSY signatures are dominantly determined by SUSY mass spectra. Therefore, we only have to care about the mass dependence, once a full decay chain is specified. In other words, setting the cross-section upper limit on each decay chain and mass spectra is no less general than considering the full parameter space of the MSSM.

<sup>4</sup>

Placing upper limits on particular decay chain  $A \rightarrow B$  is essentially equivalent to setting exclusion limit on following model called “simplified model”:

- Assuming  $\text{Br}(A \rightarrow B)$  is 100%.
- Parameters other than SUSY masses are set to arbitrary number. E.g. in LHC analysis, the EW gaugino mixing is usually set so that NLSP and LSP become wino- and bino-dominant.

Though interpretation has already been widely employed based on the simplified model in LHC searches, the critical problem is that the coverage of decay chains and mass spectra is far from complete, for instance, in case of gluino, only a few decays are considered. In this thesis, all the viable gluino decay chains will be considered, and setting the limit on each of them with full coverage of mass assumption on gluino and EW gauginos. In the following sub-section, the target decay chains are closely specified.

---

<sup>4</sup>This is the same to admit our search has no sensitivity in determining the model parameters other than masses.

### 1.5.3 Targeted Gluino Decay Chains

Under the decoupled squarks scenario, gluino always decays 3-body; 2 SM quarks and a EW gaugino via heavy virtual squarks:

$$\tilde{g} \rightarrow \begin{cases} (u\bar{d}, c\bar{s}, t\bar{b}) \times (\tilde{\chi}_{1,2}^-) \\ (d\bar{u}, s\bar{c}, b\bar{t}) \times (\tilde{\chi}_{1,2}^+) \\ (u\bar{u}, d\bar{d}, s\bar{s}, c\bar{c}, b\bar{b}, t\bar{t}) \times (\tilde{\chi}_{1-4}^0). \end{cases}$$

Including the subsequent EW gaugino decays, this will lead to an enormous number of final states, however kinematically some of them are approximately equivalent which can be merged or trimmed. For instance, the mass splitting between higgsino-dominated states or winos-dominated states are compressed, leading to the effectively the same kinematics.<sup>5</sup> This eventually reduces all gluino decays into either direct decay in which gluino directly de-excites into LSP, “1-step” decay with one intermediate EW gaugino state, and “2-step” decay in which gluino decays via two resolved intermediate EW gauginos mass states, with possible three types of scenarios in terms of the mass spectra, as schematized in Figure 13.

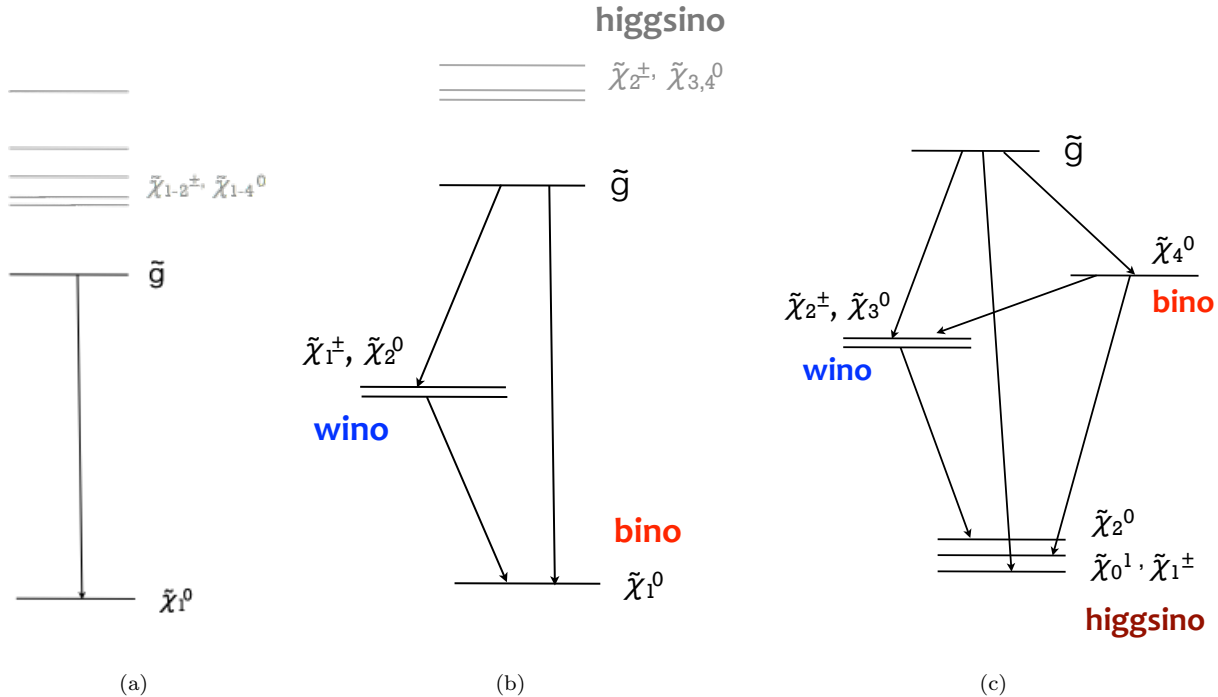


Figure 13: Possible gluino decay paths are illustrated for mass spectra where (a) all the EW gauginos are heavier than gluino (100% direct decay of gluino), (b) higgsinos are heavier than gluino while the other EW gauginos are lighter (mixture of direct decay and 1-step decays), (c) all the EW gauginos are below gluino mass (mixture of direct decay, and numerous 1-step and 2-step decays), are illustrated. The hierarchy between wino and bino in (b), or between all the EW gauginos in (c) are also allowed.

As for the scenario in Figure 13, a numerous MSSM parameters scans demonstrate that the probability of 2-step decays are generally much lower than that of direct or 1-step decays, except for some of the cases where each of the intermediate masses are aligned with relatively equal distance. Therefore, in the analysis,

<sup>5</sup>The splitting will be rarely greater than 50 GeV even when all  $M_1$ ,  $M_2$  and  $\mu$  are at the same mass leading to the maximum mixing.

we confine our scope within direct and 1-step decays.

The acceptance dependence between light quark flavors ( $u, d, s, c$ ) are also small, therefore they can be merged into a single simplified model where gluino decays with equal rate between  $u, d, s, c$ .

For subsequent gaugino decays, charginos are always assumed to emit on-shell or off-shell  $W$ -boson, while there are two options for neutralino decays via  $Z$  or  $h$ . The decays into slepton is ignored here, majorly for convenience sake of restricting the number of final states, however with a few justifications; under a general unification regime, slepton masses are in the same order of squark masses which are assumed to be decoupled here ; when respecting the observed DM relic abundance, the mass splitting between NLSP and LSP becomes naturally small (typically  $< 50$  GeV). Decays via sleptons requires sleptons masses in between NLSP and LSP, which is unlikely to happen naturally.

With all the scrutinization, the targeted gluino decay chains are reduced into Table 4 with corresponding Feynmann diagrams shown in Figure 14.

Table 4: Summary of targeted gluino decay chains. The number in the pharencethese indicates the numbers of chains in the category.

Direct decay (3)	$\tilde{g} \rightarrow (q\bar{q}, q\bar{q}, q\bar{q})\tilde{\chi}_1^0$
1-step decay (8)	$\tilde{g} \rightarrow (q\bar{q}', tb(b\bar{t})) \tilde{\chi}_1^\pm, \tilde{\chi}_1^- \rightarrow W^\mp \tilde{\chi}_1^0$ $\tilde{g} \rightarrow (q\bar{q}, b\bar{b}, t\bar{t}) \tilde{\chi}_2^0, \tilde{\chi}_2^0 \rightarrow Z \tilde{\chi}_1^0$ $\tilde{g} \rightarrow (q\bar{q}, b\bar{b}, t\bar{t}) \tilde{\chi}_2^0, \tilde{\chi}_2^0 \rightarrow h \tilde{\chi}_1^0$

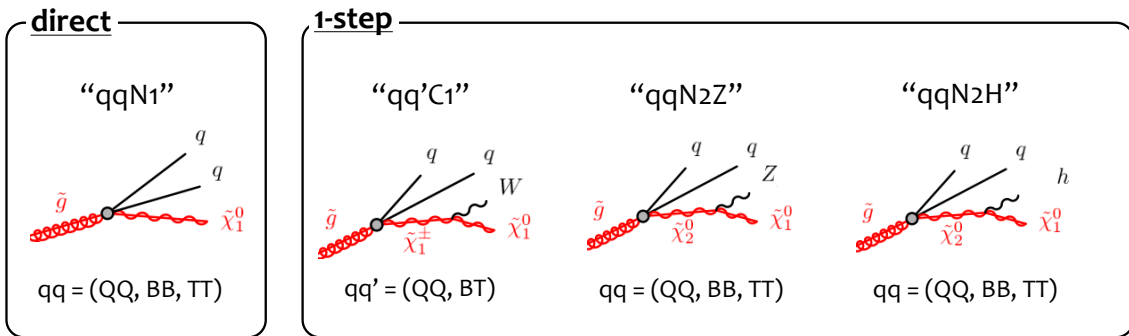


Figure 14: Target gluino decay chains.

The full decay chains of pair produced gluinos become increasingly complicated: 11 symmetric decays (two gluinos experience the same decay chains), 55 symmetric decays (two gluinos experience different decay chains). In total, 66 decay chains are identified as the candidates.

#### 1.5.4 Target Signal Models for 1-lepton Final State

In LHC, analyses are conventionally divided based on number of hard leptons in the final state, since either signal kinematics and the background strategy are drastically different. In gluino decays, ignoring the decays

into sleptons, leptons are always generated via decays of W/Z/H bosons. Therefore, giving their small leptonical branching ratio, 0-lepton or 1-lepton final state are the most promising channel for inclusive search, while 2/3-leptons final states are more specialized in specific types of scenarios such as long-chain multi-step gluino decays involving a large number of W/Z/H bosons.

This thesis focus on the final state with exactly one lepton. After excluding the decay chains with marginal branching ratio into final state with exactly 1-lepton, 45 decay chains are selected as the benchmark models for the thesis. The full list are shown in Table 5 - Table 7, with the naming convention for each decay chain defined as:

$$\begin{aligned} \text{Model name} &:= [aaXX][bbYY] \\ aa, bb &= \text{"QQ", "BB", "TT", "BT"} \\ XX, YY &= \text{"N1", "C1", "N2Z", "N2H"} \end{aligned} \quad (61)$$

where each sub-block ( $[aaXX], [bbYY]$ ) denotes the full chain of one gluino decay, corresponding to either of the topology shown in Figure 14.

They are further categorized based on the number of expected b-quarks in the final state, as the signal regions will be segmented based on the number of b-tagged jets. The reference models for each b-categories are respectively chosen as **QQC1QQC1**, **QQC1BTC1** and **TTN1TTN1** for BV, BT and 3B (Figure 15), which will be used as the reference in designing signal regions and other various studies. The Feynman diagrams for the reference models are illustrated in Figure 15.

Note that simplified models with asymmetric gluino decays are not realistic in its assumption of 100% branching ratio, since there is always branching to symmetric decays when asymmetric decays are feasible. However, it is in fact a more user (theorists?) friendly presentation since it straightforwardly describes the acceptance upper-limit for the decay chain so that the compatibility with other models can be easily tested. On the other hand, in case of an interpretation with a realistic models where many sorts of decays are mixed, one has to disentangle the decay chains to find it.

Table 5: Target models with no b-jets at tree level. The average jet multiplicity ( $n_J$ ) and b-jet multiplicity ( $n_B$ ) are calculated based on number of quarks and b-quarks appearing in the final state. The PDG values [?] are referred for branching ratio of top, W/Z/h bosons. “✓” specifies the models with the final result derived using the samples with the fast detector simulation (ATLFast 2 [?]), while the others are with emulated truth samples.

1-step decay	$n_J$	$n_B$	$\text{Br}(1\text{L})/\text{Br}(0\text{L})$	$\text{Br}(1\text{L})/\text{Br}(2\text{L})$	det sim.?
QQN1QQC1	5.5	0.0	0.33	-	
<b>QQC1QQC1</b>	7.0	0.0	0.67	6	✓
QQC1QQN2Z	7.3	0.3	0.35	3.86	✓
QQC1QQN2H	7.4	1.1	0.46	7.07	✓

## 1.6 Structure of the thesis

The rest of the sections will proceed as follows: The LHC and the ATLAS detector is firstly overviewed in Sec. 2, to have idea of typical environment that LHC provides and the precision the ATLAS detectors

Table 6: Target models with 1 or 2 b-jets at tree level. The average jet multiplicity ( $n_J$ ) and b-jet multiplicity ( $n_B$ ) are calculated based on number of quarks and b-quarks appearing in the final state. The PDG values [?] are referred for branching ratio of top, W/Z/h bosons. “✓” specifies the models with the final result derived using the samples with the fast detector simulation (ATLFast 2 [?]), while the others are with emulated truth samples.

Direct decay	$n_J$	$n_B$	$\text{Br}(1\text{L})/\text{Br}(0\text{L})$	$\text{Br}(1\text{L})/\text{Br}(2\text{L})$	det sim.?
QQN1TTN1	7.0	2.0	0.67	6	
1-step decay	$n_J$	$n_B$	$\text{Br}(1\text{L})/\text{Br}(0\text{L})$	$\text{Br}(1\text{L})/\text{Br}(2\text{L})$	det sim.?
QQN1BTC1	7.0	2.0	0.67	6	
QQN1TTN2Z	8.8	2.3	0.68	3.30	
<b>QQC1BTC1</b>	8.5	2.0	1.0	3	✓
QQC1BBN2Z	7.3	2.3	0.35	3.86	
QQC1TTN2Z	10.3	2.3	1.02	2.34	
QQN2ZTTN2Z	10.7	2.6	0.7	2.31	
BBN1QQC1	5.5	2.0	0.33	-	
BTC1QQN2Z	8.8	2.3	0.68	3.30	
TTN1QQC1	8.5	2.0	1.0	3	
TTN1QQN2Z	8.8	2.3	0.68	3.30	

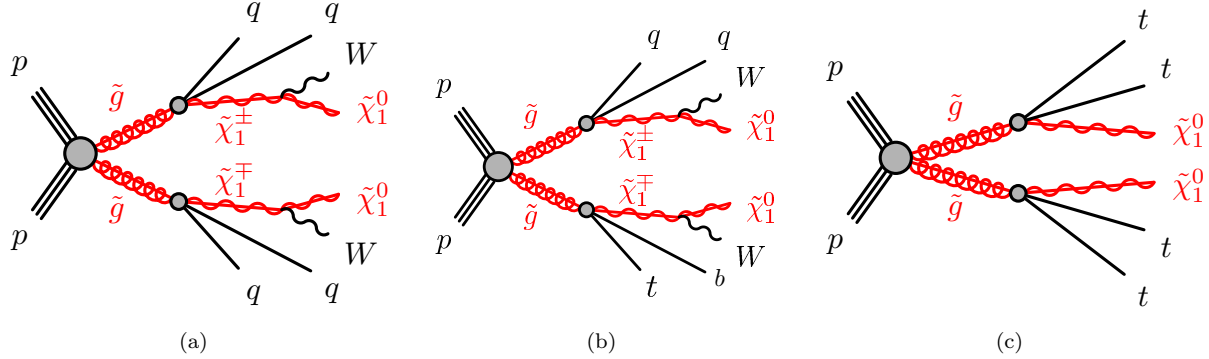


Figure 15: Feynman diagrams for the reference models (a) QQC1QQC1 (b) QQC1BTC1 (c) TTN1TTN1.

system offers ; Sec. 3 follows with describing the off-line algorithms of reconstructions and identifications for particles or jets; The detail of simulation used in analysis is summarized in Sec. 4; The description of the analysis starts with Sec. 5 in which the preselection and signal regions are designed. Sec. 6 is then involve comprehensive discussion on the background estimation, the key part of the analysis; Uncertainties associated with background estimation and signal modeling is overviewed in Sec. 7 ; finally the unblinded result and resultant limits are shown in Sec. 8; with brief concluding remarks in Sec. 9.

Table 7: Target models with 3 or more b-jets at tree level. The average jet multiplicity ( $n_J$ ) and b-jet multiplicity ( $n_B$ ) are calculated based on number of quarks and b-quarks appearing in the final state. The PDG values [?] are referred for branching ratio of top, W/Z/h bosons. “✓” specifies the models with the final result derived using the samples with the fast detector simulation (ATLFast 2 [?]), while the others are with emulated truth samples.

<b>Direct decay</b>	$n_J$	$n_B$	$Br(1L)/Br(0L)$	$Br(1L)/Br(2L)$	det sim.?
BBN1TTN1	7.0	4.0	0.67	6	
<b>TTN1TTN1</b>	10	3.9	1.33	2	✓
<b>1-step decay</b>	$n_J$	$n_B$	$Br(1L)/Br(0L)$	$Br(1L)/Br(2L)$	det sim.?
QQN1TTN2H	8.9	3.1	0.79	3.64	
QQC1BBN2H	7.4	3.1	0.46	7.07	
QQC1TTN2H	10.4	3.1	1.12	2.34	
QQN2ZTTN2H	10.8	3.4	0.8	2.56	
QQN2HTTN2H	10.8	4.3	0.91	2.70	
BBN1BTC1	7.0	4.0	0.67	6	
BBN1TTN2Z	8.8	4.3	0.68	3.30	
BBN1TTN2H	8.9	5.1	0.79	3.64	
BBN2ZTTN2Z	10.7	4.6	0.7	2.31	
BBN2ZTTN2H	10.8	5.4	0.8	2.56	
BBN2HTTN2H	10.8	6.3	0.91	2.70	
BTC1QQN2H	8.9	3.1	0.79	3.64	
BTC1BTC1	10	4.0	1.33	2	
BTC1BBN2Z	8.8	4.3	0.68	3.30	
BTC1BBN2H	8.9	5.1	0.79	3.64	
BTC1TTN2Z	11.8	4.3	1.35	1.75	
BTC1TTN2H	11.9	5.1	1.46	1.70	
TTN1QQN2H	8.9	3.1	0.79	3.64	
TTN1BTC1	10	4.0	1.33	2	
TTN1BBN2Z	8.8	4.3	0.68	3.30	
TTN1BBN2H	8.9	5.1	0.79	3.64	
TTN1TTN2Z	11.8	4.2	1.35	1.75	
TTN1TTN2H	11.9	5.1	1.46	1.70	
TTN2ZQQN2H	10.8	3.4	0.8	2.56	
TTN2ZBBN2H	10.8	5.4	0.8	2.56	
TTN2ZTTN2Z	13.7	4.5	1.36	1.55	
TTN2ZTTN2H	13.8	5.4	1.47	1.53	
TTN2HTTN2H	13.8	6.2	1.58	1.49	

## 2 Experiment Apparatus: The ATLAS Detector at the LHC

### 2.1 The Large Hadron Collider

The Large Hadron Collider (LHC) [?] is a 27 km long circular proton accelerator embedded underground of the Geneva area. It is designed to collide protons at a center-of-mass energy of  $\sqrt{s} = 14$  TeV, at the four detector cites (ATLAS [?], CMS [?], ALICE [?] and LHCb [?]) built on the accelerator ring. ATLAS and CMS are general purpose detectors designed to study a vast range of physics programs, while LHCb and ALICE are specialized in studying b-hadrons and heavy-ion collisions respectively.

The operation started in 2010, offering proton-proton (pp) collisions at a center-of-mass energies of 7 TeV and 8 TeV with  $4.7\text{fb}^{-1}$  and  $20.3\text{fb}^{-1}$  of integrated luminosity until 2012 (Run1). The center-of-mass energies has been almost doubled to 13 TeV in the runs starting from 2015 (Run2). The LHC has also delivered lead-ion (Pb-Pb) collisions with a center-of-mass energy of  $\sqrt{s_{NN}} = 2.76$  TeV and proton-lead (p-Pb) collisions with  $\sqrt{s_{NN}} = 5.02$  TeV.

The acceleration of protons stages into various steps: Protons are firstly seeded from hydrogen gas, by blowing off the electrons from the hydrogen atoms using high electric field. They are injected in the linear accelerator LINAC2 with accelerated upto 50 MeV, and sent into the Proton Synchrotron Booster (PSB) being accelerated up to an energy of 1.4 GeV. The subsequent accelerator is the Proton Synchrotron (PS) elevating the energy of the protons to 25 GeV, and injecting them into the Super Proton Synchrotron (SPS). After being accelerated to 450 GeV in SPS, the protons finally enter the two LHC beam pipes running the beam oppositely each other. The acceleration chain is illustrated in Figure 16.

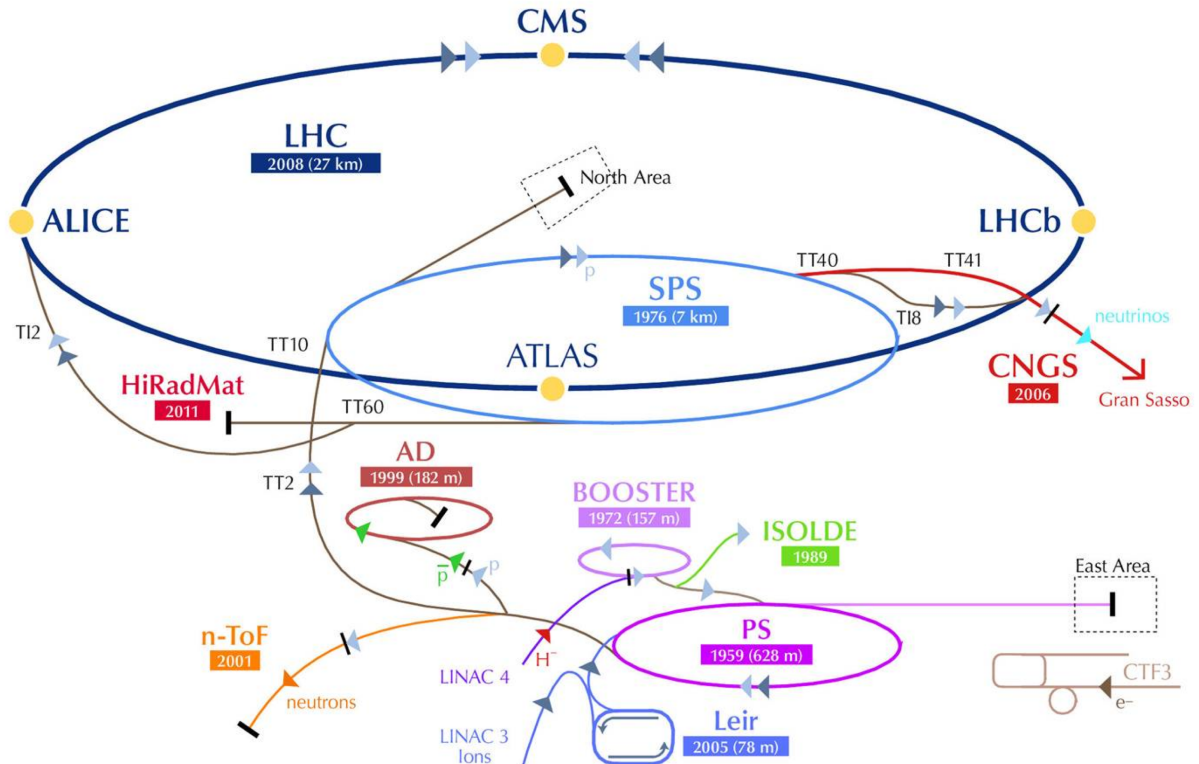


Figure 16: LHC. [?]

The LHC accelerator consists of octant-shaped 2.45 km arcs with 1232 superconducting magnets located at the curves, providing 8.33T of magnetic field to bend the proton trajectory. In total, 39 crossing-trains can be filled into the LHC simultaneously in a design conditions, with 2808 crossings per beam are brought to collision in the LHC. Each crossing contains about  $10^{11}$  protons. The beam crossings are collided with a beam crossing angle of 285 mrad. The peak luminosity amounts upto  $L = 0.7 - 1.4 \times 10^{34} \text{cm}^2\text{s}^{-1}$  in the 2015-2016 runs, as shown in Figure 17 (a).

Due to the high frequency of collisions and the dense proton crossings, multiple proton collisions can take place simultaneously within the same crossing crossing, referred as “pile-up”. The average pile-up  $\mu$ , defined as the mean number of interactions per crossing crossing, has been evolved according to the peak luminosity increase, amounting to 20 – 40 in recent runs in 2016. The  $\mu$  profile is shown in Figure 17 (b).

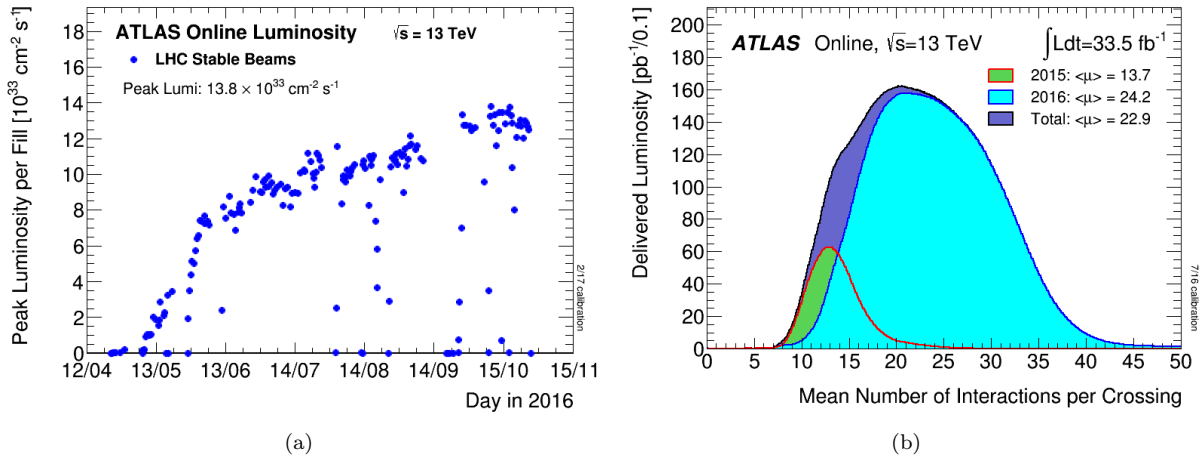


Figure 17: (a) Peak luminosity evolution in 2016 runs [?], and (b) the pile-up profile obtained in 2015-2016 runs [?].

## 2.2 Particle Measurement and The ATLAS Detector

ATLAS (A Toroidal LHC ApparatuS) is a general purpose detector, aiming to probe a wide range of physics programs from precision measurements of EW physics to the energy frontier experiments, through a dedicated measurement of particles produced in  $pp$  collisions. The detector spans over 44m in width and stand 25m in height, covering the interaction point (IP) by a cylindrical barrel and two endcaps, achieving a nearly full solid angle coverage. The total weight amounts 7000 tons including stopping materials to fully accommodate the produced particles, enabling complete measurement of particle energy. The cut-away image is shown in Figure 18.

The purposes of the detector are mainly two-fold:

- identification of particle species,
- determination of particle’s energy and momentum,

with two complemental concepts of measurement:

- fast measurement for providing trigger

- precision measurement of particle properties

To satisfy these functionalities at the same time, following sub-detectors are arranged in a designed order from the innermost toward outside with respect to the IP.

- Inner detector (and magnets) to identify and measure electrically charged particles, as well as define the primary vertices.

Charged particle can easily interact with materials by ionizing the molecules inside. The path of flight can be “imaged” as a track, by recording the position of ionization. In ATLAS, a complex of discrete layers of silicon sensors and a continuously volumed gas chambers are placed in the innermost. The momentum can be measured in addition by applying magnetic field, and quantifying the curvature of the bent trajectory.

- Calorimeters to measure the energy of electron, photon and hadrons.

Electrons and photons traveling inside materials above certain energy <sup>6</sup> lose their energy through electromagnetic showering; photons create  $e^+e^-$  pairs and electrons spew bremsstrahlung photon; the daughter electrons and photons are multiplicatively multiplied by this recursive repetition; ending up in a particle shower. Most of the energy are absorbed after traversing about 20 radiation lengths ( $X_0$ ) of material. Hadrons (mostly pions) also cause similar cascade reactions. The shower branch evolves by interacting with nucleus in the material via strong interaction, meanwhile produced  $\pi_0$ s promptly decay into two photons which shower electromagnetically. The resultant shower is combination of a long hadronic shower and small local EM clusters in it. Electromagnetic and hadronic calorimeters are set as the outer layers of the trackers, to measure such showers by absorbing them in it.

- Muon spectrometer (and the magnet) to measure the muons penetrating the detector.

Among all the particles that interact with material, muons are only exception who do not seriously deposit the energy in calorimeter. This is due to the fact that muons happen to have the mass realizing the minimum EM interaction with material (Minimum Ionizing Particle; MIP), and the corresponding critical energy for EM showering is usually at several TeV level. This is actually a lovely coincident for human being (or poor particle physicists), since they can be easily identified i.e. particles punching through the calorimeter are automatically muons. The muon spectrometer located outermost serves for identifying such muons as well as measuring the tracks together with the inner tracker described above.

- Given the total momentum conservation in transverse direction in each collision, the presence of non-interacting particles such as neutrinos and hypothetical new particles can be indirectly detected through the imbalance; This is referred to missing  $E_T$  ( $E_T^{\text{miss}}$ ), <sup>7</sup> defined by the negative of the vectoral sum of transverse momentum of all detected particles.

In the following subsections, each of the sub-detector system will be overviewed, comprehensively based on references [?] and [?].

---

<sup>6</sup>Referred to the critical energy.  $\sim 800$  MeV for typical material.

<sup>7</sup>The “ $E_T$ ” in the name is due to a historical reason; it used to be calculated only using calorimeter deposits, which is now actually outdated

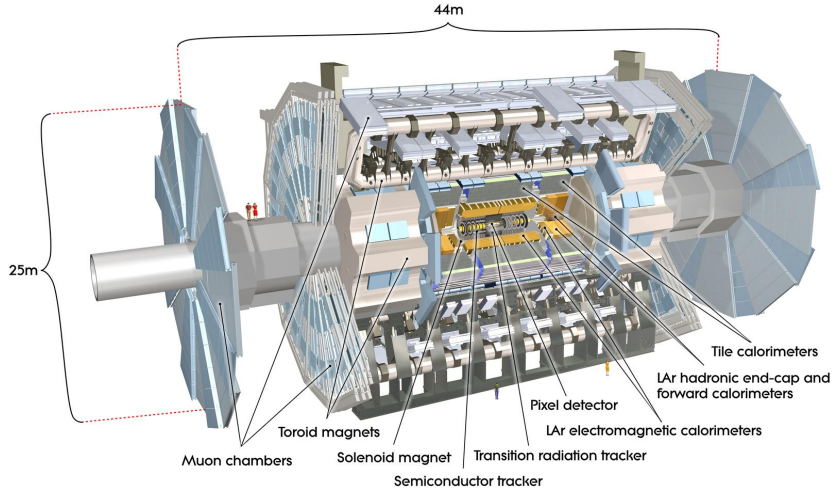


Figure 18: Full-body view of the ATLAS detector [?]. The geometry is completely forward-back symmetric.

### 2.2.1 Coordinate System

For referencing the position of the detector as well as the orientation of particles, a right-handed Cartesian coordinate system is defined with the interaction point being the origin and the x-axis pointing to the center of the LHC ring. The y-axis and z-axes are accordingly the direction of sky or the beam direction respectively. Polar angle  $\theta$  and azimuthal angle  $\phi$  are defined by the cylindrical representation  $(\theta, \phi, z)$ :  $\theta$  ranges from 0 to  $2\pi$  with respect to the z-axis, and  $\phi$  runs from  $-\pi$  to  $\pi$  from the x-axis. The two endcaps in the ATLAS detector are referred as “A-side” and “C-side”, corresponding to the position of positive and negative coordinate in the z-axis.

It is the unfortunate fate for hadron colliders that particles generated by collisions are usually highly boosted along z-axis, since the energy of the initial interacting partons inside the hadrons are asymmetric. From this point of view, a set of variables with Lorentz-invariant nature are introduced for describing momentum or position. In particular, it is useful to define the transverse component of variables, such as transverse momentum  $p_T := p \sin \theta$  or transverse energy  $E := E \sin \theta$ . The advantage over the use of  $p$  or  $E$  is obvious that they do express the intrinsic hardness of the particles in the center-of-mass frame of the reaction, and also that the vectorial sum of all particles conserves before and after the collision.

Similarly, pseudo-rapidity  $\eta$  defined below commonly serves as the coordinate of polar angle:

$$\eta := -\ln \left( \tan \frac{\theta}{2} \right). \quad (62)$$

It has two practical advantages over  $\theta$ ; the difference in pseudo-rapidity between particles  $\Delta\eta$  are invariant against the boost towards z-direction.<sup>8</sup>;  $\eta$  has an effectively wider dynamic range upto a very forward region thanks to the finer measure, where  $\theta$  suffers from the degeneracy i.e.  $\cos \theta \sim 1$ , thus more convenient in expressing the orientation of forward particles.

---

<sup>8</sup>This is true when the particles are massless, which is approximately valid given that the boost along z-axis is sourced by the momentum of order of the beam energy.

Angular distance between two particles are commonly expressed by  $R$  that is defined as:

$$\Delta R := \sqrt{(\Delta\eta)^2 + (\Delta\phi)^2}. \quad (63)$$

### 2.2.2 Inner Detectors

The inner detector (ID) is placed the inner-most of the ATLAS detector, designed to measure the tracks of charged particles, as well as precisely determining the position of vertices of the hardest scattering in interest.

It consists of a silicon tracker (the pixel detector and the semiconductor tracker ;SCT) at the inner radii, and the Transition Radiation Tracker (TRT) for continuous tracking at the outer radii. The detector arrangement is illustrated in Figure 19 and Figure 20. The outer radius is surrounded by the central solenoid, providing a magnetic field of 2T along the  $z$ -axis, to bend the tracks traveling inside the ID volume.

As a general requirement, ID has to contain material as less as possible, to avoid disturbing the measurement downstream by the energy loss. Figure 21 shows the total material profile of the ID over  $|\eta|$ . The material volume is suppressed below 2.5 radiation length and 1 nucleus interaction length, which is low enough compared with energy dropped in the calorimeter.

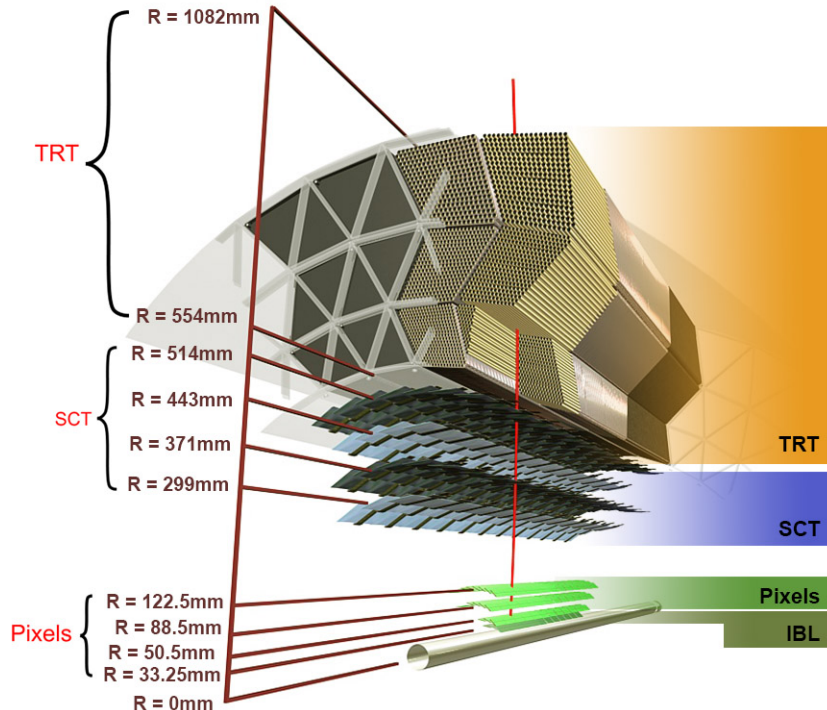


Figure 19: Cross-section of the ATLAS inner detectors [?].

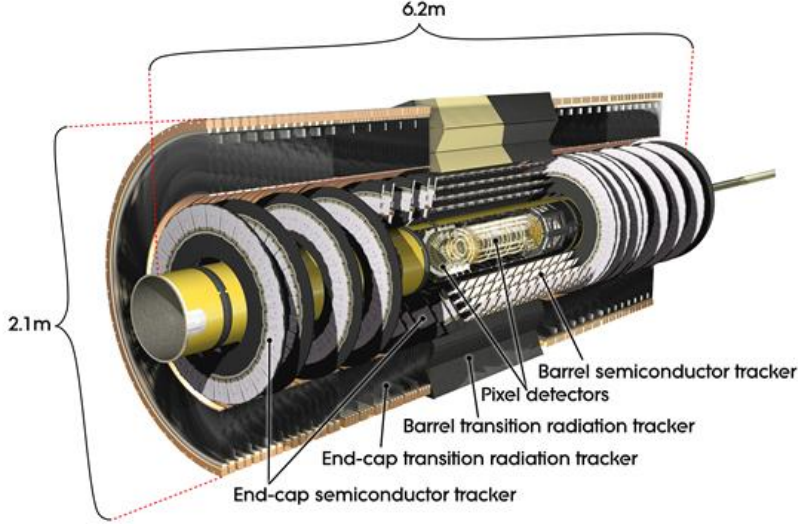


Figure 20: Cut-away view of the ATLAS inner-detector [?].

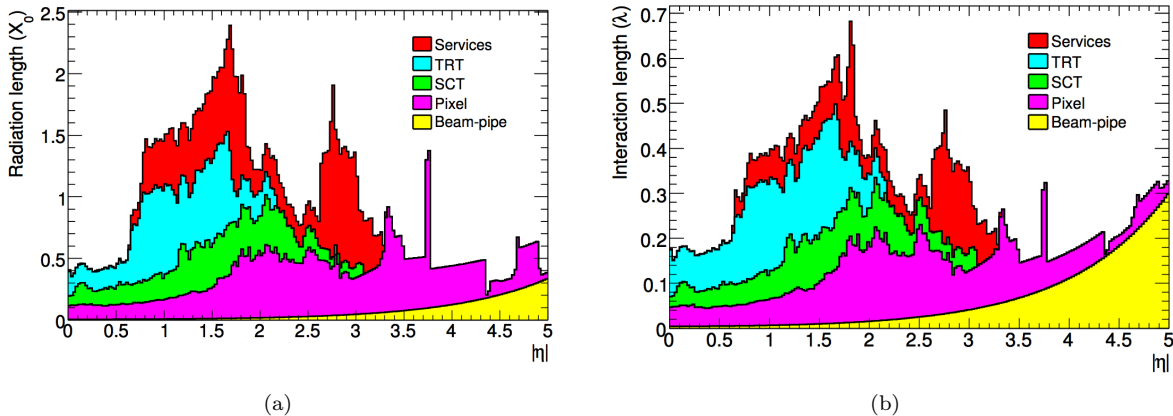


Figure 21: Simulated material profile of whole ID in unit of (a) electro-magnetic radiation length and (b) nucleus interaction length [?]. Peak  $|\eta| \sim 1.5$  corresponds to the barrel-endcap transition area through which service cables travel.

**The silicon trackers: Pixel and SCT** The detection principle of silicon detector is based on the electron-hole pair creation induced by a traverse of a charged particle. Those electron-hole pairs are inhaled by the bias voltage applied on the sensor, and transferred into an electric signal. Silicon is particularly advantageous in the choice of silicon is largely for its radiation hardness durable the enormously high radiation around the IP. On the other hand, the performance (e.g. noise level, gain) is relatively sensitive to temperature, therefore they are kept in low temperature ( $-5 \sim 0^\circ\text{C}$ ) during the operation.

The pixel detector is the unit of layers of pixelated silicon sensors located closest to the IP of all the detector component. Oxygen enriched n-in-n silicon semiconductor is used for the sensors. Four cylindrical layers are placed in the barrel at the radial distance of 31 mm - 122.5 mm with respect to the IP, and 3 disk

layers cover each side of the endcap, providing an acceptance with  $|\eta| < 2.5$ . The innermost layer in the barrel is referred as the “insertable b-layer” (IBL) installed during the long shutdown between Run1 and Run2, providing the highest precision and playing a prominent role in identifying the secondary vertex of late decaying particles ( $\tau$ ,  $b$ -hadrons etc.). The pixels are in the  $50 \times 250 \mu\text{m}$  granularity in the IBL, and  $50 \times 400 \mu\text{m}$  in the other layers. The resolution is purely determined by the pixel size. A spacial resolution of  $4 \mu\text{m}$  and  $115 \mu\text{m}$  is achieved along the radial and beam z-direction respectively, by combining the hit information from the four layers.

The SCT is located outside of the pixel detector. The sensors are made by single-sided p-on-n silicon semiconductors with 150 V of bias voltage applied. The strips of barrel SCT aligning along the z-axis with  $80 \mu\text{m}$  pitch, giving a precision position in the  $r - \phi$  plane. A slight angle stereo (40 mrad) alternated by layers is add to the arrangement, providing decent  $z$ -position determination in addition. The intrinsic resolution is  $17 \mu\text{m}$ ( $580 \mu\text{m}$ ) in  $r - \phi(z)$  direction respectively. The strips in the endcap SCT are aligned in a mesh in terms of  $x - y$ , capable of 3D position determination together with the  $z$ -coordinate of the disks.

**Trasition radiation tracker** TRT is a gaseous detector designed for tracking particles as well as identifying the species using the characteristic transition radiation. The detector is filled with 4mm-diameter straw tubes in which xenon-based active gas is confined. Ionized secondary electrons are collected by the  $30 \mu\text{m}$ -diameter gold-plated tungsten-Rhenium anode wire in the center of each straws. 73 layers of aligned straw tubes are arranged in the barrel, and 160 layers in the endcap sectors. The tube length is 144 cm (37 cm) in the barrel (endcap) region. The barrel tubes are arranged in parallel along the beam pipe, with 7 mm of interval between layers. The intrinsic position resolution per straw is about  $130 \mu\text{m}$ . A traverse of charged particle fires 36 straws on average.

Transition material is inserted between the straws.  $19 \mu\text{m}$ -diameter polypropylene fibers are used in barrel, and  $15 \mu\text{m}$ -thick polypropylene radiator foils isolated by a polypropylene net are set for the endcaps. Transition radiation can address unique sensitivity in particle identification, particularly to  $e/\pi$  separation, since the intensity is sensitive to incident particle’s velocity (proportional to  $\gamma = E/m$ ) rather than the energy or momentum. Given that the signal of transition radiation typically yield more amplitude, in the TRT two differennt thresholds are set; the lower threshold to collect the signal of normal ionization and the high threshold for transition radiation. The high threshold is carefully designed so that only electrons in the typical range of energy (0.5 GeV – 150 GeV) can fire while pions are inert to it.

Figurere 22 shows the  $\gamma$ -dependence of high threshold rate, demonstrating good separation of particles with electron-like momentum and pion-like momentum.

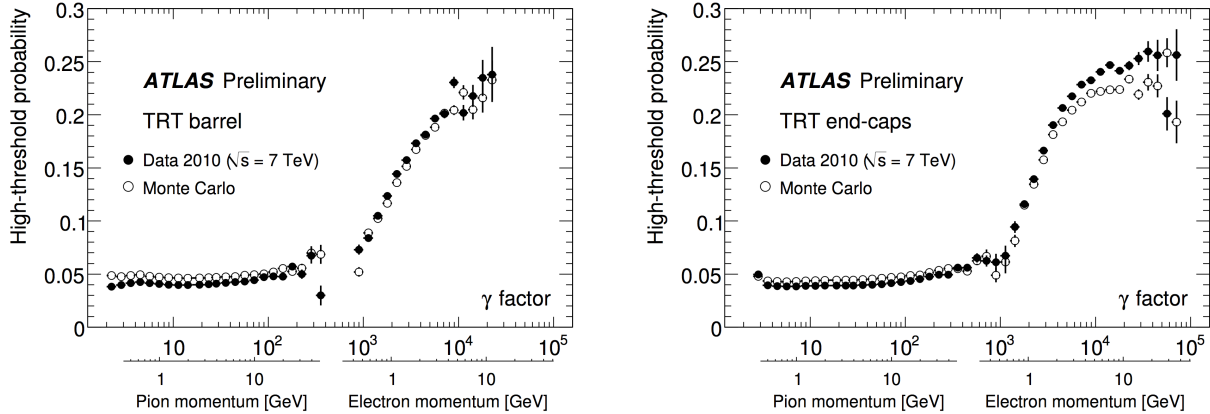


Figure 22: TRT high threshold rate as function of Lorentz factor ( $\gamma = E/m$ ) of incident particles [?]. The  $\gamma$  scale of typical pions and electrons are shown aside. Left/right plot corresponds to barrel/endcaps.

**Combined Tracking Performance** The combined tracking performance has been validated via measurement of the cosmic muons [?]. The resolution for a single muon track is obtained as function of muon transverse momentum:

$$\frac{\sigma_{p_T}}{p_T} = 1.6\% \oplus \frac{0.053\%}{\text{GeV}} \times p_T. \quad (64)$$

### 2.2.3 Calorimetry

ATLAS includes two calorimeter systems composed of the electromagnetic calorimeter (EM calorimeter) and the hadronic calorimeter (HC), located outside the ID. The whole view is given by Figure 24. EM calorimeter, the inner part of the calorimetry, is aimed to measure energy of photons and electrons by causing them to EM shower. This is done by the Liquid-Argon sampling calorimeter (LAr), alternately sandwiching the lead absorber layers and the sensor layer filled with liquid-argon. Most of the hadrons do not create EM showers and penetrate the EM calorimeter without major energy loss, which are then captured by the HC is placed downstream. The HC exploits two detection technologies: the barrel HC, covering pseudo-rapidity range of  $|\eta| < 1.7$ , is referred to the “Tile calorimeter” consisting of the sensor layers with scintillator tiles and steel absorbers; The endcap HC ( $1.5 < |\eta| < 3.2$ ) employ the technology of LAr calorimeter similar to the EM calorimeter, however in a different geometry and coarser cell granularity. In addition to the EM calorimeter and HC, the forward calorimeter located in the very forward region ( $3.2 < |\eta| < 4.9$ ) serve a supplemental function capturing the diffracted particles from jets. The detector technology used and the spatial segmentation are summarized in Table 23. Thanks to the fast response of the readout, calorimeter also provide the function of trigger, based on the fast processing of particle identification and the energy measurement using the information of individual showers, as detailed in Sec. 2.2.6.

<b>EM CALORIMETER</b>	<b>Barrel</b>	<b>End-cap</b>			
Coverage	$ \eta  < 1.475$	$1.375 <  \eta  < 3.2$			
Longitudinal segmentation	3 samplings	3 samplings	$1.5 <  \eta  < 2.5$		
		2 samplings	$1.375 <  \eta  < 1.5$		
			$2.5 <  \eta  < 3.2$		
Granularity ( $\Delta\eta \times \Delta\phi$ )					
Sampling 1	$0.003 \times 0.1$	0.025 $\times 0.1$	$1.375 <  \eta  < 1.5$		
		0.003 $\times 0.1$	$1.5 <  \eta  < 1.8$		
		0.004 $\times 0.1$	$1.8 <  \eta  < 2.0$		
		0.006 $\times 0.1$	$2.0 <  \eta  < 2.5$		
		0.1 $\times 0.1$	$2.5 <  \eta  < 3.2$		
Sampling 2	$0.025 \times 0.025$	0.025 $\times 0.025$	$1.375 <  \eta  < 2.5$		
		0.1 $\times 0.1$	$2.5 <  \eta  < 3.2$		
Sampling 3	$0.05 \times 0.025$	0.05 $\times 0.025$	$1.5 <  \eta  < 2.5$		
<b>PRESAMPLER</b>	<b>Barrel</b>	<b>End-cap</b>			
Coverage	$ \eta  < 1.52$	$1.5 <  \eta  < 1.8$			
Longitudinal segmentation	1 sampling	1 sampling			
Granularity ( $\Delta\eta \times \Delta\phi$ )	$0.025 \times 0.1$	$0.025 \times 0.1$			
<b>HADRONIC TILE</b>	<b>Barrel</b>	<b>Extended barrel</b>			
Coverage	$ \eta  < 1.0$	$0.8 <  \eta  < 1.7$			
Longitudinal segmentation	3 samplings	3 samplings			
Granularity ( $\Delta\eta \times \Delta\phi$ )					
Samplings 1 and 2	$0.1 \times 0.1$	$0.1 \times 0.1$			
Sampling 3	$0.2 \times 0.1$	$0.2 \times 0.1$			
<b>HADRONIC LAr</b>	<b>End-cap</b>				
Coverage	$1.5 <  \eta  < 3.2$				
Longitudinal segmentation	4 samplings				
Granularity ( $\Delta\eta \times \Delta\phi$ )	$0.1 \times 0.1$	$1.5 <  \eta  < 2.5$			
	$0.2 \times 0.2$	$2.5 <  \eta  < 3.2$			
<b>FORWARD CALORIMETER</b>	<b>Forward</b>				
Coverage	$3.1 <  \eta  < 4.9$				
Longitudinal segmentation	3 samplings				
Granularity ( $\Delta\eta \times \Delta\phi$ )	$\sim 0.2 \times 0.2$				

Figure 23: Summary of geometries for calorimeters [?].

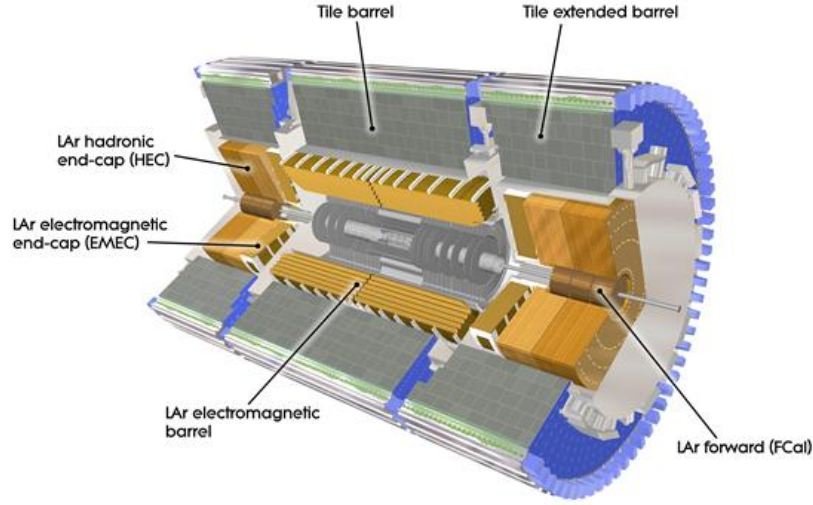


Figure 24: Cut-away view of the ATLAS calorimetry [?].

**Electromagnetic calorimeter** The basic unit of LAr calorimeter consists of a gap filled with liquid argon (1.1-2.2mm) generating the ionized electrons, a copper-kapton electrodes to collect the ionized charge, and a steel-clad lead absorber layer to develop the EM shower (1.13-1.53mm). Bias voltage of 2000V between the electrodes and the absorbers is applied, achieving the drift time of 450ns. The detector is maintained at a constant temperature of  $88K$  by the cryostats surrounding the barrel EM calorimeter.

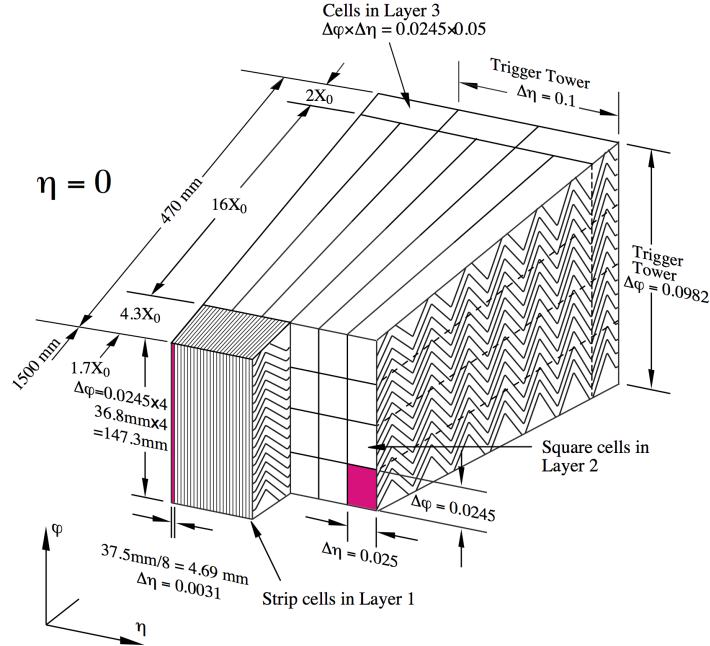


Figure 25: Geometry of barrel LAr sampling layers. Position resolution is addressed by the innermost sampling layer by the highest  $\eta - \phi$  granularity of  $0.0031 \times 0.098$ , and the energy measurement is mainly provided by the second layer with the largest volume. The third layer standing behind in the plot is the tail catcher collecting the information of shower profile. [?].

The geometry and cell segmentation varies between barrel and endcap depending on the required function. Figure 25 (b) illustrate the segmentation in the barrel ECM. 3 sampling blocks are placed along shower with different  $\eta - \phi$  segmentation. The first sampling layer has the finest  $\eta - \phi$  granularity ( $0.0031 \times 0.098$ ), identifying the precise angular position of the incident particle. The second sampling addresses the largest volume ( $16X_0$ ) layer contains the most of shower in which the energy is mainly measured. The third sampling layer is intended to measure the very tail of EM showers, providing the information about longitudinal shower profile together with the other layers. The layer units are arranged in an accordion geometry, which is the characteristic to the barrel ECM, designed to be fully hermitic in terms of angular acceptance. In order to compensate for upstream energy loss, a presampling layer is additionally located in front of the EM calorimeter for both barrel and the endcaps. The total thickness amounts to  $> 22X_0$  in the barrel and  $> 24X_0$  in the endcap, which can fully accommodate the EM showers of photons or electrons in an energy of a few TeV. The transition region between the barrel and endcaps ( $1.37 < |\eta| < 1.52$ ) is dedicated to detector services and is thus not fully instrumented.

The designed resolution is given in Eq. 67 [?]:

$$\frac{\sigma_E}{E} = \frac{10\%}{\sqrt{E}} \oplus \frac{17\%}{E} \oplus 0.7\%. \quad (65)$$

The energy resolution for the off-line objects can be further improved through the dedicated calibration exploiting the full detail of the shower and the information from the other detector. This high pointing resolution is the characteristic advantage of the ATLAS EM calorimeter, which vastly benefits the particle identification (photon, high energy tau etc.) as well as MET reconstruction.

**Hadronic Calorimeter** The ATLAS hadronic calorimeter consists of the barrel Tile HC ( $|\eta| < 1.7$ ) and endcap LAr HC. The Tile HC is the sampling calorimeter composed by a periodic units of plastic scintillators tiles and steel absorber. Figure 26 (a) schematizes one module in the Tile HC. Generated scintillation photons are read out by the photo-multiplier tubes equipped at the ends of the module via wavelength shifting fibers.

Barrel Tile HC is segmented into three sections, the central barrel section ( $|\eta| < 1.0$ ) and the two extended barrel sections ( $1.0 < |\eta| < 1.7$ ), using different channel dimensions. There are three sampling layers along the shower development with the thickness of  $1.5\lambda$ ,  $4.1\lambda$  and  $1.8\lambda$  for barrel, and  $1.5\lambda$ ,  $2.6\lambda$  and  $3.3\lambda$  for extended barrel respectively.

The endcap HC is the sampling calorimeter with liquid-argon sensor layers and copper absorber. The choice of material is dominantly based on the durability against the extremely high radiation flux in the forward region.

The intrinsic resolution of barrel Tile HC and endcap LAr HC for an individual hadron jet is given as Eq. 67 [?]:

$$\frac{\sigma_E}{E} = \frac{50\%}{\sqrt{E}} \oplus 3\%, \quad (\text{Tile HC}) \quad (66)$$

$$\frac{\sigma_E}{E} = \frac{100\%}{\sqrt{E}} \oplus 10\%, \quad (\text{Endcap LAr HC}) \quad (67)$$

**Forward Calorimeter** A set of LAr calorimeter layers are arranged in a very forward region close to the beam axis covering  $3.1 < |\eta| < 4.9$ , designed to capture the full content from jets or particles from hard scattering particles from extremely boosted center-of-mass. The location with respect to the adjacent calorimeter systems are illustrated as Figure 26 (b). Forward calorimeter is made by three sampling layers in which both functions of EM calorimeter and hadronic calorimeter are integrated; The first layer is with copper absorber working as EM calorimeter, and the later two layers are with tungsten functioning as EM calorimeter. An overlap with endcap HC is deliberated to realize smooth transition.

#### 2.2.4 Muon Spectrometer

Muon spectrometers are located outermost in the ATLAS, consisting of four sub-detectors; Monitored Drift Tube (MDT); Cathode Strip Chamber (CSC); Resistive Plate Chamber (RPC); and the Thin-Gap Chamber (TGC). The former two are dedicated to precision measurement of muon tracks and the latter two are to triggering. The spectrometer covers the pseudo-rapidity range  $|\eta| < 2.7$  and allows identification of muons with momenta above 3 GeV and precise determination of  $p_T$  up to about 1 TeV with 10% momentum resolution.

The magnetic field for tracking is sourced by the three pieces of toroidal superconducting magnets; two end-cap toroids at the ends of the detector, and a barrel toroid embedded in the space inside the muon spectrometers.  $3.9T$  and  $4.1T$  B-field is provided in the barrel and endcap region respectively. The internal volume of toroidal coils are vacant (“air-core”), in order to reduce the material with which muons experience the multiple scattering, which is one of the limiting factors of the momentum measurement. The integrated

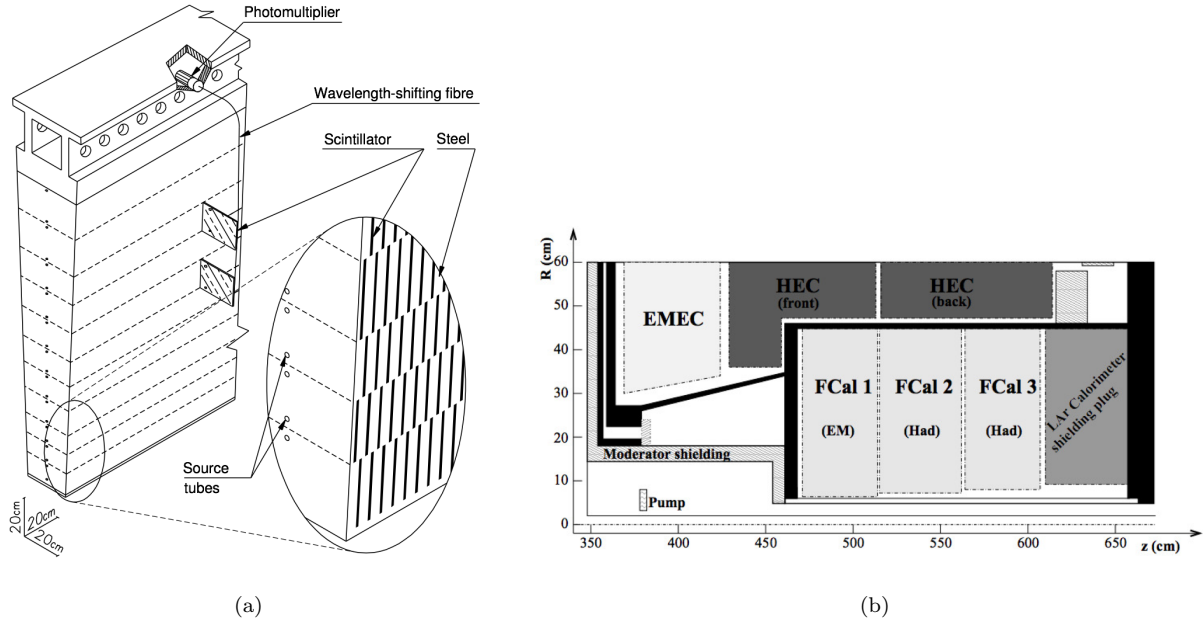


Figure 26: (a) Illustration of a Tile HC module. (b) Alignment of each detectors in an endcap; endcap LAr EM calorimeter (EMEC); endcap LAr Hadronic calorimeter (HEC); and the Forward calorimeter (FCal) [?].

B-filed profile at the position of MDT is shown in Figure 28, while the global schematic of the magnet system is given in Figure 27.

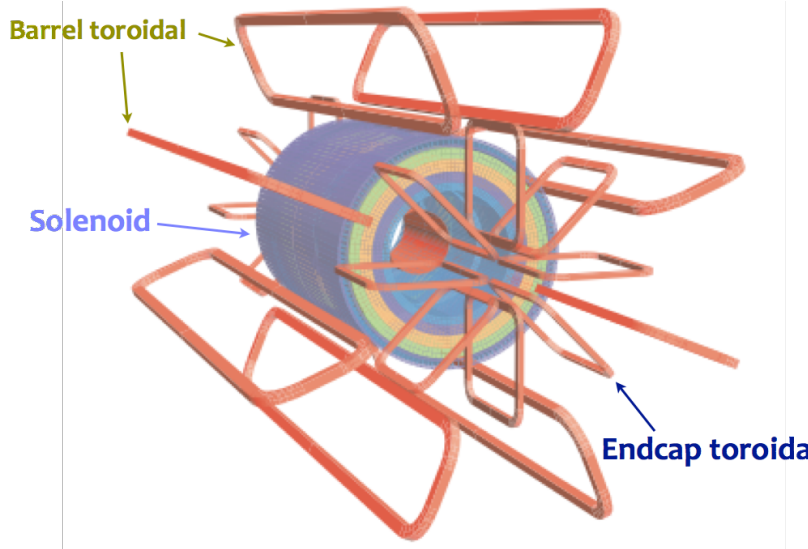


Figure 27: Schematic of the ATLAS magnet system with one central solenoid and 3 toroids (barrel+2 endcaps). [?].

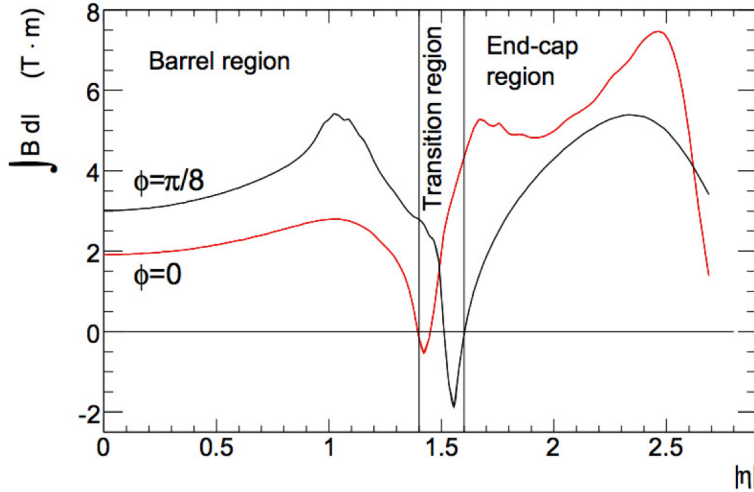


Figure 28: Simulated magnetic field integral provided by a single troid octant, from the innermost MDT layer to the outermost. [?].

**MDT** MDT is a gaseous drift chamber filled with the basic detection elements of 30 mm-diameter aluminum tubes that are covered by a 400  $\mu\text{m}$  thickness wall. Drifting electrons are absorbed in the center of a tube by a 50  $\mu\text{m}$ -diameter tungsten-Rhenium wire with a bias voltage of 3080V is applied, and read out by a low-impedance current sensitive preamplifier. The gas mixture is tuned at Ar : CO<sub>2</sub>() = 93% : 7%, maintaining the maximum drift time of 700ns. The single wire resolution is  $\sim 80 \mu\text{m}$ . There are three layers of MDT chambers located both in barrel and endcap, covering pseudo-rapidity range of  $|\eta| < 2.0$ . The limitation in the  $\eta$ -coverage is determined by its maximum durable rate ( $150 \text{ cm}^{-1} \text{s}^{-1}$ ), instead CSC takes over the role in the further forward region.

**Cathode Strip Chamber** The CSCs are multi-wire proportional chambers covering the forward region ( $|\eta| > 2.0$ ) in the endcaps, providing 2D position of incident particles. It is operated with a gas mixture of Ar (80%) and CO<sub>2</sub> (20%) and with a bias voltage of 1900V. The cells are symmetric in terms of the pitch of readout cathodes and the anode-cathode spacing, which is equally set to 2.54 mm. As the spatial resolution of the CSCs is sensitive to the inclination of tracks and the Lorentz angle, To minimize degradations of the resolution due to these effects, they will be the chamber is fixed at tilted posture so that tracks originating from the IP become orthogonal to the chamber surface.

**Resistive Plate Chamber** The RPCs are digital gaseous detectors specialized in fast timing response for triggering. They are mechanically mounted on the surface in the barrel MDT, covering the pseudo-rapidity range of  $|\eta| > 1.05$ . The elementary detection unit is a gas gap filled with non-flammable gas mixture (94.7% C<sub>2</sub>H<sub>2</sub>F<sub>4</sub>, 5% Iso – C<sub>4</sub>H<sub>10</sub>, 0.3% SF<sub>6</sub>). An uniform high electric field ( $\sim 4900 \text{ V/mm}$ ) is applied so that the ionized electrons amplify themselves by the avalanches. Signal is read out by a metal strip attached on both ends of the gaps, arranged with a pitch of 30 mm - 39.5 mm. The typical spatial and timing resolution achieves 1 cm and 2 ns respectively.

**Thin-Gap Chamber** The TGCs are a special type of multi-wire proportional chambers characterized by the notably small distance between the anode wires and the read out cathode strips (1.4mm). Together

with the highly quenching gas mixture with CO<sub>2</sub> (55%) and n-pentan (45%), a quick drain of secondary electrons is achieved with the timing response of 5 ns. TGCs also contribute to the momentum determination by supplementing the measurement in  $\phi$  by MDT. Three modules are placed per endcap, covering  $1.05 < |\eta| < 2.7$  by the innermost one and  $1.05 < |\eta| < 2.4$  by the two behind. Trigger is generated using tracks in  $1.05 < |\eta| < 2.4$ , while all tracks are utilized for momentum measurement.

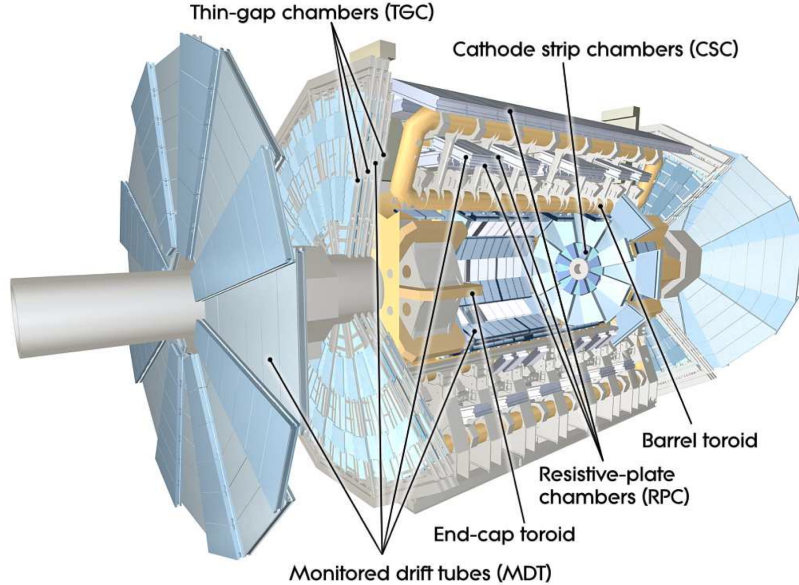


Figure 29: Global view of the ATLAS muon spectrometers [?].

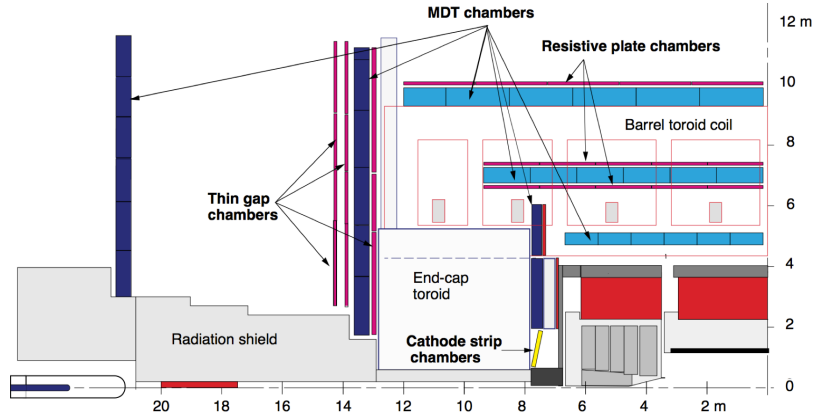


Figure 30: Cross-section of the ATLAS Muon spectrometer [?].

### 2.2.5 Luminosity Detectors

Luminosity determination is particularly important since it provides the reference in normalizing simulated dataset and enables the sensible comparison to data. The instantaneous luminosity is calculated using the formula below:

$$\mathcal{L} = \frac{\mu n_b f_b}{\sigma}, \quad (68)$$

where  $n_b$  is the number of colliding crossings and the  $f_b$  the frequency of the beam circulation.  $\sigma$  is total fiducial cross-section of  $pp$ -interaction including both elastic and inelastic scattering, and  $\mu$  is the average number of such interaction per crossing crossing. While  $\sigma$  is provided by a dedicated calibration measuring the lateral beam profile using overlapping two beams referred as the van der meer scan [?],  $\mu$  is obtained directly by exploiting the rate information from luminosity detectors located in the very forward region nearby the beam pipe. Dedicated calibration and luminosity determination algorithm studied in [?].

Two luminosity detectors mainly contribute to the luminosity measurement:

#### **LUCID** (LUminosity measurements using Cherenkov Integrating Detector)

LUCID are located at the both ends of the ATLAS detector at a distance of 17m from the IP, covering the pseudo-rapidity range of  $5.6 < |\eta| < 6.0$ . The LUCID detector consists of 16 aluminum tubes filled with  $C_4F_{10}$  gas, and designed to count the Cherenkov photons kicked out by charged particles flying along the beam axis which are mainly generated by proton-proton inelastic scattering in the IP. The measurement is translated into luminosity, which is used for online monitoring of the instantaneous luminosity as well as the beam condition.

#### **ALFA** (Absolute Luminosity For ATLAS)

ALFA is located beyond the ATLAS envelope at  $z = \pm 240$  m, sandwiching the beam pipe from top and bottom. The detectors are composed of 8 scintillating fibers, designed to mainly measure the elastic scattering component of the  $pp$ -interaction.

#### **2.2.6 Trigger and Data Acquisition System**

While ATLAS enjoys incredibly high collision rate of about 100 MHz (40 MHz beam crossing crossing together with pile-up), these data cannot entirely read out due to the limitation from data transmission as well as the computation resource. Luckily or unluckily, most of them are junk QCD reactions resulting in cheap low  $p_T$  jets, the rate can be drastically suppressed by requiring hard jets, leptons or  $E_T^{\text{miss}}$  in the events.

A highly sophisticated data acquisition system have been developed for ATLAS, referred as ATLAS Trigger and Data Acquisition System (TDAQ) [?], handling the trigger and readout. The schematic of the readout stream is shown in Figure 31. It consists of a two-staged trigger pipeline served by the hardware-based Level-1 Trigger (L1) and the software-based High-Level Trigger (HLT). The idea is to reject the major trivial QCD events in L1, based on a fast particle reconstruction with a coarse resolution, and perform further filtering in HLT based on using more sophisticated reconstruction and energy measurement, enjoying the timing latency that L1 earns. The benchmark of rate suppression is 100 kHz at the end of L1 and down to 1 kHz after the HLT on average.

The L1 consists of two independent sub-trigger systems: L1Calo, identifies the EM or hadronic clusters in calorimeter and reconstruct primitive jets, electrons, photons and taus (L1 objects) with calibrated energy in EM scale.; L1Muon, identifies and measure the tracks in the muon spectrometer, designed to accept events with muons. The object reconstruction is based on the coarsely segmented blocks of combined detector channel called “trigger tower” with  $\eta \times \phi$  granularity of  $0.1 \times 0.1$ .  $E_T^{\text{miss}}$  is also calculated at the L1 stage by the vectorial sum of the calorimeter deposits, referred as L1XE. Trigger accept is issued by the Central Trigger Processors (CTP) when the L1 objects meet certain criteria in terms of  $p_T$  threshold and number of objects.

In HLT, an offline-like algorithm is employed to refine the energy of L1 objects, or recover the mis-identified objects (typically low  $p_T$  muons) by scanning over whole detector. This is performed by a set of

custom farmwares with a processing time of 0.2s on an average. The event that is triggered by the HLT is subsequently sent to event storage infrastructures outside the ATLAS. Figure 32 illustrates the acceptance rate of HLT in 2016 operation. The performance of triggers relevant to the analysis is dedicatedly overviewed in Sec. 5.1.

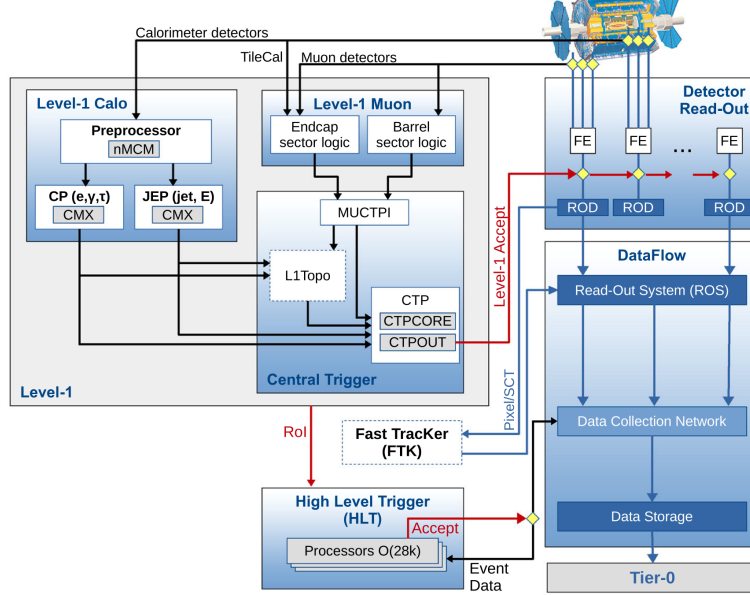


Figure 31: The logic of ATLAS trigger system [?]. Trigger detectors have separated readout line for trigger, sending input information for trigger decision to CTP. CTP reconstruct L1 objects and issue a global accept signal relieving the buffered data, once the trigger criteria are satisfied. The  $(\eta, \phi)$  position of identified trigger object is sent to downstream HLT, in which off-line like software based trigger runs to filter events further. L1 topological trigger (L1 Topo) and Fast Tracker (FTK) have been in commissioning since 2015.

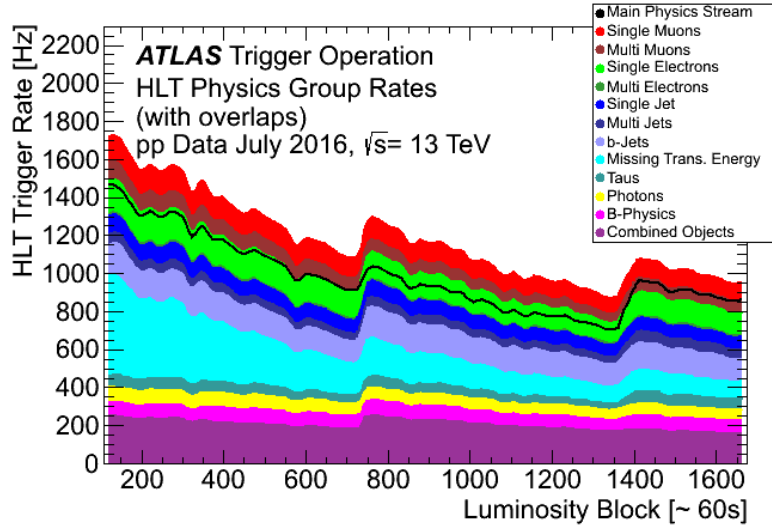


Figure 32: Rate of HLT stream for physics analysis during the 2016 data-taking [?]. Horizontal axis is in unit of lumi-clock, the smallest unit of data-taking in the same configuration.

### 2.3 Recorded Data by ATLAS

The  $pp$ -collision data analyzed in the thesis were collected by ATLAS during 2015 and 2016 at a centre-of-mass energy of 13 TeV. The evolution of the peak luminosity and corresponding average pileup increase are shown in Figure 17.

Data-quality requirements are applied based on each lumi-block, the smallest unit of data-taking defined as the period in the run configuration which varies conditions of beam and detector. Rejected data is typically at the period with more than a certain fraction of modules in the sub-detectors being disabled or in a wrong operation voltage. Integrated luminosity delivered by LHC and recorded in ATLAS during the 2016 operation is shown in Figure 33. After the quality requirement the luminosity of data used for analysis is to  $32.9 \text{ fb}^{-1}$ , to which  $3.2 \text{ fb}^{-1}$  from 2015 data taking is added, amounting to  $36.1 \text{ fb}^{-1}$  with the measurement error of 3.2%.

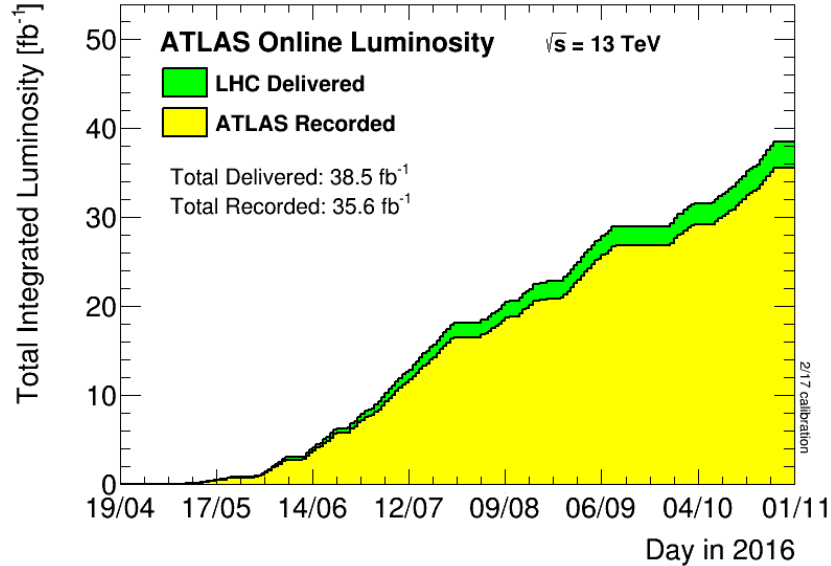


Figure 33: Evolution of integrated luminosity delivered by LHC (green) and recorded in ATLAS (yellow) in 2016 operation [?].

### 3 Object Reconstruction and Identification

The raw detector-level information of particles is translated into physics quantities through the sequence of particle reconstruction, identification and calibration. Though this is partially done at the trigger level, the recorded events are further elaborated by the sophisticated off-line algorithms, enjoying the detail of full event information and absence of limitation in computation resource and time. These particles reconstructed off-line refer to “object”. In this section, the object construction methods are extensively overviewed, particularly with focus on electrons, muons and jets that are used in the gluino search 1-lepton analysis.

#### 3.1 Tracks

Charged tracks are the fundamental units seeding almost in all the off-line particle reconstruction. Standard tracks used in ATLAS refers to ID tracks, reconstructed by the hits created in the inner detector (ID). The MS tracks for muon identification are separately reconstructed, which is described in Sec. 3.5.1. The reconstruction algorithm mainly consists of 4 steps concised as following. More detail can be found in [?].

- Based on the 3-dimensional position information and the readout charge associated to each hit in the silicon detectors, spatial charge profile is constructed event-by-event. Hits from the same particle traverse are merged, using a combination of a pattern recognition technique called connected component analysis (CCA) [?], and a neural network classifier [?]. Seed tracks are then reconstructed from three aligned clusters.
- The seed tracks are extrapolated outward, and the association with the TRT hits are tested using the Kalman fitter characterized by five tracking parameters, with a pion track hypothesis assuming the MIP energy loss in the ID material.
- If the first pattern recognition fit fails, a second fit is attempted based on an electron hypothesis with a modified algorithm that allows energy loss at each hit surface, recovering electrons with significant energy loss due to bremsstrahlung.
- Successful tracks from the Kalman Filter are rerun using the ATLAS Global  $\chi^2$  Track Fitter [?]. A pion or an electron hypothesis is used, depending on which was used successfully in the previous step.

A refined algorithm (Tracking In Dense Environment; TIDE) is used from Run2 [?], to cope with denser particle environment due to the increased pile-up and collision energy. The performance is shown red lines in Figure 34. Typically over 95% of efficiency is maintained.

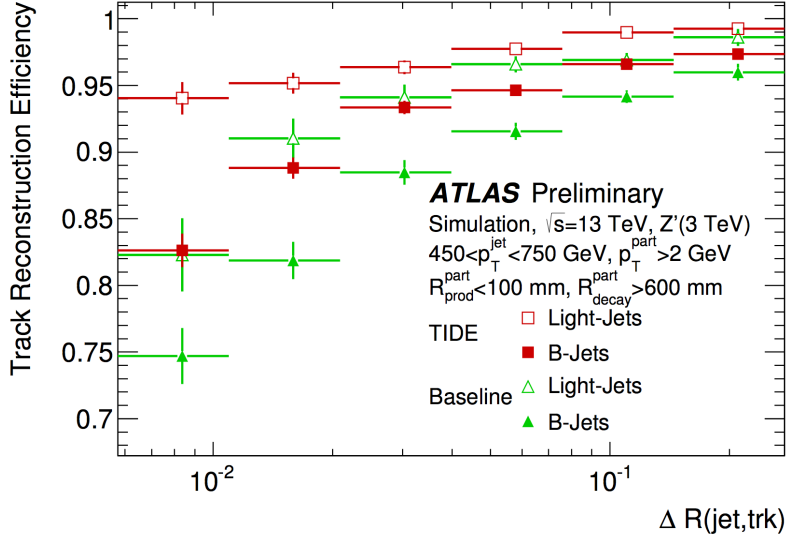


Figure 34: Reconstruction efficiency of tracks in jets as function of angular distance with respect to barycenter of the jet [?]. Red points corresponds to the tracking algorithm used from Run2.

### 3.2 Primary Vertices

The positions of  $pp$ -collisions are identified using the reconstructed ID tracks. These vertices refers to “primary vertices” (PV)<sup>9</sup> and are important for providing reference origin point of retracking and objects calibrations. PVs are reconstructed using the Iterative Vertex Finding algorithm [?] [?], identifying the peak in the  $z$  distribution of extrapolated tracks. The position of identified PVs are further elaborated using the adaptive vertex fitting algorithm [?]. The ID tracks are then re-fit taking advantage of these reconstructed PVs. The retracking procedure in principle lasts until all the tracks are associated to either of the PVs. PVs with less than two associated tracks are discard.

Though 10 – 30 PVs are reconstructed per bunch crossing, usually there is only one PV causing meaningful scattering reaction that fires the trigger. This PV is referred as the “hard-scatter” vertex identified as the PV with the highest sum of associated track  $p_T$  ( $\sum p_T$ ), and the position is used as the origin for object calibration.

### 3.3 Topo-clusters

Topo-cluster (or TC) is the basic unit of energy measurement in calorimeter and used as the input for jet clustering (Sec. 3.6.1) as well as in computing the isolation variables (Sec. 3.8). It is formed by three-dimensionally grouping the cells with significant energy deposit. The clustering algorithm proceed as follow [?]:

- Find cells with energy deposit exceeding  $4\sigma$  from the expected noise level. These cells are identified as seed cells.

---

<sup>9</sup>The “primary” is meant to distinguish with vertices generated by the late decaying particles known as “secondary-vertices”.

- Neighbouring cells touching the boundary of seed cells with energy deposit exceeding  $2\sigma$  from the expected noise level are added to the cluster and become the seed cells for the next iteration.
- Iterate the previous step until the cluster stops growing.
- Split the cluster if there are two or more local maxima with  $E_{\text{cell}} > 500$  MeV.

EM-scaled energy is assigned for TCs.

## 3.4 Electron

### 3.4.1 Reconstruction

The electron reconstruction algorithm proceeds as following, widely referred from [?]:

- **Reconstruction of a EM cluster from energy deposit in the EM calorimeter.**

This is done by the sliding window algorithm. Cells in the all four layers in the EM calorimeter are grouped into  $\eta \times \phi$  towers of  $0.025 \times 0.025$ , and a window defined by the  $3 \times 5$  units of towers are滑过 over the detector. A local maximum in the window energy above 2.5 GeV is identified as the cluster. About 95% (99%) of clustering efficiency are maintained with electrons in  $E_T = 7$  GeV ( $> 15$  GeV).

- **Track-Cluster matching and refitting.**

The EM cluster is matched with a ID track reconstructed based on the electron hypothesis (see Sec. 3.1) in the angular distance  $\Delta R = \sqrt{(\Delta\eta)^2 + (\Delta\phi)^2}$ . Closest track in  $\Delta R$  with respect to the EW cluster is chosen if multiple tracks satisfy the matching criteria. The matched track enjoys further correction by a re-tracking using the Gaussian Sum Fitter (GSF) [?] algorithm in which Bremsstrahlung is dedicated modeled.

- **Energy determination.**

The information from track momentum and calibrated EM cluster energy are combined using a multivariate algorithm [?], achieving the best available energy resolution.

The reconstruction efficiency is measured by  $Z \rightarrow ee$  events. Figure 35 presents the result together with the prediction by MC. Over 96% – 98% of efficiency is achieved for  $E_T > 20$  GeV.

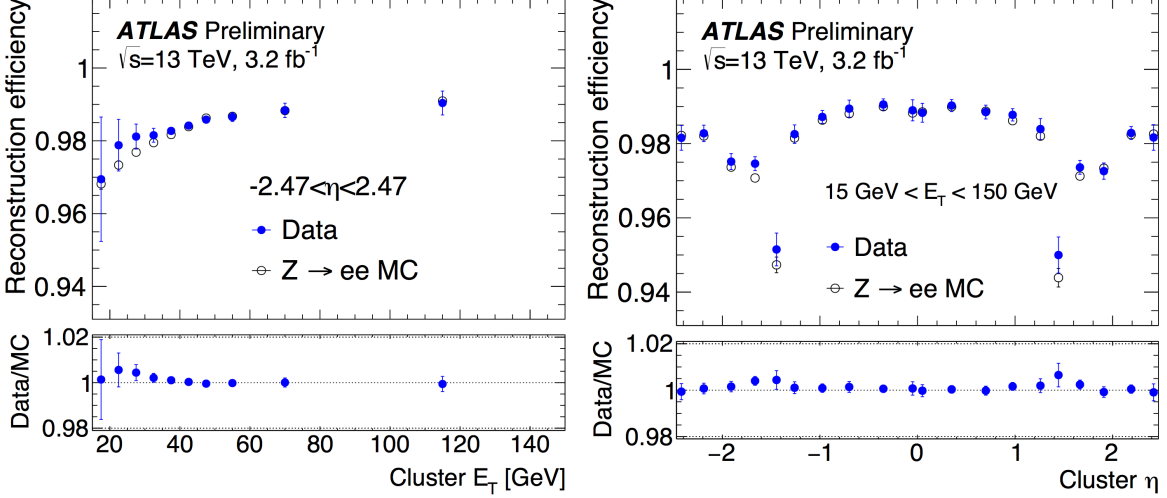


Figure 35: Reconstruction efficiency simulated (grey) or measured (blue) using  $Z \rightarrow ee$  events [?] as function of (a)  $E_T$ , and (b) pseudo-rapidity of reconstructed EM clusters.

### 3.4.2 Identification

Reconstructed electrons are dominated by fakes from pions in the jets, particularly when they are low- $E_T$ . Therefore, a powerful identification algorithm is employed in the subsequent identification, using a multi-dimensional likelihood exploiting all the relevant detector information. The number of input variables amounts up to 17, including the longitudinal and transverse EM shower profile and the number of high-threshold hits in TRT etc. The full list of input variables is found in [?]. The discriminant is given by a form of likelihood ratio, which is known to generally provide the best separation [?]. The signal and background PDF is modeled using the simulated events of  $Z \rightarrow ee$  and di-jet respectively. Figure 36 shows the efficiency of electron identification. Multiple working points are available with different cut value in the likelihood ratio. In the analysis, two working points “Loose” and “Tight” are used, which corresponds about 90% and 70% of efficiencies at  $E_T = 30$  GeV.

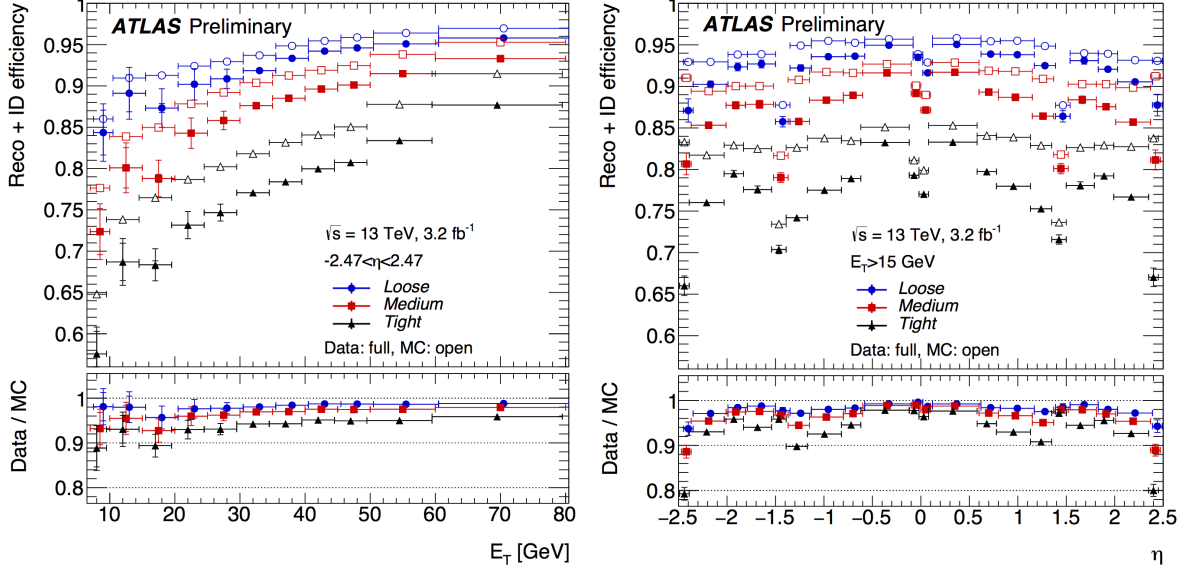


Figure 36: Electron identification efficiency as function of (a)  $E_T$ , or (b) pseudo-rapidity of reconstructed electron candidates [?].  $Z \rightarrow ee$  events are used for both MC and data.

### 3.4.3 Calibration

The electron calibration consists of several different procedures, differently applied to simulation and data. The flow of steps is illustrated in Figure 37.

#### A MC-based calibration using BDT

Though the energy of cell deposit in EM calorimeter and electron cluster is already calibrated in EM scale, it still suffers from residual due to the energy loss in the material upstream of the calorimeter, energy leakage out of the either the reconstructed clusters or EM calorimeter and so on. A multivariate algorithm (BDT regression) is employed, to estimate the true energy from the various input including the raw energy of reconstructed electron, as well as other angular position, shower profile and hit information from other auxiliary detectors such hadronic calorimeter. The full detail can be found in [?] [?].

#### Longitudinal calorimeter layer inter-calibration

The scales along longitudinal layers is equalized in data with respect to simulation, prior to the determination of the overall energy scale, in order to ensure the correct extrapolation of the response in the full  $p_T$  range. This is only applied in data.

#### Non-uniformity correction in $\phi$

A set of corrections are applied to data, to account for various on-line instrumental effects not included in simulation such as non-optimal high voltage regions, geometric effects such as the inter-module widening or biases in the LAr calorimeter electronic calibration.

#### Residual scale calibration on data / Resolution correction on simulated electrons.

The residual mis-calibration in data is corrected by shifting the energy scale so that it agrees with the expectation from simulation. This is done by comparing the mass of Z-peak in  $Z \rightarrow ee$  events.

It is found that the resolution in data is slightly worse than that in simulation using the same event sample. The corrections are derived and applied to simulation to match the data.

Numerous minor corrections follow additionally, which is detailed in [?]. The calibration is widely validated using data events of  $J/\psi \rightarrow ee$  and  $Z \rightarrow ee$ .

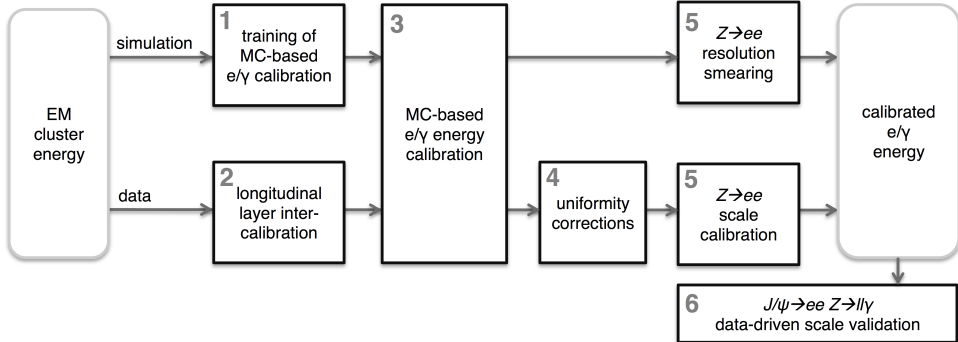


Figure 37: Flow chart of electron calibration applied respectively MC and data [?].

### 3.5 Muon

#### 3.5.1 Redconstruction

Muon tracks are reconstructed independently from ID, referred as MS-tracks. The tracking begins with finding the hits inside each MDT/CSC chamber and forming small track segments per chamber. A Hough transform is employed to convert the bending detector plane geometry into flat plane. A straight-line fit are then performed on the flattened plane for the track segments. The hits in RPC and TGC are used to determine the coordinate orthogonal to the MDT/CSC detector plane. The search algorithm employ a loosened requirement on the compatibility of the track and the hits, to account for the muon energy loss by interaction with material.

The trajectory and momentum of muons are decided by a synergy between the reconstructed MS track and the measurement by the other detectors. There are four different schemes of combination [?]:

**Combined muons:** A MS track is matched to a reconstructed track in the ID, and the measurements of the momenta are combined.

**Segment-tagged muons:** A fragmet of MS track is matched with an ID track, with the momentum taken from the ID track.

**Standalone muons:** MS tracks found outside the ID acceptance ( $2.5 < |\eta| < 2.7$ ), with the momentum quoted from the MS track.

**Calorimeter-tagged muons:** A special type of reconstruction dedicated to muons traveling to the inactive “crack of the MDT at  $|\eta| < 0.1$ . The ID tracks with  $p_T > 15$  GeV associated calorimeter deposit consistent with a minimum ionizing particle are tagged, with the momentum of ID track.

In this analysis, the combined muons is always in defining muons, while the segment-tagged muons are used for correcting the MET calculation as described in Sec. 3.9.

### 3.5.2 Identification

Additional identification requirements are imposed to purify the sample of reconstruction muons. Cuts on following three variables are applied:

$\sigma(q/p)$ : Fitting error of a tracking parameter  $q/p$  associated with the quality of measurement.

$\rho'$ :  $p_T$  difference between ID and MS track normalized by the  $p_T$  of the combined track.

$\chi^2$ : A generic measure of fit quality defined as normalized  $\chi^2$  of the combined track fit.

The Medium working point defined in [?] is used throughout the analysis, where only  $\sigma(q/p) < 7$  is required. Figure 38 summarizes the performance of reconstruction and ID for muons.

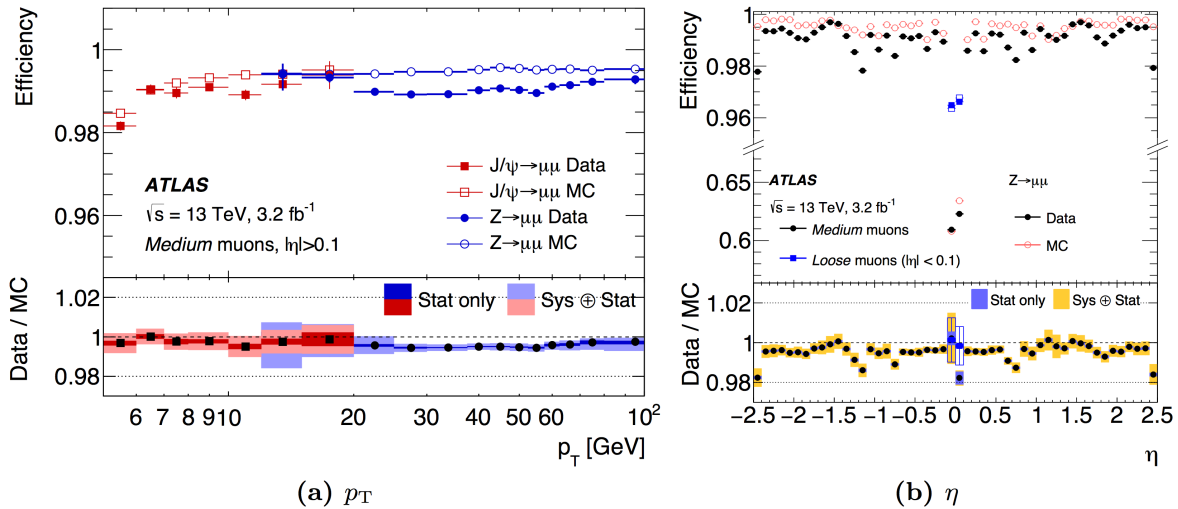


Figure 38: Simulated / measured efficiency for reconstruction and identification of muons, using  $J/\psi\mu\mu$  and  $Z \rightarrow \mu\mu$  events [?].

### 3.5.3 Calibration

As the momentum of a muon track is already well-representing the particle-level momentum of muon, the scale calibration only subjects to a series of minor corrections, accounting for the imperfect knowledge of the magnetic field integral inside the detector, and the energy loss of muons traverse through the calorimeter or other materials between the interaction point and the MS.

The momentum correction is performed on each muon based on the formula below [?]:

$$p_T^{\text{Cor.}} = \frac{s_0 + p_T^{\text{MC}}(1 + s_1)}{1 + \Delta r_0 g_0 + \Delta r_1 p_T^{\text{MC}} g_1 + \Delta r_2 (p_T^{\text{MC}})^2 g_2} \quad (69)$$

where  $p_T^{\text{MC}}$  and  $p_T^{\text{Cor.}}$  represent respectively the momentum before and after the correction, and  $g_m (m = 0, 1, 2)$  are random numbers generated by an uniform PDF ranging from 0 to 1. The numerator corresponds

to the scale correction, and the denominator is responsible for the correction of resolution modeling by MC. The parametrization of denominator is based on the fact that muon resolution obeys a  $p_T$  dependence of:

$$\frac{\sigma(p_T)}{p_T} = \frac{a}{p_T} \oplus b \oplus c \cdot p_T. \quad (70)$$

The coefficients  $s_i$ ,  $\Delta r_i$  are determined bin-by-bin in  $(\eta, \phi)$ , by applying a template fit on  $J/\psi \rightarrow \mu\mu$  and  $Z \rightarrow \mu\mu$  events.

## 3.6 Jet

### 3.6.1 Jet Clustering

Jet reconstruction starts employs the AntiKt algorithm [?] using the topo-clusters (TCs) calibrated with EM scale as input. The basic step of the algorithm is to merge the proximate two TCs based on a distance measure defined by:

$$d_{i,j} = \min(p_{T,i}^{-2}, p_{T,j}^{-2}) \frac{\Delta R_{i,j}^2}{r^2} \quad (71)$$

where  $i$  and  $j$  denote the index of topo-clusters, and  $\Delta R_{i,j}^2$  is the angular distance between the them.  $r$  is the cone parameter dictating the typical size of resultant jets, which is set to  $r = 0.4$  in the analysis. The two TCs with smallest  $d_{i,j}$  are merged in each step, and the iteration continues until it becomes:

$$\min_{i,j} [d_{i,j}] > \min_i [p_{T,i}^{-2}]. \quad (72)$$

The anti- $k_T$ jet clustering is characterized by the negative power index on the  $p_T$  in the metric  $d_{i,j}$ , where soft clusters are added in the jet at the early stage of iteration. This results in a well-defined boundary of jets, reflecting the feature that the jet clustering is insensitive to soft components on which perturbative QCD does not provide robust prediction. This collinear- and infrared-safe is an extremely welcomed feature since it provides well-defined observables allowing one to straightforwardly compare the theory and data, benefiting either the theoretical description and the jet calibration in experiment.

### 3.6.2 Energy Calibration

As the energy of TC is calibrated in the EM scale, clustered jet needs extra calibration to account for the hadronic interaction activity. Particle-level jets in simulated events (referred as “truth jets”) are used for the reference of the truth energy. They are reconstructed using the anti-kt algorithm with  $R = 0.4$  using stable, final-state particles as input. The input particles are required to have a lifetime of  $c\tau > 10m$ . Muons, neutrinos, and particles from pile-up activity are excluded. Truth jets with  $p_T > 7$  GeV and  $|\eta| < 4.5$  are used for the calibration. In simulated events, corresponding reconstructed calorimeter jets can be found by geometrically matching in terms of the  $\Delta R := \sqrt{(\Delta\eta)^2 + (\Delta\phi)^2}$

A dedicated calibration procedure detailed in [?] is employed to restore the energy to that of truth jets reconstructed at the particle-level energy scale. It mainly proceeds as following stages:

#### Origin correction

The angular coordinates assigned to each topo-cluster is based on the origin defined by the designed IP position with which the actual hard-scatter vertex is displaced in  $z$ -axis direction. The jet orientation

is recalculated based on the refined origin defined by the position of the reconstructed vertex that the jet is associated with [?].

### Pileup subtraction

The contribution of particles from pile-up jets either in the same crossing crossing (“in-time pile-up”) or those nearby (“out-of-time pile-up”) is removed using the technique of an area-based  $p_T$  density subtraction [?] applied at the per-event level, followed by a residual correction derived from the simulation. The correction is characterized as:

$$p_T^{\text{corr.}} = p_T^{\text{reco.}} - \rho \times A - \alpha \times (N_{PV} - 1) - \beta \times \mu, \quad (73)$$

where  $p_T^{\text{reco.}}$  and  $p_T^{\text{corr.}}$  are the transverse momentum before and after the correction respectively.  $A$  is the jet area which roughly corresponds to the area jet energy distributes in  $\eta - \phi$  plane calculated using the ghost-association [?].  $\rho$  is the average  $p_T$  density from the contribution of pile. The idea is to treat the pile-up as an uniform noise level over the detector, and the contribution is proportional to the area the jet is overlaying to it. The residual impact of pile-up is found to be linear in terms of the number of reconstructed primary vertices ( $N_{PV}$ ) and the average number of interactions per crossing crossings ( $\mu$ ) independent of one another. The linear coefficients  $\alpha$  and  $\beta$  are determined using the simulation as function of  $p_T$  and  $\eta$  of the jet.

### MC-based calibration

The main energy calibration is provided by comparing the energy of reconstructed jets to the corresponding truth jets in the simulated di-jet events from PYTHIA. The energy response  $R$  and  $\eta$  response  $R_\eta$  defined by

$$R = \left\langle \frac{p_T^{\text{reco.}}}{p_T^{\text{truth}}} \right\rangle, \quad R_\eta = \left\langle \frac{\eta^{\text{reco.}}}{\eta^{\text{truth}}} \right\rangle, \quad (74)$$

are calculated in various  $p_T$  and  $\eta$  bins. The obtained response is used for the scale that brings the energy of reconstructed jets to the particle-level energy scale. The conversion from the EM scale to the hadronic scale essentially happen in this stage.

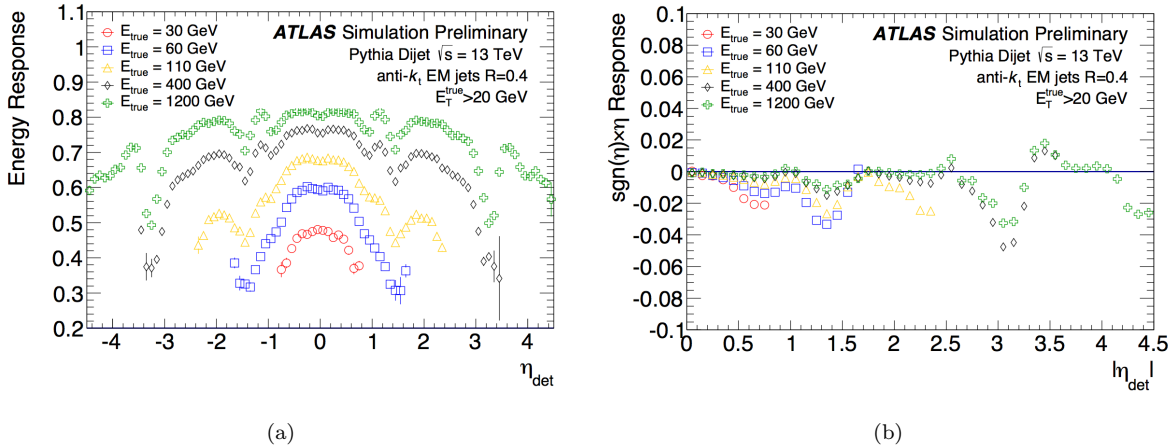


Figure 39: (a) Energy response and (b)  $\eta$  reconstruction bias defined in Eq. 74 before the MC-based calibration. [?]

## Global Sequential Calibration

While only the information on topo-clusters are used for the jet energy determination so far, further improvements are achieved by applying corrections exploiting the global detector information from calorimeter, muon detector, and reconstructed tracks from inner detector.

The procedure involves 5 independent stages, referred as the Global Sequential Calibration (GSC) [?], killing residual dependence of jet energy scale on the number of associated tracks or the spatial energy profile of the jet and etc. using the simulation.

The most important function of GSC is adding robustness against varying jet flavors, in particular between quark-initiated jets and gluon-initiated, in jet energy measurement.

## Residual in-situ calibration

A residual calibration is derived using in-situ measurements applied only to data, accounting for the differences in the jet response between data and MC simulation. The differences is quantified using data events of  $\gamma + \text{jet}$  and  $Z \rightarrow \mu\mu + \text{jet}$ , by balancing the  $p_T$  of a jet against the well-measured counterpart objects as reference.

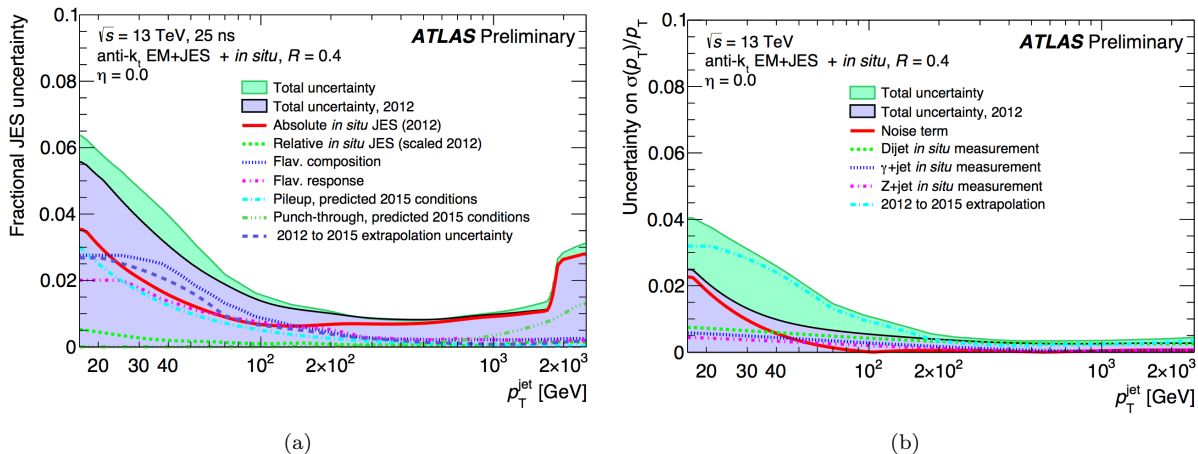


Figure 40: (a) Uncertainty on jet energy scale (JES), and (b) uncertainty on the relative resolution, with the breakdown of each sources being attached [?].

### 3.6.3 B-tagging

Hadron jets originating from  $b$ -quarks can be exclusively identified by taking advantage of the long lifetime ( $c\tau \sim 450 \mu\text{m}$ ) of  $b$ -hadrons, creating distinct secondary decay vertices. Four independent sub-algorithms (IP2D, IP3D, SV, JetFitter) exist addressing unique  $b$ -finding power. Their outcomes are combined by inputting them into a BDT classifier (MV2), which output is used as the final discriminant. Each sub-algorithm works as following (widely referred from [?] [?] [?]):

**Impact parameter based algorithm: IP2D and IP3D** IP2D and IP3D are the likelihood based classifiers using the impact parameter information of tracks associated to the jets. The track level likelihood is defined in terms of the transverse impact parameter  $d_0$  and its significance  $\sigma(d_0)$  (and longitudinal impact

parameter  $z$  for the case of IP3D), and modeled using MC respectively for the tracks in the  $b$ -jet and light-flavor jet. The jet-level likelihood is calculated by taking the product over all the associated tracks to the jet. The IP2D (IP3D) is then defined by the likelihood ratio between the  $b$ -jet and light-flavor jet hypothesis.

**Secondary vertex finding algorithm: SV** The SV algorithm [?] explores secondary vertex finding algorithm in an explicit manner. After a set of qualification requirements on tracks in the jet, all the seed tracks are paired testing the consistency with the two-track vertex hypotheses. Found vertices consistent with the decays of other long-lived particles (such as  $K_s$  or  $\Lambda$ ), photon conversions or hadronic interaction with a material are rejected. As further requirements, the sum of the two impact parameter significances of the two tracks is required greater than 2, and vertices with the invariant masses exceeding 6 GeV are removed given the masses of the  $b$ - or  $c$ -hadrons. Vertex with the highest invariant mass is chosen if multiple candidates are found.

**Decay chain multi-vertex algorithm: JetFitter** JetFitter [?] is a kinematic fittering algorithm, exploiting the topological structure of weak  $b$ - and  $c$ -hadron decays inside the jet and attempt to reconstruct the full  $b$ -hadron decay chain. Using the Kalman fitter, it finds a common line to which the PV and the bottom and charm vertices belong, approximating the  $b$ -hadron flight path, as well as their positions. The notable advantage of this approach is that the vertices of  $b$ - and  $c$ -hadron can be reconstructed, even when only a single track is attached to any of them.

**Combining algorithm: MV2** A Boosted Decision Tree (BDT) is used to combine the output from the four algorithms. The input variables includes the likelihood values from IP2D and IP3D, properties of reconstructed secondary vertex (mass, position etc.) and the associated tracks providing by SV, and the information of fitted vertices including subsequent decays of  $b$ -hadrons from JetFitter. The full list can be found in [?].

The output distribution and the performance is shown in Figure 41. Although the input information between the algorithms is highly correlated, the combined performance shows drastic improvement over those of either single algorithm.

Multiple working points are defined to provide different relative discrimination power against light-flavor jets and  $c$ -jets. For example, MV2c10 (MV2c20) are designed to address more rejection power towards  $c$ -jets, trained using the background sample with light-flavor jets admixed with  $c$ -jets by 10% (20%). The MV2c10 working point is used in the analysis.

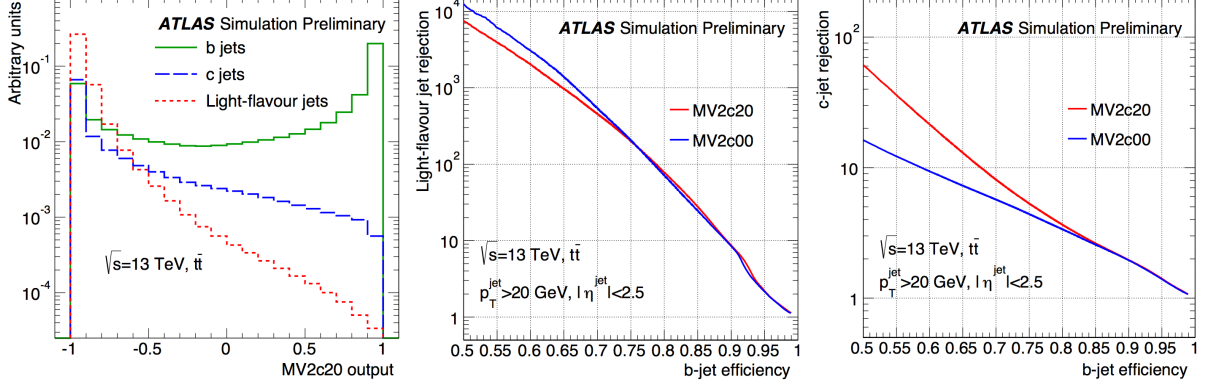


Figure 41: Left plot presents the output BDT distribution for signal (b-quark jets) and backgrounds (light flavor and c-quark jets). The score of MV2c20 is shown in which c-jets rejection is reinforced. The middle and right plot respectively show the signal efficiency vs light flavor jet rejection, and vs c-jet rejection. [?]

### 3.6.4 Pile-up Jet Tagging and Rejection

Significant fraction of reconstructed jets are originated from pile-up, particularly when they are low- $p_T$ . In order to suppress the contamination, a pile-up jet rejection is applied using the Jet Vertex Tagger (JVT) discriminant [?] exploiting the vertex information.

JVT is based on a 2D-likelihood function in terms of the corrected Jet Vertex Fraction (corr. JVT) and  $R_{p_T}$ :

$$\text{corrJVF} := \frac{\sum_k p_T^{\text{trk}_k}(\text{PV}_0)}{\sum_l p_T^{\text{trk}_l}(\text{PV}_0) + \sum p_T(\text{PU})/(\kappa \cdot n_{\text{trk}}^{\text{PU}})}, \quad \sum p_T(\text{PU}) = \sum_{n \geq 1} \sum_k p_T^{\text{trk}_k}(\text{PV}_n)$$

$$R_{p_T} := \frac{\sum_k p_T^{\text{trk}_k}(\text{PV}_0)}{p_T^{\text{jet}}}, \quad (75)$$

where  $\text{PV}_0$  denotes the hard-scatter vertex and  $\text{PV}_j (j \geq 1)$  the other primary vertices presumably due to the in-time pile-up interaction. JVF (Jet Vertex Fraction) was a variable originally used for the pile-up suppression in Run1 [?] defined by the fraction of charged tracks associated to the hard-scatter vertex:

$$\text{JVF} := \frac{\sum_k p_T^{\text{trk}_k}(\text{PV}_0)}{\sum_l p_T^{\text{trk}_l}(\text{PV}_0) + \sum p_T(\text{PU})}. \quad (76)$$

While the performance of JVF is sensitive to the pileup since  $\sum p_T(\text{PU})$  scales linearly according to number of pileup,  $\sum p_T(\text{PU})$  is divided by the number of PU tracks  $n_{\text{trk}}^{\text{PU}}$  in the corrJVF to kill the linear dependency, together with the scale factor  $\kappa = 0.01$  conserving the absolute normalization of the PU term.  $R_{p_T}$  is the charged energy fraction in the jet, design to address to the jets with small number of tracks leading to low corrJVF value. A 2D-likelihood profile in terms those two variables is respectively modeled for hard-scatter jets and pile-up jets, and the JVT is defined as likelihood ratio.

Figure 42 shows the typical separation. The JVT selection  $\text{JVT} > 0.57$  is applied for jets with  $20 \text{ GeV} < p_T < 60 \text{ GeV}$  and  $|\eta| < 2.4$ , in which the pile-up jets dominantly populates.

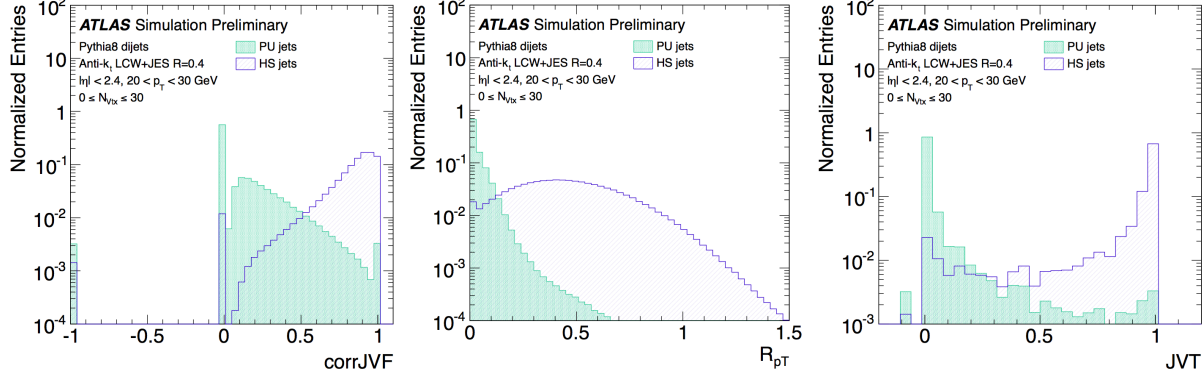


Figure 42: Left two plot display the distribution of input variables for JVT; corrJVF and  $R_\phi$ . corrJVF =  $-1$  represents the jets with no associated tracks. The right plot is resultant output likelihood score, JVT [?].

### 3.7 Overlap Removal between Reconstructed Objects

Electrons, muons and jets are reconstructed in parallel, allowing the ambiguity that an identical particle is reconstructed or identified as multiple types of particles simultaneously. For instance, electrons are typically reconstructed either as electrons and jets. This is designed to provide flexibility in the object definition to satisfy various needs by analyses.

A sequence of “overlap-removal” procedure is applied to resolve the ambiguity and avoid the double-counting, based on the angular distance  $\Delta R = \sqrt{\eta^2 + \phi^2}$  between them.

The algorithm begins with the electron-jet overlap removal. Any light-flavor jet<sup>10</sup> reconstructed within  $\Delta R < 0.2$  with respect to identified electrons is rejected. The electron is otherwise removed if the overlapping jet is b-tagged jet, to avoid rejecting b-jets due to the non-prompt lepton nearby caused by the decays of b-hadrons. Next, to remove bremsstrahlung from muons followed by a photon conversion into electron pairs, electrons lying within  $\Delta R < 0.01$  of a preselected muon are discarded.

Subsequently, the contamination of muons from heavy-flavored hadron decays is suppressed by removing muons that lie within  $\Delta R < \min(0.04 + (10 \text{ GeV})/p_T, 0.4)$  of any remaining jet, or within  $\Delta R < 0.2$  of a b-tagged jet or a jet containing more than three tracks with  $p_T > 500 \text{ MeV}$ . In the former case, the  $p_T$ -decreasing angular separation mitigates the rejection of energetic muons close to jets in boosted event topologies. Finally, jets reconstructed within  $\Delta R < 0.2$  of remaining electrons or muons are excluded.

The identification of hadronically decaying taus and photons are not exploited in the analysis, since they are not explicitly used as objects in event selections. Instead, those with sufficiently high transverse momentum pass the jet reconstruction as well as the JVT requirement, thus treated as jets in the analysis.

### 3.8 Fake Leptons and the Isolation Requirement

Light flavor leptons (electrons or muons) produced in LHC subject to two types; “prompt leptons” directly originated from the hard scattering via decays of real and virtual gauge bosons; “non-prompt leptons”

<sup>10</sup>defined as reconstructed jets with b-tagging score MV2c10<0.1758 which corresponds to 85% efficiency for real b-jets.

generated via decays of heavy flavor hadrons (contains  $b$  or  $c$  quarks) and tau leptons, or pair creation of photons (mostly stemming from  $\pi_0$  in jets). The leptons interested in the new physics or EW physics always refer to the prompt leptons, while non-prompt leptons are trivial and disturbing, degrading the use of leptons in the analysis. There are also a type of reconstructed leptons by wrongly identified pions from jets. In the thesis, these unwilling kinds of leptons (non-prompt leptons and pions) are simply referred as “fake lepton”, and suppressed by employing the extra requirement described as follows.

**Impact parameter requirement** Non-prompt leptons are generated in relatively displaced position with respect to the primary vertex. Therefore, the information of transverse impact parameters address a nice discriminating power. The selection used in the analysis is as Table 8. While the  $d_0$  and  $|z_0 \sin \theta|$  of prompt-leptons populate close to 0, those for non-prompt leptons result in wide distributions, leading many of them to be rejected.

Table 8: Summary of impact parameter requirements used in the analysis.  $d_0$  and  $z_0$  is the transverse and longitudinal impact parameter respectively.  $\sigma_{d_0}$  is defined by the error matrix of the track fit

	Electron	Muon
$ d_0/\sigma_{d_0} $	< 5	< 3
$ z_0 \sin \theta $	< 0.5 mm	< 0.3 mm

**Isolation** While the path of flight of prompt-leptons rarely overlap with other particles, fake leptons generally fly closely by jets for their origin. Relatively higher jet activity around fake leptons is expected, therefore the isolation requirement with respect to proximate cluster or tracks provide significant rejecting power of fake leptons.

Two isolation variables are defined:

**Calorimeter isolation** ( $E_T^{\text{cone } 0.2}$ ): Sum of transverse energies by the calibrated topo-clusters with  $\Delta R < 0.2$  with respect to the lepton. An  $E_T, \eta$  dependent pileup correction is applied. For electron, the energy leakage due to the bremsstrahlung is compensated.

**Track isolation** ( $p_T^{\text{cone } 0.2}$ ): Sum of transverse momentum of tracks within the angular distance of  $R = \min(0.2, 10 \text{ GeV}/p_T)$  with respect to the lepton. The variable cone size is intended to loosen the isolation cut for high- $p_T$  leptons, based on the fact that most of fake leptons are below 20 GeV.

The isolation requirement is done by applying a cut in a 2D-plane of  $E_T^{\text{cone } 0.2}$  and  $p_T^{\text{cone } 0.2}$ . In the analysis, the `GradientLoose` working point is chosen, in which a  $p_T$ -dependent cut is applied designed to recover the efficiency in high- $p_T$ . Figure 43 shows the isolation efficiency respectively for electrons and muons.

### 3.9 Missing Transverse Energy

Missing Transverse Energy ( $E_T^{\text{miss}}$ ) is an extremely important proxy to new physics since it contains the kinematical information of invisible particle.  $E_T^{\text{miss}}$  is calculated by the transverse momentum imbalance of visible particles, using the reconstructed objects as well as isolated tracks that do not associate to any

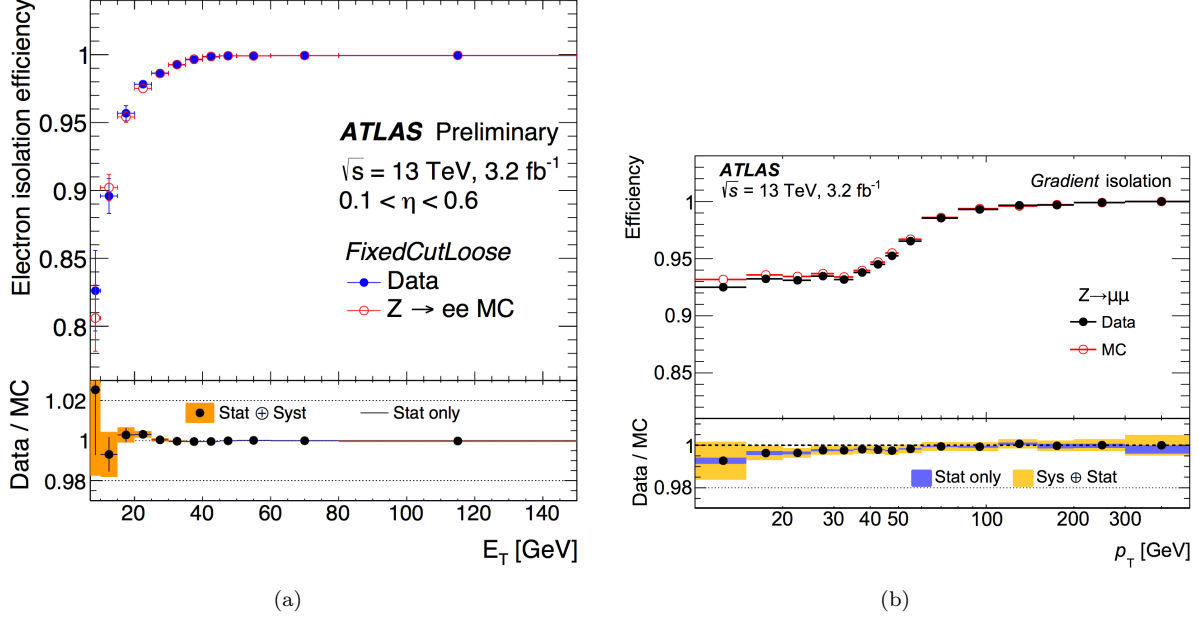


Figure 43: Measured and expected efficiency for isolation requirement for (a) electrons [?] and (b) muons [?], both using the  $Z \rightarrow ee/\mu\mu$  events. The `FixedCutLoose` working point is shown for the electrons where  $E_T^{\text{cone} 0.2}/E_T < 0.2$  and  $p_T^{\text{cone} 0.2}/E_T < 0.15$  is applied.

reconstructed objects referred as the soft term. It is constructed by four independent terms as shown in Eq. (77):

$$E_T^{\text{miss.}} := - \sum \not{E}_T^e - \sum \not{E}_T^\mu - \sum \not{E}_T^{\text{jet}} - \not{E}_T^{\text{soft}}. \quad (77)$$

Input reconstructed objects for the first three terms in Eq. (77) are fully calibrated and the ambiguity between them is resolved by the overlap removal. Jets with  $p_T > 20$  GeV are included in the jet term in the MET calculation, otherwise subjected to the soft term with the track momenta. Jets failed in the JVT selection is totally excluded from the MET calculation to prevent the contribution from pile-up.

The track soft term  $\not{E}_T^{\text{soft}}$  (TST) [?] accounts for the residual visible momentum mainly from soft jets and unidentified muons. It is constructed by the tracks that are not associated to any jet, and are isolated by  $\Delta R > 0.2$  from any reconstructed EM clusters. The momenta of tracks found to be associated with reconstructed muons are replaced into that by the combined ID+MS muon tracks. Tracks have its track momentum uncertainties larger than 40%, and high- $p_T$  tracks ( $p_T > 200$  GeV in  $|\eta| < 1.5$  or  $p_T > 150$  GeV in  $|\eta| > 1.5$ ) with questionable quality of momentum measurement satisfying following conditions are removed to prevent potential large error in the calculation:

$$p_T^{\text{cone} 0.2}/p_T > 0.1, \text{ and } \frac{E_T^{\text{cone} 0.2}}{p_T + p_T^{\text{cone} 0.2}} < 0.6, \text{ and } \frac{p_T^{\text{cone} 0.2}}{p_T + p_T^{\text{cone} 0.2}} < 0.6 \quad (78)$$

### 3.10 Object Definition in the Analysis

The requirements for objects used in the analysis is summarized in Table 9. For electrons and muons, two types of working point are defined; “baseline” is the loose selection criteria oriented to veto extra prompt

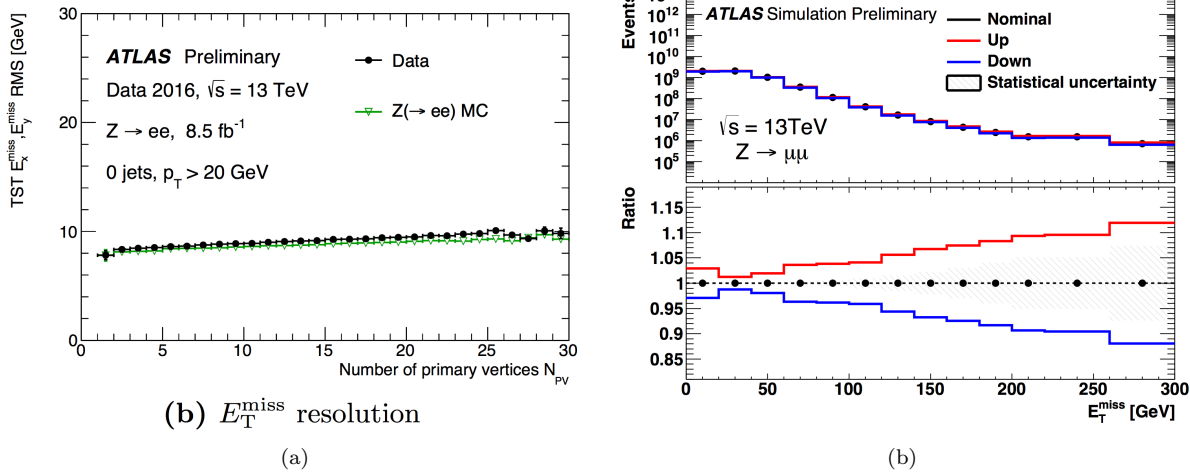


Figure 44: (a) Pile-up dependency of resolution on the met soft term, and (b) the absolute resolution, simulated or measured using  $Z \rightarrow \ell\ell$  events in which the soft terms is zero with ideal measurement [?].

leptons in the event; “signal” is the tighter working point aiming to reject fake leptons where the impact parameter cut, isolation requirement and tighter identification are imposed in on top of the baseline requirement. Signal regions are defined with exactly one baseline and signal lepton, given that the targeted signal events contain exactly one prompt lepton. Jet used in the analysis is uniquely defined. JVT cut is required to avoid the impact by pile-up on the analysis.

Table 9: Summary of all baseline and signal object selection. In addition to the listed criteria, objects are required to pass the reconstruction, identification and overlap removal. The  $p_T$ -threshold is based on the transverse momentum after calibration.

Electrons	Baseline	Signal
$p_T$	$p_T > 7 \text{ GeV}$	$p_T > 10 \text{ GeV}$
Identification	Loose <sup>11</sup>	Tight <sup>12</sup>
Isolation	-	GradientLoose
Impact parameter cuts	-	$z_0 < 0.5 \text{ mm},  d_0 /\sigma(d_0) < 5$
Muons	Baseline	Signal
$p_T$	$p_T > 6 \text{ GeV}$	$p_T > 10 \text{ GeV}$
Identification	Medium <sup>13</sup>	Medium <sup>14</sup>
Isolation	-	GradientLoose
Impact parameter cuts	-	$z_0 < 0.5 \text{ mm},  d_0 /\sigma(d_0) < 3$
Jets		
Clustering Algorithm	Anti- $k_T(r = 0.4)$	
$p_T$	$p_T > 30 \text{ GeV}$	
JVT	$\text{JVT} > 0.57$	
$b$ -tag	MV2c10 77% efficiency working point	

## 4 Monte-Carlo Simulation

Monte-Carlo (MC) simulation is a highly powerful toolkit providing theoretical prediction on particle generation and expected event kinematics, as well as detector response. The simulated event samples are used extensively from studying signal/background separation, performance evaluation to background estimation.

The MC event generation is based on the differential cross-section in terms of 4-momentum space of outcome particles (“phase space”) provided by theory. Randomly generated events over the phase space are accepted on a rate proportional to the differential cross-section in the phase space point.

In this section, an overview is given for the detail of the implementation including the phenomenological description of particle interactions in LHC, cross-section calculation and other kinematical effects in event generation (widely referred from [?] [?]), and the summary of the simulated samples used in the analysis.

### 4.1 Phenomenology in a $pp$ -collision

The processes involved in a  $pp$ -collision are schematized in Figure 45.

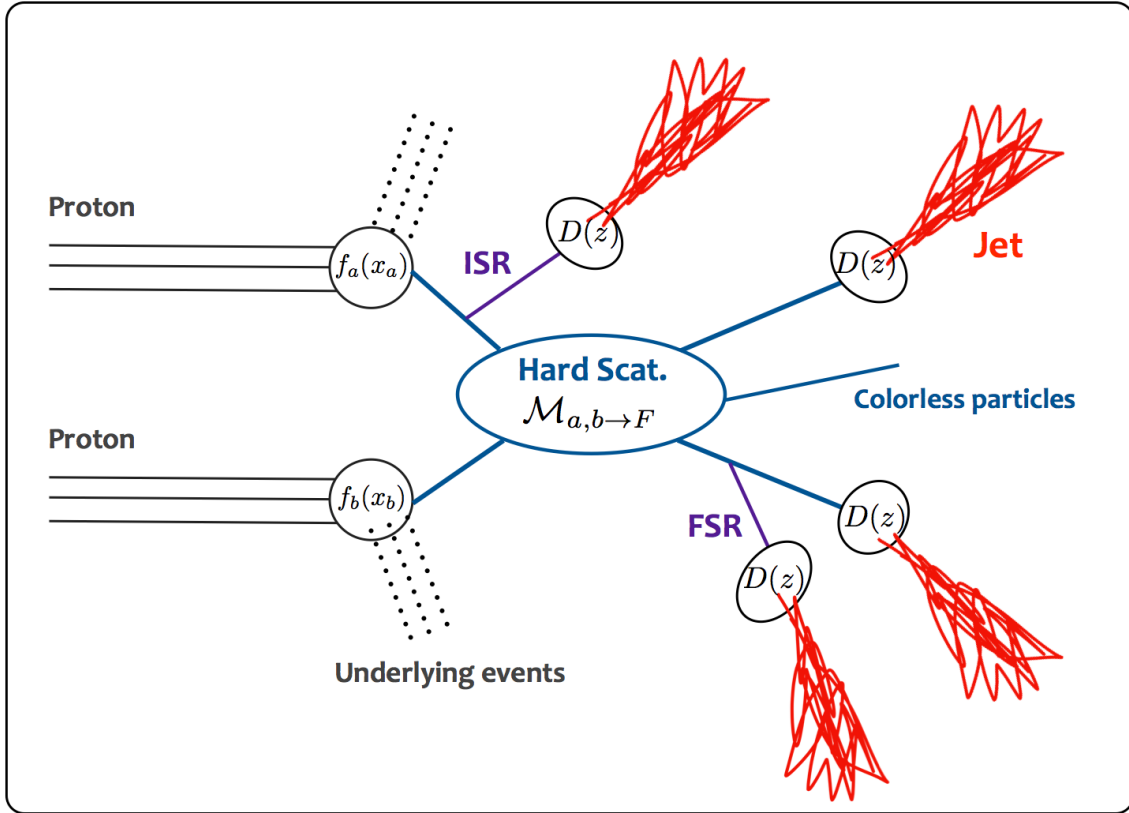


Figure 45: Schematic of involved phenomenology in a  $pp$ -collision.

Thanks to the nature of asymptotic freedom of strong interaction, a proton-proton interaction can be fully characterized by a picture of parton-parton interaction at the LHC energy. The differential cross-section describing transition from an initial state with two partons ( $a, b$ ) into a certain final state ( $F$ ) is represented

by:

$$\frac{d\hat{\sigma}_{a,b \rightarrow F}}{dy} = \frac{1}{2\hat{s}_{ab}} d\Phi |\mathcal{M}_{a,b \rightarrow F}|^2 \quad (79)$$

where  $\mathbf{y}$  represents momenta of final state particles;  $\mathcal{M}_{a,b \rightarrow f}$  the matrix-element (ME);  $d\Phi$  the phase space factor; and the flux factor  $1/2\hat{s}_{ab}$ .

The cross-section Eq. 79 is then capsulated by the Parton distribution function (PDF) to translate from the parton-level cross-section to that of  $pp$ -interaction:

$$\frac{d\sigma_{pp \rightarrow F}}{dy} = \sum_{a,b \in (q,\bar{q},g)} \int_0^1 dx_a \int_0^1 dx_b f_i(x_a) f_j(x_b) \frac{d\hat{\sigma}_{a,b \rightarrow F}}{dy}. \quad (80)$$

$x_{a,b}$  denotes the momentum fraction of protons carried by the constituent partons  $a, b$ , and  $f_i(x)$  is the proton PDF function defined by the probability density which  $x$  obeys.  $a$  and  $b$  are finally added up with possible parton flavors, reflecting our ignorance about the initial parton flavors. Note that this convolution is not the addition at the amplitude level in  $M$  but rather a statistical procedure, which is guaranteed by the factorization theorem.

Resultant quarks and gluons in the final state undergo hadronization, in which they are transformed into a collection of fragmented hadrons (“hadron jet”). This is particular the nature about strong interaction known as “confinement” where the running coupling constant becomes larger for longer distance scattering and eventually diverges at the Laudau pole  $Q^2 \sim (200 \text{ MeV})^2$ . Naively this will lead to infinite perturbative amplitudes of processes with  $Q^2 \sim (200 \text{ MeV})^2$ , including small angle diffraction and pair production of quark and anti-quark out of vacuum.<sup>15</sup> Those instantaneously generated partons are recombined eventually into hadrons with singlet color quantum number. Theoretically, hadronization can be characterized using the an universal frametation function  $D(z)$  in the same internal structure of parton distribution function, representing the probability of finding a hadron with momentum fraction of  $z$  with respect to that of seed parton.

Additionally, often additional jets accompany from splitting legs of intial and final state partons. They are referred as initial state radiation (ISR) or final state radiation (FSR).

Finally, the protons providing the hard scattering partons are completely destroyed, no longer keeping the form as protons. The remnants will experience they own hadronization, resulting in a splash of permeating hadrons known as “beam remnant”. Also, multiple parton-level hard scatterings (multiple parton interaction; MPI) occasionally take place within a single proton-proton interaction, where usually at least one of them ends up in cheap QCD scattering leaving low- $p_T$  jets. These sub-processes resulting soft remnants as the background of main HS are inclusively referred to “underlying events”.

#### 4.1.1 Parton Distribution Function

As PDF is purely determined by non-perturbative dynamic of QCD at lower scale. As the input for event simulation, it is usually taken from global fitting on experimental data of deep inelastic scatterings (DIS) or hadron-hadron collision.<sup>16</sup> Several collaborations have performed combined fits to the datasets mostly from HERA and Tevatron, with different paramerization and fitting scheme. The following sets recently

---

<sup>15</sup>This picture is incorrect giving the breakdown of perturbation, nevertheless enough to give an idea of the universal tendency toward non-perturbative region.

<sup>16</sup>The first principle calculation is strictly speaking doable by lattice QCD. Some results are presented by [?].

provide results: PDF4LHC [?], NNPDF [?], CT14 [?], MSTW [?]. The uncertainties mainly results from instrumental uncertainties in the input data, uncertainties on the strong coupling constant and the functional form of parameterization.

#### 4.1.2 Fixed-Order QCD Calculation

The matrix element in Eq. 79 is computed based on the QCD and EW theory, with truncated orders of perturbation. While the leading term in the perturbation (lowest order; “LO”) dominates over the phase space, the inclusion of high-order terms is significantly important for new physics search. This is because of the much smaller cross-section of signal productions with respect to the SM processes, forcing one to explore the phase space where the bulk SM component is suppressed, in other words the region where the LO contribution is largely suppressed and the higher-order effects addresses, to achieve a reasonable S/N.

The full calculation of higher-order terms are challenging giving the skyrocket increased number of loop diagrams. Currently, the cross-section calculation is available upto next-to-next-to-leading order (NNLO) or NNNLO for typical SM processes happening in LHC, and upto NLO level in event generation. As the largest contribution of the higher order effects are from ISR and FSR, there are a class of generators in the market particularly focusing on computing the diagrams with the additional radiations (“multi-leg generators”). Saving the computing resources by omitting the loop diagrams, they can typically afford upto 4-9 additional partons at maximum.

#### 4.1.3 Parton Showering

Aside with the straightforward QCD matrix element calculation, the parton shower (PS) regime is another useful approach of describing dynamic of additional partons emission. It is based on following two important notions:

- Soft or collinear emission provide dominant contribution to extra parton emission from a parton. In a parton-level process:  $ee \rightarrow q\bar{q}g$  for a minimal example, the differential cross-section can be expressed:

$$\frac{d\sigma_{q\bar{q}g}}{dx_1 dx_2} = \sigma_{q\bar{q}} \times \frac{\alpha_s}{2\pi} \frac{4}{3} \frac{x_q^2 + x_{\bar{q}}^2}{(1-x_q)(1-x_{\bar{q}})}, \quad x_i := 2E_i/\sqrt{s} \quad (81)$$

with  $\sqrt{s}$  being the center-of-mass energy of the  $ee$  system. The singularities correspond to collinear emission of the gluon ( $x_q \rightarrow 1$  or  $x_{\bar{q}} \rightarrow 1$ ) or soft gluon emission ( $x_q \rightarrow 1$  and  $x_{\bar{q}} \rightarrow 1$ ). These collinear and soft singularities are universal to QCD, independent from type of processes.

- In the soft/collinear regime, the cross-section with an additional parton radiation ( $d\sigma_{n+1}$ ) can be factorized by a product of the original cross-section ( $d\sigma_n$ ) and splitting factor  $P_{i \rightarrow jk}$ :

$$d\sigma_{n+1} = d\sigma_n \left[ \sum_{j,k} \frac{\alpha_s}{2\pi} \frac{dq}{q} \frac{dz}{z} P_{i \rightarrow jk}(z) \right], \quad (82)$$

where the indices  $i, j$  represent respectively the parent parton before and after the splitting, and  $k$  the emitted parton.  $z$  is the momentum fraction the emitted parton carrying from the parent, and

$q$  is the momentum transfer between the parton  $i$  and  $j$ .  $P_{i \rightarrow jk}$  is known as the Dokshitzer-Gribov-Lipatov-Altarelli-Parisi (DGLAP) evolution equations [?] [?] [?] computed from generic QCD analyses as:

$$P_{q \rightarrow qg} = \frac{4}{3} \frac{1+z^2}{1-z}, \quad (83)$$

$$P_{q \rightarrow qq} = \frac{4}{3} \frac{1+(1-z)^2}{z}, \quad (84)$$

$$P_{q \rightarrow gg} = 3 \frac{z^4 + 1 + (1-z)^4}{z(1-z)}, \quad (85)$$

$$P_{q \rightarrow q\bar{q}} = \frac{z^2 + (1-z)^2}{2}, \quad (86)$$

Based on these, the PS regimes allows one to recursively calculate in a picture of stepwise evolution, in contrast to that in the scattering amplitude approach where either initial and final state must be steadily defined beforehand. The probability of emitting an extra parton at each step can be then represented, analogous to the life time of unstable particle decay, using the Sudakov form factors [?]:

$$S_i(q_1, q_2) = 1 - \exp \left( - \sum_{j,k} \int_{q^2}^{q_{\max}^2} \frac{dQ^2}{Q^2} \int_{z_{\min}}^{z_{\max}} \frac{\alpha_s}{2\pi} P_{i \rightarrow jk}(\hat{z}) d\hat{z} \right), \quad (87)$$

where  $q_1$  and  $q_2$  denote the virtuality of parent parton between and after splitting respectively. The FSR in event simulation is implemented by stochastic evolution of final state parton legs on the probability Eq. 87, with givning an arbitrary initial virtuality  $Q$ . The evolouton is terminated typically until the virtuality becomes  $\sim 1$  GeV. ISRs are simulated in similar manner but with backward evolution with increasing virtuality  $q$  along the evolution. Generated sub-branches during the backward evolution are then evolved forward. The procedure is schematized as Figure 46.

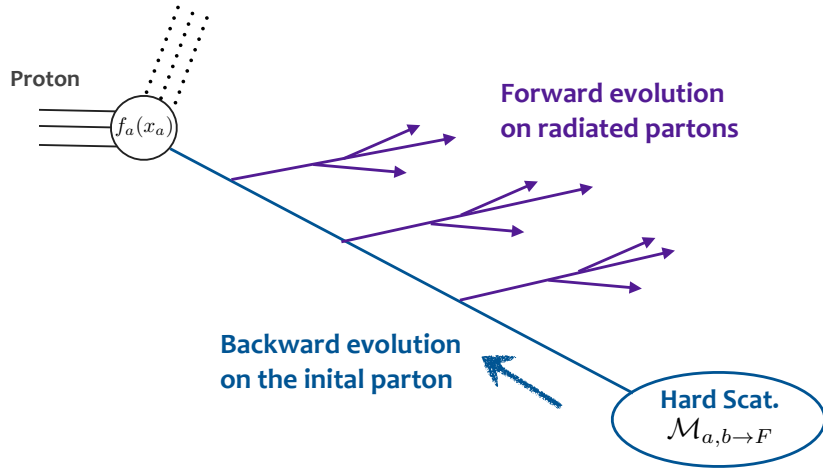


Figure 46: Schematic of the backward evolution implemented in ISR simulation. The evolution starts from hard-collided parton with increasing virtuality  $q$  along the evolution. Partons splitted from it are then evolved forward.

Various implementation for the evolution exist, leading to a subtle difference in the final state kinematics. The impact of the difference are quoted for theoretical uncertainty in the analysis. The qualification and assigned uncertainty will be discussed Sec. 7.

Note that this shower evolution is fully perturbative yet include contribution from essentially arbitrary orders of perturbation series (upto  $n$ -th order, where  $n$  is number of parton branch splitting), however it does only take care of contribution from collinear and soft singularity. This is the main motivation for multi-leg generators that provides hard ME-level additional partons to complement. One issue about this combined approach is the potential double-counting. The correction procedure commonly refers to “matching” or “merging”, and are largely categorized into two types: separating the regions that each ME and PS is responsible for, in terms of phase space or scale. The most widely used algorithm is provided by Catani-Krauss-Kuhn-Webber (CKKW) [?] algorithm or Michelangelo L. Mangano algorithm (MLM) [?]. ; Generating all jets by PS, and correct it by normalizing into the ME differential cross-section (ME correction).

#### 4.1.4 Hadronization

A phenomenological approach is usually preferred in simulating hadronization, although the it can be formulated through an universal fragmentation function that has the same internal structure as parton distribution. The most famous model is the string model [?] where the confinement between partons is represented by a gluonic string. For a quark-antiquark pair, as the partons move apart, the string is stretched leading to an increase in potential energy. When the energy becomes of the order of hadron masses, it becomes energetically favorable for the string to break and create a new quark-antiquark pair. The two segments of string will be repeatedly pulled and break again, until all energy of initial quarks is converted into newly generated fragments.

## 4.2 Event Generators and the Simulated Dataset

Signal and background event are generated using preferred generators and setups. Table 10 summarizes the configurations for datasets used in the analysis. Given that the analysis typically explores the phase space with many jets, simulation on physics processes yielding less jets (e.g.  $W/Z + \text{jets}$ ) or only soft jets at tree level (e.g. gluino production with compressed mass spectra) need dedicated modeling of ISR and FSR, therefore the multi-leg generators (SHERPA, MG5\_aMC@NLO) are preferred in general.

Table 10: Setup of simulated SUSY signal and the Standard Model background samples.  $n_{\text{ME}}^{\text{a.p.}}$  is the number of simulated additional partons in the higher order QCD processes. PS and UE are the abbreviation of parton shower and underlying events respectively.

Physics process	Generator	$n_{\text{ME}}^{\text{a.p.}}$	PDF set	PS/UE
SUSY processes	MG5_aMC@NLO2.3.3 [?] (LO)	2	NNPDF2.3 LO	PYTHIA 8.186 [?]
$W/Z + \text{jets}$	SHERPA 2.2.1 [?] (NLO)	2(NLO), +2(LO)	NNPDF3.0 NNLO [?]	SHERPA
$t\bar{t}$	POWHEG +Box v2 [?] (NLO)	1	CT10 [?]	PYTHIA 6.428 [?]
Single-top ( $Wt$ -ch.)	POWHEG +Box v2 (NLO)	1	CT10	PYTHIA 6.428
Single-top ( $s$ -ch.)	POWHEG +Box v2 (NLO)	1	CT10	PYTHIA 6.428
Single-top ( $t$ -ch.)	POWHEG +Box v1 (LO)	1	CT10f4	PYTHIA 6.428
Di-bosons	SHERPA 2.1.1 (LO)	1-2(NLO)	CT10	SHERPA
$t\bar{t} + W$	MG5_aMC@NLO2.2.3 (LO)	2	NNPDF2.3 LO	PYTHIA 8.186
$t\bar{t} + Z$	MG5_aMC@NLO2.2.3 (LO)	1	NNPDF2.3 LO	PYTHIA 8.186
$t\bar{t} + WW$	MG5_aMC@NLO2.2.3 (LO)	0	NNPDF2.3 LO	PYTHIA 8.186

The simulated samples are normalized by cross-section independently calculated typically with higher orders and soft gluon resummation upto Next-to-Leading Logarithm (NLL) or Next-to-next-to-Leading Logarithm (NNLL). Table 11 shows the summary.

Table 11: Cross-section used for the simulated processes.

Physics process	Cross-section [pb]	Order	Authors
SUSY processes	See Figure 47	NLO+NLL	[?, ?, ?, ?, ?]
$W + \text{jets}(\rightarrow \ell\nu)$	20079	NNLO	[?]
$Z + \text{jets}(\rightarrow \ell\ell)$	1950	NNLO	[?]
$t\bar{t}$	993.8	NNLO+NNLL	[?]
Single-top ( $Wt$ -channel)	75.57	NNLO+NNLL	[?]
Single-top ( $s$ -channel)	10.32	NLO	[?]
Single-top ( $t$ -channel)	216.95	NLO	[?]
Di-bosons	45.42	NLO	[?]
$t\bar{t} + W/Z/WW$	1.36	NLO	[?, ?]

Further caveats particular to each process are stated as below.

**$W/Z + \text{jets}$**  The matrix elements are calculated using the SHERPA 2.2.1 generator [?] up to two partons at NLO and four partons at LO using the Comix [?] and OpenLoops [?] generators. Parton showers are generated by the internal algorithm of SHERPA 2.2.1 [?] and merged based on the ME+PS@NLO prescription [?]. The CKKW scheme is used for ME/PS matching with matching scale set to 30 GeV.

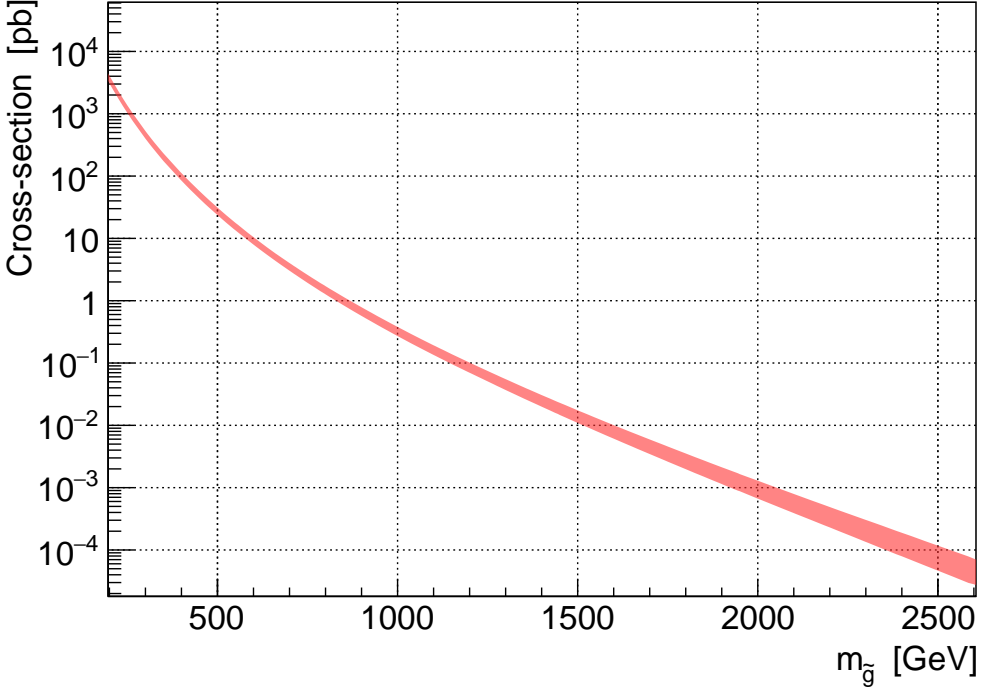


Figure 47: Cross-section for gluino pair production. Calculation is performed at NNLO+NNLL accuracy.

**Tops ( $t\bar{t}$ /single-top)** The  $h_{\text{damp}}$  parameter, which controls the  $p_T$  of the first additional emission beyond the Born configuration, is set to the mass of the top-quark [?]. The main effect of this is to regulate the emission of high  $p_T$  radiations against the  $t\bar{t}$  system recoils. The top-quark mass is set to 172.5 GeV for all the samples.

**Di-bosons: WW/WZ/ZZ** The fully-leptonic processes are simulated with five final states ( $\ell\ell\ell\ell$ ,  $\ell\ell\ell\nu$ ,  $\ell\ell\nu\nu$ ,  $\ell\nu\nu\nu$ ,  $\nu\nu\nu\nu$ ). The intermediate states are not specified therefore the contribution from Drell-Yan-like off-shell diboson and the interference between different diboson processes (e.g.  $WW \rightarrow \ell\ell\nu\nu$  and  $WZ \rightarrow \ell\ell\nu\nu$ ) are taken into account. The semi-leptonic diboson processes are simulated with designated intermediate boson states ( $W$  or  $Z$ ).

**$t\bar{t} + W/Z/WW$**  All processes are simulated by MG5\_aMC@NLO2.2.3 at LO interfaced to the PYTHIA 8.186 parton shower model, with up to two ( $t\bar{t} + W$ ), one ( $t\bar{t} + Z$ ) or no ( $t\bar{t} + WW$ ) extra partons included in the matrix element.

**SUSY signals** Decay of EW gauginos are done in PYTHIA, based on phase space with no consideration of the spin. The CKKW-L matching scheme [?] is applied for the matching of the matrix element and the parton shower, with the corresponding scale parameter set to 1/4 of the gluino mass. The cross-section uncertainty are taken from an envelope of cross-section predictions using different PDF sets and factorization

and renormalisation scales, as described in Ref. [?], considering only the four light-flavor left-handed squarks ( $\tilde{u}_L$ ,  $\tilde{d}_L$ ,  $\tilde{s}_L$ , and  $\tilde{c}_L$ ). Figure 47 shows the calculated cross-section and the associated error.

Model parameters irrelevant to SUSY masses are fixed to arbitrary reasonable values, since here we assume they do not change the kinematics as discussed in Sec. 1. The mixing parameters are set so that LSP and NLSP are bino- and wino-like.

#### 4.2.1 Pileup simulation

All simulated events are generated with a varying number of minimum-bias interactions overlaid on the hard-scattering event to model the multiple proton-proton interactions in the same and the nearby crossing crossings. The minimum-bias interactions are simulated with the soft QCD processes of PYTHIA 8.186 using the A2 tune [?] and the MSTW2008LO PDF set [?]. Corrections are applied to the samples to account for differences between data and simulation for trigger, identification and reconstruction efficiencies.

#### 4.2.2 Detector Simulation and Emulation

The detector response to generated particles is simulated by a full ATLAS detector simulation model [?] based on GEANT4 [?], for the background samples.

The ATLAS fast simulation [?] is used for signal models marked as ✓ in Table 5-7 in Sec. 1.5.3, as the economical alternative. This is based on a parametrization of the performance of the electromagnetic and hadronic calorimeters measured in the test-beam or on GEANT4 elsewhere. The difference between the full simulation is found to be marginal after examining a number of reference signal points. The subsequent procedures are identical to what is processed for the data sample.

For the signal models with no ✓ in Table 5-7, no detector simulation nor reconstruction is performed. Instead the effect is emulated by smearing the energy of truth-level particles and clustered jets, based on the resolution parametrized using the full simulated samples. The object identification is emulated by randomly accepting the candidates at the rate of the parametrized efficiency. The modeling is extensively tested by comparing the kinematic distributions with the fast simulated samples. The discrepancy is found sufficiently small, staying within 5% in general and never exceed 10%.

### 4.3 Design of SUSY Signal Grid for Interpretation

Obtained exclusion limits are presented in a form of contours in a 2-dimensional plane, usually in terms of SUSY masses. This is done by generating a set of signal samples with various SUSY masses covering the whole plane with discrete steps, referred as a signal grid. The results of the hypothetical test for the points are interpolated into a continuous limit in the end.

For limits on the direct decay models,  $m_{\tilde{g}}$  and  $m_{\tilde{\chi}_1^0}$  are chosen as x and y-axis respectively to represent (referred as “Direct” grid). The cases with 1-step decay models is a bit tricky, since they involve the third mass; the intermediate EW-gaugino  $\tilde{\chi}_1^\pm$  or  $\tilde{\chi}_2^0$ . The full 3-dimensional presentation is not realistic

from computational cost of view, due to the enormously increased number of grid points to cover the whole grid. Therefore, a couple of sensible 2D-slices are made that sufficiently capture the essence of the 3D-grid. “ $x=1/2$ ” is the grid with the intermediate EW-gaugino mass is set to midmost between gluino and the LSP, while  $x$  is defined as a parameter representing the relative mass splitting:

$$x := \Delta m(\tilde{\chi}_1^\pm / \tilde{\chi}_2^0, \tilde{\chi}_1^0) / \Delta m(\tilde{g}, \tilde{\chi}_1^0), \quad x \in [0, 1].$$

The LSP60 grid is then designed to complement the hole in high or low  $x$ , where the LSP mass is fixed to 60 GeV and the gluino mass and the intermediate EW-gaugino mass are set free. There are two additional grids DM20 and DM30 in which the intermediate EW-gaugino an the LSP are compressed ( $\Delta m(\tilde{\chi}_1^\pm / \tilde{\chi}_2^0, \tilde{\chi}_1^0) = 20, 30$  GeV respectively), respecting the dark matter relic constraint in discussed in Sec. 1.4.2. Note that these DM grids are not considered in models with  $\tilde{\chi}_2^0$  decaying to higgs, since higgs is too far off-shell thus  $\tilde{\chi}_2^0$  never almost decays via higgs in the situation.

To summarize, four types of signal grid are designed in the analysis, as shown in Table 12.

Table 12: List of signal grids used for limit setting. Direct is for the direct decay model, and the others are for the 1-step decay models. The latter is four-fold:  $x=1/2$ , a grid with EW gaugino mass fixed to the middle of gluino and LSP; LSP60 , in which LSP mass is fixed to 60 GeV; DM20 and DM30 are grids with  $\Delta m(\tilde{\chi}_1^\pm / \tilde{\chi}_2^0, \tilde{\chi}_1^0) = 20, 30$  GeV which are considered only in models without  $\tilde{\chi}_2^0$  decay into higgs.

Grid name	x-axis	y-axis	Slicing	Note
Direct	$m_{\tilde{g}}$	$m_{\tilde{\chi}_1^0}$	-	-
$x=1/2$	$m_{\tilde{g}}$	$m_{\tilde{\chi}_1^0}$	$\Delta m(\tilde{g}, \tilde{\chi}_1^0)/2 = \Delta m(\tilde{\chi}_1^\pm / \tilde{\chi}_2^0, \tilde{\chi}_1^0)$	-
LSP60	$m_{\tilde{g}}$	$\Delta m(\tilde{\chi}_1^\pm / \tilde{\chi}_2^0, \tilde{\chi}_1^0) / \Delta m(\tilde{g}, \tilde{\chi}_1^0)$	$m_{\tilde{\chi}_1^0} = 60$ GeV	-
DM20 ,DM30	$m_{\tilde{g}}$	$m_{\tilde{\chi}_1^0}$	$\Delta m(\tilde{\chi}_1^\pm / \tilde{\chi}_2^0, \tilde{\chi}_1^0) = 20, 30$ GeV	For models without $h$ -mediated $\tilde{\chi}_2^0$ decays.

## 5 Event Selection

### 5.1 Trigger Selection

The missing ET trigger (MET trigger) is primarily used throughout the analysis. Since the lowest unprescaled trigger kept evolved according to the increased instantaneous luminosity during the 2016 data taking, a number of different triggers are used in combination. The list of the triggers are shown in Table 13,

Table 13: Summary of MET triggers used in the analysis along the peak luminosity evolution. Corresponding on-line and off-line threshold are shown altogether.

Period	Peak lumi. [ $\text{cm}^{-2} \text{s}^{-1}$ ]	Int. lumi. [ $\text{fb}^{-1}$ ]	L1 (HLT) item	L1/HLT/Off-line threshold [GeV]
2015	$0.50 \times 10^{34}$	3.19	L1XE50 (xe70_mht)	50 / 70 / 200
2016 A-D1	$0.99 \times 10^{34}$	6.12	L1XE50 (xe90_mht)	50 / 90 / 200
2016 D1-F1	$1.03 \times 10^{34}$	6.55	L1XE50 (xe100_mht)	50 / 100 / 200
2016 F2-	$1.21 \times 10^{34}$	20.2	L1XE50 (xe110_mht)	50 / 110 / 200

The efficiency curve as function of off-line  $E_T^{\text{miss}}$  is shown in Figure 48 with the example of HLT\_xe100\_mht. Thanks to the fact that MET is calculated from global information of an event, rather than the feature of a single particular particle, the plateau efficiency amounts almost 100 %. This is a significant advantage over the use of leptonic trigger where efficiency is typically 70%  $\sim$  90%. Generally the downside of MET trigger is on the other hand its slow turn-on in terms of the off-line MET that needs nearly 200 GeV to assure the plateau efficiency despite much lower trigger threshold ( $< 110$  GeV). This is due to the deteriorated resolution of on-line MET which is purely based on calorimeter clusters, with respect to the off-line one which is take into muons and soft tracks into account. The signal acceptance by the trigger requirement is  $> 95\%$  except when gluino mass and LSP mass are compressed. Nevertheless, given that it is impossible for such signal to be discriminated against background without the MET generated by associated ISRs, the loss in trigger is not problematic.

The single-lepton trigger (SLT) is also used for supplemental purpose, including the efficiency measurement of MET trigger and closure tests of data-driven background estimation. The trigger turn-on is about 28 GeV (26 GeV) for single-electron (muon) in its transverse momentum and 30 GeV (28 GeV) is required as off-line threshold.

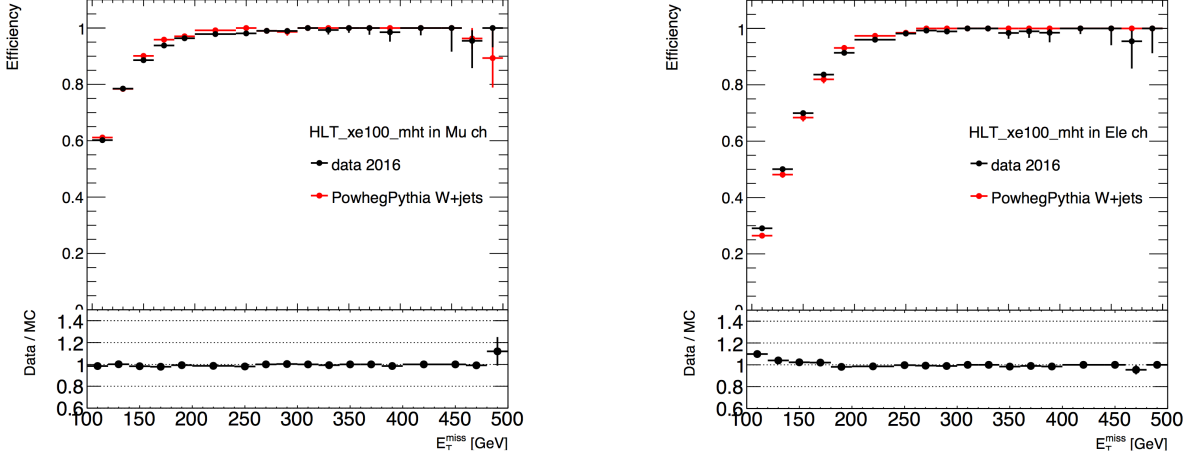


Figure 48: Turn-on of MET trigger HLT\_xe100\_mht simulated or measured using  $W + \text{jets}$  events by performing the tag-and-probe technique. (a) events with exactly one muon, and (b) events with exactly one electron.

## 5.2 Event Cleaning and the Pre-selection

Event cleaning is applied to get rid of funky data events that are either in bad quality due to inappropriate detector status and badly measured objects, or with objects stemming from somewhere other than the hard collision such as cosmic muons and beam-induced background. As those events could result in extraordinary observables, for instance extremely high jet pt or MET, they are generally critical for search analyses probing the high-end of kinematics where only a few background events in signal regions are in discussion where therefore even a single event of the accidental contamination makes huge impact on the final result. The list of procedure and cut efficiencies are summarized in Table 14.

Table 14: List of cuts applied as event cleaning. Data and MC shows different efficiencies up-to the top four since MC does not emulate bad data quality and cosmic muons in it.

Cut	Efficiency (Data) [%]	Efficiency (MC, $t\bar{t}$ ) [%]
Veto bad lumi-clocks	95.12	100.0
Veto bad DAQ events	99.81	100.0
Veto events with no primary vertex	100.0	100.0
Veto events with cosmic muons	95.83	98.52
Veto events with badly measured jets	99.49	99.65
Veto events with badly measured muons	99.99	98.56

Lumi-blocks with more than 10% of the detector in the bad status are firstly removed. Events affected by noise bursts in LAr and SCT, corrupted data transmission in LAr and the Tile calorimeter are then vetoed subsequently.

Cosmic muon are vetoed by requiring the muon track passing reasonably close-by the primary vertex i.e.

$$|z_0| < 1 \text{ mm}, \quad d_0 < 0.2 \text{ mm}.$$

The beam induced backgrounds are events with muons that are generated by the secondary cascades of protons traveling upstream of the interaction point. The energy depositions created by these muons can be reconstructed as jets with energy as high as the beam energy therefore becomes highly signal-like. To reject

the fake jets, event with jets flagged as ‘‘BadLoose’’ described in [?] are vetoed.

High energy muons with poor momentum measurement quality are also a source of fake high MET ranging upto a few TeV. Those muons are selected as ones with  $\sigma(q/p)/(q/p) > 0.2$  where  $q$  is muon charge,  $p$  the momentum and  $\sigma(q/p)$  is the fitting error. The entire events will be vetoed if containing at least one bad muon.

Figure 49 demonstrate the performance of bad muon veto. While bad muon events typically peak in  $\Delta\phi(l, E_T^{\text{miss}})$  since the fake MET aligns with the muon, it is exclusively resolved by the veto. Also, the role of bad muon veto is shown to be very important in this analysis as the 1-muon high MET phase space generally suffers from severe contaminaton by bad muon events upto about 20% (90%) with  $E_T^{\text{miss}} > 1(2)$  TeV.

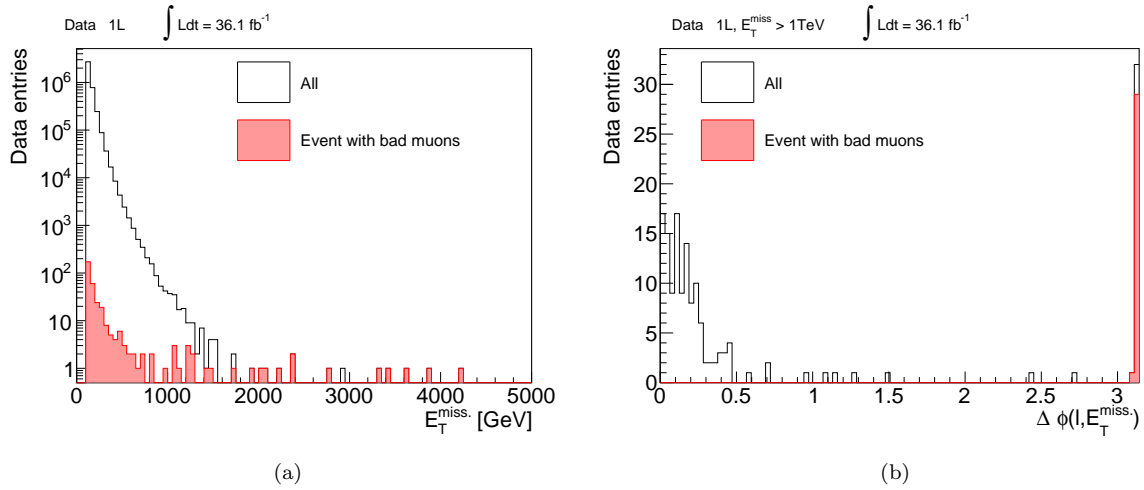


Figure 49: (a) MET distribution after requiring exactly one signal muon and MET trigger, and (b)  $\Delta\phi(l, E_T^{\text{miss}})$  distribution with  $E_T^{\text{miss}} > 1$  TeV being applied. The pink histogram corresponds to events dropped by the bad muon veto. The veto looks working reasonably considering the apparent spike due to the fake MET:  $\Delta\phi \sim \pi$  is cleared.

The pre-selection is the common selection for all the signal regions in the analysis, which is defined as Table 15.

Table 15: List of requirements for the 1-lepton pre-selection.

---

Event cleaning	
Pass the MET trigger and $E_T^{\text{miss}} > 250$ GeV	
At least one signal electron (muon) with $p_T > 7(6)$ GeV.	
At least two jets with $p_T > 30$ GeV.	

---

### 5.3 Signal Region Definition

#### 5.3.1 Binning Strategy

To inclusively address to all the 45 decay models and all possible mass spectra, a set of tailored multi-bin signal regions (SRs) are employed. Specifically, different decay models are covered by splitted the signal

regions in terms of b-jet multiplicity (“categories”), and various scenario of mass spectra in the models are coped with the division in terms of kinematical cuts (“towers”). SR bins are basically designed to be exclusive for each other, aiming at an easy combination afterward so that no signals are lost due to the binning.

The definition of the b-jet based categories: b-vetoed (BV), b-tagged (BT) and 3B follows Table 16. The main customers of these categories are respectively the models in Table 5, 6 and 7 in Sec. 1.5.3, which are referred as “BV”, “BT” and “3B” benchmark models from now on. The b-jet multiplicity for the reference signal models versus background at the pre-selection level is shown in Figure 50. Note that despite a fraction of signal events falling into other categories than the benchmarked one, they will not be wasted thanks to the combined fit performed in deriving the final result. As the S/N ratio and the background kinematics in BV/BT are found to be more or less similar, further kinematical selections in those categories are set to identical for simplicity. On the other hand, different selection strategy is adopted for the 3B categories since the background level is significantly lower and also the composition is very different.

Table 16: The definition of the b-jet based categories and the main backgrounds there.

Category	b-jet multiplicity	Main background
B-vetoed (BV)	0	$W + \text{jets}$
B-tagged (BT)	1-2	$t\bar{t}$
3B	$\geq 3$	$t\bar{t}, t\bar{t} + cc/bb$

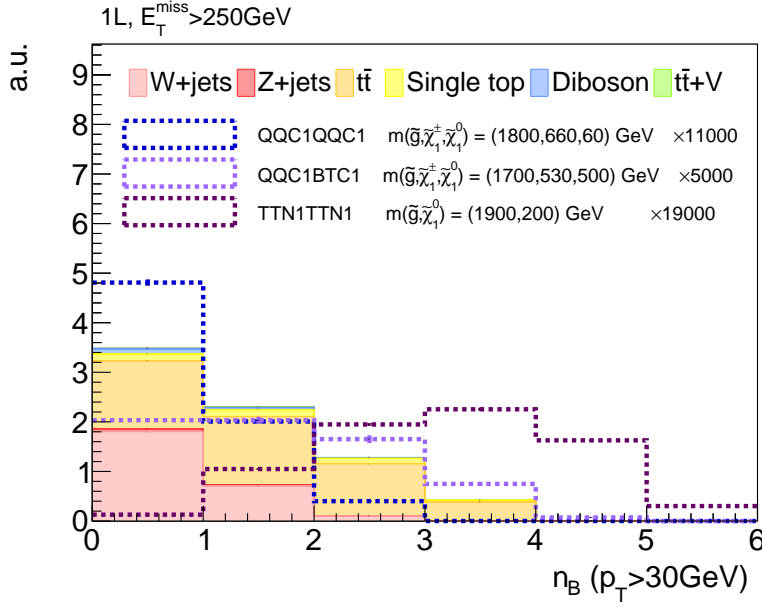


Figure 50: B-tagged jet multiplicity for the standard model backgrounds and the reference signals (QQC1QQC1 for the BV, QQC1BTC1 for the BT and TTN1TTN1 for the 3B categories respectively) after the 1-lepton pre-selection.

The BV/BT categories are further divided into 4 “towers”, to tackle the 4 typical configurations of the mass spectra for gluino and the LSP (and the intermediate EW gauginos in case of 1-step decays). The relation is schematized in Figure 51, with the benchmark model “QQC1QQC1” being the example. Each of them is further detailed as below:

1. The mass of intermediate EW gaugino is roughly in the middle of those of gluino and the LSP ( $x \sim 1/2$ ). This is the most standard configuration where particles from both gluino and the intermediate EW gaugino decays are hard enough to pass the criteria of hard lepton ( $> 35$  GeV) and jets ( $p_T > 30$  GeV). As the signals targeted by the BV/BT categories typically result in 4 – 10 jets at the tree-level, a tower **6J** with  $n_J \geq 6$  is defined.
2. Gluino and EW gauginos are all compressed. From either trigger and background separation point of view, hard ISRs are indispensable for probing this type of signatures so that the  $\tilde{g}\tilde{g}$  system gets kicked and resulting in large MET. On the other hand, as the kicked gluinos are typically enough heavy to be non-relativistic, the transverse momentum of the boosted  $\tilde{g}\tilde{g}$  system is almost solely converted into MET. As a result the particles from gluino decays stay soft. The **2J** tower consisting of a soft lepton, at least two hard jets and large MET is defined for targeting the signature.
3. ,4 The intermediate EW gaugino and either gluino or LSP are compressed ( $x \sim 0, 1$ ). There are also extreme cases where the intermediate EW gaugino mass is degenerate toward either of gluino or LSP and decoupled from the other. Two signal region towers: *High* –  $x$  and *Low* –  $x$  are employed to cover the scenarios.

Similar discussion holds for direct gluino decay models as well i.e. the tower **2J** covers the scenario of compressed mass spectra while the tower **6J** is used for general cases.

In contrast to the BV/BT category, the 3B does not undergo the additional classification in towers since the targeted signal models usually involve top quarks that can result in hard jets, leptons and MET. Therefore the kinematics does not dramatically vary between the mass configurations unless the top-quarks are on-shell. The only exception is when gluino and the intermediate EW gaugino get compressed, and the top-quarks turn to off-shell ending up in only soft particles. However such events are then covered by the BV and BT towers instead, thanks to the dropped  $\geq 3$  b-jet acceptance according to the decreasing b-quarks’  $p_T$ .

To summarize, 5 towers (2J/6J/Low-x/High-x/3B) are defined in total out of 3 categories (BV/BT/3B) as in Table 17.

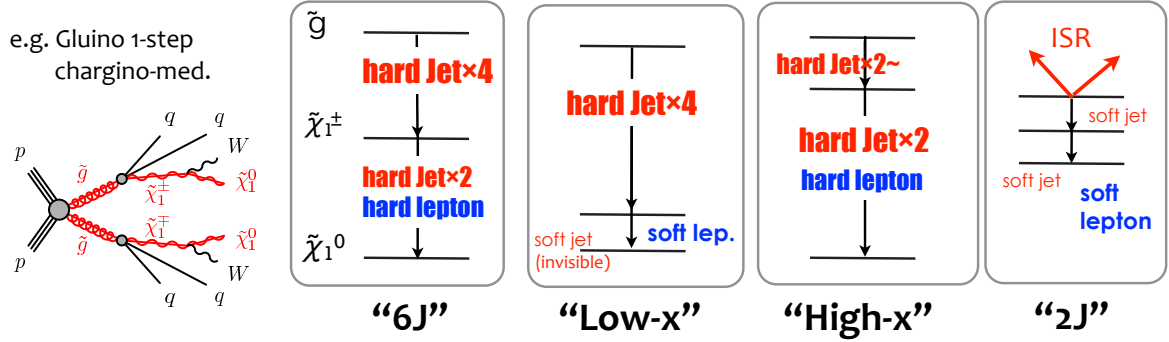


Figure 51: The 4 signal region towers for the BT/BV categories, and their targeted mass configuration.

Table 17: List of defined towers in each b-category and t kinematical selection required. **2J** and **6J**, **Low-x** and **High-x** are orthogonal to each other. **3B** are orthogonal to all the other towers.

Category	Tower	Electron (muon) $p_T$ [GeV]	$n_J (p_T > 30 \text{ GeV})$
BV/BT	2J	$\in [7(6), 35]$	$\geq 2$
	6J	$> 35$	$\geq 6$
	Low-x	$\in [7(6), 35]$	$\geq 4$
	High-x	$> 35$	$\geq 4$
3B	3B	$> 15$	$\geq 7$

Finally, the towers further experience the binning in terms of  $m_{\text{eff}} := E_T^{\text{miss}} + \sum_i p_T(j_i)$  to accommodate different absolute scale of mass splitting. The “2J/6J” and “3B” tower are segmented into 3 and 2 bins respectively while “Low-x” and “High-x” are single-binned as their low  $m_{\text{eff}}$  bins have too much overlap with “2J” and “6J” in phase space which does not provide unique sensitivity. The bin widths of  $m_{\text{eff}}$  are set to be 400 GeV – 500 GeV driven by the width of  $m_{\text{eff}}$  distribution for signals that the lower  $m_{\text{eff}}$  bins typically target ( $\Delta m(\tilde{g}, \tilde{\chi}_1^0) = 1 \text{ TeV} \sim 1.5 \text{ TeV}$ ). The “3B” tower enjoys an exceptionally wider bin width with 750 GeV, compromising with limited statistics in corresponding control regions.

To conclude, the signal regions end up in 5 tower-structured bins as schematized as Figure 52, where  $3 \times 2$  bins in  $m_{\text{eff}} \times (\text{BV}/\text{BT})$  reside in the tower ”**2J**” and ”**6J**”,  $1 \times 2$  bins in ”**Low-x**” and ”**High-x**”, and  $2 m_{\text{eff}}$  bins in ”**3B**”. Since all the SRs bins in the towers ”2J/6J/3B” or ”Low-x/High-x/3B” are statistically independent, they can be straightforwardly combined in a simultaneous fit. Figures 53-54 schematize the mass regions in the signal grids that each signal region tower or bin is supposed to address the sensitivity for the benchmark models.

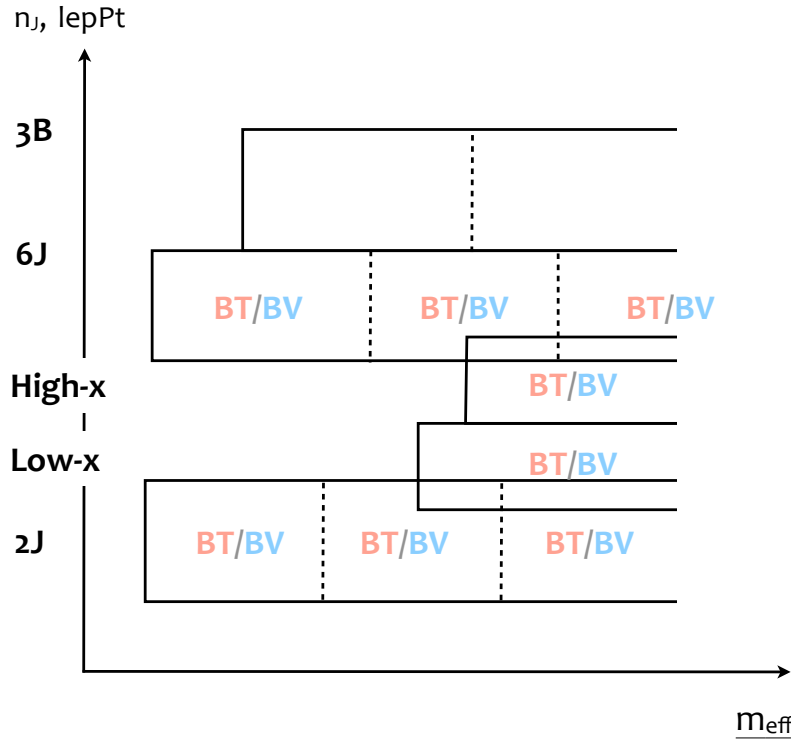


Figure 52: Tower structure and the  $m_{\text{eff}}$  binning of signal regions.

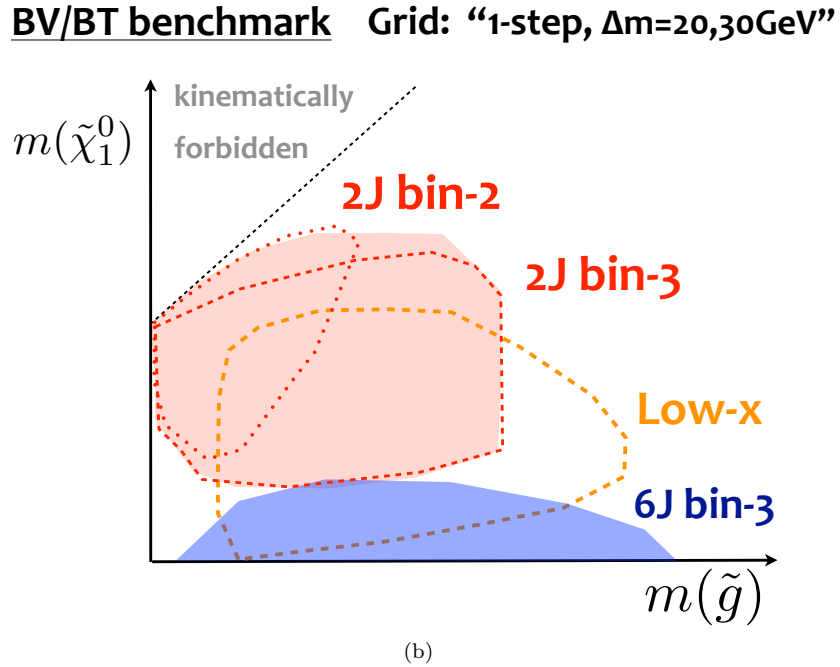
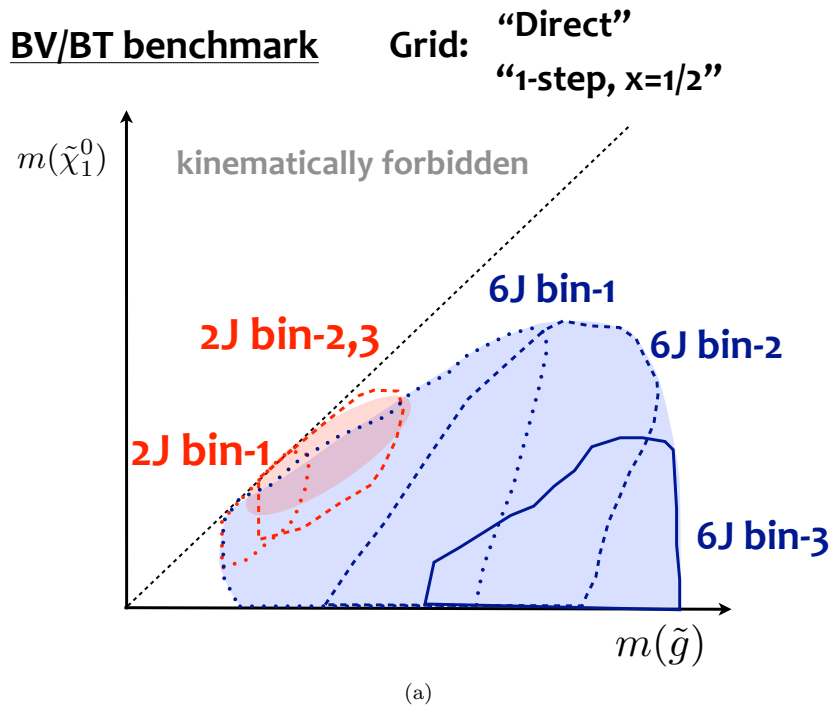


Figure 53: Sensitivity coverage by individual signal region towers or  $m_{\text{eff}}$ -bins in the (a) the **Direct** and  $x=1/2$  grid, and in (b) the **DM20**, **DM30** grid of the BT/BV benchmark models. Dashed contours and shaded areas schematize the regions that the individual tower or  $m_{\text{eff}}$ -bin addresses the sensitivity.

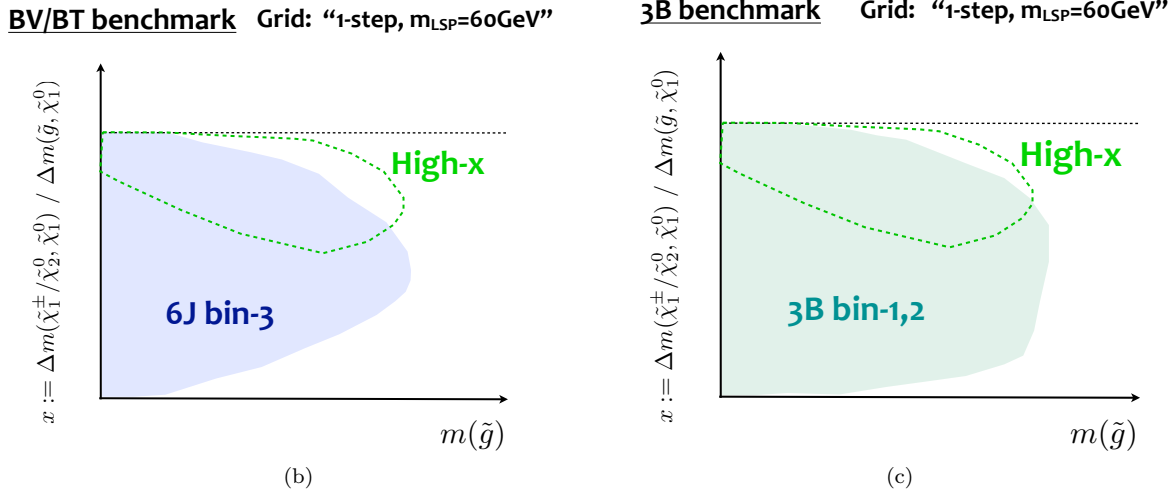
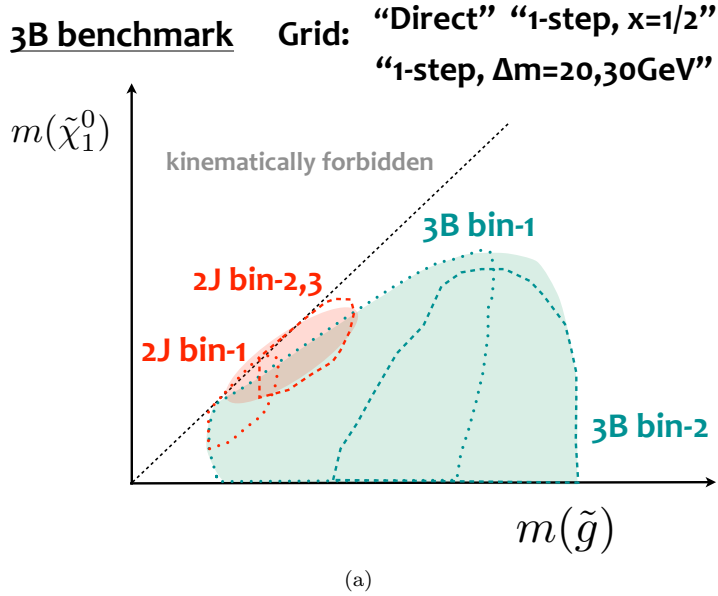


Figure 54: Sensitivity coverage by individual signal region towers or  $m_{\text{eff}}$ -bins in the (a) Direct ,  $x=1/2$  , DM20 and DM30 grids of the 3B benchmark models, (b) the LSP60 grid of the of the BT/BV benchmark models, and in (c) the LSP60 grid of the 3B benchmark models. Dashed contours and shaded areas schematize the regions that the individual tower or  $m_{\text{eff}}$ -bin addresses the sensitivity.

### 5.3.2 Discriminating variables

Kinamtical variables used for background rejection as well as defining control regions are overviewed. The distributions of backgrounds overlaid with benchmark signals at the preselection are presented in Figure 56 - 57. In addition to the pre-selection, a soft lepton ( $p_T(\ell) \in [6, 35]$ ) is required in Figure 57 (b),  $m_{\text{eff}} > 1500$  GeV in for Figure 57 (b), and  $n_B \geq 3$   $m_T > 125$  GeV are applied in Figure 57 (c) and (d). The definition and the purpose of the variables are as below:

**n<sub>J</sub>** Jet multiplicity often shows the great discriminating power since the standard model processes suffer a sharp cut-off. However one should mind that the optimum cut is significantly dependent on the gluino decay mode, and also that the aggressive cut will enhance the contribution from higher order effect, putting the modeling at the risk of large theoretical uncertainty. Therefore, it is kept to a moderated use as means of background rejection.

**E<sub>T</sub><sup>miss</sup>** Signal events result in large  $E_T^{\text{miss}}$  reflecting the presence of hard additional undetected LSP when  $\Delta m(\tilde{g}, \tilde{\chi}_1^0)$  is large. At analysis level, this is also true for the compressed case given that the MET via ISRs is nevertheless required for the trigger sake as described above.

**m<sub>eff</sub>**  $m_{\text{eff}}$  is the variable best reflecting the magnitude of absolute mass splitting  $\Delta m(\tilde{g}, \tilde{\chi}_1^0)$ , providing the best separation against backgrounds. Meanwhile it is also noticeable that the magnitude of  $m_{\text{eff}}$  is almost uniquely determined by  $\Delta m(\tilde{g}, \tilde{\chi}_1^0)$ , regardless of the relative mass splitting and gluino decays, therefore the optimal cut in  $m_{\text{eff}}$  is highly universal.

**m<sub>T</sub>(p<sub>T</sub>(ℓ), E<sub>T</sub><sup>miss</sup>)** Invariant mass of  $E_T^{\text{miss}}$  and the lepton with the z-momentum set to 0. Analogous to ordinary invariant mass peaking at the mass of the parent particle, the end point of  $m_T$  represents the parent mass when they share the same origin. Since SM 1-lepton process is always with a leptonically decaying W-boson without additional hard missing particles, the bulk component experiences a sharp cut-off in  $m_T$  around  $m_W = 81.4$  GeV, therefore the cut above  $m_W$  is tremendously effective.

**E<sub>T</sub><sup>miss</sup>/m<sub>eff</sub>**  $E_T^{\text{miss}}/m_{\text{eff}}$  separates backgrounds and signals targeted by the **2J** and **High-x** where jet activity is relatively low compared with the magnitude of MET required.

**Aplanarity** Aplanarity [?] is a variable characterizing the 3-dimensionality of an event in terms of the final state particles. It is defined by the thirtial eigenvalue of the normalized momentum tensor  $S$  constructed from 3-momenta of jets and leptons:

$$\begin{aligned} S^{\alpha\beta} &:= \frac{\sum_{i \in j, \ell} p_i^\alpha p_i^\beta}{\sum_i |\mathbf{p}_i|^2}, \\ P^{-1} S P &= \begin{pmatrix} \lambda_1 & & \\ & \lambda_2 & \\ & & \lambda_3 \end{pmatrix}, \quad \lambda_1 > \lambda_2 > \lambda_3, \\ \text{Aplanarity} &:= \frac{3}{2} \times \lambda_3, \end{aligned} \tag{88}$$

where  $P$  stands for the  $3 \times 3$  matrix diagonalizing  $S$ ,  $\lambda_i$  for the eigenvalues of  $S$ . It ranges from  $0 < A < 1/2$ ;  $A = 0$  corresponds to events with jets distributed in the common plain, and  $A = 0.5$  represents the isotropically distributed event topology. Aplanarity is an effective discriminator after requiring tight selection in  $m_{\text{eff}}$  or  $E_T^{\text{miss}}$ , where the remnant SM events (particularly  $W + \text{jets}$ ) are typically heavily kicked by hard ISR radiations, leading to a highly linear event topology in their center-of-mass frame. These events end up in a planar topology in the lab frame once getting boosted toward the beam direction, as a result populating in low aplanarity region accordingly. On the other hand, the decay of gluino pairs keep relatively spherical thus the aplanarity distributing rather flatly, which reflects the fact the gluinos are too heavy to be boosted.

**$n_J/p_T(\ell_1)$**  Since the hardness of lepton and jets are positively correlated in normal processes in SM, it is relatively rare to end up in a soft lepton and hard jet activity simultaneously, while it is the case for the compressed gluino signature. A variable  $n_J/p_T(\ell_1)$  helps visualize the different correlations, and used in the **2J** signal region towers to improve the sensitivity of the compressed gluino signatures.

$\min_{i=1-4} \Delta\phi(j_i, \mathbf{E}_T^{\text{miss}})$  A variable intended to reject the remnant  $t\bar{t}$  events after requiring tight selection of  $m_{\text{eff}}$  and  $E_T^{\text{miss}}$ . As such  $t\bar{t}$  events typically have hard ISR jets to boost the  $t\bar{t}$  system, the jets from  $t\bar{t}$  decays and associated soft radiation tend to be collimated each other. Conversely, the jets from the gluino decays almost never get collimated as due to the heavy mass of gluino.

**Topness** One of the most important background in 1-lepton analysis is di-leptonic  $t\bar{t}$  events with a hadronically decaying tau lepton or a lepton that fails the baseline requirement. To reject those events, a  $\chi^2$ -based di-leptonic  $t\bar{t}$  tagger “topness” has been designed in context of scalar-top search since Run1 [?]. The  $\chi^2$  function is defined as:

$$\begin{aligned}
S(p_W^x, p_W^y, p_W^z, p_\nu^z) \\
= & \chi^2(m_{t,1}^2) + \chi^2(m_{t,2}^2) + \chi^2(m_{W,1}^2) + \chi^2(\hat{s}(t\bar{t})) \\
= & \frac{(m_t^2 - (p_{b,1} + p_\ell + p_\nu)^2)^2}{a_t^4} \\
& + \frac{(m_t^2 - (p_{b,2} + p_W)^2)^2}{a_t^4} \\
& + \frac{(m_W^2 - (p_\ell + p_\nu)^2)^2}{a_W^4} \\
& + \frac{(4m_t^2 - (p_\ell + p_\nu + p_{b,1} + p_{b,2} + p_W)^2)^2}{a_{t\bar{t}}^4}, \tag{89}
\end{aligned}$$

assuming an event topology as shown Figure 55 where one of the lepton are totally undetected and the momentum does fully contribute to MET.

It consists of four gaussian constraints imposing the mass constraint of top-quark and W-boson, and the center-of-mass for the  $t\bar{t}$  system being close to its minimum threshold ( $2m_t$ ). The width parameters are set to  $(a_t, a_W, a_{t\bar{t}}) = (15, 5, 1000)$  GeV, accounting for the Breit-Wigner widths of top-quark and W-boson as well as the tail of  $\hat{s}(t\bar{t})$  distribution. Although there are three missing particles in the topology, the number of unknown degree of freedom can be reduced into 4 by combining the missing lepton ( $\ell_2$ ) and the paired neutrino ( $\nu'$ ) into a single onshell W-boson and imposing the vectorial sum of transverse momenta of missing

particles being equal to  $E_T^{\text{miss}}$ . Topness is then defined as the minimum  $\chi^2$  when scanning over the four DOFs parametrized by  $p_W$  and  $p_\nu^z$ :

$$\text{Topness} := \min_{p_W^x, p_W^y, p_W^z, p_\nu^z} \ln[S]. \quad (90)$$

Events in the topology assumed are supposed to have solutions  $(p_W^x, p_W^y, p_W^z, p_\nu^z)$  that satisfy the four constraints at the same time while scanning, however it is not necessarily the case for the other type of events. Figure 55 shows typical separation between di-leptonic  $t\bar{t}$  and signals. Although di-leptonic  $t\bar{t}$  does have a fraction of unfortunate events on the pile of higher values due to the fact that the energy of missing leptons or tau leptons does not entirely contribute to MET, the majority resides on the left pile while signals typically populate more in the opposite one.

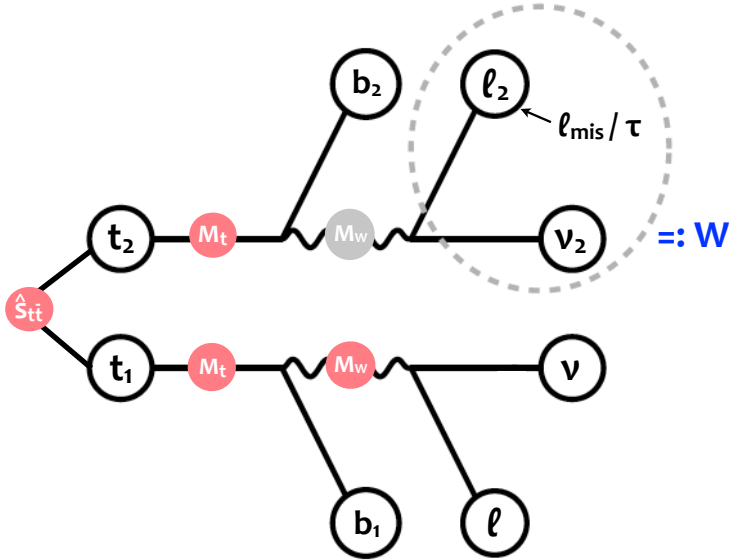


Figure 55: Di-leptonic  $t\bar{t}$  topology assumed in the topness calculation where one lepton is tagged ( $\ell_1$ ) and the other lepton ( $\ell_2$ ) is not identified as any objects with its momentum fully contributing to MET. Topness is defined as minimum summed  $\chi^2$  of three mass shell constraints for the top, anti-top and the W-boson decaying into  $\ell_1$ , as well as one pseudo-mass constraint in terms of the  $t\bar{t}$  systems (labeled as pink circles), while scanning over the momenta space of missing particles. The degrees of freedom by  $\ell_2$  and the associated neutrino ( $\nu_2$ ) are combined into a 4-momentum  $p_W$  with the mass fixed to  $m_W = 81.2$  GeV, and the scan is performed in terms of  $p_W^x, p_W^y, p_W^z$  and  $p_\nu^z$  from  $-4$  TeV to  $4$  TeV respectively.

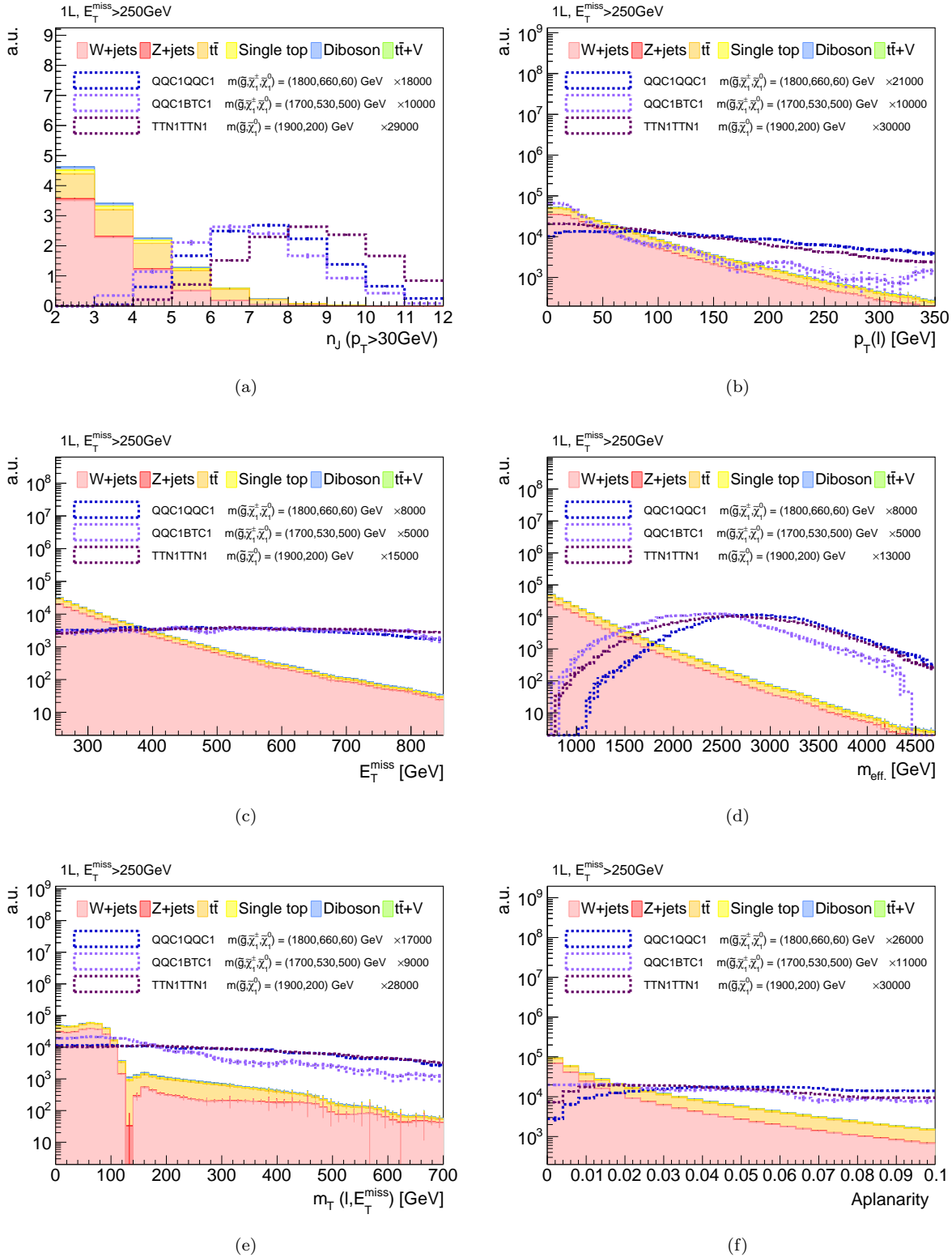


Figure 56: Distributions of discriminating variables for reference signal and backgrounds, at the preselection level. (a)  $n_J$ , (b) Lepton  $p_T$ , (c)  $E_T^{\text{miss}}$ , (d)  $m_{\text{eff.}}$ , (e)  $m_T$  and (f) aplanarity are respectively shown.

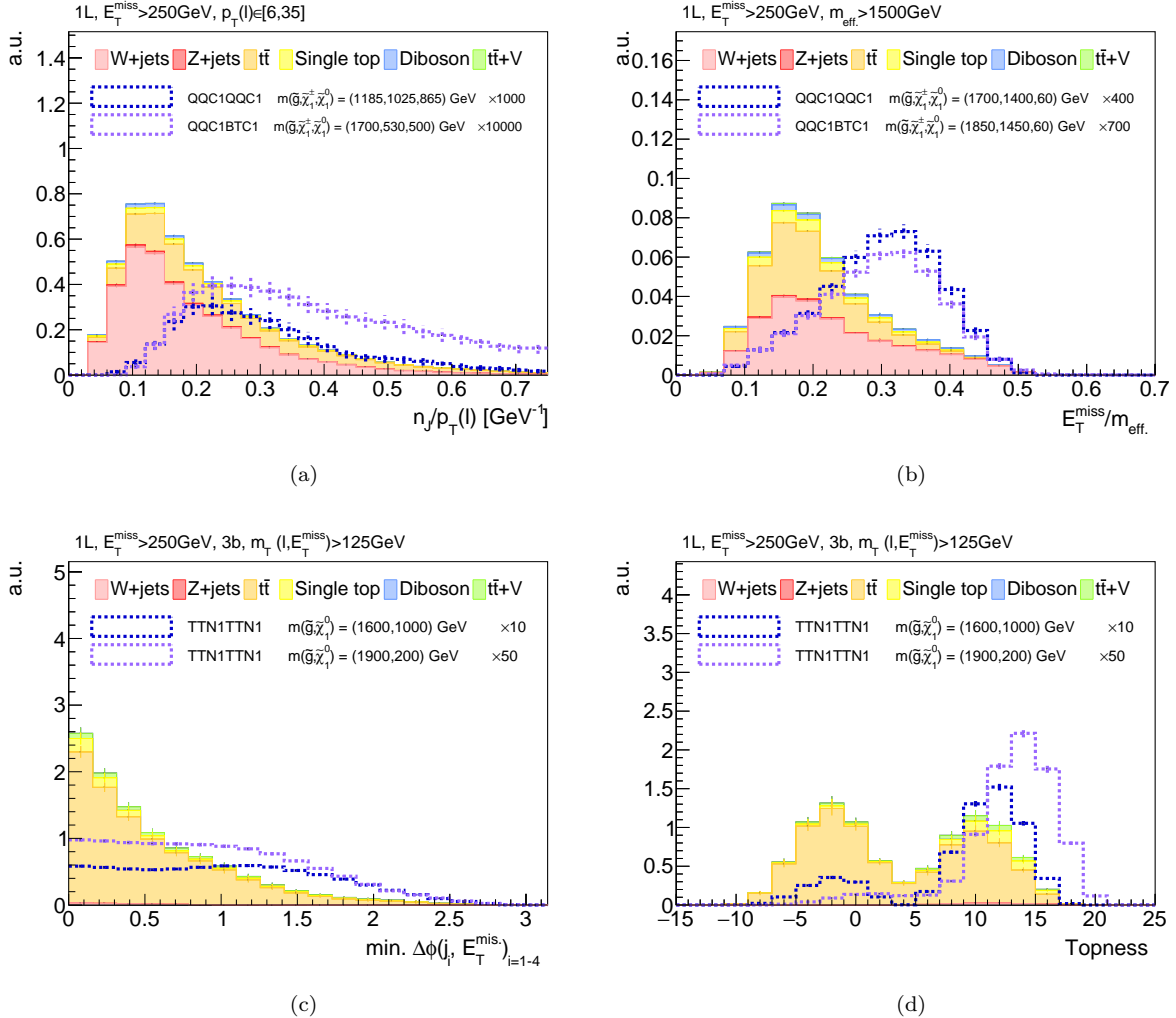


Figure 57: Distributions of discriminating variables at the preselection level. Soft lepton requirement:  $p_T(\ell) \in [6, 35]$  is applied for (b), and  $n_B \geq 3$   $m_T > 125$  GeV is applied for (c).

### 5.3.3 Cut Optimization

The cut values for the kinematic variables listed above are optimized, including the lower  $m_{\text{eff}}$  cut for the highest  $m_{\text{eff}}$ -bin. Reference signal points are defined in Table 18, to which the sensitivity is optimized. The optimization procedure proceeds as following.

1. The binning of  $m_{\text{eff}}$  is roughly decided so that the sensitivities for all the reference points in the same tower are maintained.
2. Cuts values in other variables are then optimized by a simultaneous grid scan using machinery. The initial values are chosen based on the target mass regions of each signal region (as depicted by Figure 53-Figure 54), and the typical kinematics of such signals as shown in Figure 154-157 in Appendix A. The sensitivity as the reference of the optimization is defined by the combined significance of  $m_{\text{eff}}$  bins such as :

$$Z_{N,\text{comb.}} = \sqrt{\sum_i Z_{N,i}^2},$$

$$Z_{N,i} := S_i / \sqrt{B_i + \alpha^2 B_i^2}, \quad (91)$$

where  $Z_{N,i}$  is the significance provided by a single  $m_{\text{eff}}$  bin, with  $S_i$ ,  $B_i$  being the signal and background yields in the  $m_{\text{eff}}$  bin.  $\alpha$  is relative uncertainty on the background expectation in each  $m_{\text{eff}}$  bin, which is set to 30% given the typical level systematic uncertainty. The cut between BT and BV bins in the same tower and  $m_{\text{eff}}$ -bin are always set to common.

3. All the cuts including the  $m_{\text{eff}}$  binning are re-optimized by perturbing them from the optimum configuration obtained in the previous step simultaneously.
4. Optimum cuts are different between reference points in the same  $m_{\text{eff}}$  tower. An adjustment is therefore applied for the best compromise, as well as to avoid the over-optimization on specific signal points.
5. Another minor adjustment is done afterwards, required from the context of background estimation. Some of the cuts are loosened to facilitate the control region definition.

Finalized definition of signal regions are shown in Table 19-23. The  $m_{\text{eff}}$  distribution in the optimized signal regions are displayed in Figure 58-62 for backgrounds with the reference signal points overlaid. The segmentation of  $m_{\text{eff}}$ -bin is found to successfully address the sensitivity in different mass region in the signal grid.

The optimized selection is also validated by a set looking at the kinematic distribution Figure 63-71 in which the one of the cuts is loosened from the optimized signal regions. The sensitivity is calculated as function of the cut position of the removed cut. The decided cuts are shown by the red arrows, which are more or less at the optimum position for all the reference signals.

Table 18: The reference signal points for each signal regions to which the selection is optimized to.

Model	$(m_{\tilde{g}}, m_{\tilde{\chi}_1^\pm}, m_{\tilde{\chi}_1^0}), (m_{\tilde{g}}, m_{\tilde{\chi}_1^0})$ [GeV]
<b>2J BV</b>	
QQC1QQC1	(1550,580,550)
QQC1QQC1	(1065,1025,985)
TTN1TTN1	(1000,915)
<b>2J BT</b>	
QQC1BTC1	(1400,830,800)
QQC1BTC1	(1550,780,750)
<b>6J BV</b>	
QQC1QQC1	(1945,1105,265)
QQC1QQC1	(1850,1350,850)
QQC1QQC1	(1700,1300,900)
<b>6J BT</b>	
QQC1BTC1	(1850,1050,250)
QQC1BTC1	(1700,1300,900)
<b>Low-x BV</b>	
QQC1QQC1	(1700,460,60)
QQC1QQC1	(1600,260,60)
QQC1QQC1	(1700,530,500)
<b>Low-x BT</b>	
QQC1BTC1	(1700,730,700)
QQC1BTC1	(1700,530,500)
<b>High-x BV</b>	
QQC1QQC1	(1800,1600,60)
QQC1QQC1	(1800,1460,60)
QQC1QQC1	(1800,1260,60)
<b>High-x BT</b>	
QQC1BTC1	(1850,1750,60)
QQC1BTC1	(1850,1450,60)
<b>3B</b>	
TTN1TTN1	(2000,0)
TTN1TTN1	(1900,800)
TTN1TTN1	(1500,1000)

Table 19: Definition of signal/control/validation regions (SRs/CRs/VRs) for tower "2J"

	SR (BV/BT)	WR/TR	VR $E_T^{\text{miss}}$	VRb	VR QCD	VR DB
$n_{\ell,\text{base.}}$	1	1	1	1	1	2
$n_{\ell,\text{sig.}}$	1	1	1	1	0	2
$p_T(\ell)$			[6, 35]			-
$n_J(p_T > 30 \text{ GeV})$			$\geq 2$			$\geq 1$
$n_B(p_T > 30 \text{ GeV})$	0/[1,2]	0/[1,2]	-	-	-	0
$E_T^{\text{miss}}$	$> 430$	[250, 430]	[250, 430]	$> 430$	$> 430$	$> 250$
$m_{\text{eff}}$			[1100, 1500], [1500, 1900], $> 1900$			
$m_T(p_T(\ell), E_T^{\text{miss}})$	$> 100$	[30, 100]	$> 100$	[30, 100]	$> 100$	-
$E_T^{\text{miss}}/m_{\text{eff}}$	$> 0.25$	$> 0.15$	$> 0.1$	$> 0.2$	$> 0.25$	-
$n_J/p_T(\ell)$		$> 0.2$		$> 0.15$		$> 0.2$
Topness	$> 4$	-	-	$> 4$	$> 4$	

Table 20: Definition of signal/control/validation regions (SRs/CRs/VRs) for tower "6J"

	SR (BV/BT)	WR/TR	VRa	VRb	VR QCD	VR DB
$n_{\ell,\text{base.}}$	1	1	1	1	1	2
$n_{\ell,\text{sig.}}$	1	1	1	1	0	2
$p_T(\ell)$			$> 35$			
$n_J(p_T > 30 \text{ GeV})$			$\geq 6$			$\geq 5$
$n_B(p_T > 30 \text{ GeV})$	0/[1,2]	0/[1,2]	-	-	-	0
$E_T^{\text{miss}}$	$> 350$	$> 300$	$> 250$	$> 350$	$> 350$	$> 250$
$m_{\text{eff}}$			[1100, 1600], [1600, 2100], $> 2100$			
$m_T(p_T(\ell), E_T^{\text{miss}})$	$> 175$	[40, 125]	[125, 400]	[40, 125]	$> 125$	-
Aplanarity	$> 0.06$	$< 0.06$	$< 0.04$	$> 0.06$	$> 0.06$	$< 0.06$
Topness	$> 4$	-	-	$> 4$	$> 4$	

Table 21: Definition of signal/control/validation regions (SRs/CRs/VRs) for tower "Lowx"

	SR (BV/BT)	WR/TR	VRa	VRb	VR QCD	VR DB
$n_{\ell,\text{base.}}$	1	1	1	1	1	2
$n_{\ell,\text{sig.}}$	1	1	1	1	0	2
$p_T(\ell)$			[6, 35]			-
$n_J (p_T > 30 \text{ GeV})$			$\geq 4$			$\geq 3$
$n_B (p_T > 30 \text{ GeV})$	$0/[1,2]$	$0/[1,2]$	-	-	-	0
$p_T(j_4)$			$> 80$			-
$E_T^{\text{miss}}$	$> 350$	$> 300$	$> 300$	$> 350$	$> 350$	$> 250$
$m_{\text{eff}}$				$> 1900$		
$m_T(p_T(\ell), E_T^{\text{miss}})$	$> 100$	[30, 100]	[100, 450]	[30, 100]	$> 100$	-
Aplanarity	$> 0.02$	$< 0.02$	$< 0.02$	$> 0.02$	$> 0.02$	$< 0.04$
Topness	$> 4$	-	-	$> 4$	$> 4$	

Table 22: Definition of signal/control/validation regions (SRs/CRs/VRs) for tower "Highx"

	SR (BV/BT)	WR/TR	VRa	VRb	VR QCD	VR DB
$n_{\ell,\text{base.}}$	1	1	1	1	1	2
$n_{\ell,\text{sig.}}$	1	1	1	1	0	2
$p_T(\ell)$				$> 35$		
$n_J (p_T > 30 \text{ GeV})$			$\geq 4$			$\geq 3$
$n_B (p_T > 30 \text{ GeV})$	$0/[1,2]$	$0/[1,2]$	-	-	-	0
$E_T^{\text{miss}}$	$> 300$	$> 300$	$> 300$	$> 300$	$> 300$	$> 250$
$m_{\text{eff}}$				$> 2000$		
$m_T(p_T(\ell), E_T^{\text{miss}})$	$> 300$	[30, 125]	[125, 600]	[30, 125]	$> 450$	-
$E_T^{\text{miss}}/m_{\text{eff}}$	$> 0.25$	$> 0.2$	$> 0.15$	$> 0.25$	$> 0.25$	$> 0.2$
Aplanarity	$> 0.01$	$< 0.01$	$< 0.01$	$> 0.01$	$> 0.01$	$< 0.02$
Topness	$> 4$	-	-	$> 4$	$> 4$	

Table 23: Definition of signal/control/validation regions (SRs/CRs/VRs) for tower "3B"

	SR	TR	VR $m_T$	VRb	VR QCD
$n_{\ell,\text{base.}}$	1	1	1	1	1
$n_{\ell,\text{sig.}}$	1	1	1	1	0
$p_T(\ell)$			$> 15$		
$n_J (p_T > 30 \text{ GeV})$			$\geq 7$		
$n_B (p_T > 30 \text{ GeV})$			$\geq 3$		
$E_T^{\text{miss}}$	$> 300$	$> 250$	$> 250$	$> 250$	$> 300$
$m_{\text{eff}}$			$[1000, 1750], > 1750$		
$m_T(p_T(\ell), E_T^{\text{miss}})$	$> 175$	$[30, 125]$	$[125, 450]$	$[30, 125]$	$> 175$
Aplanarity	$> 0.01$	-	-	$> 0.01$	$> 0.01$
$\min_{i=1-4} \Delta\phi(j_i, E_T^{\text{miss}})$	$> 0.45$	$< 0.45$	$< 0.45$	$> 0.3$	$> 0.45$
Topness	$> 6$	-	-	$> 6$	$> 6$

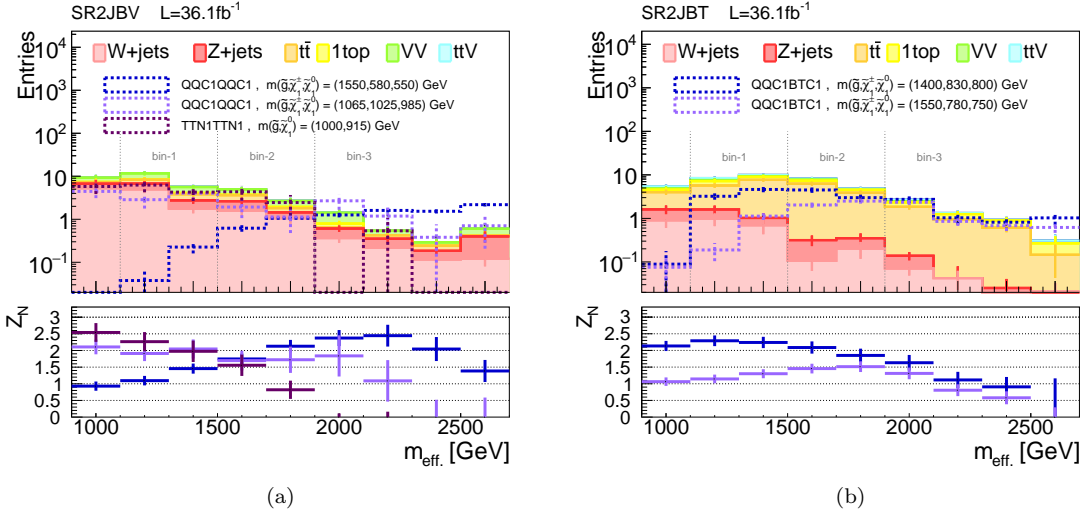


Figure 58:  $m_{\text{eff}}$  distribution in the (a) b-vetoed (BV) and (b) b-tagged (BT) slices of the optimized **2J** signal region. Bottom row display the sensitivity  $Z_N := S/\sqrt{B + \alpha^2 B^2}$  for each reference signals.

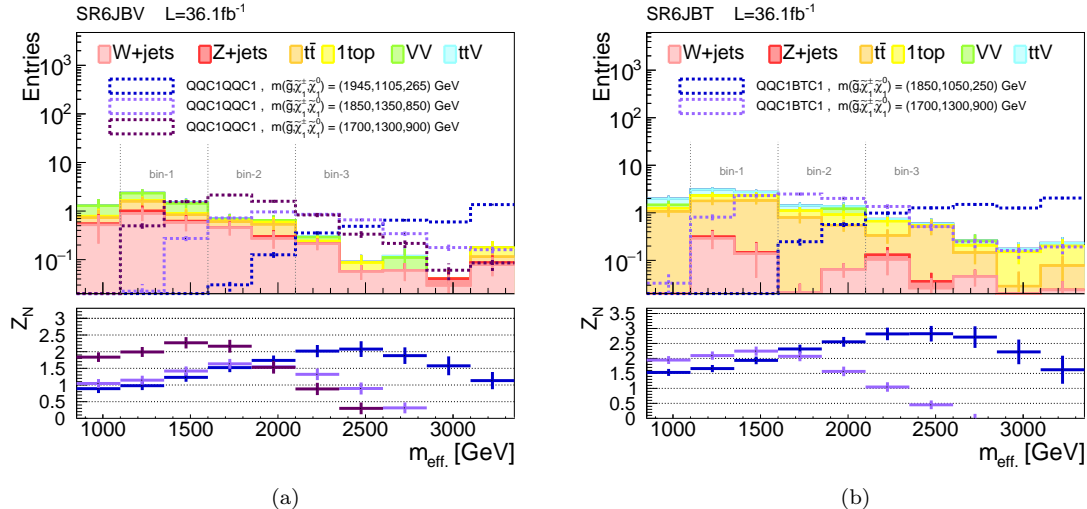


Figure 59:  $m_{\text{eff}}$  distribution in the (a) b-vetoed (BV) and (b) b-tagged (BT) slices of the optimized **6J** signal region. Bottom row display the sensitivity  $Z_N := S/\sqrt{B + \alpha^2 B^2}$  for each reference signals.

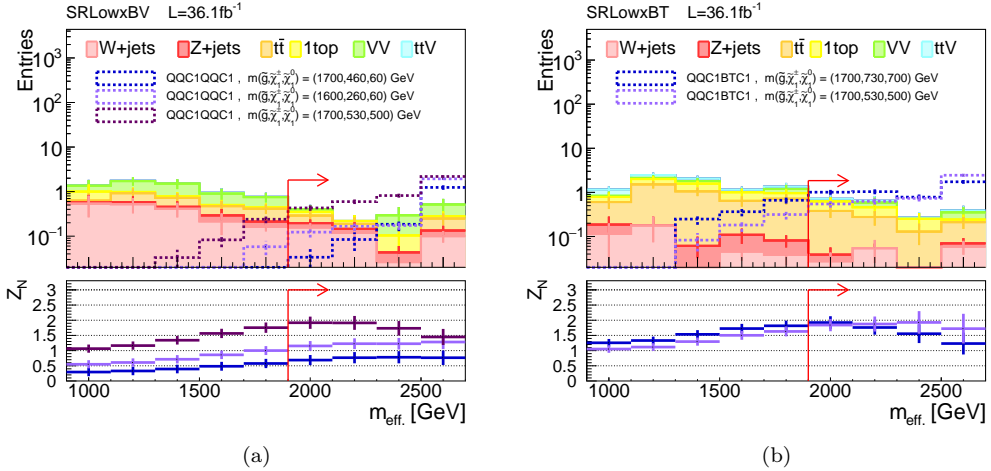


Figure 60:  $m_{\text{eff}}$  distribution in the (a) b-vetoed (BV) and (b) b-tagged (BT) slices of the optimized **Low-x** signal region. The red arrow indicates the cut position of  $m_{\text{eff}}$ . Bottom row display the sensitivity  $Z_N := S/\sqrt{B + \alpha^2 B^2}$  for each reference signals.

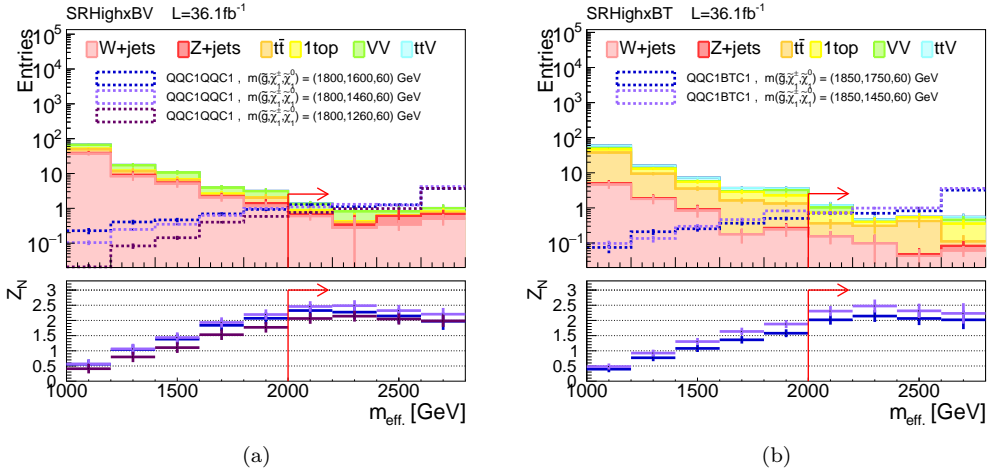
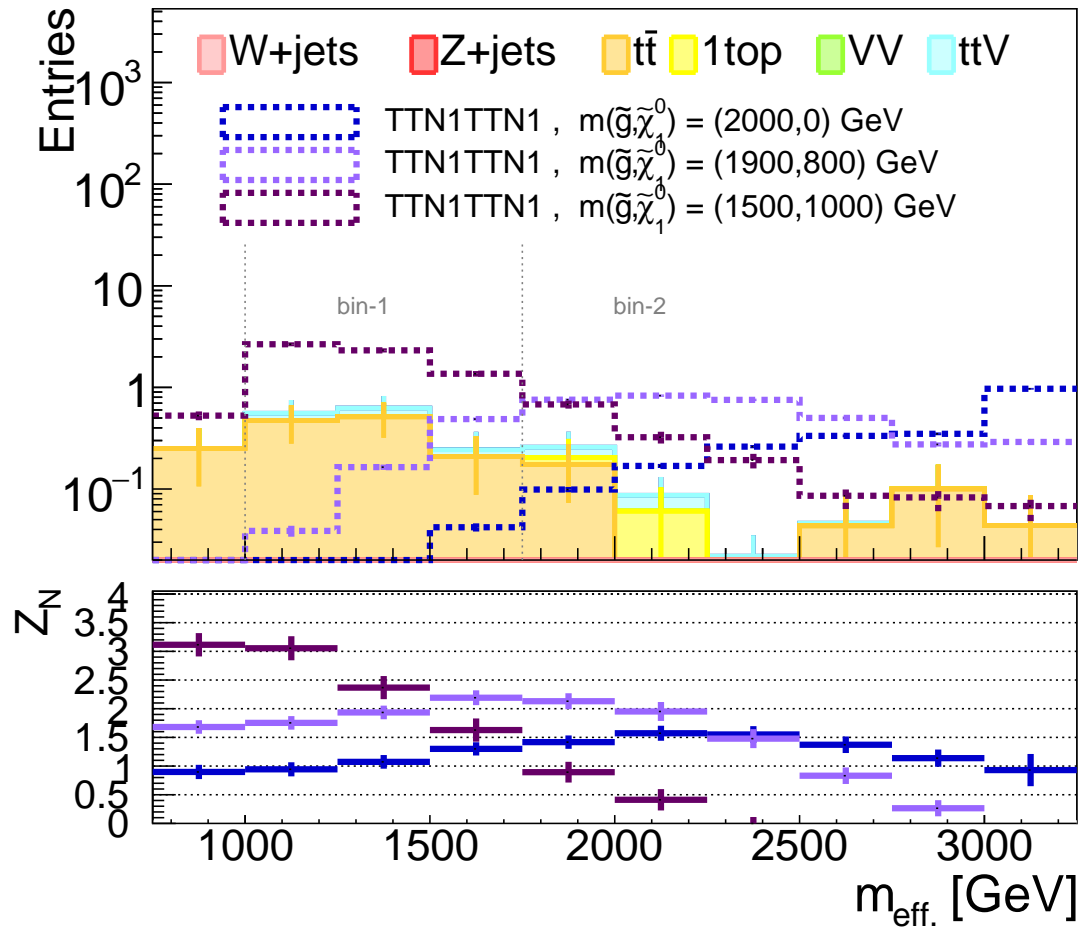


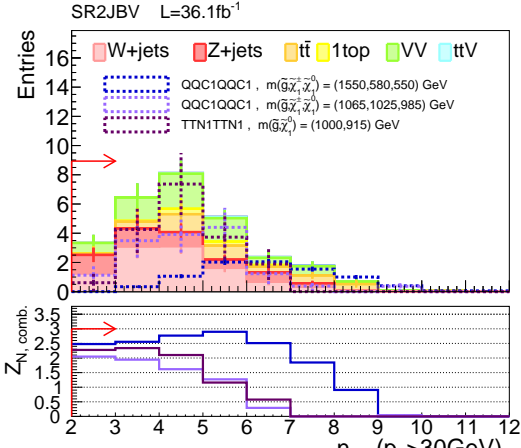
Figure 61:  $m_{\text{eff}}$  distribution in the (a) b-vetoed (BV) and (b) b-tagged (BT) slices of the optimized **High-x** signal region. The red arrow indicates the cut position of  $m_{\text{eff}}$ . Bottom row display the sensitivity  $Z_N := S/\sqrt{B + \alpha^2 B^2}$  for each reference signals.

SR3B L=36.1fb<sup>-1</sup>

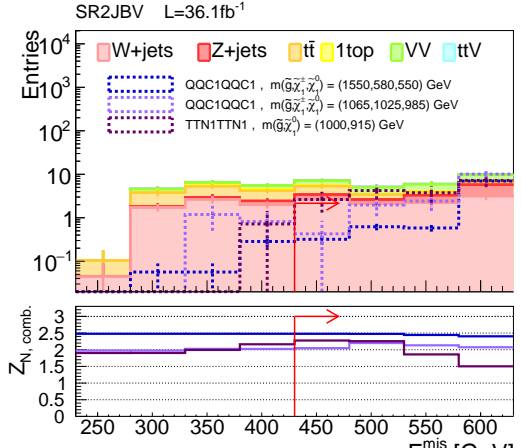


(a)

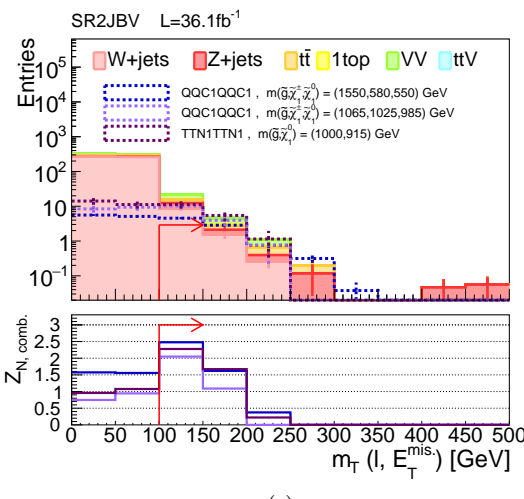
Figure 62:  $m_{\text{eff.}}$  distribution in the (a) b-vetoed (BV) and (b) b-tagged (BT) slices of the optimized **3B** signal region. Bottom row display the sensitivity  $Z_N := S/\sqrt{B + \alpha^2 B^2}$  for each reference signals.



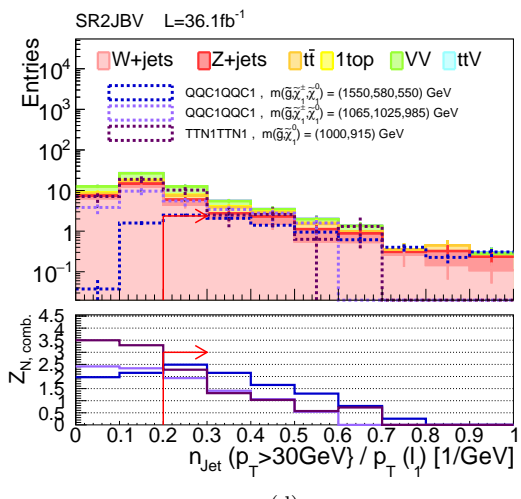
(a)



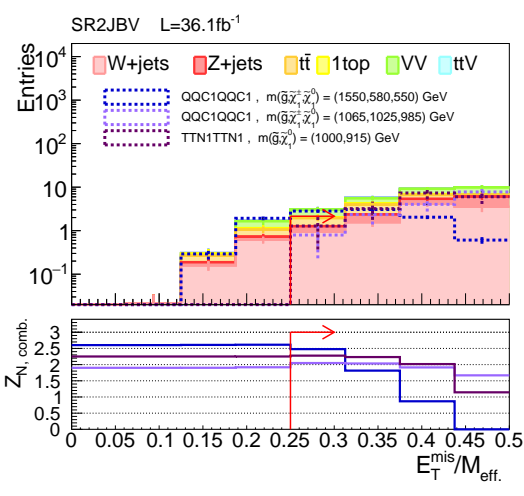
(b)



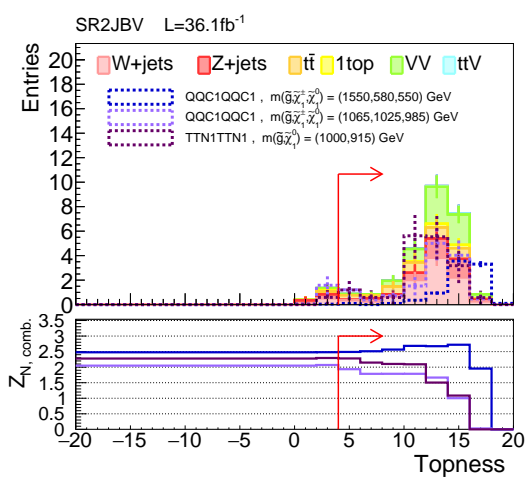
(c)



(d)

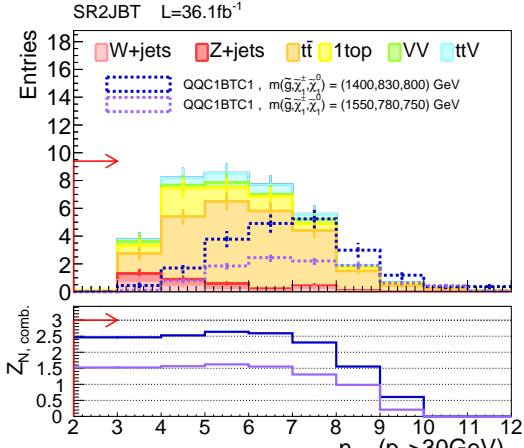


(e)

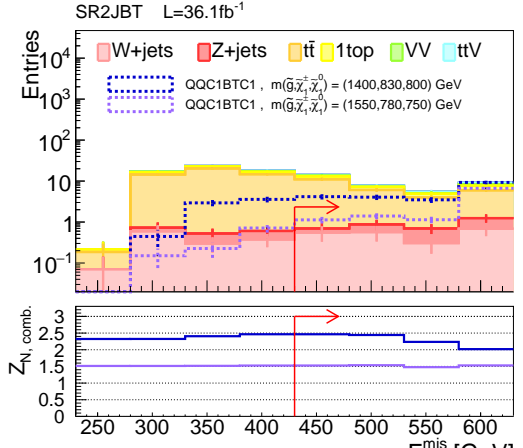


(f)

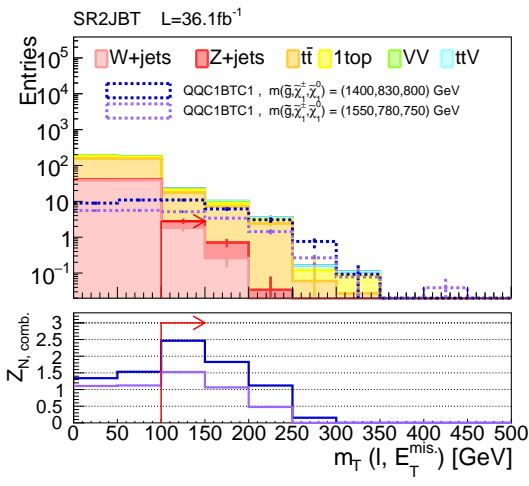
Figure 63: N-1 plots for the b-vetoed (BV) slices of the optimized **2J** signal regions. Bottom row presents the combined significance over the  $m_{\text{eff}}$  bins defined in Eq. 91.



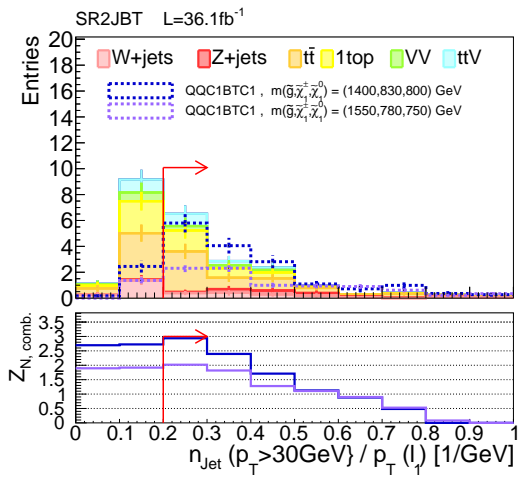
(a)



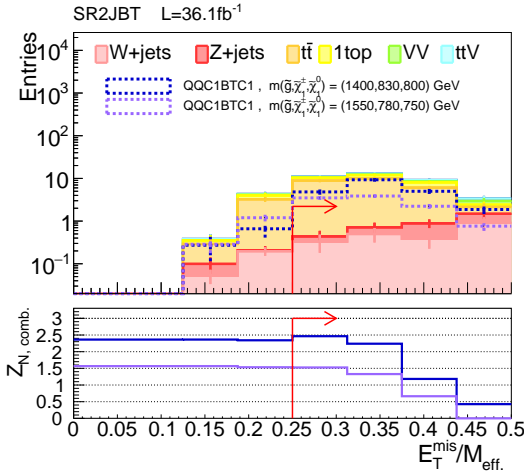
(b)



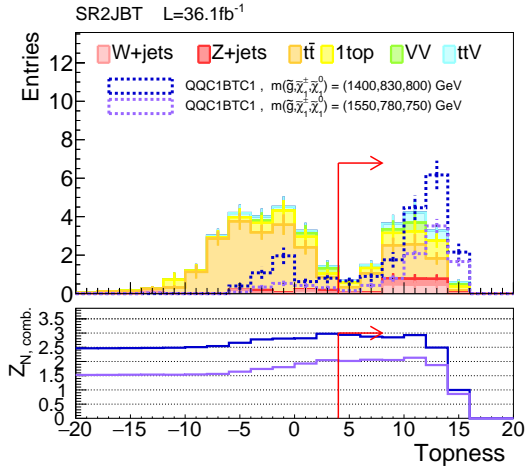
(c)



(d)



(e)



(f)

Figure 64: N-1 plots for the b-tagged (BT) slices of the optimized **2J** signal regions. Bottom row presents the combined significance over the  $m_{\text{eff}}$  bins defined in Eq. 91.

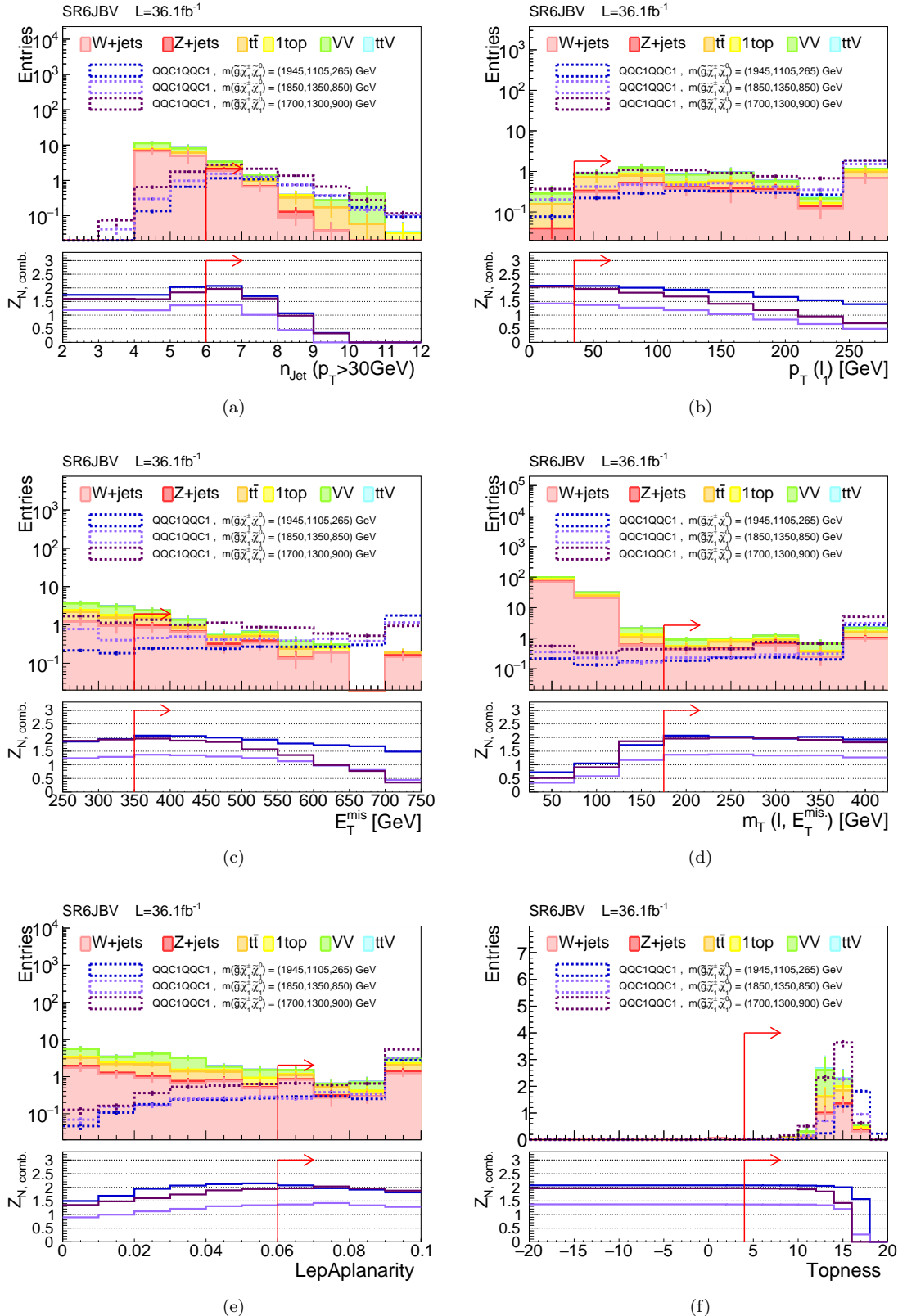


Figure 65: N-1 plots for the b-vetoed (BV) slices of the optimized **6J** signal regions. Bottom row presents the combined significance over the  $m_{\text{eff}}$  bins defined in Eq. 91.

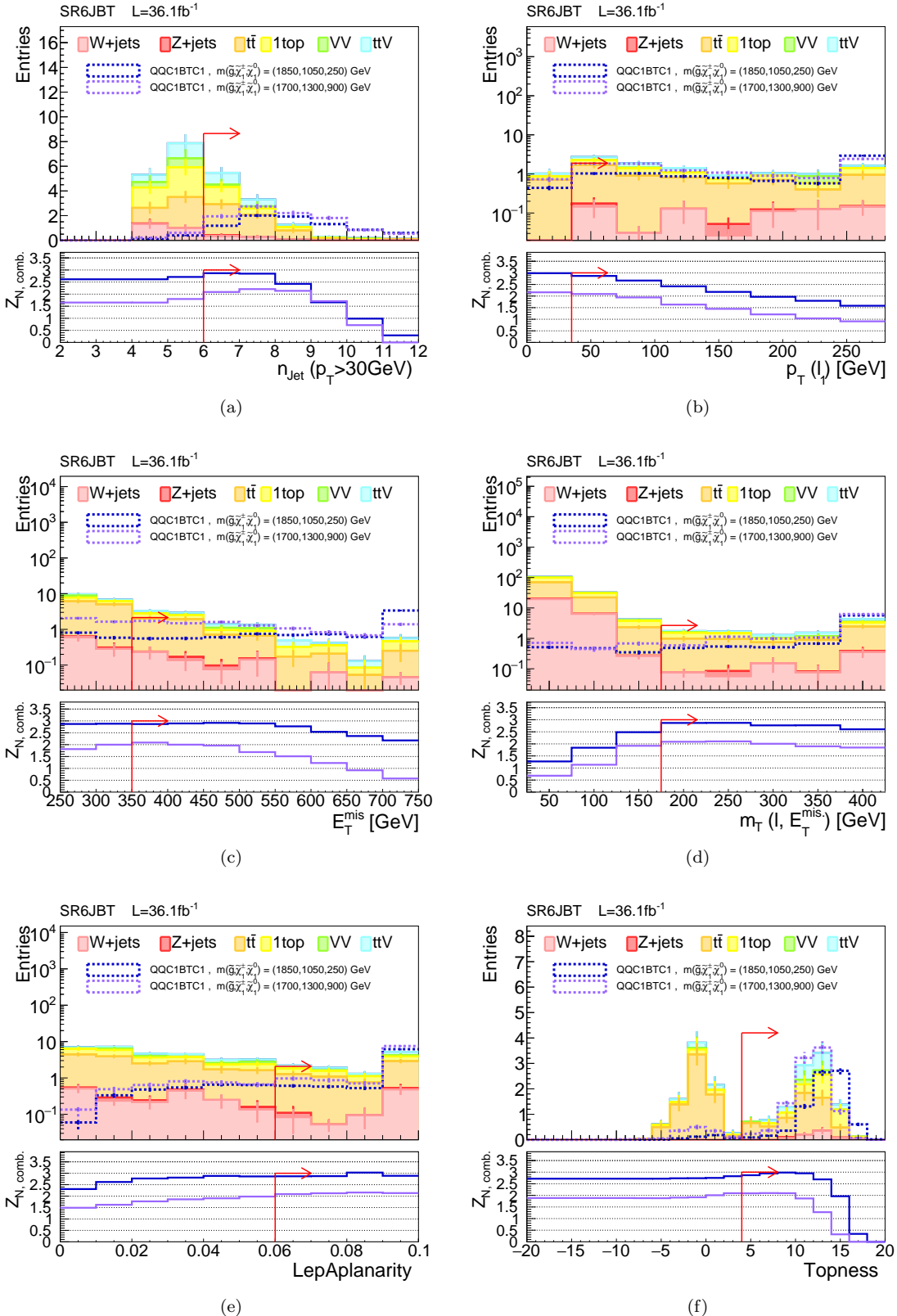


Figure 66: N-1 plots for the b-tagged (BT) slices of the optimized **6J** signal regions. Bottom row presents the combined significance over the  $m_{\text{eff}}$  bins defined in Eq. 91.

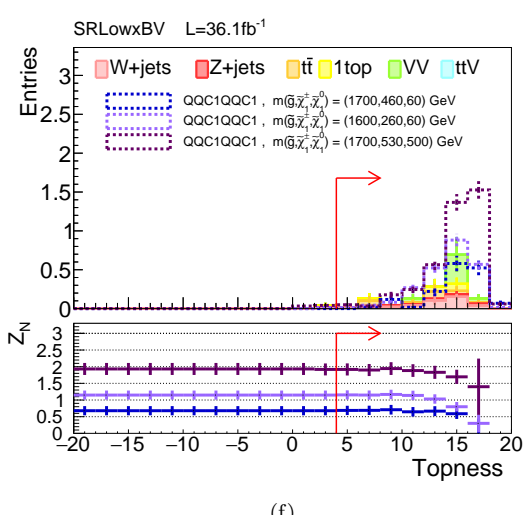
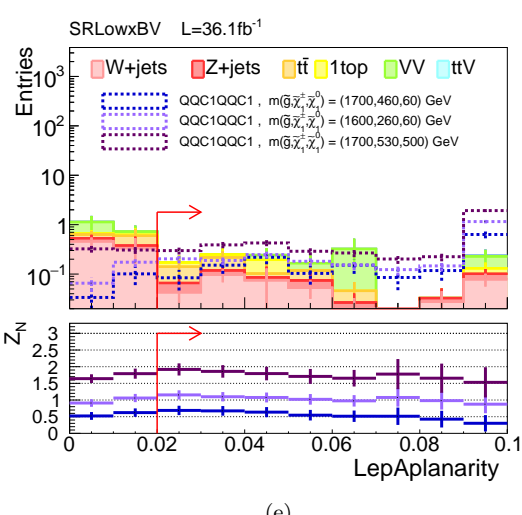
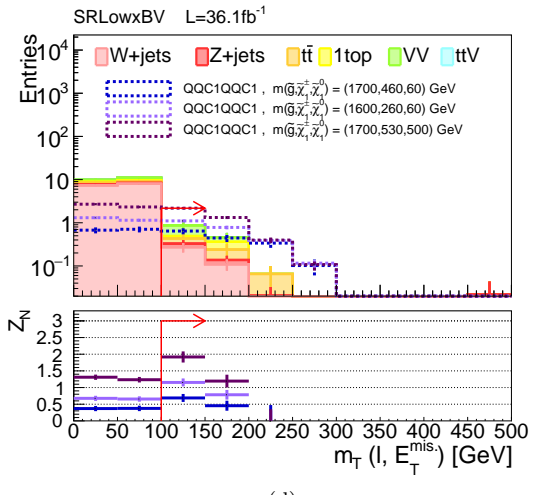
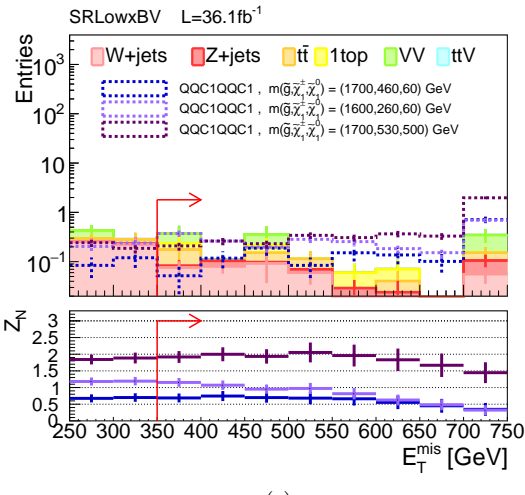
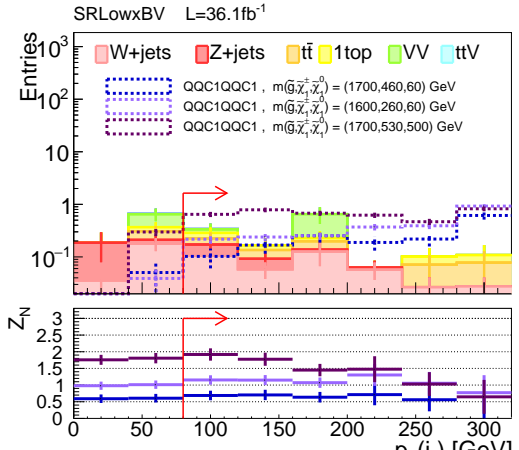
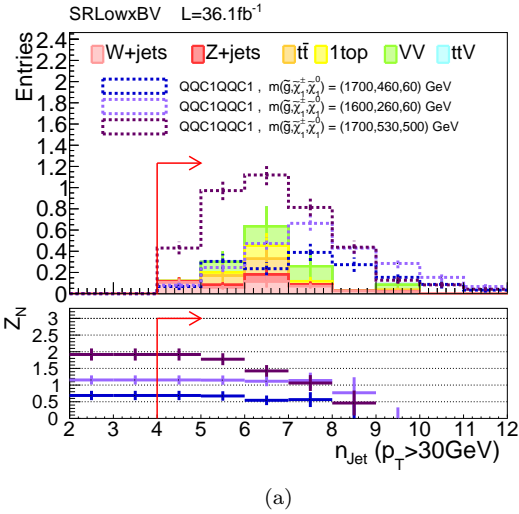


Figure 67: N-1 plots for the b-vetoed (BV) slices of the optimized **Low-x** signal region. Bottom row presents the single  $m_{\text{eff}}$  bin significance defined in Eq. 91.

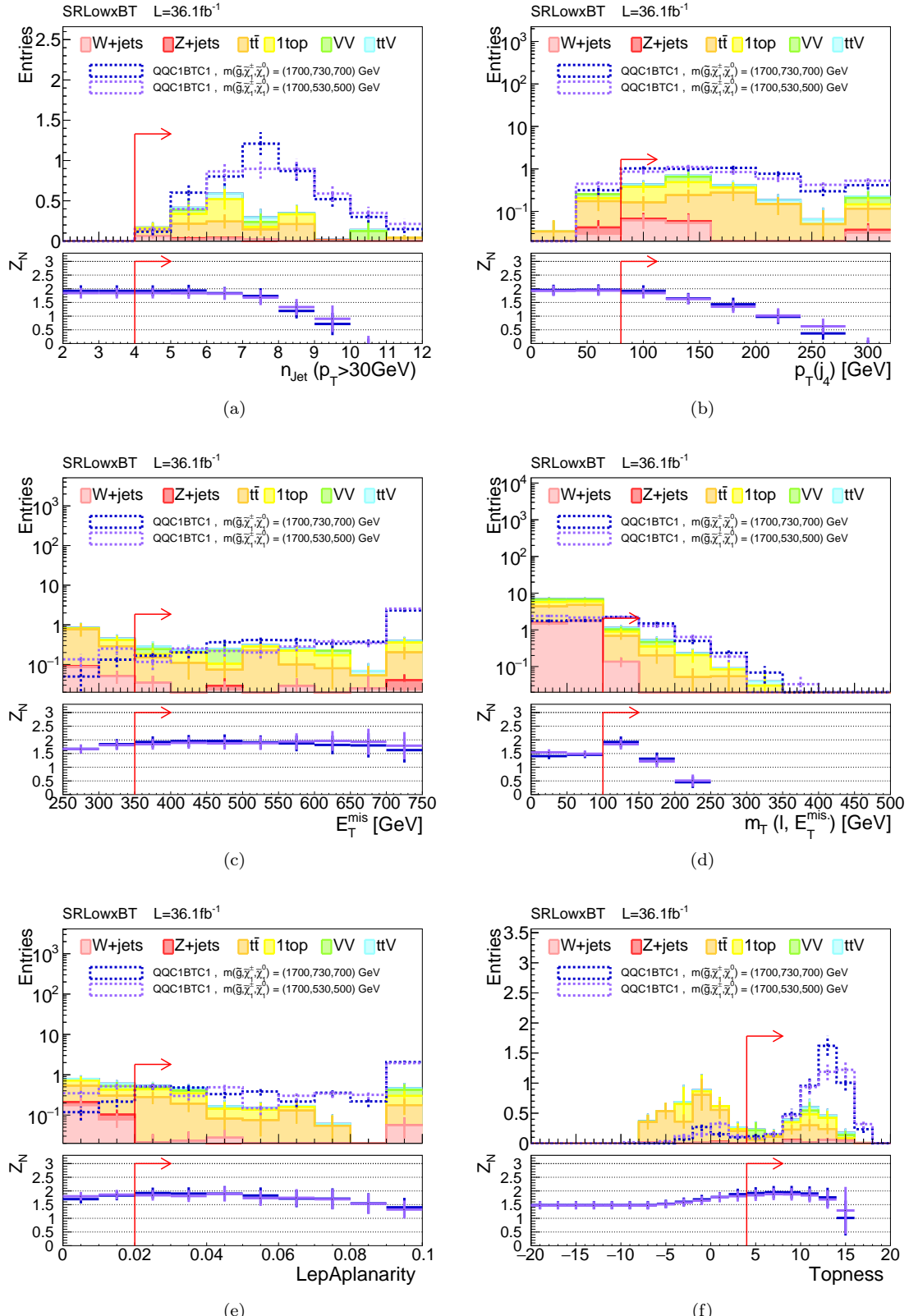
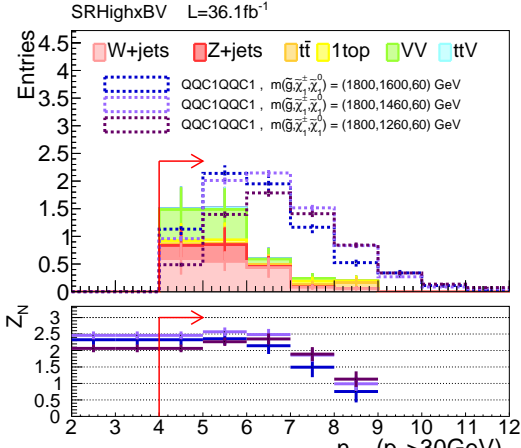
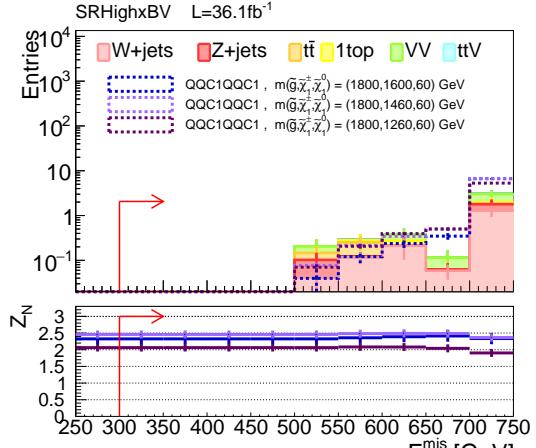


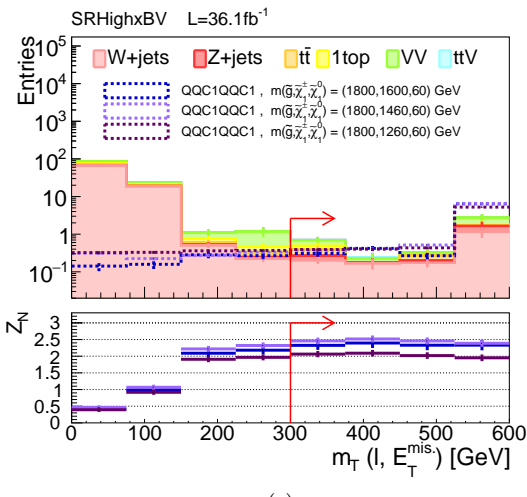
Figure 68: N-1 plots for the b-tagged (BT) slices of the optimized **Low-x** signal region. Bottom row presents the single  $m_{\text{eff}}$  bin significance defined in Eq. 91.



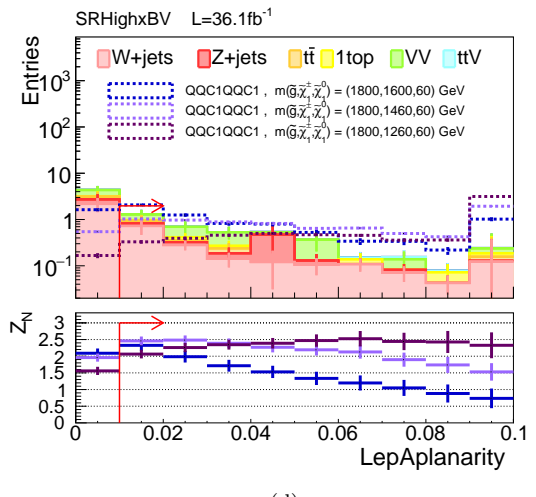
(a)



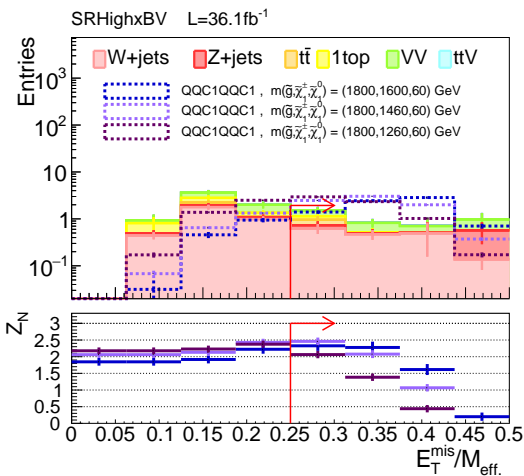
(b)



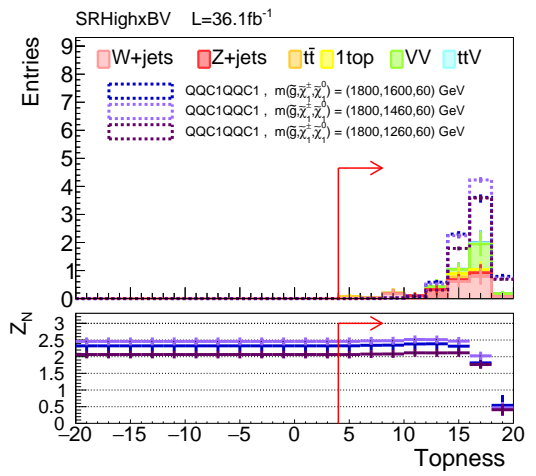
(c)



(d)

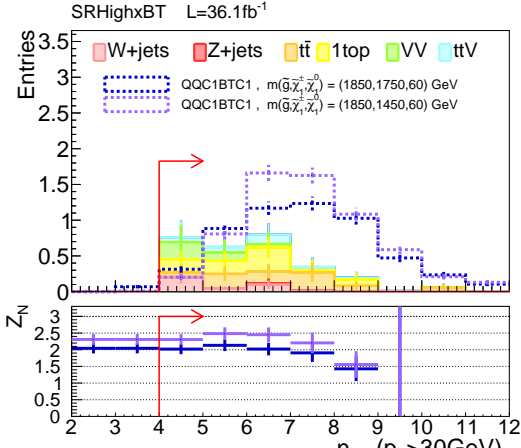


(e)

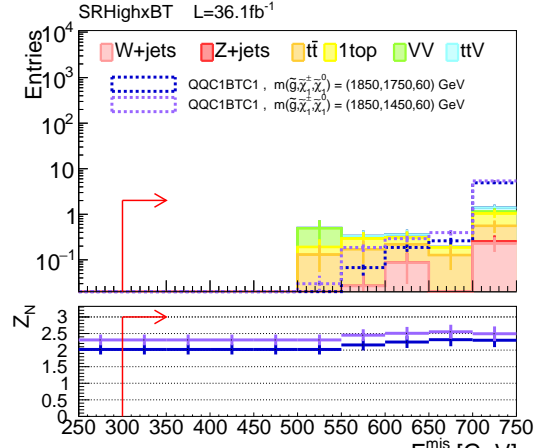


(f)

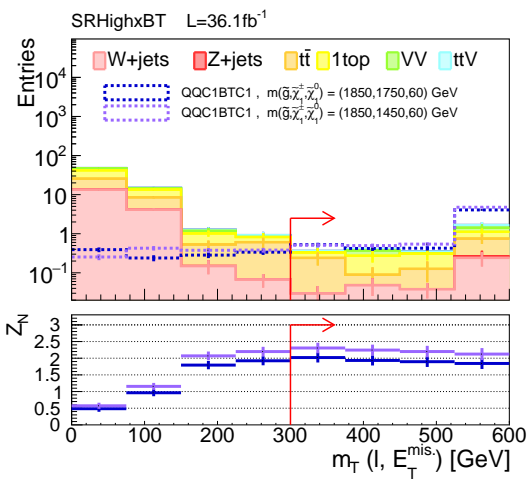
Figure 69: N-1 plots for the b-vetoed (BV) slices of the optimized **High-x** signal region. Bottom row presents the single  $m_{\text{eff}}$  bin significance defined in Eq. 91.



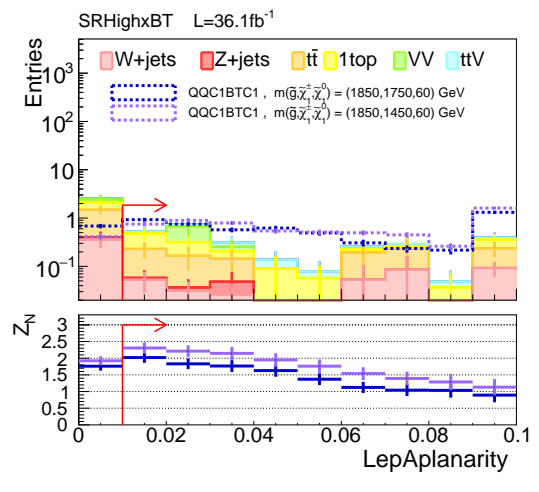
(a)



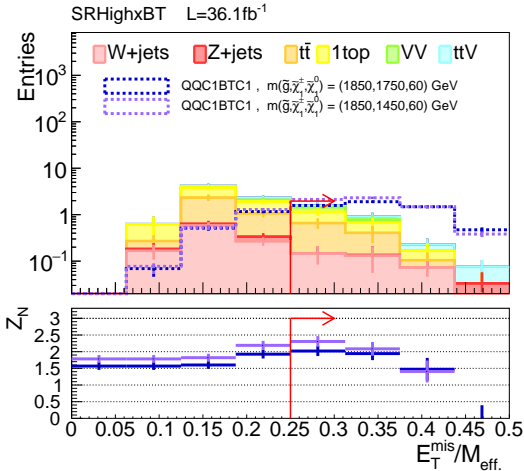
(b)



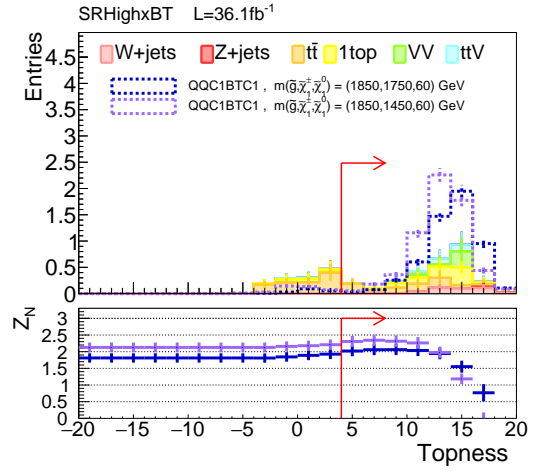
(c)



(d)



(e)



(f)

Figure 70: N-1 plots for the b-tagged (BT) slices of the optimized **High-x** signal region. Bottom row presents the single  $m_{\text{eff}}$  bin significance defined in Eq. 91.

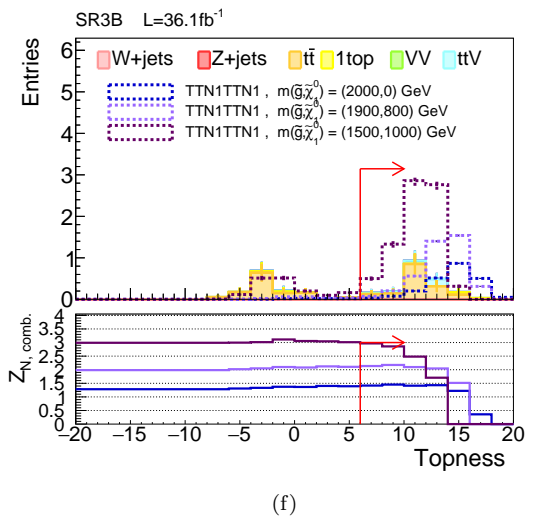
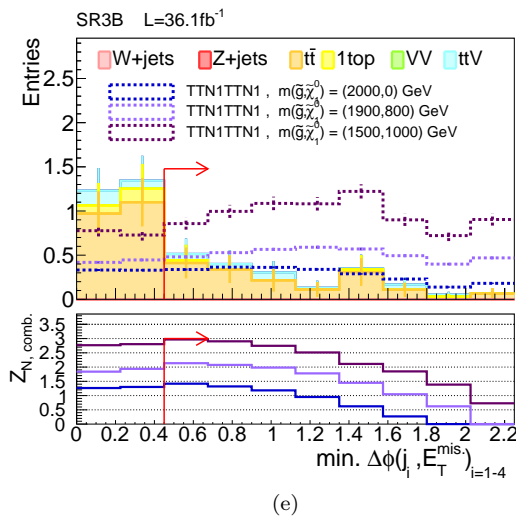
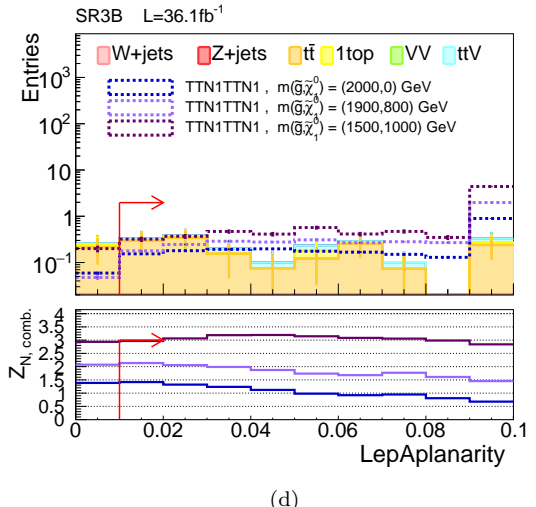
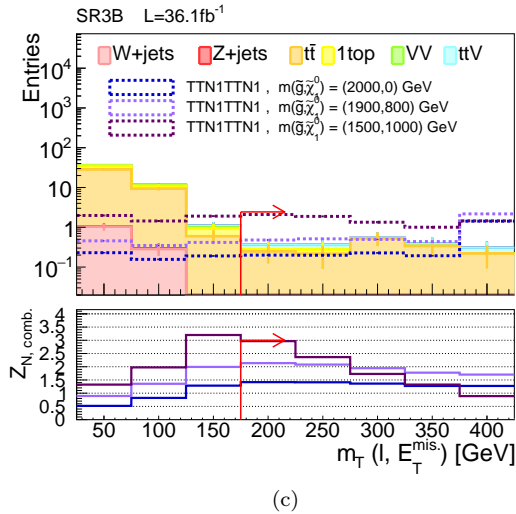
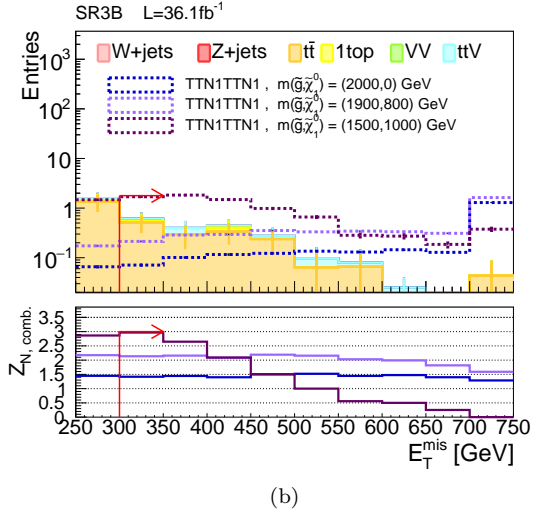
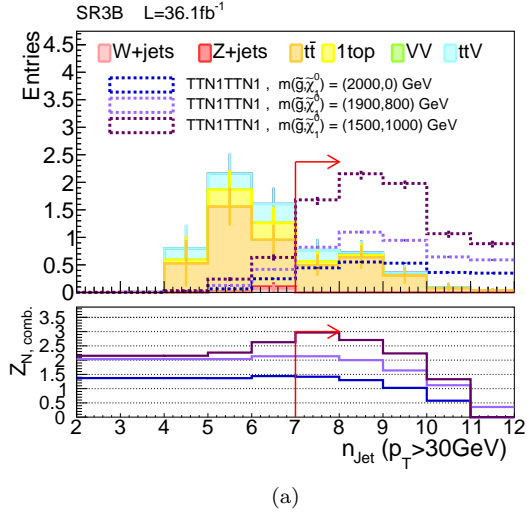


Figure 71: N-1 plots for the optimized **3B** signal regions. Bottom row presents the combined significace over the  $m_{\text{eff}}$  bins defined in Eq. 91.

### 5.3.4 Expected Sensitivity

The limits expected by the optimized signal regions are calculated for the grids of reference models. The expected exclusion limit with  $L = 36.1\text{fb}^{-1}$  for the TTN1TTN1 Direct grid is shown in 72. The dashed lines on the left plots indicate the exclusion provided by a single  $m_{\text{eff}}$  bin, and the solid lines being the limit given by respective signal region towers with combined bins. The ultimately sensitivity provided by the combined towers are shown in the right plots. Since the all five towers are not completely orthogonal (**2J** and **Low-x**, **6J** and **High-x** are partially overlapped), there are four possible way of combining orthogonal towers: {**2J**, **6J**, **3B**}, {**2J**, **High-x**, **3B**}, {**Low-x**, **6J**, **3B**}, and {**Low-x**, **High-x**, **3B**}. The final result will be provided using the combination with best expected sensitivity. The expected sensitivity for QQC1QQC1 and QQC1BTC1 are presented in Figure 73 and Figure 74. Nice complementality between the signal region towers are shown. No suspicious structure indicating local over-optimization onto specific mass region is found, ensuring the inclusive sensitivity of the search.

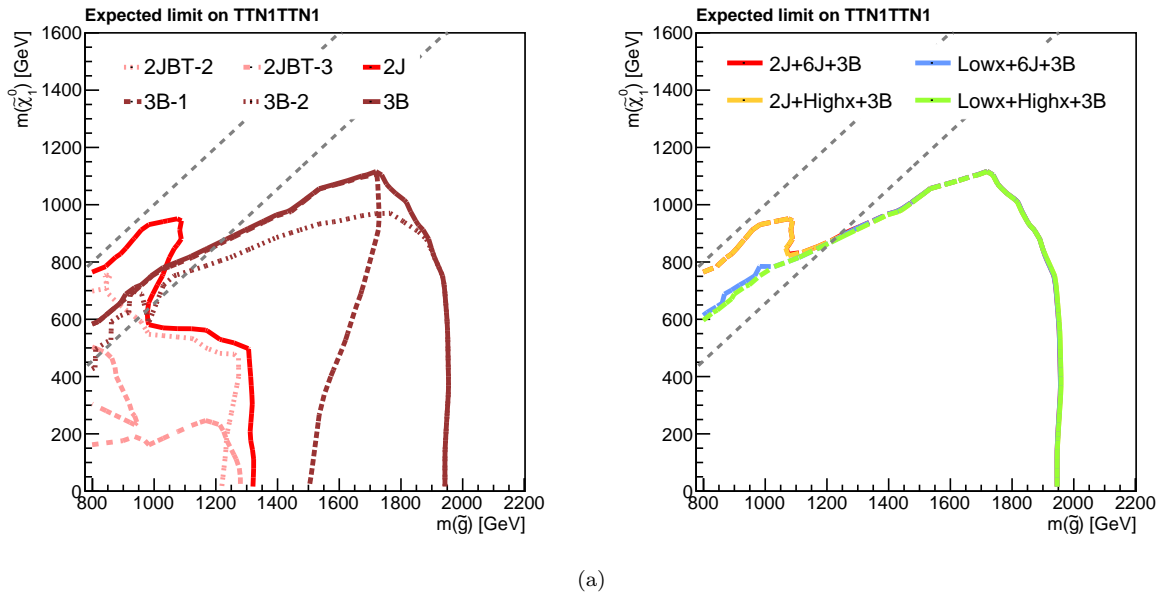
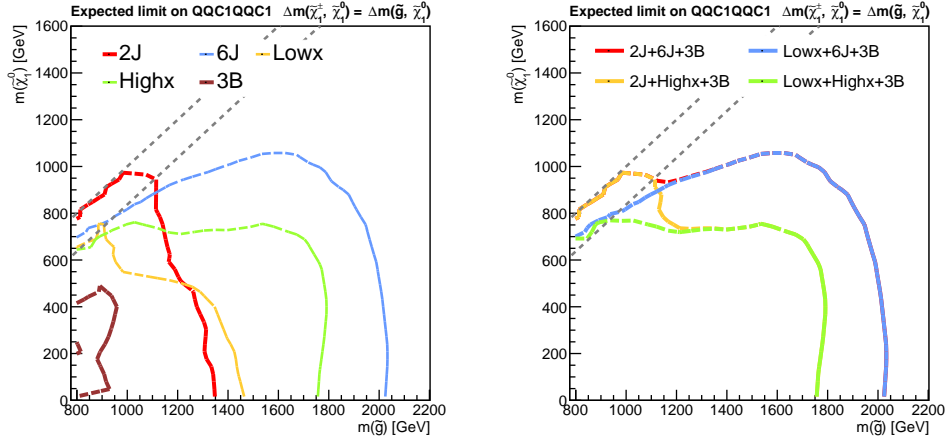
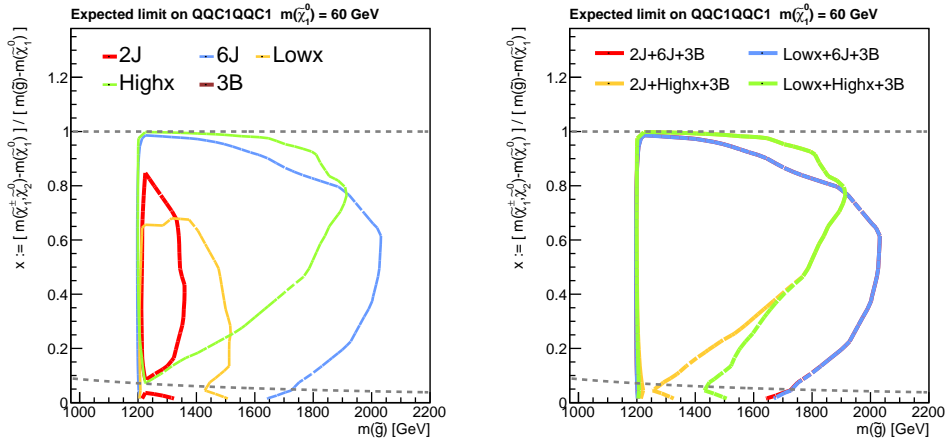


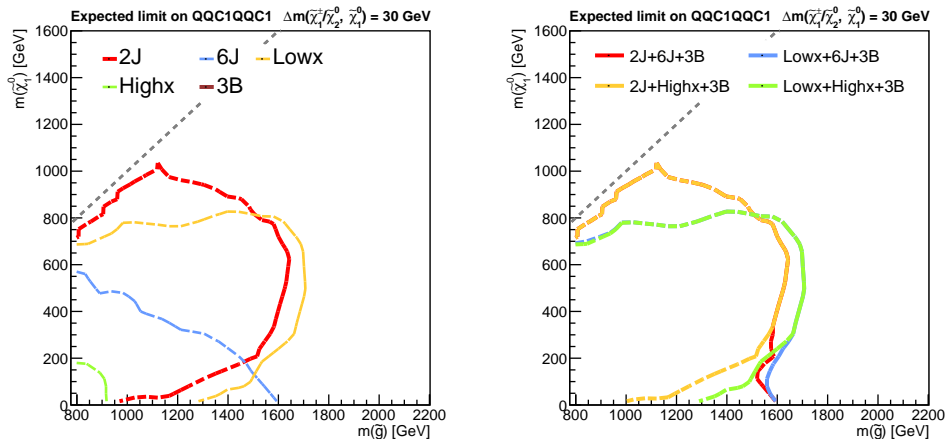
Figure 72: Expected exclusion (95%CL) for the benchmark model TTN1TTN1. The left plot shows the exclusion limit set by individual signal region  $m_{\text{eff}}$ -bin (dashed) or a tower (solid). The contours in the right plot display the ultimate sensitivity provided by the combined fit. The hypothetical test will be carried out using the best performed combination, in deriving the final result.



(a)

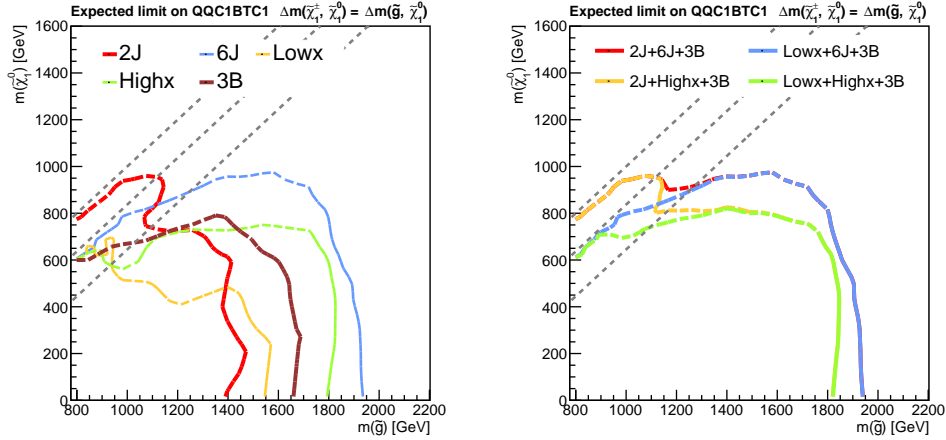


(b)

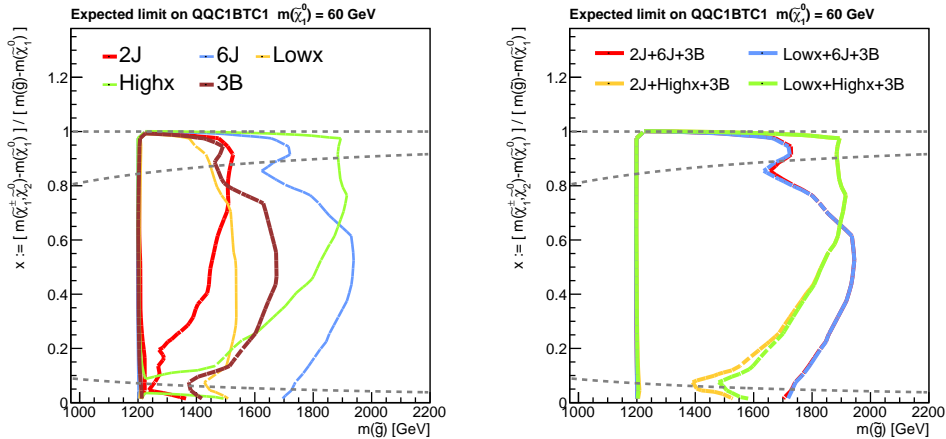


(c)

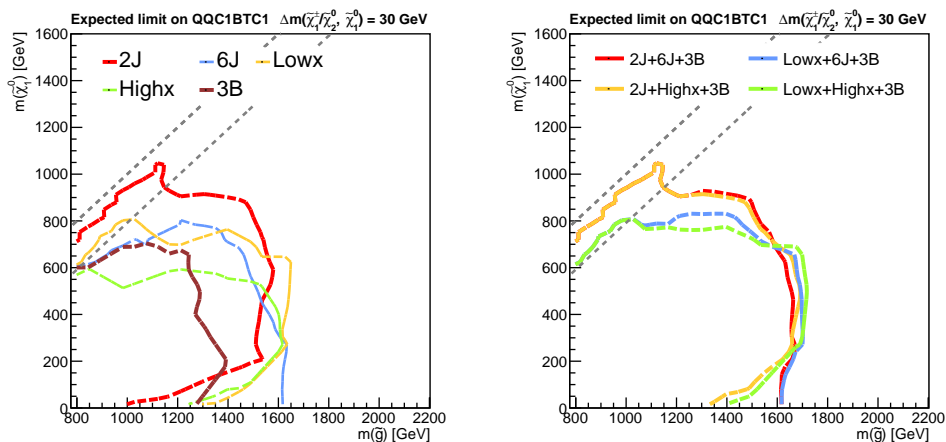
Figure 73: Projected expected exclusion (95%CL) for the benchmark model QQC1QQC1 onto the (a)  $x = 1/2$  (b)  $m_{\tilde{\chi}_1^0} = 60$  GeV (c)  $\Delta m(\tilde{\chi}_1^\pm, \tilde{\chi}_1^0) = 30$  GeV grid. The contours in the right plot display the ultimate sensitivity provided by the combined fit. The hypothetical test will be carried out using the best performed combination, in deriving the final result.



(a)



(b)



(c)

Figure 74: Projected expected exclusion (95%CL) for the benchmark model QQC1BTC1 onto the (a)  $x = 1/2$  (b)  $m_{\tilde{\chi}_1^0} = 60$  GeV (c)  $\Delta m(\tilde{\chi}_1^\pm, \tilde{\chi}_1^0) = 30$  GeV grid. The contours in the right plot display the ultimate sensitivity provided by the combined fit. The hypothetical test will be carried out using the best performed combination, in deriving the final result.

## 6 Standard Model Background Estimation

Due to the enormously large cross-section of SM processes with respect to the signal, it is a fate for new physics searches to keep exploring the phase space with tight event selections. The consequence is the highly untypical kinematics for the remained SM backgrounds, and the modeling is usually challenging since the standard MC simulation is not necessarily reliable as we will see in Sec. 6.2.1.

This is why (semi-)data-driven approach is remarkably motivated in search analyses. The most commonly done practice over the past analyses is to apply an in-situ correction to MC using the data events around signal region (“control region”). The prediction in signal regions is given by the corrected MC, assuming the modeling on the phase space between the control region and the signal region is correct. We refer this semi-data driven method as “**kinematical extrapolation method**”. The advantage of the kinematical extrapolation method is that the prediction does not suffer from statistical fluctuation leading to relatively smaller total uncertainty. However the drawback is that it has to still rely on MC in the extrapolation from control regions to signal regions, which uncertainty is rather difficult to capture and quantify.

Since statistical error often dominates the uncertainty in the signal regions, it has no point in competing on a few percent precision in the estimation. Instead, it is more sensible to pursue the robustness avoiding risk to introducing unknown systematic effects, even if it will result in larger estimation uncertainty. A nearly fully data-driven method (“**object replacement method**”) is meant to that purpose, estimating particular background components by a simplified extrapolation in which the use of MC is minimized. We promise to use this method as much as possible, and cover the rest of all by the kinematical extrapolation method.

This section will go through the overall backgrounds estimation procedure for the analysis. After reviewing the breakdown in the signal regions and how they evade the event selection, both estimation methods will be detailed. Finally, we demonstrate the performance by comparing the estimation and the observed data, using a set of validation regions.

### 6.1 Background Breakdown in the Signal Regions

The breakdown of physics processes in the signal regions are shown in Figure 76.  $W + \text{jets}$  and  $t\bar{t}$  dominate over the b-tagged and b-vetoed regions respectively in general, while dibosons and single-top (mostly  $Wt$ -channel) are sub-dominant. The **3B** towers are completely dominated by  $t\bar{t}$ , where 60 % of them are with heavy flavor jets via radiative gluon splitting ( $t\bar{t} + cc/bb$ ) while the rest are with one light flavor jet or hadronically decaying  $\tau$  faking into b-tagged jet ( $t\bar{t} + b_{\text{fake}}$ ).

Backgrounds also follow the categorization depending on the mechanism they pass the selection as listed in Table 24, based on which the estimation method is decided.

The “**semi-leptonic**” category is defined by events with exactly one real light flavor lepton ( $e, \mu$ ). In the SM, these are uniquely provided by processes with leptonically decaying W-boson, such as from  $W + \text{jets}$  and  $t\bar{t}$ . This is by far the dominant component at 1-lepton preselection level, however is drastically suppressed after a tight  $m_T$  cut since they are largely truncated at  $m_W$ . After the  $m_T$  cut, the remnant events are typically either: 1) Drell-Yan process with virtual heavy intermediate W boson, or 2) events with badly measured MET leading to prolonged tail in  $m_T$ . The former contribution is typically larger although the

Table 24: Background classification in terms of the origin.

Category		Origin	Main physics process	Estimation method
“Semi-leptonic”		On-shell W with diluted $m_T$ / High-mass Drell-Yan	$(W, t\bar{t}, VV) \rightarrow \ell\nu + \text{jets}$	Kine. expt. / MC
“Di-leptonic”	$\ell\ell_{\text{mis.}}$	”Out Acc.” ”Mis. Reco.” ”Mis. ID” ”Mis. OR”	$(t\bar{t}, Wt, WW) \rightarrow \ell\nu\ell\nu + \text{jets}$	Kine. expt. Obj. rep. Obj. rep. Kine. expt.
	$\ell\tau_h$	1 real-lepton + $\tau_h$	$t\bar{t}, Wt, WW \rightarrow \ell\nu\tau\nu + \text{jets}$	Obj. rep.
“Fake”		0 real-lepton + 1 fake-lepton.	$W \rightarrow \tau\nu, Z \rightarrow \nu\nu$	MC

latter addresses more with increasing jet activity, as shown in Figure 75. The dominant processes  $W + \text{jets}$  and  $t\bar{t} + Wt$  are estimated by a semi-data driven approach referred as “kinematical extrapolation method” as detailed in following sub-section, while the other processes are taken from pure MC prediction since they are minor.

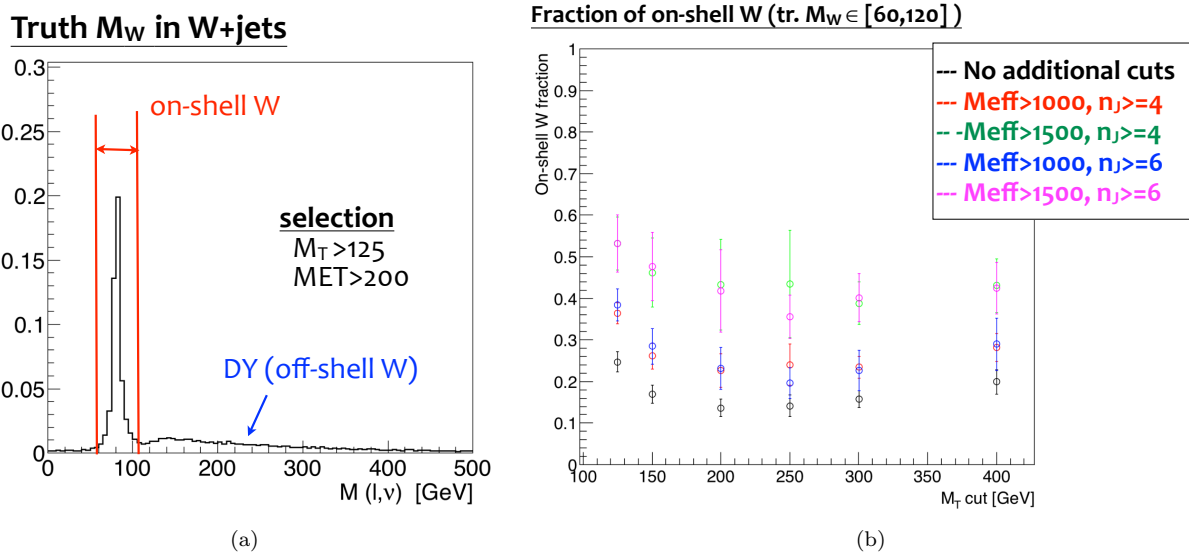


Figure 75: (a) Truth invariance mass  $m(\ell, \nu)$  of high- $m_T$   $W + \text{jets}$  events. Ideally there are only high-mass Drell-Yan type of events, however due to the finite detector resolution, a fraction of on-shell W events with badly measured MET sneak into regions with  $m_T > m_W$ . (b) The fraction of on-shell events defined by  $m(\ell, \nu) \in [60, 125]$ , as a function of the  $m_T$  cut. It is generally below 50 %, however increases with higher jet activity in the event.

The “di-leptonic” category consists of processes with real two leptons including  $\tau$ , mainly from di-leptonic decaying  $t\bar{t}$ ,  $Wt$  and  $WW$ . The presence becomes highly significant with respect to the “semi-leptonic” after the  $m_T$  cut, since the source of missing transverse momentum is multiple thus they have no reason to cut-off at  $m_W$ .

They fall into 1-lepton regions through two channels, namely “ $\ell\ell_{\text{mis.}}$ ”: events with two real light flavor leptons and one of them fails the “baseline” requirement (“missing lepton”), and “ $\ell\tau_h$ ”: events with a real

light flavor lepton and a hadronically decaying tau lepton.

The origin of “missing lepton” is further four-fold and symbolized as follow:

#### “Out Acc.”

Leptons going outside the acceptance of “baseline” requirement i.e.  $p_T > 7(6)$  GeV,  $|\eta| < 2.47(2.5)$  for electrons (muons).

#### “Mis. Reco”

Leptons within the  $p_T - \eta$  acceptance but failing the reconstruction i.e a truth lepton that can not be associated with any of reconstructed electrons/muons in the xAOD container.

#### “Mis. ID”

Reconstructed leptons within the  $p_T - \eta$  acceptance but failing the electron/muon ID for the “baseline” requirement.

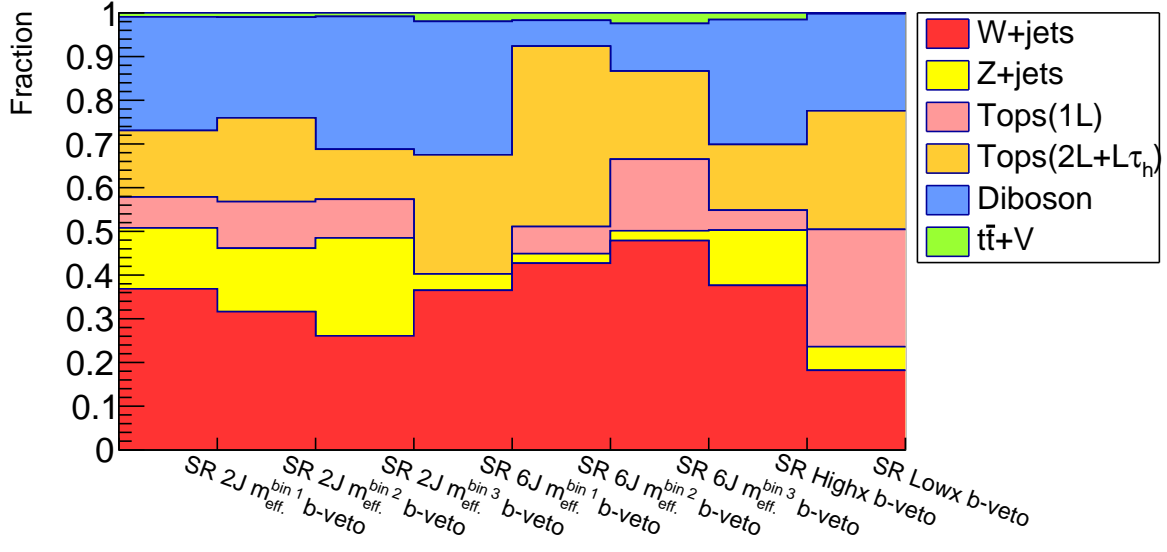
#### “Mis. OR”

Reconstructed leptons within the  $p_T - \eta$  acceptance passing the ID for ”baseline” requirement, but killed in the overlap removal (Sec. 3.7).

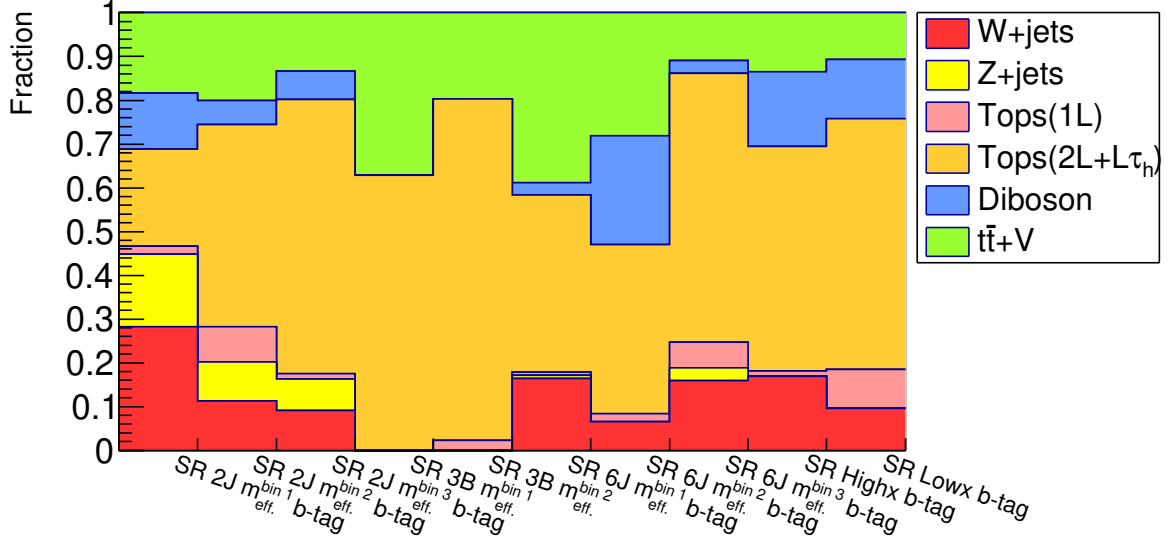
One nice thing about this “**di-leptonic**” components is that 2-lepton regions are available for control regions in the estimation. Since no signal regions are set there, exactly the same phase space with respect to SRs can be exploited. This is performed by the “object replacement method” as detailed in the following sub-section, although “Out Acc.” and “Mis. OR” are challenging for some technical reasons thus are estimated altogether with the “**semi-leptonic**” events.

The third category “**fake**” involves events with a fake lepton, which is negligible except regions dealing with soft leptons (“**2J**” and “**Low-x**”). Dominant contribution is from  $W \rightarrow \tau\nu$  and  $Z \rightarrow \nu\nu$  which accompanies a large MET from neutrinos. While the contribution from the multi-jets process is supposed to be negligible, it is dedicatedly cross-checked since the impact could be hazardous due to the huge cross-section. This is done using a series of validation regions referred as VRs-QCD, shown in Appendix B.

The relative popularity over the sub-categories in the signal regions are summarized in Figure 77 illustrates, where “**semi-leptonic**” and “**di-leptonic**” (particularly “ $\ell\tau_h$ ”) are overwhelmingly dominant in BV and BT signal regions respectively.

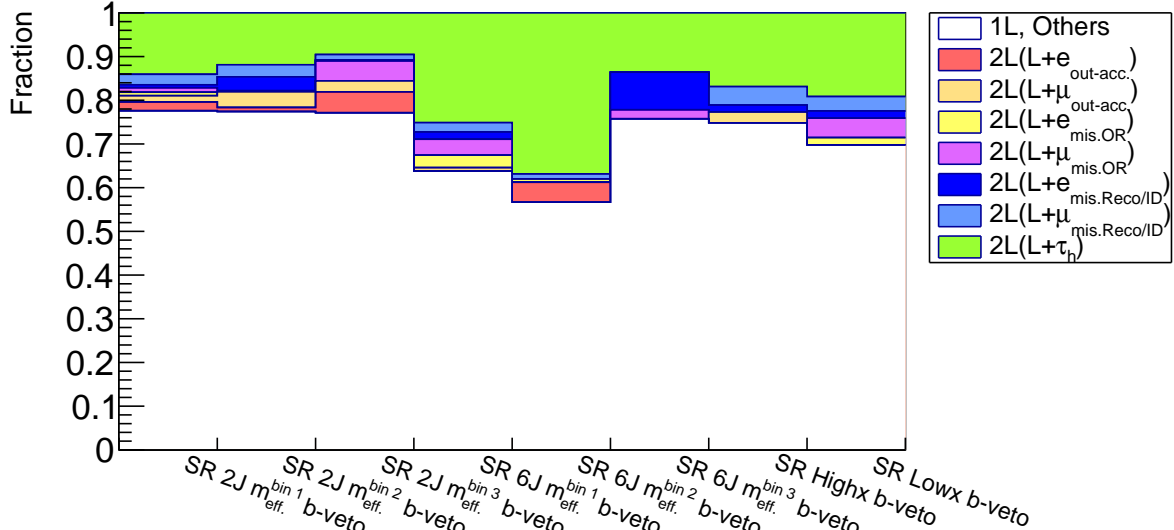


(a)

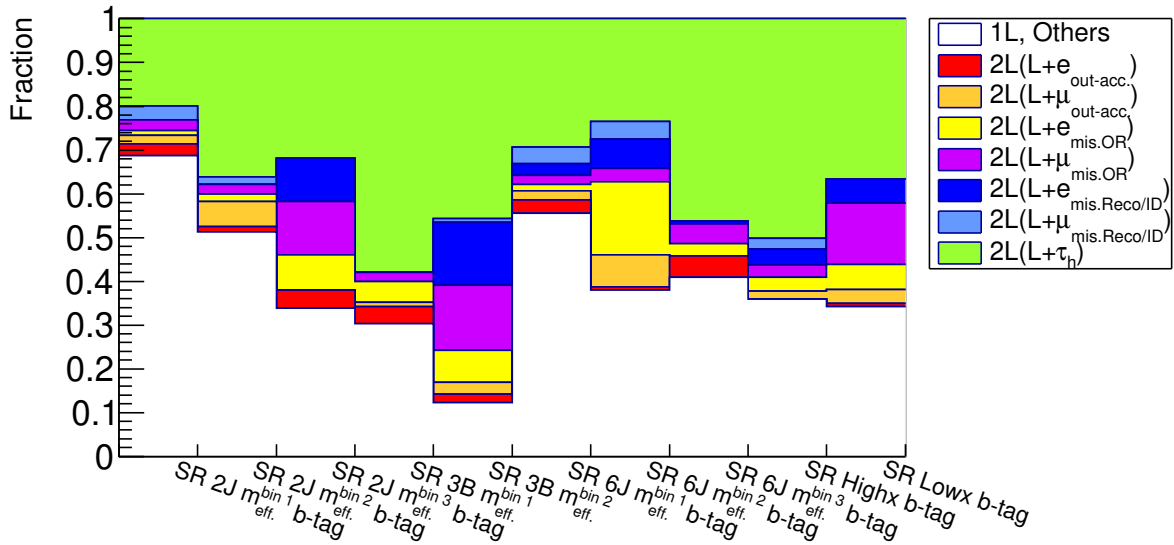


(b)

Figure 76: Background composition in terms of physics processes in the (a) BV, and (b) BT/3B signal regions.  $t\bar{t}$  and single-top are merged as “Tops”, and the semi-leptonic and di-leptonic components are respectively labeled as “semi-leptonic” and “ $2L + L\tau_h$ ”.



(a)



(b)

Figure 77: Background breakdown in the (a) BV, and (b) BT/3B signal regions based on the classification in Table 24. While the BV signal regions are dominated by the “semi-leptonic” category, BT/3B signal regions are mainly with “di-leptonic” especially the “ $\ell\tau_h$ ” component.

## 6.2 The Kinematical Extrapolation Method

The design of kinematical extrapolation method begins with control region definition. It is basically a procedure where one specifies kinematical variables well-modeled by MC that are suitable for the extrapolation from control region (CR) to signal region (SR), and tuning the selection in those variables under a couple of rules and considerations. These are discussed in Sec. 6.2.1 and Sec. 6.2.2 respectively. While MC is normalized to data in the determined CRs, the most important thing is that the behavior (or the cause) of the MC mis-modeling is more or less understood. Therefore, an extensive investigation in the MC mis-modeling modeling is simultaneously done in Sec. 6.2.1.

### 6.2.1 MC vs Data Comparison and the MC mis-modeling

The MC modeling of dominant background processes ( $W + \text{jets}$  and  $t\bar{t}$ ) is examined in pre-selection regions defined in Table 25. Each pre-selection region is intended to be dominated by the process being tested.

Table 25: Definition of pre-selection regions and corresponding tested physics processes. MET trigger requirement, event cleaning described Sec. 5.2,  $n_J \geq 2$  and  $E_T^{\text{miss}} > 250$  are applied as common selection.

Region name	$n_{\ell, \text{base.}}$	$n_{\ell, \text{sig.}}$	$p_T(\ell_1)$ [GeV]	$n_B$ ( $p_T > 30$ GeV)	Tested processes
1LBV (hardLep/softLep)	1	1	$> 35 / [7(6), 35]$ for $e$ ( $\mu$ )	0	$W + \text{jets}$
1LBT (hardLep/softLep)	1	1	$> 35 / [7(6), 35]$ for $e$ ( $\mu$ )	[1, 2]	$t\bar{t}$
2LBT	2	2	-	[1, 2]	$t\bar{t}$
1L3B	1	1	$> 15$	$\geq 3$	$t\bar{t} + cc/bb, t\bar{t} + b_{\text{fake}}$

**W + jets** Figure 78 - 79 show the kinematic distribution of the pre-selection region **1LBV hardLep** where  $W + \text{jets}$  is enriched. While the bulk phase space is well-described by MC, there is a striking tendency of overestimation by MC in the tail. Discrepancy is mainly observed in distributions related to the jet activity, particularly in jet multiplicity when it is above 3. Considering that they here are all from ISRs or FSRs, and that the jet multiplicity in the event roughly corresponds to the number of QCD-order of the processes, this directly implies the mis-modeling in higher order effects beyond next-to-next-to-leading order (NNLO) level. This might not be surprising giving that the MC sample (Sherpa 2.2.1 generator) does not include loop diagrams beyond NLO and neither diagrams with more than 5 partons in the final state, due to computational limitation.

Therefore, an order-by-order cross-section correction should be helpful as the first aid. In fact, a simple MC reweighting in terms of jet multiplicity turns to work quite nicely. The reweighting function is derived by fitting linearly the observed data/MC in Figure 78 (a):

$$w = 1 - 0.1 \times (n_J - 2), \quad (92)$$

where  $n_J$  is the number of jets with transverse momenta greater than 30 GeV. While the jet multiplicity distribution is fully corrected by construction, the other discrepancies can be resolved almost perfectly as well, as shown in 80.

Another observed aspect of the mis-modeling is that it is more striking in terms of soft radiations rather than the hard ones. For example, the average jet transverse momentum distribution (Figure 80 (c)) is well-modeled above  $\sim 200$  GeV, while the slope of data over the MC for jet multiplicity distribution is rather persistent. This in fact backups that reweighting in other mis-modeled variables than jet multiplicity, such as  $m_{\text{eff}}$ , actually does not work as successfully, since their tails are basically determined by hard jets.

Although this simple linear  $n_J$  reweighting demonstrated above seems qualitatively reasonable, it is not seriously used as correction due to the technical drawbacks that the optimum coefficients in Eq. 92 has slight phase space dependence, and that it is difficult to validate them around signal regions since the data statistics is limited. However, it is still a good enough approximation as well as a useful reference expression to understand the behavior and correlation of mis-modeling between variables. The reweighting with Eq. 92 is then used for emulating the mis-modeling when designing the data-driven background estimation as described in the following sub-sections.

Variables that do not scale with transverse momenta of outgoing particles, such as  $m_T$  or aplanarity, keep relatively well-modeled up to the tails. Particularly,  $m_T$  is by construction insensitive to most of the kinematics since the tail is determined by the mass-line of  $W$ -boson and MET resolution. Aplanarity is also supposed to be robust by itself since it takes a form of ratio of jet momentum. Therefore, these variables are decided to be used for the extrapolation from control regions to signal regions. Note that the  $m_T$  cut-off ( $m_T \sim m_W$ ) is slightly mis-modeled typically when tighter selections are applied, presumably due to the simplified treatment of the mass-line in calculating diagrams with many additional partons. The effect becomes visible especially in CR (e.g. Figure 107) and b-vetoed SRs.

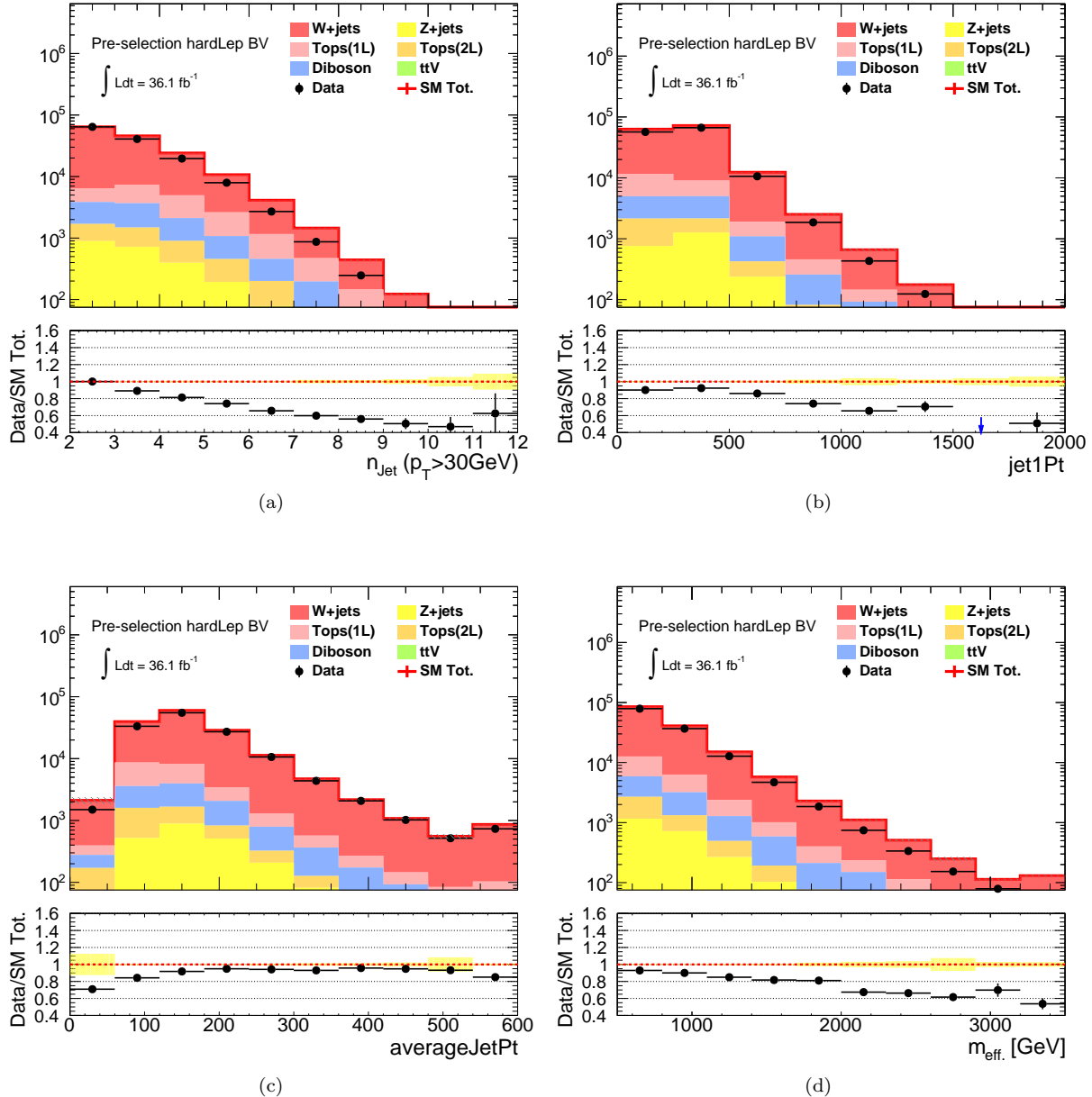


Figure 78: Kinematical distribution of (a) Jet multiplicity ( $p_T > 30$  GeV) (b) leading-jet  $p_T$  (c) average jet  $p_T$  ( $p_T > 30$  GeV) (d)  $m_{\text{eff.}}$  in the hard lepton b-vetoed pre-selection region.

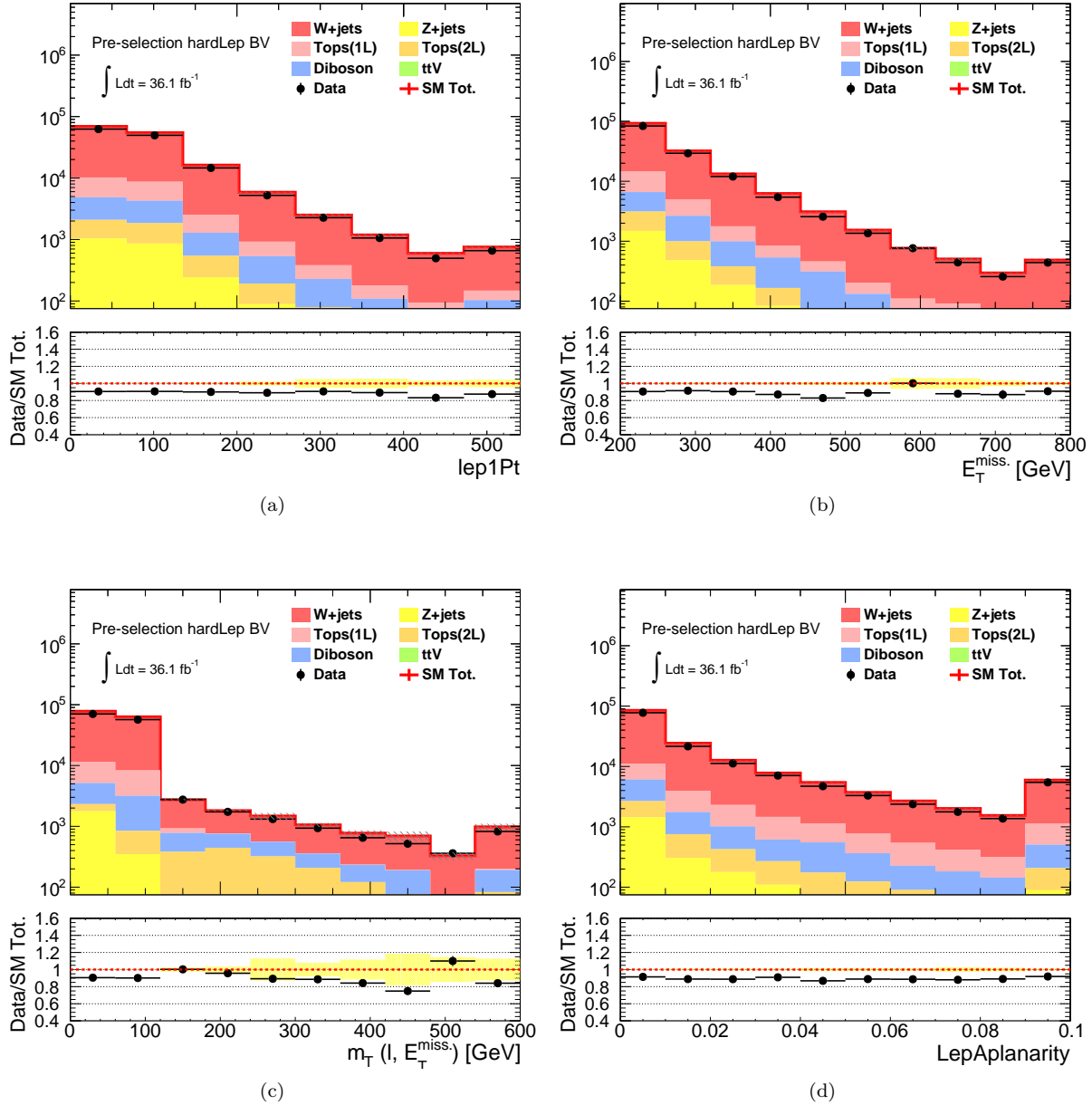


Figure 79: Kinematical distribution of (a) leading-lepton pt (b)  $E_T^{\text{miss}}$  (c)  $m_T$  (d) aplanarity in the hard lepton b-vetoed pre-selection region.

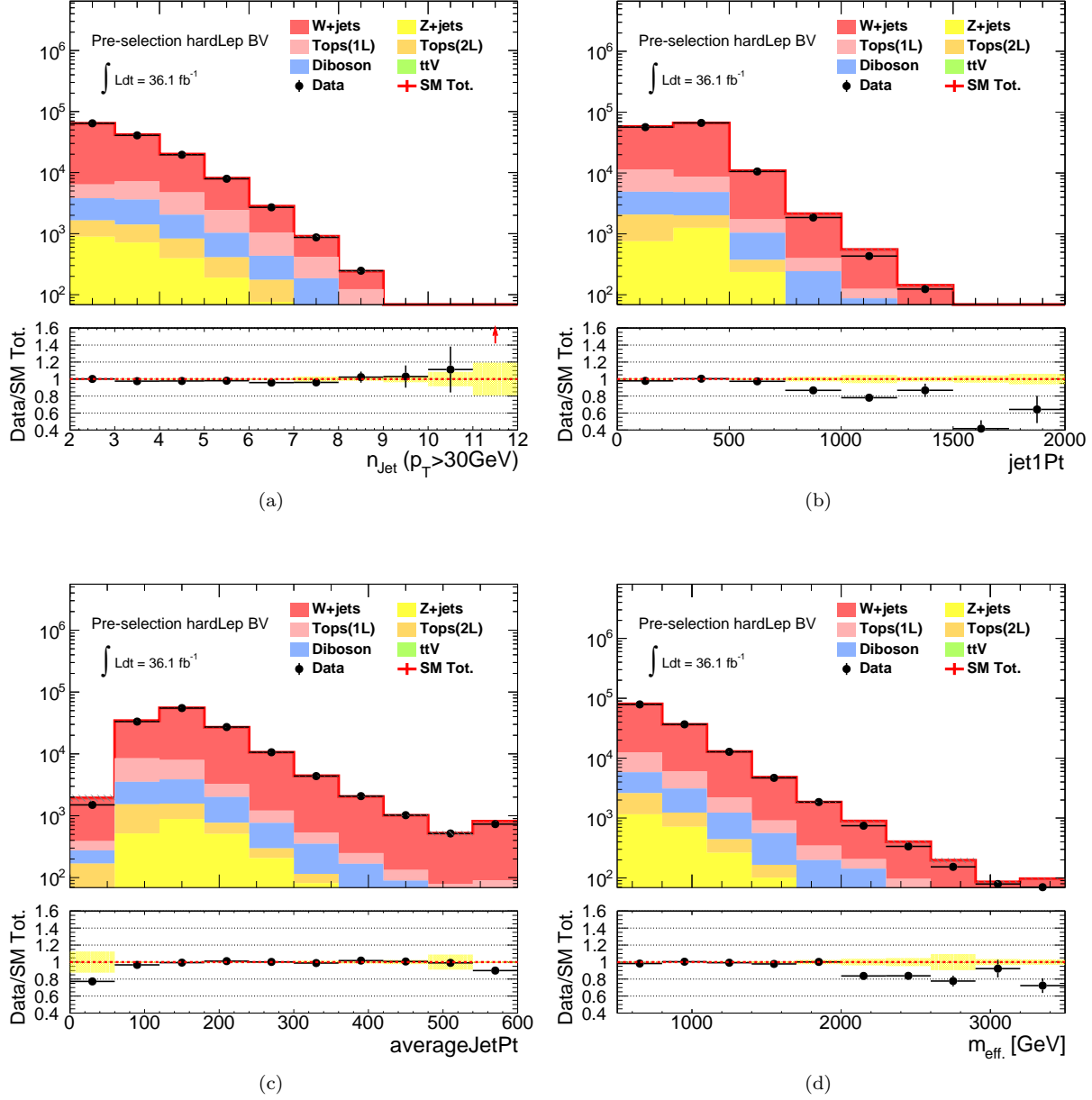


Figure 80: Kinematical distribution of (a) Jet multiplicity ( $p_T > 30$  GeV) (b) leading-jet pt (c) average jet pt ( $p_T > 30$  GeV) (d)  $m_{\text{eff}}$  in the hard lepton b-vetoed pre-selection region, with the reweighting  $w = 1 - 0.1 \times (n_J - 2)$  (Eq.(92)) being applied for  $W + \text{jets}$  MC.

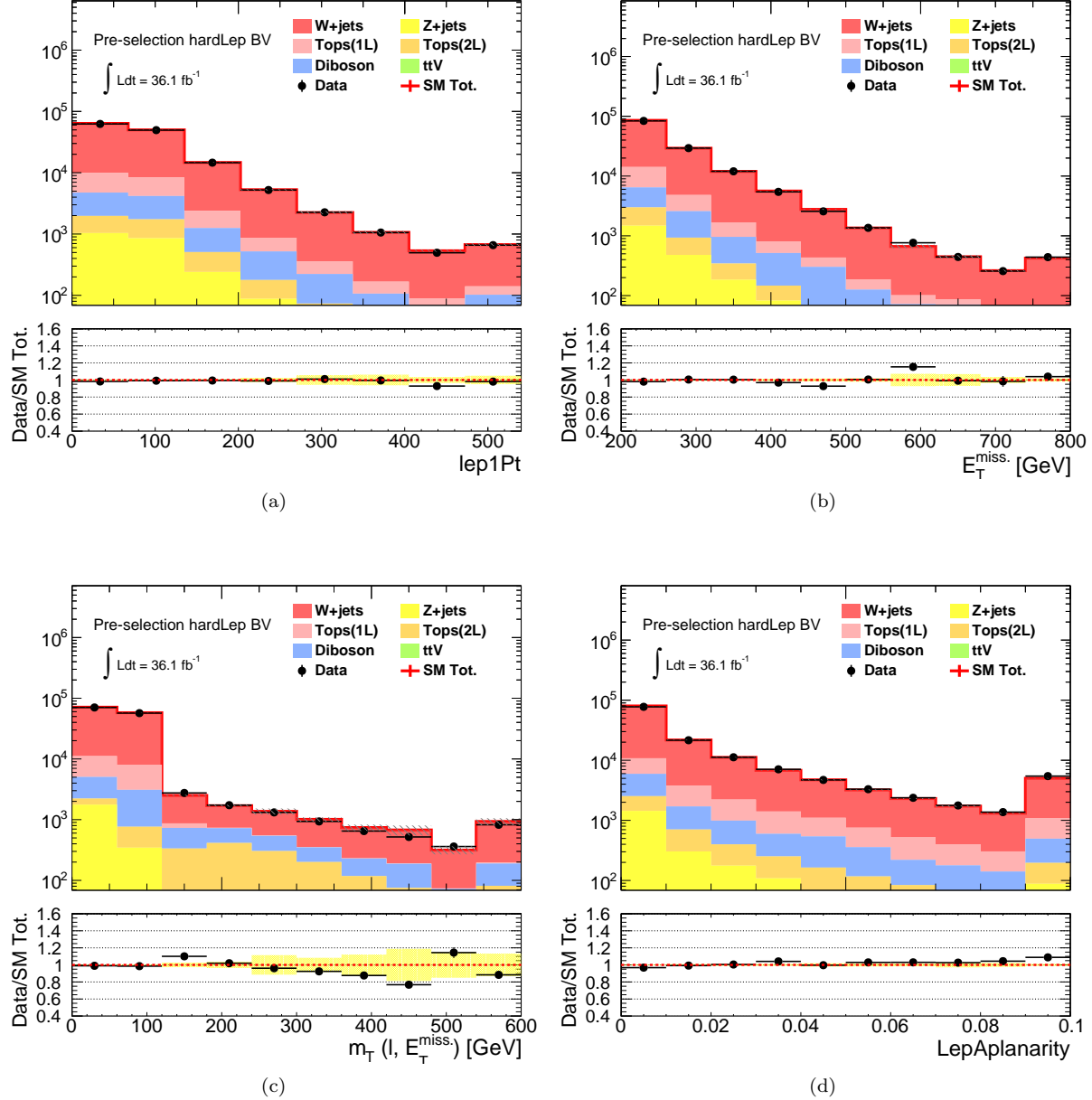


Figure 81: Kinematical distribution of (a) leading-lepton pt (b)  $E_T^{\text{miss}}$  (c)  $m_T$  (d) aplanarity in the **hard lepton b-vetoed** pre-selection region, with the reweighting  $w = 1 - 0.1 \times (n_J - 2)$  (Eq.(92)) being applied for  $W + \text{jets}$  MC.

**Tops** Figure 78 - 79 are the kinematic distributions in the pre-selection region **1LBT hardLep** dominated by  $t\bar{t}$ . It is seen that MC is overshooting the data with increasing transverse momenta of outgoing particles such as jets, lepton and MET.

In particular, the mis-modeling in  $m_{\text{eff}}$  distribution is significant. This is concerning given that the signal regions are designed to exploit its shape therefore We first try to understand the mis-modeling in  $m_{\text{eff}}$ . The leading source of the mis-modeling is suspected to be in the description of ISR or FSR radiation. This is because hard jets ( $p_T > 200 \text{ GeV}$ ) become more often non- $t\bar{t}$  origin in the tail of  $m_{\text{eff}}$ , as demonstrated by Figure 82, although  $t\bar{t}$  does have 2-4 jets in its tree-level decay.

This is in fact also supported by a series of MC reweighting studies shown in Figure 83 where linear reweighting in various top kinematic variables is attempted to correct the slope of data/MC in  $m_{\text{eff}}$ . It turns that  $p_T(t\bar{t})$  is the variable most sensitive to the mis-modeling, while reweighting in other variables can only change the normalization but the slope. This strongly indicates that the primary problem is in the radiation recoiling the  $t\bar{t}$  rather than in the internal kinematics of the  $t\bar{t}$  system.

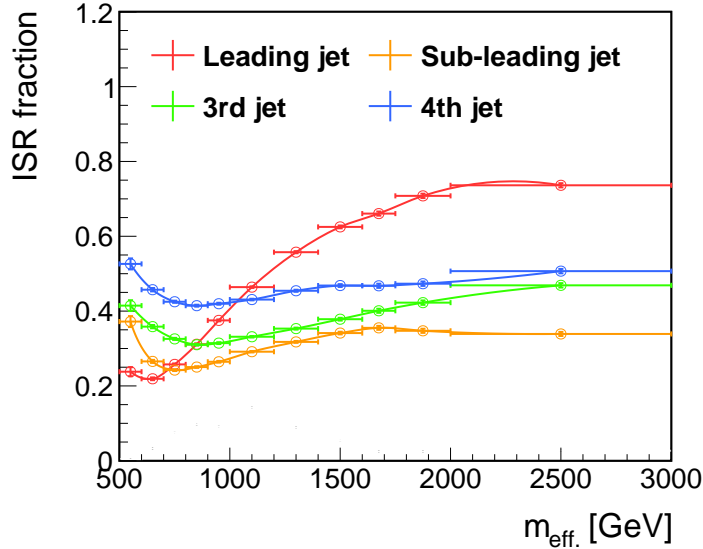


Figure 82: Fraction of ISR and FSR jets in the 4 leading jets with the largest transverse momenta, defined by  $N_{\text{events}}(i\text{-th jets in the } p_T \text{ range that do not match either jets from } t\bar{t} \text{ decay by } \Delta R < 0.2) / N_{\text{events}}(\text{all } i\text{-th jets in the } p_T \text{ range})$ .

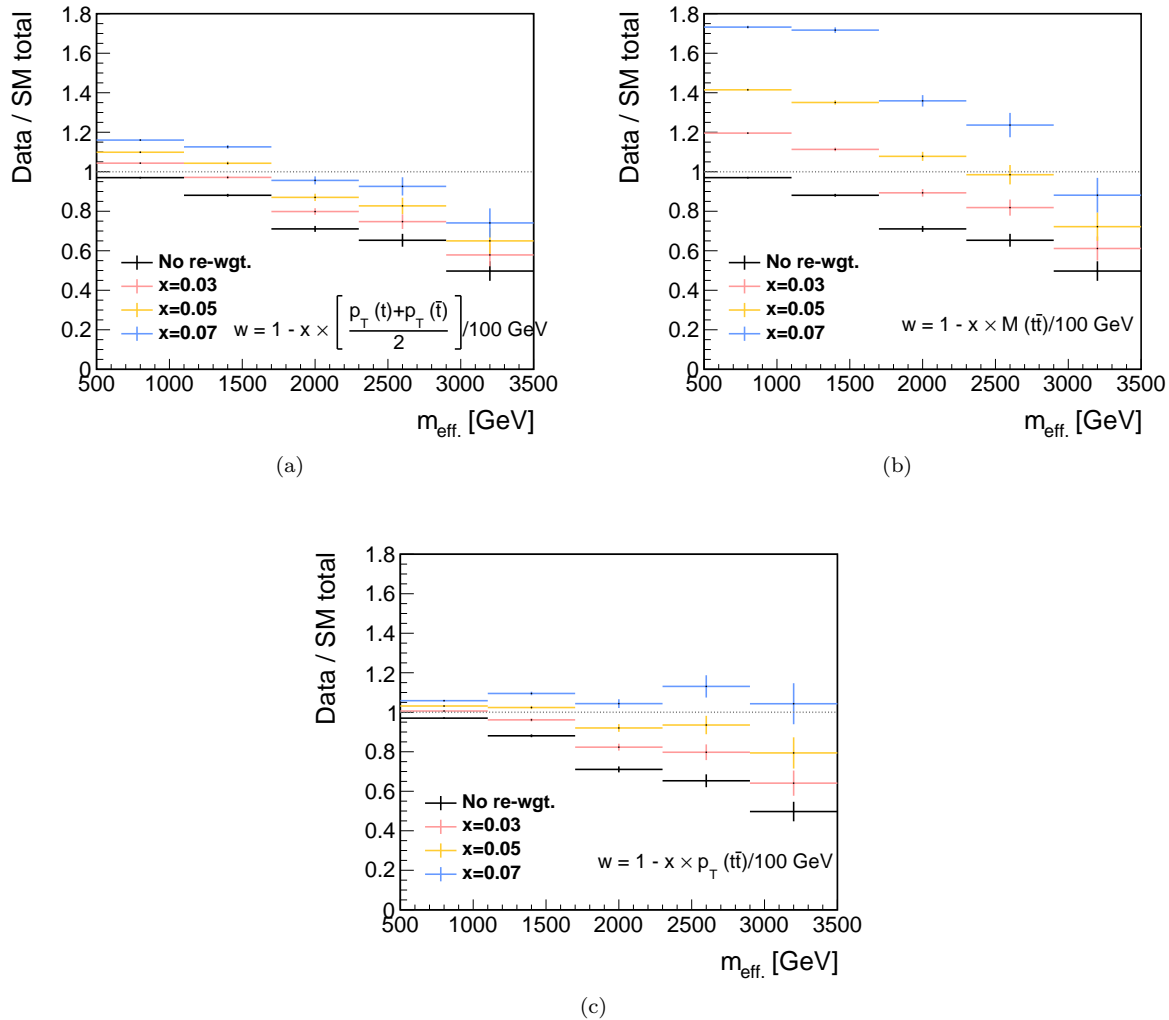


Figure 83: Response of data/MC in  $m_{\text{eff}}$  by reweighting  $t\bar{t}$  events in terms of (a) average top transverse momentum  $((p_T(t) + p_T(\bar{t}))/2)$ , (b) invariant mass of  $t\bar{t}$  system ( $m_{t\bar{t}}$ ) and (c) transverse momentum of  $t\bar{t}$  system ( $p_T(t\bar{t})$ ).  $p_T(t\bar{t})$  is found to be sensitive to the slope of  $m_{\text{eff}}$  and improve the data/MC discrepancy, while the other are only capable of shifting the normalization.

The  $p_T(t\bar{t})$ -based reweighting is found also capable of restoring the discrepancy in other distribution other than  $m_{\text{eff}}$ . Applying the reweighting function optimum for correcting the  $m_{\text{eff}}$ :

$$w = 1.05 \times [1 - 0.061 \times p_T(t\bar{t})], \quad (93)$$

good data-MC agreement is seen in overall spectra regarding to jets and MET as shown in Figure [86](#) - [87](#).

The mis-modelling in lepton transverse momentum distribution seems to have the other origin, seen as the residual discrepancy .

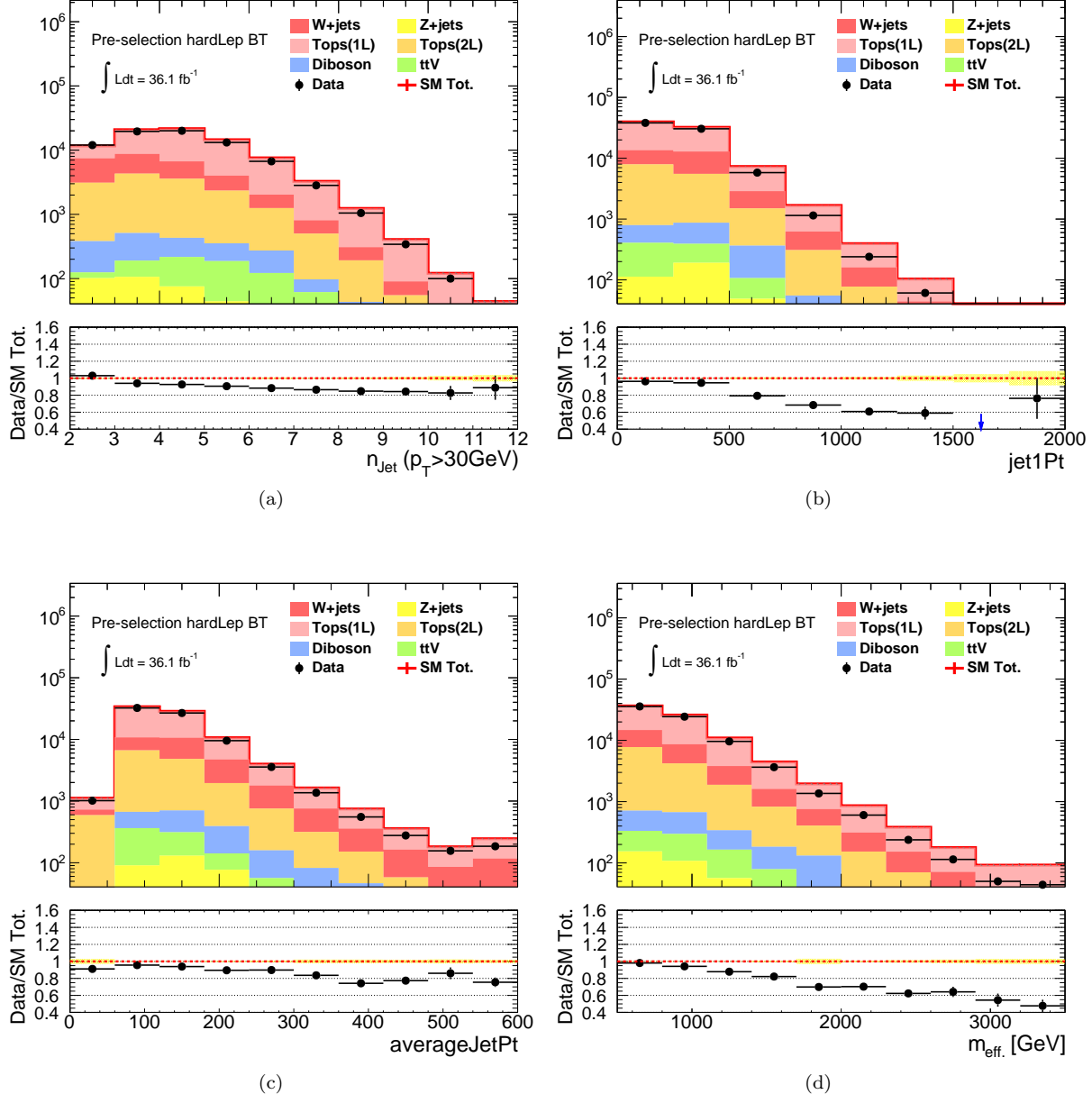


Figure 84: Kinematical distribution of (a) Jet multiplicity ( $p_T > 30$  GeV) (b) leading-jet pt (c) average jet pt ( $p_T > 30$  GeV) (d)  $m_{\text{eff.}}$  in the hard lepton b-tagged pre-selection region.

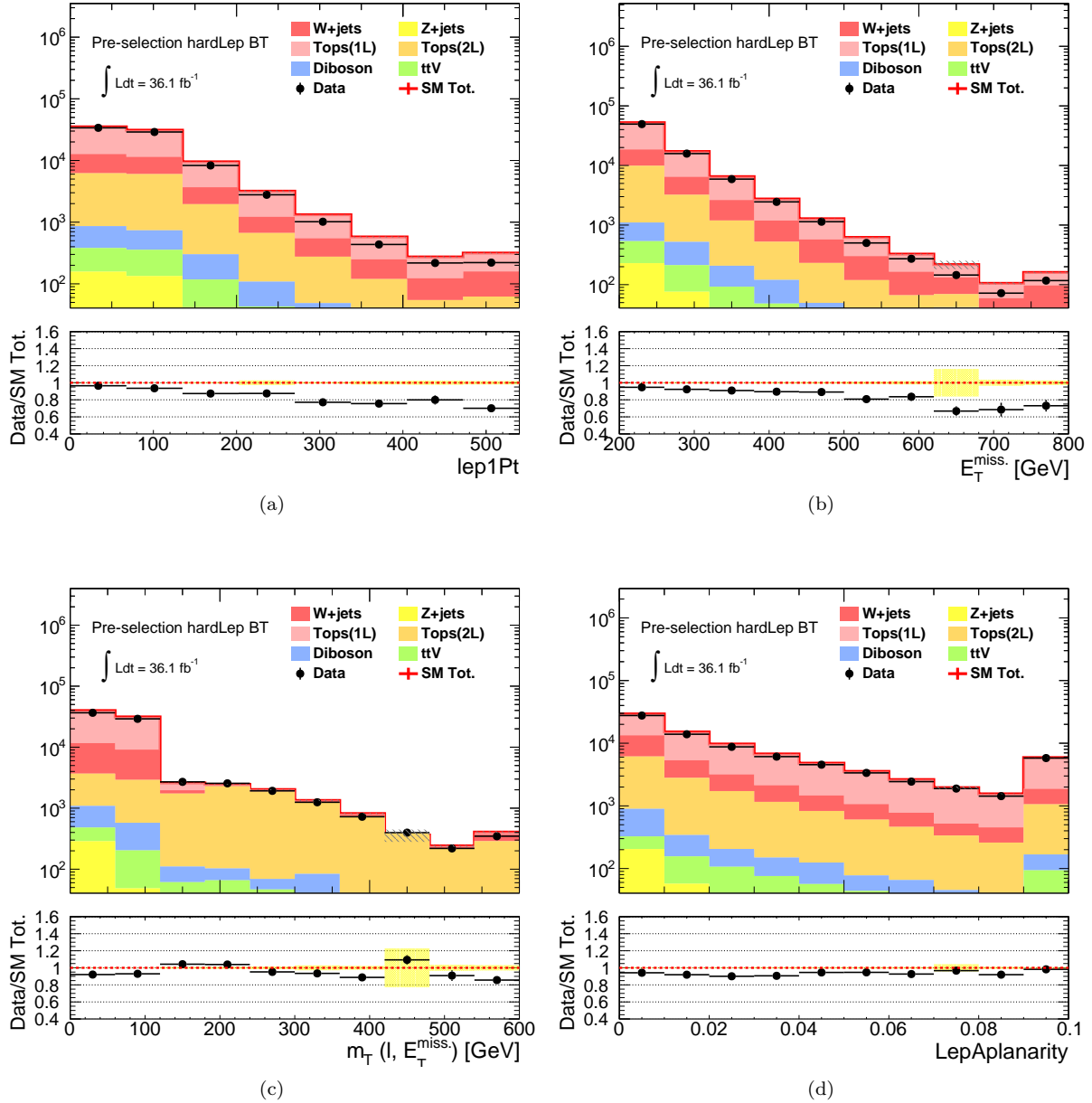


Figure 85: Kinematical distribution of (a) leading-lepton pt (b)  $E_T^{\text{miss}}$  (c)  $m_T$  (d) aplanarity in the hard lepton b-tagged pre-selection region.

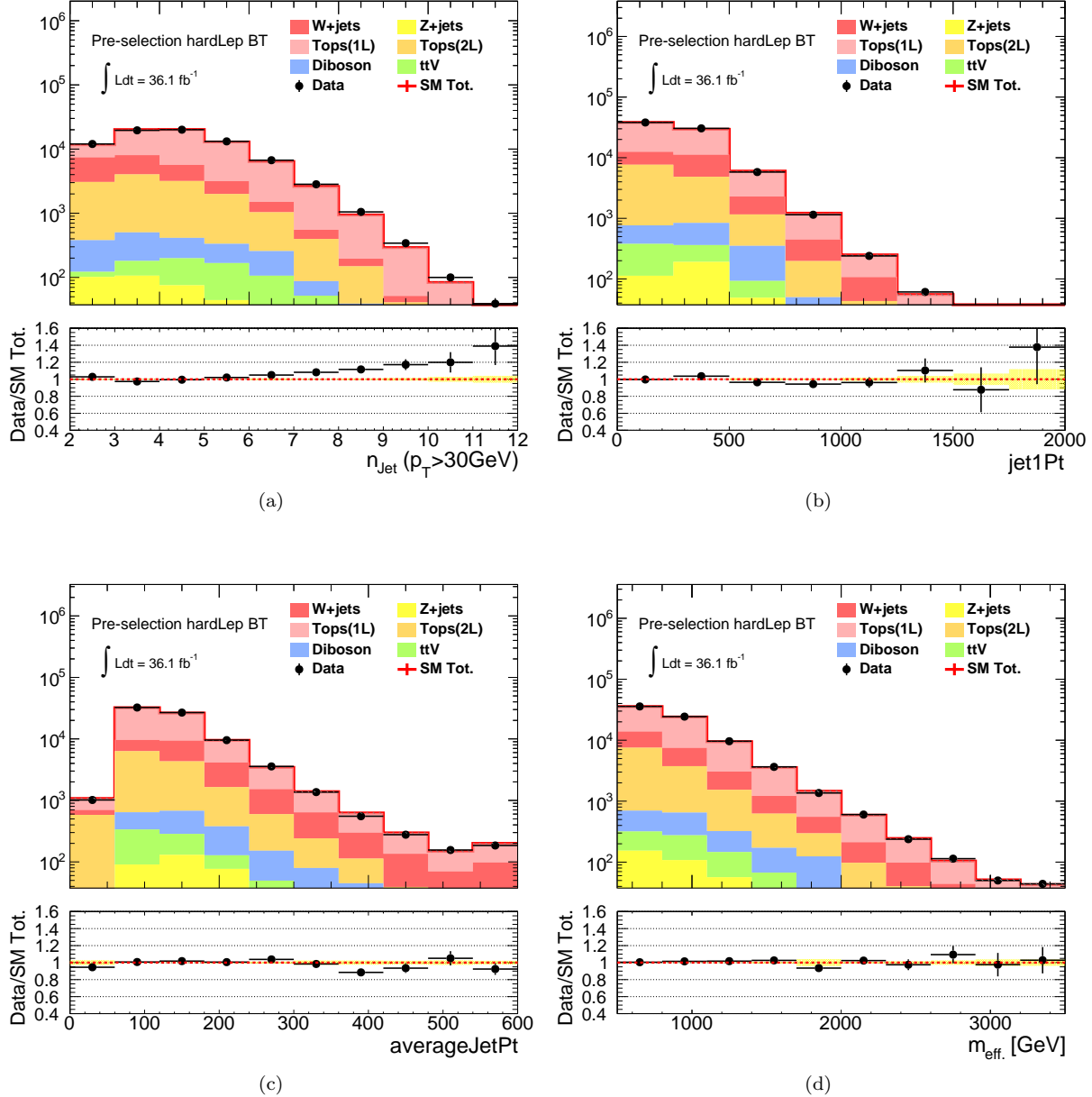


Figure 86: Kinematical distribution of (a) Jet multiplicity ( $p_T > 30$  GeV) (b) leading-jet pt (c) average jet pt ( $p_T > 30$  GeV) (d)  $m_{\text{eff}}$  in the hard lepton b-tagged pre-selection region, with the reweighting  $w = 1.05 \times [1 - 0.061 \times p_T(t\bar{t})]$  (Eq.(93)) being applied for  $t\bar{t}$  MC.

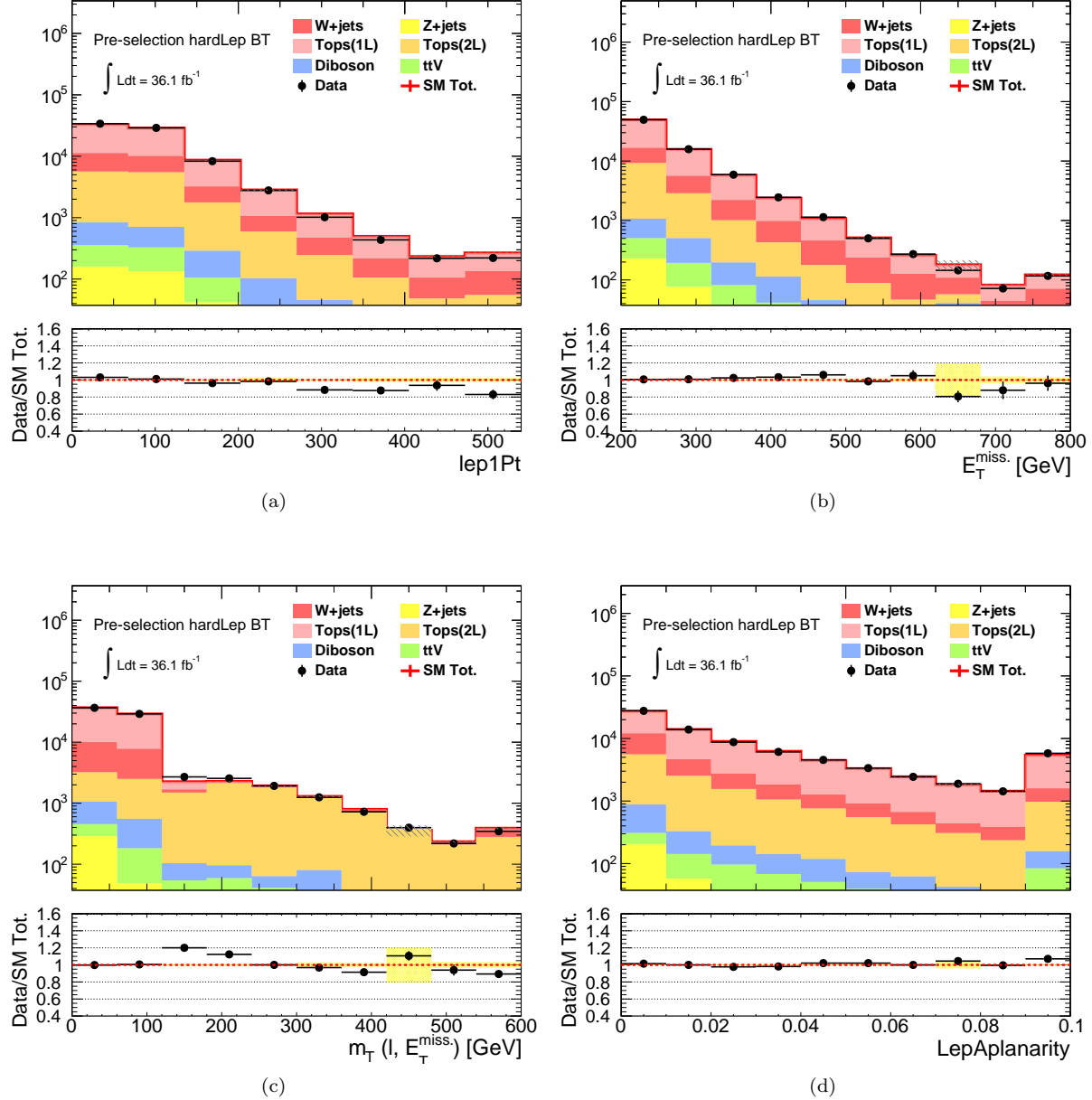


Figure 87: Kinematical distribution of (a) leading-lepton pt (b)  $E_T^{\text{miss}}$  (c)  $m_T$  (d) aplanarity in the **hard lepton b-vetoed** pre-selection region, with the reweighting  $w = 1.05 \times [1 - 0.061 \times p_T(t\bar{t})]$  (Eq.(93)) being applied for  $t\bar{t}$  MC.

The same trend is observed also in the di-leptonic channel. Figures 88-89 plot the kinematic distributions in the 2-lepton b-tagged preselection region (**2LBT**), and constant slopes in data/MC are seen in jet transverse momenta and  $m_{\text{eff}}$  distributions. It might be worth noting that the slope in jet transverse momenta and  $m_{\text{eff}}$  can also be corrected by the same reweighting function Eq. 93 as the semi-leptonic case. Figures 90-91 show the distributions with the reweighting applied, where the data-MC discrepancy related to jet kinematics are fairly recovered, and the lepton transverse momentum enjoys much poorer restoration. This universality strongly implies that the cause of mis-modeling in  $t\bar{t}$  is highly likely in the kinematics before the W-bosons decay, which is an important underlying assumption of the object replacement method to be described later.

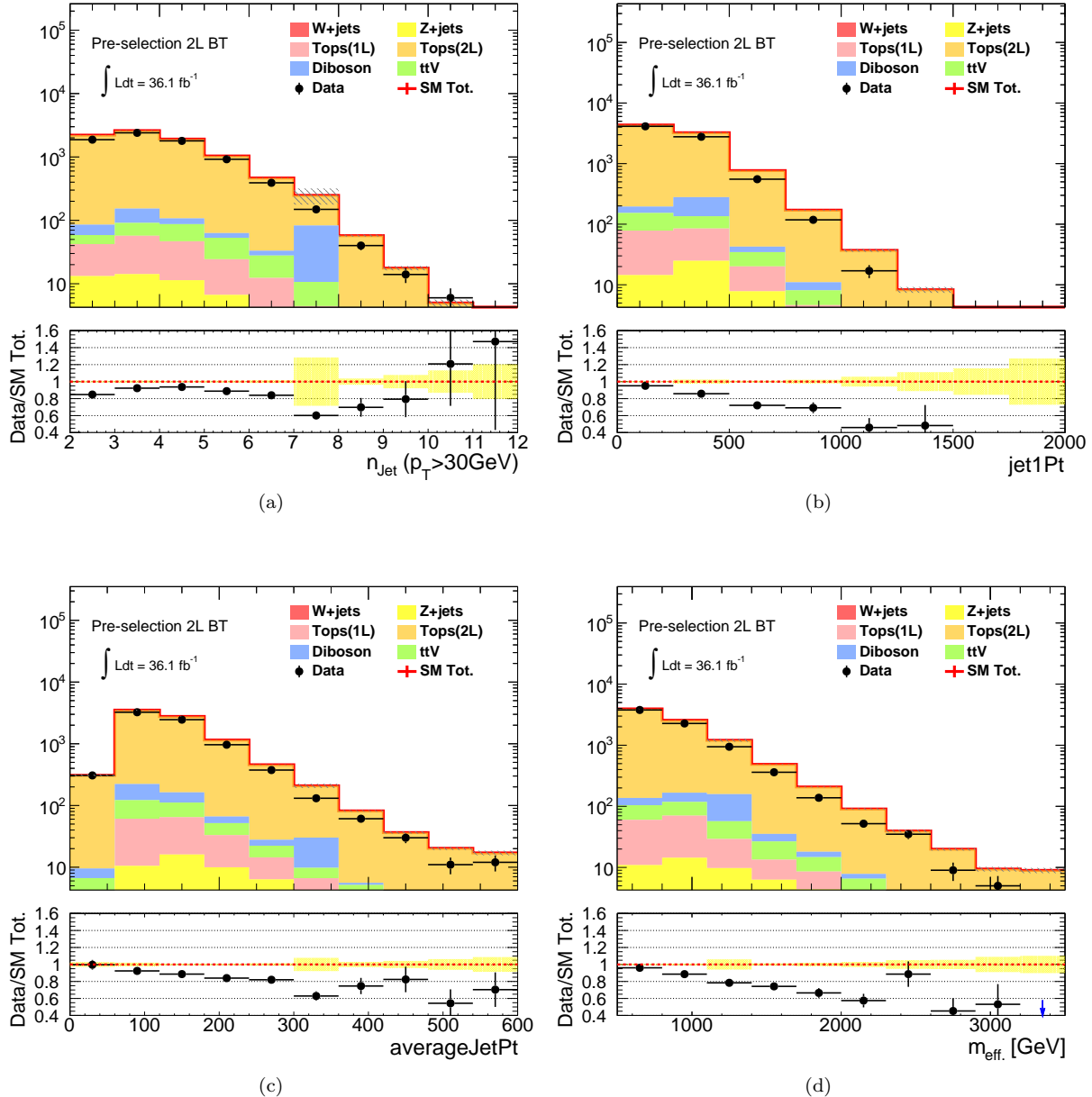


Figure 88: Kinematical distribution of (a) Jet multiplicity ( $p_T > 30$  GeV) (b) leading-jet pt (c) average jet pt ( $p_T > 30$  GeV) (d)  $m_{\text{eff.}}$  in the hard lepton b-tagged pre-selection region.

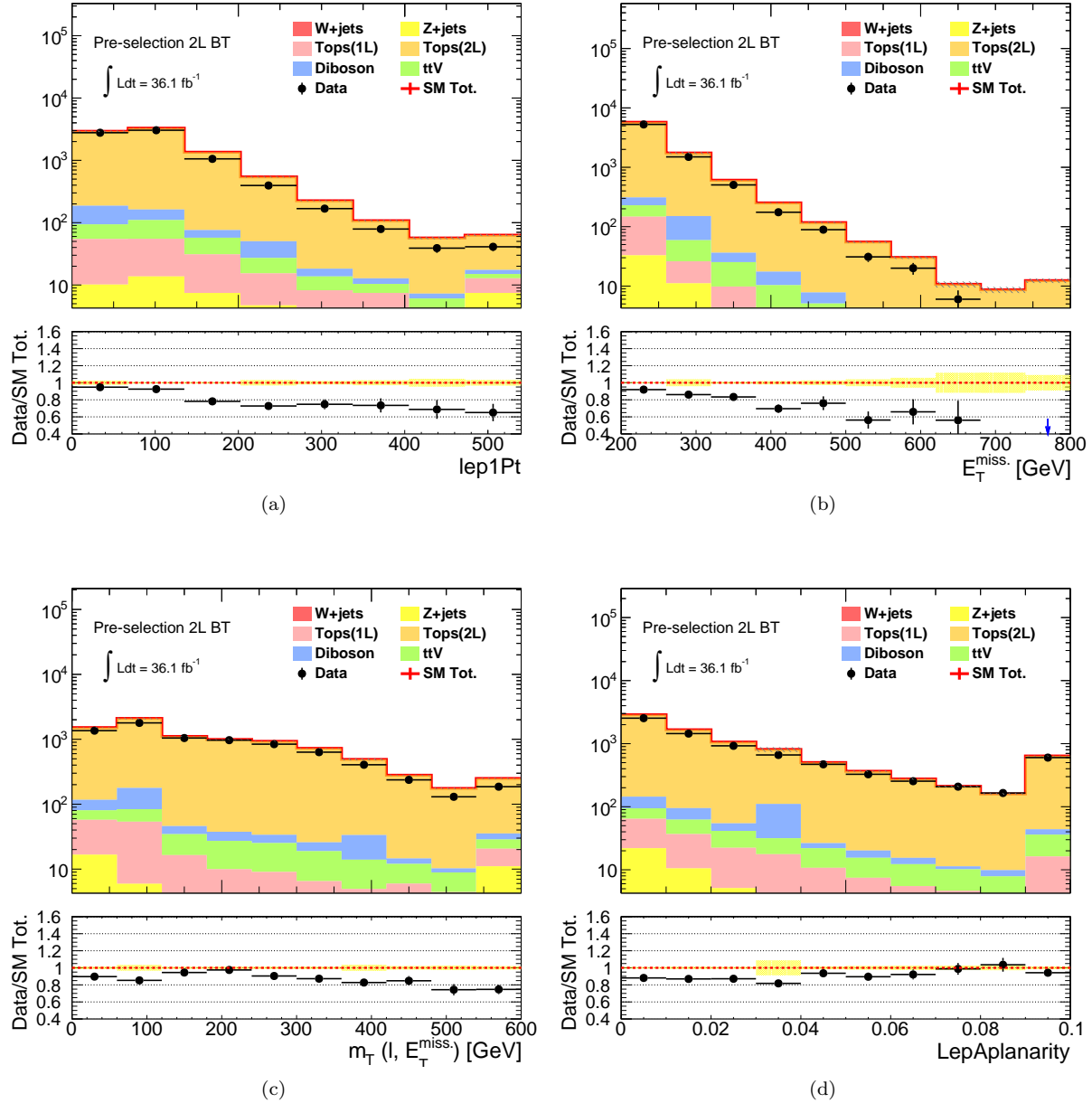


Figure 89: Kinematical distribution of (a) leading-lepton pt (b)  $E_T^{\text{miss}}$  (c)  $m_T$  (d) aplanarity in the hard lepton b-tagged pre-selection region.

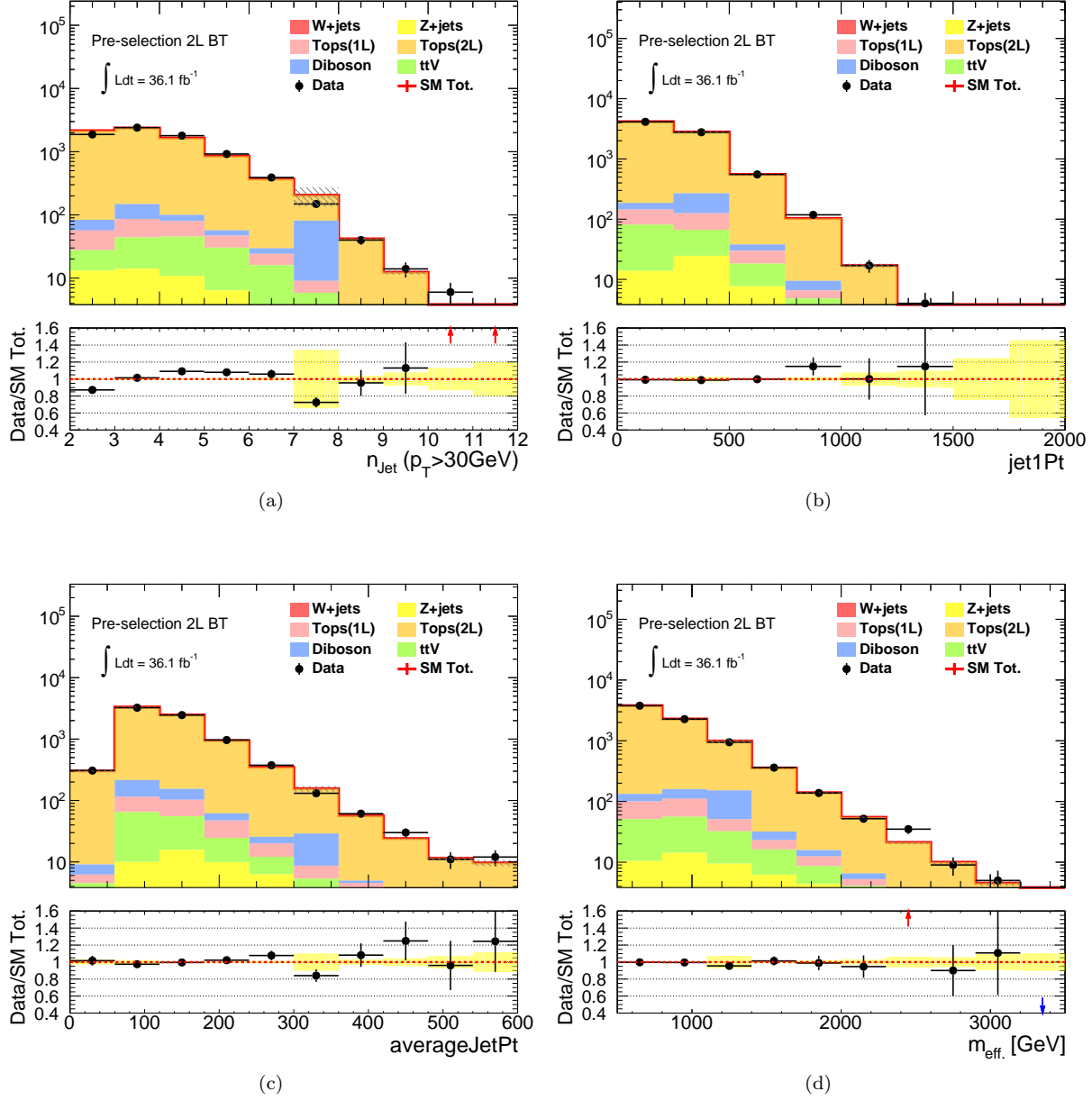


Figure 90: Kinematical distribution of (a) Jet multiplicity ( $p_T > 30$  GeV) (b) leading-jet pt (c) average jet pt ( $p_T > 30$  GeV) (d)  $m_{\text{eff.}}$  in the hard lepton b-tagged pre-selection region, with the reweighting:  $w = 1.05 \times [1 - 0.061 \times p_T(t\bar{t})]$  (Eq.(93)) being applied for  $t\bar{t}$  MC.

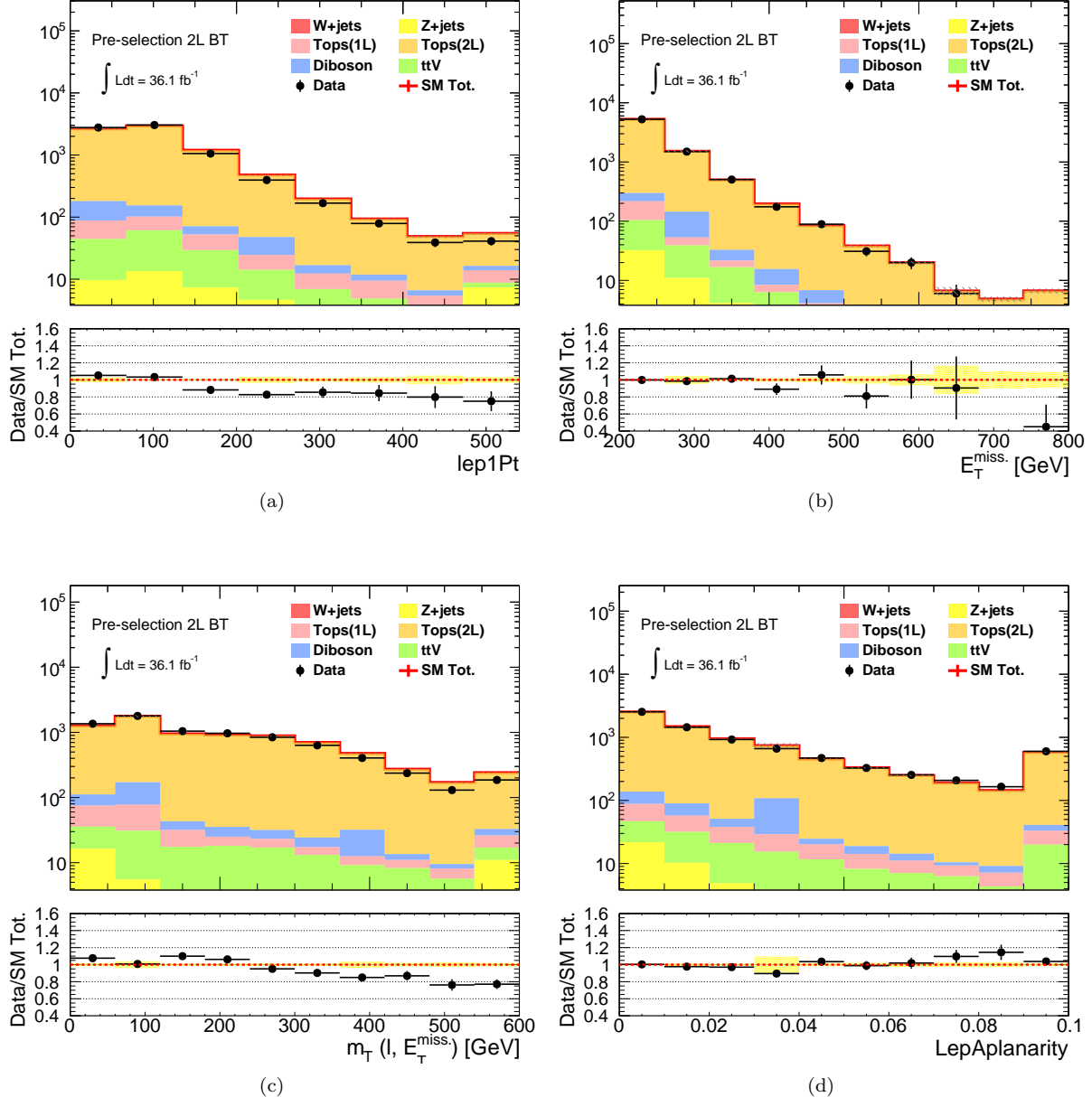


Figure 91: Kinematical distribution of (a) leading-lepton pt (b)  $E_T^{\text{miss.}}$  (c)  $m_T$  (d) aplanarity in the hard lepton b-tagged pre-selection region, with the reweighting:  $w = 1.05 \times [1 - 0.061 \times p_T(t\bar{t})]$  (Eq.(93)) being applied for  $t\bar{t}$  MC.

In contrast to variables that scale with transverse momenta of outgoing particles,  $m_T$  and aplanarity look relatively well-modeled among ones used in signal regions definition. Therefore, the same estimation strategy is taken as the case of  $W + \text{jets}$ , which is namely extrapolating in these variables from control regions to signal regions. However, note that the modeling of  $m_T$  is still not as perfect. For instance in Figure 79 or 81, there is a small bump-like structure in the ratio plot around  $m_T = 100 \sim 200$  GeV corresponding the cut-off of the semi-leptonic  $t\bar{t}$ . This is suspected to be due to the interference between  $t\bar{t} + Wt \rightarrow WWbb$  and other  $WWbb$  diagrams which is not accounted by the generator, which effect is addressing in regions where bulk  $t\bar{t}$  amplitude is suppressed. Corresponding uncertainty is evaluated in Sec. 7.2.1 and assigned as theory systematics.

$m_T$  in the bulk di-leptonic component suffers from another issue: while the tail in the  $m_T$  distribution of  $W + \text{jets}$  is only determined by jet energy resolution and the mass-line of  $W$ -boson, that of  $t\bar{t}$  is dominated by the di-leptonic component whose  $m_T$  simply scales with lepton transverse momentum and MET without any cut-off structure. As a result, the  $m_T$  distribution of di-leptonic  $t\bar{t}$  is affected by the mis-modeling rather more severely than the semi-leptonic component in general. The emerged data/MC discrepancy can be seen in Figure 89 (c).

To avoid the impact by the mis-modeling in  $m_T$ , in this analysis di-leptonic components are decided to be estimated by the other “object replacement” method as much as possible, and only small portion (“Out Acc.” and “Mis. OR” in Table 24) of them is covered by the kinematical extrapolation.

Modeling of  $tt + cc/bb$  and  $t\bar{t} + b_{\text{fake}}$  are exclusively examined using a preselected region with 3 or more b-jets (**1L3B**). Figure 95 - 96 displays the data-vs-MC comparison in the region. While the shapes seem to be affected by the same type of mis-modeling as observed in inclusive  $t\bar{t}$  selection above, the normalization is also underestimated by about 20% which is thought to be due to the modeling error of  $t\bar{t} + cc/bb$  cross-section.

#### Reweighting function

$$w = 1.4 \times [1 - 0.061 \times p_T(t\bar{t})], \quad (94)$$

is found to well correct the discrepancy, in which only the normalization coefficient varies from Eq. 93 accounting for the cross-section correction for  $tt + cc/bb$ . Meanwhile, the invariance of the slope coefficient implies that the source of the shape mis-modeling is common to the bulk  $t\bar{t}$  component as seen above.

Despite the  $t\bar{t}$  components in 3B regions suffer from such even more complex mis-modeling than the bulk, the impact on the final result is not dramatic since the majority of them are di-leptonic components in the signal regions which can be estimated largely by the object replacement method.

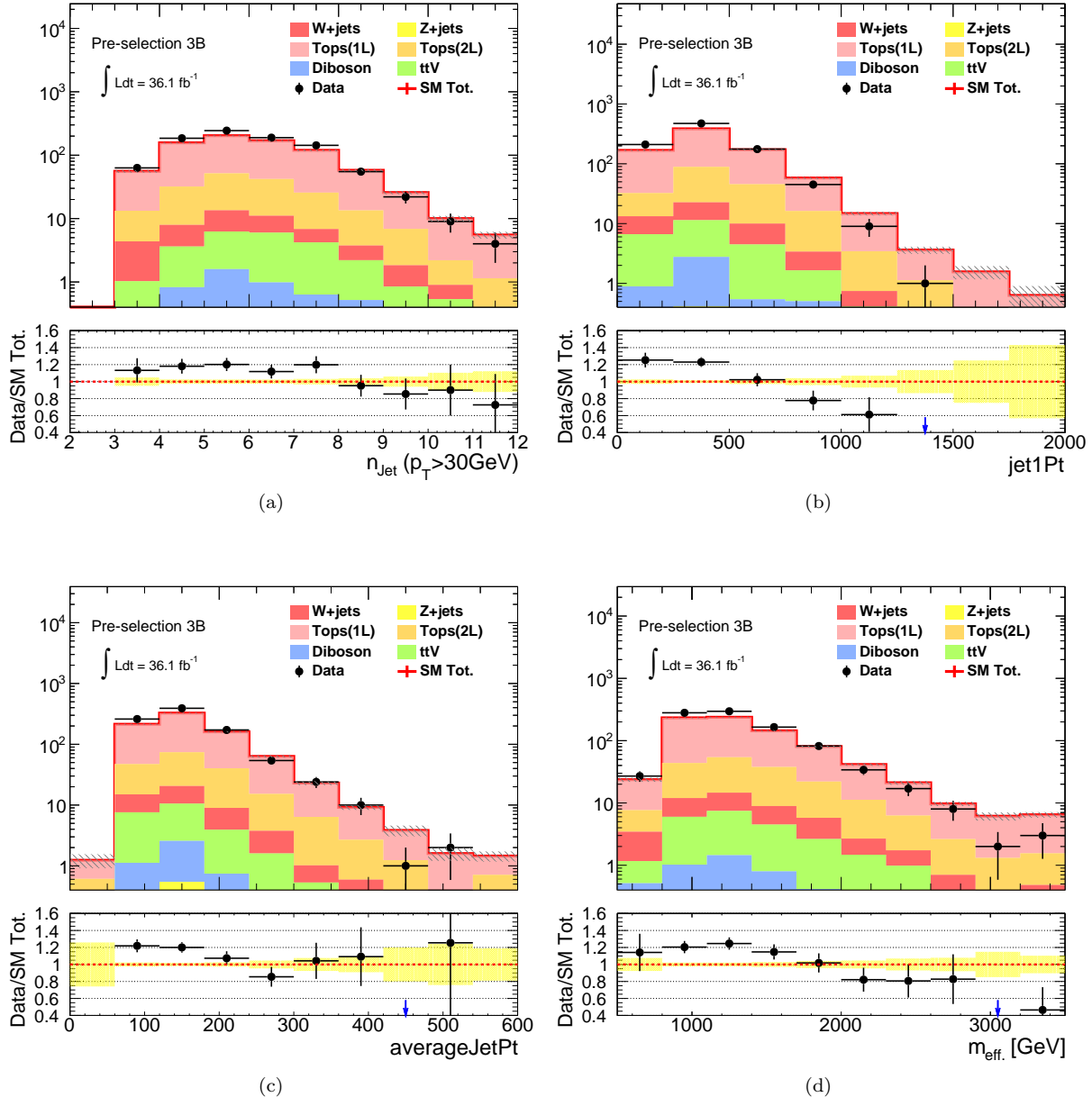


Figure 92: Kinematical distribution of (a) Jet multiplicity ( $p_T > 30$  GeV) (b) leading-jet pt (c) average jet pt ( $p_T > 30$  GeV) (d)  $m_{\text{eff}}$  in the 3b-tagged pre-selection region.

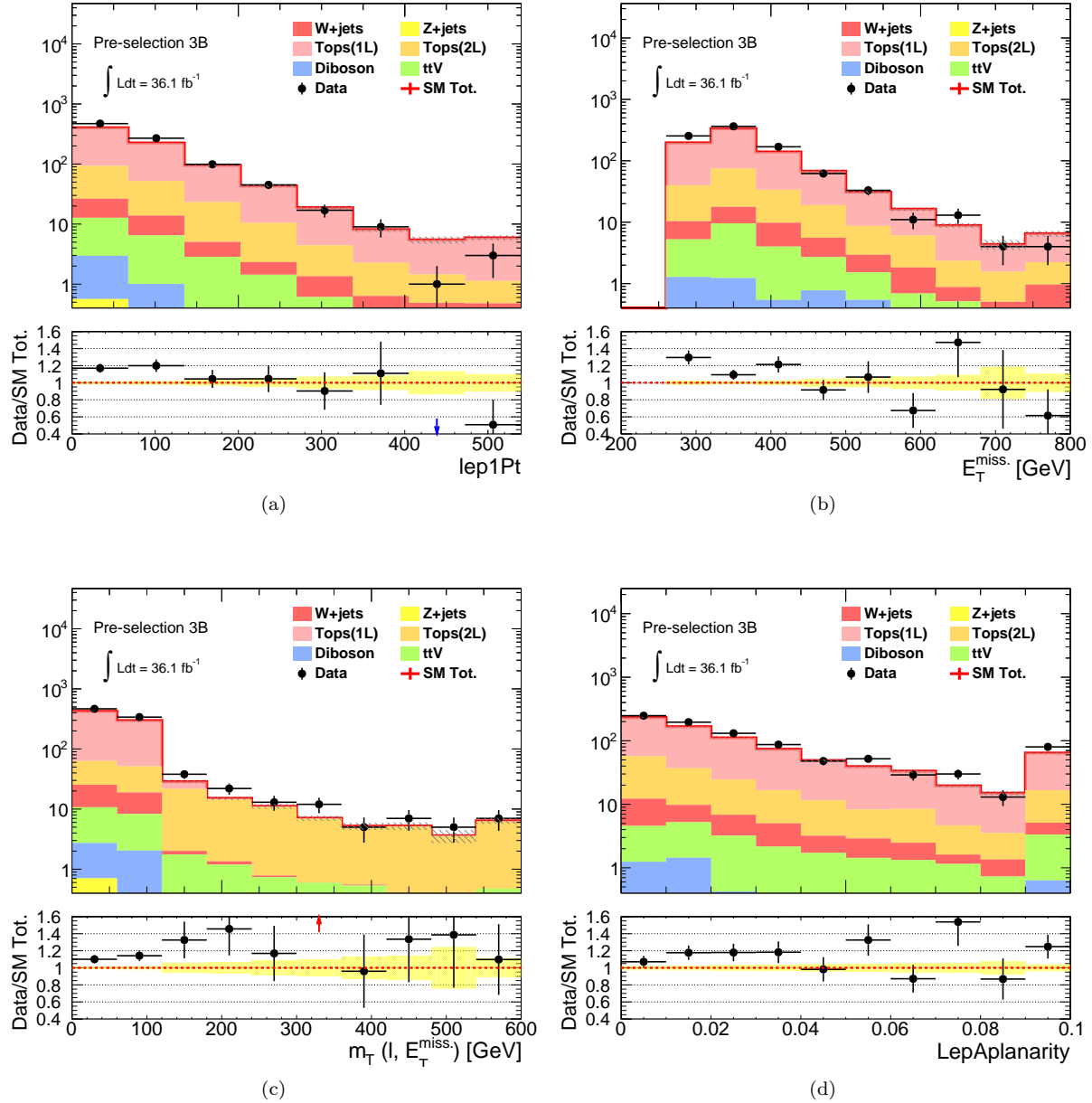


Figure 93: Kinematical distribution of (a) leading-lepton  $p_T$  (b)  $E_T^{\text{miss}}$  (c)  $m_T$  (d) aplanarity in the 3b-tagged pre-selection region.

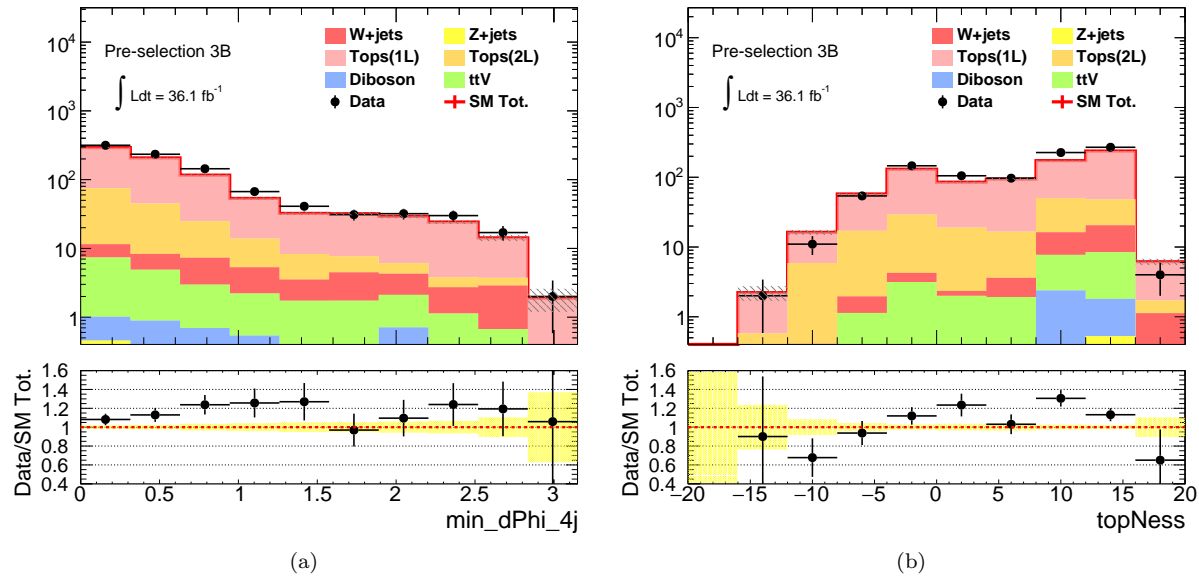


Figure 94: Kinematical distribution of (a)  $\min_{i=1-4} \Delta\phi(j_i, E_T^{\text{miss}})$  (b) Topness in the 3b-tagged pre-selection region.

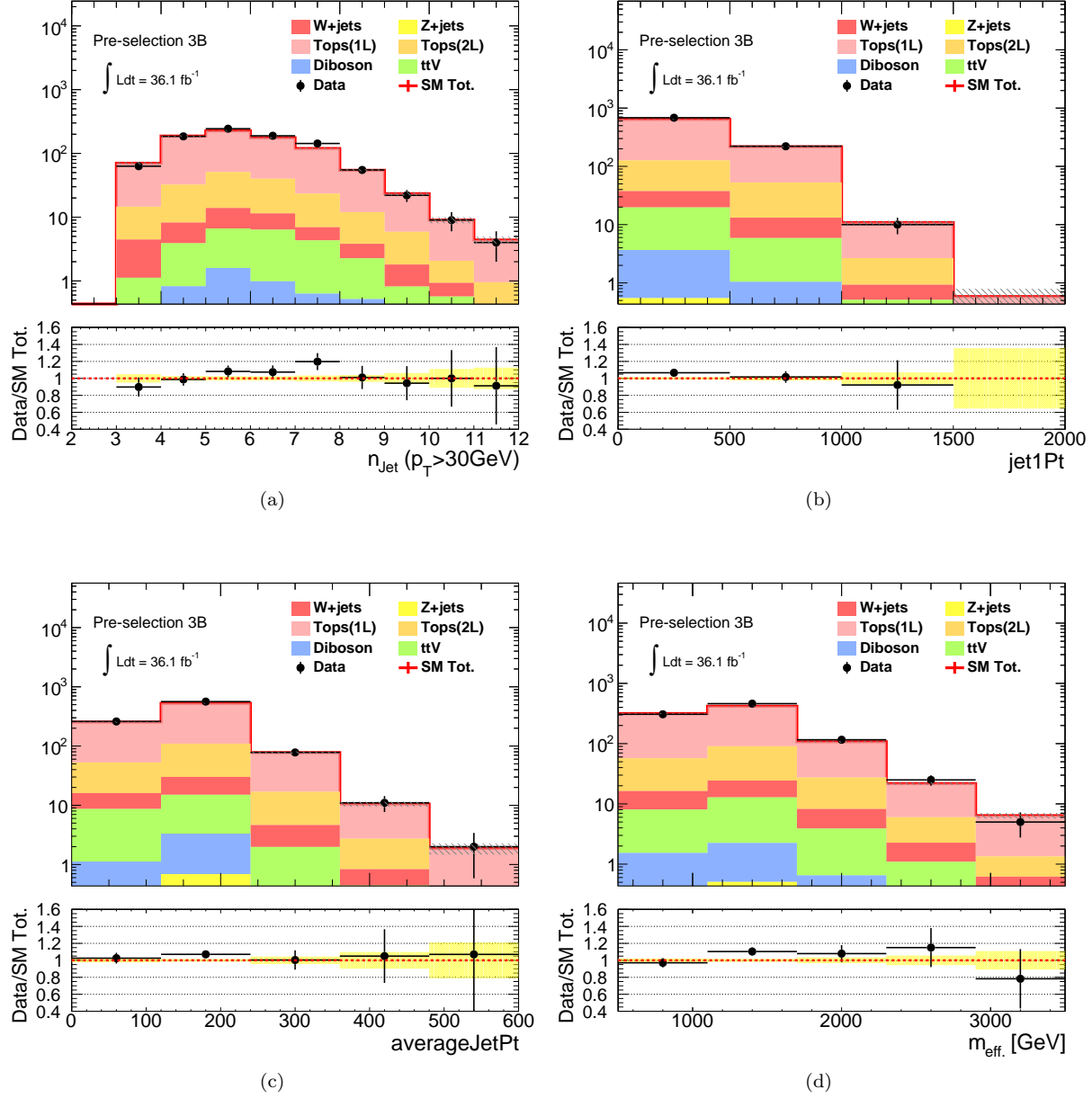


Figure 95: Kinematical distribution of (a) Jet multiplicity ( $p_T > 30$  GeV) (b) leading-jet pt (c) average jet pt ( $p_T > 30$  GeV) (d)  $m_{\text{eff}}$  in the **3b-tagged pre-selection region**, with the reweighting  $w = 1.4 \times [1 - 0.061 \times p_T(t\bar{t})]$  (Eq.(94)) being applied for  $t\bar{t}$  MC.

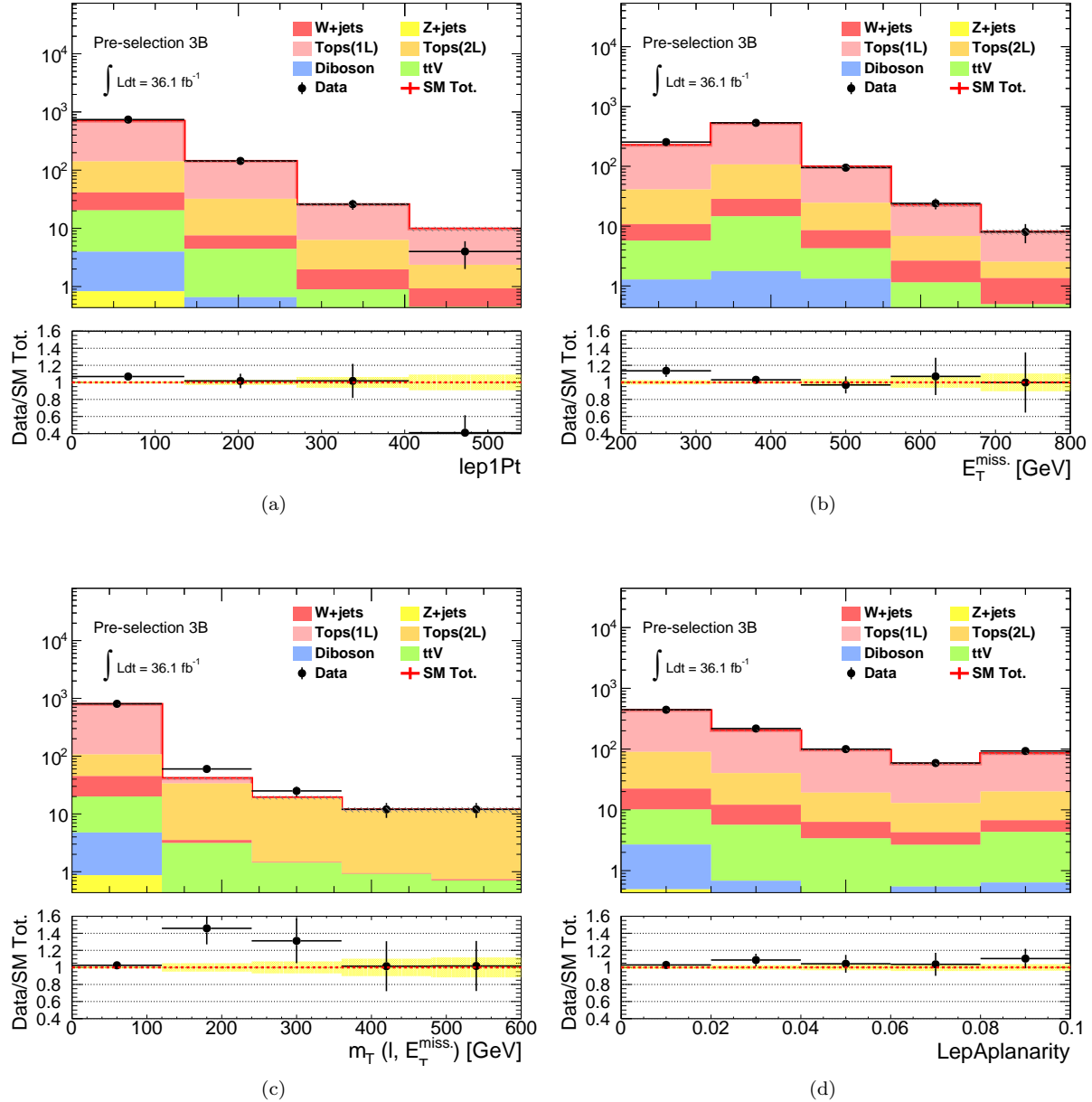


Figure 96: Kinematical distribution of (a) leading-lepton pt (b)  $E_T^{\text{miss}}$  (c)  $m_T$  (d) aplanarity in the **3b**-tagged pre-selection region, with the reweighting:  $w = 1.4 \times [1 - 0.061 \times p_T(t\bar{t})]$  (Eq.(94)) being applied for  $t\bar{t}$  MC.

### 6.2.2 Definition of Control Regions and Validation Regions

The key assumption in this method is that the relative modeling of MC between CRs and SRs are correct. In other words, both CRs and SRs suffer from the same mis-modeling, so that the normalization factor measured in CR is applicable to SR. Therefore, the most important requirement in CR definition is having the similar phase space with respect to corresponding SR in terms of the mis-modeling.

The easiest realization of CR is to revert the SR cuts in kinematical variables that are well-modeled by MC. In this analysis,  $m_T$ , aplanarity and topness (and also  $\min_{i=1-4} \Delta\phi(j_i, E_T^{\text{miss}})$  for the “3B” tower) are chosen as the baseline extrapolation variables. A exception is in the “2J” tower where  $E_T^{\text{miss}}$  is used instead of aplanarity, since it is not used in the signal regions selection.

A couple of minor modifications follow based on following supplemental requirements:

- CR statistics have to be sufficient.

Typically, about 10 times more data statistics in CRs with respect to SRs are desired to make the correction stable particularly in cases where multiple components are corrected simultaneously (in this analysis,  $W + \text{jets}$  and  $t\bar{t} + Wt$ ). For this sake, cuts in variables fatally sensitive to the mis-modeling is loosened in some of the CRs, even at some cost of being hit by the mis-modeling. MET is for example always a good candidate to loosen since the gain in statistics increase is large. Although it is affected by the mis-modeling through jet transverse momenta which is known to be the most ill-modeled, the influence is much diluted through the vectorial summation of them, instead of the scalar sum.  $E_T^{\text{miss}}/m_{\text{eff}}$  is also loosened in “2J” and “High-x” since it is in a form of ratio which is supposed to be robust against simultaneous variation of the numerator and the denominator. The impact by the mis-modeling due to these loosened cuts are evaluated in Sec 6.2.3. On the other hand, it is promised that  $n_J$  ( $p_T > 30$  GeV) and  $m_{\text{eff}}$  are never touched since they are critical to the mis-modeling.

- Lower cut in  $m_T$  to reduce the contribution from fake leptons.

Low- $m_T$  regions are typically have higher abundance of events with fake leptons for  $W + \text{jets}$  and  $t\bar{t}$ . As the MC modeling on the fake rate is generally less reliable,  $m_T > 30 \sim 40$  GeV is applied in CR to get rid of the influence.

CRs are defined for each tower and  $m_{\text{eff}}$  bins independently, however are shared between b-tagged and b-vetoed SR bins. Normalization is applied only on  $W + \text{jets}$ ,  $t\bar{t}$  and single-top while raw MC prediction is quoted for diboson and the other minor backgrounds.  $t\bar{t}$  and single-top share the normalization factors as their relative breakdown is similar in CRs and SRs. The normalization factors are determined by a simultaneous fit on the b-vetoed and b-tagged slice of a CR (“WR” and “TR”) in which  $W + \text{jets}$  and  $t\bar{t}$  is dominant respectively. During the fit, all the normalization factors and nuisance parameters characterizing theoretical and experimental systematics are allowed to flow. The detail of the statistical procedure is described in Sec. 8.1.

There are the third type of regions referred as “validation regions” designed to confirm the validity of the background estimation procedure by comparing with the data. They are typically set in between the CR and SR, with the cut in one of the extrapolation variable is freed with respect to CRs and kept for the other one. VRa and VRb respectively validates the extrapolation in  $m_T$  and aplanarity ( $E_T^{\text{miss}}$  for “2J”). Upper cut on  $m_T$  is set in some VRa to suppress the signal contamination. VRs-QCD are the regions to examine

the contribution from QCD multi-jet processes in SRs which is supposedly negligible. The detail is found in Sec. B.

The finalized CRs and VRs are summarized together with the corresponding SRs in Table 19 - 23, with the graphical schematics being shown in Figure 97. While SRs are carefully designed to be orthogonal to CRs and VRs, it is allowed to have overlap between CRs and VRs once the CRs are found to have much larger statistics than that of the VRs so that the overlapped events have no influence to the normalization. For instance, CR and VRa are overlapped in “3B”. This is intended to secure the CR statistics, while the number of events in VRa is small enough so that they are still nearly statistically independent.

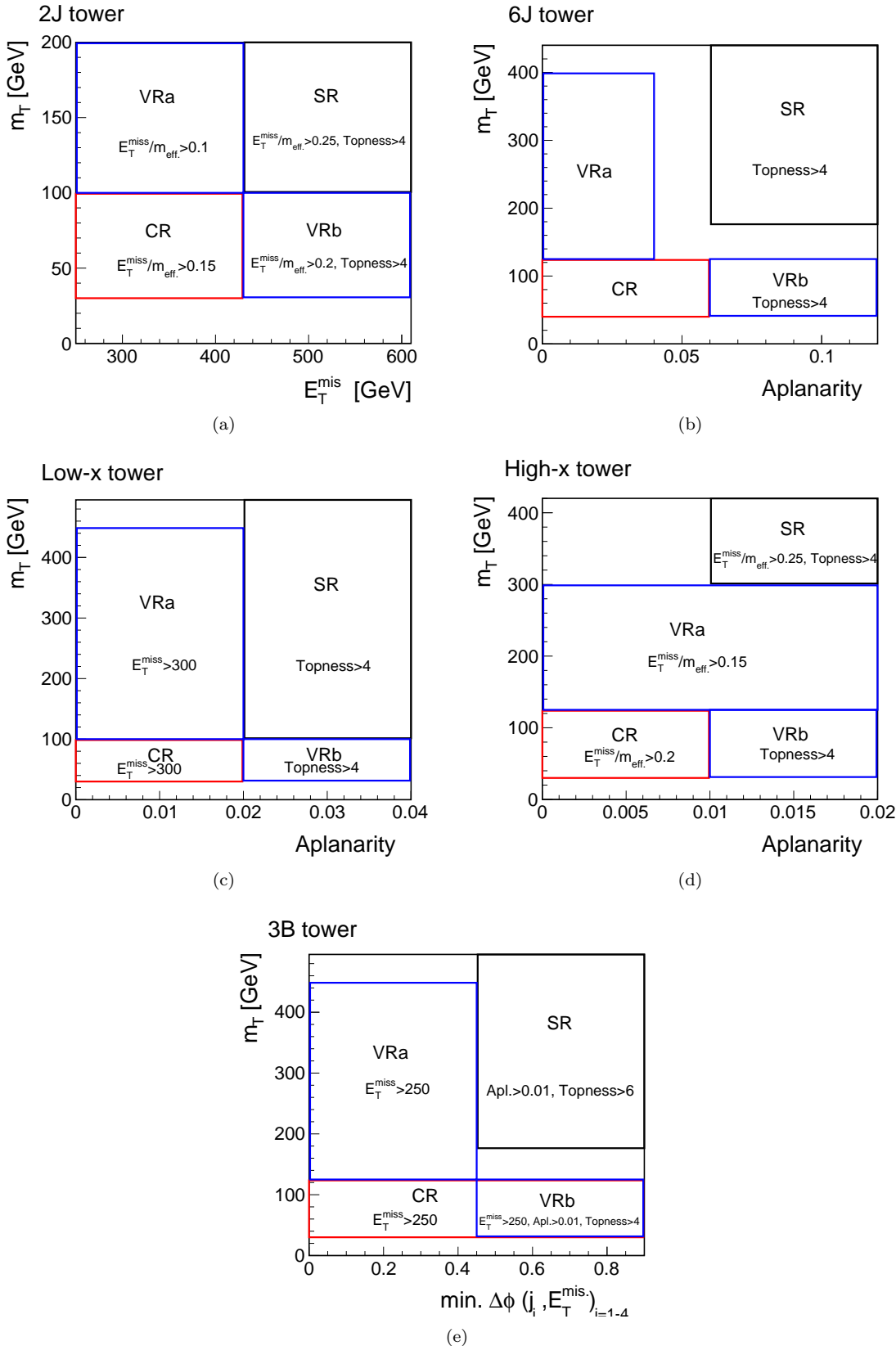


Figure 97: Schematics of CR/VR/SR in each signal region tower. Two major extrapolation variables are chosen to illustrate the difference between the regions. Extrapolation in the other variables are explicitly mentioned in the label. Note that the control region in the “3B” tower contains the VRa in it.

### 6.2.3 Evaluation of the Extrapolation Error

Although the good modeling on the extrapolation variables is confirmed in the pre-selection regions, the question is whether they are still good when the signal region selections are applied. In fact, there is correlation between the well-modeled variables ( $m_T$ , aplanarity etc.) and the ill-modeled ones ( $n_J$ , jet transverse momenta,  $m_{\text{eff}}$  etc.) that are not evident at preselection level, however could be addressing in some particular phase space. The extrapolation is also affected by the loosened cuts in variables that are already known to be poorly modeled such as MET, so the associated uncertainty needs be quantified.

In this sub-section, the extrapolation error is evaluated by injecting an artificial variation in MC compared to the observed MC mis-modeling, and then measure the yield change in a CR and the corresponding SR. Ideally, they show the same response against the injected variation, so that the normalization in CR can perfectly compensate the effect of mis-modeling in SR. Otherwise, the relative difference in their yield variation directly corresponds to the amount of extrapolation error.

Figures 98 - 101 present the results where the  $W + \text{jets}$  and  $t\bar{t}$  MC are varied by reweighting the events with:

$$\begin{aligned} w &= 1 - x \times (n_J - 2), & x \in [0, 0.18] && (W + \text{jets}) \\ w &= 1 - x \times p_T(t\bar{t})/100 \text{ GeV}, & x \in [0, 0.09] && (t\bar{t}), \end{aligned} \quad (95)$$

respectively. The vertical axis on the top panels show the amount of relative change that CR or SR experience by the injected MC variation as a function of  $x$ . The relative variation in CR (orange) compares to the normalization factor actually obtained via the fit to data, while that in SR (blue) to the ideal normalization factor need to fully correct the SR. The bottom panel display the ratio, namely the resultant extrapolation error. The realistic  $x$  is approximately  $x_W = 0.1$  and  $x_{t\bar{t}} = 0.06$  for  $W + \text{jets}$  and  $t\bar{t}$  respectively, based on the observation of data/MC in Sec. 6.2.1 as Eq. (92), (93) and (94). B-tagging requirement is removed to maintain sufficient statistics, assuming the kinematics are invariant with it. For the  $t\bar{t}$  process, component estimated by the object replacement method is excluded from the test. The extrapolation error from CRs to corresponding VRs are shown in Appendix Sec.C.

Observed extrapolation error is generally small, which stays within 10% (20%) for  $W + \text{jets}$  ( $t\bar{t}$ ) at the reference magnitude of mis-modeling ( $x_W = 0.1$ ,  $x_{t\bar{t}} = 0.06$ ). These are quoted as systematics error associated with the method in the fit, which is summarized in Table 48 of Sec. 7.3.1.

Note that this check is only quantifying the error in the methodology; how much the MC mis-modeling in terms of jet activities can be corrected if the other MC description is perfect. In reality, the shape of  $m_T$  or aplanarity distribution can be varies by the other reasons, and the uncertainties have to be assigned additionally. This will be discussed in Sec. 7.

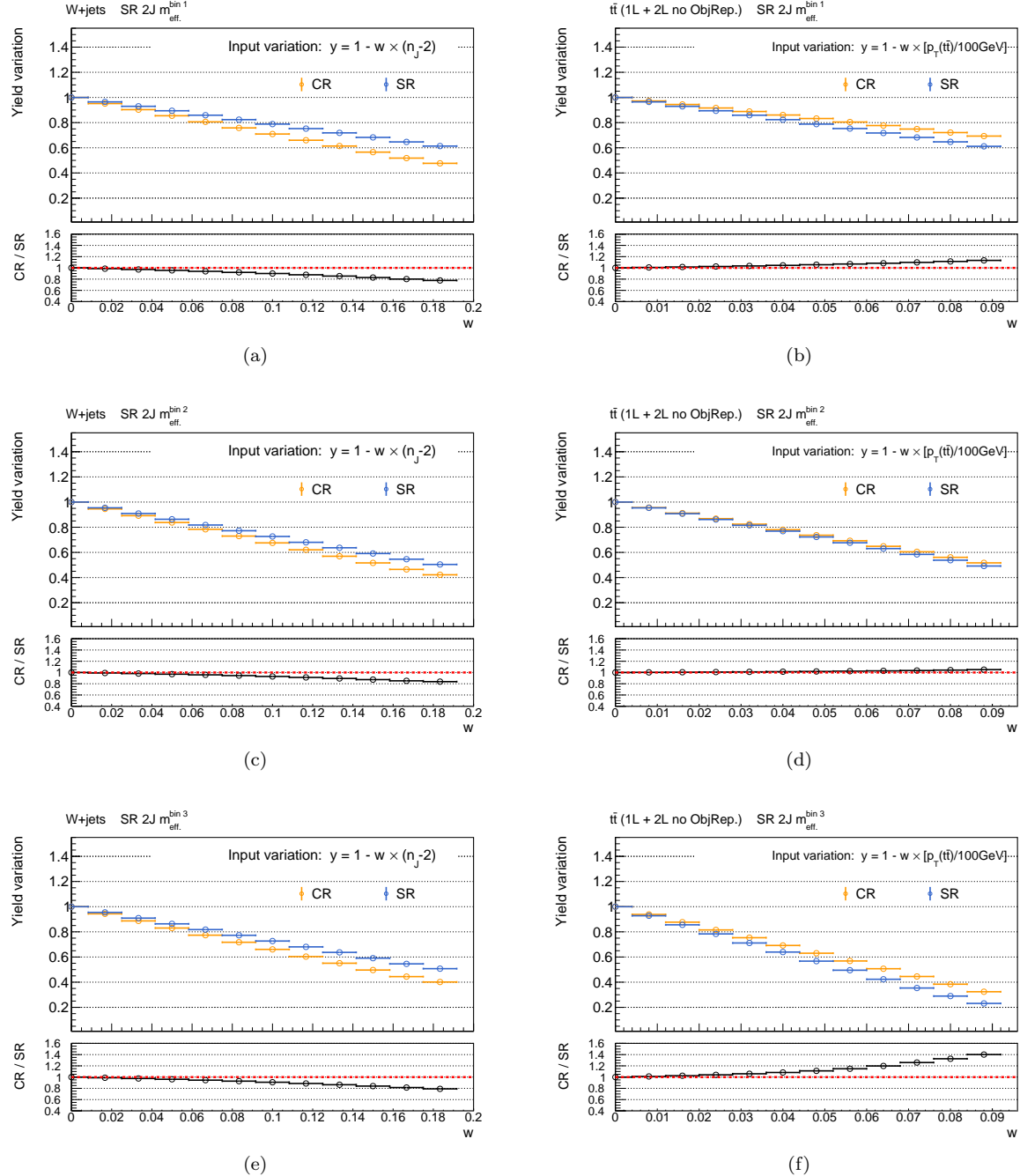


Figure 98: Extrapolation error in SR/CR 2J. B-tagging requirement is removed. Top pannels show the yield variation of (a)  $W + \text{jets}$  and (b)  $t\bar{t}$  when injecting the variation by reweighting the MC with Eq. 95. Bottom rows are the relative difference in their response against the injected variation, namely the extrapolation errir. For the  $t\bar{t}$  process, component estimated by the object replacement method is removed.

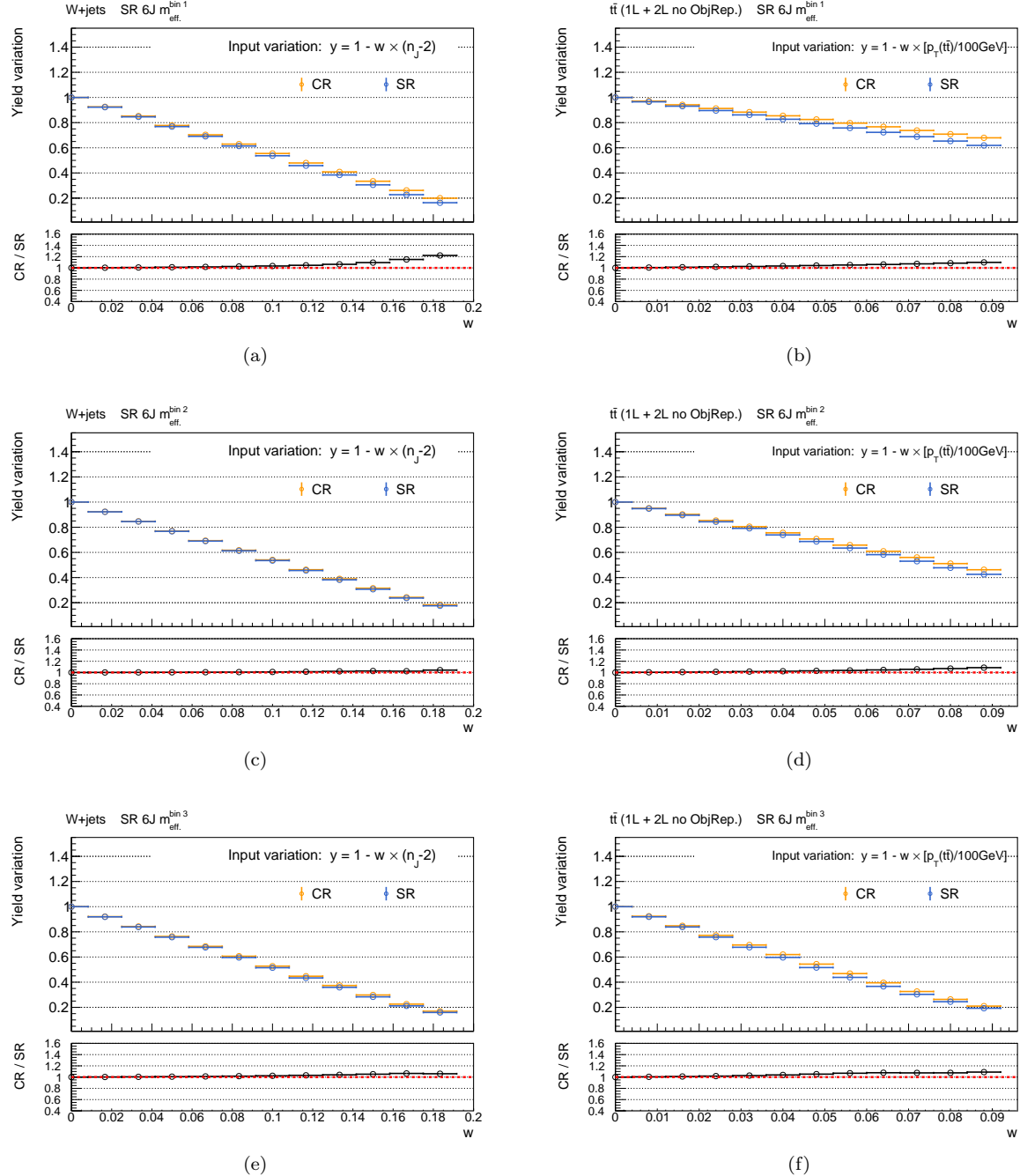


Figure 99: Extrapolation error in SR/CR 6J. B-tagging requirement is removed. Top pannels show the yield variation of (a)  $W + \text{jets}$  and (b)  $t\bar{t}$  when injecting the variation by reweighting the MC with Eq. 95. Bottom rows are the relative difference in their response against the injected variation, namely the extrapolation errir. For the  $t\bar{t}$  process, component estimated by the object replacement method is removed.

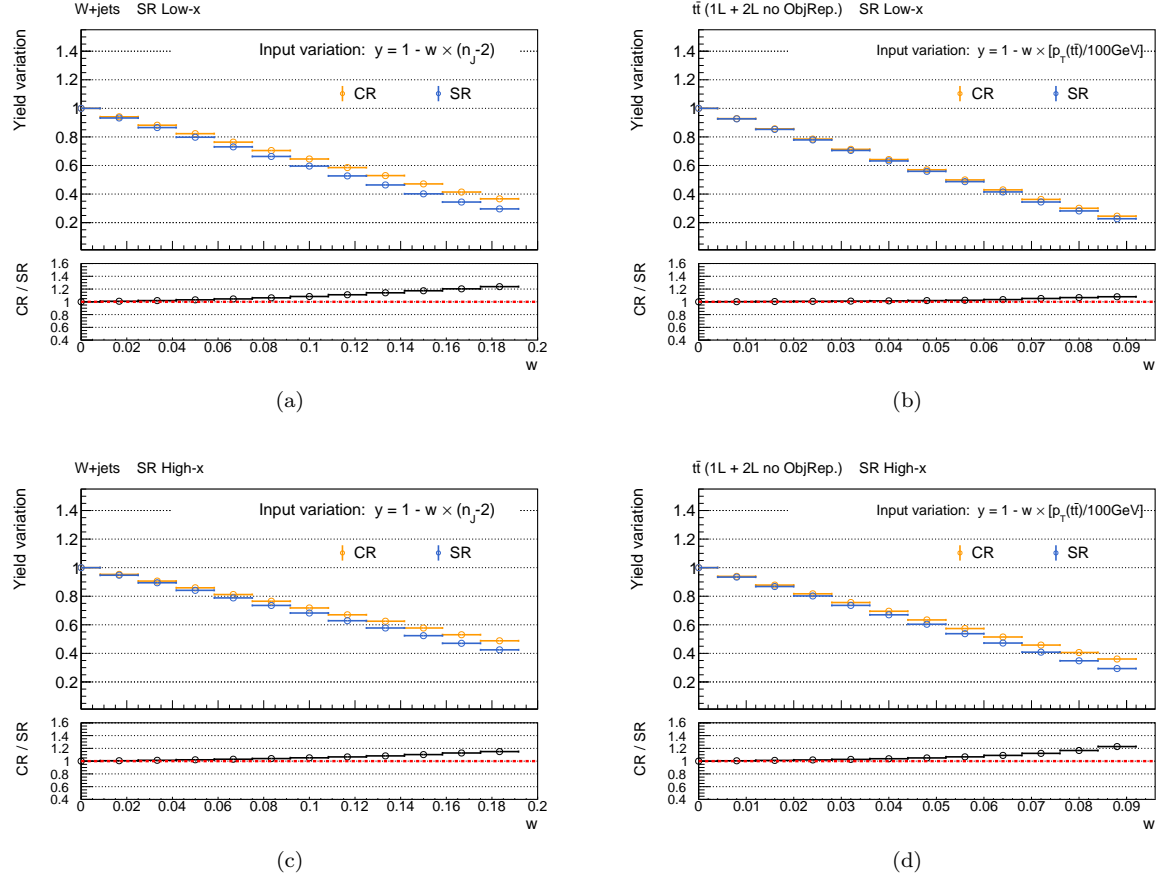


Figure 100: Extrapolation error in SR/CR (a)(b) Low-x, and (c)(d) High-x. B-tagging requirement is removed. Top pannels show the yield variation of  $W + \text{jets}$  (left) and  $t\bar{t}$  (right) when injecting the variation by reweighting the MC with Eq. 95. Bottom rows are the relative difference in their response against the injected variation, namely the extrapolation error. For the  $t\bar{t}$  process, component estimated by the object replacement method is removed.

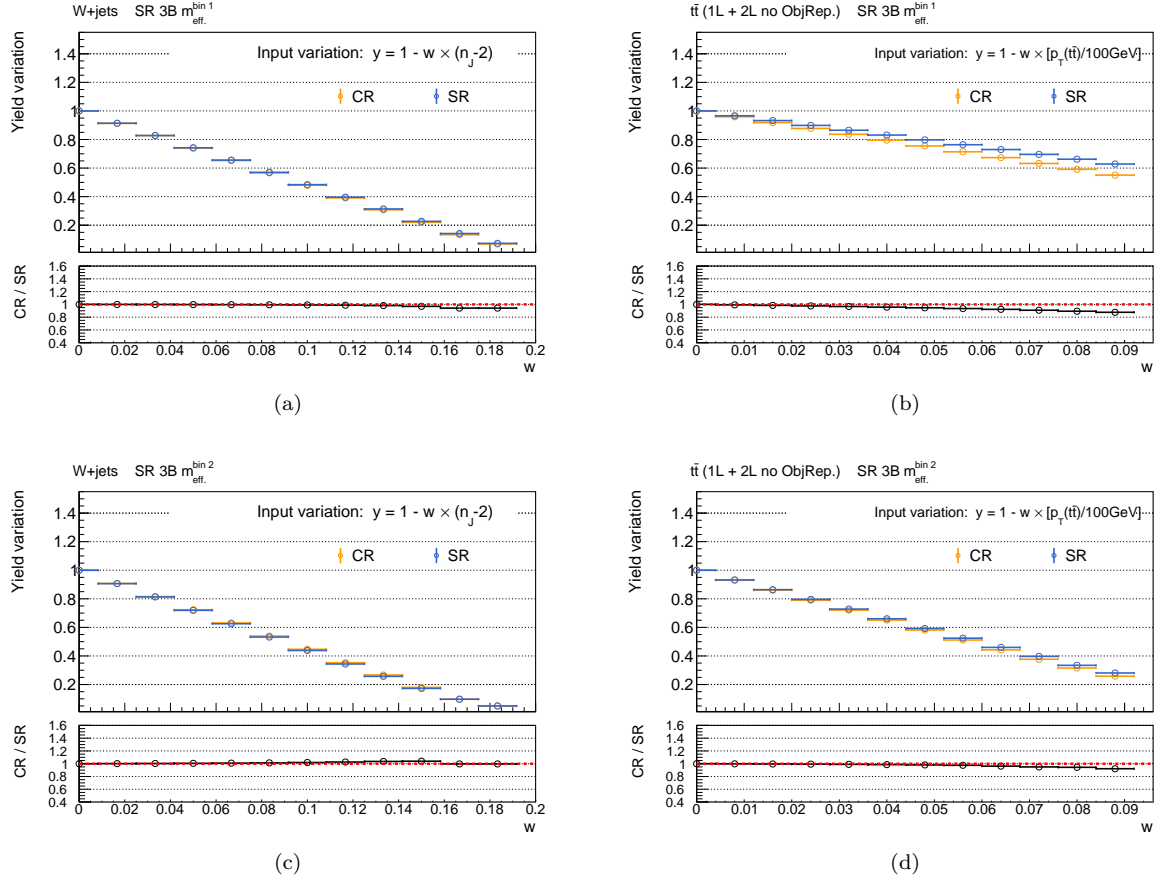


Figure 101: Extrapolation error in SR/CR 3B. B-tagging requirement is removed for  $W + \text{jets}$ . Top pannels show the yield variation of  $W + \text{jets}$  (left) and  $t\bar{t}$  (right) when injecting the variation by reweighting the MC with Eq. 95. Bottom rows are the relative difference in their response against the injected variation, namely the extrapolation errir. For the  $t\bar{t}$  process, component estimated by the object replacement method is removed.

#### 6.2.4 Result of Background-only Fit

The data yields in control regions are summarized in Table 26 - 30, accompanied with the pre-fit and post-fit prediction by MC. Note that only  $W + \text{jets}$  and top backgrounds ( $t\bar{t}$  and single-top) are normalized and the yield of other processes are kept during the fit. The effect of signal contamination in control regions is neglected therefore referred as “background-only fit”.

Fitted normalization factors are summarized in Figure 102. Generally they decrease with elevating  $m_{\text{eff}}$ -bin, consistent to the data-MC observation where MC is systematically over-predict in high  $m_{\text{eff}}$  regions.

Figure 103-110 are the post-fit distributions for variables used in the extrapolation in each region. Blue arrows indicate the CRs that the MC is normalized.

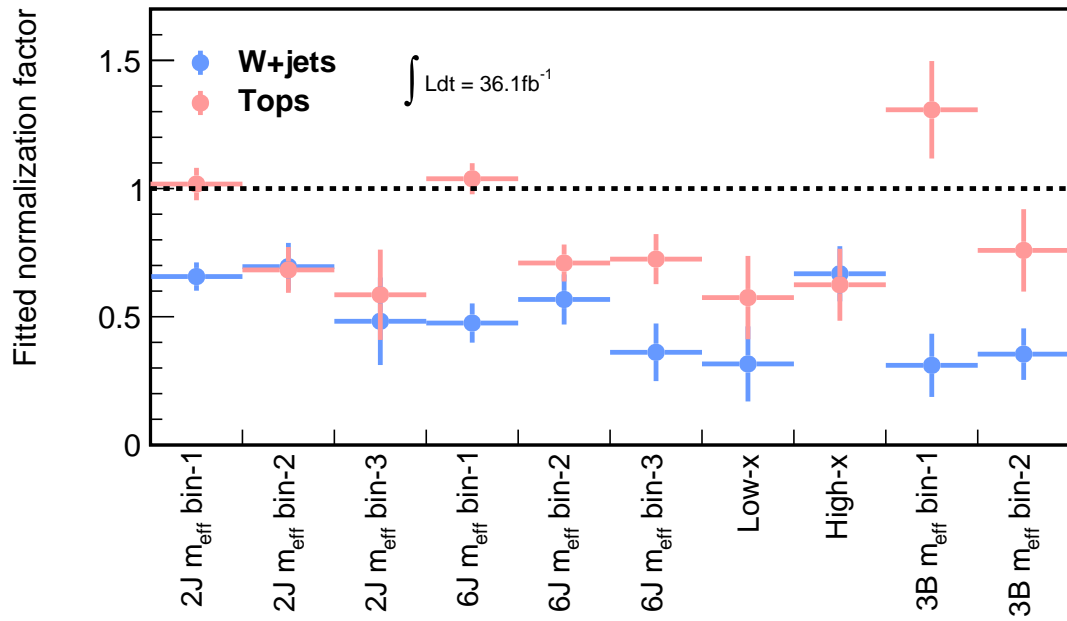


Figure 102: Fitted normalization factors for  $W + \text{jets}$  and top backgrounds ( $t\bar{t}$  plus single-top). The error bars represent combined systematic and statistical uncertainties.

Table 26: Event yields and the background-only fit results in the “2J” control regions. Each column corresponds to a bin in  $m_{\text{eff}}$ . Uncertainties in the MC estimates combine statistical (in the simulated event yields) and systematic uncertainties discussed in Sec 7. The uncertainties in this table are symmetrised for propagation purposes but truncated at zero to remain within the physical boundaries.

<b>WR 2J</b>	$m_{\text{eff}} \in [1100, 1500]$	$m_{\text{eff}} \in [1500, 1900]$	$m_{\text{eff}} > 1900$
Observed data	620	127	17
MC total (post-fit)	$620.06 \pm 24.93$	$126.89 \pm 11.28$	$17.01 \pm 4.14$
$W + \text{jets}$	$462.0 \pm 34.1$	$99.7 \pm 12.6$	$12.6 \pm 4.4$
$Z + \text{jets}$	$14.3 \pm 3.9$	$2.6 \pm 0.7$	$0.5 \pm 0.1$
Tops	$100.9 \pm 17.1$	$14.9 \pm 3.2$	$2.6 \pm 0.9$
Di-boson	$41.7 \pm 13.7$	$9.3 \pm 3.6$	$1.3 \pm 0.4$
$t\bar{t} + V$	$1.2 \pm 0.3$	$0.3 \pm 0.1$	$0.1 \pm 0.0$
MC total (pre-fit)	$859.70 \pm 30.91$	$177.49 \pm 7.33$	$32.40 \pm 1.67$
$W + \text{jets}$	$703.35 \pm 19.15$	$143.40 \pm 4.39$	$26.19 \pm 1.22$
$Z + \text{jets}$	$14.26 \pm 3.92$	$2.58 \pm 0.72$	$0.45 \pm 0.13$
Tops	$99.27 \pm 13.32$	$21.88 \pm 3.16$	$4.42 \pm 0.75$
Di-boson	$41.63 \pm 13.69$	$9.32 \pm 3.55$	$1.26 \pm 0.44$
$t\bar{t} + V$	$1.18 \pm 0.25$	$0.30 \pm 0.07$	$0.06 \pm 0.02$
<b>TR 2J</b>	$m_{\text{eff}} \in [1100, 1500]$	$m_{\text{eff}} \in [1500, 1900]$	$m_{\text{eff}} > 1900$
Observed data	972	150	22
MC total (post-fit)	$971.82 \pm 31.18$	$150.01 \pm 12.27$	$22.00 \pm 4.71$
$W + \text{jets}$	$99.5 \pm 35.0$	$23.2 \pm 8.4$	$3.3 \pm 1.7$
$Z + \text{jets}$	$3.9 \pm 1.0$	$0.9 \pm 0.2$	$0.2 \pm 0.1$
Tops	$846.1 \pm 48.2$	$120.2 \pm 15.3$	$17.4 \pm 5.2$
Di-boson	$11.9 \pm 4.4$	$2.7 \pm 0.9$	$0.7 \pm 0.3$
$t\bar{t} + V$	$10.3 \pm 1.8$	$3.1 \pm 0.6$	$0.4 \pm 0.1$
MC total (pre-fit)	$1009.13 \pm 52.94$	$216.02 \pm 11.81$	$37.88 \pm 2.67$
$W + \text{jets}$	$151.50 \pm 48.57$	$33.30 \pm 10.57$	$6.91 \pm 2.25$
$Z + \text{jets}$	$3.86 \pm 1.05$	$0.85 \pm 0.23$	$0.17 \pm 0.05$
Tops	$831.49 \pm 14.93$	$176.11 \pm 4.06$	$29.70 \pm 1.15$
Di-boson	$11.94 \pm 4.35$	$2.67 \pm 0.92$	$0.68 \pm 0.27$
$t\bar{t} + V$	$10.34 \pm 1.81$	$3.08 \pm 0.58$	$0.43 \pm 0.11$

Table 27: Event yields and the background-only fit results in the “6J” control regions. Each column corresponds to a bin in  $m_{\text{eff}}$ . Uncertainties in the MC estimates combine statistical (in the simulated event yields) and systematic uncertainties discussed in Sec 7. The uncertainties in this table are symmetrised for propagation purposes but truncated at zero to remain within the physical boundaries.

<b>WR 6J</b>	$m_{\text{eff}} \in [1100, 1600]$	$m_{\text{eff}} \in [1600, 2100]$	$m_{\text{eff}} > 2100$
Observed data	248	120	53
MC total (post-fit)	$248.06 \pm 15.84$	$120.02 \pm 11.21$	$52.98 \pm 7.30$
$W + \text{jets}$	$147.5 \pm 22.0$	$83.3 \pm 13.9$	$30.6 \pm 9.2$
$Z + \text{jets}$	$2.5 \pm 1.0$	$1.1 \pm 0.5$	$0.7 \pm 0.3$
Tops	$71.7 \pm 11.5$	$22.9 \pm 4.4$	$14.3 \pm 3.1$
Di-boson	$25.3 \pm 7.5$	$12.1 \pm 5.8$	$7.1 \pm 3.8$
$t\bar{t} + V$	$1.1 \pm 0.2$	$0.6 \pm 0.2$	$0.3 \pm 0.1$
MC total (pre-fit)	$408.20 \pm 19.21$	$192.94 \pm 10.30$	$112.45 \pm 7.11$
$W + \text{jets}$	$310.29 \pm 11.30$	$146.84 \pm 5.42$	$84.62 \pm 4.04$
$Z + \text{jets}$	$2.54 \pm 1.03$	$1.10 \pm 0.46$	$0.72 \pm 0.33$
Tops	$69.12 \pm 8.78$	$32.38 \pm 4.37$	$19.72 \pm 2.80$
Di-boson	$25.19 \pm 7.45$	$12.05 \pm 5.78$	$7.10 \pm 3.80$
$t\bar{t} + V$	$1.06 \pm 0.24$	$0.57 \pm 0.17$	$0.29 \pm 0.09$
<b>TR 6J</b>	$m_{\text{eff}} \in [1100, 1600]$	$m_{\text{eff}} \in [1600, 2100]$	$m_{\text{eff}} > 2100$
Observed data	647	232	117
MC total (post-fit)	$646.88 \pm 25.46$	$231.79 \pm 15.24$	$116.91 \pm 10.85$
$W + \text{jets}$	$43.2 \pm 16.5$	$25.1 \pm 9.7$	$11.6 \pm 5.5$
$Z + \text{jets}$	$0.9 \pm 0.4$	$0.6 \pm 0.2$	$0.4 \pm 0.2$
Tops	$586.2 \pm 31.2$	$193.1 \pm 18.7$	$98.8 \pm 12.8$
Di-boson	$8.1 \pm 2.5$	$8.2 \pm 2.7$	$3.9 \pm 1.7$
$t\bar{t} + V$	$8.5 \pm 1.5$	$4.7 \pm 1.1$	$2.3 \pm 0.6$
MC total (pre-fit)	$672.53 \pm 31.35$	$329.86 \pm 16.23$	$174.76 \pm 11.54$
$W + \text{jets}$	$90.62 \pm 28.71$	$44.24 \pm 14.02$	$31.99 \pm 10.13$
$Z + \text{jets}$	$0.88 \pm 0.36$	$0.58 \pm 0.23$	$0.41 \pm 0.20$
Tops	$564.43 \pm 9.95$	$272.12 \pm 5.74$	$136.21 \pm 3.91$
Di-boson	$8.11 \pm 2.51$	$8.21 \pm 2.69$	$3.84 \pm 1.69$
$t\bar{t} + V$	$8.48 \pm 1.53$	$4.71 \pm 1.14$	$2.30 \pm 0.63$

Table 28: Event yields and the background-only fit results in the “Low-x” control regions. Each column corresponds to a bin in  $m_{\text{eff}}$ . Uncertainties in the MC estimates combine statistical (in the simulated event yields) and systematic uncertainties discussed in Sec 7. The uncertainties in this table are symmetrised for propagation purposes but truncated at zero to remain within the physical boundaries.

CR Low-x	WR	TR
Observed data	15	25
MC total (post-fit)	$15.02 \pm 3.89$	$24.97 \pm 5.03$
$W + \text{jets}$	$9.3 \pm 4.2$	$2.9 \pm 1.8$
$Z + \text{jets}$	$0.4 \pm 0.2$	$0.2 \pm 0.1$
Tops	$2.7 \pm 0.9$	$20.4 \pm 5.7$
Di-boson	$2.6 \pm 0.8$	$1.0 \pm 1.0$
$t\bar{t} + V$	$0.0 \pm 0.0$	$0.5 \pm 0.1$
MC total (pre-fit)	$37.17 \pm 2.56$	$46.38 \pm 3.87$
$W + \text{jets}$	$29.51 \pm 1.84$	$9.26 \pm 3.05$
$Z + \text{jets}$	$0.38 \pm 0.15$	$0.17 \pm 0.07$
Tops	$4.62 \pm 0.75$	$35.47 \pm 1.52$
Di-boson	$2.61 \pm 0.79$	$0.99 \pm 0.98$
$t\bar{t} + V$	$0.05 \pm 0.02$	$0.48 \pm 0.11$

Table 29: Event yields and the background-only fit results in the “High-x” control regions. Each column corresponds to a bin in  $m_{\text{eff}}$ . Uncertainties in the MC estimates combine statistical (in the simulated event yields) and systematic uncertainties discussed in Sec 7. The uncertainties in this table are symmetrised for propagation purposes but truncated at zero to remain within the physical boundaries.

CR High-x	WR	TR
Observed data	92	73
MC total (post-fit)	$91.91 \pm 9.61$	$72.97 \pm 8.57$
$W + \text{jets}$	$72.4 \pm 11.1$	$17.0 \pm 6.5$
$Z + \text{jets}$	$1.1 \pm 0.4$	$0.3 \pm 0.1$
Tops	$10.2 \pm 2.9$	$52.0 \pm 11.3$
Di-boson	$8.0 \pm 3.5$	$2.7 \pm 1.4$
$t\bar{t} + V$	$0.2 \pm 0.1$	$1.0 \pm 0.4$
MC total (pre-fit)	$134.04 \pm 6.41$	$112.69 \pm 9.52$
$W + \text{jets}$	$108.42 \pm 3.88$	$25.52 \pm 8.13$
$Z + \text{jets}$	$1.13 \pm 0.39$	$0.29 \pm 0.13$
Tops	$16.32 \pm 2.19$	$83.19 \pm 3.25$
Di-boson	$7.99 \pm 3.50$	$2.70 \pm 1.35$
$t\bar{t} + V$	$0.18 \pm 0.08$	$0.99 \pm 0.37$

Table 30: Event yields and the background-only fit results in the “3B” control regions. Each column corresponds to a bin in  $m_{\text{eff}}$ . Uncertainties in the MC estimates combine statistical (in the simulated event yields) and systematic uncertainties discussed in Sec 7. The uncertainties in this table are symmetrised for propagation purposes but truncated at zero to remain within the physical boundaries.

<b>WR 3B</b>	$m_{\text{eff}} \in [1000, 1750]$	$m_{\text{eff}} > 1750$
Observed data	368	107
MC total (post-fit)	$368.18 \pm 19.69$	$107.05 \pm 10.56$
$W + \text{jets}$	$146.4 \pm 59.3$	$58.3 \pm 16.7$
$Z + \text{jets}$	$5.3 \pm 1.5$	$2.4 \pm 0.4$
Tops	$176.6 \pm 52.2$	$33.1 \pm 11.5$
Di-boson	$37.7 \pm 9.9$	$12.5 \pm 3.3$
$t\bar{t} + V$	$2.2 \pm 0.5$	$0.8 \pm 0.2$
MC total (pre-fit)	$651.86 \pm 28.54$	$223.90 \pm 10.02$
$W + \text{jets}$	$471.51 \pm 7.38$	$164.58 \pm 2.94$
$Z + \text{jets}$	$5.29 \pm 1.45$	$2.39 \pm 0.38$
Tops	$135.10 \pm 21.31$	$43.59 \pm 7.33$
Di-boson	$37.74 \pm 9.93$	$12.53 \pm 3.26$
$t\bar{t} + V$	$2.21 \pm 0.52$	$0.80 \pm 0.22$
<b>TR 3B</b>	$m_{\text{eff}} \in [1000, 1750]$	$m_{\text{eff}} > 1750$
Observed data	234	47
MC total (post-fit)	$233.97 \pm 15.57$	$46.98 \pm 6.95$
$W + \text{jets}$	$1.4 \pm 1.0$	$0.9 \pm 0.5$
$Z + \text{jets}$	$0.1 \pm 0.1$	$0.1 \pm 0.1$
Tops	$227.5 \pm 15.8$	$44.1 \pm 7.1$
Di-boson	$0.2^{+0.3}_{-0.2}$	$0.2 \pm 0.1$
$t\bar{t} + V$	$4.7 \pm 1.2$	$1.7 \pm 0.4$
MC total (pre-fit)	$183.60 \pm 23.01$	$62.71 \pm 8.28$
$W + \text{jets}$	$4.54 \pm 1.87$	$2.62 \pm 1.00$
$Z + \text{jets}$	$0.12 \pm 0.05$	$0.10 \pm 0.06$
Tops	$174.00 \pm 21.42$	$58.15 \pm 7.43$
Di-boson	$0.20^{+0.27}_{-0.20}$	$0.18 \pm 0.08$
$t\bar{t} + V$	$4.75 \pm 1.17$	$1.66 \pm 0.43$

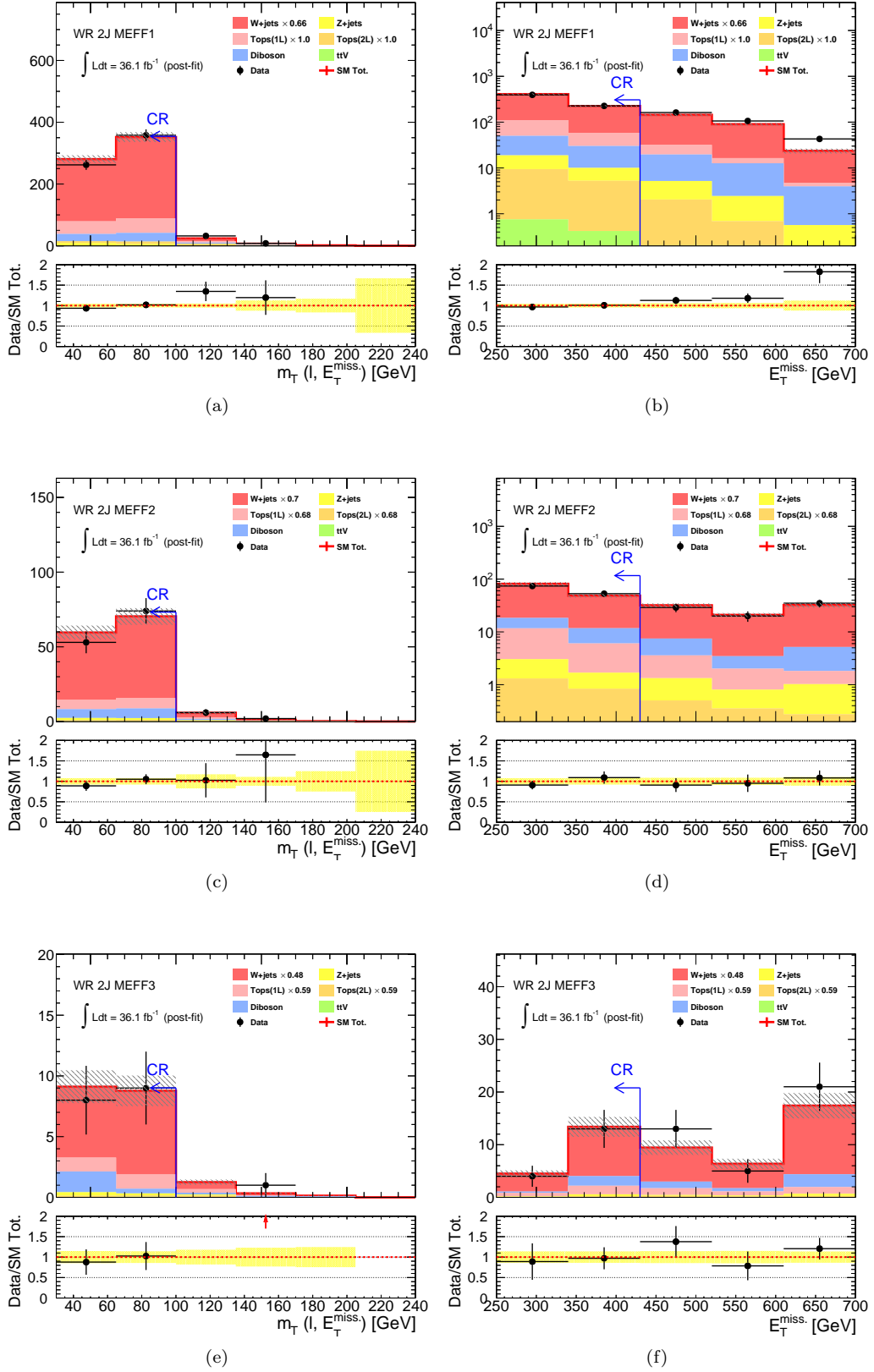


Figure 103: Post-fit distribution of (left)  $m_T$  (right)  $E_T^{\text{miss}}$ . (a,b) WR 2J- $m_{\text{eff}}^{\text{bin}1}$ . (c,d) WR 2J- $m_{\text{eff}}^{\text{bin}2}$ . (e,f) WR 2J- $m_{\text{eff}}^{\text{bin}3}$ . The yellow band in the bottom panel represents only statistical error. The overflow is included in the highest bin.

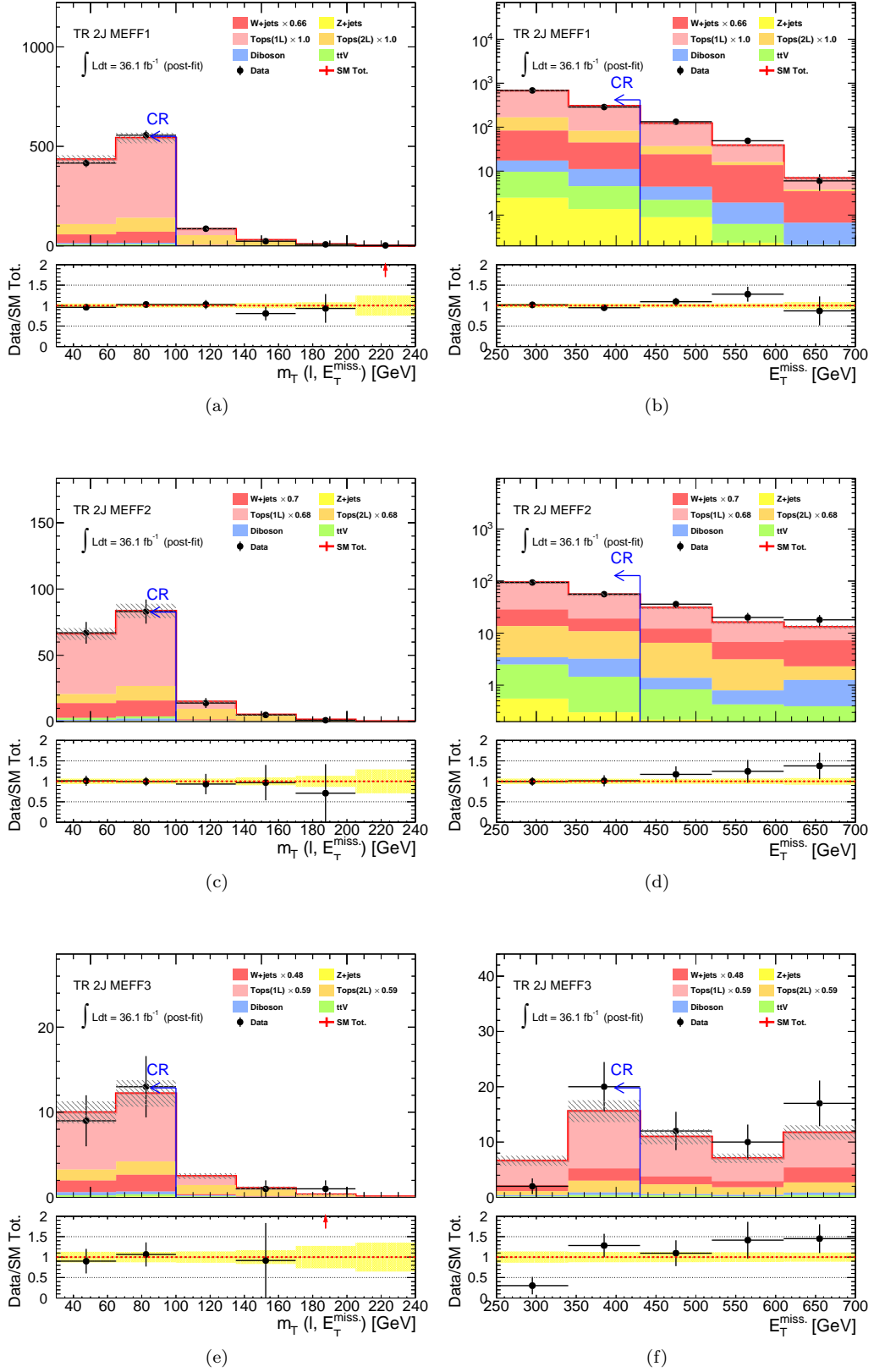


Figure 104: Post-fit distribution of (left)  $m_T$  (right)  $E_T^{\text{miss}}$ . (a,b) TR 2J- $m_{\text{eff}}^{\text{bin}1}$ . (c,d) TR 2J- $m_{\text{eff}}^{\text{bin}2}$ . (e,f) TR 2J- $m_{\text{eff}}^{\text{bin}3}$ . The yellow band in the bottom panel represents only statistical error. The overflow is included in the highest bin.

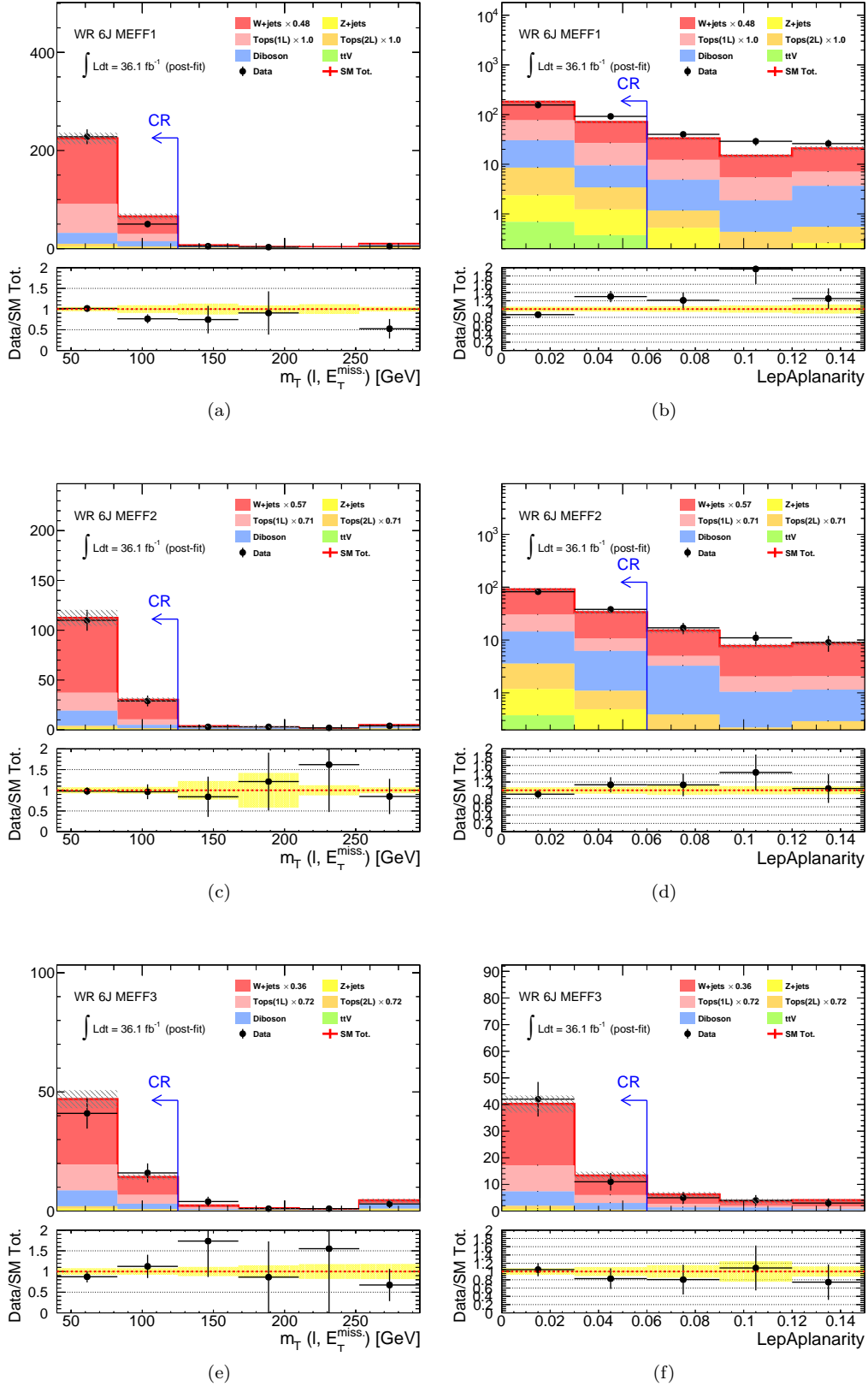


Figure 105: Post-fit distribution of (left)  $m_T$  (right) aplanarity. (a,b) WR 6J- $m_{\text{eff}}^{\text{bin}1}$ . (c,d) WR 6J- $m_{\text{eff}}^{\text{bin}2}$ . (e,f) WR 6J- $m_{\text{eff}}^{\text{bin}3}$ . The yellow band in the bottom panel represents only statistical error. The overflow is included in the highest bin.

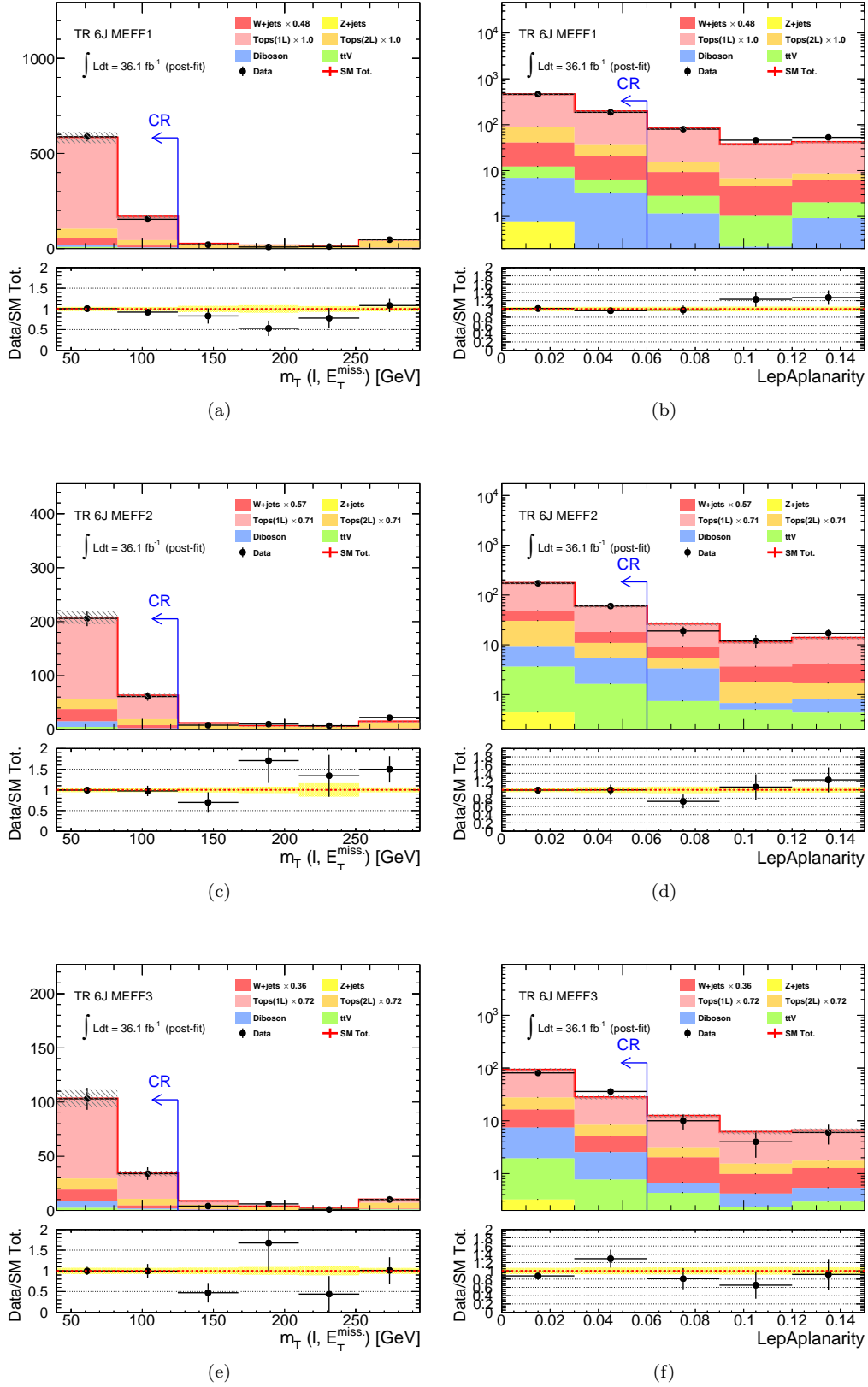


Figure 106: Post-fit distribution of (left)  $m_T$  (right) aplanarity. (a,b) TR 6J- $m_{\text{eff}}^{\text{bin}1}$ . (c,d) TR 6J- $m_{\text{eff}}^{\text{bin}2}$ . (e,f) TR 6J- $m_{\text{eff}}^{\text{bin}3}$ . The yellow band in the bottom panel represents only statistical error. The overflow is included in the highest bin.

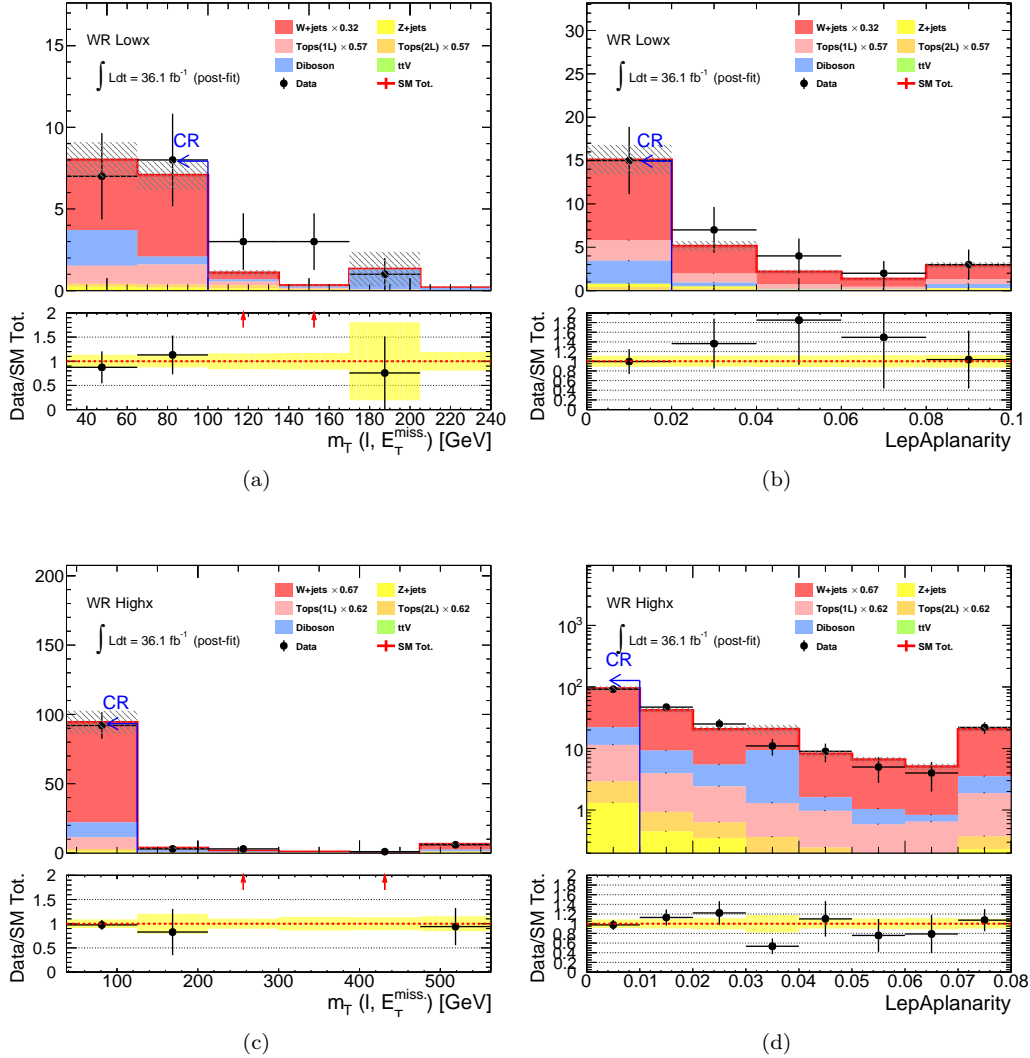


Figure 107: Post-fit distribution of (left)  $m_T$  (right) aplanarity. (a,b) WR Low-x. (c,d) WR High-x. The yellow band in the bottom panel represents only statistical error. The overflow is included in the highest bin.

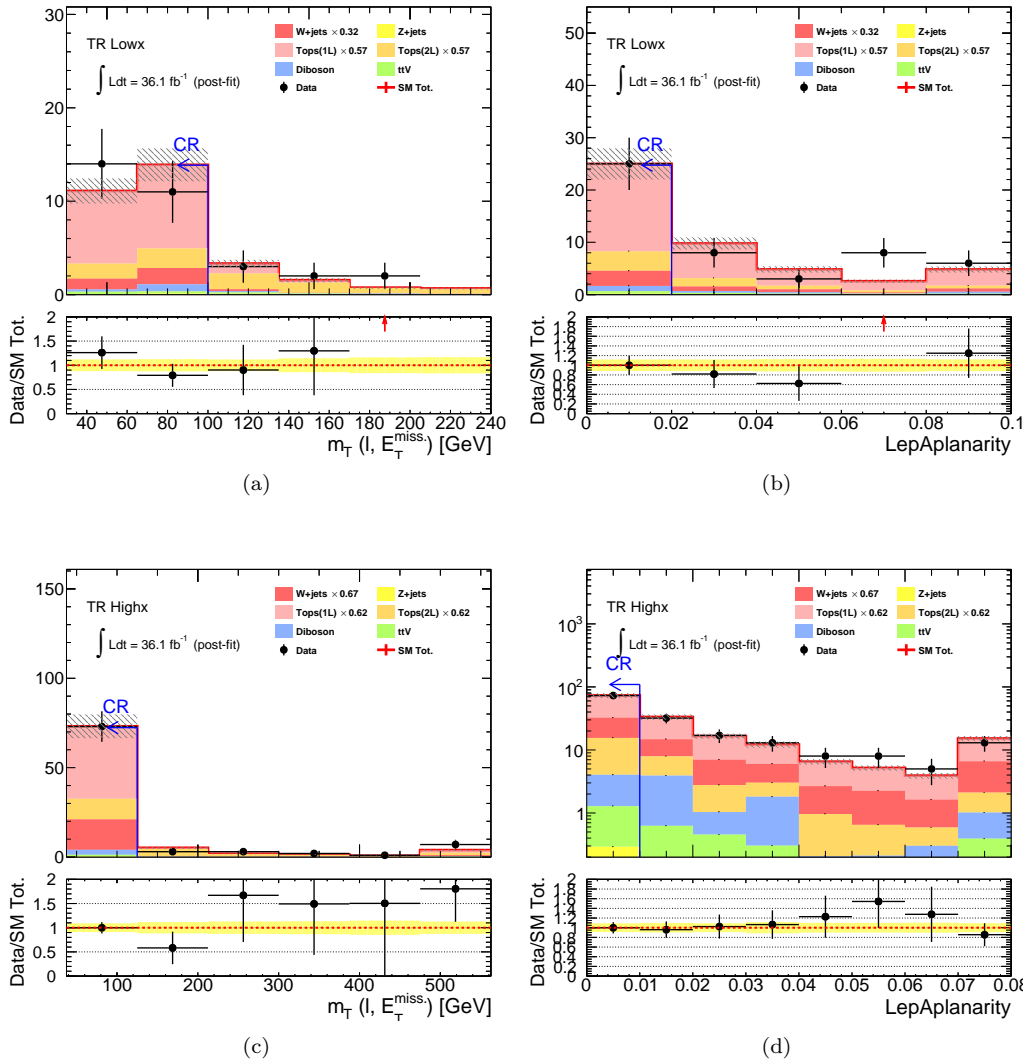


Figure 108: Post-fit distribution of (left)  $m_T$  (right) aplanarity. (a,b) TR Low-x. (c,d) TR High-x. The yellow band in the bottom panel represents only statistical error. The overflow is included in the highest bin.

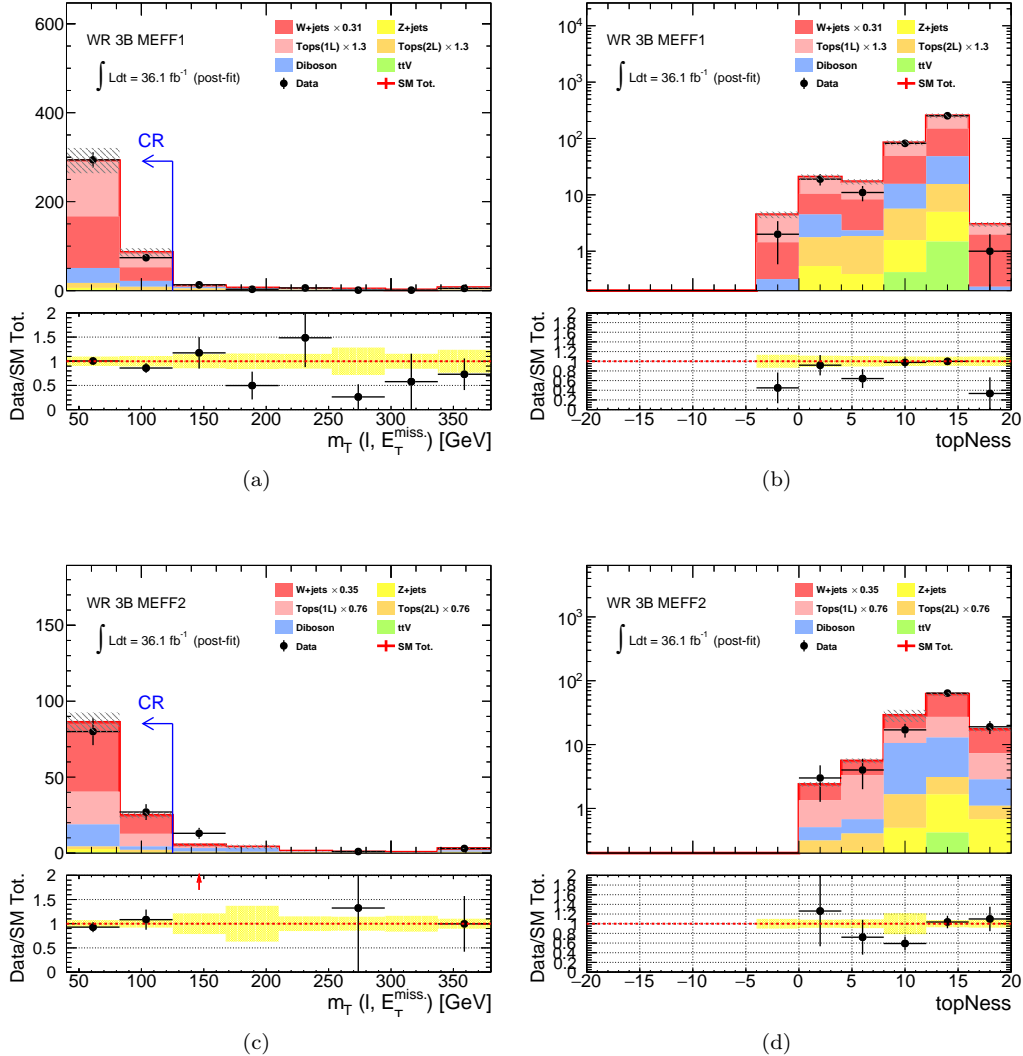


Figure 109: Post-fit distribution of (left)  $m_T$  (right) topness. (a,b) WR 3B- $m_{\text{eff}}^{\text{bin}1}$ . (c,d) WR 3B- $m_{\text{eff}}^{\text{bin}2}$ . The yellow band in the bottom panel represents only statistical error. The overflow is included in the highest bin.

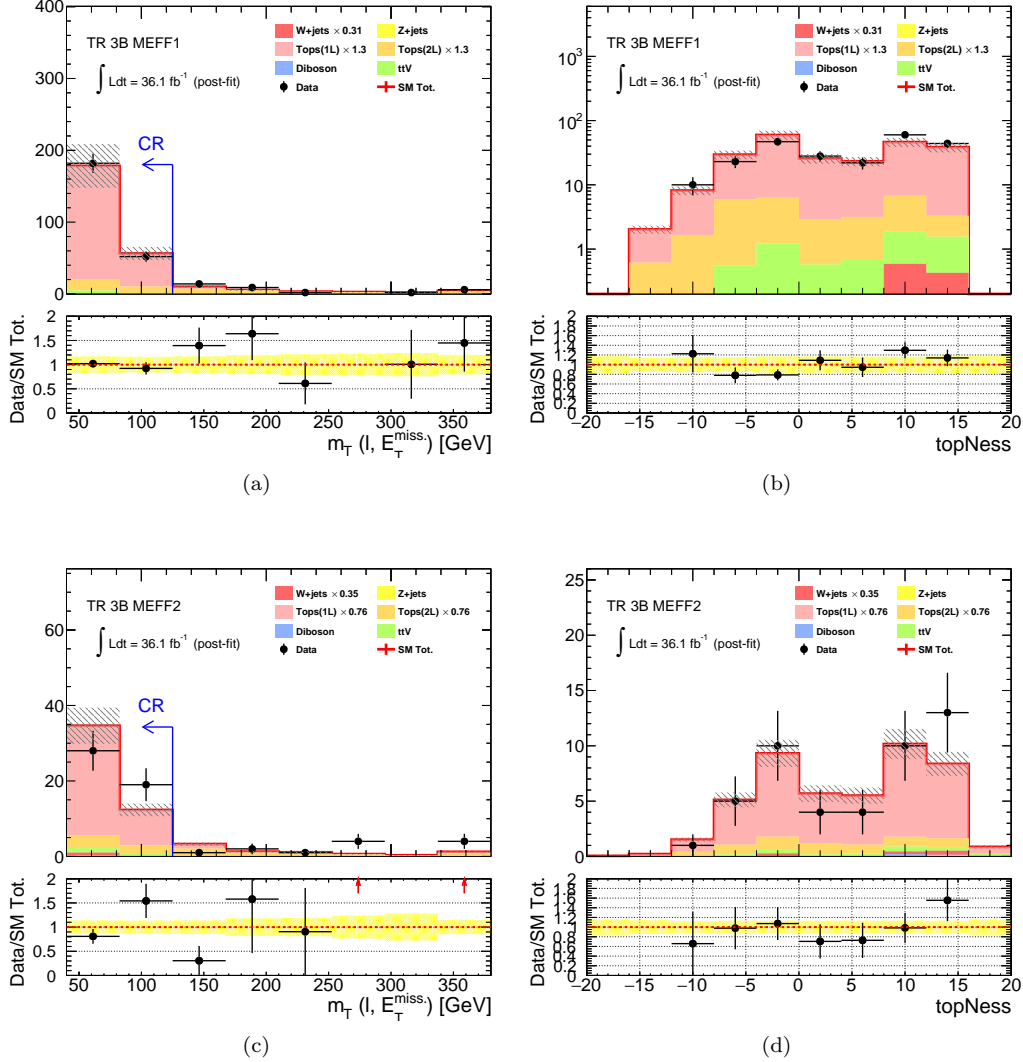


Figure 110: Post-fit distribution of (left)  $m_T$  (right) topness. (a,b) TR 3B- $m_{\text{eff}}^{\text{bin}1}$ . (c,d) TR 3B- $m_{\text{eff}}^{\text{bin}2}$ . The yellow band in the bottom panel represents only statistical error. The overflow is included in the highest bin.

### 6.3 The Object Replacement Method

A potential concern over the kinematical extrapolation method is that it is still fully relies on MC in the extrapolation. In particular, in case of estimating the “di-leptonic” background by extrapolating in  $m_T$ , this follows that:

- The MC modeling itself is questionable.

As observed in Figure 89 (c), MC tends to be overestimating in the tail, reflecting the fact that in case of di-leptonic channel,  $m_T$  scales with the lepton transverse momentum and MET in which MC is found to be is-modeling.

- Different particles contribute to observables between the semi-leptonic and di-leptonic processes. For instance, MET is sourced by a single neutrino in the semi-leptonic channel while it is by a vectorial sum of two neutrinos in the di-leptonic one. More seriously, the number of ISR/FRS jets is different under the same jet multiplicity. For example in  $t\bar{t}$ , the semi-leptonic channel yields 4 jets by its decay while the di-leptonic channel can only lead to 2 (or 3 if hadronic decay product from  $\tau$  is tagged as a jet). The differences are summarized in Table 31. Note that these differences also propagate to the other composite variables using jets and MET (e.g.  $m_{\text{eff}}$  and  $m_T$  etc.). Therefore, applying the same selection between CRs and SRs no longer guarantee that CRs grasp the same phase space as SRs.

Table 31: Comparison of constituents of MET and  $n_J$  between the semi-leptonic  $t\bar{t}$  and di-leptonic  $t\bar{t}$  as example. “1LCR” refers to the control regions used in the kinematical extrapolation method, and “2LCR” is its 2-lepton version with the same kinematical selection. Note that the other composite variables using jet and MET (e.g.  $m_{\text{eff}}$  and  $m_T$  etc.) are also affected by the difference accordingly.

	SR	1L CR	2LCR
Dominant $t\bar{t}$ component	$t\bar{t} \rightarrow b\ell\nu_1 b\tau\nu_2, \tau \rightarrow \tau_h \nu_\tau$	$t\bar{t} \rightarrow bqq\ell\nu$	$t\bar{t} \rightarrow b\ell\nu_1 b\ell\nu_2$
$n_J$ $E_T^{\text{miss}}$	$\sim 2(3) + n_{\text{ISR/FSR}}$ $ \mathbf{p}_T(\nu_1) + \mathbf{p}_T(\nu_2) + \mathbf{p}_T(\nu_\tau) $	$\sim 4 + n_{\text{ISR/FSR}}$ $ \mathbf{p}_T(\nu) $	$\sim 2 + n_{\text{ISR/FSR}}$ $ \mathbf{p}_T(\nu_1) + \mathbf{p}_T(\nu_2) $

The use of 2-lepton control regions (2LCRs) is then naturally motivated. However, the region-based approach where CRs apply similar kinematical selections with respect to SRs does not dramatically improve the situation, since a fixed region can not express the behavior of taus or missing leptons that differ event-by-event, as schematized in Table 31.

Instead, the method of event-by-event emulation, introduced in this sub-section referred as “object replacement method”, can perfectly accommodate the problem. It is an integrated method consisting of:

- “missing lepton replacement” to estimate a part of  $\ell\ell_{\text{mis}}$  events (“Mis. Reco.” and “Mis. ID”),
- “tau replacement” to estimate  $\ell\tau_h$ ,

where one of the lepton of data events in 2LCR is replaced into a virtual missing lepton or a simulated hadronic tau decay respectively, as outlined in Figure 111. The detector responses and behavior in object reconstruction of those replaced objects are carefully emulated so that the replaced event can directly mimic the events in the signal regions.

The object replacement method is a nearly full data-driven method where the use of MC is limited in an area of tau decays and modeling of instrumental effects, such as lepton efficiency and jet energy scale. The MC modeling is highly reliable where the data/MC agreement is closely examined and the discrepancies are typically sub-percent level which are also mostly well-understood. The reliance of MC ensures the extrapolation much more robust, compared with the kinematical extrapolation method where the mis-modeling in kinematic tail is always critical.

Note that the whole method relies on the orthogonality between kinematics and object properties:

$$\frac{d\sigma(\ell\ell)}{dx} \propto \frac{d\sigma(\ell\ell_{ID})}{dx} \propto \frac{d\sigma(\ell\ell_{mis.})}{dx} \quad (96)$$

and the lepton universality:

$$\frac{d\sigma(\ell\ell)}{dx} \propto \frac{d\sigma(\ell\tau)}{dx}, \quad (97)$$

where  $\ell\ell_{ID}$  and  $\ell\ell_{mis-ID}$  represents the seed events and the missing lepton events respectively, and  $x$  symbolizes kinematical variables. Particularly, the kinematics-object orthogonality (Eq. 96) is of paramount importance, since it allows to extrapolate the object properties measured in a very inclusive phase space into any phase space including extreme cases such as the signal regions in this analysis. As long as the lepton reconstruction and identification is concerned, the statement is more or less true because their result generally obeys the statistical behavior of detector responses such as fluctuating number of hits or energy deposit, which does not depend on global event kinematics, but rather on the nature of the particle itself (usually only on its momentum) as well as the local material configuration in the detector. Therefore, it is usually enough to parametrize the efficiency of reconstruction or identification simply by the momentum ( $p_T, \eta, \phi$ ) of the particles. This is however not the case when coming to the probability of lepton being beyond the  $p_T - \eta$  acceptance (“Out-Acc”) or being dropped in the overlap removal (“Mis. OR”), since they do depend on the momentum of parent particle or the proximity to the nearest jet. Hence, the class of seed events do not fully represent the kinematics of “Out-Acc” and “Mis. OR”. This is the reason why these events can not be covered by the object replacement method.

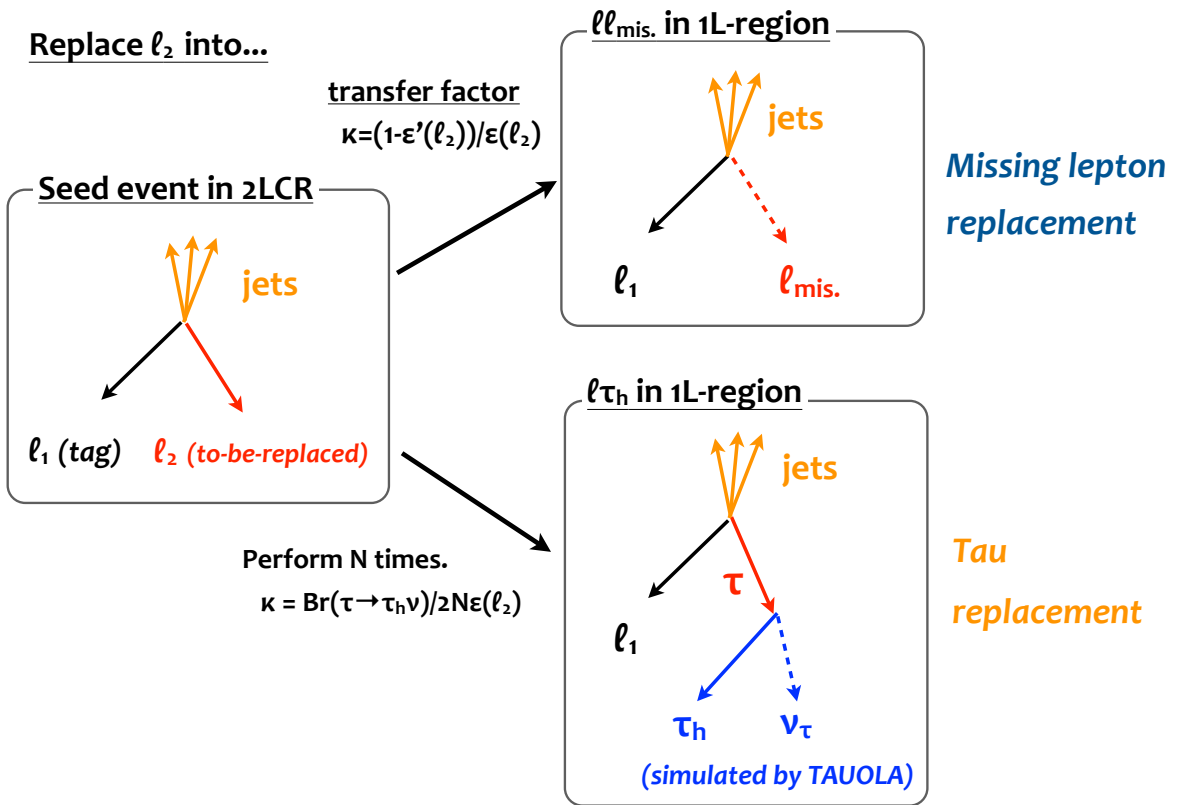


Figure 111: Schematic of the object replacement method.

### 6.3.1 The Replacement Procedure and the Per-event Logic

Figure 112 presents the work flow for the replacement procedure in a single seed event, which follows as below steps.

1. Pick up a 2LCR event ("seed event").
2. Replace a lepton of the seed event into a virtual missing lepton or a simulated hadronic decay of tau lepton, if the two leptons satisfy a certain criteria. This replaced event is called "sub-event".
3. (For tau replacement) Apply the calibration for the hadronic tau.
4. Re-calculate the event-level kinematics such as  $E_T^{\text{miss}}$  or  $m_{\text{eff}}$  etc.
5. Assign a weight  $\kappa$  for each sub-event as the transfer factor from 2LCR to 1L regions.
6. Change the roles (tagged/replaced) between the two leptons and repeat 2-5. Generated sub-events are filled in a single "event-level histogram".
7. (For tau replacement) Repeat the step 2-6 above by  $N = 50$  times and take the average, in order to fully accommodate the statistical nature of tau decay. Note that the number of iteration  $N$  only defines the level of "smoothing" thus has no essential impact on the final result. The average is taken by scaling the  $\kappa$  by  $1/N$ .
8. Apply the analysis level selection (e.g. signal region selection when one wants to estimate the yield in the signal region) and the post-selection (discussed below) on the generated sub-events.
9. Collect the accepted sub-events and fill them into an event-level histogram. 100% of statistical uncertainty is assigned for each bin of the event-level histogram, accounting for all the sub-events are generated from the common seed event.
10. Loop over all seed event and sum up all the event-level histograms with ordinary statistical treatment where the uncertainty is quadratically summed for each bin of the histogram.

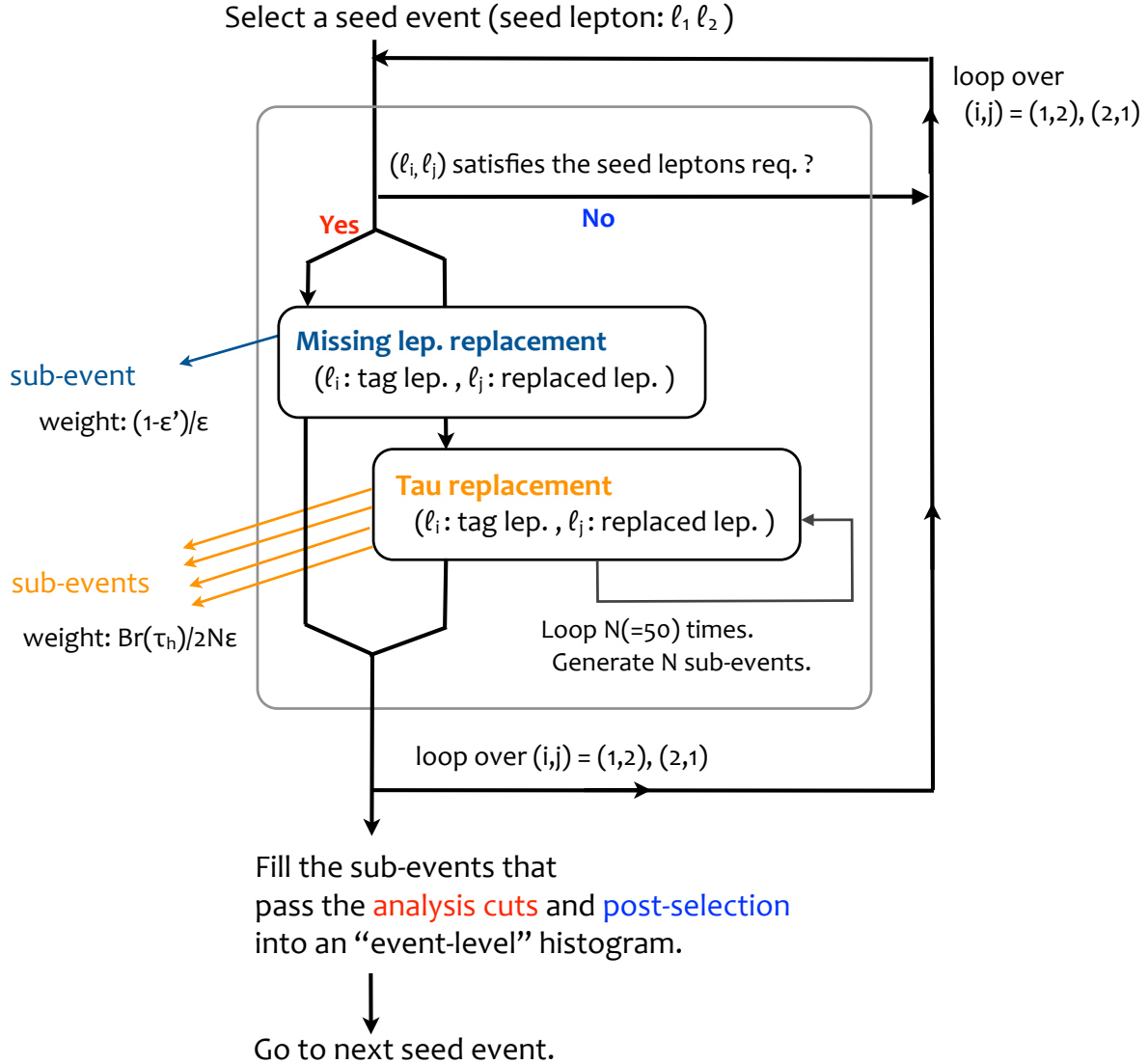


Figure 112: Work flow in the replacement procedure for a single seed event.

More detail and caveats about each step are as following:

#### Seed event selection and trigger

For seed event selection, looser kinematical selection is generally preferred, to collect the seed events necessary for estimating the regions in interest as completely as possible. In particular, as MET and  $m_T$  change their values the most during the replacement, those cuts have to be drastically relaxed with respective to signal regions. For instance, Figure 113 shows the MET distribution for corresponding seed events of the  $\ell\ell_{\text{mis}}$  and  $\ell\tau_h$  events with  $E_T^{\text{miss}} > 250$  GeV. About 40% of seeds are with seed MET below 250 GeV, meaning that it will be underestimated by 40% if naively selecting seeds by  $E_T^{\text{miss}} > 250$  GeV in 2LCR.

While MET trigger is available for collecting the bulk events above its off-line threshold  $E_T^{\text{miss}} > 250$  GeV, the single-lepton trigger (SLT) is introduced to complement the seeds events with  $E_T^{\text{miss}} < 250$  GeV. In spite

of its relatively low efficiency 70% – 90% and the off-line threshold of  $p_T > 28(26)$  GeV for single-electron (muon), SLT is still fully efficient for the seed events since there are two leptons being the candidate to fire the trigger. Eventually, as shown in Figure 113, more than 95% of the overall trigger efficiency can be maintained.

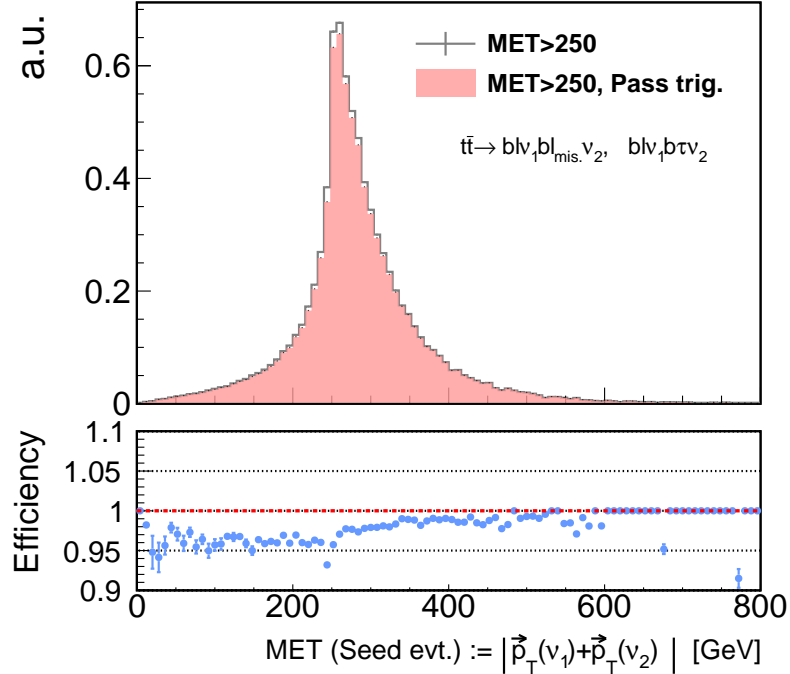


Figure 113: Seed MET distribution (gray) for the  $\ell\ell_{\text{mis.}}/\ell\tau_h$  events from  $t\bar{t}$  resulting in  $E_T^{\text{miss}} > 250$  GeV. The seed MET is defined by the MET component only by neutrinos from top decays:  $|\mathbf{p}_T(\nu_1) + \mathbf{p}_T(\nu_2)|$ , which is roughly equivalent to the MET in corresponding seed events ( $t\bar{t} \rightarrow b\ell\nu_1\bar{b}\ell\nu_2$ ). Over 95% of the seed events are shown to be accepted by the combined trigger strategy defined in Table 32 (pink).

Although the enhanced backgrounds due to the lowered MET selection for 2LCR does not impact as much on the final result since most of them are skimmed out in the analysis-level selection applied after the replacement, the decent cut  $E_T^{\text{miss}} > 100$  is required to suppress the bulk background components in 2LCR (Z+jets, 1L+fake lepton etc.) and make sure avoiding the large uncertainty from MC subtraction. The seed event loss due to the selection  $E_T^{\text{miss}} > 100$  is negligible when estimating SRs/VRs.

Table 32 shows the definition of common 2LCR.

Table 32: Definition of 2-lepton control region for MC closure test.

---

$n_{\ell,\text{baseline}} = 2, n_{\ell,\text{signal}} \geq 1$
MET trigger, $E_T^{\text{miss}} > 250$ GeV
or
At least 1 signal lepton with $p_T > 28$ GeV firing the single-lepton trigger, $E_T^{\text{miss}} > 100$ GeV

---

### Requirement on seed leptons for the replacement

A seed event with lepton  $\ell_1\ell_2$  have two choices of the replacement namely 1) keeping  $\ell_1$ /replacing  $\ell_2$  or 2) keeping  $\ell_2$ /replacing  $\ell_1$ . The replacement is proceeded only if the lepton to-be-replaced (“replaced lepton”) and the lepton to-be-kept (“tag lepton”) satisfy a certain condition as noted below. Note that the replacement can happen twice from the identical seed event if the both combinations (tag,rep.)= $(\ell_1\ell_2)$ ,  $(\ell_2\ell_1)$  are eligible.

As the tag lepton eventually corresponds to the single lepton used in the analysis in 1-lepton regions, it has to undergo the consistent object definition as that used in signal region definition, which is namely in Table 9. On the other hand, no such requirement is needed for the replaced lepton, instead, looser definition is preferred from the CR statistics point of view. Therefore, only the baseline lepton requirement when estimating the b-inclusive or b-tagged regions, while the signal lepton requirement is still applied in case of estimating b-vetoed regions since the impact of fake lepton background in 2LCR is relatively large otherwise. The replaiton between and the working point of lepton definition is summarized in Table 33.

Table 33: Lepton definition used for tag and replaced lepton versus the type of regions to be estimated.

	B-tagged, b-inclusive	b-vetoed
Tag lepton	signal	signal
Replaced lepton	baseline	signal

### Treatment of virtual missing lepton

As mentioned in Sec. 3.7, electrons are usually also identified as jets, and the doubly-counted object, either an electron or a jet, is discarded during the overlap removal. Therefore, electrons failing the reconstruction or identification will simply recognized as jets without experiencing the overlap removal. To emulate this effect, in case of replacing an electron in a seed event, the record that the electron is reconstructed as a jet candidate is retrieved, and the 4-vector of electron is replaced into the that of the jet candidate. As the jet candidate is fully calibrated in the hadronic scale, no more correction is needed. In some occasion, electrons do not have corresponding jet candidates typically when the low transverse momentum is too low. In such cases, the electron is replaced into a missing particle with the 4-momentum of original electron.

Muons failing the reconstruction or identification are almost never identified as any other objects. Instead, they are included in the MET track soft term in the MET calculation, and in principle this needs to be emulated in the missing muon replacement. This is technically possible, however the bottleneck is that the muon track quality is totally different between well-identified muons and unidentified ones, and particularly it is difficult to reproduce the resolution of bad muon track from good one with a meaningful correction. As it turns that simply including the 4-momentum replaced muon into the MET soft term even leads to worse performance than not including at all (as demonstrated in Figure 126), replaced muons are decided to be simply treated as a virtual missing particle in the same momentum, and added in MET. Although this rough treatment causes a non-zero error in the estimation as one will see in Sec. 6.3.3, fortunately the impact on final estimation is marginal because the rate of missing muon events are generally very low, compared with the other components (missing electron events or  $\ell\tau_h$ ) due to the very high efficiency of muon reconstruction and identification.

### Simulation of tau decays and the $\tau_h$ -to-jet calibration

Tau decays are simulated by TAUOLA [?] [?] [?] assuming the taus are unpolarized. This assumption is incorrect given the parent W-bosons are left-handed, however the impact on the final result is found to be marginal. This is discussed in Sec. 6.3.3. Branching for leptonic decay is set to zero to reduce the number of loops.

Given that the analysis is without explicit tau selections, hadronic taus within the  $p_T$ - $\eta$  acceptance undergo the reconstruction, b-tagging and calibration as an (b-tagged) anti-Kt4 jets, once they pass the JVT cut (Sec. 3.6.4). On the other hand, the output of TAUOLA is merely a 4-vector of truth level hadronic tau. Therefore, following pseudo-calibration is applied for the truth-level  $\tau_h$ , to emulate the effect either of the detector response, jet calibration, and the b-tagging.

1. Scale the transverse momentum of truth  $\tau_h$ .

The scale of a truth  $\tau_h$  to an anti-Kt4 jets is derived using the  $t\bar{t}$  MC samples, by comparing the transverse momenta of truth hadronic taus and that of  $\Delta R$ -matched reconstructed jet by  $\Delta R < 0.2$ . It is defined by the mean value of the residual distribution (Figure 114) and parametrized in terms of  $p_T$  and  $\eta$  of truth hadronic taus (Figure 115). The scale is always positive and rises significantly in the low- $p_T$  limit, due to the fact that the anti-Kt4 jet contains extra underlying tracks inside that become the pedestal. The difference in the calibration between light jets and b-tagged jets are ignored.

2. Smear the  $p_T$  of hadronic tau.

After applying the scale above, smearing is subsequently adopted for to account for the detector resolution. The resolution is taken from the Gaussian-fitted RMS of the residual distribution on which the scale above is defined as well (Figure 114), and likewise parametrized as function of  $p_T$  and  $\eta$  of truth hadronic taus (Figure 116). The smearing is applied based on the Gaussian profile centered at with RMS being the resolution.

3. Emulation on the JVT cut and b-tagging.

After the sequence of the  $p_T$ -scaling and smearing, hadronic taus with  $p_T > 30$  GeV,  $|\eta| < 2.8$  are selected as the signal jet candidates. Signal jets are then randomly identified from them, based on the efficiency of JVT cut derived from signal jet candidates matched with truth hadronic taus by  $\Delta R < 0.2$  in the simulated  $t\bar{t}$  sample (Figure 117). A random b-tagging is further performed on the signal jets, by assigning a random b-tagging score (MV2c10) following according to the profile obtained from the  $t\bar{t}$  MC sample using the same technique (Figure 118). While the JVT cut efficiency is mapped as a function of  $p_T$  and  $\eta$  of signal jet candidates, the b-tagging score profile is measured separately by different tau decay modes (1-prong and 3-prong).

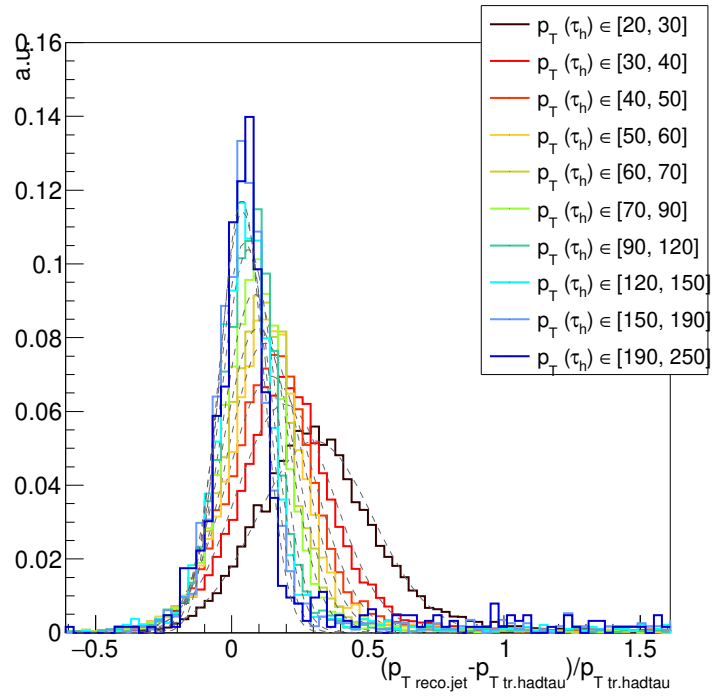


Figure 114: The residual of tau momentum measurement:  $p_T(\text{reco.}\tau - \text{jet}) - p_T(\text{tr.}\tau_h)/p_T(\text{tr.}\tau_h)$  calculated using the simulated  $t\bar{t}$  sample.  $p_T(\text{tr.}\tau_h)$  is the transverse momentum of truth-level hadronic tau defined as  $|\mathbf{p}(\tau) - \mathbf{p}(\nu_\tau)|$  and  $p_T(\text{reco.}\tau - \text{jet})$  is the corresponding reconstructed anti-Kt4 jet matched by  $\Delta R < 0.2$ .

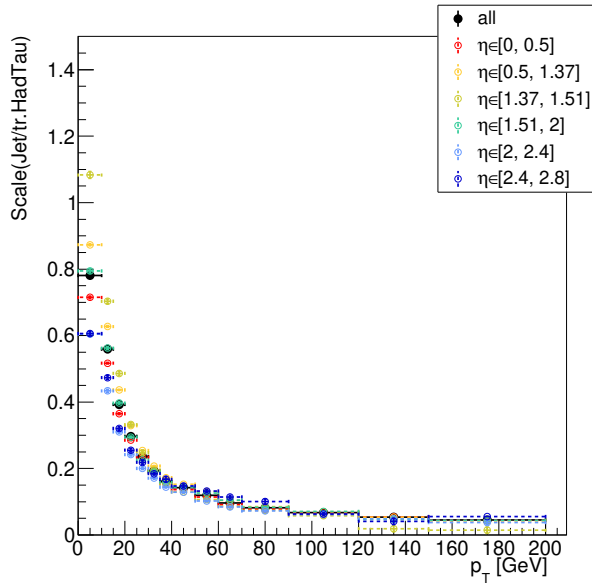


Figure 115: Scale of anti-Kt4 jets for truth hadronic taus, defined as the mean of the residual distribution 114. Both  $\eta$ -inclusive and  $\eta$ -dependent curves are derived.

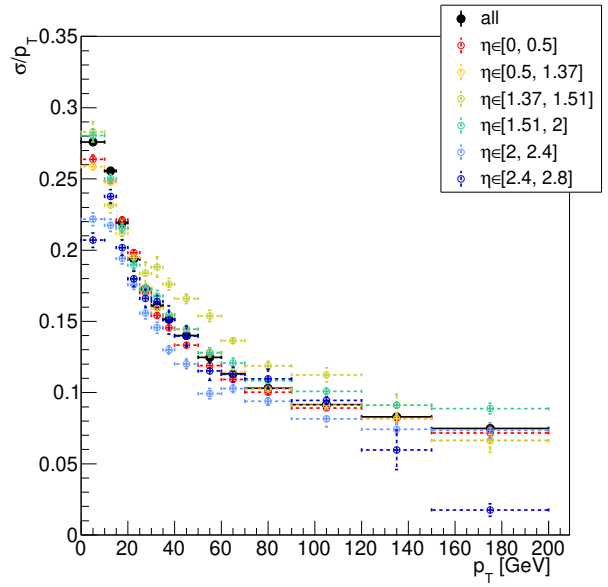


Figure 116: Resolution of hadronic tau, defined by the Gaussian-fitted RMS of the residual distribution 114. Both  $\eta$ -inclusive and  $\eta$ -dependent curves are derived.

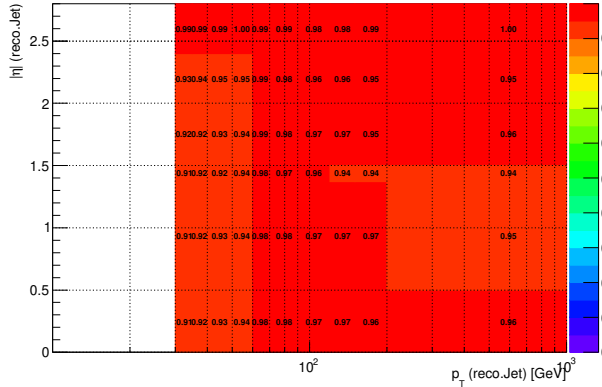


Figure 117: The JVT cut efficiency map for a reconstructed hadronic tau jet as function of its  $p_T$  and  $\eta$ , calculated using the  $t\bar{t}$  MC sample. The efficiency is defined by the fraction of signal jet candidates  $\Delta R$ -matched to the truth hadronic tau by  $\Delta R < 0.2$  that pass the signal jet requirement.

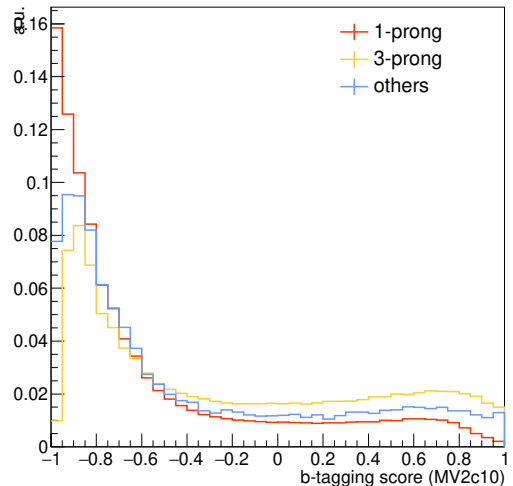


Figure 118: Profile of b-tagging score (MV2c10) for signal jets originated from hadronic tau decays. Only the dependency on the decay modes (1-prong or 3-prong) is taken into account. The threshold for the b-tagging is at 0.44. The 3-prong events result in a higher fake rate into b-tagging jets, reflecting the secondary vertex structure more resembling to that of b-hadrons. The simulated  $t\bar{t}$  MC sample is used to derive the profiles.

## Transfer factor

A weight  $\kappa$  is assigned to each sub-event, to account for the different probability of occurrence between the seed event and the replaced sub-event. For instance, in the missing lepton replacement, this corresponds to the difference between probability of a lepton being identified and failing the identification. The  $\kappa$  is therefore the inefficiency over the efficiency:

$$\kappa = \frac{1 - \epsilon_{\text{baseline}}(\mathbf{p}_T(\ell_{\text{rep.}}))}{\epsilon_{\text{rep.}}(\mathbf{p}_T(\ell_{\text{rep.}}))}.$$

Note that the efficiency appearing in the enumerator is for the working point used for the second lepton veto (namely “baseline”), and that in the denominator is for one used for requiring replaced lepton which can be either “baseline” and “signal” depending on cases (see Table 33).

As for the tau replacement, the transfer factor is

$$\kappa = \frac{\text{Br}(\tau \rightarrow \tau_h \nu)}{2N\epsilon_{\text{rep.}}(\ell_{\text{rep.}})},$$

where  $N$  is number of iterations per replacement, and  $\epsilon_{\text{rep.}}$  the efficiency for working point used for requiring replaced lepton. The factor 2 originates from the fact that two channels ( $e\ell$  and  $\mu\ell$ ) are available as seeds for estimating a single channel  $\tau\ell$  (see Table 34).

Letting  $N_{\text{acc.}}$  the typical number of accepted sub-events after the post selection,  $N_{\text{acc.}}/\kappa$  gives a rough idea on the effective statistics in CR with respect to the SR. It is typically 5 – 10 for the missing lepton replacement, and about 1.4 ( $\sim 1/\text{Br}(\tau \rightarrow \tau_h \nu)$ ) for the tau replacement. It will be enhanced by about factor of 2 when regions  $m_T > 100$  GeV are interested since  $m_T(\ell_2, E_T^{\text{miss}})$  is almost never exceed  $m_W$  for standard model processes thus half of the sub-events will be discarded. Therefore, the effective CR statistics is found about 3 times more than the SR statistics. This factor of 3 gain in statistics is in fact not very sufficient as it immediately leads to 20% – 50% statistical uncertainty by itself in typical signal regions where only a few events are expected. Therefore CR statistic is always the biggest source of uncertainty in this method.

Table 34: The flavor correspondence between the seed events and the estimated component in case of  $t\bar{t}$ .

Seed	Estimated by mis. lep. rep.	Estimated by tau rep.
$e^+ e^-$	$e^+ e_{\text{mis}}^-$ $e_{\text{mis}}^+ e^-$	$e^+ \tau^-$ $\tau^+ e^-$
$e^+ \mu^-$	$e^+ \mu_{\text{mis}}^-$ $e_{\text{mis}}^+ \mu^-$	$e^+ \tau^-$ $\tau^+ \mu^-$
$\mu^+ e^-$	$\mu^+ e_{\text{mis}}^-$ $\mu_{\text{mis}}^+ e^-$	$\mu^+ \tau^-$ $\tau^+ e^-$
$\mu^+ \mu^-$	$\mu^+ \mu_{\text{mis}}^-$ $\mu_{\text{mis}}^+ \mu^-$	$\mu^+ \tau^-$ $\tau^+ \mu^-$

### Lepton efficiency

The lepton efficiency used in the transfer factor calculation is calculated using  $t\bar{t}$  MC sample as well. The efficiency of ID/baseline/signal lepton requirement is respectively defined as the fraction of truth leptons that are  $\Delta R$ -matched with reconstructed passing the ID / identified / signal lepton requirement by  $\Delta R < 0.2$ . Leptons overlapped with jets (if the nearest jet closer than  $\Delta < 0.4$ ) are excluded since their efficiency is biased. The efficiencies are parametrized as a function of lepton flavor ( $e/\mu$ ),  $p_T$  and  $\eta$  of truth leptons. The data/MC scale factor measured by  $Z \rightarrow ee/\mu\mu$  are applied. The resultant efficiency maps are shown in Figure 119.

### Event-level histogram and the statistical treatment

Multiple sub-events are generated by both missing lepton replacement and tau replacement from a single seed event. Those passing the analysis selections are collected and filled into a common histogram, referred as “event-level” (this corresponds to a one-bin histogram when one only wants to estimate the yield in a particular region). To account for their full statistical correlation between the filled sub-events, 100% error is then assigned to each bin of the event-level histogram. The summed event-level histograms over all seed events will be the desired distribution. While the statistical error on each bin is simply the quadratic sum of those over the all event-level histograms, there is generally also the inter-bin correlation since the bins of event-level histograms are not statistically independent between each other. This correlated uncertainty in fact needs to be modeled when performing the combined fit with multiple signal bins, which is examined and summarized in Sec. 136.

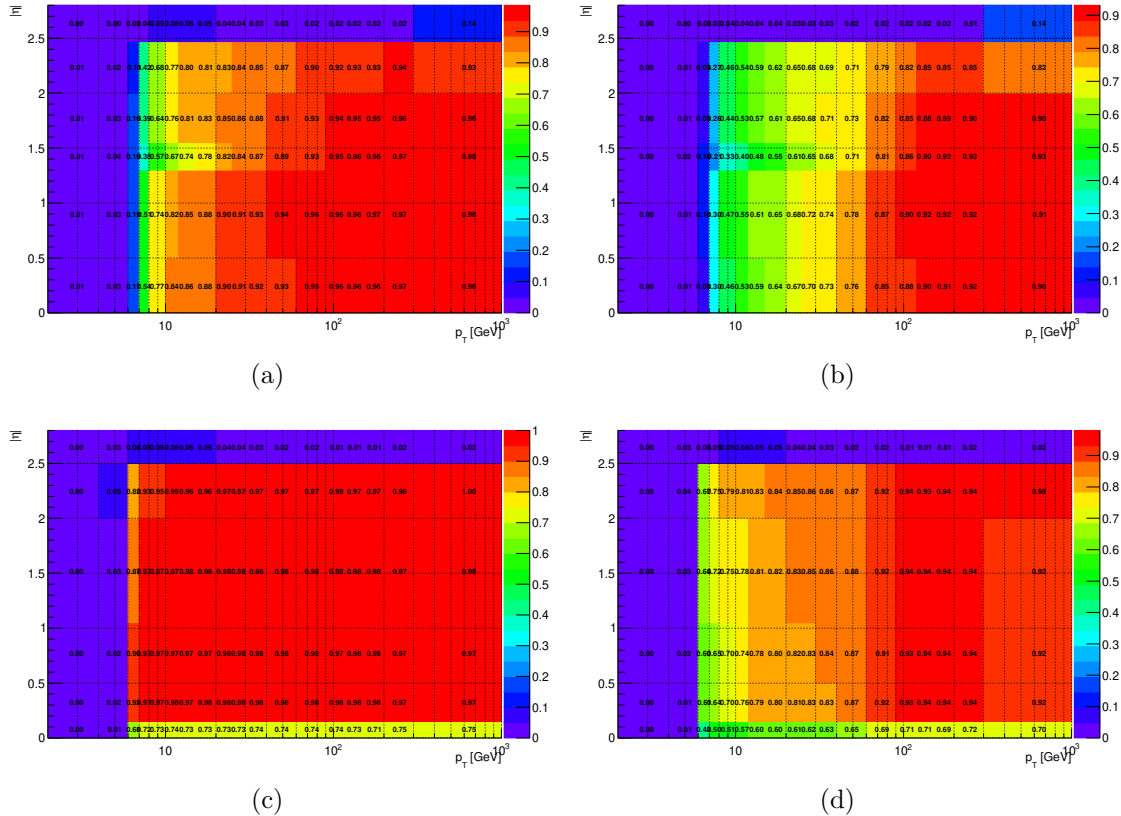


Figure 119: Off-line selection efficiency used in transfer factor calculation. (a) Efficiency of electrons passing reconstruction and ID. (b) Efficiency of electrons passing signal lepton requirement. (c) Efficiency of muons passing reconstruction and ID. (d) Efficiency of muons passing signal lepton requirement.

### Example of an event-level histogram

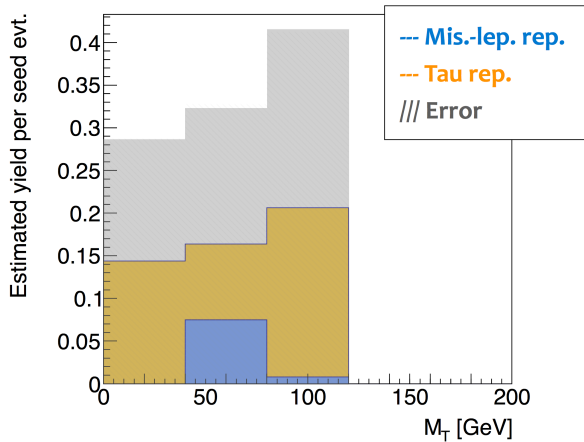


Figure 120: An example of event-level histogram. 100% uncertainty is assigned for each bin to account for the fact that all the entries are from the same seed. Final estimation is given by the sum of the event-level histograms over all seed events.

### 6.3.2 Closure Test using $t\bar{t}$ MC Samples

The methodologies are tested by comparing yields in regions with exactly one baseline lepton, between the estimation using the seed events in 2LCR and the actual  $\ell\ell_{\text{mis.}}/\ell\tau_h$  events. The test is referred as “closure test” where the level of disagreement (non-closure) indicates the generic accuracy about this method. The evaluated non-closure is assigned as systematics uncertainty. In the MC closure test, simulated  $t\bar{t}$  sample is used in both seed events and the  $\ell\ell_{\text{mis.}}/\ell\tau_h$  events. All the other processes are absent thus no subtraction is taken. The common 2LCR selection as defined in Table 32 is applied for seed events selection, except that the MET cut is removed in order to boost the statistics.

Figure 121 ~ 123 show the result with  $p_T > 35$  GeV is required for the tag lepton. The test result for the case with a soft lepton ( $p_T \in [6, 35]$  GeV) is displayed in the Appendix E.1.

Good closure is seen in overall kinematics. Non-closure generally stay within 10% (5%), and never exceeds 30% (10%) significantly for the missing lepton replacement (the tau replacement). Although the closure of missing lepton replacement is worse than that of tau replacement, it is not worrisome since the contribution of  $\ell\ell_{\text{mis.}}$  is typically 5 ~ 10 times smaller than  $\ell\tau_h$ .

Closure tests are also performed in phase space close to signal regions. Figure 124 ~ 125 are the btag/bveto-split closure in various regions requiring high MET,  $m_T$ ,  $m_{\text{eff.}}$  etc. The non-closure stay within 30% (10%) for the missing lepton replacement (the tau replacement).

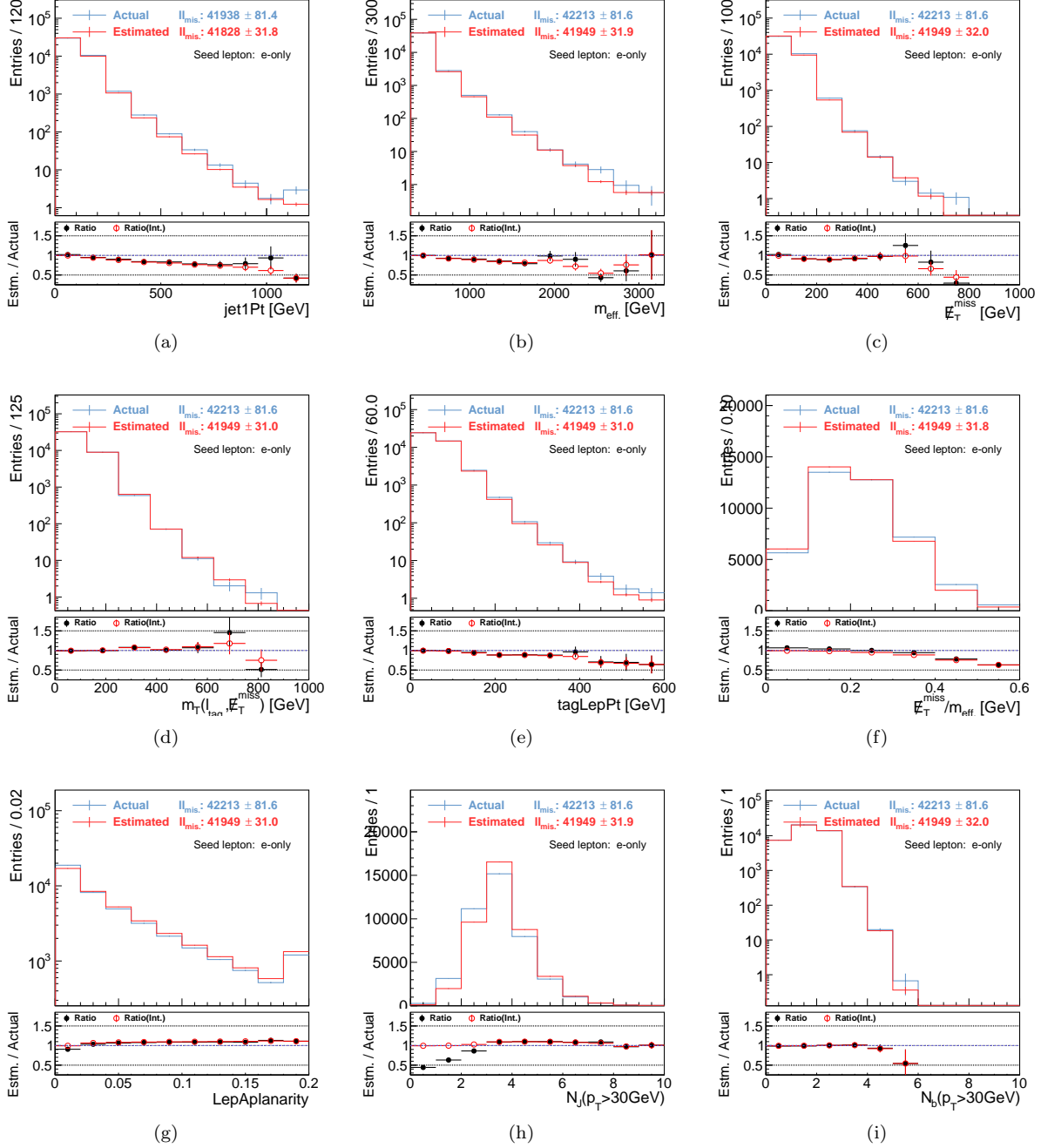


Figure 121: MC closure test for **missing lepton replacement** using  $t\bar{t}$  MC sample. Seed events are collected by the single-lepton trigger.  $p_T > 35$  GeV for the leading lepton is required. **Only electrons in the seed events are replaced.** Red points in the bottom plots show the ratio of integrated yields for the two histograms above the x-position that the point indicates.

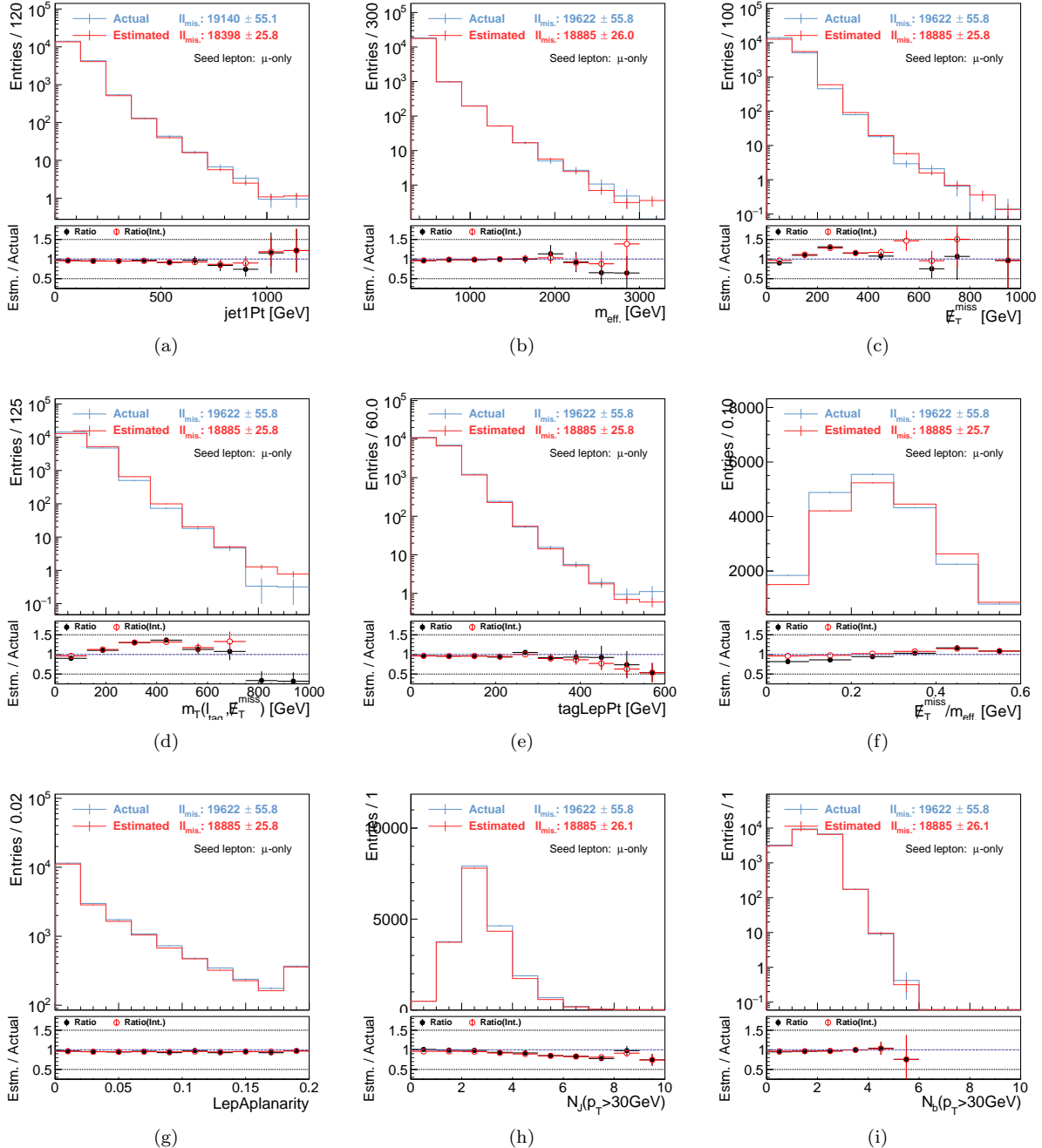


Figure 122: MC closure test for **missing lepton replacement** using  $t\bar{t}$  MC sample. Seed events are collected by the single-lepton trigger.  $p_T > 35$  GeV for the leading lepton is required. **Only muon in the seed events are replaced.** Red points in the bottom plots show the ratio of integrated yields for the two histograms above the x-position that the point indicates.

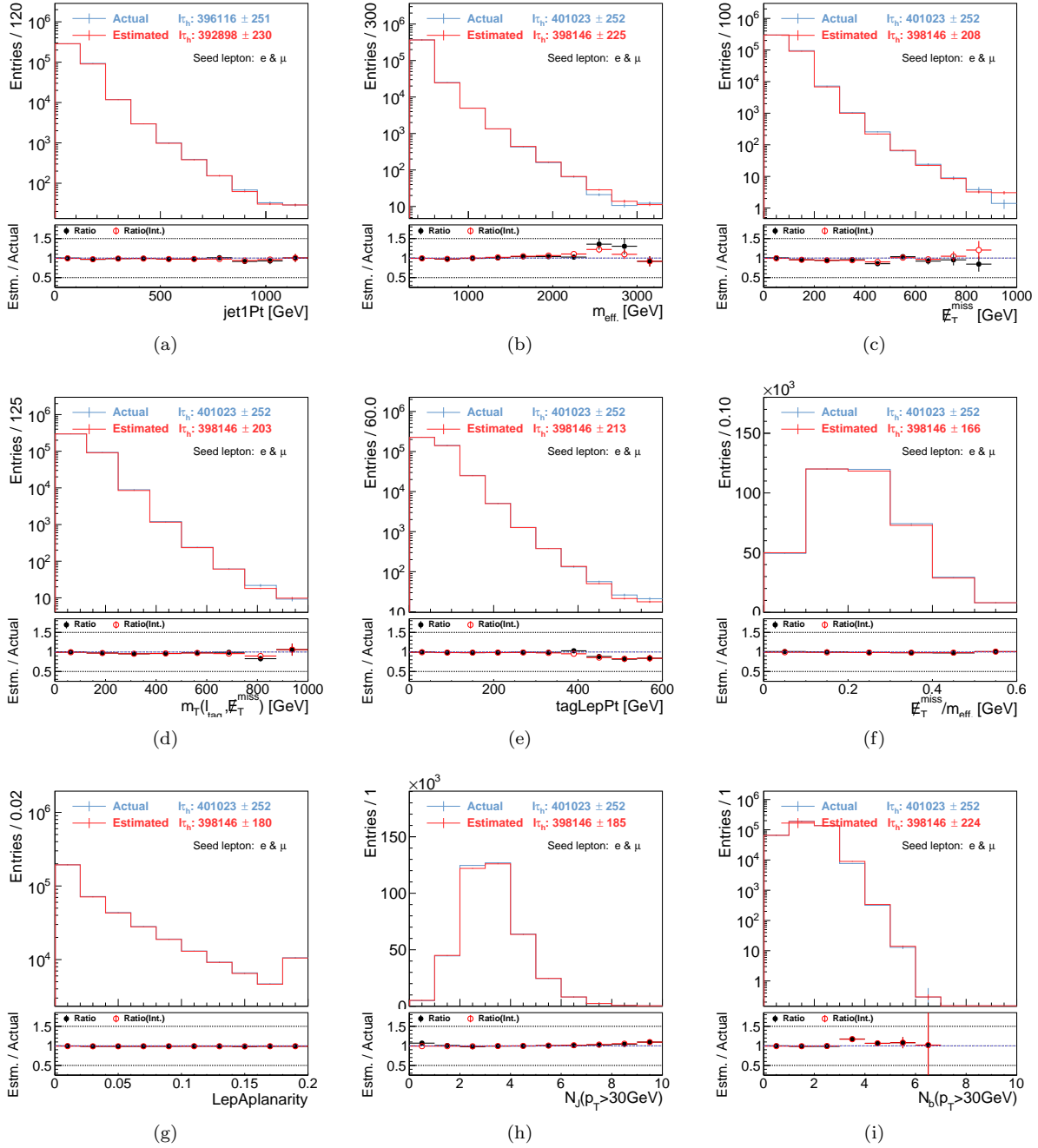
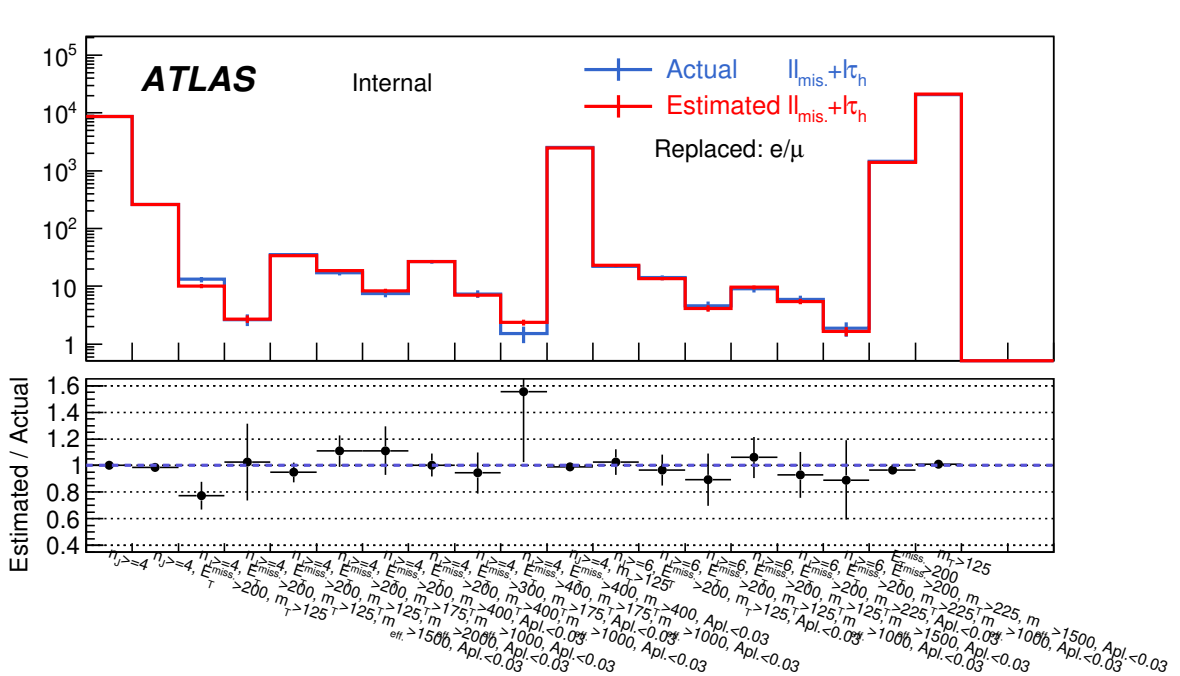
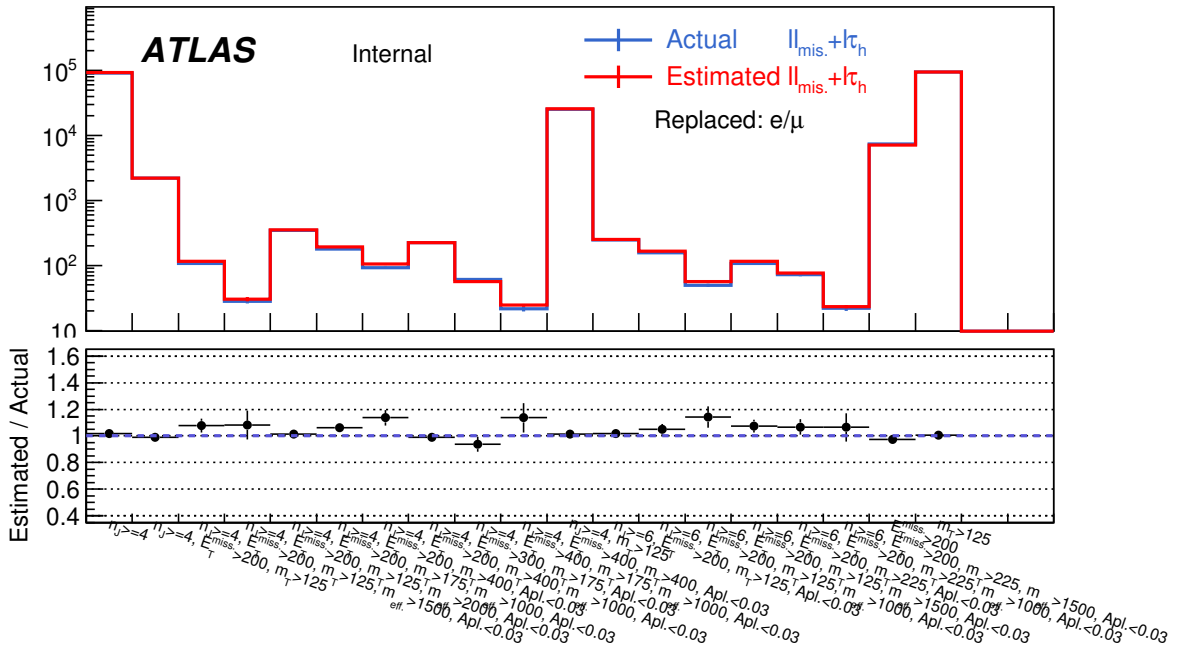


Figure 123: MC closure test for tau replacement using  $t\bar{t}$  MC sample. Seed events are collected by the single-lepton trigger.  $p_T > 35$  GeV for the leading lepton is required. **Both electrons and muons in the seed events are replaced.** Red points in the bottom plots show the ratio of integrated yields for the two histograms above the x-position that the point indicates.



### 6.3.3 Source of non-closure

Visible non-closures are found in some distributions such as MET and jet transverse momenta, and the cause is nailed down as following:

#### Kinematical bias triggered by the two lepton requirement in seed event selection (All)

Though the orthogonality between kinematics and object properties (Eq. 96) generally hold as a good approximation, there is still some exception. The most notable example is when the parent particles of the two leptons in a seed event are heavily boosted, the leptons get collimated and overlapped each other. This leads to a deteriorated reconstruction/ID efficiency, therefore selecting events with exactly two leptons already discard the seed events in such phase space. The estimated spectra is biased and generally become softer. Electrons address more severe effect because the efficiency drop in the boosted environment is more distinct than the case of muons.

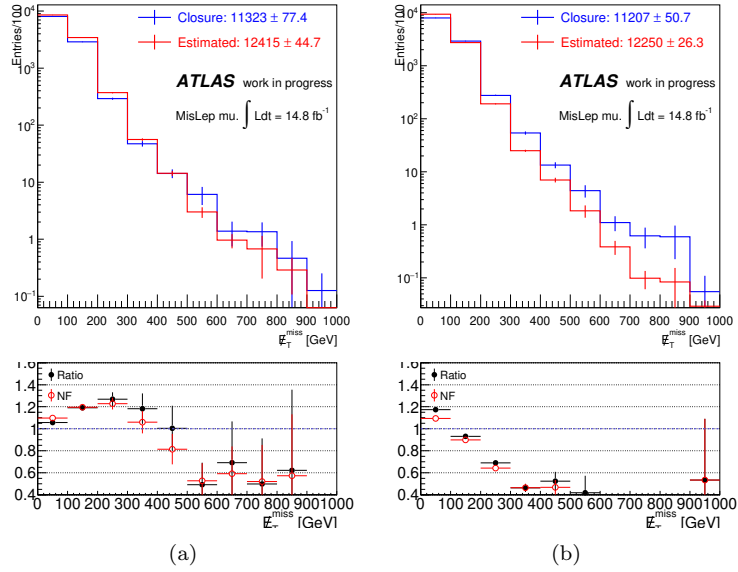
#### Treatment of missing muon

While the emulated missing muons are completely regarded as invisible particles in the replacement algorithm, the momenta of real unidentified muons do contribute to MET since their tracks are often included in the track soft term. This imperfect emulation leads to a non-closure around MET-related variables in the missing muon replacement. Naively thinking, this can be improved by simply stopping adding the missing muons momenta into MET. However, this is unfortunately not the case, as shown in Figure 126 where the improvement is limited in bulk region of the MET spectrum and the closure in the tail gets even worse. This is mainly because the poor momentum resolution of high  $p_T$  unidentified muons is not emulated in the replacement. As the implementation of the full emulation is too costly compared with the small portion of missing muons backgrounds in the estimated regions, it is decided to keep the original treatment. Instead, the 30% of non-closure error is additionally quoted to the estimation of the missing muon background.

#### Wrong assumption on tau polarization (tau replacement)

For technical simplicity, tau leptons are assumed to be unpolarized during the decay, which is not true given that tau leptons in consideration are mostly generated through weak decays of W-bosons. For example, the case of Figure 127 (a) shows the visible tau fraction  $x := E(\tau_h)/E(\tau)$ , a variable sensitive to tau polarization, for taus in the  $t\bar{t}$  process in a blue line, and for the case of unpolarized hypothesis in a red line. This discrepancy is known to eventually propagate to the non-closures in the tail of MET and  $m_T(p_T(\ell), E_T^{\text{miss}})$  such as the left plots in Figure 127 and Figure 128. On the other hand, these non-closure can be cured by a simple reweighting in terms of  $x$ , as they are purely caused by the issue of polarization modeling. Obtaining the reweighting function by fitting the non-closure in  $x$  with a third polynomial as shown in Figure 127 (c), nicely recovered closures in MET and  $m_T(p_T(\ell), E_T^{\text{miss}})$  are confirmed as in the right plots in Figure 127 and Figure 128 respectively.

This  $x$ -reweighting is however not brought into practice, because the  $x$ -profile varies by the physics processes (e.g.  $t\bar{t}$ ,  $Wt$  or  $WW$  etc.) and the information of their relative breakdown needs to be provided from MC which uncertainty is not easy to evaluate. Fortunately, since the impact of this non-closure is marginal in estimating VRs and SRs ( $< 5\%$ ), it is decided to be left as it is.



(a)

(b)

Figure 126: The MC closure of MET distribution for the missing muon sub-events, with (a) the default treatment of missing muons where they are fully counted as invisible particles, and (b) the alternative method where the momenta of missing muons are fully included in the MET soft term and no addition is applied to MET.

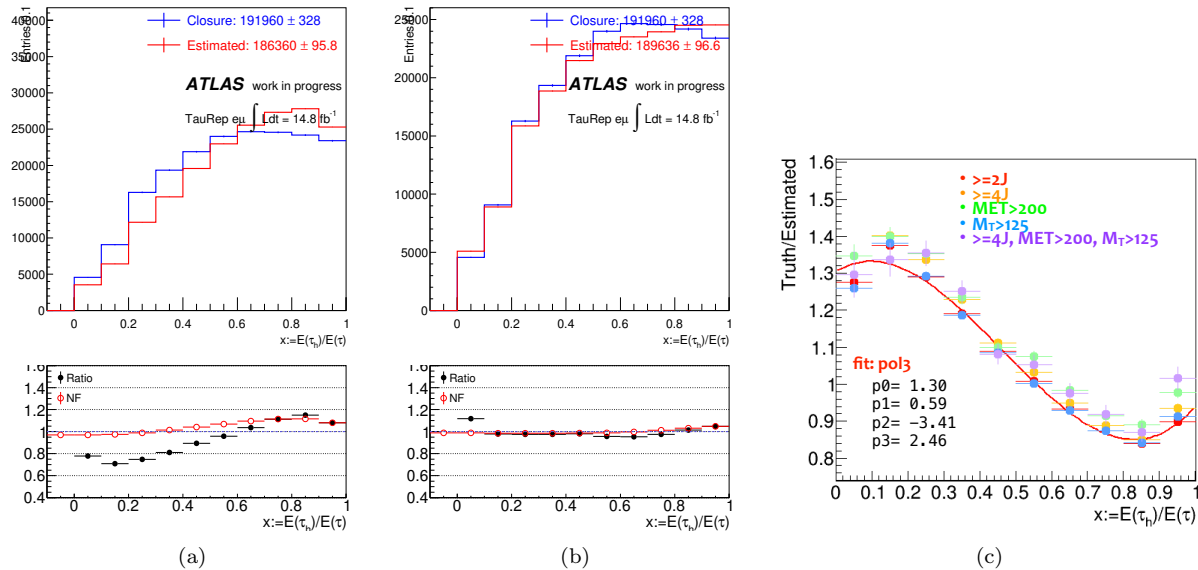


Figure 127: Reweighting in terms of the visible tau fraction  $x := E(\tau_h)/E(\tau)$ . (a)  $x$  distribution before the reweighting, (b)  $x$  distribution after the reweighting. (c) An ad hoc fit of the reweighting function by third order polynomial. The reweighting function is almost invariant in terms of phase space.

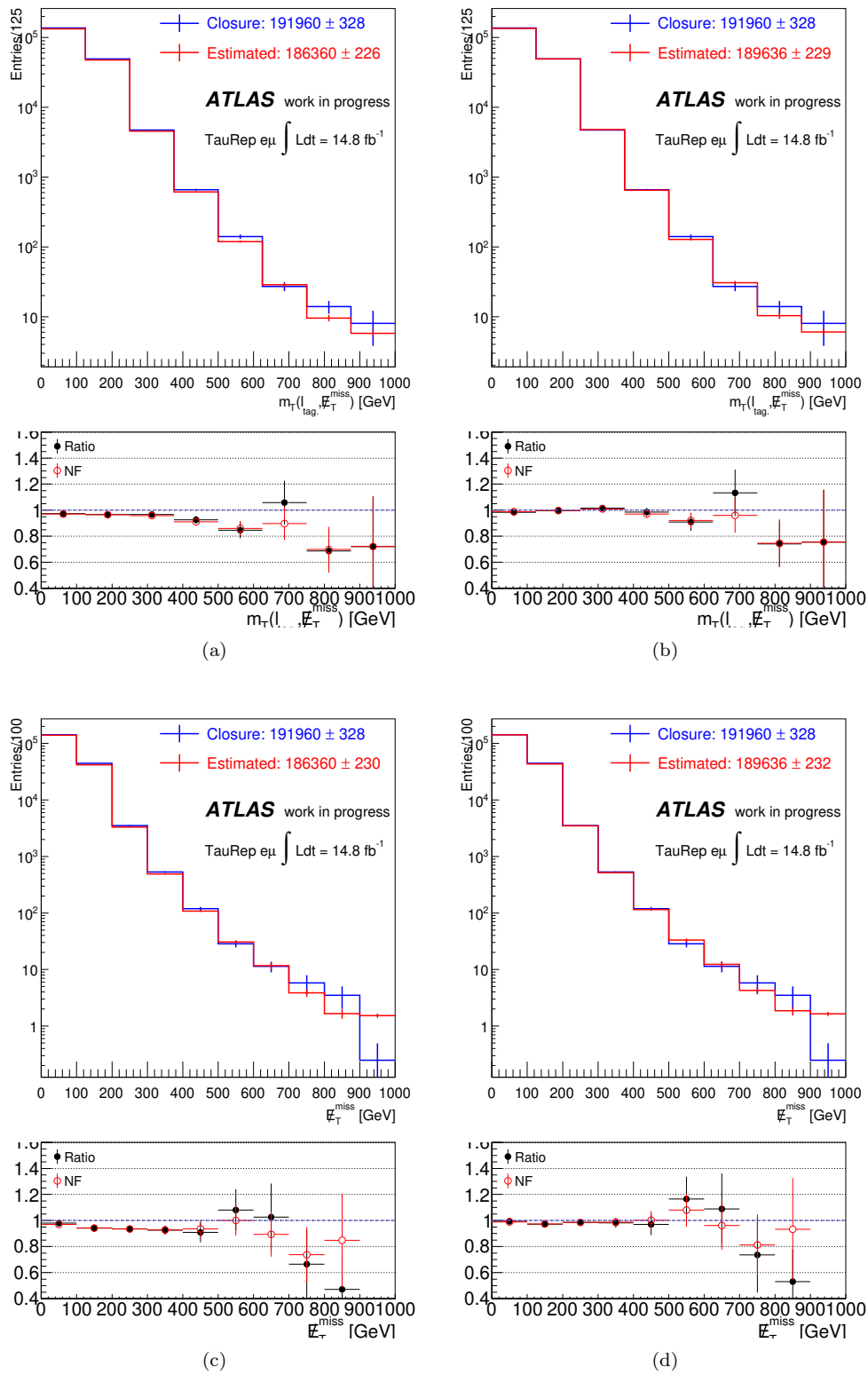


Figure 128: (a)  $m_T$  and (c) MET distribution before the reweighting in  $x$ , and (b)(d) after the reweighting.

### 6.3.4 Subtraction of Bogus Sub-events

Although the object replacement method is designed to estimate the di-leptonic decays of  $t\bar{t} + Wt$  and  $WW$  which are the dominant “di-leptonic” backgrounds in b-tagged and b-vetoed regions, it is also applicable to estimate the other minor backgrounds such as  $t\bar{t} + W$ . Basically any leptons in 2LCR are eligible to be replaced, since the replaced sub-event could exist for most of the case. However, there are couple of exceptions: if the replaced lepton is from  $Z$ , sub-events of tau replacement will lead to a bogus topology of  $Z \rightarrow \tau_h \ell$  ( $\ell = e, \mu$ ) which never happens, thus these sub-events (bogus sub-events) are need to be subtracted.

Likewise, seed leptons from leptonic tau decays ( $\tau \rightarrow \tau_\ell \nu \bar{\nu}$ ) have the same issue that tau replacement leads to bogus sub-event where tau decays into tau again. Replacing fake lepton will only end up in bogus sub-events. The summary of legal and illegal replacement is given in Table 35 where bogus sub-events are label as “ $\times$ ”. Note that the decision is made on each sub-event level (not seed event level), therefore even  $W(\rightarrow \ell\nu) + \ell_{\text{fake}}$  can be seed events as long as one replaces  $\ell$  rather than  $\ell_{\text{fake}}$ .

While the subtraction takes place on sub-event basis, it can be only done statistically i.e. evaluate total contribution from bogus sub-events and subtract once. The largest source of bogus sub-events are seed events with  $\tau_\ell$ . The contribution is quite large, accounting for  $10\% \sim 20\%$  of the estimated yields by the tau replacement. Therefore, a naive MC subtraction could introduce culprits from the MC mis-modeling, for example on  $t\bar{t}$  as overviewed in Sec. 6.2.1. Instead, to avoid the impact, the subtraction is done in a form of ratio, such as:

$$y_\ell^{\text{Data}} = y_{\ell+\tau_\ell}^{\text{Data}} \times \frac{y_\ell^{\text{MC}}}{y_\ell^{\text{MC}} + y_{\tau_\ell}^{\text{MC}}} \quad (98)$$

where  $y_\ell^{\text{Data}}$  ( $y_{\ell+\tau_\ell}^{\text{Data}}$ ) denote the total yield estimated by tau replacement using data before (after) the subtraction, and  $y_\ell^{\text{MC}}$  ( $y_{\tau_\ell}^{\text{MC}}$ ) the contribution from legal (bogus) sub-events of tau replacement estimated by MC.

The subtraction of the  $\ell\ell_{\text{fake}}$  is a little sensitive as MC modeling on fake leptons is less reliable in general. Therefore, relatively more aggressive suppression is applied at the stage of seed selection (Table 33) by requiring tighter isolation, in case that it could be addressing.

Table 35: Correspondence between origin of seed lepton and estimated components by the missing lepton replacement or the tau replacement.  $X$  represents any arbitrary particles. “ $\times$ ” indicates that the generated sub-events represent non-existing processes (“bogus sub-events”) that requires the subtraction. The subscripts mis. denote missing leptons (leptons categorized in “Mis. Reco” and “Mis. ID” defined in Table 24).

Parent of seed lepton	Sub-events of mis. lep. rep.	Sub-events of tau rep.
$W(\rightarrow \ell\nu)$	$W + X, W \rightarrow \ell_{\text{mis.}} \nu$	$W + X, W \rightarrow \tau_h \nu$
$Z(\rightarrow \ell\ell)$	$Z + X, Z \rightarrow \ell_{\text{mis.}} \ell$	$\times$
$\tau(\rightarrow \tau_\ell \nu)$	$\tau_{\ell, \text{mis.}} + X$	$\times$
Fake	$\times$	$\times$

### 6.3.5 Closure Test using Data in the Loose Validation Regions.

In order to demonstrate the procedures beyond the ideal MC closure tests done in Sec. 6.3.2 such as the subtraction, another validation study is done using the data events.

Since the nominal VRs (Table 19 - 23) tends to have too tight selections with small data statistics, a set of high- $m_T$  regions “VR-objRep” with relatively loose selections are deliberately defined, in which the object replacement estimation and data is compared. 9 complemental bins are defined as in Table 36.

It is populated by  $\ell\ell_{\text{mis}}/\ell\tau_h$  events with the purity of  $\sim 50\%$ , and the rest of backgrounds that are not covered by the object replacement (namely the “semi-leptonic”, “2L-Out. Acc” and “2L-Mis. OR” components) are estimated by a kinematics extrapolation where the MC of  $W + \text{jets}$  and  $t\bar{t} + Wt$  is normalized in the corresponding control region bins (“CR-objRep”) which are only different in  $m_T$  with respect to VR-objRep, as defined in Table 36. An upper cut in aplanarity is set in either the VRs and the CRs so that the signal contamination is subdued. Statistical uncertainty from the control region statistics, and flat 5% non-closure error is assigned for the object replacement estimation in all the VR bins.

Table 36: Definition of VRs(CRs) objRep. MC of  $W + \text{jets}$  and  $t\bar{t} + Wt$  are normalized in corresponding CR-objRep.

	$n_J (p_T > 30 \text{ GeV})$	$E_T^{\text{miss}} [\text{GeV}]$	$m_T [\text{GeV}]$ (CR-objRep)	$m_{\text{eff}} [\text{GeV}]$	Aplanarity
bin-1	$\geq 4$	$> 200$	$> 125 (\in [60, 125])$	$> 1500$	$< 0.03$
bin-2	$\geq 4$	$> 200$	$> 125 (\in [60, 125])$	$> 2000$	$< 0.03$
bin-3	$\geq 4$	$> 200$	$> 175 (\in [60, 125])$	$> 1000$	$< 0.03$
bin-4	$\geq 4$	$> 200$	$> 400 (\in [60, 125])$	—	$< 0.03$
bin-5	$\geq 4$	$> 200$	$> 400 (\in [60, 125])$	$> 1000$	$< 0.03$
bin-6	$\geq 4$	$> 300$	$> 175 (\in [60, 125])$	—	$< 0.03$
bin-7	$\geq 4$	$> 400$	$> 175 (\in [60, 125])$	$> 1000$	$< 0.03$
bin-8	$\geq 6$	$> 400$	$> 400 (\in [60, 125])$	—	$< 0.03$
bin-9	$\geq 6$	$> 200$	$> 125 (\in [60, 125])$	$> 1500$	$< 0.03$

The result is presented in Figure 129. The agreement with data is found within the uncertainty.

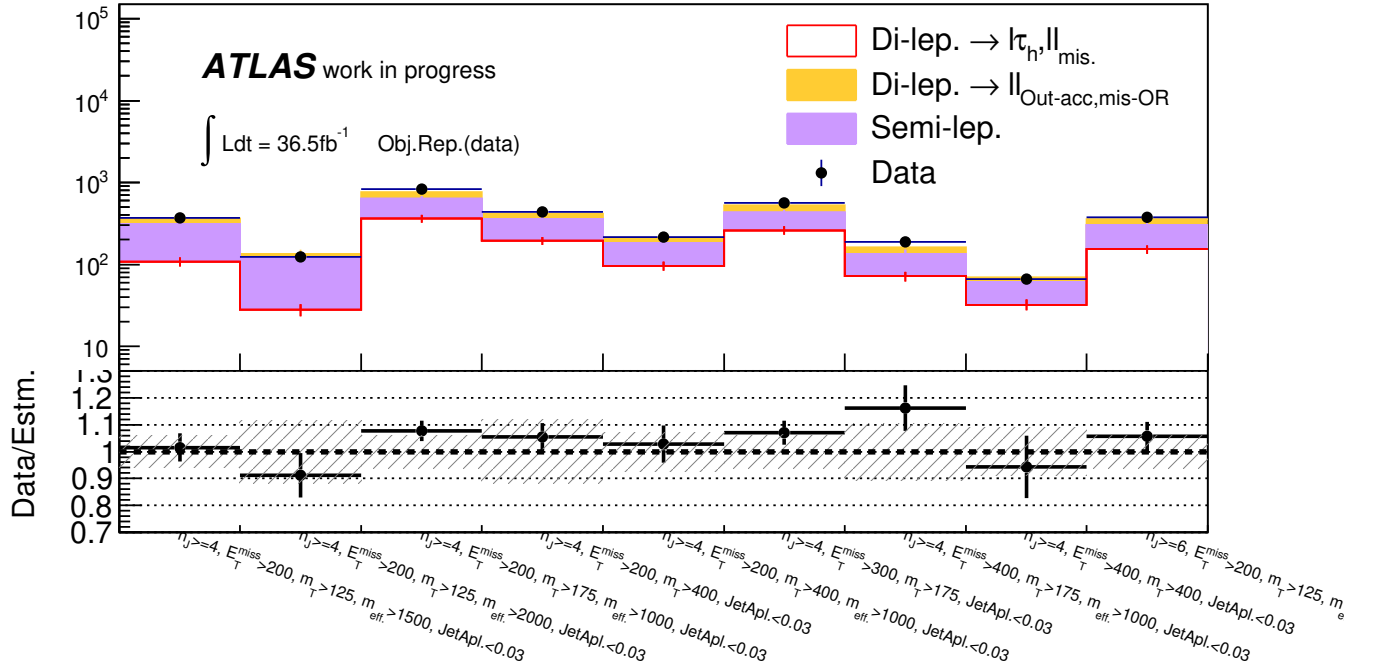


Figure 129: Closure test in VRs objRep bins. The white component shows the yield of the  $\ell\ell_{\text{mis}}, \ell\tau_h$  events that are estimated by the object replacement, while the colored represents the “semi-leptonic” (purple) and “2L-Out. Acc / Mis. OR” components (orange) respectively. The bottom row plots the ratio between the estimated yield and actual number of data. The gray dashed band shows the uncertainty in the estimation which is statistical error due to the CR statistics and flat 5% non-closure for the object replacement.

## 6.4 Unblinded Validation Regions

The background estimation is inclusively tested in validation regions VRa and VRb defined in Table 19 - 23, where the phase space are close enough to the signal regions, giving the sensible demonstration of the estimation.

Table 55 - 59 show the data yields and the expected background together with the breakdowns. The components estimated by the object replacement are merged and denoted as “Di-leptonic” in the tables, while the yields for the other components provided by the kinematical extrapolation are exclusively listed by physic processes. The errors are all post-fit uncertainty with the nuisance parameters profiled (detail found in Sec. 8.1).

The visualized comparison between data and background expectation is illustrated in 130, together with the pulls defined by the number of gaussian-equivalent deviation. The tension with respect to data never exceed  $2\sigma$ , which is still consistent to ascribing to the effects that the systematic uncertainties are paying for. For instance, the trend of underestimating  $W + \text{jets}$  in some of the VRb (in particular 2J) can be understood by the biased extrapolation due to the correlation with the ill-modeled variations, as discussed previously in Sec. 6.2. 15% of uncertainty is in fact assigned for this effect (based on Figure 164, with the mis-modeling parameter  $x$  to be at  $\sim 0.1$ ). Another source of systematical underestimation is understood by the potential MC mis-modeling in the  $m_T$  shape as mentioned in Sec. 6.2.1; for  $W + \text{jets}$ , the cut-off  $m_T \sim m_W$  is sharper for the MC supposedly due to the narrow mass width approximation in the matrix-element calculation in SHERPA. No theoretical uncertainties are dedicatedly assigned for this effect however could be explained by assigned theoretical uncertainties given the  $\sim 1\sigma$  discrepancy; for  $t\bar{t} + Wt$ , lack of full description of interference between  $WWbb$  diagrams could potential lead to underestimation in the tail of semi-leptonic component for which  $5\% \sim 30\%$  of uncertainty is assigned. All in all, underestimation upto  $1\sigma$  is expected therefore we don't regard this as an issue.

Figure ??-?? display the kinematical distributions of data overlaid with the prediction, for variables which VRs are designed to test i.e.  $m_T$  for VRa and aplanarity/topness etc. for VRb.

Table 37: Event yields and the background-only fit results in the “2J” control regions. Each column corresponds to a bin in  $m_{\text{eff}}$ . Uncertainties in the MC estimates combine statistical (in the simulated event yields) and systematic uncertainties discussed in Sec 7. The uncertainties in this table are symmetrised for propagation purposes but truncated at zero to remain within the physical boundaries.

<b>VRa 2J</b>	$m_{\text{eff}} \in [1100, 1500]$	$m_{\text{eff}} \in [1500, 1900]$	$m_{\text{eff}} > 1900$
Observed data	222	46	23
Expected background	$209.88 \pm 21.80$	$38.67 \pm 5.51$	$17.28 \pm 3.25$
Di-leptonic	$91.5 \pm 11.1$	$11.7 \pm 2.6$	$5.7 \pm 1.6$
$W + \text{jets}$	$20.9 \pm 3.8$	$8.0 \pm 2.6$	$3.2 \pm 1.3$
$Z + \text{jets}$	$2.6 \pm 0.7$	$0.8 \pm 0.2$	$0.3 \pm 0.1$
Tops	$85.6 \pm 18.0$	$15.6 \pm 3.8$	$6.9 \pm 2.8$
Di-boson	$6.0 \pm 2.2$	$1.5 \pm 0.5$	$0.8 \pm 0.3$
$t\bar{t} + V$	$3.2 \pm 0.5$	$0.9 \pm 0.2$	$0.4 \pm 0.1$
<b>VRb 2J</b>	$m_{\text{eff}} \in [1100, 1500]$	$m_{\text{eff}} \in [1500, 1900]$	$m_{\text{eff}} > 1900$
Observed data	390	113	52
Expected background	$314.33 \pm 36.92$	$104.33 \pm 13.80$	$41.34 \pm 8.95$
Di-leptonic	$10.5 \pm 2.4$	$3.0 \pm 1.1$	$3.7 \pm 1.3$
$W + \text{jets}$	$219.5 \pm 34.9$	$76.8 \pm 13.0$	$24.9 \pm 9.2$
$Z + \text{jets}$	$5.1 \pm 1.3$	$2.0 \pm 0.6$	$0.8 \pm 0.2$
Tops	$56.7 \pm 14.1$	$15.7 \pm 4.5$	$8.1 \pm 3.2$
Di-boson	$21.3 \pm 7.4$	$6.3 \pm 4.5$	$3.5 \pm 1.1$
$t\bar{t} + V$	$1.2 \pm 0.2$	$0.5 \pm 0.1$	$0.4 \pm 0.1$

Table 38: Event yields and the background-only fit results in the “6J” control regions. Each column corresponds to a bin in  $m_{\text{eff}}$ . Uncertainties in the MC estimates combine statistical (in the simulated event yields) and systematic uncertainties discussed in Sec 7. The uncertainties in this table are symmetrised for propagation purposes but truncated at zero to remain within the physical boundaries.

<b>VRa 6J</b>	$m_{\text{eff}} \in [1100, 1600]$	$m_{\text{eff}} \in [1600, 2100]$	$m_{\text{eff}} > 2100$
Observed data	130	60	31
Expected background	$134.22 \pm 18.17$	$48.27 \pm 7.79$	$28.71 \pm 4.57$
Di-leptonic	$71.9 \pm 15.2$	$24.7 \pm 6.8$	$11.5 \pm 3.5$
$W + \text{jets}$	$7.6 \pm 1.8$	$4.0 \pm 1.0$	$2.5 \pm 0.9$
$Z + \text{jets}$	$0.6 \pm 0.2$	$0.3 \pm 0.1$	$0.2 \pm 0.1$
Tops	$45.7 \pm 9.8$	$16.0 \pm 3.7$	$12.0 \pm 2.9$
Di-boson	$4.6 \pm 1.5$	$2.1 \pm 0.7$	$1.6 \pm 0.7$
$t\bar{t} + V$	$3.8 \pm 0.7$	$1.2 \pm 0.3$	$0.9 \pm 0.2$
<b>VRb 6J</b>	$m_{\text{eff}} \in [1100, 1600]$	$m_{\text{eff}} \in [1600, 2100]$	$m_{\text{eff}} > 2100$
Observed data	99	53	26
Expected background	$84.21 \pm 10.42$	$43.22 \pm 5.50$	$25.15 \pm 3.89$
Di-leptonic	$0.9 \pm 0.4$	$1.0 \pm 0.8$	$0.5 \pm 0.4$
$W + \text{jets}$	$32.9 \pm 6.5$	$21.8 \pm 4.7$	$8.6 \pm 2.9$
$Z + \text{jets}$	$0.4 \pm 0.2$	$0.3 \pm 0.1$	$0.2 \pm 0.1$
Tops	$43.1 \pm 9.0$	$16.3 \pm 3.8$	$13.0 \pm 3.4$
Di-boson	$5.6 \pm 2.6$	$2.9 \pm 1.8$	$2.3 \pm 1.1$
$t\bar{t} + V$	$1.3 \pm 0.3$	$0.9 \pm 0.2$	$0.5 \pm 0.2$

Table 39: Event yields and the background-only fit results in the “Low-x” control regions. Each column corresponds to a bin in  $m_{\text{eff}}$ . Uncertainties in the MC estimates combine statistical (in the simulated event yields) and systematic uncertainties discussed in Sec 7. The uncertainties in this table are symmetrised for propagation purposes but truncated at zero to remain within the physical boundaries.

<b>VR Low-x</b>	VRa	VRb
Observed data	20	23
Expected background	$14.91 \pm 2.09$	$15.77 \pm 3.31$
Di-leptonic	$6.5 \pm 1.2$	$0.6 \pm 0.3$
$W + \text{jets}$	$1.5 \pm 0.8$	$6.9 \pm 3.3$
$Z + \text{jets}$	$0.5 \pm 0.2$	$0.5 \pm 0.2$
Tops	$5.0 \pm 1.7$	$6.1 \pm 2.1$
Di-boson	$1.0 \pm 0.3$	$1.4 \pm 0.4$
$t\bar{t} + V$	$0.4 \pm 0.1$	$0.4 \pm 0.1$

Table 40: Event yields and the background-only fit results in the “High-x” control regions. Each column corresponds to a bin in  $m_{\text{eff}}$ . Uncertainties in the MC estimates combine statistical (in the simulated event yields) and systematic uncertainties discussed in Sec 7. The uncertainties in this table are symmetrised for propagation purposes but truncated at zero to remain within the physical boundaries.

<b>VR High-x</b>	<b>VRa</b>	<b>VRb</b>
Observed data	66	119
Expected background	$49.33 \pm 8.80$	$102.12 \pm 13.40$
Di-leptonic	$18.9 \pm 5.4$	$0.0 \pm 0.0$
$W + \text{jets}$	$8.8 \pm 1.8$	$70.6 \pm 13.3$
$Z + \text{jets}$	$0.4 \pm 0.1$	$0.7 \pm 0.3$
Tops	$16.0 \pm 6.8$	$21.5 \pm 7.5$
Di-boson	$4.2 \pm 1.6$	$8.5 \pm 3.2$
$t\bar{t} + V$	$1.1 \pm 0.4$	$0.8 \pm 0.3$

Table 41: Event yields and the background-only fit results in the “3B” control regions. Each column corresponds to a bin in  $m_{\text{eff}}$ . Uncertainties in the MC estimates combine statistical (in the simulated event yields) and systematic uncertainties discussed in Sec 7. The uncertainties in this table are symmetrised for propagation purposes but truncated at zero to remain within the physical boundaries.

<b>VRa 3B</b>	$m_{\text{eff}} \in [1000, 1750]$	$m_{\text{eff}} > 1750$
Observed data	11	8
Expected background	$12.46 \pm 5.81$	$5.31 \pm 1.58$
Di-leptonic	$7.3 \pm 5.5$	$2.7 \pm 1.3$
$W + \text{jets}$	$0.0^{+0.0}_{-0.0}$	$0.0 \pm 0.0$
$Z + \text{jets}$	$0.0 \pm 0.0$	$0.0 \pm 0.0$
Tops	$4.8 \pm 1.7$	$2.4 \pm 0.9$
Di-boson	$0.1^{+0.1}_{-0.1}$	$0.0 \pm 0.0$
$t\bar{t} + V$	$0.2 \pm 0.1$	$0.2 \pm 0.0$
<b>VRb 3B</b>	$m_{\text{eff}} \in [1000, 1750]$	$m_{\text{eff}} > 1750$
Observed data	69	12
Expected background	$60.09 \pm 15.83$	$9.55 \pm 2.77$
Di-leptonic	$3.3 \pm 1.4$	$0.8 \pm 0.6$
$W + \text{jets}$	$0.8 \pm 0.5$	$0.4 \pm 0.2$
$Z + \text{jets}$	$0.1 \pm 0.0$	$0.0 \pm 0.0$
Tops	$54.1 \pm 15.7$	$7.8 \pm 2.7$
Di-boson	$0.1 \pm 0.1$	$0.2 \pm 0.1$
$t\bar{t} + V$	$1.7 \pm 0.4$	$0.4 \pm 0.1$

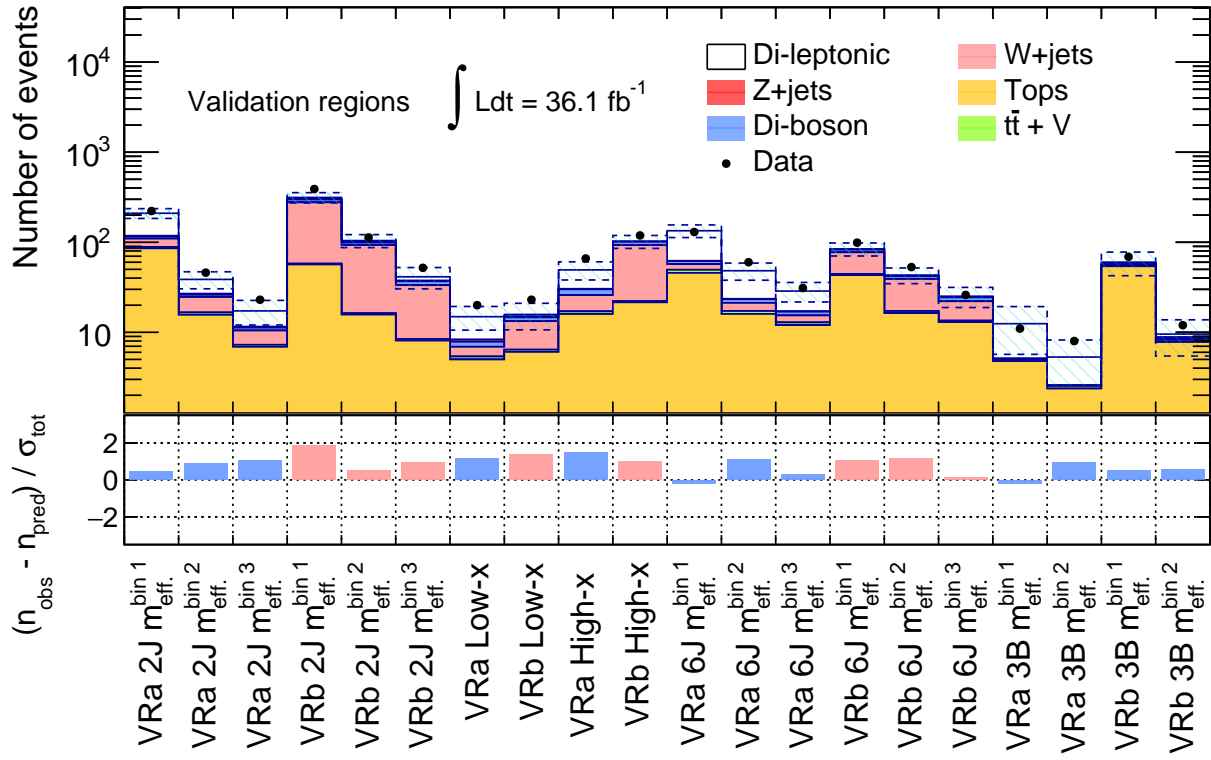


Figure 130: (Top) Observed data and the estimated yields in the nominal validation regions (VRa/VRb). The white component is the backgrounds estimated by the object replacement method, while the colored ones are by the kinematical extrapolation method. The dashed band represents the combined statistical and systematic uncertainty on the total estimated backgrounds. (Bottom) Pull between the data and the estimation. Pulls in regions dominated by  $W + \text{jets}$  and tops are painted by pink and blue respectively.

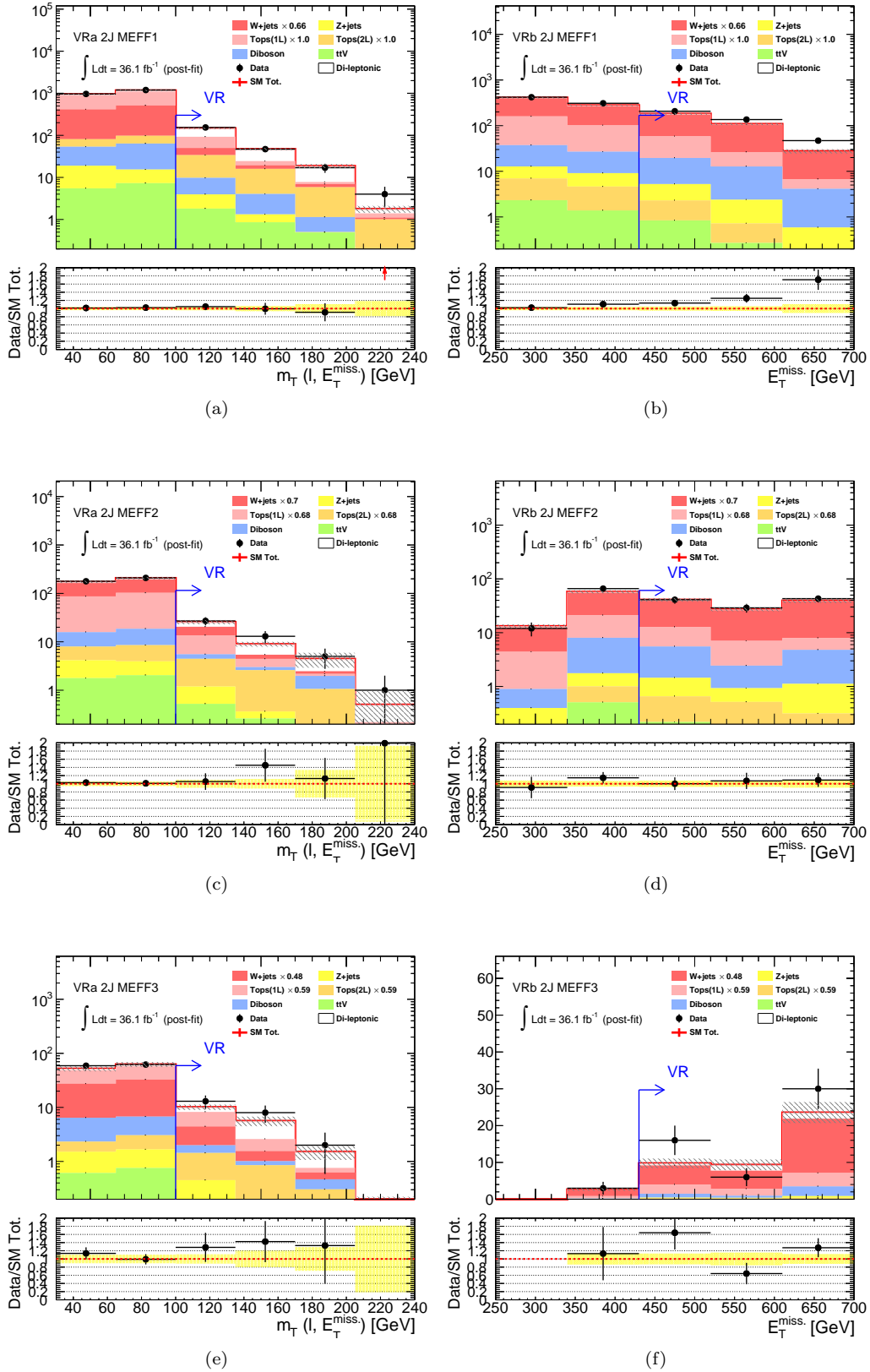


Figure 131: Post-fit distribution of (left)  $m_T$  in VRa, and (right)  $E_T^{\text{miss}}$  in VRb. (a,b) VR 2J- $m_{\text{eff}}^{\text{bin}1}$ . (c,d) VR 2J- $m_{\text{eff}}^{\text{bin}2}$ . (e,f) VR 2J- $m_{\text{eff}}^{\text{bin}3}$ . The yellow band in the bottom panel represents statistical error. The overflow is included in the highest bin.

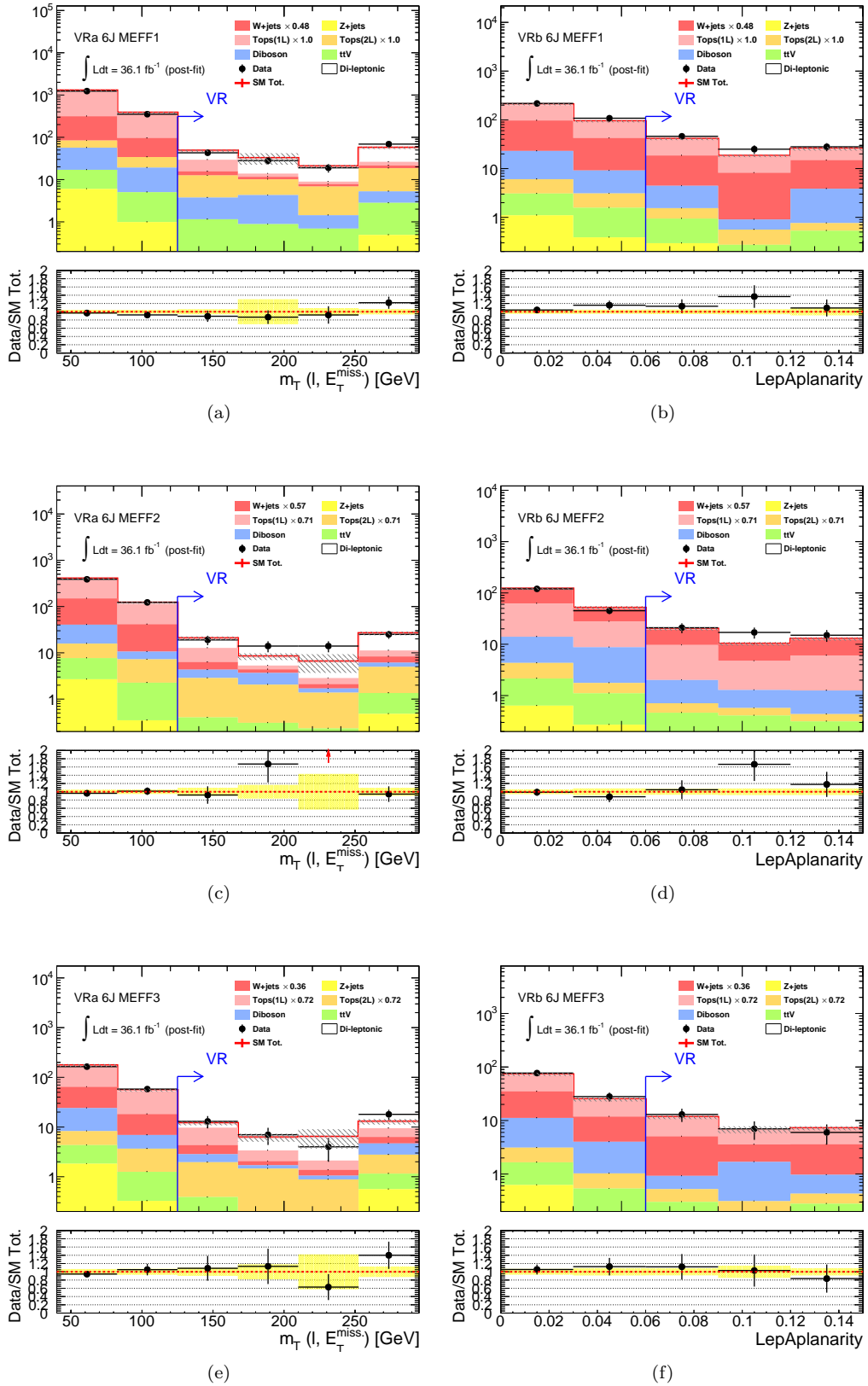


Figure 132: Post-fit distribution of (left)  $m_T$  in VRa, and (right) aplanarity in VRb. (a,b) VR 6J- $m_{\text{eff}}^{\text{bin}1}$ . (c,d) VR 6J- $m_{\text{eff}}^{\text{bin}2}$ . (e,f) VR 6J- $m_{\text{eff}}^{\text{bin}3}$ . The yellow band in the bottom panel represents only statistical error. The overflow is included in the highest bin.

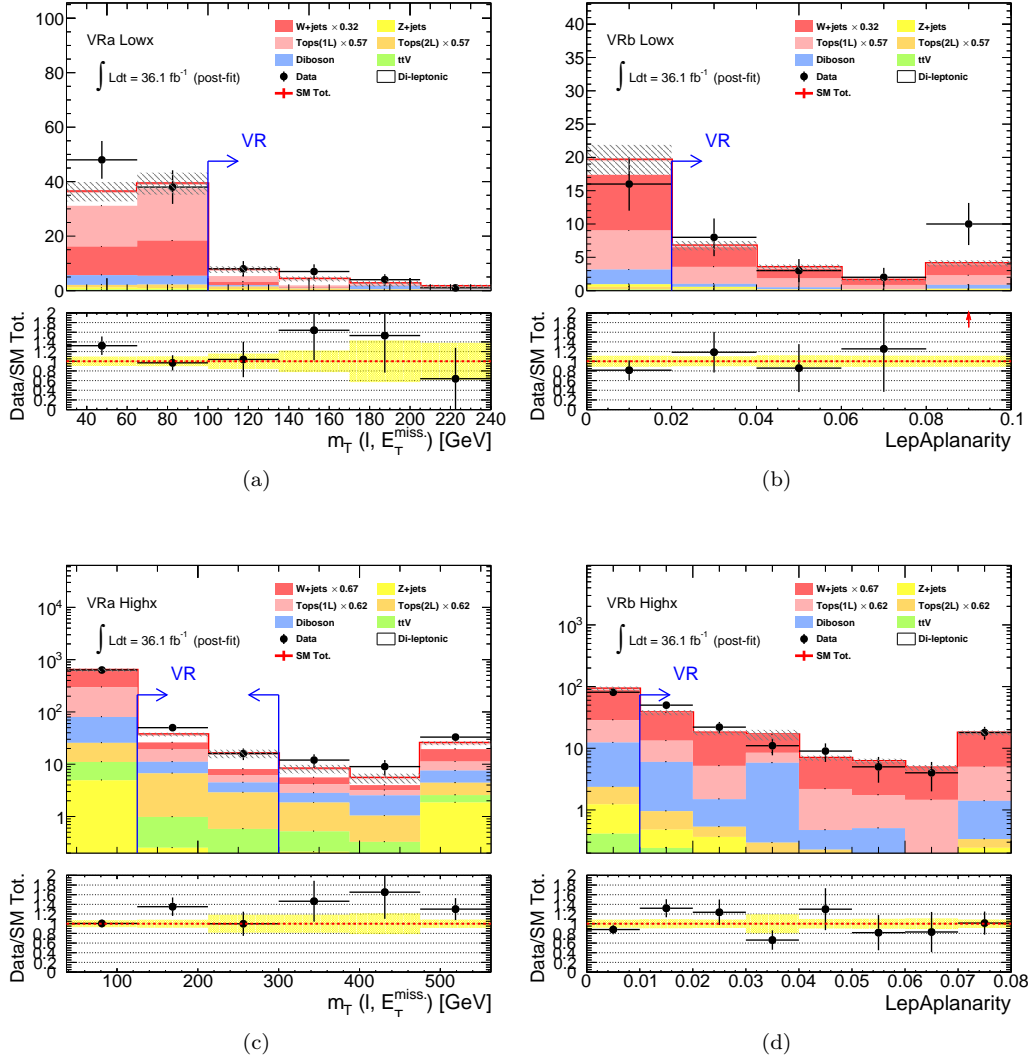


Figure 133: Post-fit distribution of (left)  $m_T$  in VRa, and (right) aplanarity in VRb. (a,b) VR Low-x. (c,d) VR High-x. The yellow band in the bottom panel represents only statistical error. The overflow is included in the highest bin.

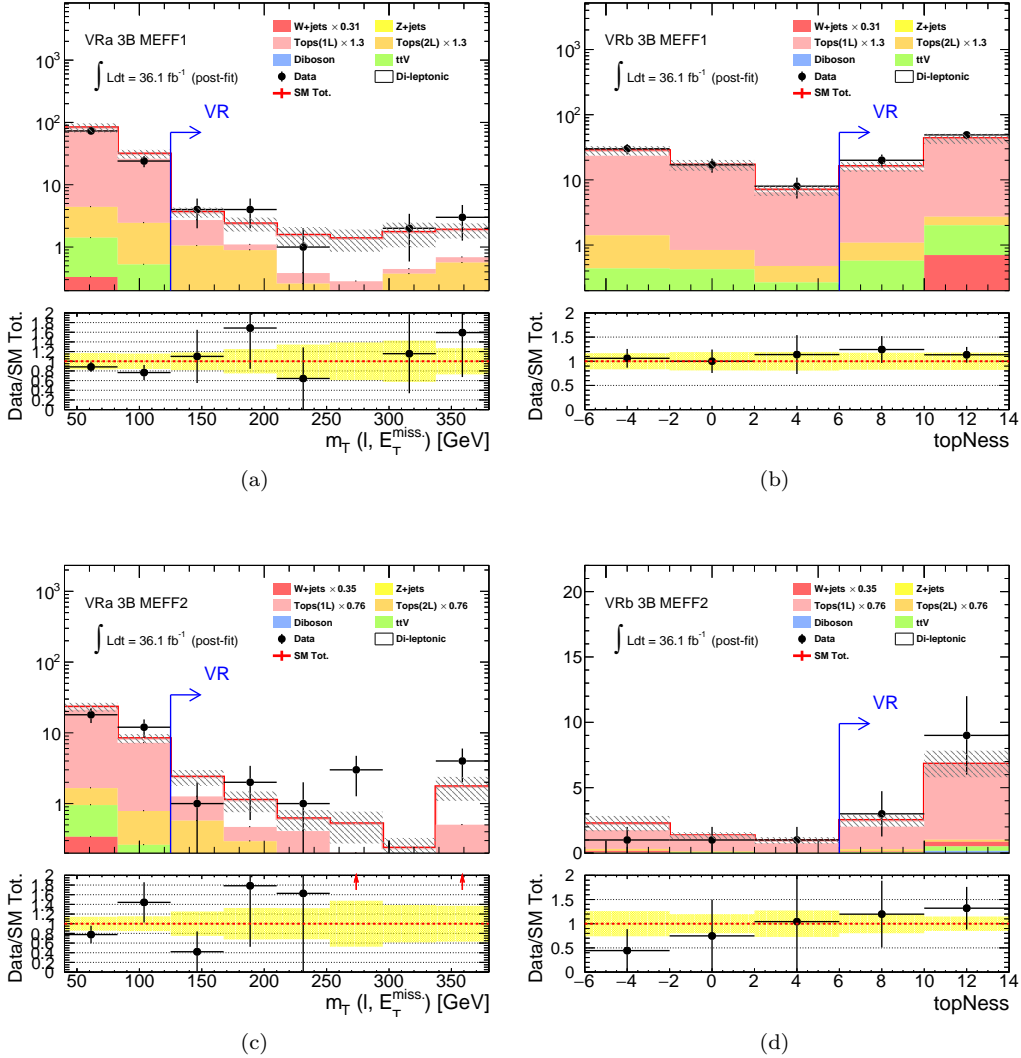


Figure 134: Post-fit distribution of (left)  $m_T$  in VRa, and (right) topness in VRb. (a,b) VR 3B- $m_{\text{eff}}^{\text{bin}1}$ . (c,d) VR 3B- $m_{\text{eff}}^{\text{bin}2}$ . The yellow band in the bottom panel represents only statistical error. The overflow is included in the highest bin.

## 7 Systematic Uncertainties

Uncertainties associated with background estimations and the signal modeling is dedicatedly discussed in this section. They are largely three-fold: instrumental uncertainties, theoretical uncertainties and the generic uncertainties for the background estimation methods.

### 7.1 Instrumental Uncertainty

Instrumental uncertainties are the systematic uncertainty regarding to the experiment, including the imperfection of calibration and mis-modeling of detector response and so on.

#### 7.1.1 Jets

Despite the dedicated calibration procedures as described in Sec. 3.6, the residual uncertainty on the jet energy scale (JES) is often the largest source of instrumental uncertainty. While 87 independent uncertainties are modeled from each step in the sequential calibration, those showing the similar behavior are then combined. In the analysis, 8 combined nuisance parameters are input in the fit. The sub-leading jet uncertainty is on the jet energy resolution (JER). While JER is measured using different multiple physics processes, the uncertainty is quoted by the difference in the outcomes. Systematics dealing with the flavor tagging are also important since the analysis deeply relies on the classification in b-tagged jet multiplicity. There are a couple of additional uncertainties dealing with the jet eta-scale and the modeling of the JVT (Jet Vertex Tagger, Sec. 3.6) profile etc. that are also taken into account, though the impacts on the final result are usually negligible.

#### 7.1.2 Electrons

Electrons involve three efficiency uncertainties on reconstruction, identification and isolation, as well as the uncertainties on the energy scale and resolution modeling. The efficiencies are measured by exploiting the  $Z \rightarrow \ell\ell$  process with the tag-probe technique as described in Sec. 3.4, and the uncertainties are derived from the difference between the expected measured efficiencies by MC and the observed ones. The uncertainties on the energy scale and resolution are evaluated based on the discrepancy between simulated and observed response of the EM calorimeter in Run2.

#### 7.1.3 Muons

Four efficiency uncertainties and two separated scale uncertainties are associated to muons. All the uncertainties are derived from the difference between the expectation and observed measurement outcome using  $Z \rightarrow \mu\mu$  process by the tag-probe technique similarly to the case of electrons. The efficiency uncertainties involve the reconstruction, identification, isolation and TTVA (Tracks-To-Vetex-Association), while the two scale uncertainties corresponds to the statistical and systematic uncertainty in the measurement.

#### 7.1.4 MET

On top of the propagated uncertainties on the scales and resolutions of the reconstructed objects, MET suffers from additional uncertainty regarding to the modeling of the soft term defined in Sec. 3.9. This is measured using the  $Z(\rightarrow \ell\ell) + \text{jets}$  events, by comparing the expected momentum profile of soft terms and the observed ones.

#### 7.1.5 Implementation and the Impact

Instrumental uncertainties are implemented by generating the corresponding MC variations in which the scale, resolution or the efficiency for objects are tuned event-by-event. The expected yields in the CRs and SRs (VRs) by the variated samples are then input into the fit, and the difference with respect to those of nominal sample is taken as the  $1\sigma$  deviation by the systematics.

The impact on kinematical extrapolation is relatively sizable, amounting upto  $5\% \sim 15\%$  in signal regions, though the nomalization applied for the main background in CRs helps a lot. On the other hand, instrumental uncertainties have tiny impact on the estimation by the object replacement method, though they do affect the modeling of lepton efficiencies and the tau response that are fully based on MC. The effect is examined by comparing the MC closure between the nominal setup and the cases with systematical variations being applied using the  $t\bar{t}$  MC samples.

The impact on signal modeling is generally marginal compared with the cross-section error and the shape uncertainties as described below. Therefore, the instrumental uncertainties are not implemented for the non-benchmark models, otherwise the computation cost will skyrocket due to the enormous signal points.

## 7.2 Theoretical Uncertainty

There are two types of uncertainties subjecting to theoretical uncertainty: the cross-section uncertainty affecting the global normalization, and the uncertainty on kinematics modeling affecting the acceptance referred as “shape” uncertainty. Their impacts are evaluated either on signal yields and background expectation in the SRs and VRs, and implemented in the final fit. As for the backgrounds, uncertainties are assigned only for the components estimated by the kinematical extrapolation method, since the object replacement method experiences no theory dependency by construction.

The cross-section uncertainties are provided by the associated calculation error in the references that the cross-section is quoted by. The primary source contributing to it is the missing higher-order terms in the calculation, such as terms beyond NNLO for the NLO calculation, or the absence of soft gluon resummation. The other typical sources are from PDF, and measurement precision on standard model parameters, particularly in strong coupling constant and quark masses for higher order QCD correction.

The shape uncertainties are evaluated using the MC samples with specific systematic variations applied. Different recepes for the variation are prepared for each physics process and the generator, and is carefully designed to minimize the double-counting as possible.

For the normalized backgrounds ( $W + \text{jets}$  and  $t\bar{t}$ ), the uncertainties on the extrapolation between CRs to SRs/VRs are considered as the only source of theoretical uncertainty, since the other uncertainties (cross-section uncertainty and the shape uncertainties on CR yields) will be cancelled through the normalization in CRs. On the other hand, the full uncertainties are assigned for the other non-normalized backgrounds ( $Z + \text{jets}$ , di-bosons and  $t\bar{t} + W/Z/WW$ ) and the SUSY processes, as they are free from any constraints in the analysis. Note that all these theoretical uncertainties are assigned on the post-fit yields without any constraint by the fit.

### 7.2.1 Normalized Backgrounds

The shape uncertainties for the normalized backgrounds ( $W + \text{jets}$  and  $t\bar{t}$ ) are given by computing the variation in the ratio of MC yields between in a CR and a SR (or VR), resulting from the systemtical variations applied. The uncertainties are evaluated in respective SR and VR, however, some of the cuts are removed to suppress the statistical fluctuation in MC to a sensible level, which is not trivial given that the evaluated variations are often at the level of 5% – 10%. The b-jet requirement is then removed, based on the fact that it is generally orthogonal to kinematics. Though it is much less trivial, the  $m_{\text{eff}}$  cut can also be removed in addition to it. This is because the kinematical extrapolation method is by concept relying on the weak correlation in the behaviors between the extrapolating variables and the other presumably ill-modeled variables including  $m_{\text{eff}}$ , thus the effect of loosened  $m_{\text{eff}}$  cut is supposed to be sub-dominant with respect to the systematic variations in interest. Therefore, the evaluated systematics are common to all the bins in the same tower eventually.

The menu of theoretical variations for  $W + \text{jets}$  are as following:

- Choice of renormalization, factorization and resummation scale for soft gluon.  
The  $1\sigma$  up/down variations are generated by independently shifting those scales from the default values  $\mu_0$  to either  $0.5\mu_0$  or  $2\mu_0$  respectively.

- Choice of CKKW matching scale.

The default matching scale for CKKW is 20 GeV, while it is set to 15 GeV and 30 GeV respectively for variations.

The theoretical variations considered for  $t\bar{t}$  are as below:

- Choice of renormalization/factorization scale.

In POWHEG +Box generator, these scales are set to common default values of  $\mu_0 = \sqrt{m_t^2 + p_{T,t}^2}$  where  $m_t$  and  $p_{T,t}$  are the mass and transverse momentum of top quark. The  $1\sigma$  up/down variations are generated by simultaneously shifting those scales by factor of 2 or 0.5 respectively.

- Parton shower scheme.

The dependency on parton showering scheme is evaluated by comparing the default scheme (PYTHIA 6.428) with one used in HERWIG. The difference is taken as  $1\sigma$  variation.

- Interference between top-like  $WWbb$  diagrams, and the inclusive  $WWbb$  ones.

The diagrams of  $t\bar{t} + Wt$  and the other  $WWbb$  diagrams are allowed to interfere each other since they lead to the common final states. This effect is a missed piece in the MC description, however is known to become significant in phase space where the bulk  $t\bar{t}$  component is suppressed, for which signal regions are actually designed for. In particular, the topness selection is essentially rejecting the  $t\bar{t}$  with the both top quarks being on-shell, in other words, significantly enhancing the contribution from the off-shell tail of top quarks where the interference effect is addressed. The impact is evaluated by comparing two truth-level MadGraph samples: one with the only diagrams of  $t\bar{t} + Wt$ , and the other with inclusive  $WWbb$  diagrams. The difference is taken as  $1\sigma$  variation.

The evaluated uncertainties are listed in Table 42 and 43 for  $W +$  jets and  $t\bar{t}$  respectively. Systematics contributing below 5% or 5 times less than that of the leading uncertainty in the region are ignored.

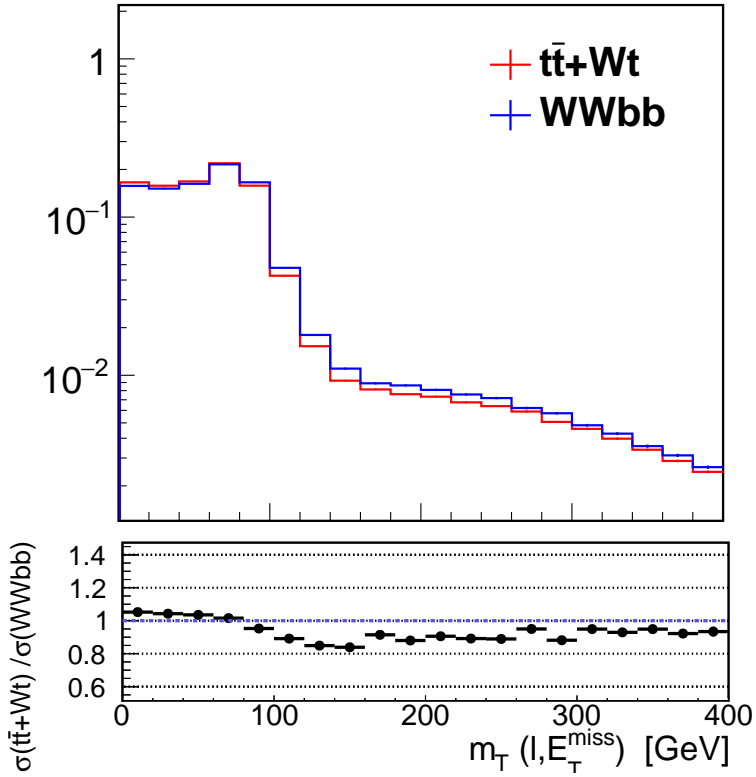


Figure 135: Comparison of the  $m_T$  shape between  $t\bar{t} + Wt \rightarrow WWbb$  (red) and  $WWbb$  (blue).

Table 42: Theory systematics assigned for the post-fit yields for  $W + \text{jets}$  [%]. The numbers are shared by all the  $m_{\text{eff}}$ -bins in the same SR/VR tower. Systematics contributing below 5% or 5 times less than that of the leading uncertainty in the region are ignored (labeled as "-").

	Factorization scale	Resummation scale	Renormalization scale	CKKW matching scale
SR 2J	-	7	7	9
SR 6J	9	-	23	-
SR Low-x	-	11	-	6
SR High-x	19	7	-	-
SR 3B	36	15	-	19
VRa 2J	-	8	12	-
VRa 6J	13	11	-	-
VRa Low-x	9	-	8	8
VRa High-x	-	6	-	9
VRa 3B	20	16	7	6
VRb 2J	-	4	3	7
VRb 6J	5	-	5	6
VRb Low-x	-	5	6	5
VRb High-x	5	-	-	5
VRb 3B	-	5	5	5

Table 43: Theory systematics assigned for the post-fit yields for  $t\bar{t} + Wt$  [%]. The numbers are shared by all the  $m_{\text{eff}}$ -bins in the same SR/VR tower. Systematics contributing below 5% or 5 times less than that of the leading uncertainty in the region are ignored (labeled as "-").

	Renormalization/factorization scale	$tt+Wtb$ vs WWbb	Parton shower
SR 2J	22	17	8
SR 6J	21	24	25
SR Low-x	15	13	10
SR High-x	15	17	28
SR 3B	27	25	13
VRa 2J	12	5	10
VRa 6J	15	7	9
VRa Low-x	10	12	6
VRa High-x	17	10	-
VRa 3B	13	26	8
VRb 2J	-	21	10
VRb 6J	-	19	5
VRb Low-x	-	18	5
VRb High-x	-	23	8
VRb 3B	-	25	7

### 7.2.2 Non-normalized Backgrounds

**Cross-section uncertainty** The cross-section uncertainty for  $Z + \text{jets}$ , di-bosons and  $t\bar{t} + W/Z/WW$  amounts upto level of 5% [?], 6% [?] and 13% [?] respectively.

**Shape uncertainty** The shape uncertainties for non-normalized background components are dominantly seen in spectra regarding to jet activity, in particular jet-multiplicity and  $m_{\text{eff}}$ , while the impact on the spectra of other variables are rather limited. Therefore, the shape uncertainties are evaluated in SRs/VRs with the cuts in  $m_T$ , aplanarity and topness are removed, as well as the b-tagging requirement.

The variations considered for  $Z + \text{jets}$  and di-bosons are the same as those for  $W + \text{jets}$  as described above, except for that CKKW matching for dibosons. The menu of variations for  $t\bar{t} + W/Z/WW$  is minimal since it is the smallest backgrounds:

- Choice of renormalization and factorization scale The  $1\sigma$  up/down variations are generated by simultaneously shifting these scales from the default value  $\mu_0$  to  $0.5\mu_0$  and  $2\mu_0$ .
- Hard process description. As  $t\bar{t} + W/Z/WW$  have not dedicatedly measured in precision using data, additional uncertainty is quoted by comparing with the sample generated by the alternative hard process modeling by Sherpa.

The uncertainties derived for each  $m_{\text{eff}}$ -bin of SR and VR, as in Table 44, 45 and 46 for  $Z + \text{jets}$ , di-bosons and  $t\bar{t}$  respectively. Systematics contributing below 5% or 5 times less than that of the leading uncertainty in the region are ignored.

Table 44: Theory systematics assigned for the yields of  $Z + \text{jets}$  [%]. The uncertainty is shared by SRs and corresponding VRs. Systematics contributing below 5% or 5 times less than that of the leading uncertainty in the region are ignored (labeled as "-"). The uncertainties in the 3B towers are not evaluated since the  $Z + \text{jets}$  contribution is negligible.

	Factorization scale	Resummation scale	Renormalization scale	CKKW matching scale
2J $m_{\text{eff}}^{\text{bin}1}$	-	-	23	7
2J $m_{\text{eff}}^{\text{bin}2}$	-	-	25	-
2J $m_{\text{eff}}^{\text{bin}3}$	-	-	25	-
6J $m_{\text{eff}}^{\text{bin}1}$	-	-	35	-
6J $m_{\text{eff}}^{\text{bin}2}$	10	-	35	-
6J $m_{\text{eff}}^{\text{bin}3}$	-	-	39	15
Low-x	-	-	33	10
High-x	-	-	32	-

Table 45: Theory systematics assigned for the yields of Di-boson [%]. The uncertainty is shared by SRs and corresponding VRs. Systematics contributing below 5% or 5 times less than that of the leading uncertainty in the region are ignored (labeled as "-").

	Factorization scale	Resummation scale	Renormalization scale
2J $m_{\text{eff}}^{\text{bin}1}$	-	-	16
2J $m_{\text{eff}}^{\text{bin}2}$	21	-	21
2J $m_{\text{eff}}^{\text{bin}3}$	-	-	23
6J $m_{\text{eff}}^{\text{bin}1}$	8	9	19
6J $m_{\text{eff}}^{\text{bin}2}$	8	7	26
6J $m_{\text{eff}}^{\text{bin}3}$	9	11	37
Low-x	13	-	22
High-x	-	12	34
3B $m_{\text{eff}}^{\text{bin}1}$	-	7	29
3B $m_{\text{eff}}^{\text{bin}2}$	13	-	35

Table 46: Theory systematics assigned for the yields of  $t\bar{t} + V$  [%]. The uncertainty is shared by SRs and corresponding VRs. Systematics contributing below 5% or 5 times less than that of the leading uncertainty in the region are ignored (labeled as "-").

	Renormalization/factorization scale	Hard processes
2J $m_{\text{eff}}^{\text{bin}1}$	-	9
2J $m_{\text{eff}}^{\text{bin}2}$	5	10
2J $m_{\text{eff}}^{\text{bin}3}$	-	16
6J $m_{\text{eff}}^{\text{bin}1}$	-	8
6J $m_{\text{eff}}^{\text{bin}2}$	-	17
6J $m_{\text{eff}}^{\text{bin}3}$	-	22
Low-x	-	16
High-x	-	33
3B $m_{\text{eff}}^{\text{bin}1}$	5	5
3B $m_{\text{eff}}^{\text{bin}2}$	-	13

### 7.2.3 SUSY signal

The cross-section uncertainty of gluino pair production amounts up-to 15%  $\sim$  35%, as shown in Figure 47 in Sec. 4.2.

The shape uncertainty is evaluated by examining following systematic variations:

- Choice of renormalization and factorization scale.

The variations are generated by independently shifting those scales by factor of 2 or 0.5 respectively.

- Parton shower tuning.

Five variations are generated by tuning the MadGraph internal parameters dealing with parton shower.

The Uncertainties are added in quadrature.

They are evaluated over the signal points in the  $x=1/2$  grid of the model QQC1QQC1, and found to be typically marginal compared with the cross-section uncertainty. This is because the jet activity is predominantly sourced by gluino decays rather than the ISRs and FSRs for most of the cases. The only exception is found in low  $m_{\text{eff}}$ -bins in SR **2J** where the target signals are with highly compressed mass splitting between gluino and LSP ( $\Delta m(\tilde{g}, \tilde{\chi}_1^0) < 50$  GeV) that have to rely on the additional radiation to enter the signal regions. In such case, the acceptance can vary upto by 20% by the theoretical variation. Table 47 presents the assigned shape uncertainties, which are common to all the signal models and mass points.

Table 47: Shape uncertainties assigned for SUSY signal processes [%]. The uncertainties are common to all the signal models.

	Scale in Fac./Renom.	Parton shower
SR 2J $m_{\text{eff}}^{\text{bin}1}$	15	20
SR 2J $m_{\text{eff}}^{\text{bin}2}$	10	10
SR 2J $m_{\text{eff}}^{\text{bin}3}$	-	5
The other regions	-	-

## 7.3 Other Uncertainties

### 7.3.1 Uncertainty Generaic to the Estimation Methods

The generic errors of the estimation method need to be quoted as additional uncertainties in the background expectation. In the kinematical extrapolation method, this refers to the extrapolation error as already discussed in Sec. 6.2.3. The assigned uncertainty to each SR and VR are decided as Table 48, based on the as shown in Figure 98 - 101 and the observed level of mis-modeling ( $x_W = 0.1$ ,  $x_{t\bar{t}} = 0.06$  in Eq. 95).

Table 48: Assigned uncertainty for  $t\bar{t}$  and  $W + \text{jets}$  for the kinematical extrapolation from CRs to corresponding VRs and SRs [%], based on the result in Sec 6.2.3.

	$W + \text{jets}$	$t\bar{t}$		$W + \text{jets}$	$t\bar{t}$		$W + \text{jets}$	$t\bar{t}$
SR 2J $m_{\text{eff}}^{\text{bin}1}$	15	5	VRa 2J $m_{\text{eff}}^{\text{bin}1}$	-	10	VRb 2J $m_{\text{eff}}^{\text{bin}1}$	10	5
SR 2J $m_{\text{eff}}^{\text{bin}2}$	15	-	VRa 2J $m_{\text{eff}}^{\text{bin}2}$	5	10	VRb 2J $m_{\text{eff}}^{\text{bin}2}$	5	10
SR 2J $m_{\text{eff}}^{\text{bin}3}$	15	20	VRa 2J $m_{\text{eff}}^{\text{bin}3}$	-	20	VRb 2J $m_{\text{eff}}^{\text{bin}3}$	5	10
SR 6J $m_{\text{eff}}^{\text{bin}1}$	-	5	VRa 6J $m_{\text{eff}}^{\text{bin}1}$	-	5	VRb 6J $m_{\text{eff}}^{\text{bin}1}$	-	-
SR 6J $m_{\text{eff}}^{\text{bin}2}$	-	10	VRa 6J $m_{\text{eff}}^{\text{bin}2}$	-	5	VRb 6J $m_{\text{eff}}^{\text{bin}2}$	5	5
SR 6J $m_{\text{eff}}^{\text{bin}3}$	-	-	VRa 6J $m_{\text{eff}}^{\text{bin}3}$	-	5	VRb 6J $m_{\text{eff}}^{\text{bin}3}$	5	10
SR Low-x	10	-	VRa Low-x	-	5	VRb Low-x	10	5
SR High-x	-	10	VRa High-x	-	30	VRb High-x	5	10
SR 3B $m_{\text{eff}}^{\text{bin}1}$	-	5	VRa 3B $m_{\text{eff}}^{\text{bin}1}$	30	-	VRb 3B $m_{\text{eff}}^{\text{bin}1}$	20	10
SR 3B $m_{\text{eff}}^{\text{bin}2}$	-	10	VRa 3B $m_{\text{eff}}^{\text{bin}2}$	30	5	VRb 3B $m_{\text{eff}}^{\text{bin}2}$	30	15

For the object replacement method, the observed non-closure error discussed throughout Sec. 6.3.2 - 6.3.3 are included as systematics as listed in Table 49.

Table 49: Summary of non-closure errors in the object replacement method [%].

	BV/BT	3B
Tau replacement	5	20
Missing electron replacement	15	
Missing muon replacement	30	

### 7.3.2 Control region statistics

In both of the background estimation methods, reflecting the (semi-)data driven nature, the statistical error in CRs often becomes the primary uncertainty in the estimation. This typically occurs in case of the high  $m_{\text{eff}}$  bins, for instance the yields in the CRs for the kinematical extrapolation end up in about 15 events, immediately resulting in 20% – 30% of uncertainty. The tendency is more striking concerning to the object replacement method where the uncertainty is solely dominated by the seed event statistical error that amounts 20% – 60% in SRs depending on the tightness of selection. Furthermore, one has to mind that the statistical error in the object replacement method is not independent between the regions given that the sub-events from a single seed event can fall into different regions. The correlated statistical error between two signal regions is then evaluated by identifying the fraction of common seed events between their estimation. Table 136 shows the correlation coefficient in the estimated yields between  $\text{SR}_i$  and  $\text{SR}_j$  defined

as:

$$\rho := \frac{\sum_e \sqrt{w_e^i w_e^j}}{\sqrt{\sum_e w_e^i} \sqrt{\sum_e w_e^j}}$$

where  $e$  runs over all seed events, and  $w_e^i$  denotes the sum of weighted sub-events falling into SR $_i$  generated by the seed event  $e$ . Correlation is mainly found in adjacent  $m_{\text{eff}}$ -bins, high  $m_{\text{eff}}$  BT/3B bins, and high  $m_{\text{eff}}$  hard lepton / soft lepton bins. This correlation is taken into account in the final fitting. Though large inter-bin correlation can potentially destroy the sensitivity in the shape fit, the impact on the final result to this analysis is limited, since the signal points rarely lay over multiple bins with equal abundance.

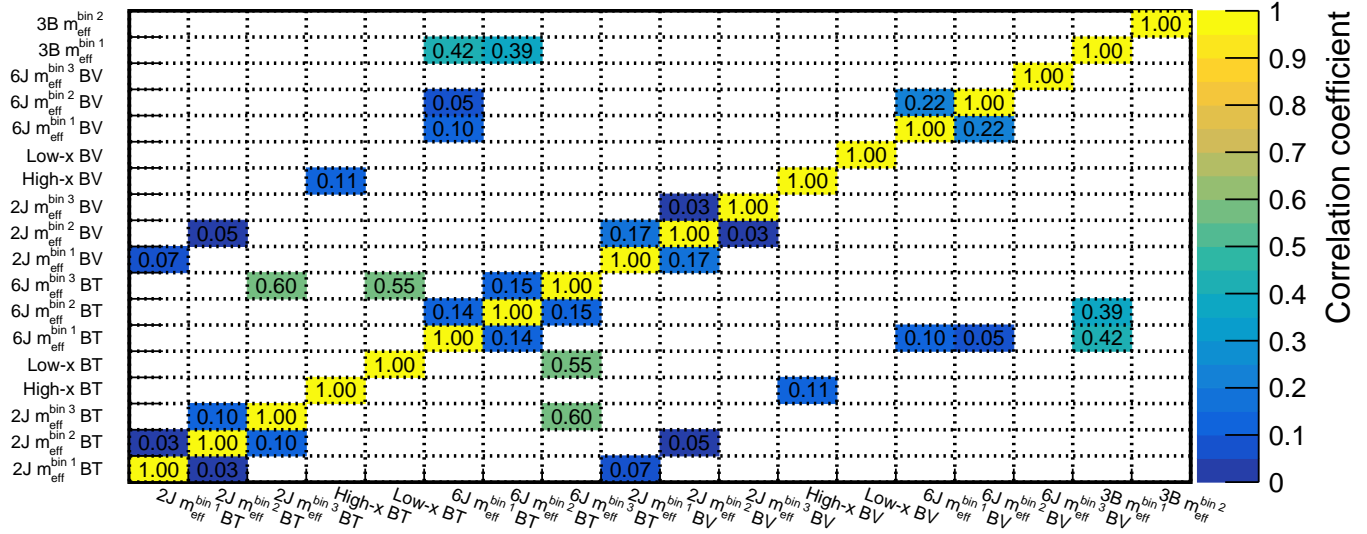


Figure 136: The correlation coefficient in the estimated yields between two signal regions, indicating the level of correlated statistical fluctuation.

### 7.3.3 MC statistics

Limited MC statistics lead to non-negligible uncertainty in signal and background yields in regions with tight selection. The largest impact is found in SR 3B  $m_{\text{eff}}^{\text{bin}_2}$  amounting up to 15%, which is still minor compared with the other systematics sources. The statistical behavior is carefully taken into account in the fit, as detailed in the Sec. 8.1.

## 8 Result

### 8.1 Statical Analysis and Hypothetical Test

**The Profile Likelihood and Treatment of Systematics** Statistical tests are performed to examine the consistency of observed data with respect to prediction of SM or that with specific signal being overlayed. This is implemented via a likelihood function based on the probability desnsity distribution (PDF) in terms of number of observed events in each signal region bin. The full representation of the likelihood is given by Eq. 99:

$$\begin{aligned}
\mathcal{L}(\mu; \mu_W^i, \mu_{\text{Top}}^i, \boldsymbol{\theta}) &= \mathcal{L}(\mathbf{n}^{\text{SR}}, \mathbf{n}^{\text{WR}}, \mathbf{n}^{\text{TR}} | \mu, \mu_W^i, \mu_{\text{Top}}^i, \boldsymbol{\theta}) \\
&= \mathcal{P}_{\text{SR}} \times \mathcal{P}_{\text{CR}} \times \prod_{k \in \text{syst.}} \rho(\theta_k), \\
\mathcal{P}_{\text{SR}} &= \prod_{i \notin \mathbf{3B}} \left[ \prod_{b \in \text{BT,BV}} \text{Pois}(n_{i,b}^{\text{SR}} | \mu s_{i,b}^{\text{SR}}(\boldsymbol{\theta}) + \mu_W^i w_{i,b}^{\text{SR}}(\boldsymbol{\theta}) + \mu_{\text{Top}}^i t_{i,b}^{\text{SR}}(\boldsymbol{\theta}) + b_{i,b}^{\text{SR}}(\boldsymbol{\theta})) \right] \\
&\quad \times \prod_{i \in \mathbf{3B}} \text{Pois}(n_i^{\text{SR}} | \mu s_i^{\text{SR}}(\boldsymbol{\theta}) + \mu_W^i w_i^{\text{SR}}(\boldsymbol{\theta}) + \mu_{\text{Top}}^i t_i^{\text{SR}}(\boldsymbol{\theta}) + b_i^{\text{SR}}(\boldsymbol{\theta})) \\
\mathcal{P}_{\text{CR}} &= \prod_i \text{Pois}(n_i^{\text{TR}} | \mu s_i^{\text{WR}}(\boldsymbol{\theta}) + \mu_W^i w_i^{\text{WR}}(\boldsymbol{\theta}) + \mu_{\text{Top}}^i t_i^{\text{WR}}(\boldsymbol{\theta}) + b_i^{\text{WR}}(\boldsymbol{\theta})) \\
&\quad \times \text{Pois}(n_i^{\text{WR}} | \mu s_i^{\text{TR}}(\boldsymbol{\theta}) + \mu_W^i w_i^{\text{TR}}(\boldsymbol{\theta}) + \mu_{\text{Top}}^i t_i^{\text{TR}}(\boldsymbol{\theta}) + b_i^{\text{TR}}(\boldsymbol{\theta})) \tag{99}
\end{aligned}$$

where  $\mathbf{n}^{\text{SR}}$ ,  $\mathbf{n}^{\text{WR}}$  and  $\mathbf{n}^{\text{TR}}$  are respectively the numbers of observed events in SRs, corresponding CRs such as WRs and TRs, with the vetro indices running over regions ;  $s_r$  is the expected signal yield in region  $r$  in the signal model to be tested;  $w_r$  and  $t_r$  are respectively the expectated yields of  $W + \text{jets}$  and  $t\bar{t}$  in region  $r$  before the normalization, with the components derived by the object replacement method being exluded;  $b_r$  are the expectated yields of the other backgrounds in region  $r$ ;  $\boldsymbol{\theta}$  is the vector of nuisance parameters for each systematic uncertainty;  $\mu_W^i$  and  $\mu_{\text{Top}}^i$  are the normalization factors for  $W + \text{jets}$  and  $t\bar{t}$  which are allowed to vary between  $i$ ; and  $\mu$  is the signal strength, a parameter describing relative normalization with respect to the signal model to be tested i.e.  $\mu = 0$  corresponds to a background-only hypothesis and  $\mu = 1$  to a hypothesis with the nominal signal level expected by the signal model. Index  $i$  runs along signal region bins joining the combined fit that are orothogonal to each other s.t. :

$$\begin{aligned}
i \in & \{ \text{ 2J, 6J, 3B } \} \\
& \text{or } \{ \text{ 2J, High-x, 3B } \} \\
& \text{or } \{ \text{ Low-x, 6J, 3B } \} \\
& \text{or } \{ \text{ Low-x, High-x, 3B } \} \tag{100}
\end{aligned}$$

where

$$\begin{aligned}
\mathbf{2J} &= \{ 2J \cdot m_{\text{eff}}^{\text{bin1}}, 2J \cdot m_{\text{eff}}^{\text{bin2}}, 2J \cdot m_{\text{eff}}^{\text{bin3}} \} \\
\mathbf{6J} &= \{ 6J \cdot m_{\text{eff}}^{\text{bin1}}, 6J \cdot m_{\text{eff}}^{\text{bin2}}, 6J \cdot m_{\text{eff}}^{\text{bin3}} \} \\
\mathbf{Low-x} &= \{ \text{Low-x} \} \\
\mathbf{High-x} &= \{ \text{High-x} \} \\
\mathbf{3B} &= \{ 3B \cdot m_{\text{eff}}^{\text{bin1}}, 3B \cdot m_{\text{eff}}^{\text{bin2}} \}
\end{aligned} \tag{101}$$

The normalization factors for  $W + \text{jets}$  and  $t\bar{t}$  backgrounds are simultaneously determined by the fit, in order to correlate the behavior of systematics. Therefore the CRs terms are also placed in the common likelihood with an identical representation as SRs.

The statistical behavior of the PDF is fully characterized by a set of independent poisson PDF, namely:

$$\text{Pois}(n|\nu) := \frac{\nu^n}{n!} e^{-\nu}$$

with  $\nu$  and  $n$  being the expected yield and observed number respectively.

The effect of a systematics (indexed by  $k$ ) are then incorporated by shifting the poisson means  $\nu$ , via a corresponding nuisance parameter  $\theta_k$  so as:

$$\nu(\theta_k) := f(\theta_k), \tag{102}$$

with  $f(\theta_k)$  being a continuous function satisfying:

$$\begin{aligned}
f(\theta_k = 0) &= \nu(0) \\
f(\theta_k = \pm 1) &= \nu(\pm 1\sigma).
\end{aligned} \tag{103}$$

$\nu(0)$  is the nominal expectation yields, while  $\nu(\pm 1\sigma)$  is given by that with the systematic variation applied by  $\pm 1\sigma$  which are evaluated beforehand.  $f(\theta_k)$  in the other  $\theta_k$  is then interpolated or extrapolated using the three points by a polynomial or an exponential function, providing a continuous functional form of  $\mathcal{L}$  in terms of  $\boldsymbol{\theta}$ .

What is here intend to do is to perform a global fit on data, simultaneously determining  $\mu, \mu_W^i, \mu_{\text{Top}}^i$  and  $\boldsymbol{\theta}$  by minimizing the likelihood  $\mathcal{L}$  (Eq. 99). While the  $\mu, \mu_W^i$  and  $\mu_{\text{Top}}^i$  are allowed to flow based on our total ignorance, the shifts of the nuisance parameters  $\boldsymbol{\theta}$  need to be restricted reflecting the level of our confidence. This is implemented by the last terms in the likelihood  $\rho(\theta_k)$  known as the “penalty terms” serving as the prior constraints for the likelihood. The form of the penalty terms depends on the statistical nature of each systematics:

- A Gaussian PDF is commonly assumed for most systematic uncertainties:

$$\rho(\theta) = \frac{1}{\sqrt{2\pi}\sigma} \exp\left(-\frac{\theta^2}{2}\right) \tag{104}$$

- The Gamma PDF is used to describe uncertainties following according to Poisson distribution, typically associated with the number of data events in control regions, or selected MC events:

$$\rho(a) = \frac{\nu^a}{a!} e^{-\nu} \tag{105}$$

where  $a$  is related with  $\theta$  using the symmetrized uncertainty  $\sigma$  by

$$\theta = \frac{a - \nu}{\sigma} \quad (106)$$

A multi-dimensional minimization over the parameter spaces of all the normalization factors, nuisance parameters and signal strength <sup>17</sup> is performed by the Minuit2 algorithm [?] interfaced by a number wrapper packages; HistFitter [?], HistFactory [?] and RooFit [?]. Signal strength and the background normalization factors are allowed to range  $0 \sim 5$ , while nuisance parameters are to moved by  $-5\sigma \sim 5\sigma$  during the fit. Systematics found have tiny enough impact on the yields in the SRs/CRs region bins (evaluated by the Kolmogorov-Smirnov test) are excluded from the fit so as to reduce the redundant dimensions of scan (“pruning”).

**Hypothetical Testing** A hypothetical test against a hypothesis  $H$  is done by examining the compatibility with observation, via p-value. P-value for testing hypothesis  $H$  is commonly defined as the probability to find even rarer outcome than the observation under  $H$ . For the simplest one bin counting experiment where signal is manifested as an data excess, the p-value is then:

$$p_\mu := \sum_{n=n_{\text{obs}}}^{\infty} L(n|\mu) \quad (107)$$

using the number of observed events  $n_{\text{obs}}$  as the test static. One would claim a discovery against the null hypothesis  $H_0$  if the  $p_0$  is significantly low that the observation can be hardly ascribed to statistical fluctuation out of  $H_0$ . In the field of high energy physics experiment, this is usually set to one corresponding to  $5\sigma$  gaussian standard deviation ( $\sim 10^{-7}$ ).

On the other hand, one can claim the exclusion of a signal hypothesis  $H_1$  when  $p_1$  is reasonably low.  $p_1 < 0.05$  is conventionally used as the threshold, equivalent to an exclusion with 95% confidence level. There are circumstances where observation does not agree with either  $H_0$  and  $H_1$  due to statistical fluctuation or more seriously poor understanding to backgrounds, and result in strong exclusion power typically when data undershoots the expectation. In LHC, in order to prevent such potentially unreasonably strong exclusion, a modified measure  $\text{CL}_s$  is used:

$$\text{CL}_s := \frac{p_1}{p_0}, \quad (108)$$

and  $\text{CL}_s < 0.05$  is accepted as the equivalence of an exclusion at 95% confidence level.

In presence of multiple test statics ( $\mathbf{n}^{\text{SR}}$ ) together with bunches of nuisance parameters, it is not obvious how to define the “rareness” on the multi-dimension of space. In such cases, likelihood is often chosen as the test static projecting n-dimension observables into 1 dimension, as well as providing a well-defined measure

---

<sup>17</sup>Remind that we have 8 – 16 normalization factors and  $\sim 150$  nuisance parameters in case of combined fit over all SR towers.

of ‘‘reareness’’ by definition. In LHC analysis, a normalized likelihood test static  $\lambda_\mu$  is widely used:

$$\lambda_\mu = \begin{cases} \frac{\mathcal{L}(\mu, \hat{\theta}(\mu))}{\mathcal{L}(\hat{\mu}, \hat{\theta})} & (\hat{\mu} > 0) \\ \frac{\mathcal{L}(\mu, \hat{\theta}(\mu))}{\mathcal{L}(0, \hat{\theta}(0))} & (\hat{\mu} < 0) \end{cases} \quad (109)$$

where  $\hat{\theta}(\mu)$  denotes the best-fit nuisance parameters with fixed  $\mu$ , while  $\hat{\mu}$  and  $\hat{\theta}$  the best-fit parameters with  $\mu$  is allowed to float.  $\mathcal{L}(\mu, \hat{\theta}(\mu))$  presents the conditional likelihood normalized by the  $\mu$ -agonistic denominator  $\mathcal{L}(\hat{\mu}, \hat{\theta})$ , forcing the range of  $\lambda_\mu$  to  $0 < \lambda_\mu < 1$ .

The p-value is finally defined as:

$$p_\mu := \int_{q_{\mu, \text{obs}}}^{\infty} f(q_\mu | \mu) dq_\mu \quad (110)$$

where  $q_\mu$  is:

$$q_\mu = \begin{cases} -2 \log \lambda(\mu) & (\hat{\mu} < \mu) \\ 0 & (\hat{\mu} > \mu) \end{cases}. \quad (111)$$

$f(q_\mu)$  is the PDF that  $q_\mu$  obeys, defined by the variation of  $q_\mu$  when suffering from both the statistical fluctuation as well as systematics. Unlike the PDF in the simplest counting experiment Eq. 107,  $f(q_\mu)$  is in generally unknown neither modeled analytically thus needs a bunch of toy experiments to determine; scanning from  $\mu = 0$  upto  $\mu = 5 \sim 10$  with a finite step, on each of which a number of the likelihood fits are performed with different fluctuating data statistics and systematic variation applied. This is an incredibly crazy course of computation, and we have to go relying on some analytical approximation after all.

<sup>18</sup>

Fortunately, there are a couple of powerful approximation formula known as Wald’s approximation [?]:

$$q_\mu = -2 \log \lambda(\mu) = \frac{\mu - \hat{\mu}}{\sigma^2} + O(1/\sqrt{N}) \quad (112)$$

and the asymptotic formula based on the Asimov dataset [?]:

$$\begin{aligned} f(q_\mu, \mu) &= \frac{1}{\sqrt{q_\mu}} \frac{1}{\sqrt{2\pi}} \left[ \exp \left( -\frac{1}{2} (\sqrt{q_\mu} + \sqrt{R}) \right) + \exp \left( -\frac{1}{2} (\sqrt{q_\mu} - \sqrt{R}) \right) \right], \\ R &:= \frac{(\mu - \hat{\mu})^2}{\sigma^2}, \end{aligned} \quad (113)$$

with Wald’s approximation 112 being applied.  $\sigma$  is the fitting error on  $\hat{\mu}$  and  $N$  symbolizes the magnitude of number of events in signal regions, with which the PDF  $f(q_\mu)$  can be determined by only one fit.

One disclaimer is however about the validity of the approximation where  $O(1/\sqrt{N})$  terms are ignored. This may not be the case given that the signal regions typically contains events less than 5. In the thesis, the result for background-only hypothesis (shown in Sec. 8.2) is derived using the rigid toy experiments, however the Asimov’s formula (Eq.113) is nevertheless used for limit setting due to the unrealistic computing time required for the toy experiments.<sup>19</sup>

<sup>18</sup>Each likelihood fit takes approximately 8-15 minutes.

<sup>19</sup>This is in fact how ATLAS/CMS provides the result. We have to admit the imperfection but this is the best thing we could afford to do.

## 8.2 Unblinded Signal Regions with Background-only Hypothesis

The background expectation in signal regions for null singal hypothesis are determined tower-by-tower, by performing a simoultaneous fit on the normalization factors ( $\mu_W$ ,  $\mu_{Top}$ ) as well as the nuisance parameters associated to systematics uncertainties, using all the relevant bins of control regions and signal regions. The post-fit uncertainties are summarized in Figure 137.

For the low  $m_{\text{eff}}$ -bins, typically the estimation precision is at 20% level where theory systematics is the main souce. The signal region bins with tightest selection end up in 40%  $\sim$  60% of total uncertainty, dominated by the control region statistics in the object replacement method.

The unblinded yields of observed data together with the expected backgrounds in the signal regions are shown in Table 50 - 52. Observed data are found to be consistent in general, with no signal regions exhibiting the deviation more than  $2\sigma$ . The pulls between data and expectation is shown in Figure 145.

Figure ??-?? show the kinematical distributions of either data and prediction in unblinded signal regions.

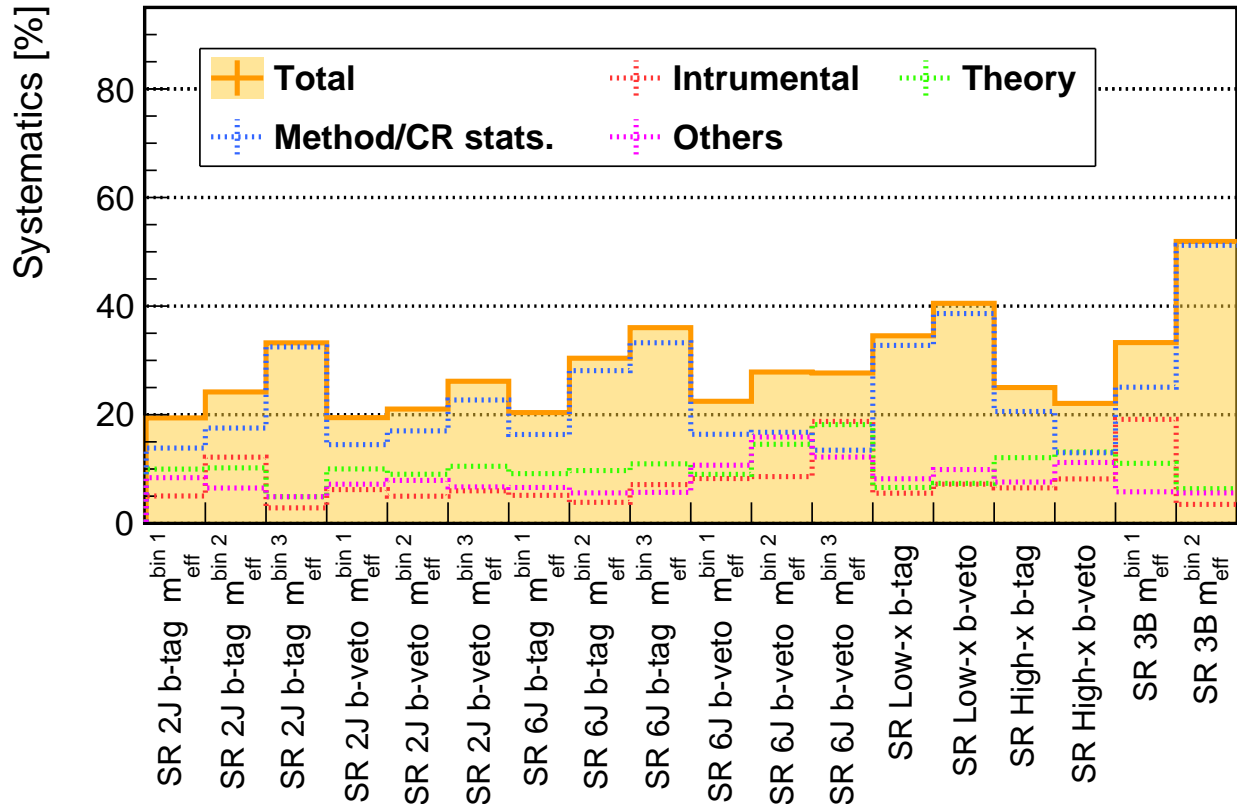


Figure 137: Post-fit systematic uncertainty with respective to the expected yield in the signal regions. Total systematics uncertainty is shown by the filled orange histogram, and the breakdowns are by dashed lines. While the systematics in b-tagged bins are purely dominated by control region statistics, it is comparable to the other sources in the b-veto bins. The overall uncertainty ranges between 20%  $\sim$  50%.

Table 50: Observed yields and backgrounds expectation in the signal region bins in tower **2J** and **6J**. Background component estimated by the object replacement are denoted as “Di-leptonic”, while the others are derived from the kinematical extrapolation method. Displayed errors are only systematics uncertainty.

<b>SR 2J</b> <i>b</i> -tag	$m_{\text{eff.}} \in [1100, 1500]$	$m_{\text{eff.}} \in [1500, 1900]$	$m_{\text{eff.}} > 1900$
Observed data	8	2	1
Expected background	$7.20 \pm 1.40$	$2.46 \pm 0.60$	$2.31 \pm 0.77$
Di-leptonic	$2.4 \pm 1.0$	$0.8 \pm 0.4$	$1.7 \pm 0.7$
$W + \text{jets}$	$1.0 \pm 0.5$	$0.1^{+0.2}_{-0.1}$	$0.0 \pm 0.0$
$Z + \text{jets}$	$0.6 \pm 0.2$	$0.2 \pm 0.0$	$0.1 \pm 0.0$
Tops	$2.1 \pm 0.7$	$0.8 \pm 0.3$	$0.4 \pm 0.2$
Di-boson	$0.4 \pm 0.1$	$0.2 \pm 0.2$	$0.1 \pm 0.0$
$t\bar{t} + V$	$0.8 \pm 0.2$	$0.3 \pm 0.1$	$0.1 \pm 0.0$
<b>SR 2J</b> <i>b</i> -veto	$m_{\text{eff.}} \in [1100, 1500]$	$m_{\text{eff.}} \in [1500, 1900]$	$m_{\text{eff.}} > 1900$
Observed data	25	8	6
Expected background	$13.33 \pm 2.59$	$6.84 \pm 1.44$	$2.53 \pm 0.66$
Di-leptonic	$2.4 \pm 1.8$	$2.3 \pm 1.1$	$0.7 \pm 0.6$
$W + \text{jets}$	$4.2 \pm 1.1$	$1.6 \pm 0.4$	$0.4 \pm 0.2$
$Z + \text{jets}$	$2.3 \pm 0.7$	$1.0 \pm 0.3$	$0.6 \pm 0.2$
Tops	$1.1 \pm 0.4$	$0.3 \pm 0.1$	$0.2 \pm 0.1$
Di-boson	$3.2 \pm 1.1$	$1.6 \pm 0.5$	$0.7 \pm 0.2$
$t\bar{t} + V$	$0.1 \pm 0.0$	$0.1 \pm 0.0$	$0.0 \pm 0.0$
<b>SR 6J</b> <i>b</i> -tag	$m_{\text{eff.}} \in [1100, 1600]$	$m_{\text{eff.}} \in [1600, 2100]$	$m_{\text{eff.}} > 2100$
Observed data	7	3	0
Expected background	$5.09 \pm 1.04$	$2.14 \pm 0.65$	$2.46 \pm 0.89$
Di-leptonic	$2.6 \pm 0.8$	$1.1 \pm 0.6$	$1.5 \pm 0.8$
$W + \text{jets}$	$0.4 \pm 0.2$	$0.1 \pm 0.1$	$0.1 \pm 0.1$
$Z + \text{jets}$	$0.0^{+0.0}_{-0.0}$	$0.0 \pm 0.0$	$0.0^{+0.0}_{-0.0}$
Tops	$1.0 \pm 0.4$	$0.5 \pm 0.2$	$0.6 \pm 0.3$
Di-boson	$0.2 \pm 0.1$	$0.1 \pm 0.1$	$0.1^{+0.1}_{-0.1}$
$t\bar{t} + V$	$0.8 \pm 0.2$	$0.3 \pm 0.1$	$0.1 \pm 0.0$
<b>SR 6J</b> <i>b</i> -veto	$m_{\text{eff.}} \in [1100, 1600]$	$m_{\text{eff.}} \in [1600, 2100]$	$m_{\text{eff.}} > 2100$
Observed data	5	0	1
Expected background	$3.93 \pm 0.88$	$1.28 \pm 0.36$	$0.65 \pm 0.18$
Di-leptonic	$1.5 \pm 0.6$	$0.2^{+0.2}_{-0.2}$	$0.0 \pm 0.0$
$W + \text{jets}$	$1.1 \pm 0.5$	$0.6 \pm 0.3$	$0.3 \pm 0.1$
$Z + \text{jets}$	$0.2 \pm 0.1$	$0.0 \pm 0.0$	$0.0 \pm 0.0$
Tops	$0.3 \pm 0.1$	$0.1 \pm 0.1$	$0.1 \pm 0.1$
Di-boson	$0.7 \pm 0.2$	$0.3 \pm 0.1$	$0.2 \pm 0.1$
$t\bar{t} + V$	$0.1 \pm 0.0$	$0.0 \pm 0.0$	$0.0 \pm 0.0$

Table 51: Observed yields and backgrounds expectation in the signal region bins in tower **Low-x** and **High-x**. Background component estimated by the object replacement are denoted as “Di-leptonic”, while the others are derived from the kinematical extrapolation method. Displayed errors are only systematics uncertainty.

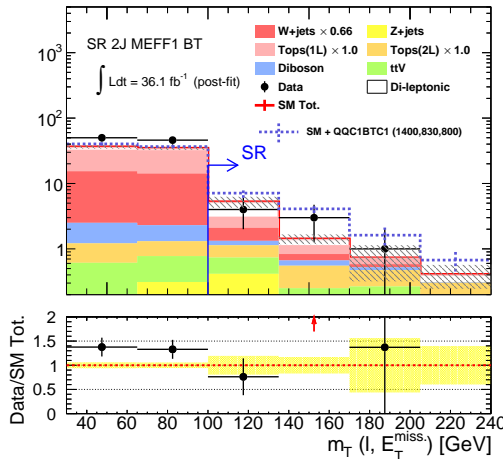
<b>SR Low-x</b>	<i>b</i> -tag	<i>b</i> -veto
Observed data	0	3
Expected background	$2.04 \pm 0.70$	$1.46 \pm 0.59$
Di-leptonic	$1.2 \pm 0.7$	$0.6 \pm 0.5$
$W + \text{jets}$	$0.1 \pm 0.0$	$0.2 \pm 0.1$
$Z + \text{jets}$	$0.0 \pm 0.0$	$0.1 \pm 0.0$
Tops	$0.6 \pm 0.2$	$0.4 \pm 0.2$
Di-boson	$0.1 \pm 0.0$	$0.2 \pm 0.1$
$t\bar{t} + V$	$0.1 \pm 0.0$	$0.0 \pm 0.0$

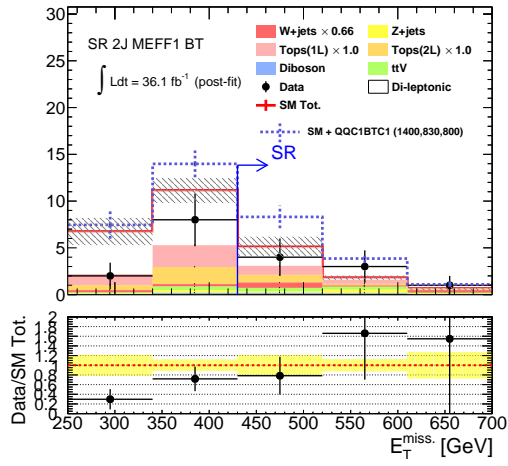
<b>SR High-x</b>	<i>b</i> -tag	<i>b</i> -veto
Observed data	6	4
Expected background	$2.35 \pm 0.59$	$4.27 \pm 0.94$
Di-leptonic	$0.8 \pm 0.5$	$0.8 \pm 0.5$
$W + \text{jets}$	$0.3 \pm 0.1$	$1.7 \pm 0.5$
$Z + \text{jets}$	$0.0^{+0.0}_{-0.0}$	$0.5 \pm 0.2$
Tops	$0.5 \pm 0.2$	$0.1 \pm 0.1$
Di-boson	$0.4 \pm 0.2$	$1.1 \pm 0.5$
$t\bar{t} + V$	$0.3 \pm 0.1$	$0.1 \pm 0.0$

Table 52: Observed yields and backgrounds expectation in the signal region bins in tower **3B**. Background component estimated by the object replacement are denoted as “Di-leptonic”, while the others are derived from the kinematical extrapolation method. Displayed errors are only systematics uncertainty.

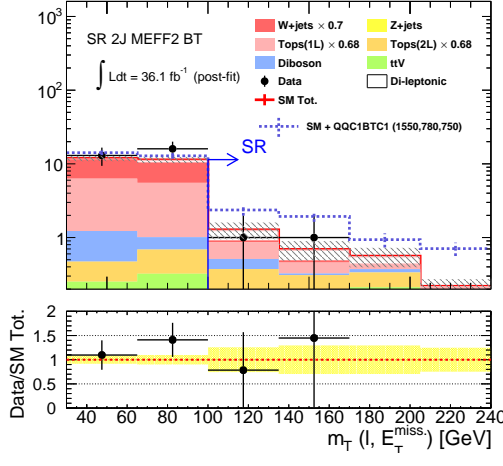
<b>SR 3B</b>	$m_{\text{eff.}} \in [1000, 1750]$	$m_{\text{eff.}} > 1750$
Observed data	2	1
Expected background	$2.06 \pm 0.68$	$1.00 \pm 0.52$
Di-leptonic	$1.3 \pm 0.5$	$0.8 \pm 0.5$
$W + \text{jets}$	$0.0 \pm 0.0$	$0.0 \pm 0.0$
$Z + \text{jets}$	$0.0 \pm 0.0$	$0.0 \pm 0.0$
Tops	$0.6 \pm 0.4$	$0.2 \pm 0.1$
Di-boson	$0.0 \pm 0.0$	$0.0 \pm 0.0$
$t\bar{t} + V$	$0.2 \pm 0.1$	$0.1 \pm 0.0$



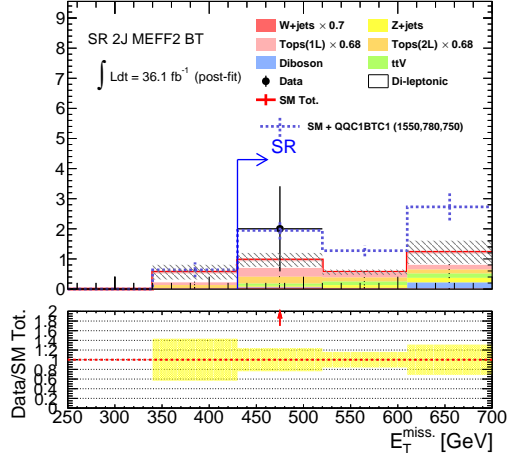
(a)



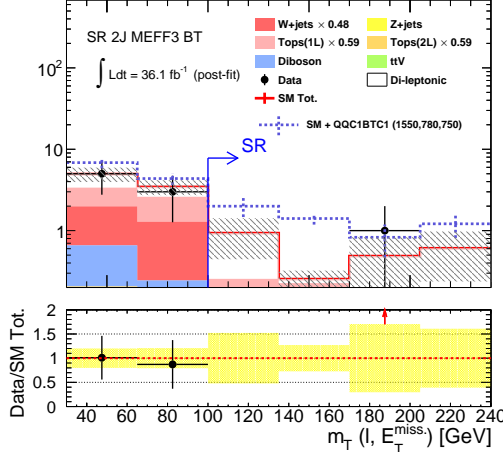
(b)



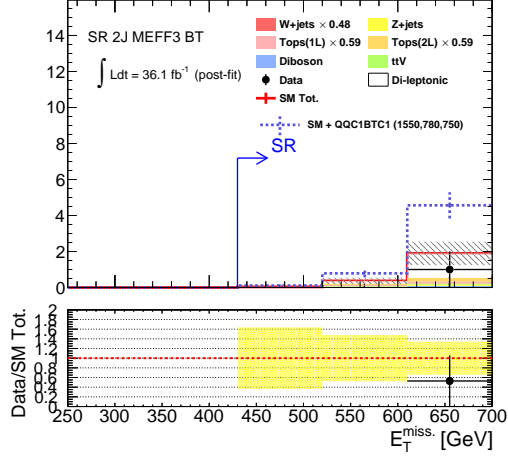
(c)



(d)



(e)



(f)

Figure 138: Post-fit distribution of (left)  $m_T$ , and (right)  $E_T^{\text{miss}}$ . (a,b) SR 2J- $m_{\text{eff}}^{\text{bin}1}$  BT. (c,d) SR 2J- $m_{\text{eff}}^{\text{bin}2}$  BT. (e,f) SR 2J- $m_{\text{eff}}^{\text{bin}3}$  BT. The yellow band in the bottom panel represents statistical error. The overflow is included in the highest bin.

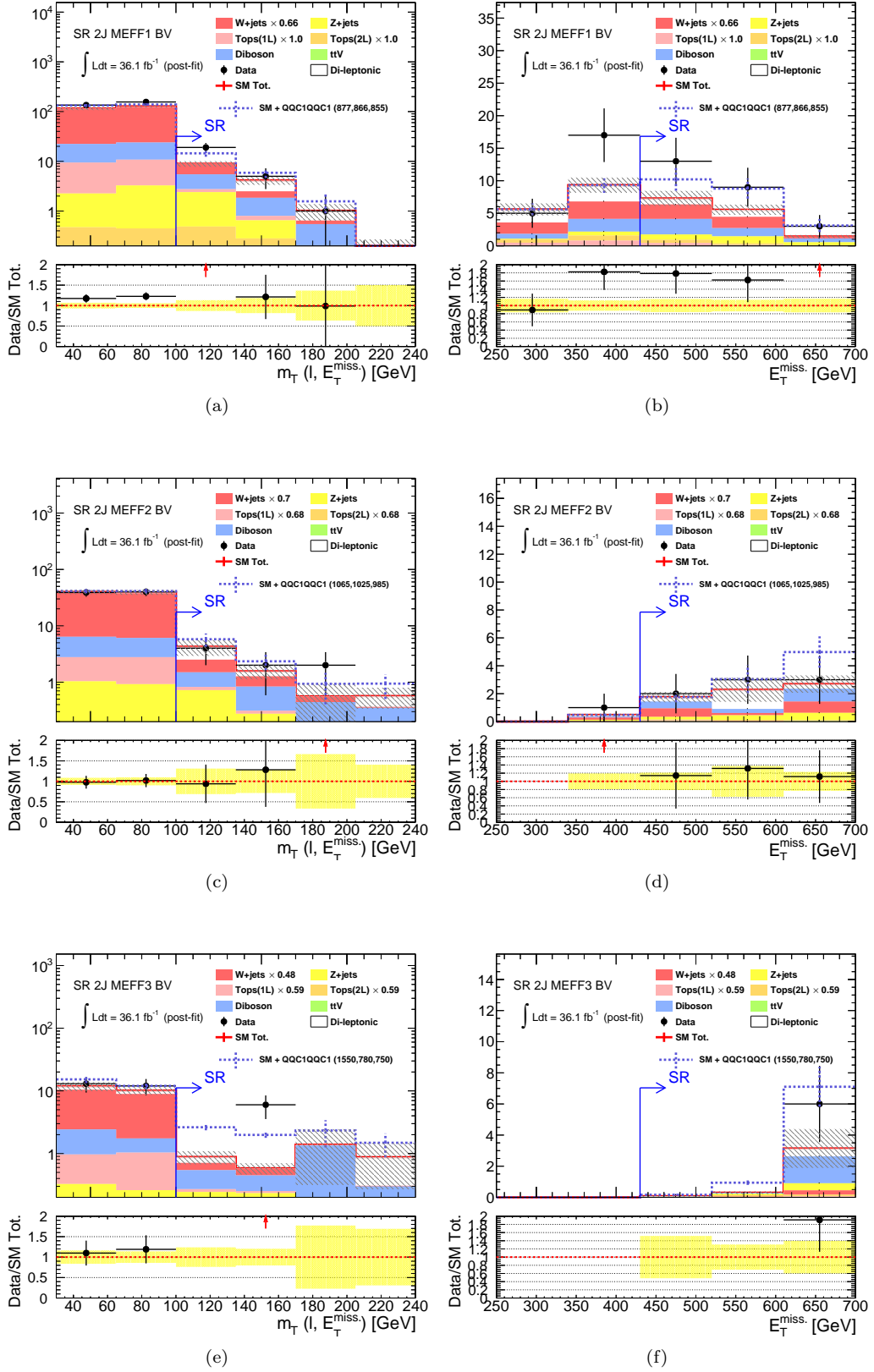


Figure 139: Post-fit distribution of (left)  $m_T$ , and (right)  $E_T^{\text{miss}}$ . (a,b) SR 2J- $m_{\text{eff}}^{\text{bin}1}$  BV. (c,d) SR 2J- $m_{\text{eff}}^{\text{bin}2}$  BV. (e,f) SR 2J- $m_{\text{eff}}^{\text{bin}3}$  BV. The yellow band in the bottom panel represents statistical error. The overflow is included in the highest bin.

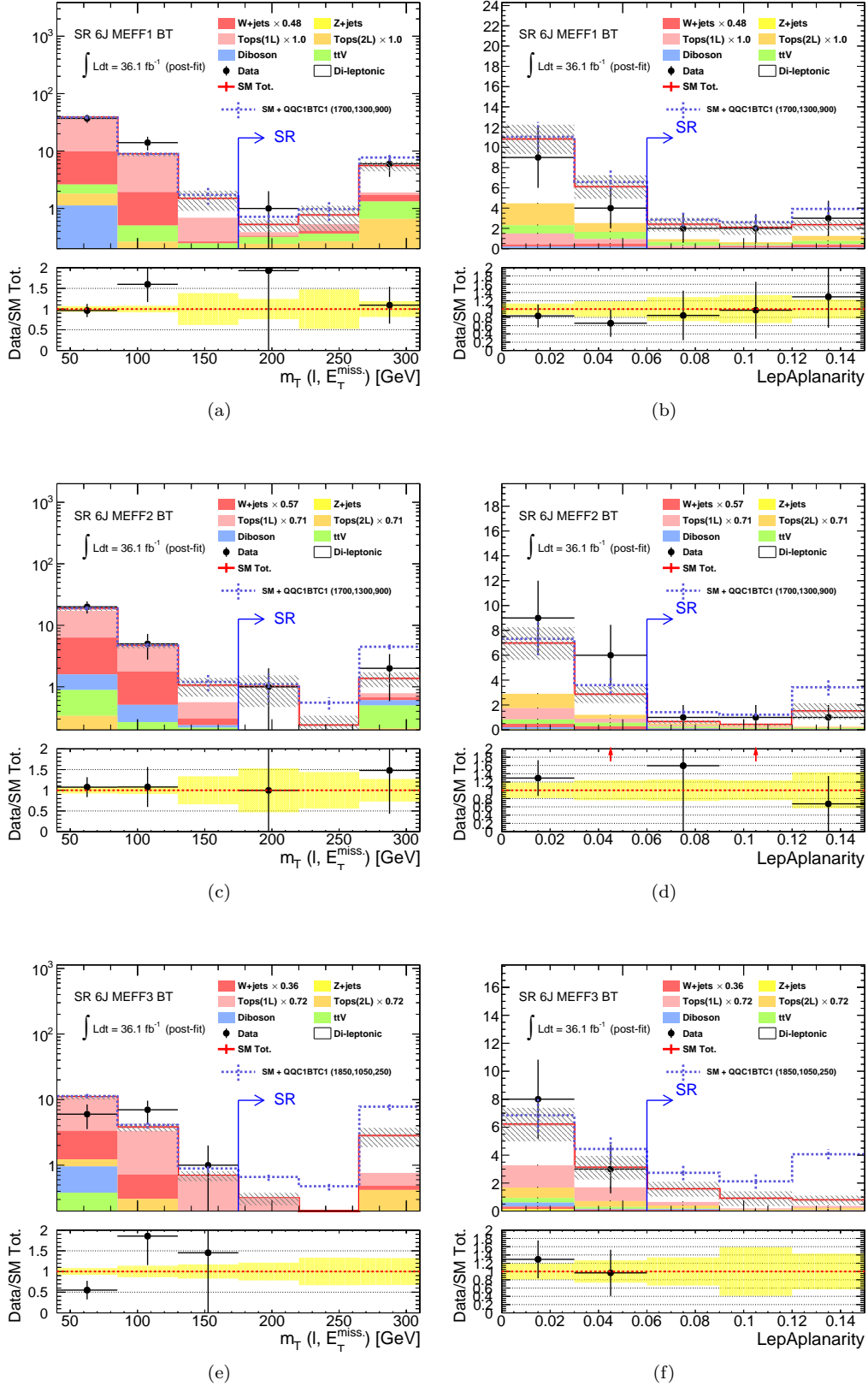


Figure 140: Post-fit distribution of (left)  $m_T$ , and (right) aplanarity. (a,b) SR 6J- $m_{\text{eff}}^{\text{bin}1}$  BT. (c,d) SR 6J- $m_{\text{eff}}^{\text{bin}2}$  BT. (e,f) SR 6J- $m_{\text{eff}}^{\text{bin}3}$  BT. The yellow band in the bottom panel represents only statistical error. The overflow is included in the highest bin.

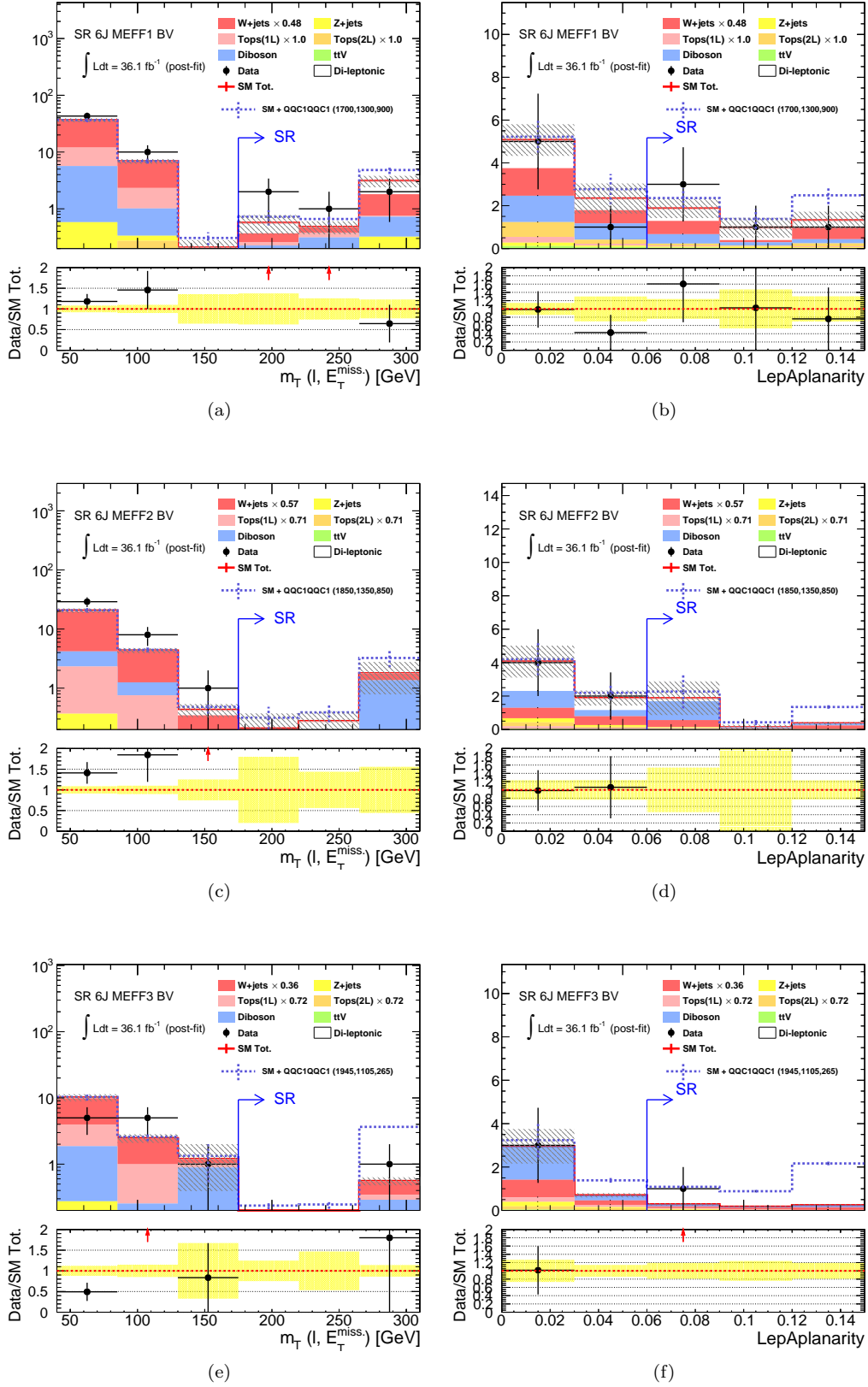


Figure 141: Post-fit distribution of (left)  $m_T$ , and (right) aplanarity. (a,b) SR 6J- $m_{\text{eff}}^{\text{bin}1}$  BV. (c,d) SR 6J- $m_{\text{eff}}^{\text{bin}2}$  BV. (e,f) SR 6J- $m_{\text{eff}}^{\text{bin}3}$  BV. The yellow band in the bottom panel represents only statistical error. The overflow is included in the highest bin.

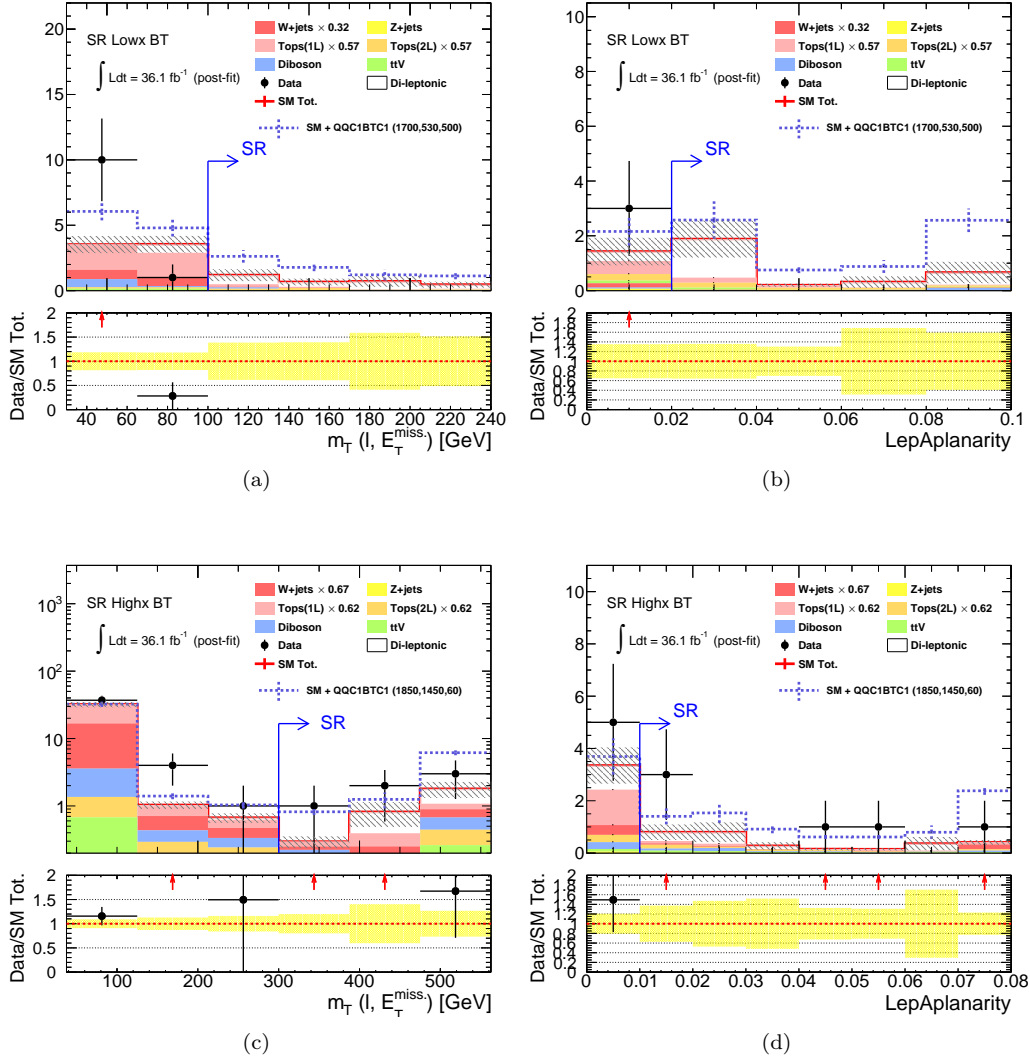


Figure 142: Post-fit distribution of (left)  $m_T$  and (right) aplanarity. (a,b) SR Low-x BT. (c,d) SR High-x BT. The yellow band in the bottom panel represents only statistical error. The overflow is included in the highest bin.

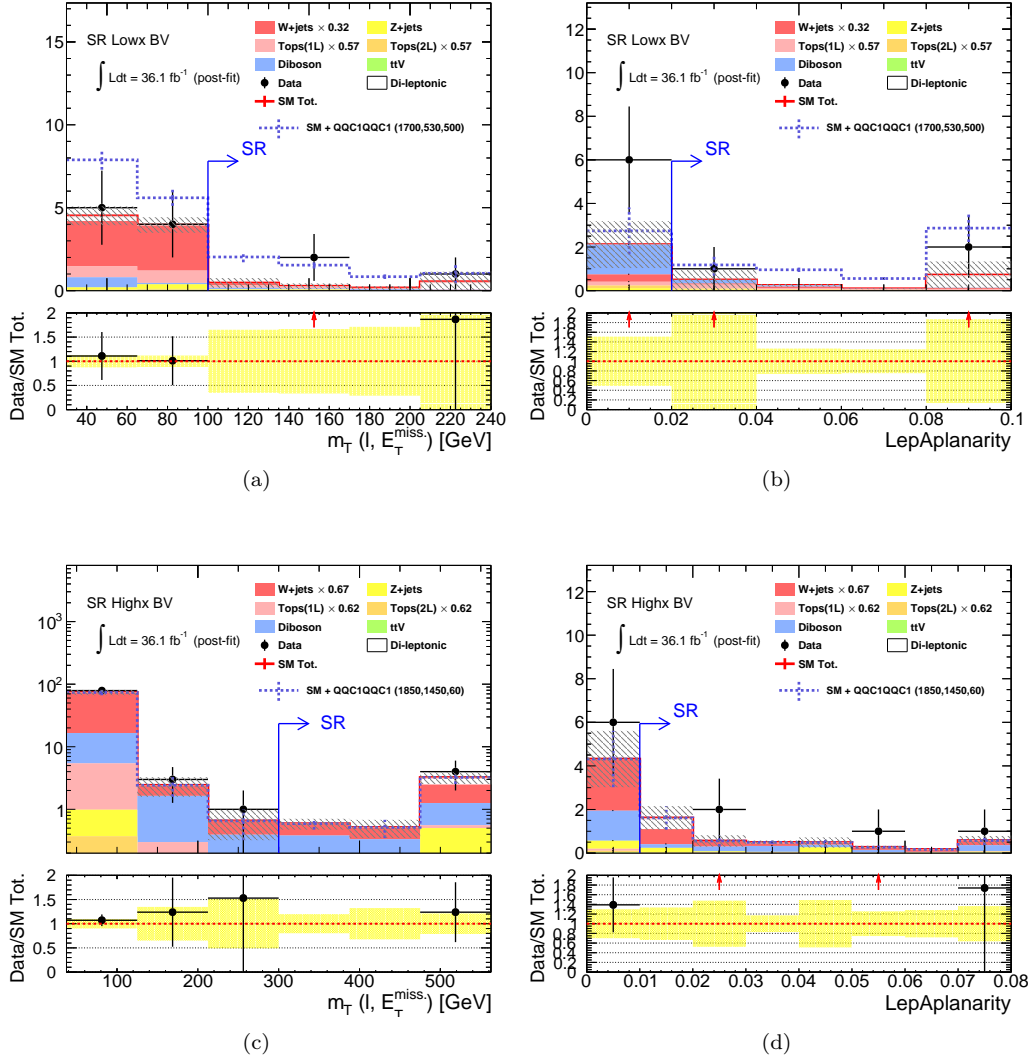


Figure 143: Post-fit distribution of (left)  $m_T$  and (right) aplanarity. (a,b) SR Low-x BV. (c,d) SR High-x BV. The yellow band in the bottom panel represents only statistical error. The overflow is included in the highest bin.

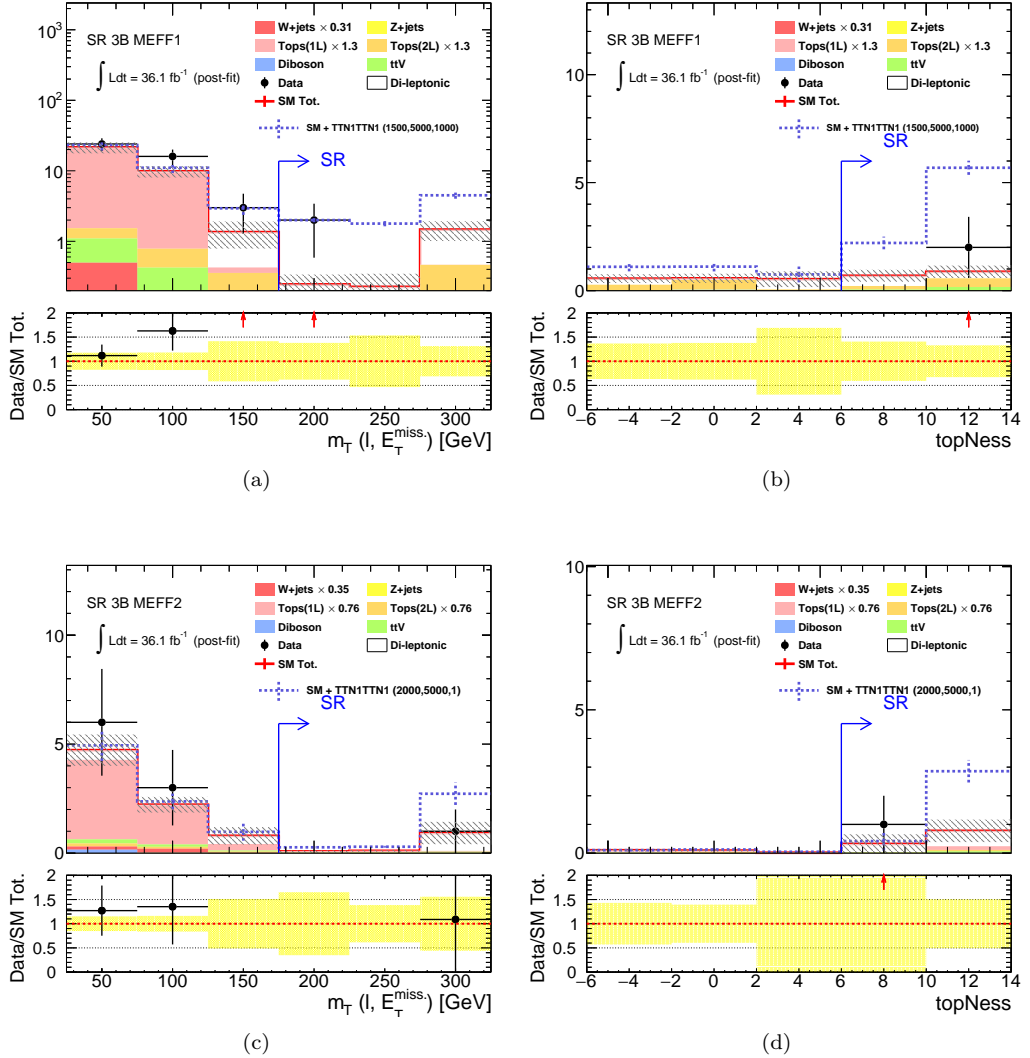


Figure 144: Post-fit distribution of (left)  $m_T$ , and (right) topness. (a,b) SR 3B- $m_{\text{eff}}^{\text{bin}1}$ . (c,d) SR 3B- $m_{\text{eff}}^{\text{bin}2}$ . The yellow band in the bottom panel represents only statistical error. The overflow is included in the highest bin.

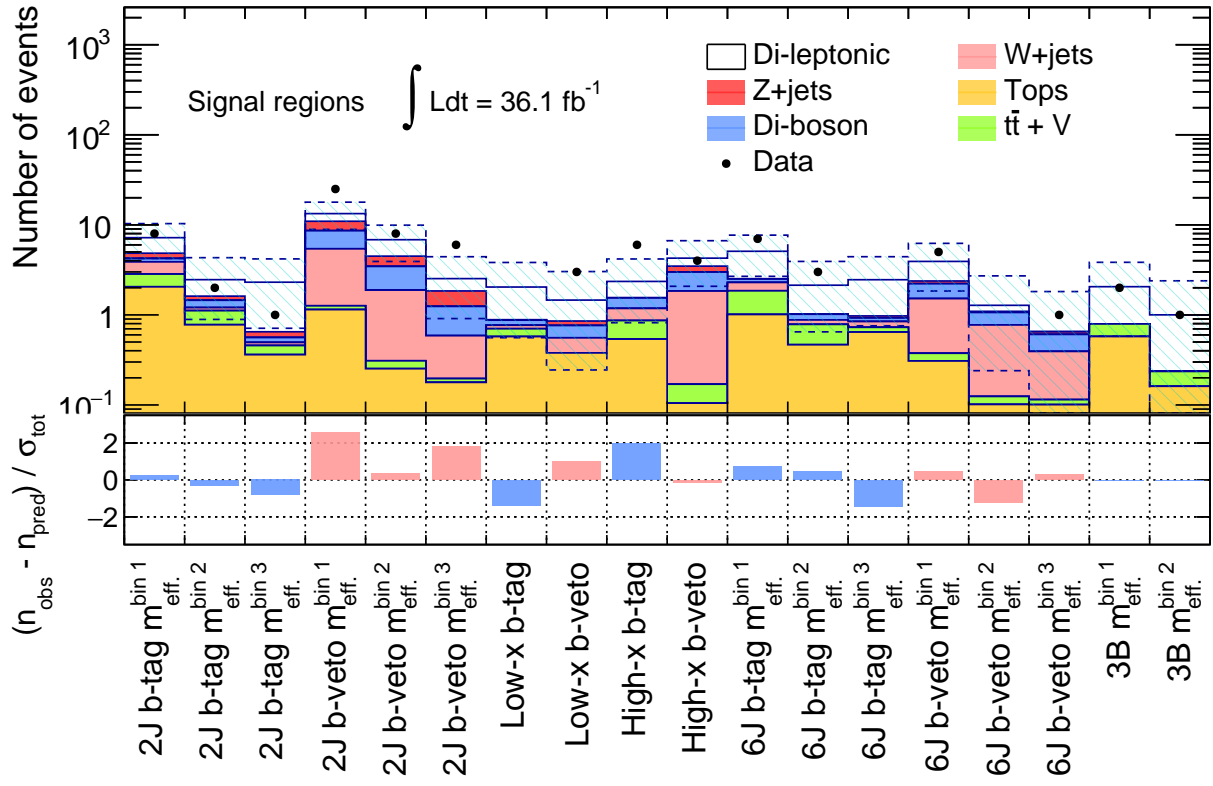


Figure 145: (Top) Observed yields and the background expectation in signal regions. The white component is the backgrounds estimated by the object replacement method, while the colored ones are by the kinamtical extrapolation method. The dashed band represents the combined statistical and systematic uncertainty on the total estimated backgrounds. (Bottom) Pull between the observed data and the expectation. No significant deviation from expectation exceeding  $2\sigma$ .

### 8.3 Constraints on the Benchmark Models

The observed results are then interpreted into constraints on the benchmark models listed in Table 5 - 7.

Figure 146 presents the exclusion limit on QQC1QQC1, the reference model for BV benchmarks (Table 5). Hypothetical tests are done with each signal point using the combination of signal regions that gives the best expected sensitivity. The excluded region is defined by areas with  $CL_s < 0.05$ , corresponding to 95% confidence level. The associated expected limit is represented by a yellow band, showing the range of obtained limit if observed data is consistent to the expectation within  $\pm 1\sigma$ . Observed limits are typically worse than the expected ones in the mass region where sensitivity is primarily driven by SR **2J** and SR **High-x**, namely the diagonal region in the  $x=1/2$  grid, and the high- $x$  region in the LSP60 grid respectively, reflecting the observed excess there which weakens the exclusion power. For the  $x=1/2$  and the LSP60 grid, limits are compared with the up-to-date published result provided by ATLAS [?], shown as grey shades. The exclusion limits are pushed forward by about 200 GeV  $\sim$  300 GeV in gluino mass. Obviously, this owes a lot to the increased data statistics by factor of 2.5 though, the benefit by the improved analysis can also be acknowledged, given that the cross-section of gluino pair production falls more rapidly with respect the gluino mass increase, which is roughly 1/3 by every 200 GeV. Up to 2 TeV of gluino mass is excluded at the most optimistic massless LSP scenario, while it also reaches about 1.9 TeV of gluino mass for the more realistic case with  $0 < m_{\tilde{\chi}_1^0} < 1$  TeV. The constraints on the scenario where EW-gauginos are compressed, represented by the DM30, DM20 grids, are explicitly investigated for the first time, which will provide useful input for a number of dark matter oriented SUSY phenomenological models, such as the well-tempered neutrino scenario. Though the limit is weaker than the typical signatures in  $x=1/2$  and LSP60, sensitivity is addressed without loopholes.

Likewise, Figure 147 exhibits the limits for model QQC1BTC1, the reference model for BT benchmarks (Table 5). As the sensitivity is mainly driven by the b-tagged bins for this model, it is relatively more affected by the  $\sim 1.9\sigma$  excess observed in the SR High-x BT, which drastically weakens the limit in the LSP60 grid. Nevertheless, the overall exclusion reach is comparable to QQC1QQC1, amounting to  $1.9 \sim 2$  TeV in gluino mass for  $m_{\tilde{\chi}_1^0} < 1$  TeV. As the asymmetric decays of gluino have never been interpreted before, this is the first explicit constraint on such class of models.

The exclusion limit for the model TTN1TTN1, the reference model for the 3B benchmarks (Table 5) is shown in Figure 148. The observed and expected limits agree as the global feature. The most prominent update from the past result [?] by ATLAS (shaded area in the plot) is around the diagonal region with the mass splitting  $\Delta m(\tilde{g}, \tilde{\chi}_1^0)$  below 400 GeV, where the explicit limit is set for the first time by the exploring the  $\geq 3$  b-tagged jets signature. On the other hand, there is seemingly no improvement in the direction toward high gluino mass despite the increased data, which is because the compared limit is provided by the combination of both 0-lepton and 1-lepton channel in the analysis. The sensitivities driven by 1-lepton channel are comparable between the analyses.

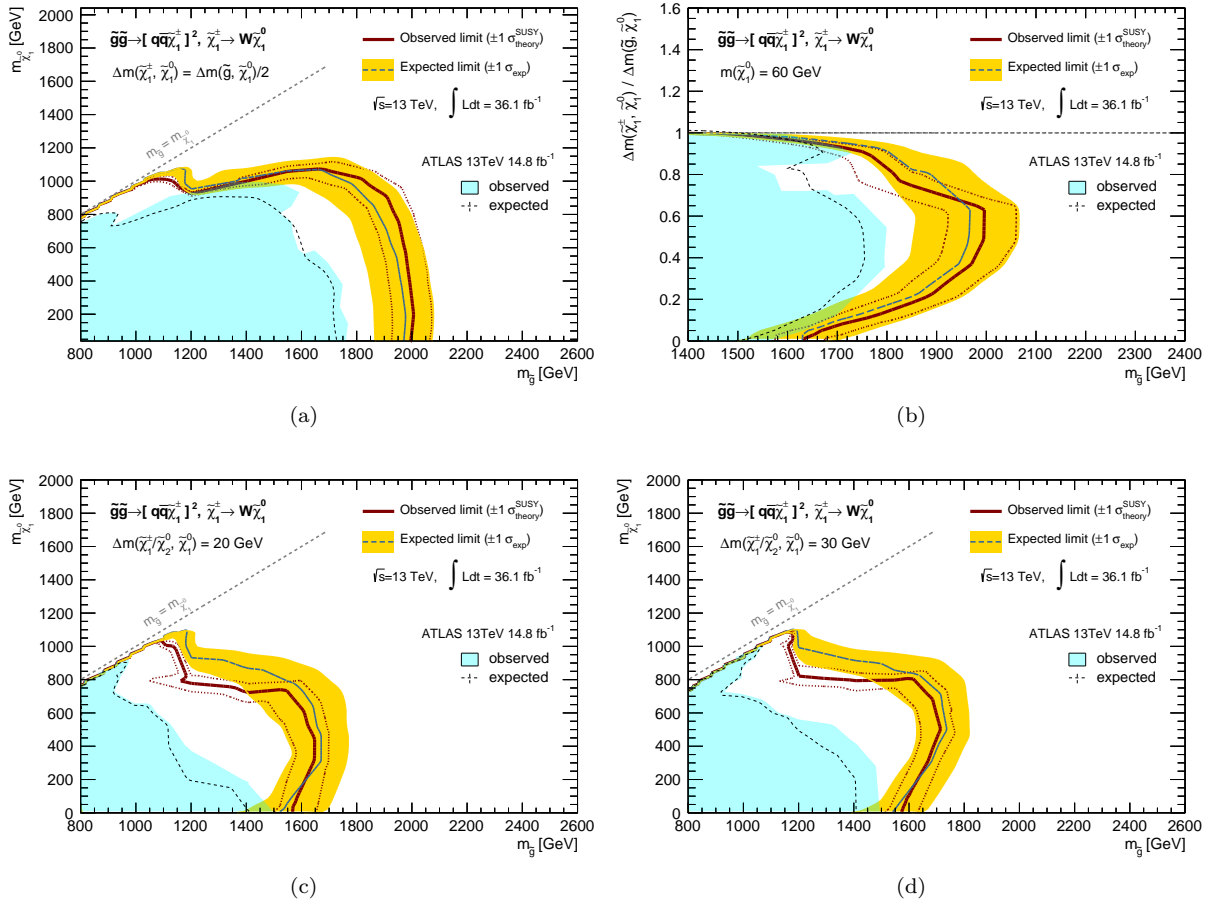


Figure 146: Exclusion limit for the benchmark model **QQC1QQC1** presented in the (a)  $x=1/2$  (b) LSP 60 (c) DM20 (d) DM30 grids. Observed limit is shown by the solid red line, while the expected limit are expressed by the dashed blue line with the yellow band describing the variation due to the deviation within  $\pm 1\sigma$ . The up-to-date published result provided by ATLAS [?] is overlaid (observed limit: grey shade, expected limit: black dashed line). All limits correspond to 95% CL.

The exclusion limits for all the 45 models and grids are calculated similarly. Observed limits are compared in Figure 149-153. Models in the same BV/BT/3B type (defined by the different tables in Table 5 - 7) are overlaid in the same plot. Though the acceptance after the 1-lepton pre-selection are similar between them, the final sensitivity does vary depending on the branching into 1-lepton final state of the model which has relatively a wide variety. This ends up in  $300 \text{ GeV} \sim 400 \text{ GeV}$  of difference in gluino mass at the largest. This on the other hand means that the models with less sensitivity can be fully recovered by the combination with 0-lepton final state. Aside such several models with small 1-lepton branches, the variation is typically  $100 \text{ GeV} \sim 200 \text{ GeV}$ , which indicates inclusive acceptance by the analysis.

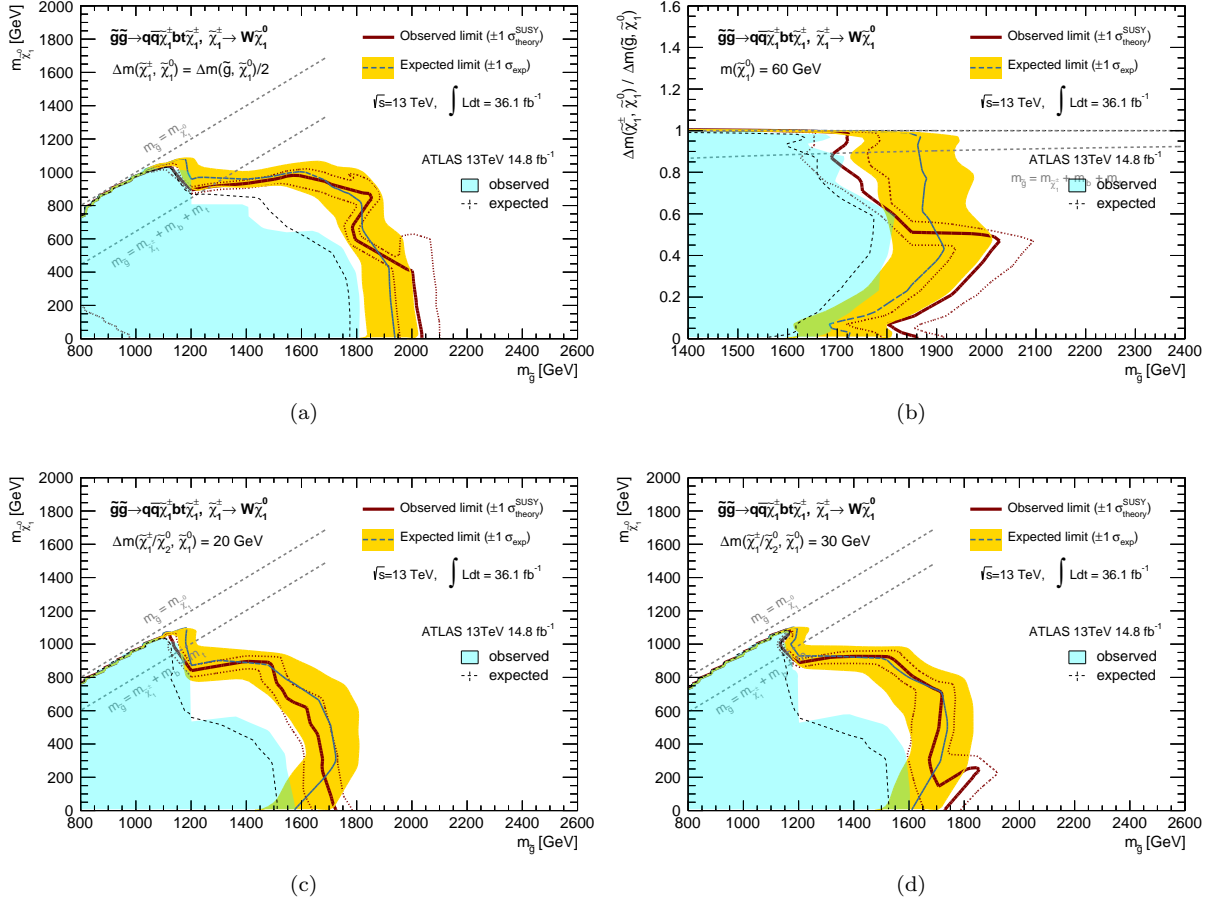


Figure 147: Projected exclusion limit (95% CL) for benchmark model **QQC1BTC1** presented in (a)  $x=1/2$  (b) LSP 60 (c) DM20 (d) DM30 . Observed limit is shown by the solid red line, while the expected limit are expressed by the dashed blue line with the yellow band describing the variation due to the deviation within  $\pm 1\sigma$ . All limits correspond to 95% CL.

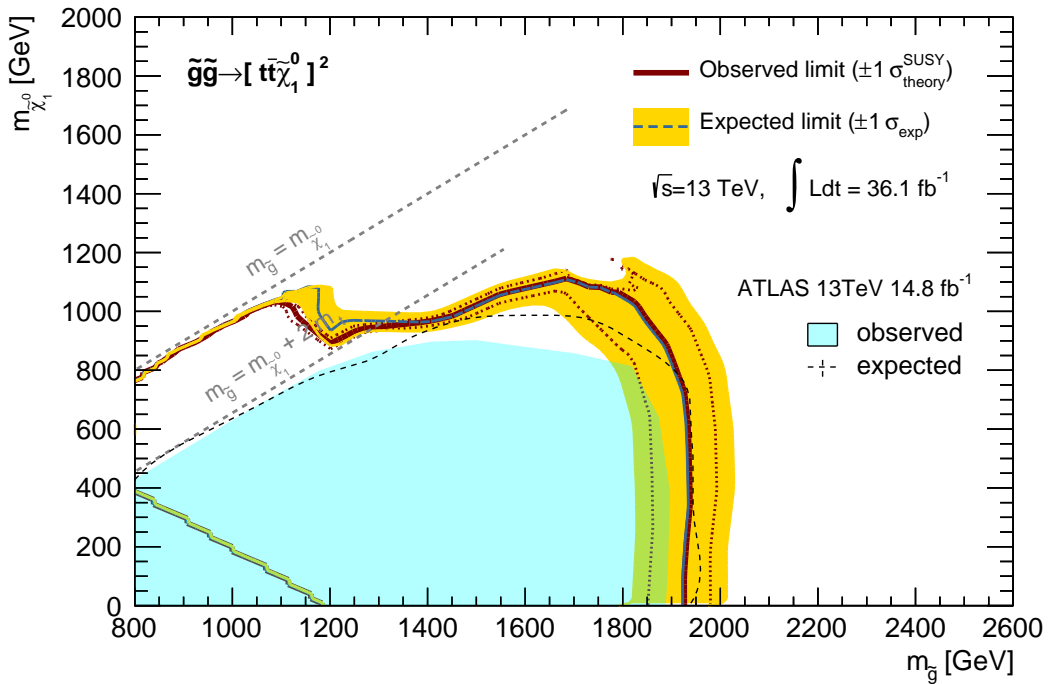


Figure 148: Exclusion limit for benchmark model **TTN1TTN1**. Observed limit is shown by the solid red line, while the expected limit are expressed by the dashed blue line with the yellow band describing the variation due to the deviation within  $\pm 1\sigma$ . The up-to-date published result provided by ATLAS [?] is overlaid (observed limit: grey shade, expected limit: black dashed line), which is given by the combination of 0-lepton and 1-lepton analyses. All limits correspond to 95% CL.

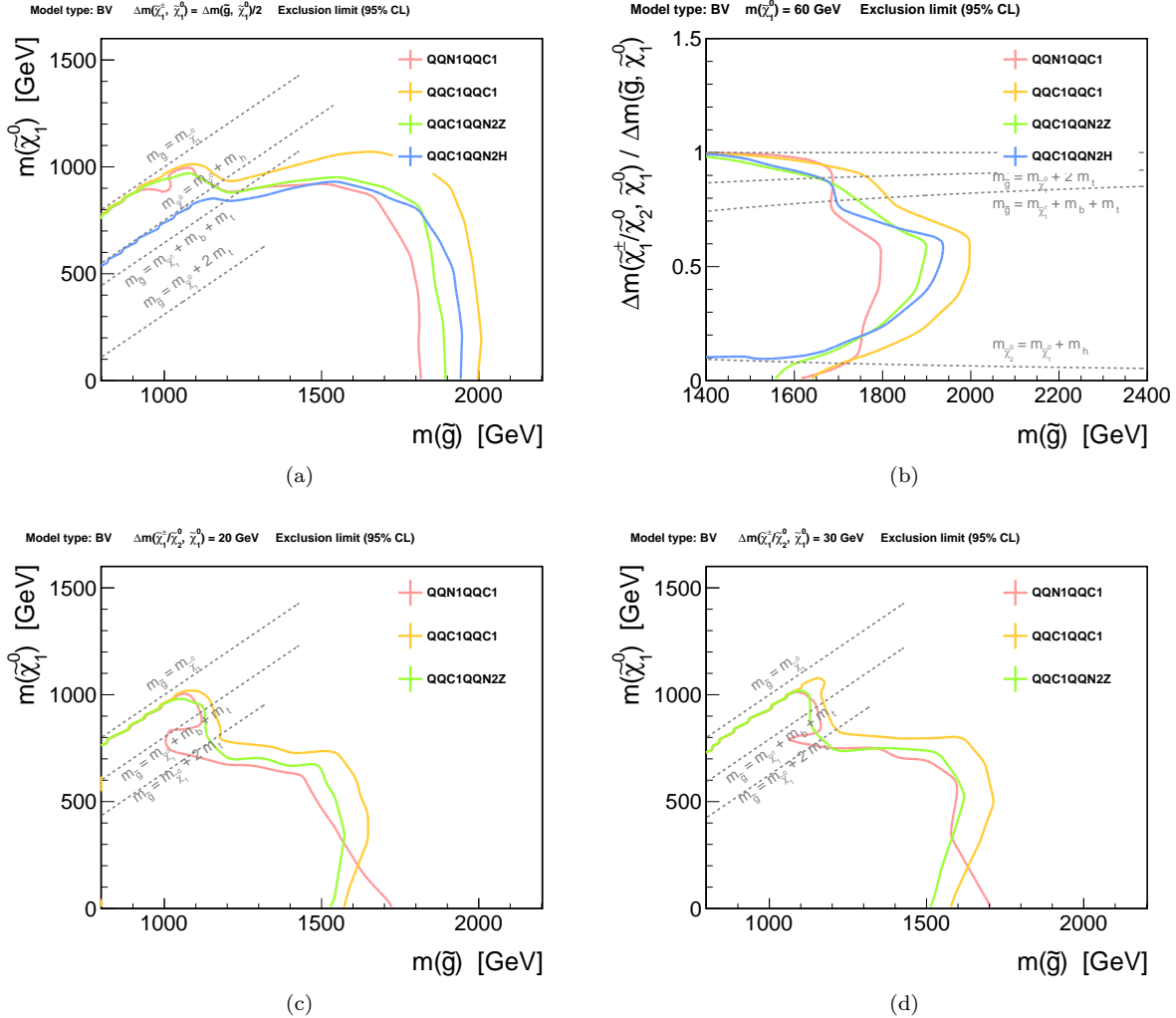


Figure 149: Observed limit for benchmark models belonging to “BV”-type in the (a)  $x=1/2$  (b) LSP 60 (c) DM20 (d) DM30 grid.

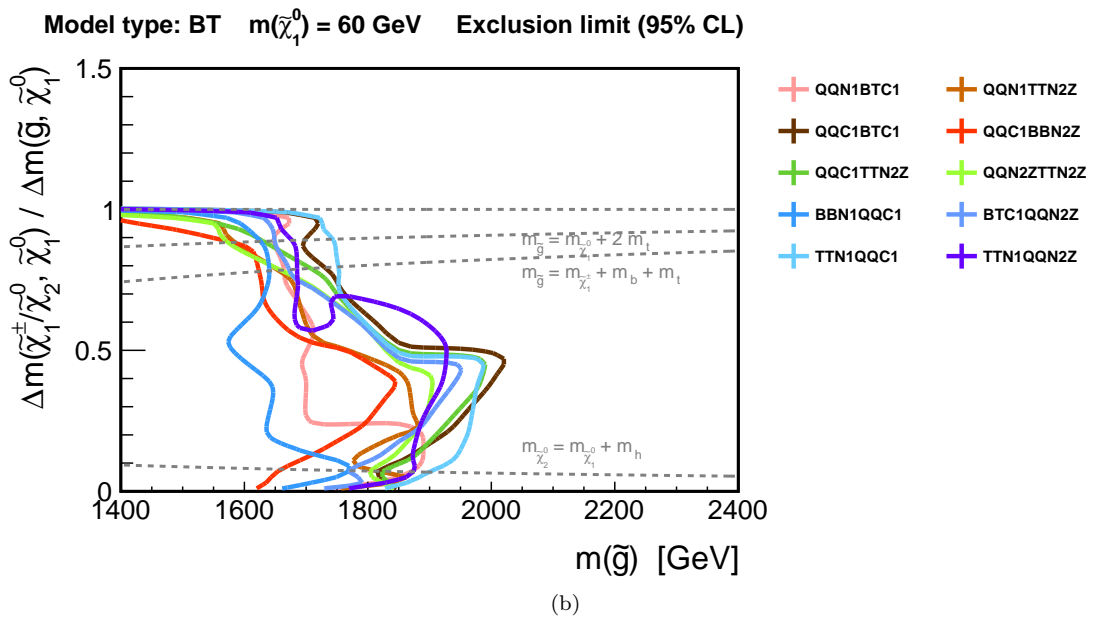
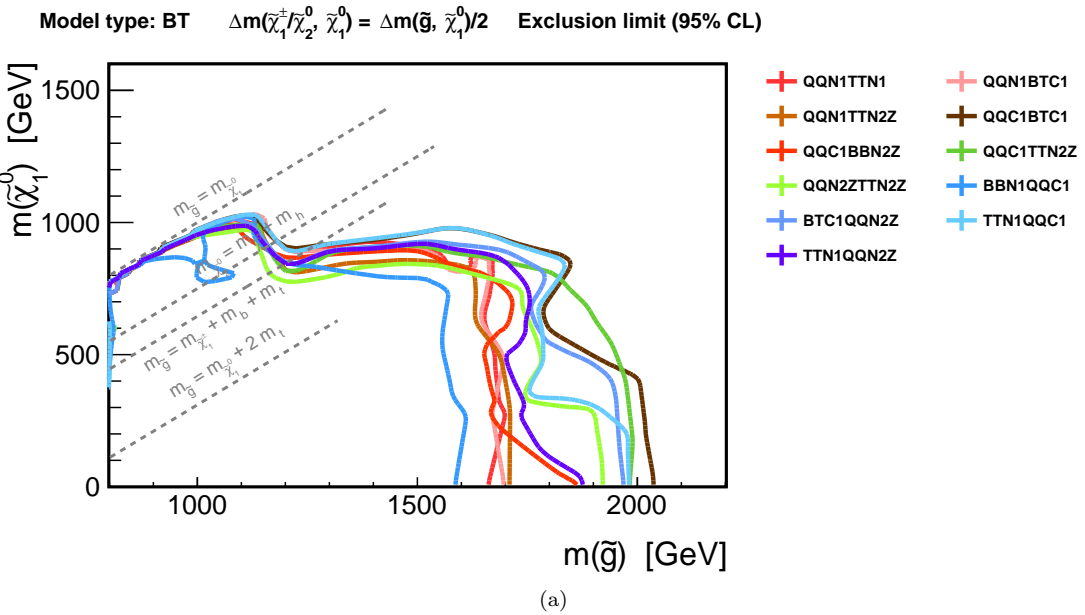


Figure 150: Observed limit for benchmark models belonging to “BT”-type in the (a)  $x=1/2$  (b) LSP 60 grid.

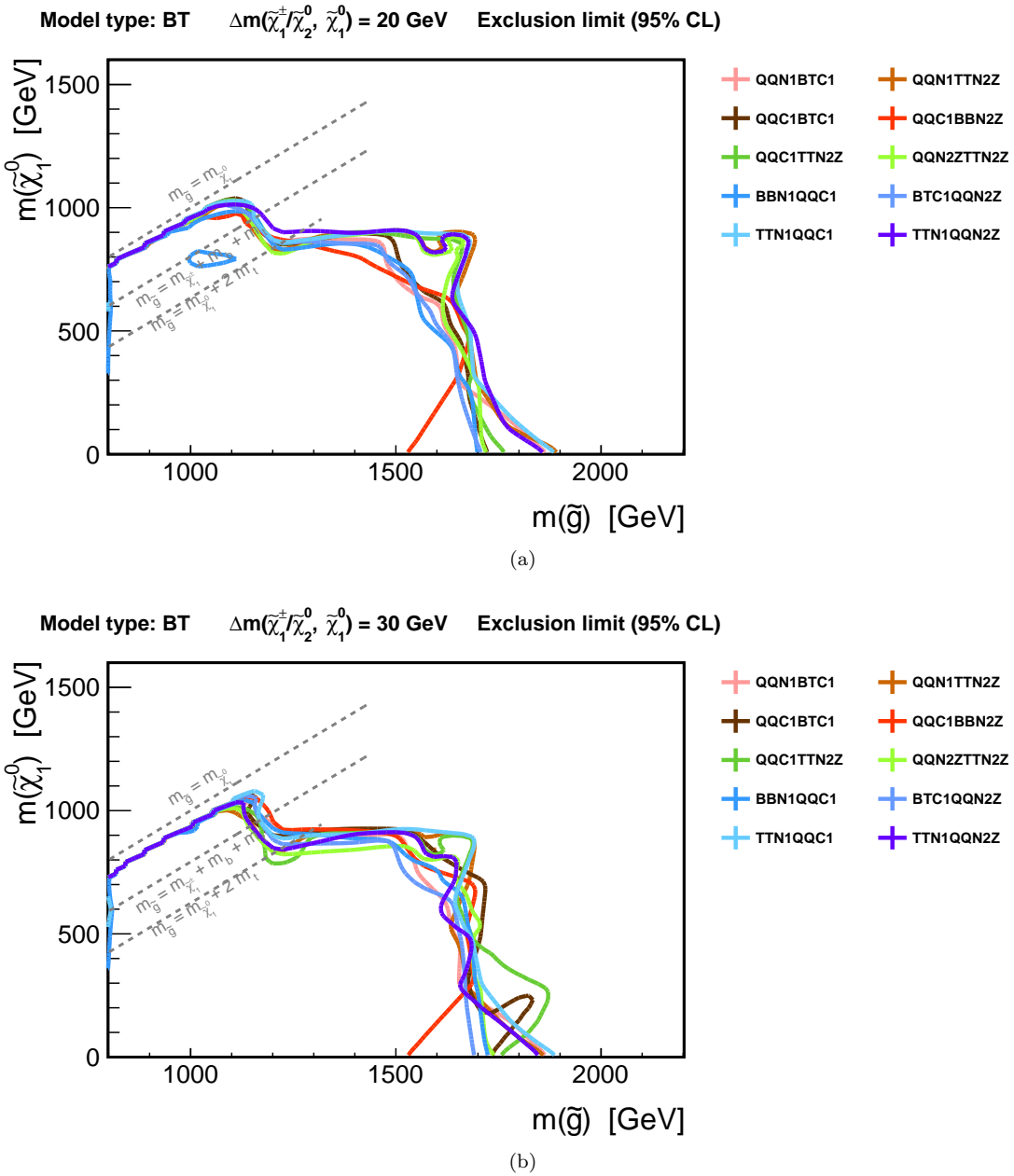


Figure 151: Observed limit for benchmark models belonging to “BT”-type in the (a) DM20 (b) DM30 grid.

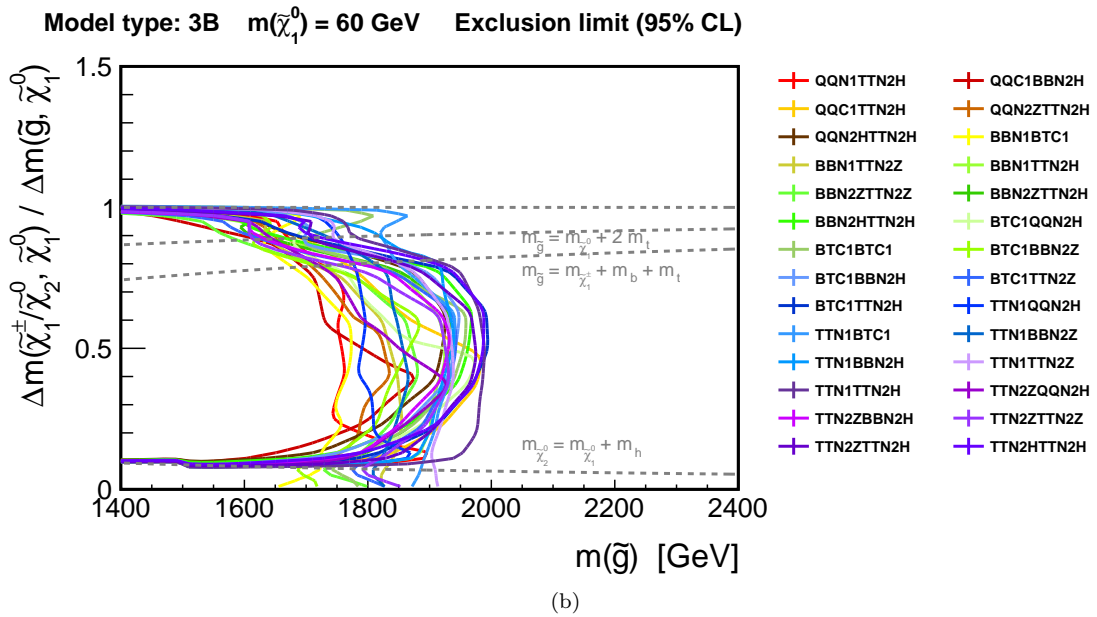
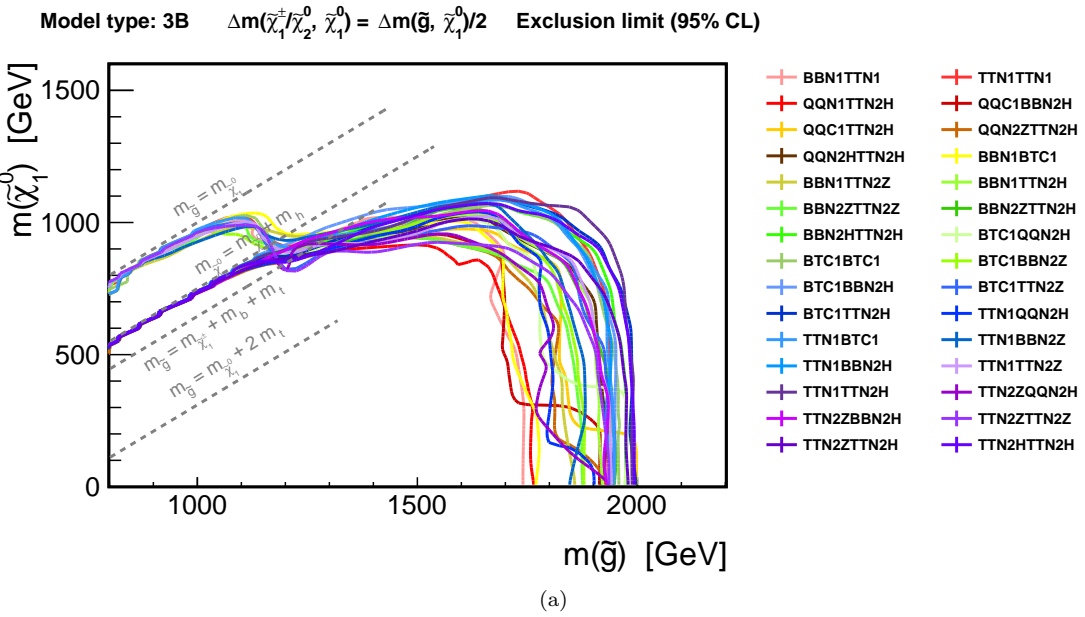


Figure 152: Observed limit for benchmark models belonging to “3B”-type in the (a)  $x=1/2$  (b) LSP 60 grid.

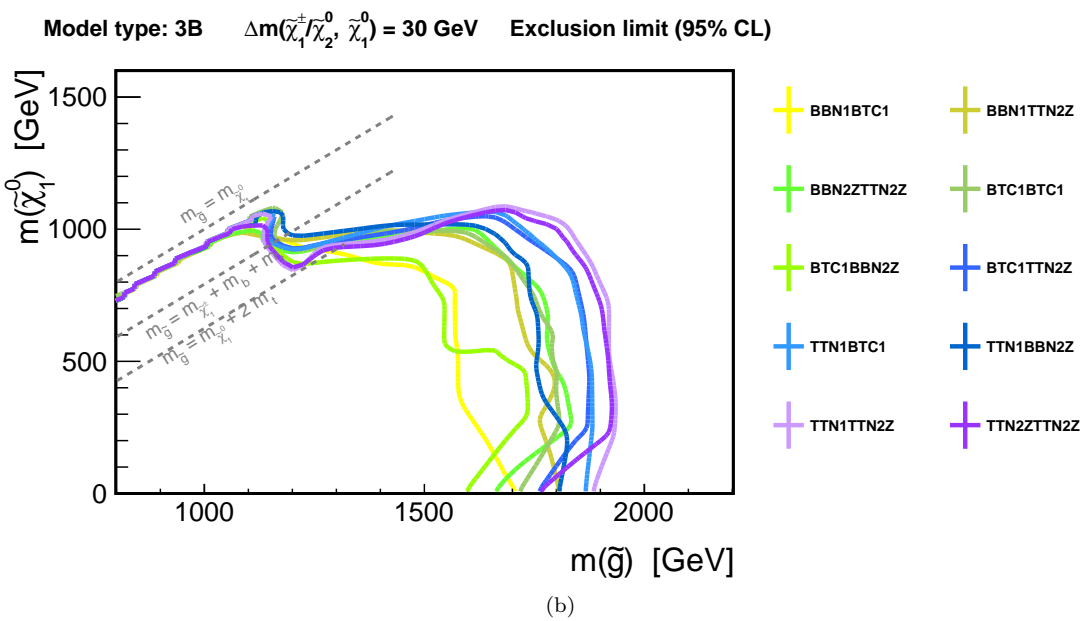
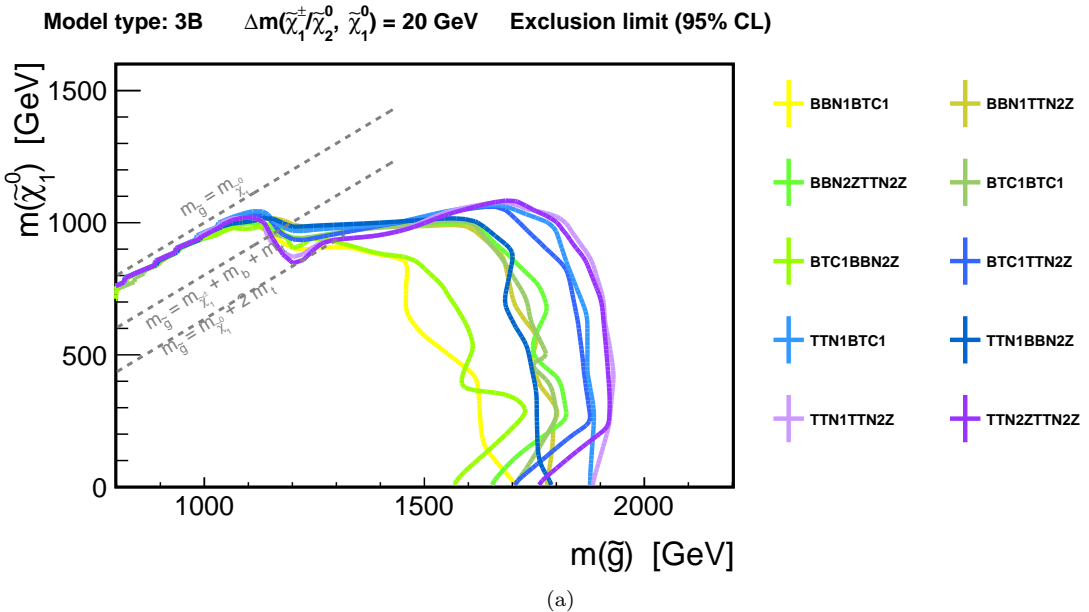


Figure 153: Observed limit for benchmark models belonging to “3B”-type in the (a) DM20 (b) DM30 grid.

## 9 Conclusion

This thesis presented the search for gluinos using proton-proton collisions in the Large Hadron Collider (LHC) at the center-of-mass energy of  $\sqrt{s} = 13$  TeV collected in the ATLAS detector. Focusing on the final state with one leptons, all relevant 45 decay chains for pair produced gluinos are explored, together with various scenarios of the mass spectra, aiming to provide the most general result achievable in principle.

The highlight of the analysis is designing a dedicated data-driven background estimation method, reinforce the confidence on the estimation by reducing the reliance on simulation which typically less performing in an extreme phase space.

Analysis is performed with dataset with  $36.1 \text{ fb}^{-1}$  of integrated luminosity. In the unblinded signal regions, no significant excess is found. Constraints are set on each of the 45 models of gluino decay chain. Exclusion upto 1.7 TeV – 2.0 TeV in gluino mass, and upto  $\sim 1$  TeV in the lightest neutralino mass is widely confirmed with typical mass spectra of gluino and EW gauginos, while upto 1.5 TeV – 1.9 TeV in gluino mass is excluded in case of compressed EW gaugino masses ( $\Delta M \sim 20 - 30$  GeV) which is motivated by dark matter relic observations.

# Acknowledgement

The appreciation from the author to people for the contribution of this work is summarized in Table 53-54.

Table 53: List of guys I want to thank.

Name	Relation with the author	The author thanks for ...
<b>Tokyo Group</b>		
Sachio Komamiya	Supervisor	Encouraging the author to jump in the field, reviewing this thesis.
Yoshio Kamiya	Semi-boss	Providing initial how-tos (programing, DAQ, statistics etc.) at the beginning of master
Daniel Jeans	Semi-boss	Teaching physics and software while in master. Proof reading of CV.
Junping Tian	Neighbor desk (Nov. 2016-)	Discussing the prospect of ILC.
Tokyo Computing Team	Host	Maintaining the incredibly efficient server.
Kono-san	Secretary	Handling numerous paper works for trips, and contact to JPS.
Shiota-san	Secretary	Handling numerous paper works for trips.
Chihiro Kozakai	Colleague	Sharing the tough feeling of Ph.D.
Yusuke Suda	Colleague	Sharing the tough feeling of Ph.D.
Yuya Kano	Colleague	Instruct the author how to say “hello” in a cool manner in the US, and the impact of saying f⊕⊕k in public.

Table 54: List of guys I want to thank.

Name	Relation with the author	The author thanks for ...
<b>People in CERN</b>		
Shoji Asai	Local Supervisor in CERN	Suggestion on topics for the Ph.D project.
Junichi Tanaka	Local Supervisor in CERN	Secretly generating samples exerting the privilege of MC coordinator. Maintaining the server for Tokyo group in CERN.
Takashi Yamanaka	Supervising role in the analysis	Answering every technical question from the author, discussing physics in deep, polishing many new/preliminary ideas.
Tomoyuki Saito	Supervising role in the analysis	Constant consultant on plans in analysis, co-developer of the object replacement.
Shimpei Yamamoto	Staff of ICEPP (-2015)	Comprehensive assistance in the initiation of the analysis. Maintaining the server for Tokyo group in CERN.
Yuji Enari	Staff of ICEPP, kebab mate	Providing keen comments to the analysis. Promoting eating kekabs as the desert of a dinner.
Yasu Okumura	Staff of ICEPP	Consultant on post-doc app., proof reading of CV and research proposals.
Keisuke Yoshihara Till Eifert	Foreseen colleague in UPenn SUSY convener	Secure author's life after the Ph. D. Encouraging agreeable ideas. Teaching the author that the life does not end even if SUSY is not found.
Stefano Zambito Moritz Backe Jeanette Lorentz Da Xu Nikolai Hartmann Valentina Tudorache Masahiro Morinaga	Analysis Contact	Cool coordination.
K. Onogi	Colleague	Closely working with the most.
Chikuma Kato Shadachi Minegishi (Minegy)	Room mate	Cooking 10 kg Bolonese per week. Throwing mushrooms from window.
Kazuki Motohashi Dai Kobayashi T. Nobe T. Nitta	Room mate	Keep the rooms comfortable. Suggesting interesting comics to the author.
	Soul mate	Sharing the tough feeling of Ph.D.
	Student of Tokyo ICEPP	Exploring Iceland (2016).
	Student of Tokyo ICEPP	Exploring Iceland (2016).
	Buddy	Exploring Iceland (2015).
	Buddy	Exploring Iceland (2015).
	Famous hip-hopper in Japan	Preaching a notion that money is all.
	Famous climber in Japan	Teaching basic movement of climbing.
<b>Others</b>		
Chun Chen / Ying Chen	Parents	Feeding the author for > 25 years.

# Appendix

## A Kinematics dependence on Signal Mass Configuration

The trend of the kinematical variables over the mass grids are shown in Figure 154-157. The color scale (z-axis) indicates the mean of the distribution in the variables, for the signal process in the mass point designated by the xy-coordinate. Three QQC1QQC1 grids ( $x=1/2$ , LSP60, DM30) and one TTN1TTN1 grid are displayed as the benchmark model for BV/BT signal regions and the 3B signal regions respectively.

One can find that the variables related to transverse momenta of outgoing particles such as  $m_{\text{eff}}$ ,  $p_T(\ell)$  and  $E_T^{\text{miss}}$  simply scale with the mass splitting, while the other variables such as aplanarity and  $E_T^{\text{miss}}/m_{\text{eff}}$  etc. are sensitive to the relative mass splitting, therefore helpful in defining SR **Low-x/High-x**.

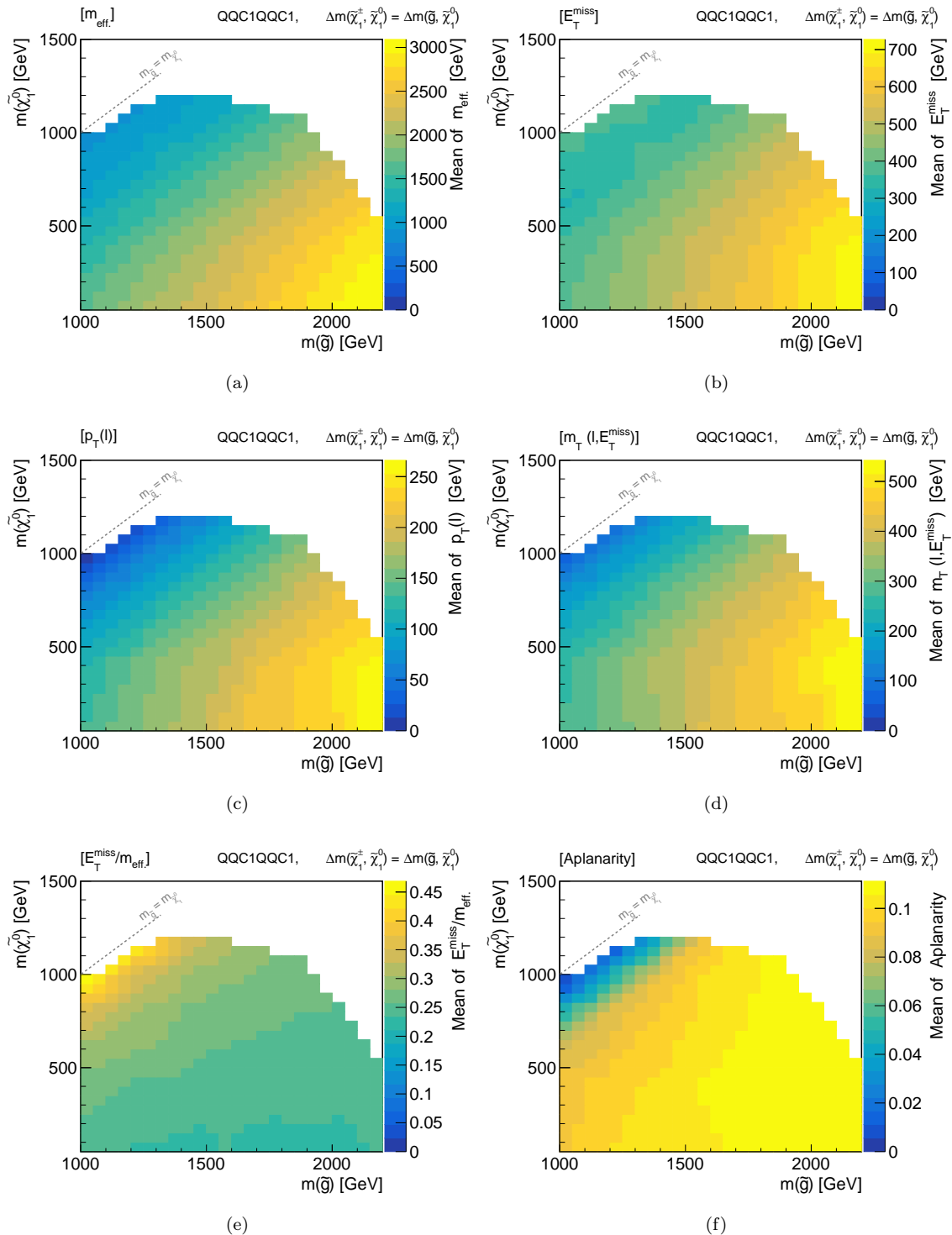


Figure 154: Mean of (a)  $m_{\text{eff.}}$  (b)  $E_T^{\text{miss}}$  (c)  $p_T(\ell)$  (d)  $m_T$  (e)  $E_T^{\text{miss}}/m_{\text{eff.}}$  (f) aplanarity, for the QQC1QQC1  $x=1/2$  grid, after the pre-selection.

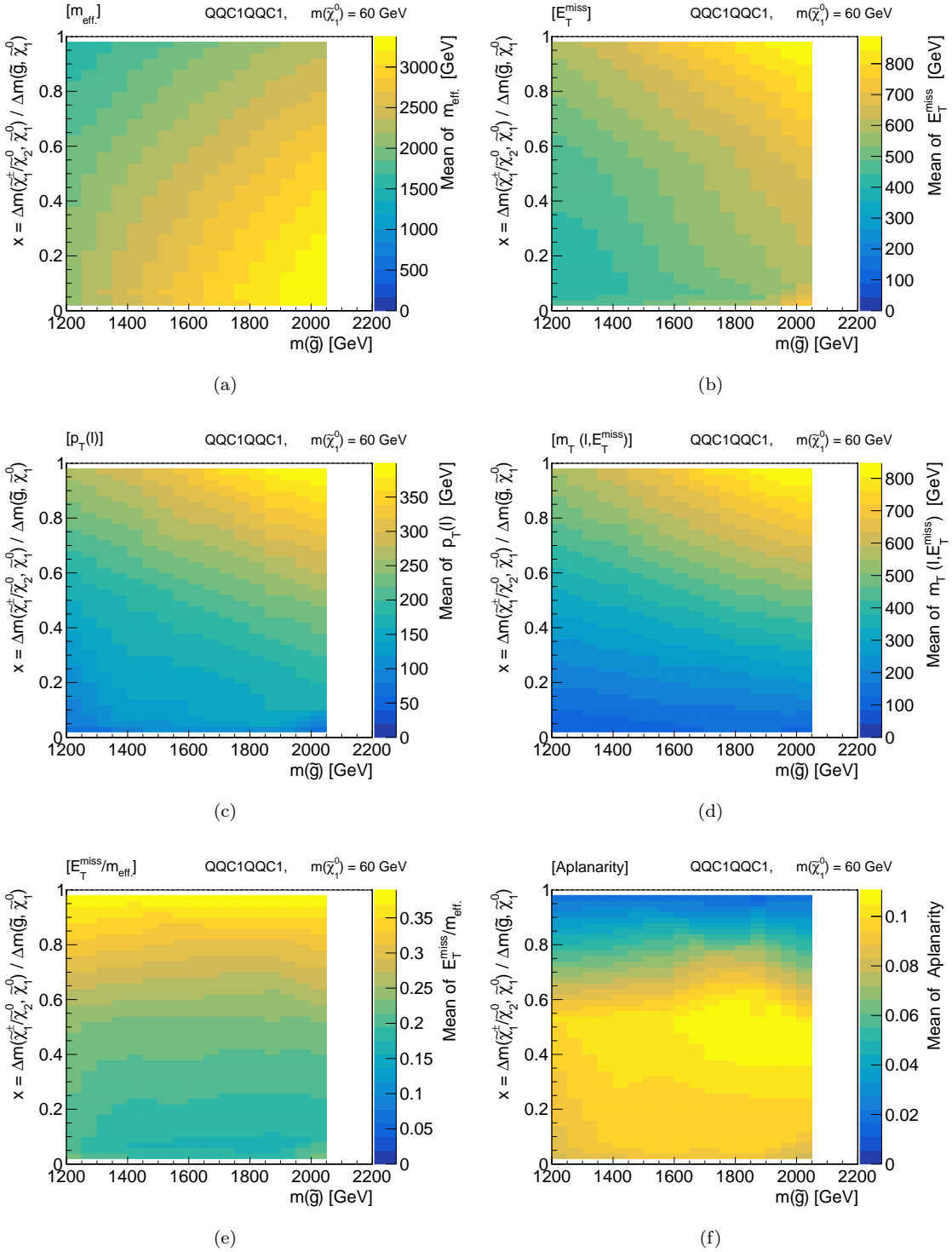


Figure 155: Mean of (a)  $m_{\text{eff}}$  (b)  $E_T^{\text{miss}}$  (c)  $p_T(\ell)$  (d)  $m_T$  (e)  $E_T^{\text{miss}}/m_{\text{eff}}$  (f) aplanarity, for the QQC1QQC1 LSP 60 grid, after the pre-selection.

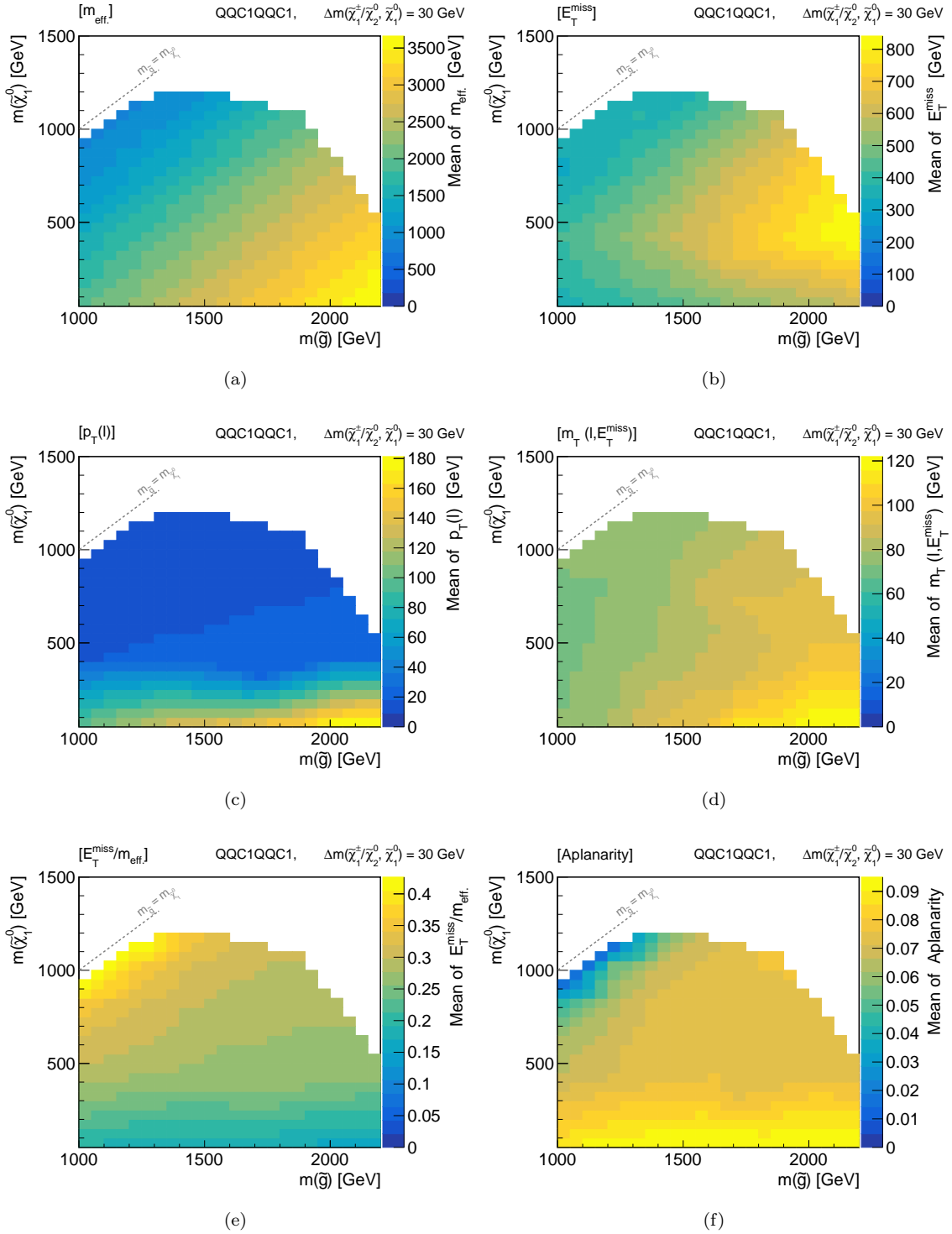


Figure 156: Mean of (a)  $m_{\text{eff.}}$  (b)  $E_T^{\text{miss}}$  (c)  $p_T(\ell)$  (d)  $m_T$  (e)  $E_T^{\text{miss}}/m_{\text{eff.}}$  (f) aplanarity, for the QQC1QQC1 DM30 grid, after the pre-selection.

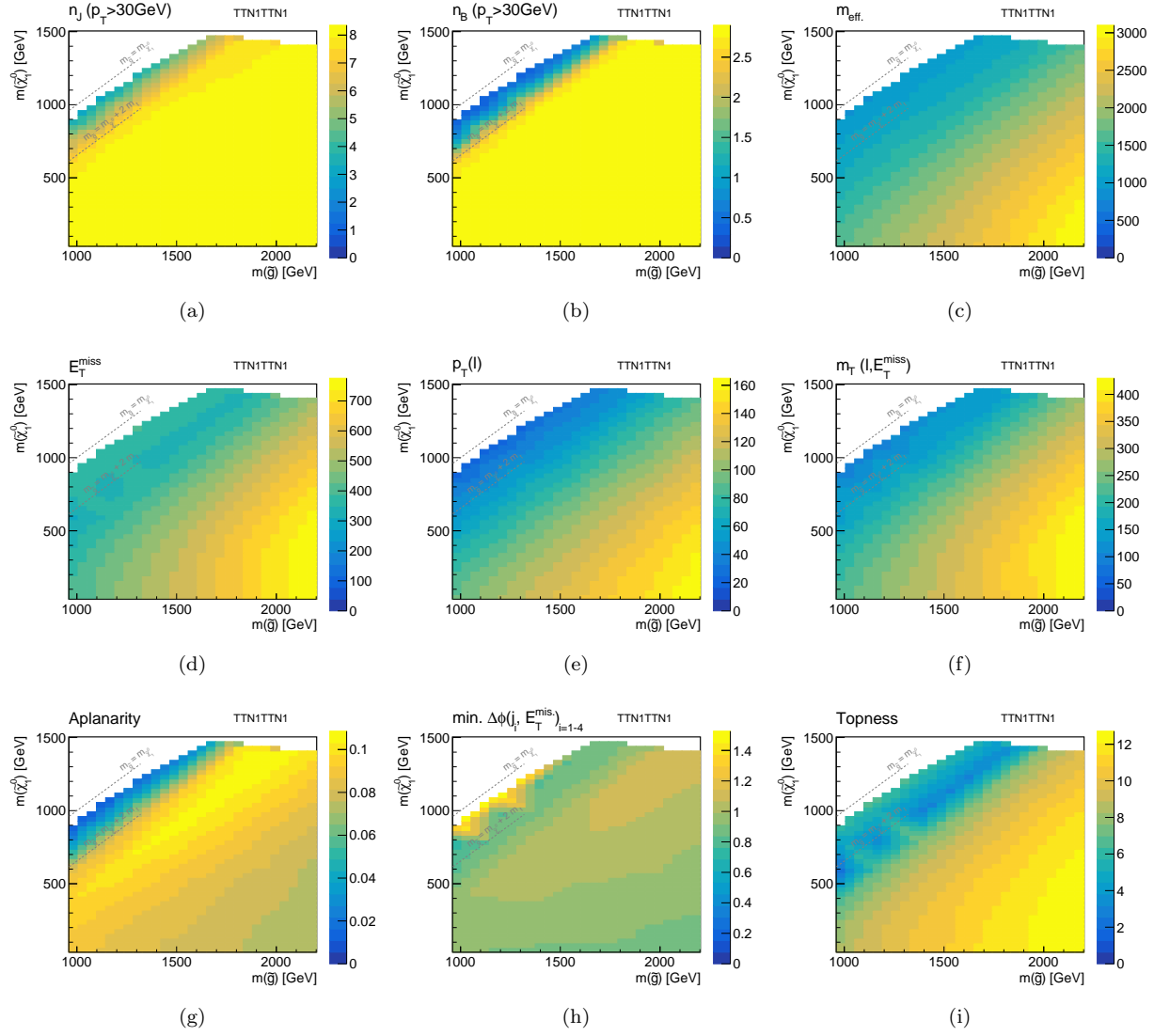


Figure 157: Mean of (a) jet-multiplicity ( $p_T > 30$  GeV) (b) bjet-multiplicity ( $p_T > 30$  GeV) (c)  $m_{\text{eff}}$  (d)  $E_T^{\text{miss}}$  (e)  $p_T(\ell)$  (f)  $m_T$  (g) aplanarity (h)  $\min_{i=1-4} \Delta\phi(j_i, E_T^{\text{miss}})$  (i) topness, for the TTN1TTN1 Direct grid, after the pre-selection.

## B Multi-jet Validation using Data

Among the “fake” backgrounds defined in Table 24, the multi-jets background including QCD di-jet and full-hadronic decays of  $V + \text{jets}$  or  $t\bar{t}$ , is ignored in the estimation since it is supposed to be negligible after requiring one signal lepton and  $E_T^{\text{miss}} > 250$  in the events, based on the MC study and the past Run2 ATLAS 1-lepton analyses [?] [?]. However, the cross-check is always worthwhile since the impact could be fatal once it turns to contribute because of its huge cross-section. The other components, dominated by  $W \rightarrow \tau\nu$  and  $Z \rightarrow \nu\nu$ , are estimated by the kinematical extrapolation method in which the normalization factors in Figure 102 are applied for  $W + \text{jets}$  and top MC. Note that the normalization factors are intended to correct the mis-modeling in the hard process kinematics, but not the modeling on the fake rate of lepton candidates where MC is known to be sometimes unreliable. Therefore, a data-driven validation is performed in a set of specific validation regions (VR-QCD) to check those estimation.

VR-QCDs are defined by inverting the isolation requirement on the final state lepton with respect to the SRs, as shown in Table 19 - 23. The abundance of “fake” components is enhanced by around factor of 10 with respect to the SRs, due to the high rejection factor of isolation that is typically 10 – 20 (5 – 10) for fake electrons (muons).

Figure 158 - 159 are the result for each  $m_{\text{eff}}$  bin of VRs-QCD. Nice agreement between the estimation and data is seen overall, implying the good MC modeling on fake lepton. Note that the multi-jets process is not included in MC thus the contribution would emerge as excess in data if it is significant, which is fortunately not the case.

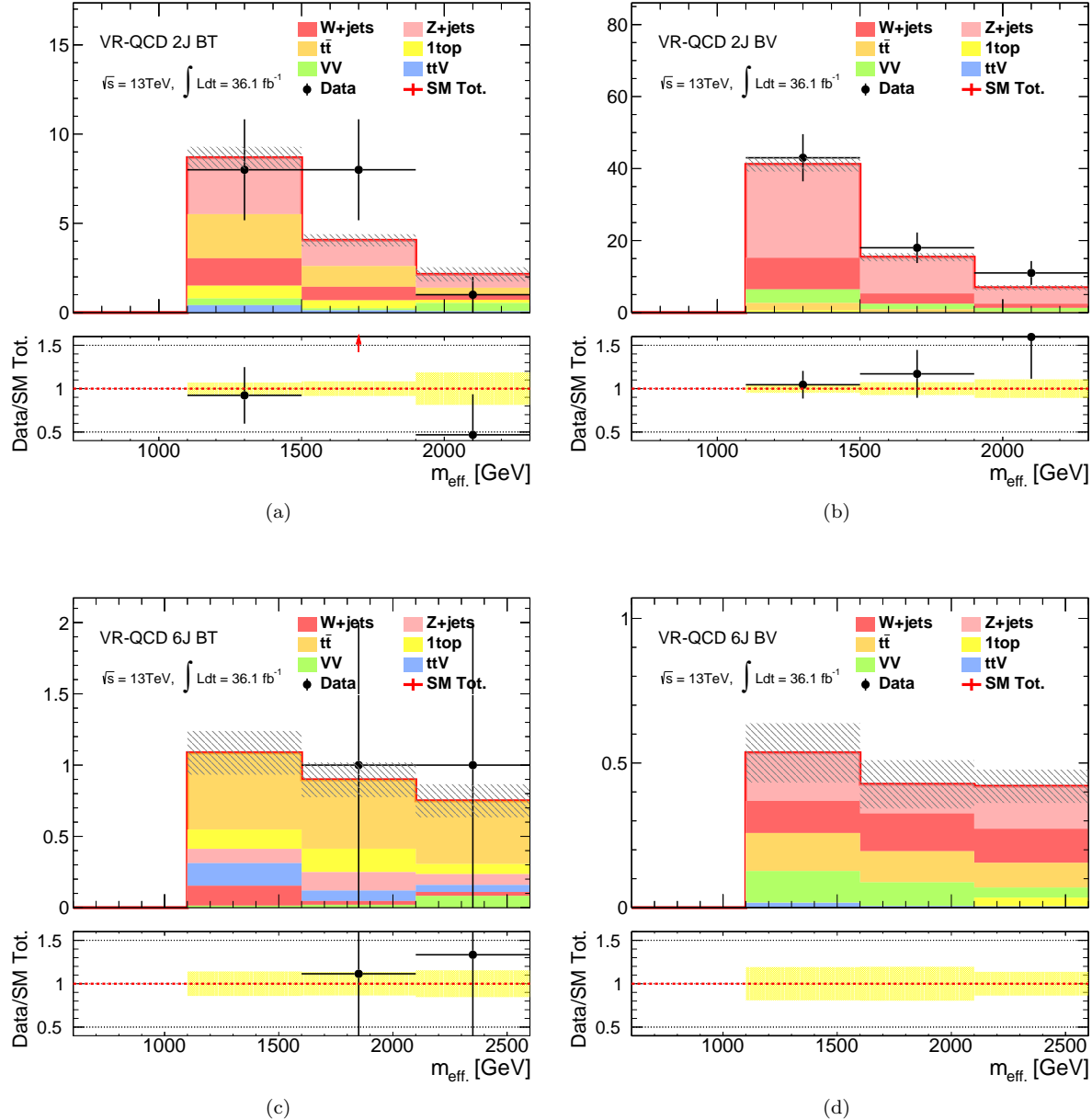


Figure 158: VR-QCD for towers (a) 2JBT (b) 2JBV (c) 6JBT (d) 6JBV.

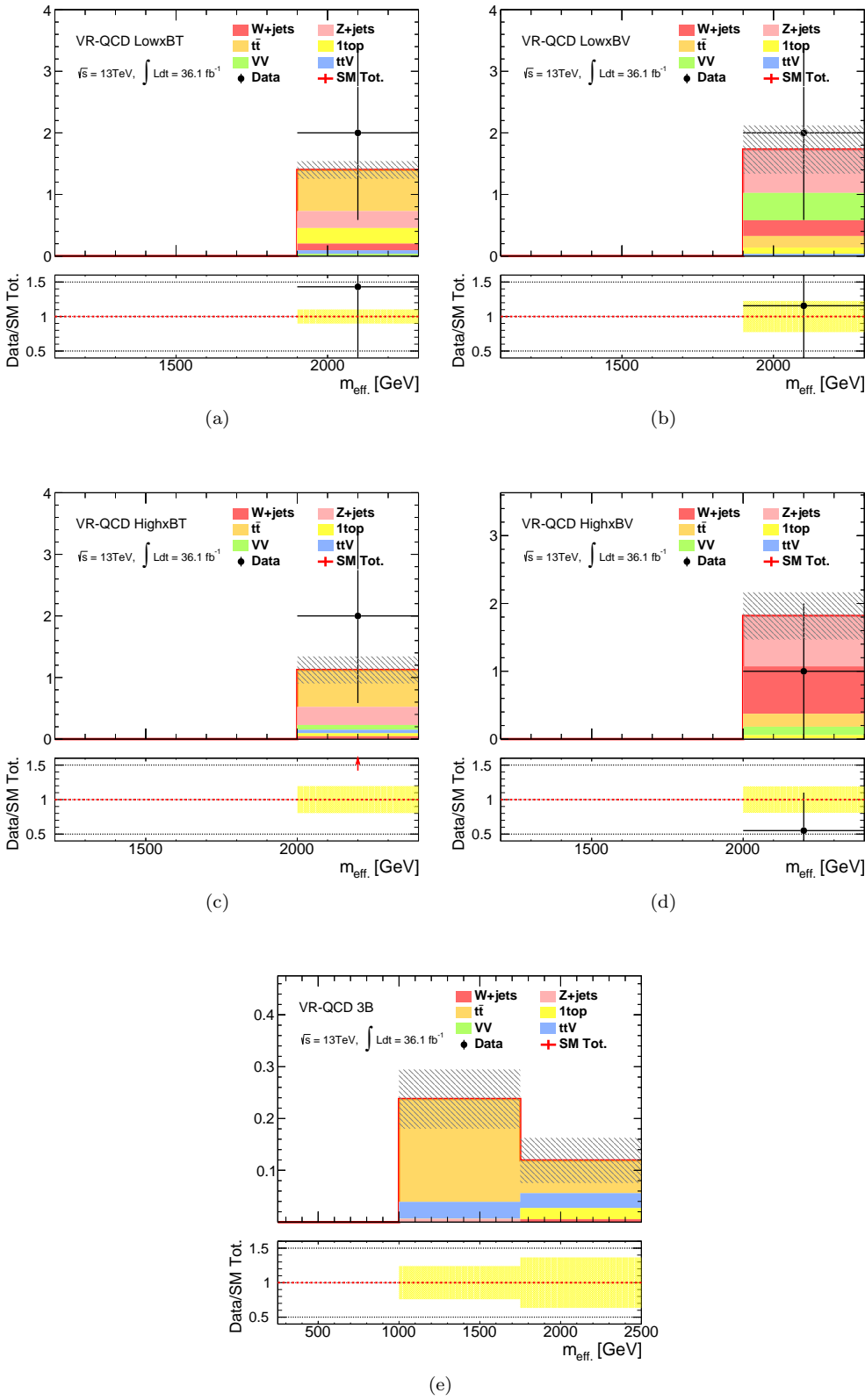


Figure 159: VR-QCD for towers (a) LowxBT (b) LowxBV (c) HighxBT (d) HighxBV (e) 3B.

## C Evaluation of the Extrapolation Error in VRs

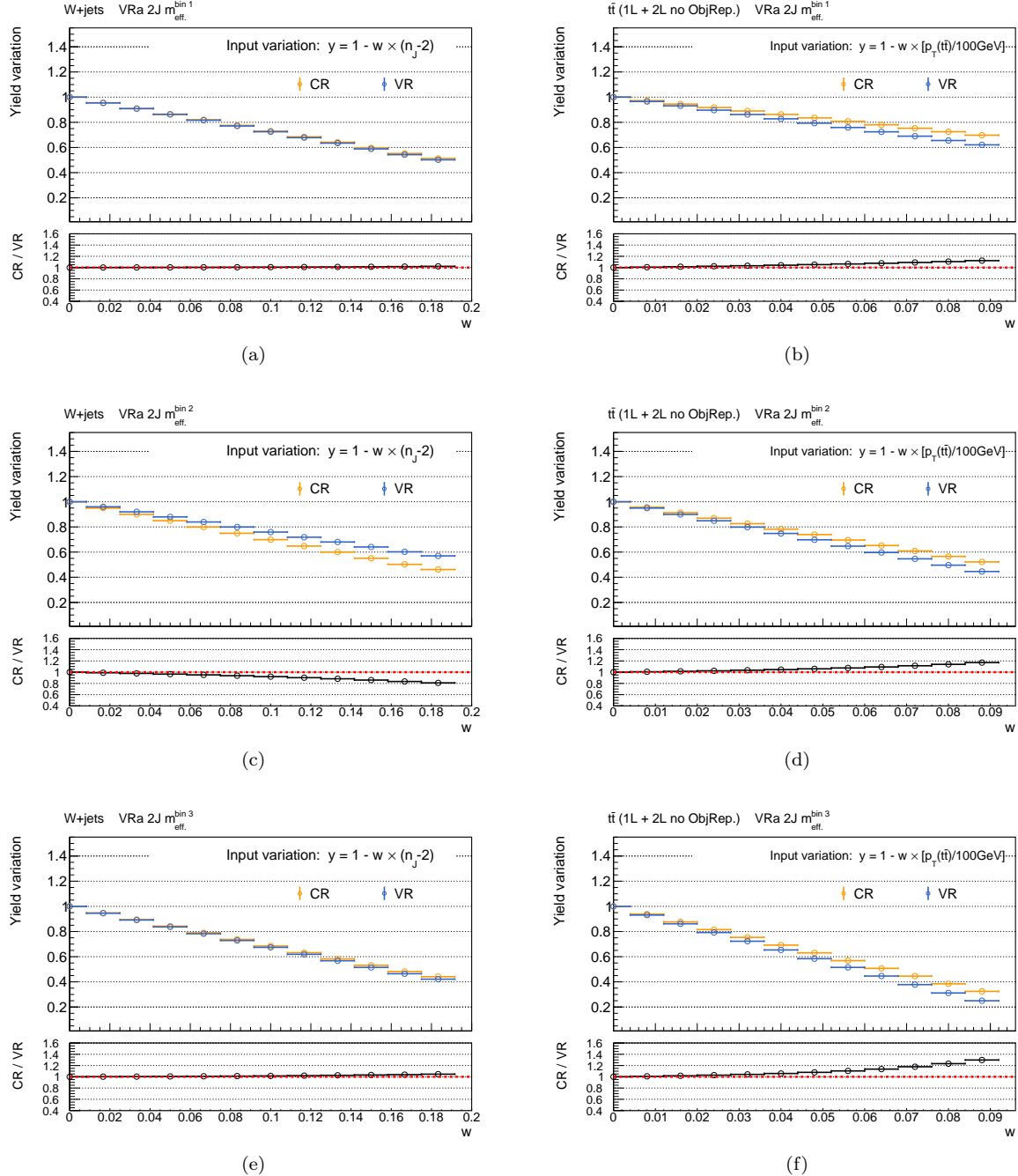


Figure 160: Extrapolation error in VRa/CR 2J. B-tagging requirement is removed. Top pannels show the yield variation of (a)  $W + \text{jets}$  and (b)  $t\bar{t}$  when injecting the variation by reweighting the MC with Eq. 95. Bottom rows are the relative difference in their response against the injected variation, namely the extrapolation errir. For the  $t\bar{t}$  process, component estimated by the object replacement method is removed.

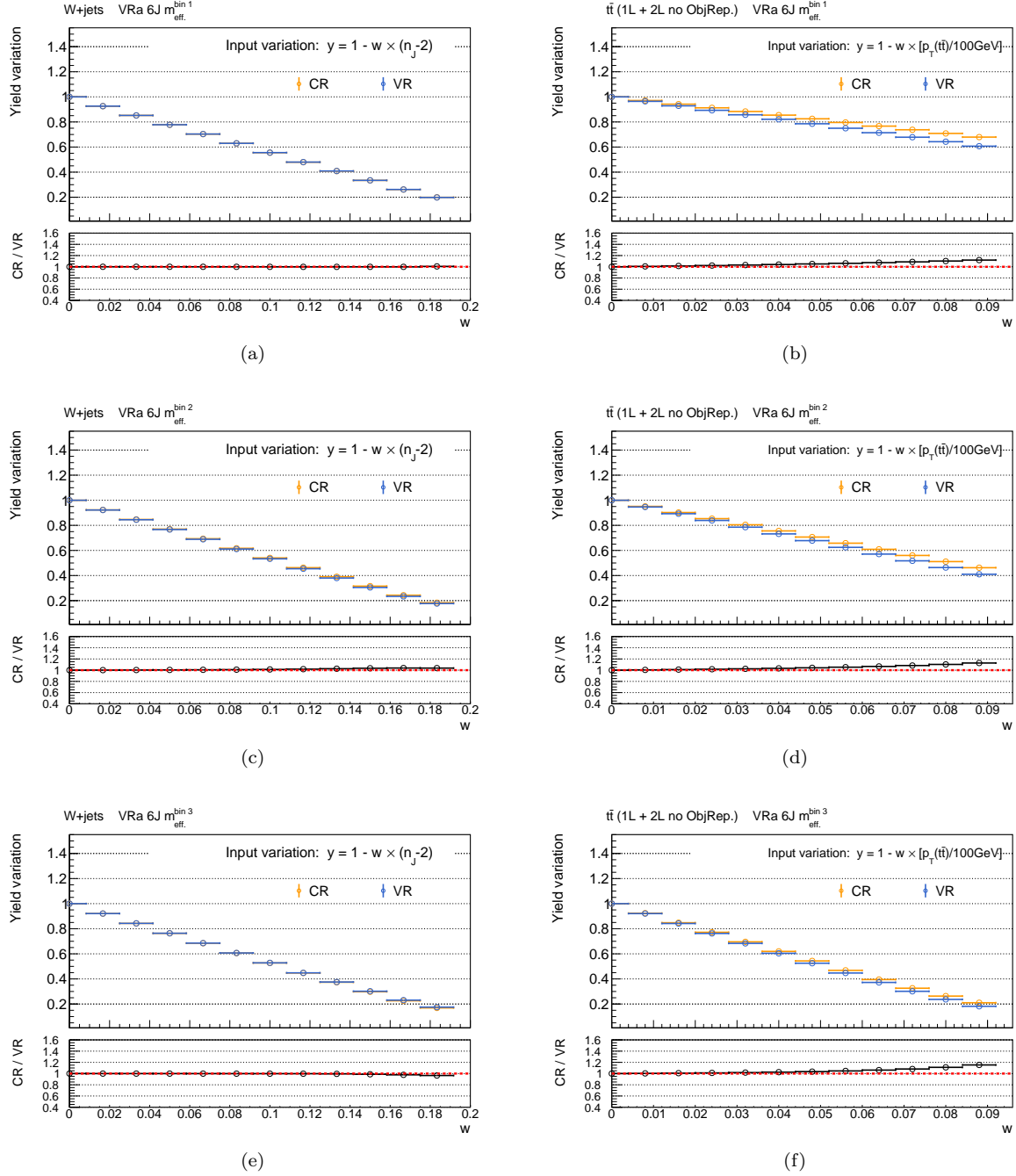


Figure 161: Extrapolation error in VRa/CR 6J. B-tagging requirement is removed. Top pannels show the yield variation of (a)  $W + \text{jets}$  and (b)  $t\bar{t}$  when injecting the variation by reweighting the MC with Eq. 95. Bottom rows are the relative difference in their response against the injected variation, namely the extrapolation errir. For the  $t\bar{t}$  process, component estimated by the object replacement method is removed.

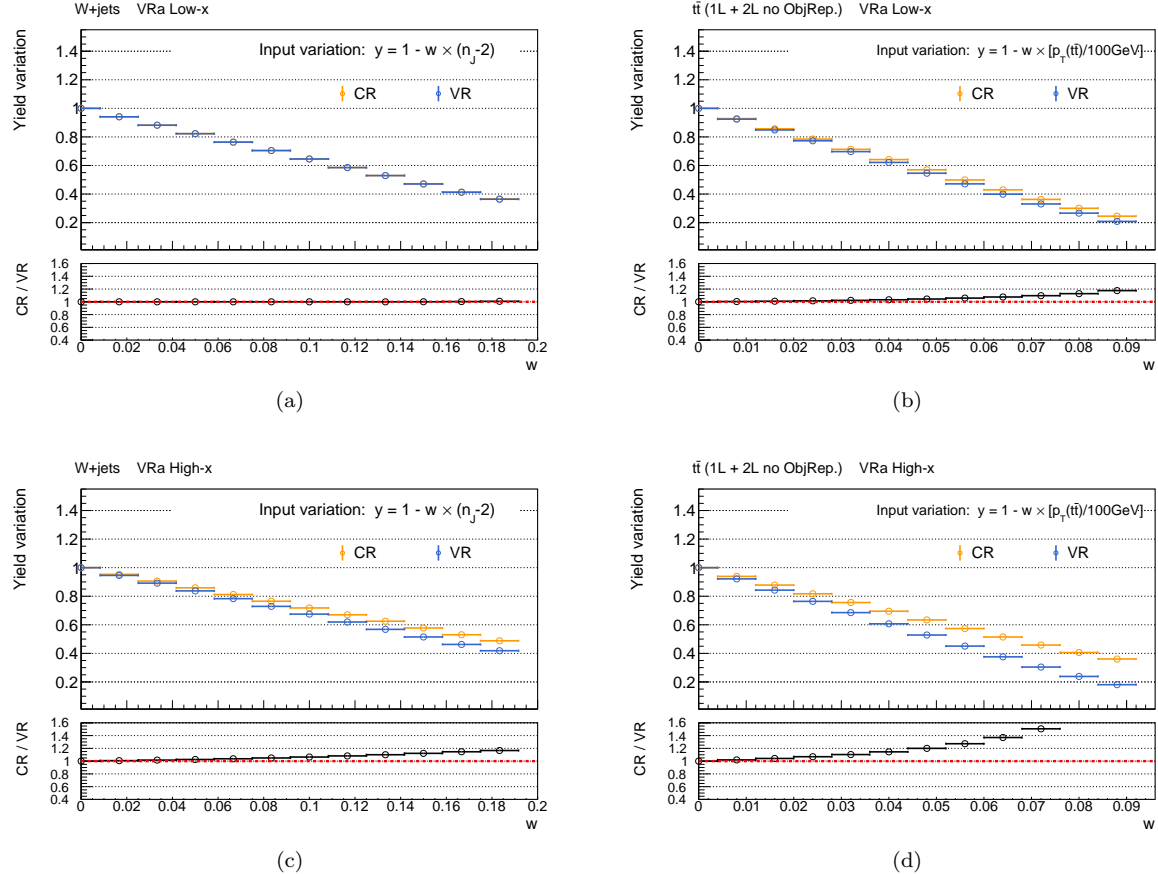


Figure 162: Extrapolation error in VRa/CR (a)(b) Low-x, and (c)(d) High-x. B-tagging requirement is removed. Top pannels show the yield variation of  $W + \text{jets}$  (left) and  $t\bar{t}$  (right) when injecting the variation by reweighting the MC with Eq. 95. Bottom rows are the relative difference in their response against the injected variation, namely the extrapolation error. For the  $t\bar{t}$  process, component estimated by the object replacement method is removed.

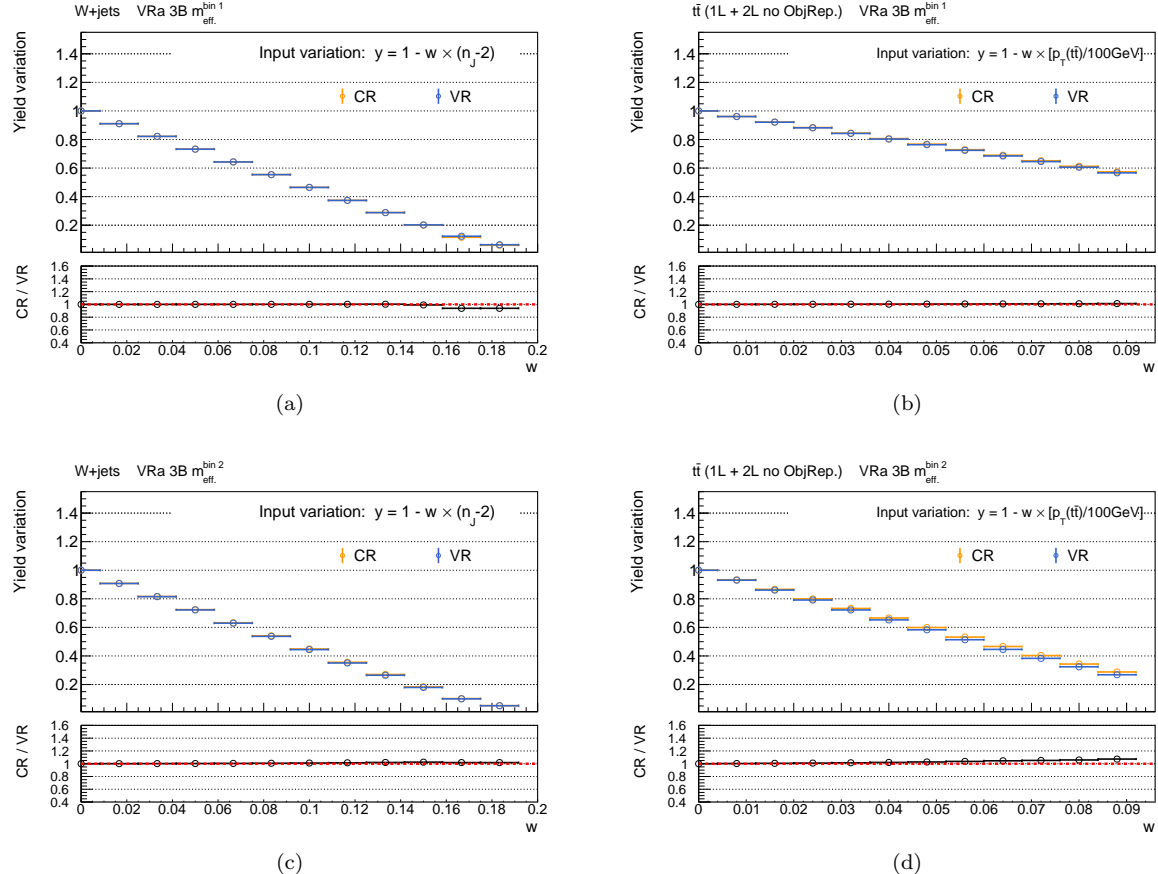


Figure 163: Extrapolation error in VRa/CR 3B. B-tagging requirement is removed for  $W + \text{jets}$ . Top pannels show the yield variation of  $W + \text{jets}$  (left) and  $t\bar{t}$  (right) when injecting the variation by reweighting the MC with Eq. 95. Bottom rows are the relative difference in their response against the injected variation, namely the extrapolation errir. For the  $t\bar{t}$  process, component estimated by the object replacement method is removed.

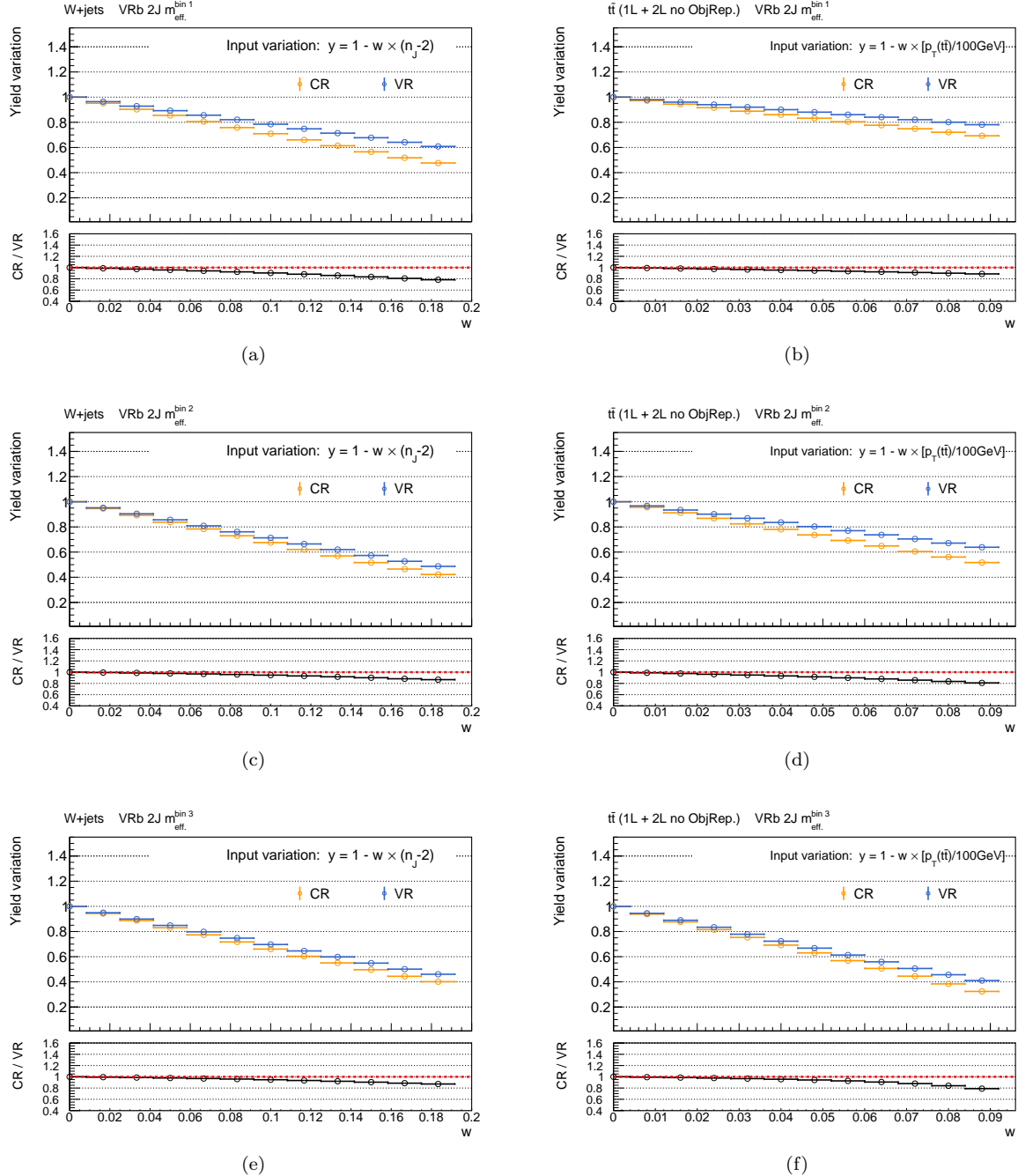


Figure 164: Extrapolation error in VRb/CR 2J. B-tagging requirement is removed. Top pannels show the yield variation of (a)  $W + \text{jets}$  and (b)  $t\bar{t}$  when injecting the variation by reweighting the MC with Eq. 95. Bottom rows are the relative difference in their response against the injected variation, namely the extrapolation errir. For the  $t\bar{t}$  process, component estimated by the object replacement method is removed.

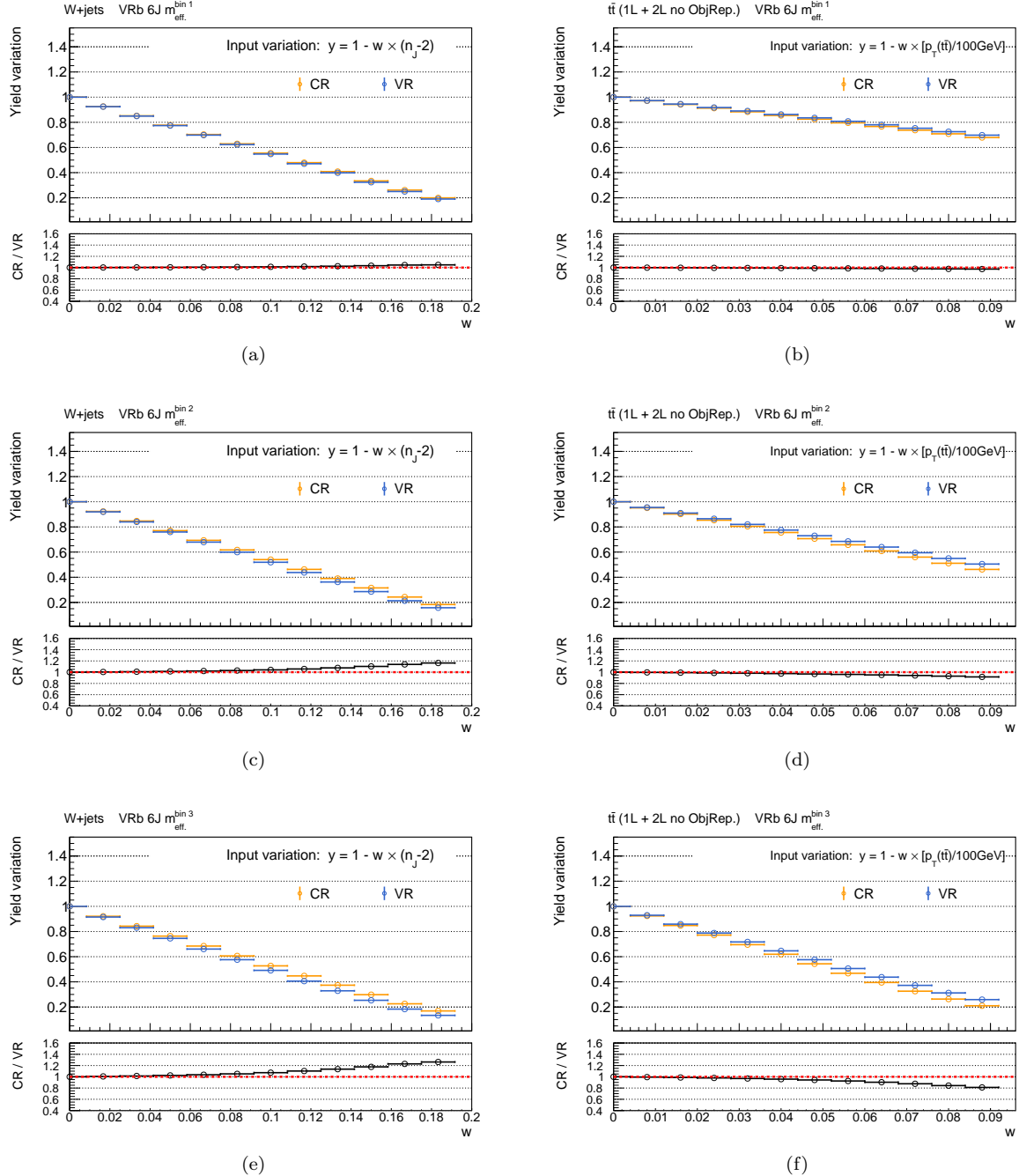


Figure 165: Extrapolation error in VRb/CR 6J. B-tagging requirement is removed. Top pannels show the yield variation of (a)  $W + \text{jets}$  and (b)  $t\bar{t}$  when injecting the variation by reweighting the MC with Eq. 95. Bottom rows are the relative difference in their response against the injected variation, namely the extrapolation errir. For the  $t\bar{t}$  process, component estimated by the object replacement method is removed.

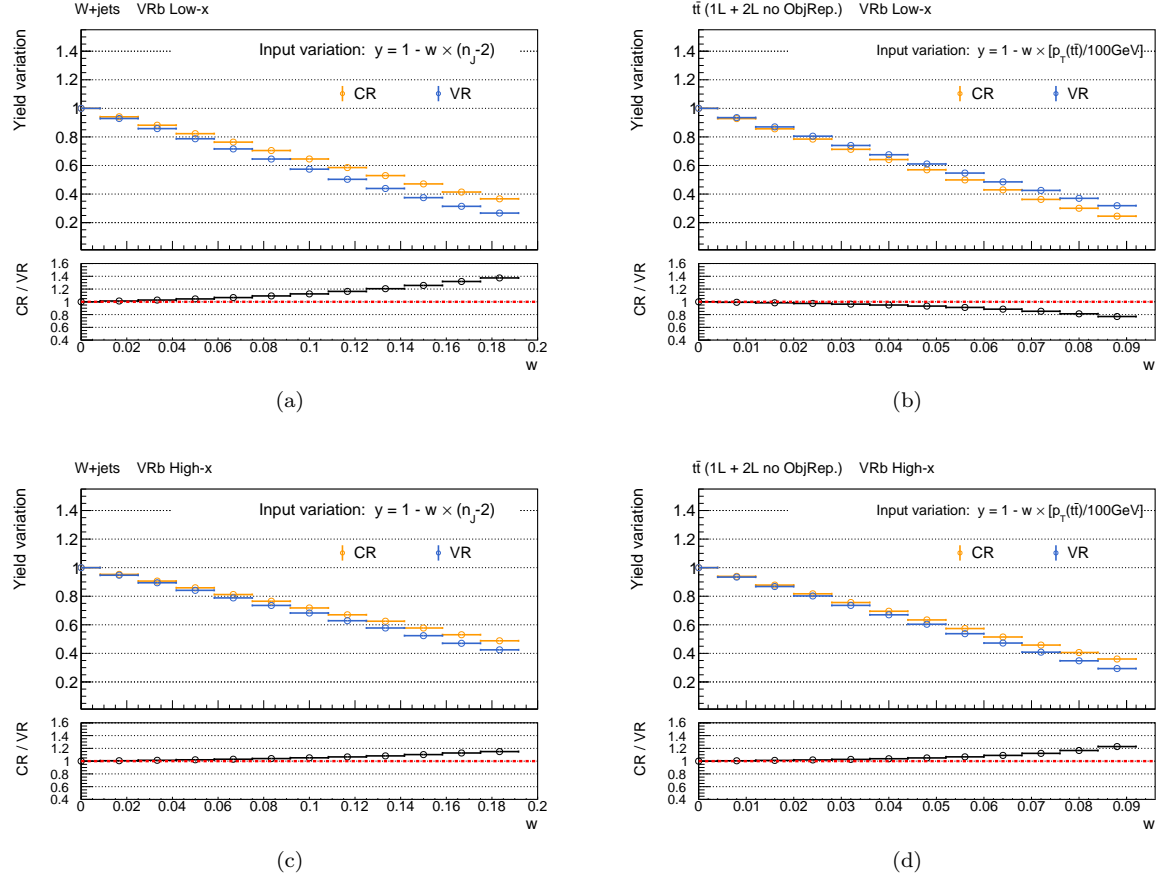


Figure 166: Extrapolation error in VRb/CR (a)(b) Low-x, and (c)(d) High-x. B-tagging requirement is removed. Top pannels show the yield variation of  $W + \text{jets}$  (left) and  $t\bar{t}$  (right) when injecting the variation by reweighting the MC with Eq. 95. Bottom rows are the relative difference in their response against the injected variation, namely the extrapolation error. For the  $t\bar{t}$  process, component estimated by the object replacement method is removed.

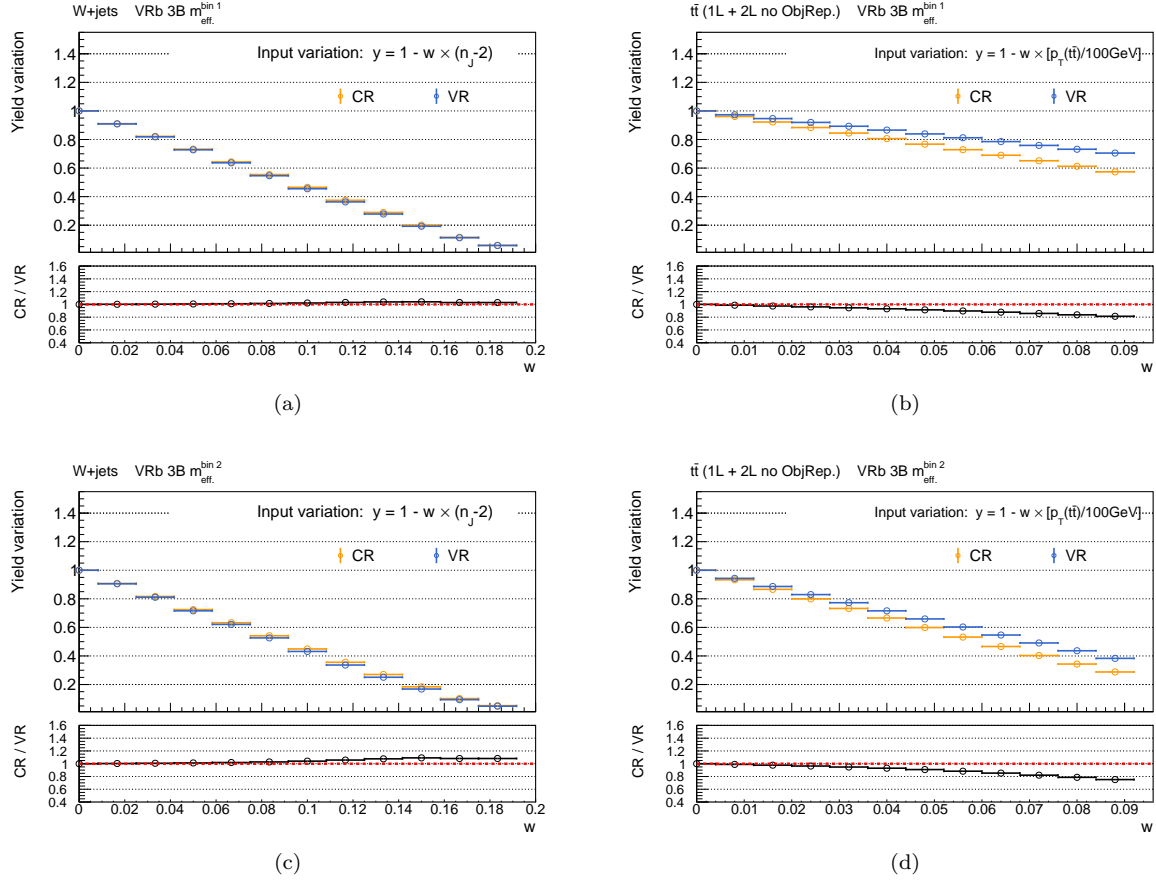


Figure 167: Extrapolation error in VRb/CR 3B. B-tagging requirement is removed for  $W + \text{jets}$ . Top pannels show the yield variation of  $W + \text{jets}$  (left) and  $t\bar{t}$  (right) when injecting the variation by reweighting the MC with Eq. 95. Bottom rows are the relative difference in their response against the injected variation, namely the extrapolation error. For the  $t\bar{t}$  process, component estimated by the object replacement method is removed.

## D Cross-check of Background Estimation by fully using the Kinematical Extrapolation

For cross-check of the background estimation, the SRs/VRs yields fully predicted by the kinamtical extrapolation method are presented. The same normalization factors are obtained in Sec. 6.2.4 are used. The results are fairly consistent with that shown in the main sections derived by a combination of the kinamtical extrapolation and object replacement.

### D.1 Validation Regions

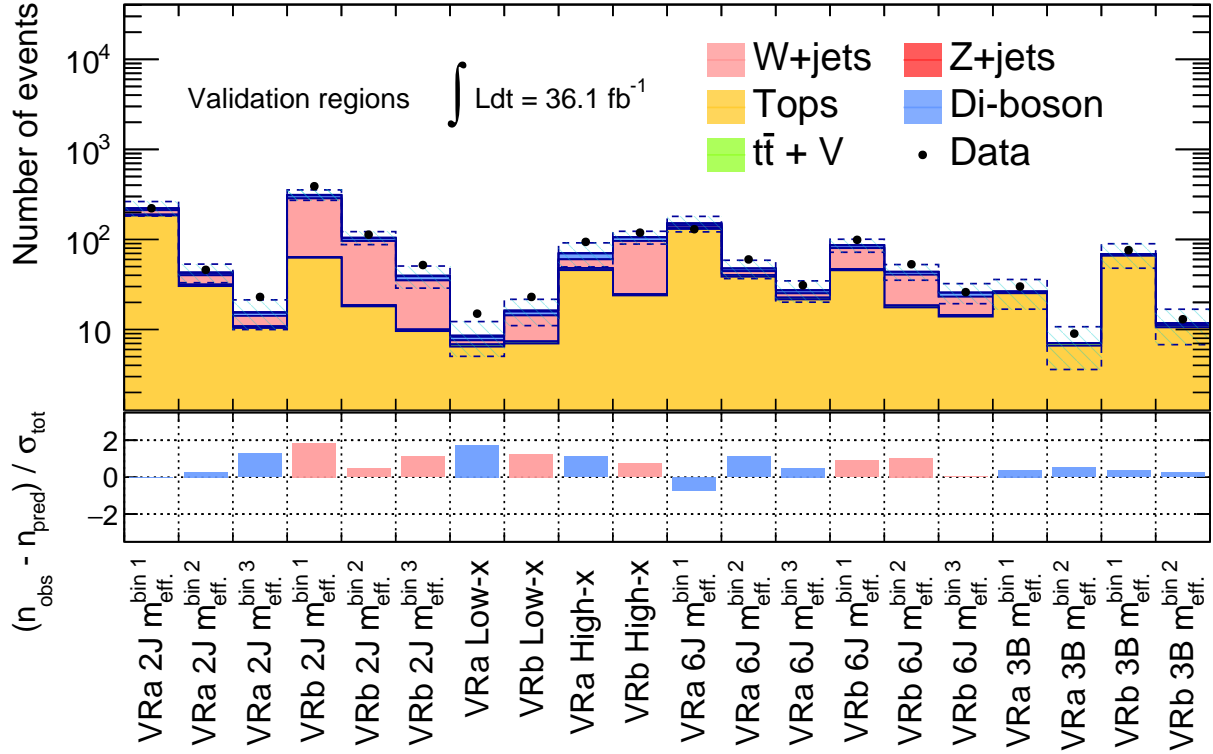


Figure 168: (Top) Observed data and the estimated yields in the nominal validation regions (VRa/VRb). All backgrounds all estimated by the kinematical extrapolation method. The dashed band represents the combined statistical and systematic uncertainty on the total estimated backgrounds. (Bottom) Pull between the data and the estimation. Pulls in regions dominated by  $W + \text{jets}$  and tops are painted by pink and blue respectively.

Table 55: Event yields and the background-only fit results in the “2J” control regions. Each column corresponds to a bin in  $m_{\text{eff}}$ . Uncertainties in the MC estimates combine statistical (in the simulated event yields) and systematic uncertainties discussed in Sec 7. The uncertainties in this table are symmetrised for propagation purposes but truncated at zero to remain within the physical boundaries.

<b>VRa 2J</b>	$m_{\text{eff}} \in [1100, 1500]$	$m_{\text{eff}} \in [1500, 1900]$	$m_{\text{eff}} > 1900$
Observed data	222	46	23
Expected background	$222.82 \pm 38.03$	$43.15 \pm 7.67$	$15.62 \pm 4.07$
$W + \text{jets}$	$21.9 \pm 3.9$	$8.4 \pm 2.6$	$3.3 \pm 1.3$
$Z + \text{jets}$	$2.6 \pm 0.7$	$0.8 \pm 0.2$	$0.3 \pm 0.1$
Tops	$184.5 \pm 37.8$	$30.3 \pm 7.3$	$10.4 \pm 4.2$
Di-boson	$9.3 \pm 3.1$	$2.4 \pm 0.8$	$1.2 \pm 0.4$
$t\bar{t} + V$	$4.6 \pm 0.8$	$1.3 \pm 0.3$	$0.5 \pm 0.1$
<b>VRb 2J</b>	$m_{\text{eff}} \in [1100, 1500]$	$m_{\text{eff}} \in [1500, 1900]$	$m_{\text{eff}} > 1900$
Observed data	390	113	52
Expected background	$313.50 \pm 37.61$	$104.86 \pm 13.92$	$39.73 \pm 8.96$
$W + \text{jets}$	$221.5 \pm 35.2$	$77.2 \pm 13.0$	$25.1 \pm 9.3$
$Z + \text{jets}$	$5.1 \pm 1.3$	$2.0 \pm 0.6$	$0.8 \pm 0.2$
Tops	$62.6 \pm 15.5$	$18.0 \pm 5.2$	$9.6 \pm 3.8$
Di-boson	$22.9 \pm 7.9$	$6.9 \pm 4.6$	$3.9 \pm 1.3$
$t\bar{t} + V$	$1.4 \pm 0.2$	$0.6 \pm 0.1$	$0.4 \pm 0.1$

Table 56: Event yields and the background-only fit results in the “6J” control regions. Each column corresponds to a bin in  $m_{\text{eff}}$ . Uncertainties in the MC estimates combine statistical (in the simulated event yields) and systematic uncertainties discussed in Sec 7. The uncertainties in this table are symmetrised for propagation purposes but truncated at zero to remain within the physical boundaries.

<b>VRa 6J</b>	$m_{\text{eff}} \in [1100, 1600]$	$m_{\text{eff}} \in [1600, 2100]$	$m_{\text{eff}} > 2100$
Observed data	130	60	31
Expected background	$150.89 \pm 26.88$	$47.73 \pm 8.59$	$27.36 \pm 5.08$
$W + \text{jets}$	$7.8 \pm 1.9$	$4.1 \pm 1.1$	$2.5 \pm 0.9$
$Z + \text{jets}$	$0.6 \pm 0.2$	$0.3 \pm 0.1$	$0.2 \pm 0.1$
Tops	$130.5 \pm 27.1$	$38.5 \pm 8.6$	$21.6 \pm 5.2$
Di-boson	$7.0 \pm 2.2$	$3.1 \pm 1.0$	$1.9 \pm 0.8$
$t\bar{t} + V$	$5.0 \pm 0.9$	$1.7 \pm 0.4$	$1.1 \pm 0.3$
<b>VRb 6J</b>	$m_{\text{eff}} \in [1100, 1600]$	$m_{\text{eff}} \in [1600, 2100]$	$m_{\text{eff}} > 2100$
Observed data	99	53	26
Expected background	$86.31 \pm 10.82$	$43.92 \pm 5.64$	$25.80 \pm 4.05$
$W + \text{jets}$	$33.2 \pm 6.5$	$22.0 \pm 4.7$	$8.7 \pm 2.9$
$Z + \text{jets}$	$0.4 \pm 0.2$	$0.3 \pm 0.1$	$0.2 \pm 0.1$
Tops	$45.4 \pm 9.5$	$17.6 \pm 4.0$	$13.9 \pm 3.7$
Di-boson	$5.9 \pm 2.7$	$3.1 \pm 1.8$	$2.4 \pm 1.1$
$t\bar{t} + V$	$1.4 \pm 0.3$	$0.9 \pm 0.2$	$0.6 \pm 0.2$

Table 57: Event yields and the background-only fit results in the “Low-x” control regions. Each column corresponds to a bin in  $m_{\text{eff}}$ . Uncertainties in the MC estimates combine statistical (in the simulated event yields) and systematic uncertainties discussed in Sec 7. The uncertainties in this table are symmetrised for propagation purposes but truncated at zero to remain within the physical boundaries.

<b>VR Low-x</b>	VRa	VRb
Observed data	20	23
Expected background	$13.74 \pm 3.14$	$16.30 \pm 3.43$
$W + \text{jets}$	$1.6 \pm 0.8$	$6.9 \pm 3.4$
$Z + \text{jets}$	$0.5 \pm 0.2$	$0.5 \pm 0.2$
Tops	$9.8 \pm 3.3$	$7.0 \pm 2.4$
Di-boson	$1.3 \pm 0.4$	$1.5 \pm 0.4$
$t\bar{t} + V$	$0.6 \pm 0.1$	$0.4 \pm 0.1$

Table 58: Event yields and the background-only fit results in the “High-x” control regions. Each column corresponds to a bin in  $m_{\text{eff}}$ . Uncertainties in the MC estimates combine statistical (in the simulated event yields) and systematic uncertainties discussed in Sec 7. The uncertainties in this table are symmetrised for propagation purposes but truncated at zero to remain within the physical boundaries.

<b>VR High-x</b>	VRa	VRb
Observed data	66	119
Expected background	$51.14 \pm 14.47$	$106.03 \pm 13.79$
$W + \text{jets}$	$8.8 \pm 1.8$	$71.3 \pm 13.5$
$Z + \text{jets}$	$0.4 \pm 0.1$	$0.7 \pm 0.3$
Tops	$34.2 \pm 14.5$	$23.9 \pm 8.3$
Di-boson	$6.1 \pm 2.3$	$9.3 \pm 3.4$
$t\bar{t} + V$	$1.6 \pm 0.6$	$0.8 \pm 0.3$

Table 59: Event yields and the background-only fit results in the “3B” control regions. Each column corresponds to a bin in  $m_{\text{eff}}$ . Uncertainties in the MC estimates combine statistical (in the simulated event yields) and systematic uncertainties discussed in Sec 7. The uncertainties in this table are symmetrised for propagation purposes but truncated at zero to remain within the physical boundaries.

<b>VRa 3B</b>	$m_{\text{eff}} \in [1000, 1750]$	$m_{\text{eff}} > 1750$
Observed data	11	8
Expected background	$14.82 \pm 4.63$	$5.18 \pm 1.76$
$W + \text{jets}$	$0.0^{+0.0}_{-0.0}$	$0.0 \pm 0.0$
$Z + \text{jets}$	$0.0 \pm 0.0$	$0.0 \pm 0.0$
Tops	$14.3 \pm 4.6$	$4.9 \pm 1.8$
Di-boson	$0.1^{+0.1}_{-0.1}$	$0.0 \pm 0.0$
$t\bar{t} + V$	$0.5 \pm 0.1$	$0.2 \pm 0.1$
<b>VRb 3B</b>	$m_{\text{eff}} \in [1000, 1750]$	$m_{\text{eff}} > 1750$
Observed data	69	12
Expected background	$59.45 \pm 16.51$	$9.50 \pm 2.92$
$W + \text{jets}$	$0.8 \pm 0.5$	$0.4 \pm 0.2$
$Z + \text{jets}$	$0.1 \pm 0.0$	$0.0 \pm 0.0$
Tops	$56.7 \pm 16.5$	$8.4 \pm 2.9$
Di-boson	$0.1 \pm 0.1$	$0.2 \pm 0.1$
$t\bar{t} + V$	$1.8 \pm 0.4$	$0.5 \pm 0.1$

## D.2 Signal Regions

The unblinded yields of observed data together with the expected backgrounds in the signal regions are shown in Table 60 - 62. Observed data are found to be consistent in general, with no signal regions exhibiting the deviation more than  $2\sigma$ . The pulls between data and expectation is shown in Figure 170.

Table 60: Observed yields and backgrounds expectation in the signal region bins in tower **2J** and **6J**. Backgrounds are all estimated by the kinematical extrapolation.

<b>SR 2J b-tag</b>	$m_{\text{eff.}} \in [1100, 1500]$	$m_{\text{eff.}} \in [1500, 1900]$	$m_{\text{eff.}} > 1900$
Observed data	8	2	1
Expected background	$7.83 \pm 1.64$	$3.42 \pm 0.82$	$1.46 \pm 0.51$
$W + \text{jets}$	$1.1 \pm 0.6$	$0.3 \pm 0.2$	$0.1 \pm 0.0$
$Z + \text{jets}$	$0.6 \pm 0.2$	$0.2 \pm 0.0$	$0.1 \pm 0.0$
Tops	$4.7 \pm 1.5$	$2.2 \pm 0.7$	$1.1 \pm 0.5$
Di-boson	$0.4 \pm 0.2$	$0.3 \pm 0.2$	$0.1 \pm 0.0$
$t\bar{t} + V$	$0.9 \pm 0.2$	$0.4 \pm 0.1$	$0.1 \pm 0.0$
<b>SR 2J b-veto</b>	$m_{\text{eff.}} \in [1100, 1500]$	$m_{\text{eff.}} \in [1500, 1900]$	$m_{\text{eff.}} > 1900$
Observed data	25	8	6
Expected background	$14.54 \pm 2.28$	$6.27 \pm 1.09$	$2.42 \pm 0.46$
$W + \text{jets}$	$5.0 \pm 1.3$	$2.0 \pm 0.5$	$0.5 \pm 0.2$
$Z + \text{jets}$	$2.3 \pm 0.7$	$1.0 \pm 0.3$	$0.6 \pm 0.2$
Tops	$2.9 \pm 1.0$	$1.1 \pm 0.4$	$0.5 \pm 0.2$
Di-boson	$4.1 \pm 1.4$	$2.1 \pm 0.7$	$0.8 \pm 0.3$
$t\bar{t} + V$	$0.1 \pm 0.0$	$0.1 \pm 0.0$	$0.0 \pm 0.0$
<b>SR 6J b-tag</b>	$m_{\text{eff.}} \in [1100, 1600]$	$m_{\text{eff.}} \in [1600, 2100]$	$m_{\text{eff.}} > 2100$
Observed data	7	3	0
Expected background	$5.83 \pm 1.78$	$2.53 \pm 0.82$	$2.00 \pm 0.71$
$W + \text{jets}$	$0.4 \pm 0.2$	$0.1 \pm 0.1$	$0.1 \pm 0.1$
$Z + \text{jets}$	$0.0^{+0.0}_{-0.0}$	$0.0 \pm 0.0$	$0.0^{+0.1}_{-0.0}$
Tops	$4.1 \pm 1.7$	$1.8 \pm 0.8$	$1.6 \pm 0.7$
Di-boson	$0.3 \pm 0.1$	$0.2 \pm 0.1$	$0.1^{+0.1}_{-0.1}$
$t\bar{t} + V$	$1.0 \pm 0.2$	$0.4 \pm 0.1$	$0.1 \pm 0.0$
<b>SR 6J b-veto</b>	$m_{\text{eff.}} \in [1100, 1600]$	$m_{\text{eff.}} \in [1600, 2100]$	$m_{\text{eff.}} > 2100$
Observed data	5	0	1
Expected background	$3.62 \pm 0.80$	$1.68 \pm 0.38$	$0.99 \pm 0.24$
$W + \text{jets}$	$1.1 \pm 0.5$	$0.6 \pm 0.3$	$0.3 \pm 0.1$
$Z + \text{jets}$	$0.2 \pm 0.1$	$0.0 \pm 0.0$	$0.0 \pm 0.0$
Tops	$1.0 \pm 0.5$	$0.4 \pm 0.2$	$0.3 \pm 0.1$
Di-boson	$1.2 \pm 0.3$	$0.6 \pm 0.2$	$0.4 \pm 0.2$
$t\bar{t} + V$	$0.1 \pm 0.0$	$0.0 \pm 0.0$	$0.0 \pm 0.0$

Table 61: Observed yields and backgrounds expectation in the signal region bins in tower **Low-x** and **High-x**. Backgrounds are all estimated by the kinematical extrapolation.

<b>SR Low-x</b>	<i>b</i> -tag	<i>b</i> -veto
Observed data	0	3
Expected background	$1.62 \pm 0.46$	$1.23 \pm 0.29$
$W + \text{jets}$	$0.1 \pm 0.0$	$0.2 \pm 0.1$
$Z + \text{jets}$	$0.0 \pm 0.0$	$0.1 \pm 0.0$
Tops	$1.2 \pm 0.5$	$0.6 \pm 0.3$
Di-boson	$0.2 \pm 0.1$	$0.3 \pm 0.1$
$t\bar{t} + V$	$0.2 \pm 0.0$	$0.0^{+0.0}_{-0.0}$
<b>SR High-x</b>	<i>b</i> -tag	<i>b</i> -veto
Observed data	6	4
Expected background	$2.90 \pm 0.77$	$4.43 \pm 0.96$
$W + \text{jets}$	$0.3 \pm 0.1$	$1.7 \pm 0.5$
$Z + \text{jets}$	$0.0^{+0.0}_{-0.0}$	$0.5 \pm 0.2$
Tops	$1.7 \pm 0.7$	$0.4 \pm 0.2$
Di-boson	$0.5 \pm 0.2$	$1.7 \pm 0.7$
$t\bar{t} + V$	$0.4 \pm 0.1$	$0.1 \pm 0.0$

Table 62: Observed yields and backgrounds expectation in the signal region bins in tower **3B**. Backgrounds are all estimated by the kinematical extrapolation.

<b>SR 3B</b>	$m_{\text{eff.}} \in [1000, 1750]$	$m_{\text{eff.}} > 1750$
Observed data	2	1
Expected background	$1.74 \pm 0.77$	$0.52 \pm 0.19$
$W + \text{jets}$	$0.0 \pm 0.0$	$0.0 \pm 0.0$
$Z + \text{jets}$	$0.0 \pm 0.0$	$0.0 \pm 0.0$
Tops	$1.5 \pm 0.7$	$0.4 \pm 0.2$
Di-boson	$0.0 \pm 0.0$	$0.0 \pm 0.0$
$t\bar{t} + V$	$0.3 \pm 0.1$	$0.1 \pm 0.0$

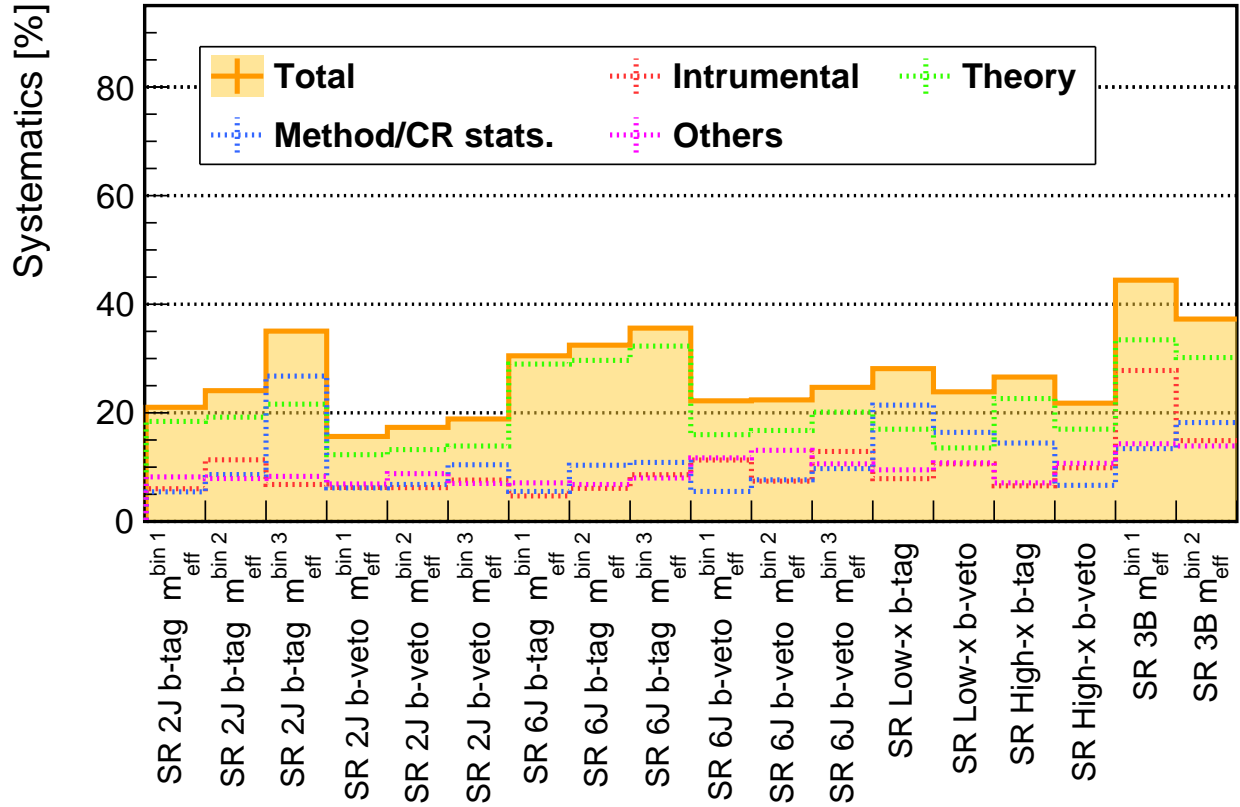


Figure 169: Post-fit systematic uncertainty with respective to the expected yield in the signal regions. Total systematics uncertainty is shown by the filled orange histogram, and the breakdowns are by dashed lines. While the systematics in b-tagged bins are purely dominated by control region statistics, it is comparable to the other sources in the b-veto bins. The overall uncertainty ranges between 20%  $\sim$  50%.

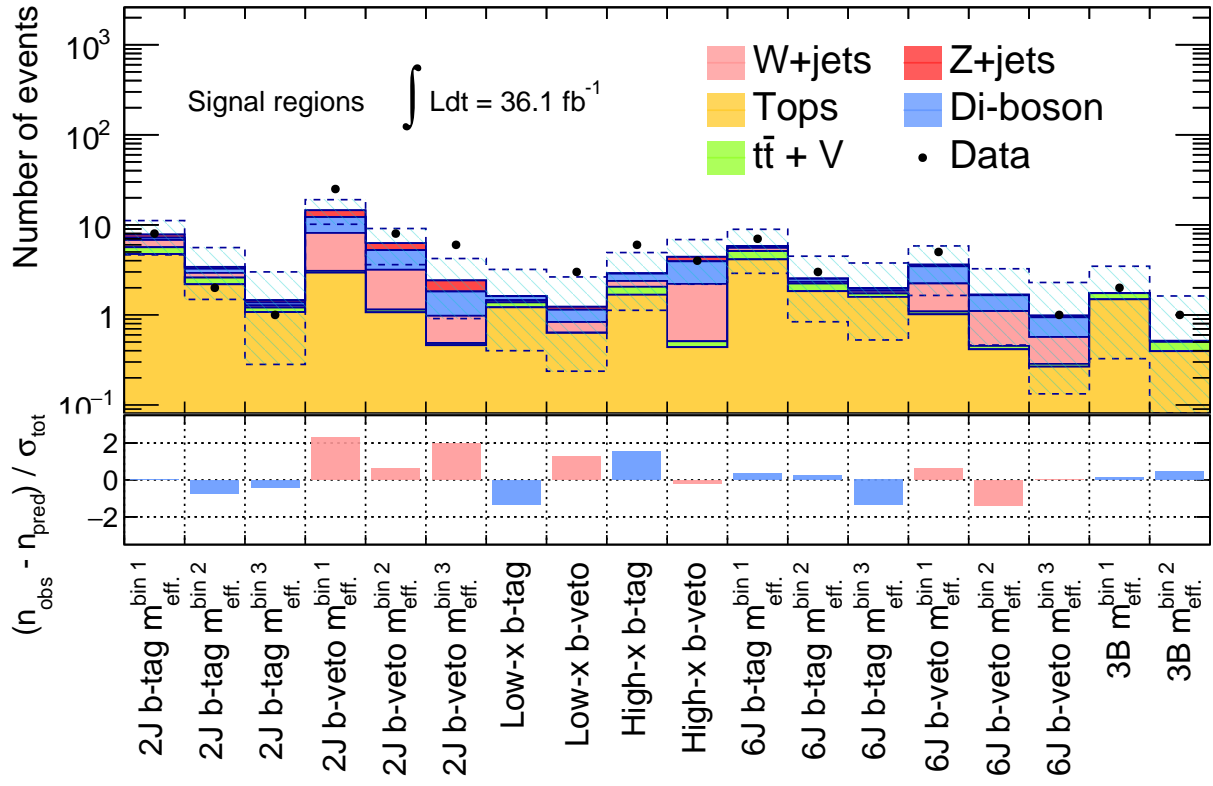


Figure 170: (Top) Observed yields and the background expectation in signal regions. The white component is the backgrounds estimated by the object replacement method, while the colored ones are by the kinamtical extrapolation method. The dashed band represents the combined statistical and systematic uncertainty on the total estimated backgrounds. (Bottom) Pull between the observed data and the expectation. No significant deviation from expectation exceeding  $2\sigma$ .

## E MC Closure Test for the Object Replacement Method

### E.1 MC Closure Test with the Soft Lepton Selection

Figure 171 ~ 173 show the closure test estimating a region with a soft lepton ( $p_T \in [6, 35]$  GeV).

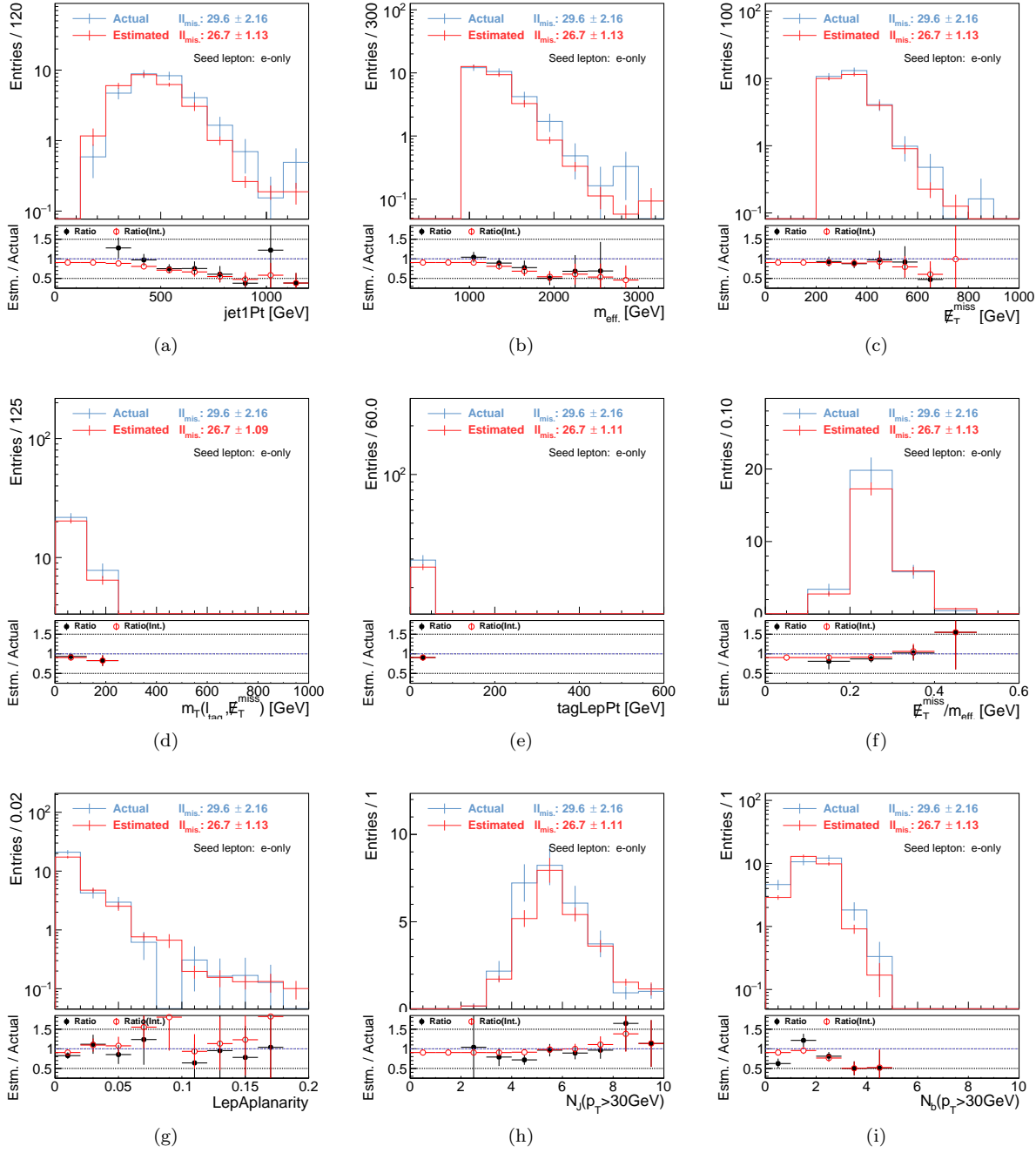


Figure 171: MC closure test for **missing lepton replacement** using  $t\bar{t}$  MC sample. Seed events are collected by the use of MET trigger.  $p_T < 35$  GeV for the leading lepton is required. **Only electrons in the seed events are replaced.** Red points in the bottom plots show the ratio of integrated yields for the two histograms above the x-position that the point indicates.

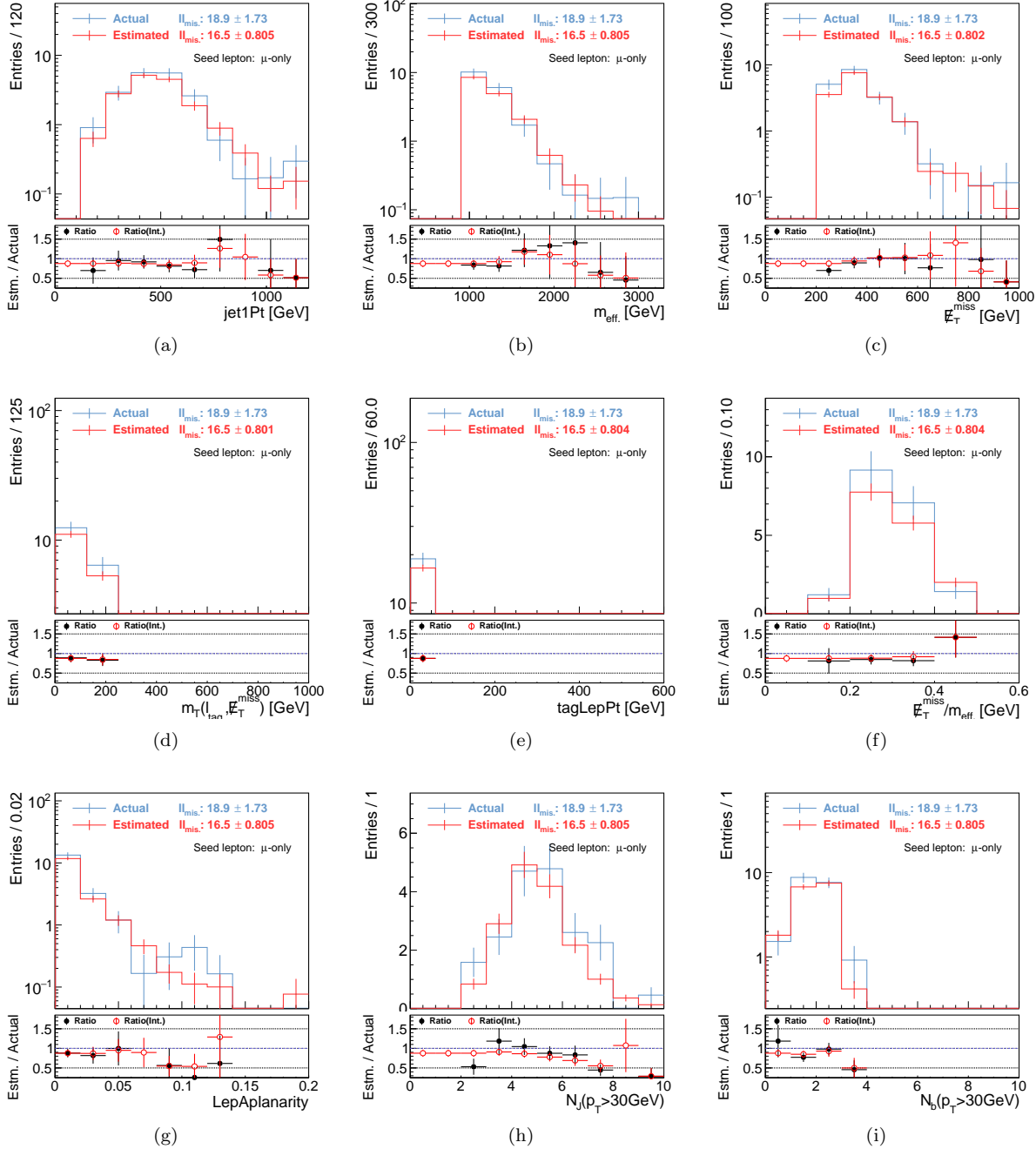


Figure 172: MC closure test for **missing lepton replacement** using  $t\bar{t}$  MC sample. Seed events are collected by the use of MET trigger.  $p_T < 35$  GeV for the leading lepton is required. **Only muon in the seed events are replaced**. Red points in the bottom plots show the ratio of integrated yields for the two histograms above the x-position that the point indicates.

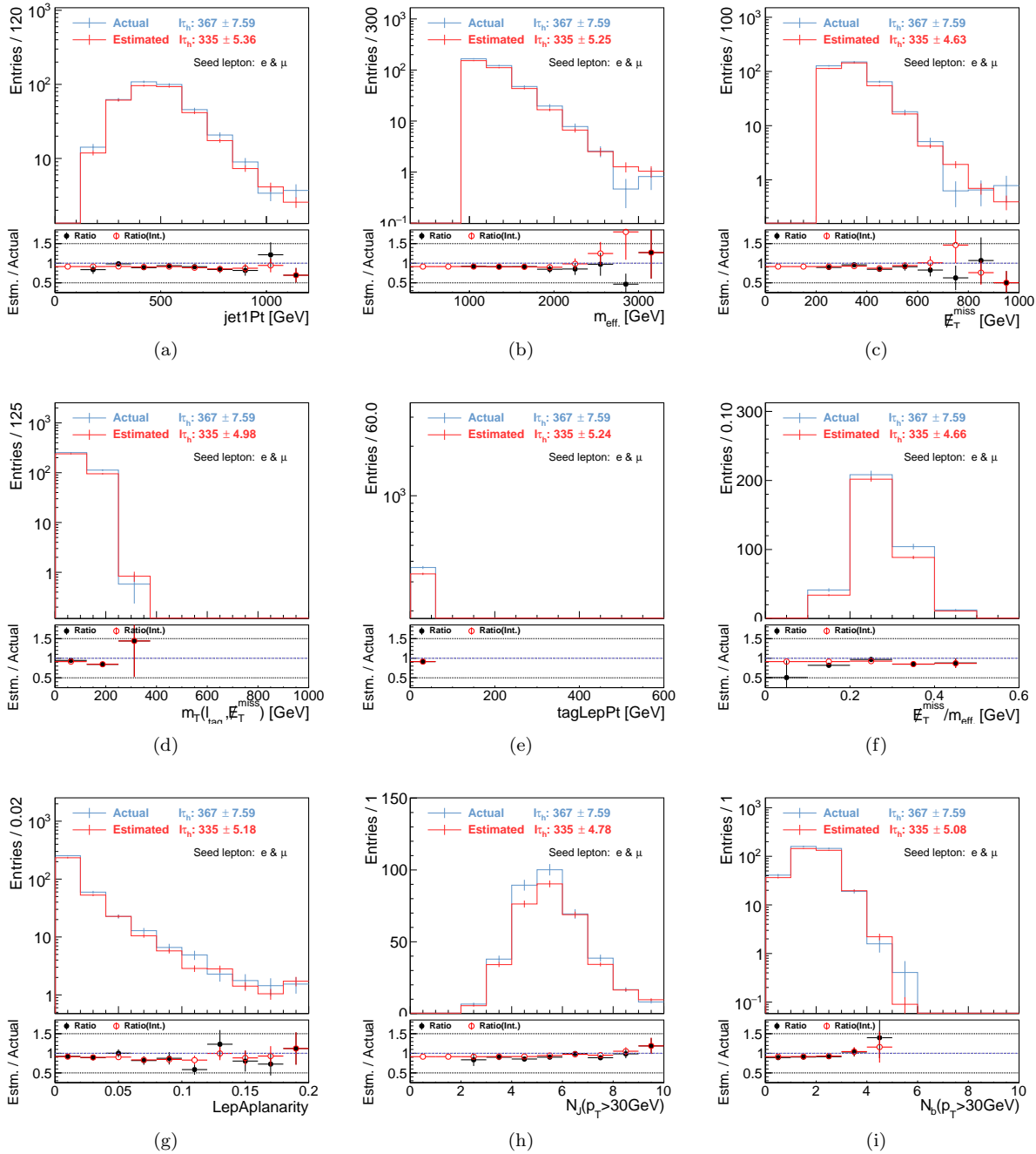


Figure 173: MC closure test for tau replacement using  $t\bar{t}$  MC sample. Seed events are collected by the use of MET trigger.  $p_T < 35$  GeV for the leading lepton is required. **Both electrons and muons in the seed events are replaced.** Red points in the bottom plots show the ratio of integrated yields for the two histograms above the x-position that the point indicates.

## E.2 Combined Test of Missing Lepton Replacement and Tau Replacement

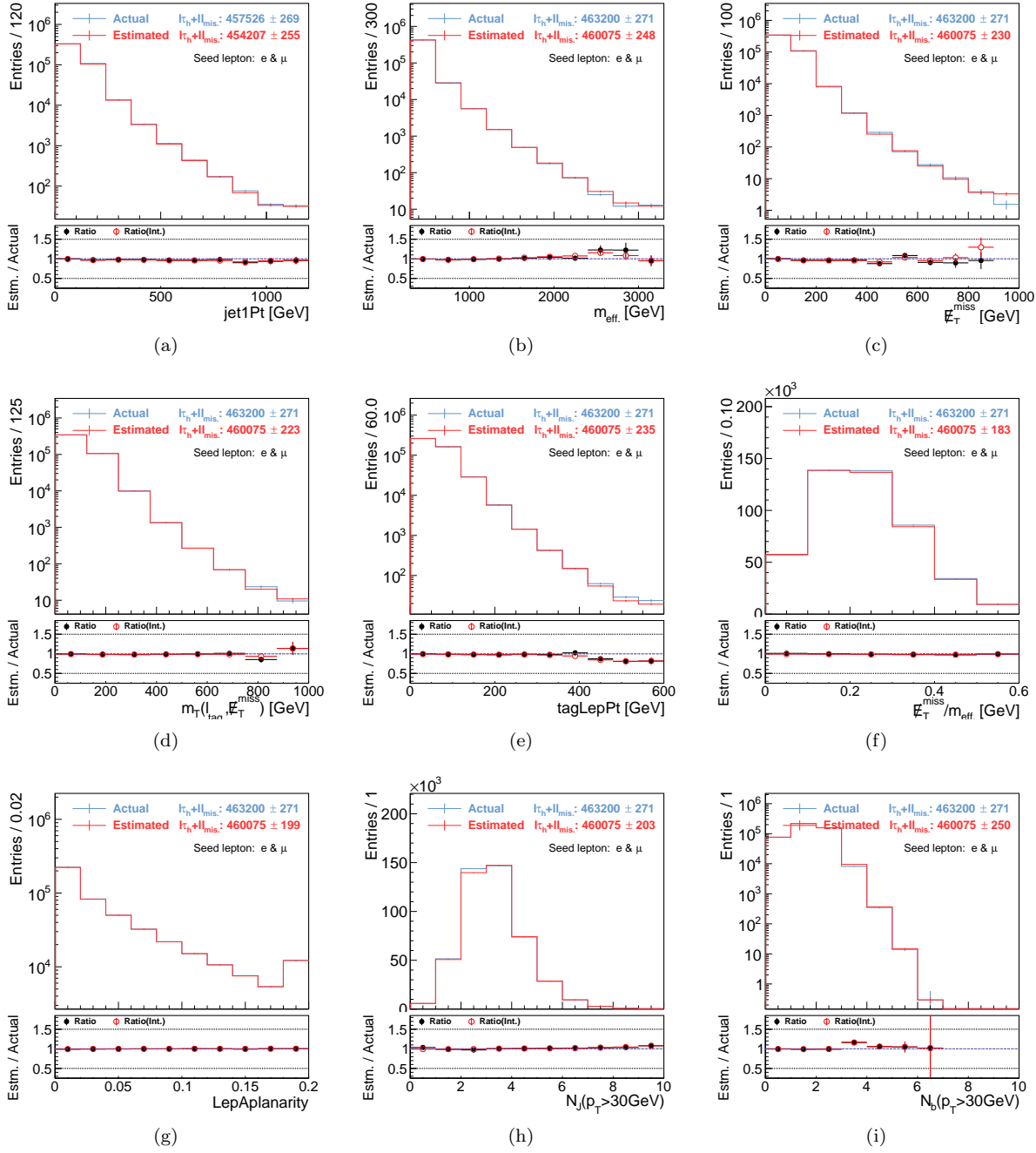


Figure 174: MC closure test for **combined estimation of missing lepton rep. and tau rep.** using  $t\bar{t}$  MC sample. Seed events are collected by the single-lepton trigger.  $p_T > 35$  GeV for the leading lepton is required. **Both electrons and muons in the seed events are replaced.** Red points in the bottom plots show the ratio of integrated yields for the two histograms above the x-position that the point indicates.

## F Obtained Cross-section Upper-limit

In a hypothetical test, the  $\text{CL}_s$  values are calculated for multiple points in  $\mu_{\text{sig.}}$ , ranging from  $0 \sim 10$ .  $\text{CL}_s$  is then modeled as function of  $\mu_{\text{sig.}}$ , therefore the upper limit on  $\mu_{\text{sig.}}$  can be defined by:

$$\mu_{\text{sig.},95} := \mu_{\text{sig.}}(\text{CL}_s = 0.05),$$

for each signal points in the model. This can be straightforwardly interpreted into cross-section upper limit ( $\sigma_{95}$ ), which can be model-independently ultimately by computing  $\sigma_{95}$  as the function of masses of gluino and EW-gauginos including the LSP, for all the decay model of gluino. Figurere 175-Figurere 177 present the results for the reference models QQC1QQC1, QQC1BTC1 and TTN1TTN1.

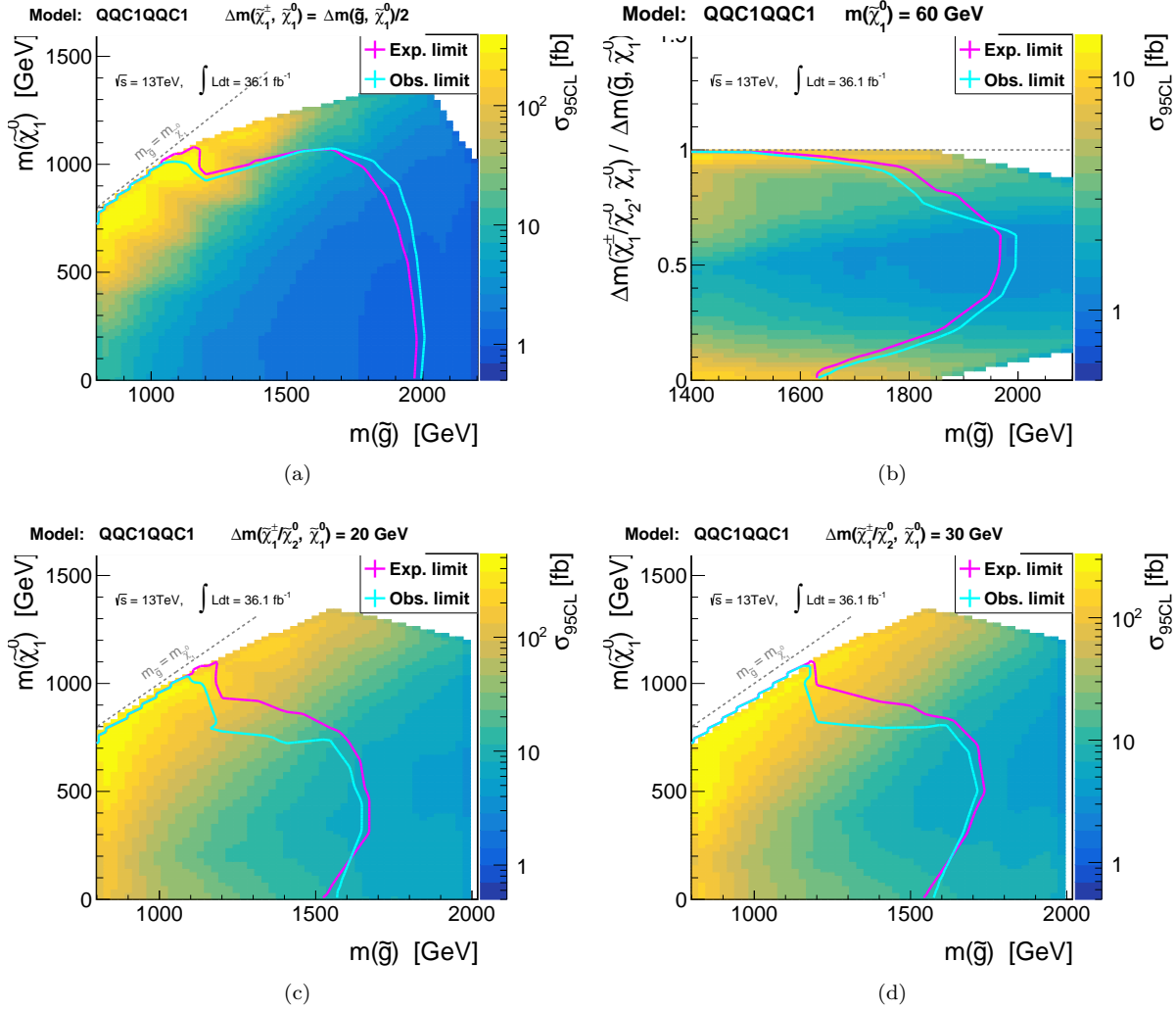


Figure 175: Upper limit of excluded cross-section (95%CL) as the function of the SUSY masses, for benchmark model **QQC1QQC1**, presented in the grids (a)  $x = 1/2$  (b)  $m_{\tilde{\chi}_1^0} = 60\text{ GeV}$  (c)  $\Delta m(\tilde{\chi}_1^\pm, \tilde{\chi}_1^0) = 20\text{ GeV}$  (d)  $\Delta m(\tilde{\chi}_1^\pm, \tilde{\chi}_1^0) = 30\text{ GeV}$ .

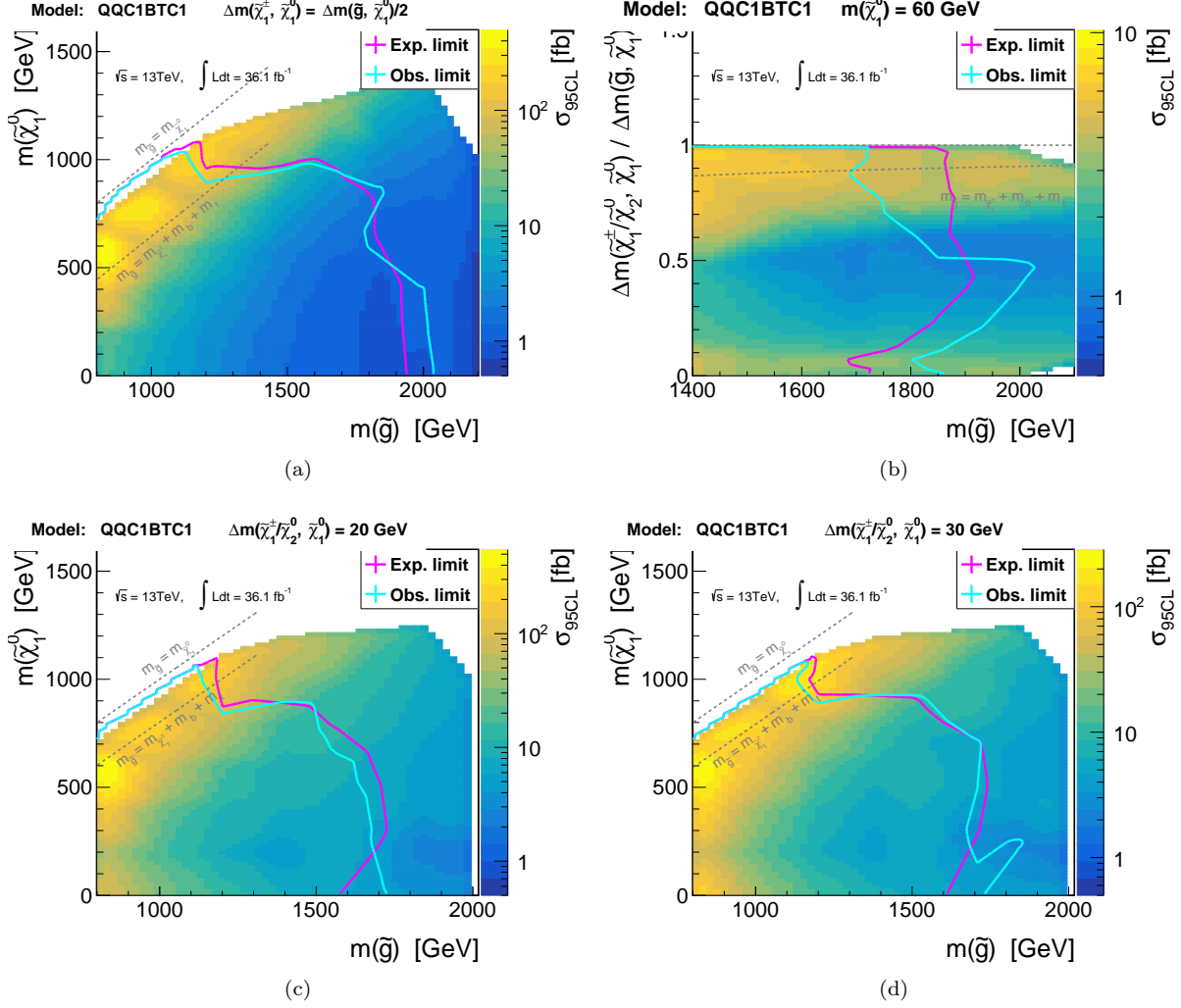


Figure 176: Upper limit of excluded cross-section (95%CL) as the function of the SUSY masses, for benchmark model **QQC1BTC1**, presented in the grids (a)  $x = 1/2$  (b)  $m_{\tilde{\chi}_1^0} = 60\text{ GeV}$  (c)  $\Delta m(\tilde{\chi}_1^\pm, \tilde{\chi}_1^0) = 20\text{ GeV}$  (d)  $\Delta m(\tilde{\chi}_1^\pm, \tilde{\chi}_1^0) = 30\text{ GeV}$ .

**Model: TTN1TTN1**

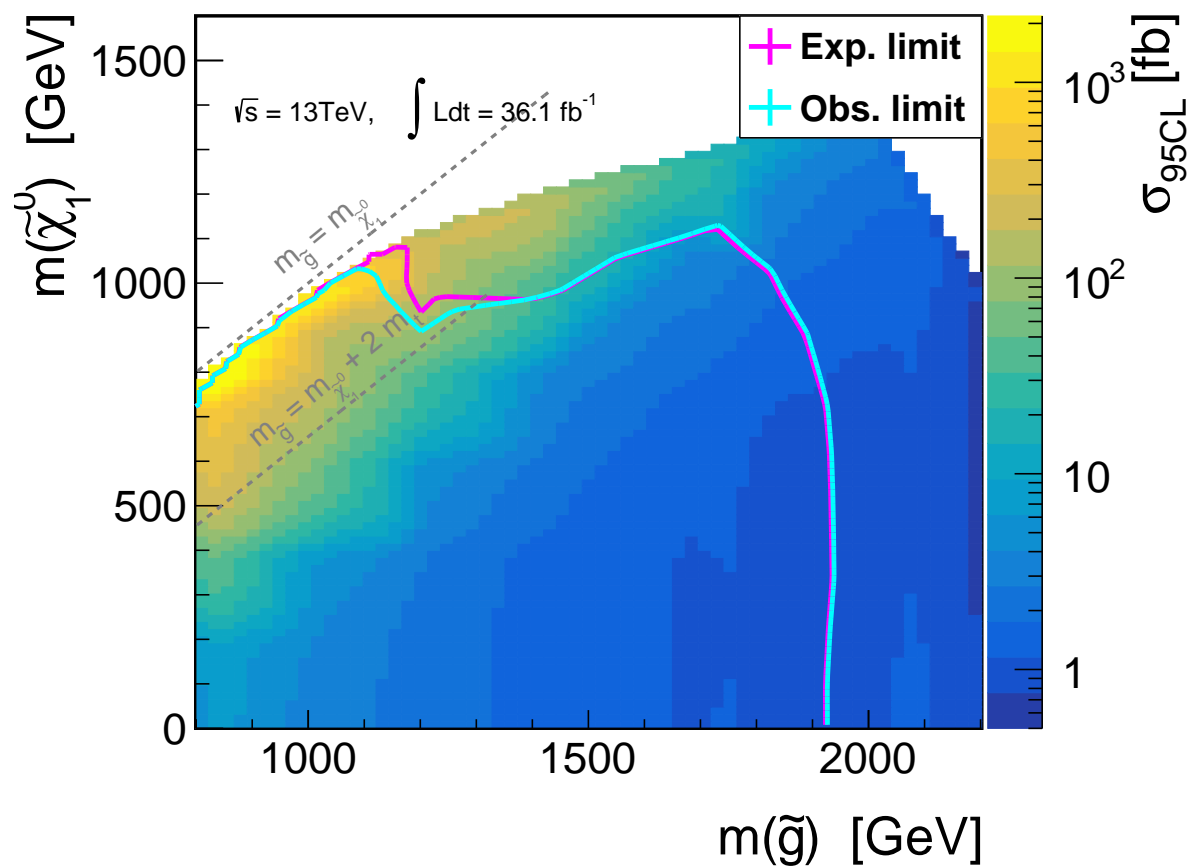


Figure 177: Upper limit of excluded cross-section (95% CL) as the function of the SUSY masses, for benchmark model **TTN1TTN1**.

## G Observed Constraints on All Benchmark Models

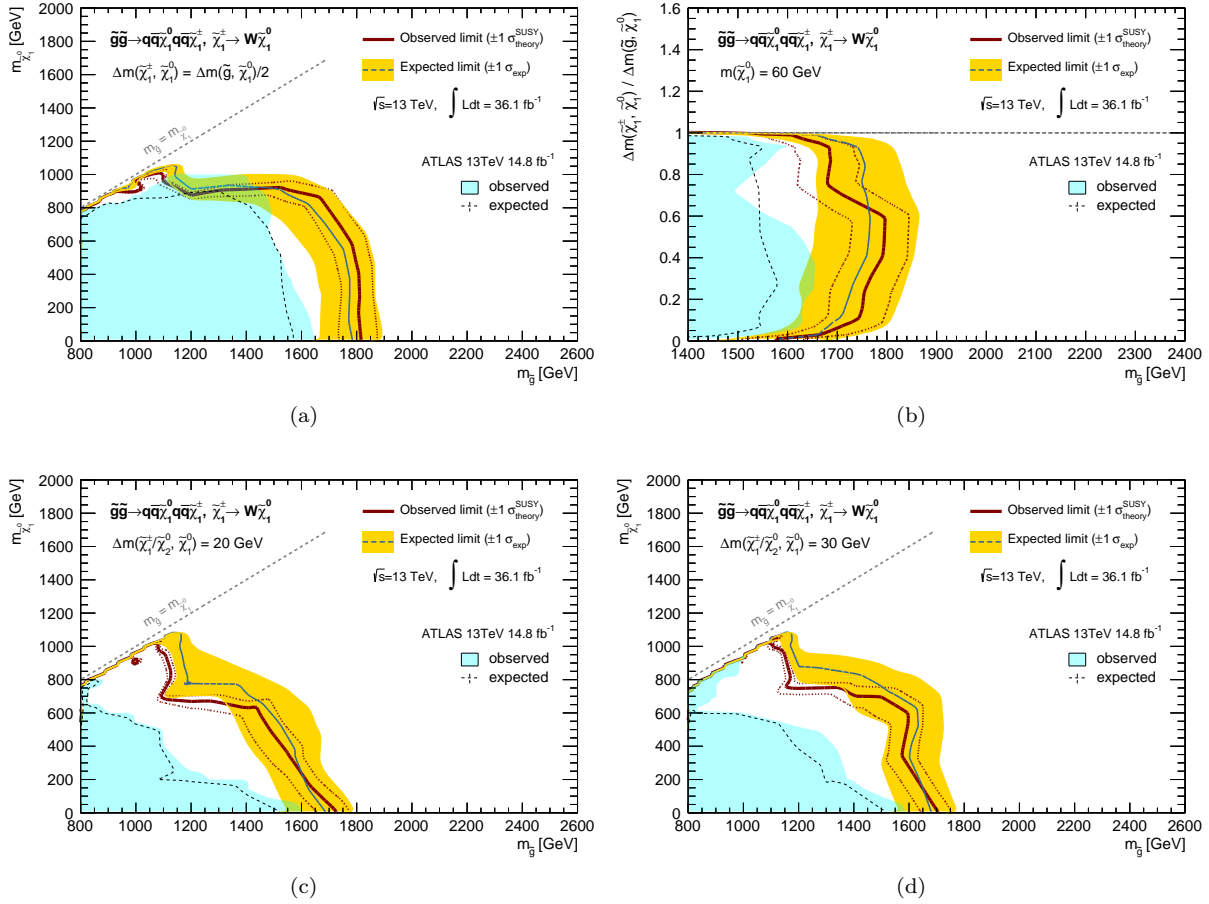


Figure 178: Exclusion limit (95% CL) on the benchmark model **QQN1QQC1** for the grids (a)  $x=1/2$ , (b)  $m_{\tilde{\chi}_1^0} = 60 \text{ GeV}$ , (c)  $\Delta m(\tilde{\chi}_1^\pm, \tilde{\chi}_1^0) = 20 \text{ GeV}$ , (d)  $\Delta m(\tilde{\chi}_1^\pm, \tilde{\chi}_1^0) = 30 \text{ GeV}$ .

## QQN1QQC1

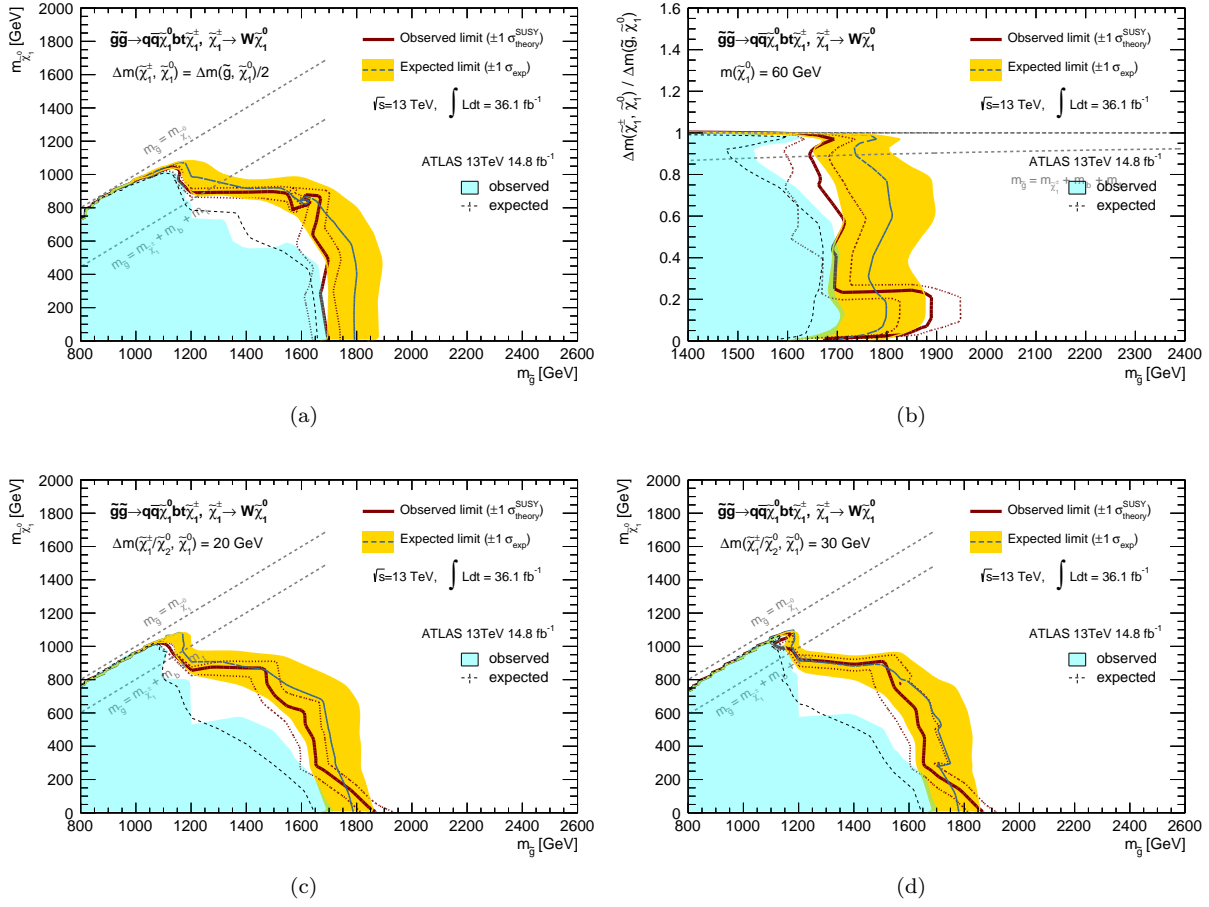
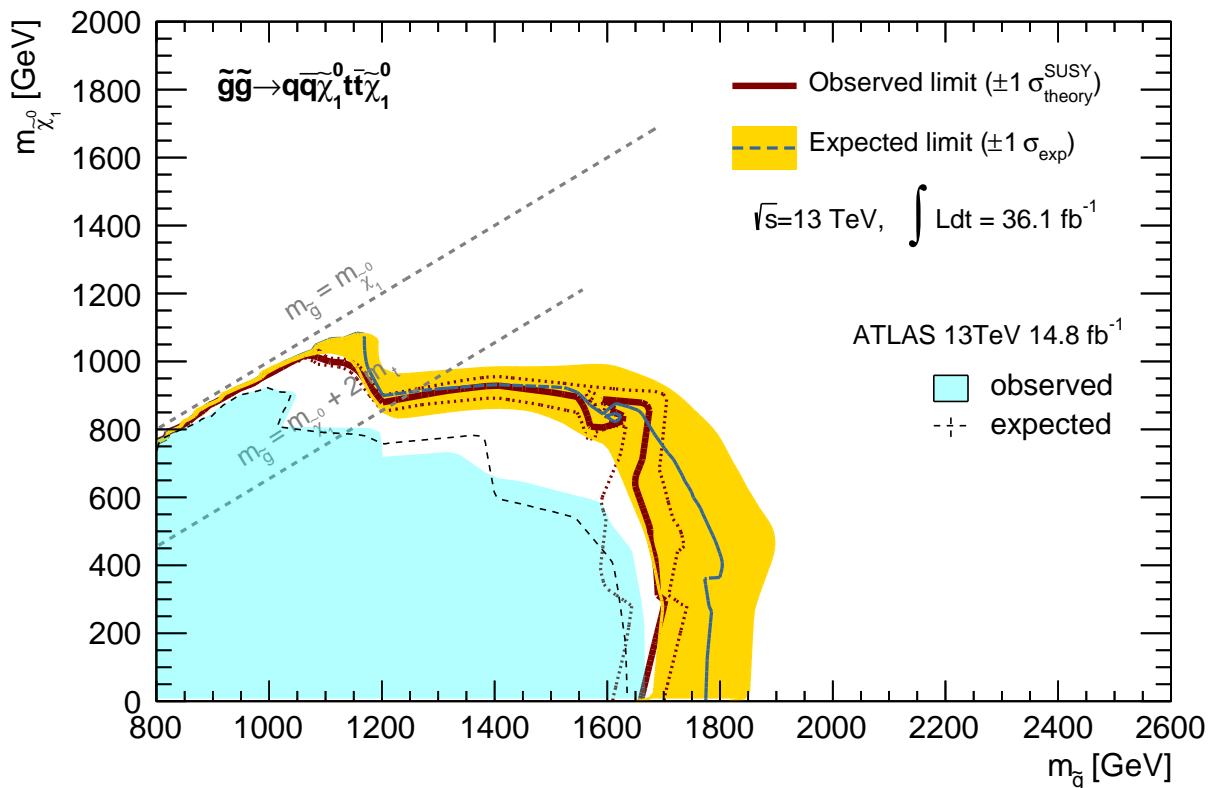


Figure 179: Exclusion limit (95% CL) on the benchmark model **QQQN1BTC1** for the grids (a)  $x=1/2$ , (b)  $m_{\tilde{\chi}_1^0} = 60$  GeV, (c)  $\Delta m(\tilde{\chi}_1^\pm, \tilde{\chi}_1^0) = 20$  GeV, (d)  $\Delta m(\tilde{\chi}_1^\pm, \tilde{\chi}_1^0) = 30$  GeV.

### QQQN1BTC1



(a)

Figure 180: Exclusion limit (95% CL) on the benchmark model **QQN1TTN1**.

**QQN1TTN1**

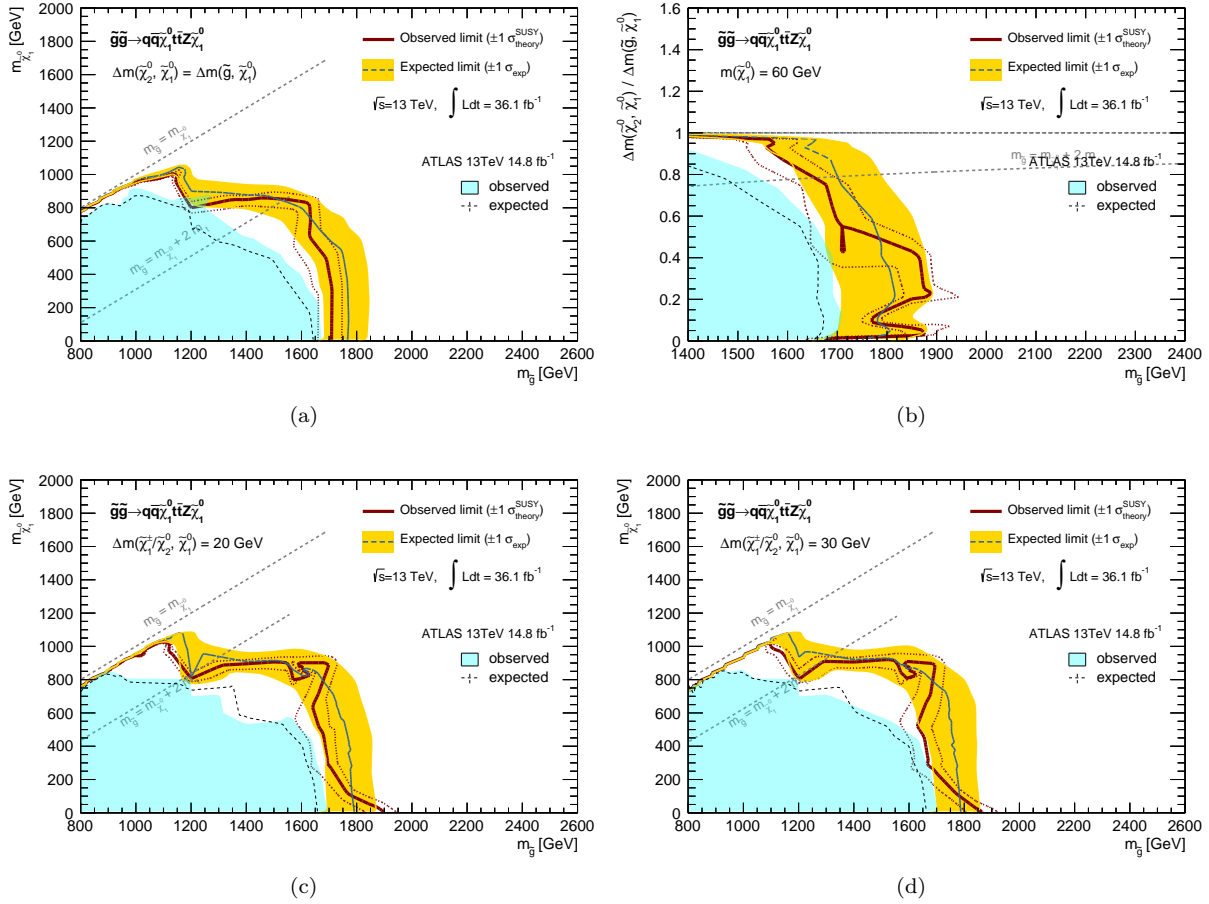
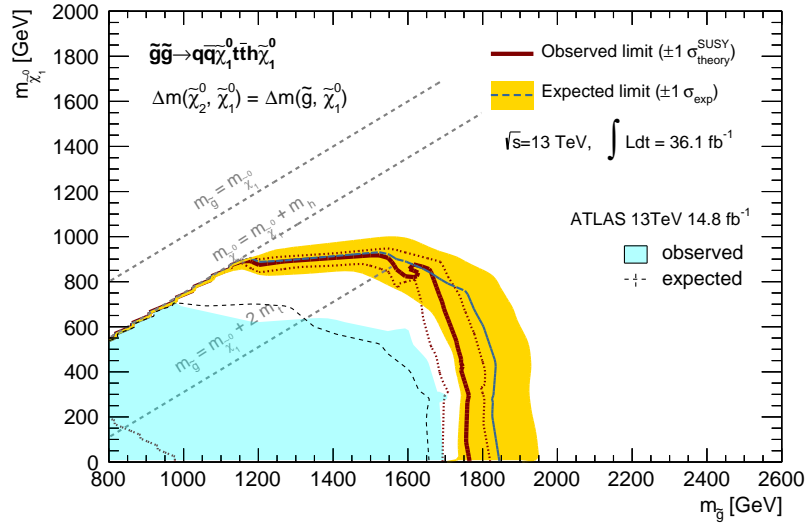
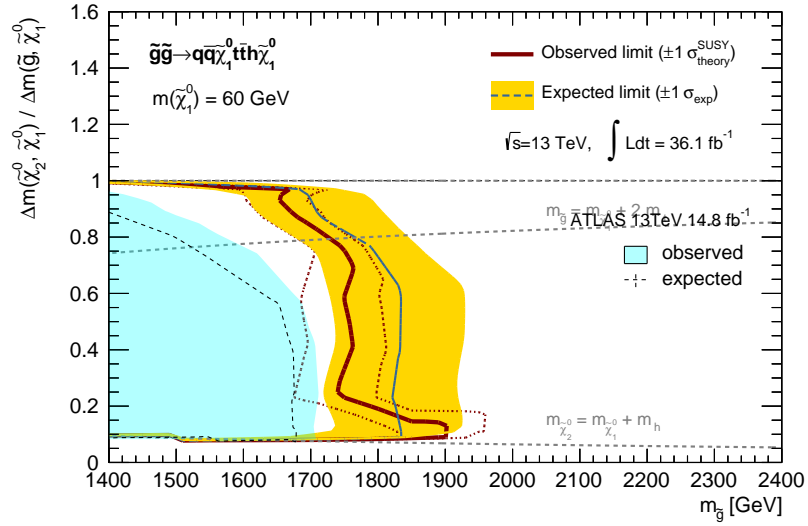


Figure 181: Exclusion limit (95% CL) on the benchmark model **QQQN1TTN2Z** for the grids (a)  $x=1/2$ , (b)  $m_{\tilde{\chi}_1^0} = 60$  GeV, (c)  $\Delta m(\tilde{\chi}_1^\pm, \tilde{\chi}_1^0) = 20$  GeV, (d)  $\Delta m(\tilde{\chi}_1^\pm, \tilde{\chi}_1^0) = 30$  GeV.

## QQQN1TTN2Z



(a)



(b)

Figure 182: Exclusion limit (95% CL) on the benchmark model **QQN1TTN2H** for the grids (a)  $x=1/2$ , (b)  $m_{\tilde{\chi}_1^0} = 60$  GeV.

## QQN1TTN2H

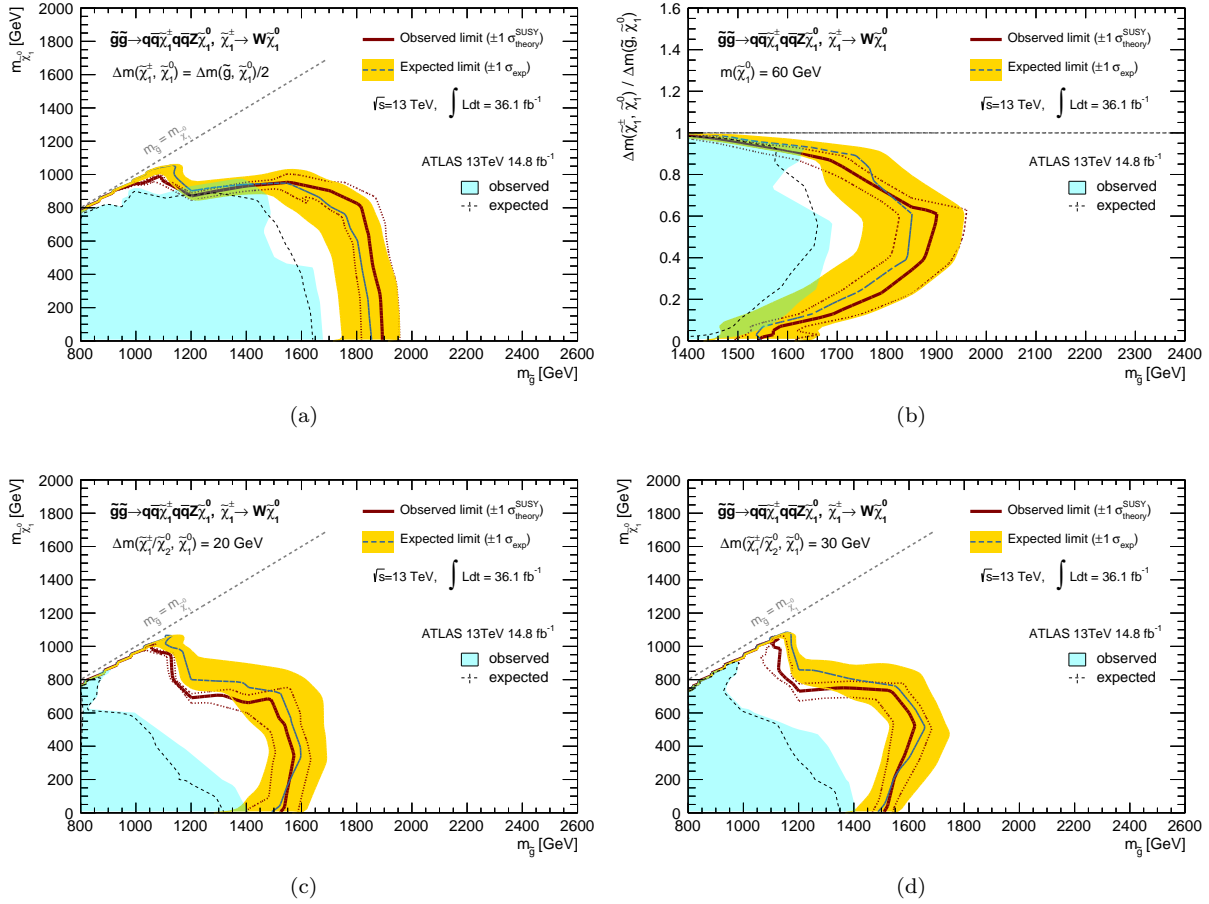


Figure 183: Exclusion limit (95% CL) on the benchmark model **QQC1QQN2Z** for the grids (a)  $x=1/2$ , (b)  $m_{\tilde{\chi}_1^0} = 60$  GeV, (c)  $\Delta m(\tilde{\chi}_1^\pm, \tilde{\chi}_1^0) = 20$  GeV, (d)  $\Delta m(\tilde{\chi}_1^\pm, \tilde{\chi}_1^0) = 30$  GeV.

## QQC1QQN2Z

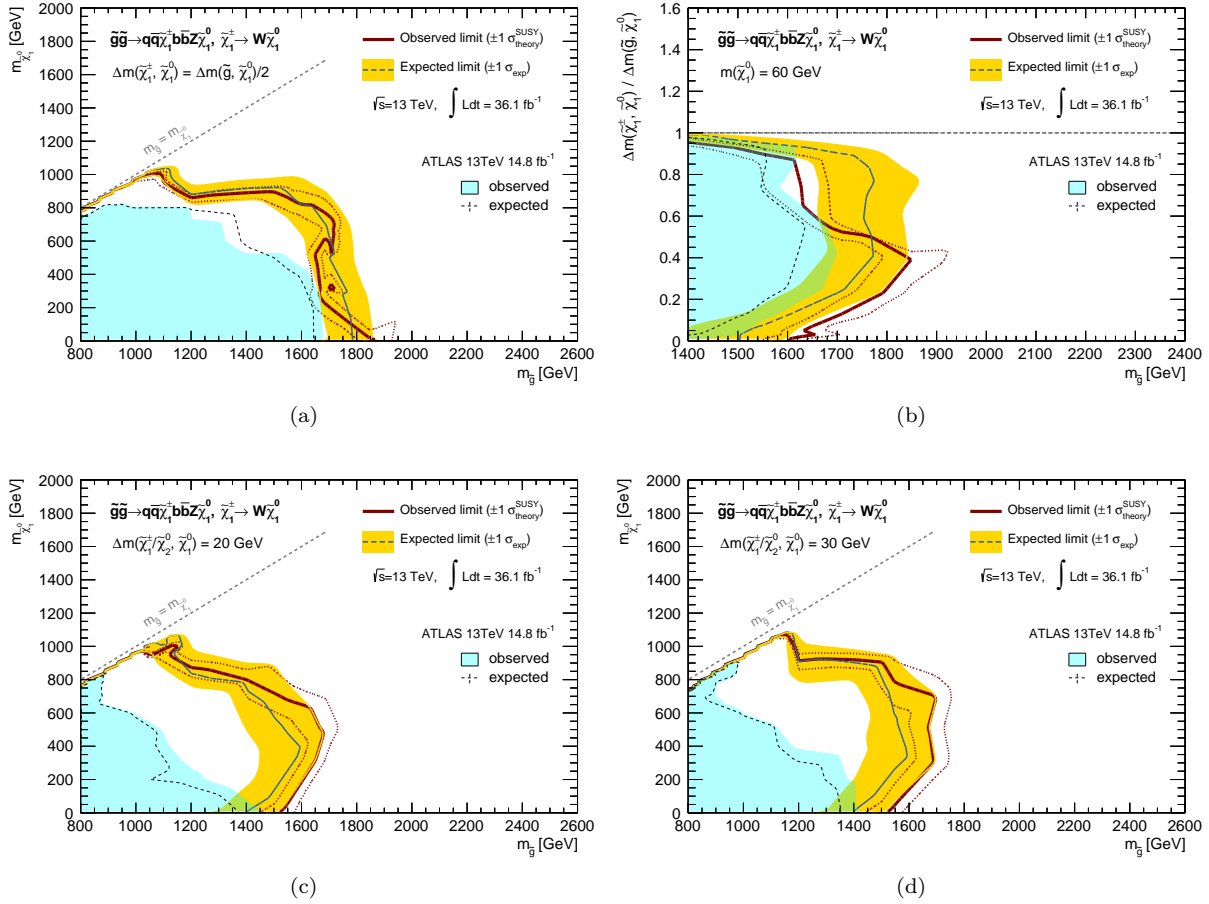


Figure 184: Exclusion limit (95% CL) on the benchmark model **QQC1BBN2Z** for the grids (a)  $x=1/2$ , (b)  $m_{\tilde{\chi}_1^0} = 60$  GeV, (c)  $\Delta m(\tilde{\chi}_1^\pm, \tilde{\chi}_2^0) = 20$  GeV, (d)  $\Delta m(\tilde{\chi}_1^\pm, \tilde{\chi}_2^0) = 30$  GeV.

## QQC1BBN2Z

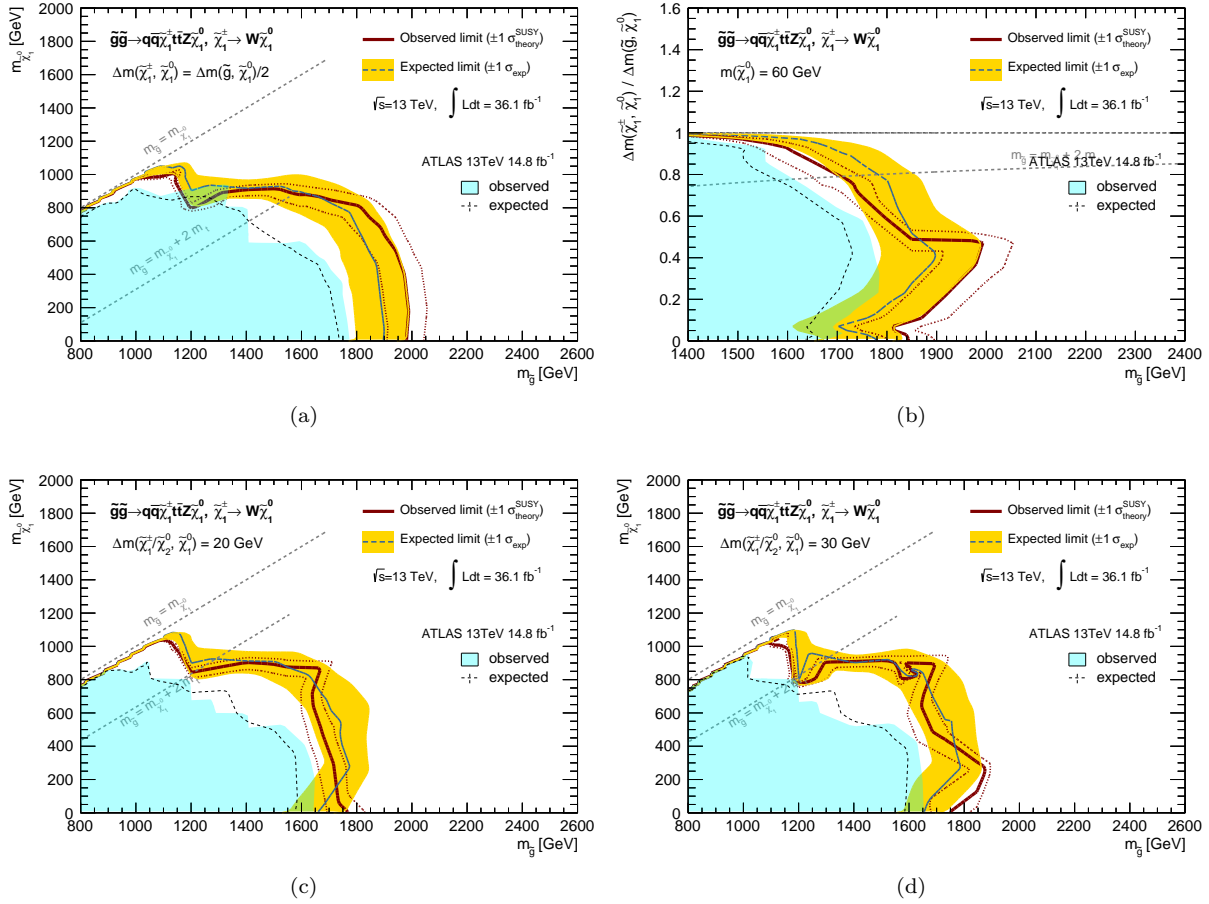
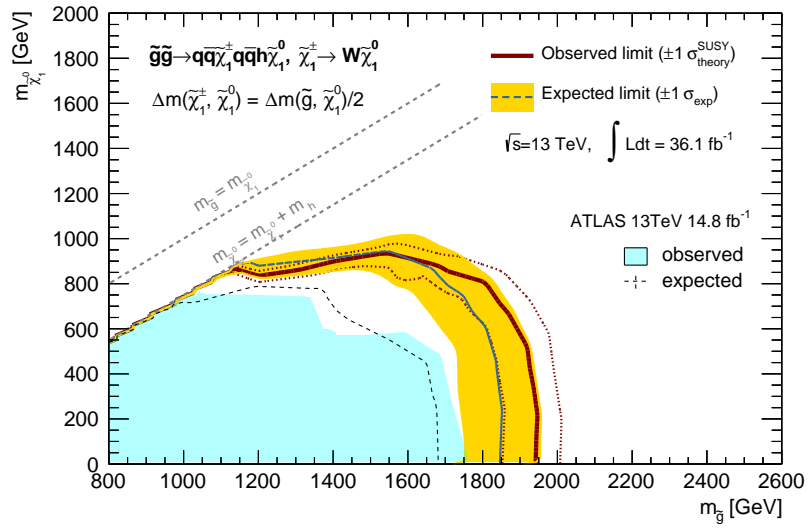
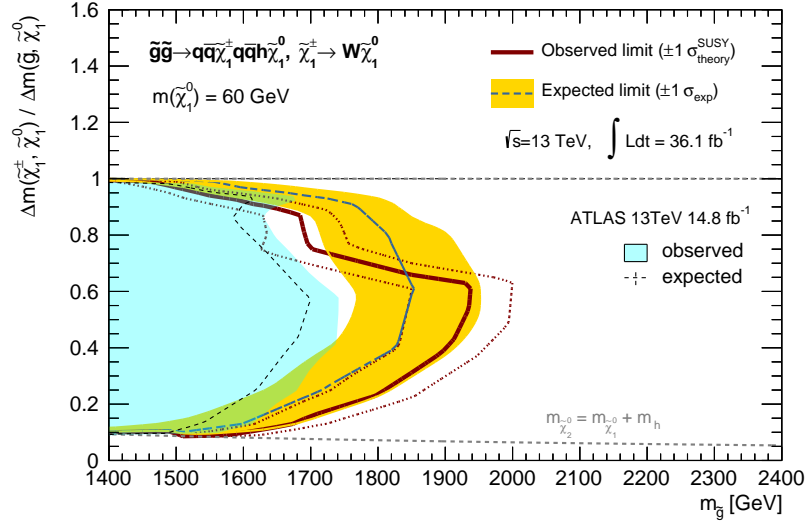


Figure 185: Exclusion limit (95% CL) on the benchmark model **QQC1TTN2Z** for the grids (a)  $x=1/2$ , (b)  $m_{\tilde{\chi}_1^0} = 60$  GeV, (c)  $\Delta m(\tilde{\chi}_1^\pm, \tilde{\chi}_1^0) = 20$  GeV, (d)  $\Delta m(\tilde{\chi}_1^\pm, \tilde{\chi}_1^0) = 30$  GeV.

## QQC1TTN2Z



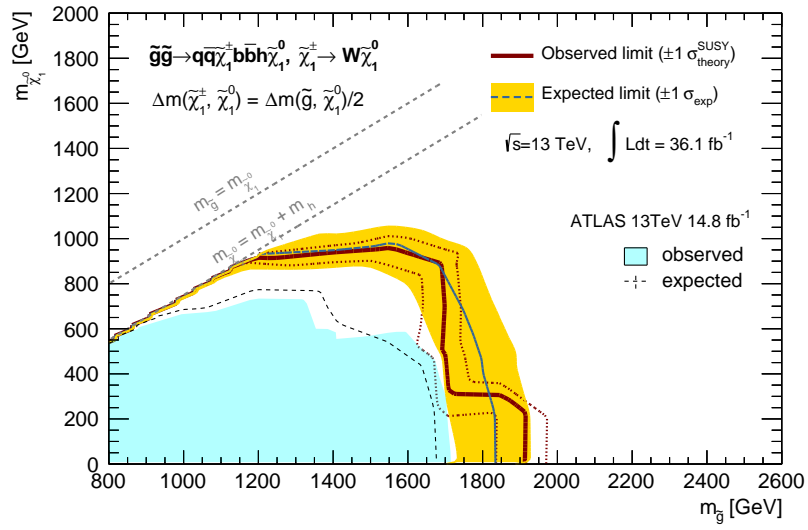
(a)



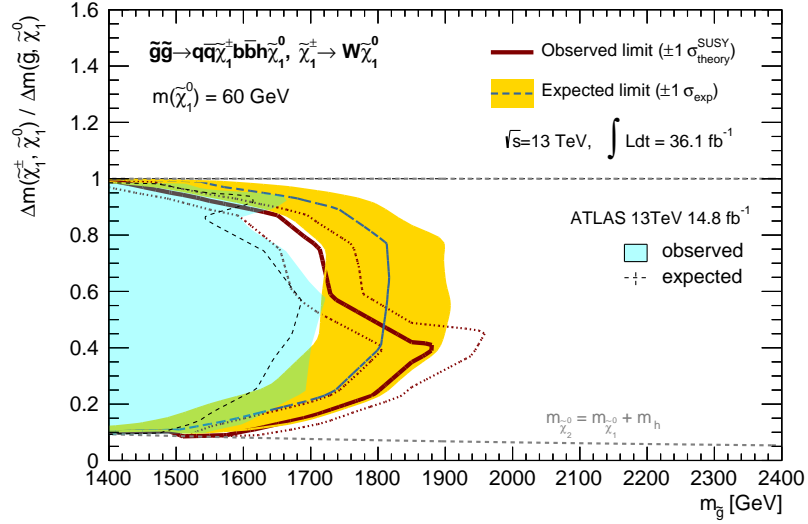
(b)

Figure 186: Exclusion limit (95% CL) on the benchmark model **QQC1QQN2H** for the grids (a)  $x=1/2$ , (b)  $m_{\tilde{\chi}_1^0} = 60$  GeV.

**QQC1QQN2H**



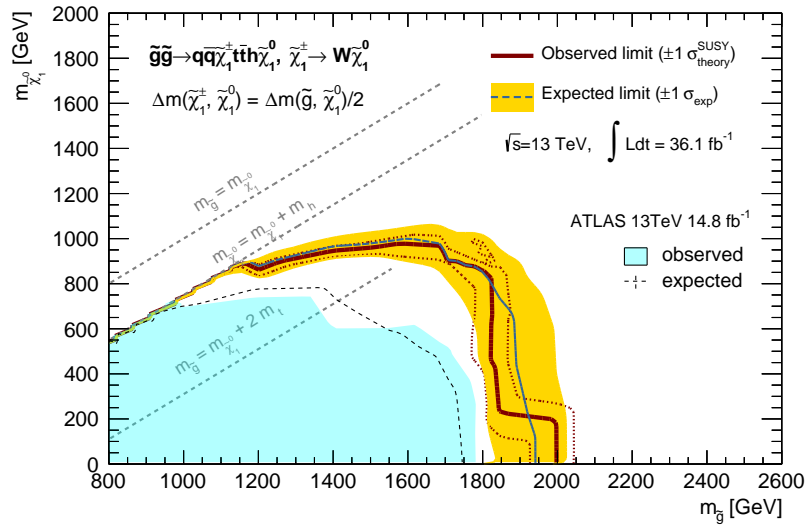
(a)



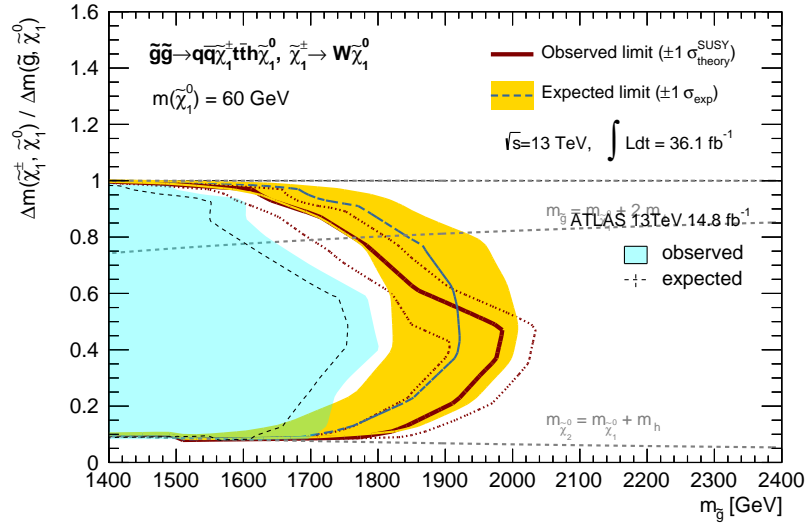
(b)

Figure 187: Exclusion limit (95% CL) on the benchmark model **QQC1BBN2H** for the grids (a)  $x=1/2$ , (b)  $m_{\tilde{\chi}_1^0} = 60$  GeV.

### QQC1BBN2H



(a)



(b)

Figure 188: Exclusion limit (95% CL) on the benchmark model **QQC1TTN2H** for the grids (a)  $x=1/2$ , (b)  $m_{\tilde{\chi}_1^0} = 60$  GeV.

### QQC1TTN2H

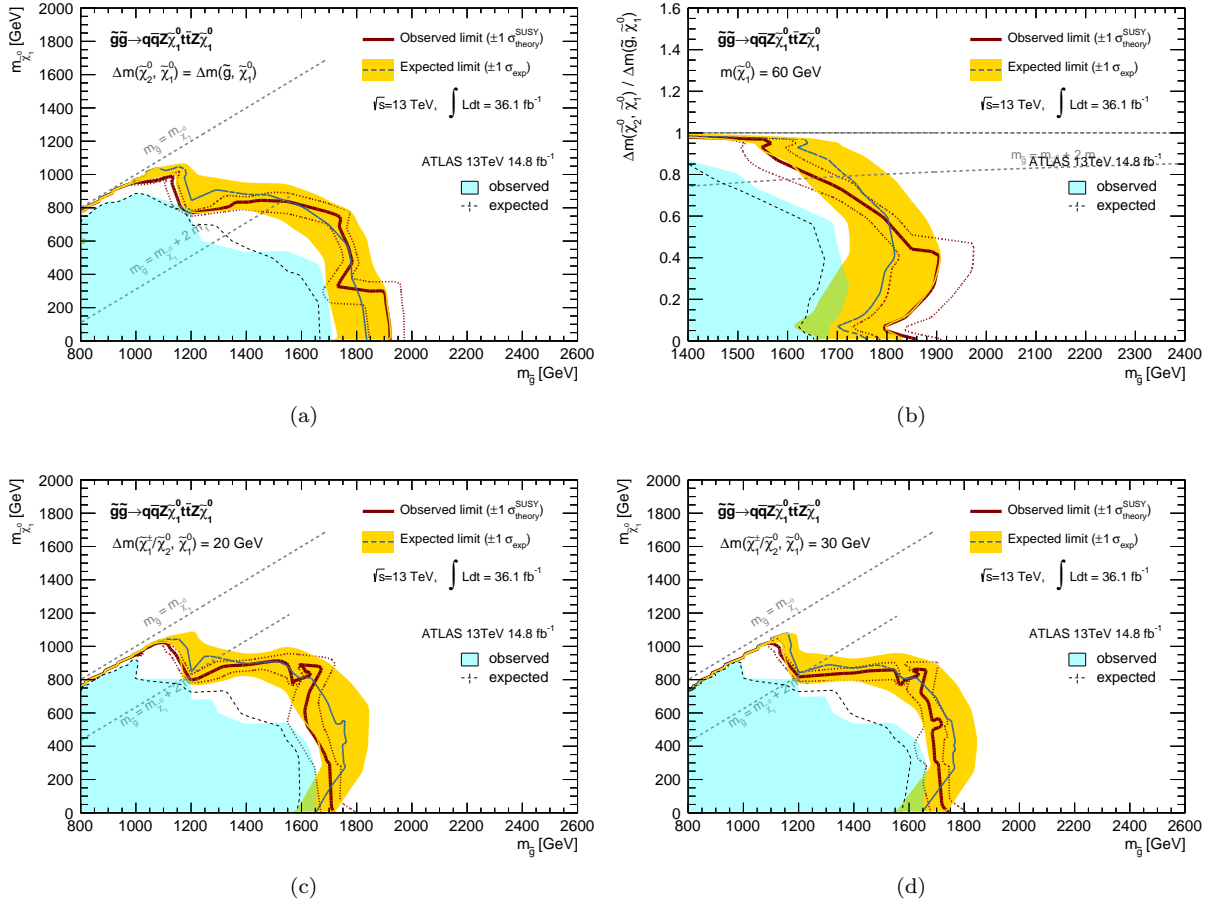
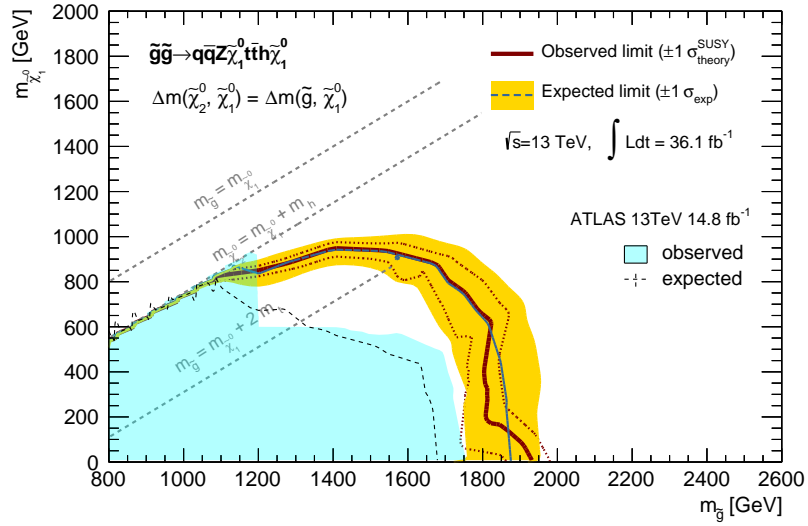
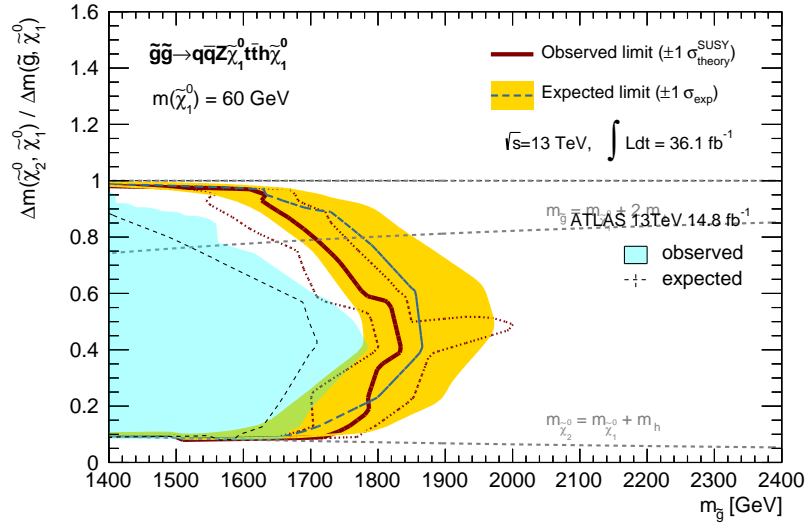


Figure 189: Exclusion limit (95% CL) on the benchmark model **QZN2ZTTN2Z** for the grids (a)  $x=1/2$ , (b)  $m_{\tilde{\chi}_1^0} = 60$  GeV, (c)  $\Delta m(\tilde{\chi}_1^\pm, \tilde{\chi}_1^0) = 20$  GeV, (d)  $\Delta m(\tilde{\chi}_1^\pm, \tilde{\chi}_1^0) = 30$  GeV.

## QZN2ZTTN2Z



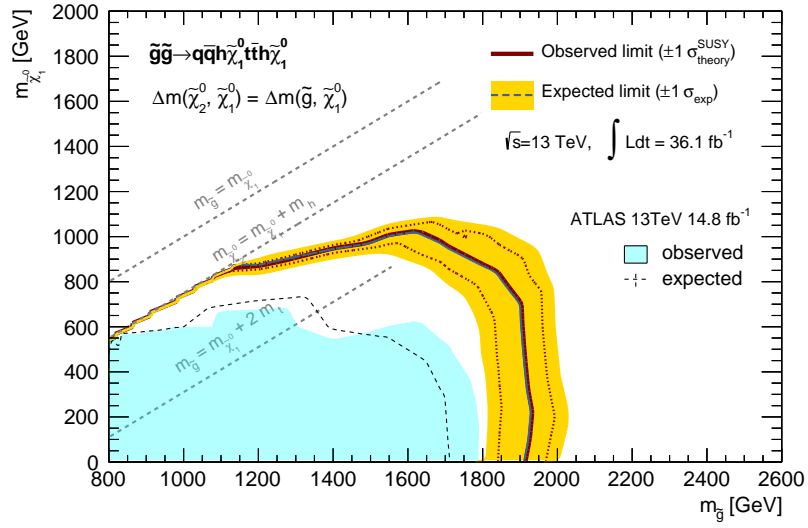
(a)



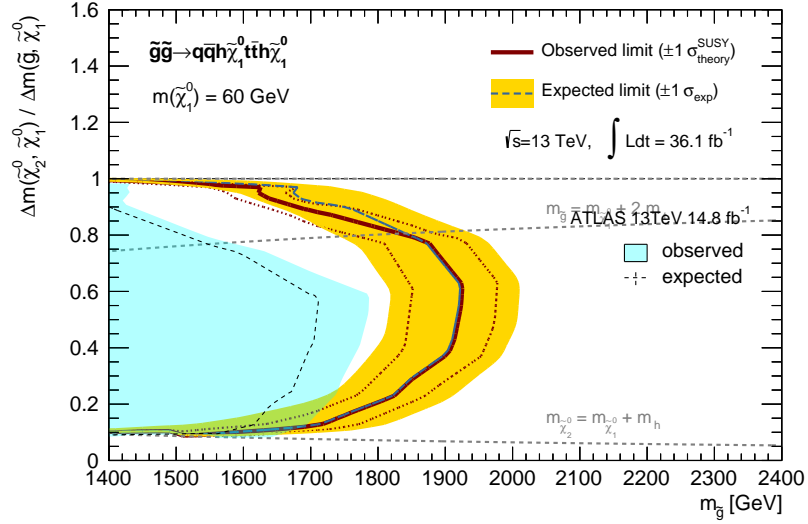
(b)

Figure 190: Exclusion limit (95% CL) on the benchmark model **QZN2ZTTN2H** for the grids (a)  $x=1/2$ , (b)  $m_{\tilde{\chi}_1^0} = 60$  GeV.

### QZN2ZTTN2H



(a)



(b)

Figure 191: Exclusion limit (95% CL) on the benchmark model **QQN2HTTN2H** for the grids (a)  $x=1/2$ , (b)  $m_{\tilde{\chi}_1^0} = 60$  GeV.

### QQN2HTTN2H

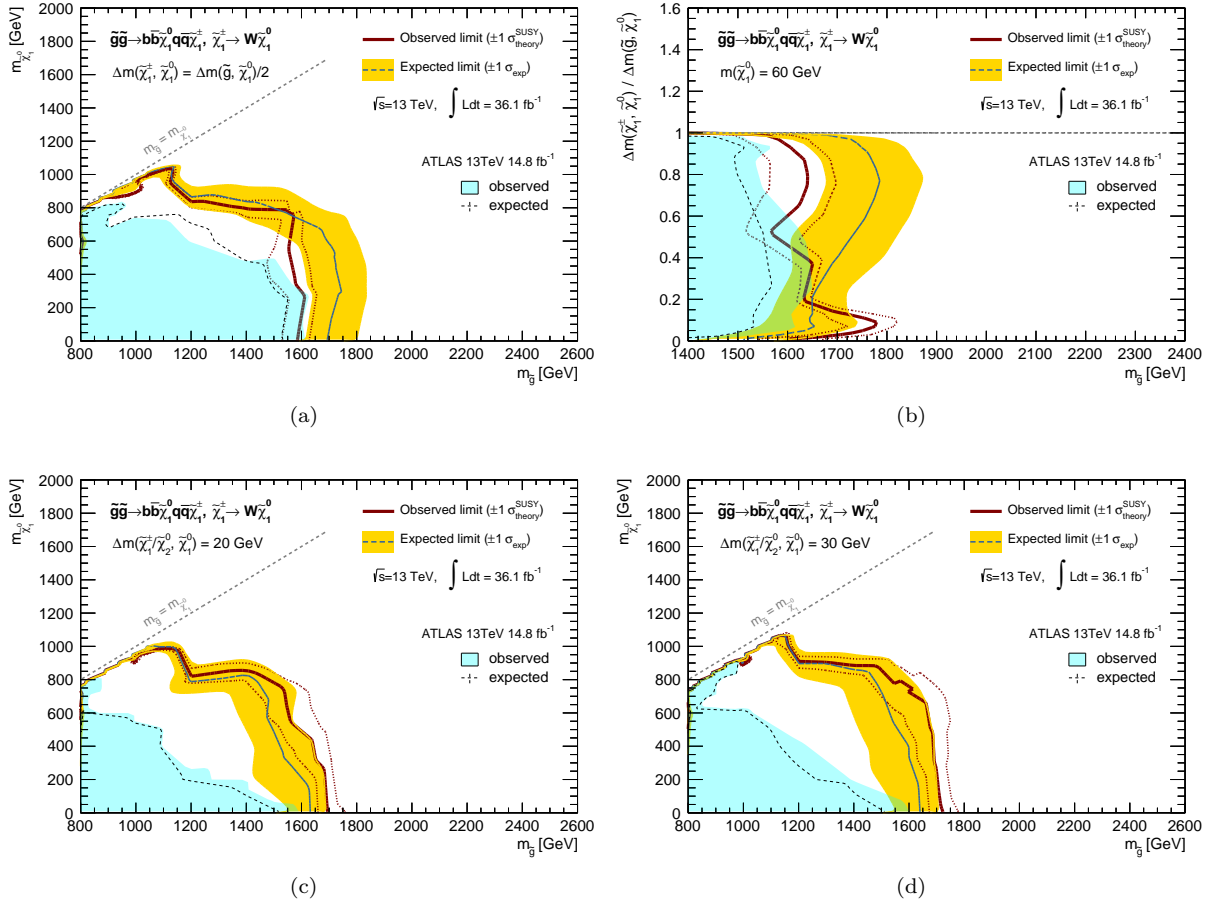


Figure 192: Exclusion limit (95% CL) on the benchmark model **BBN1QQC1** for the grids (a)  $x=1/2$ , (b)  $m_{\tilde{\chi}_1^0} = 60 \text{ GeV}$ , (c)  $\Delta m(\tilde{\chi}_1^\pm, \tilde{\chi}_1^0) = 20 \text{ GeV}$ , (d)  $\Delta m(\tilde{\chi}_1^\pm, \tilde{\chi}_1^0) = 30 \text{ GeV}$ .

## BBN1QQC1

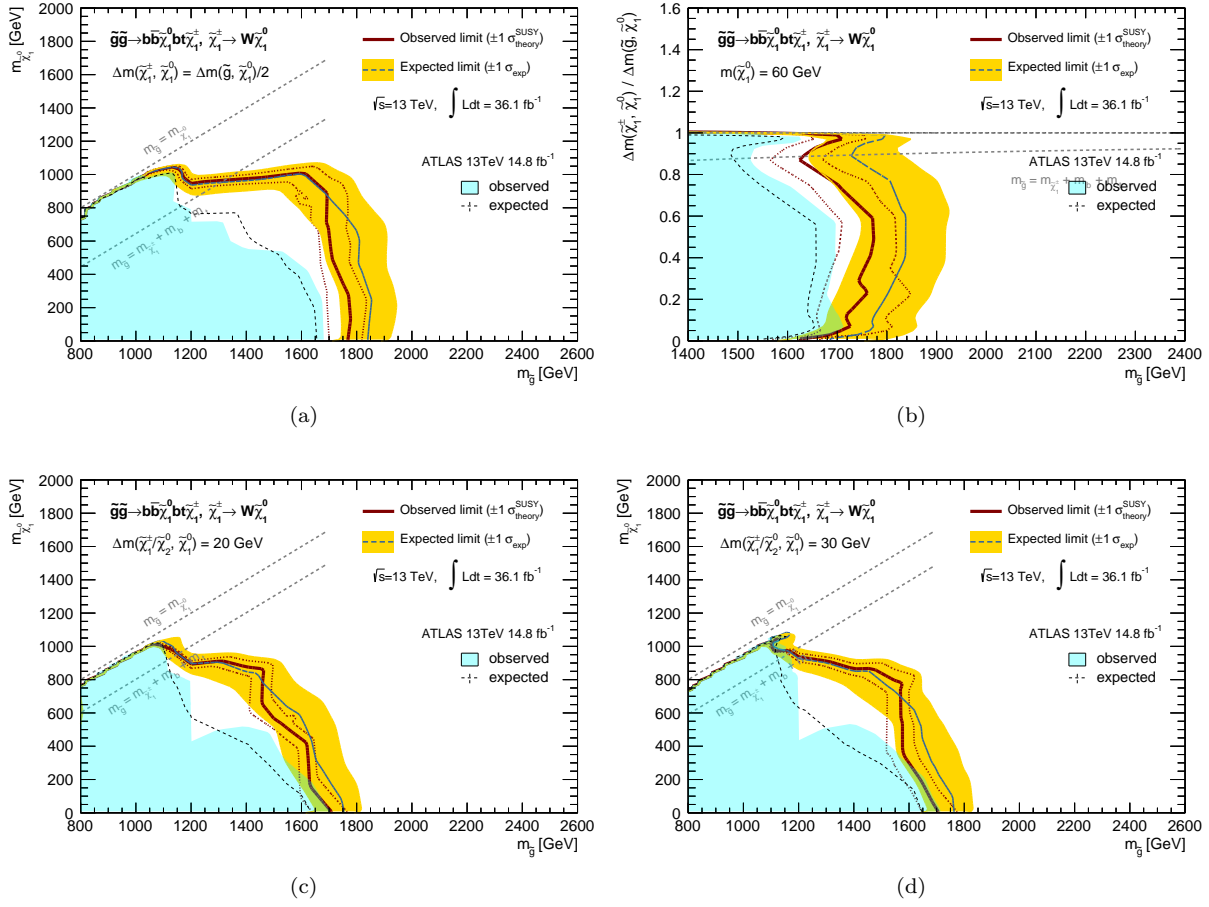
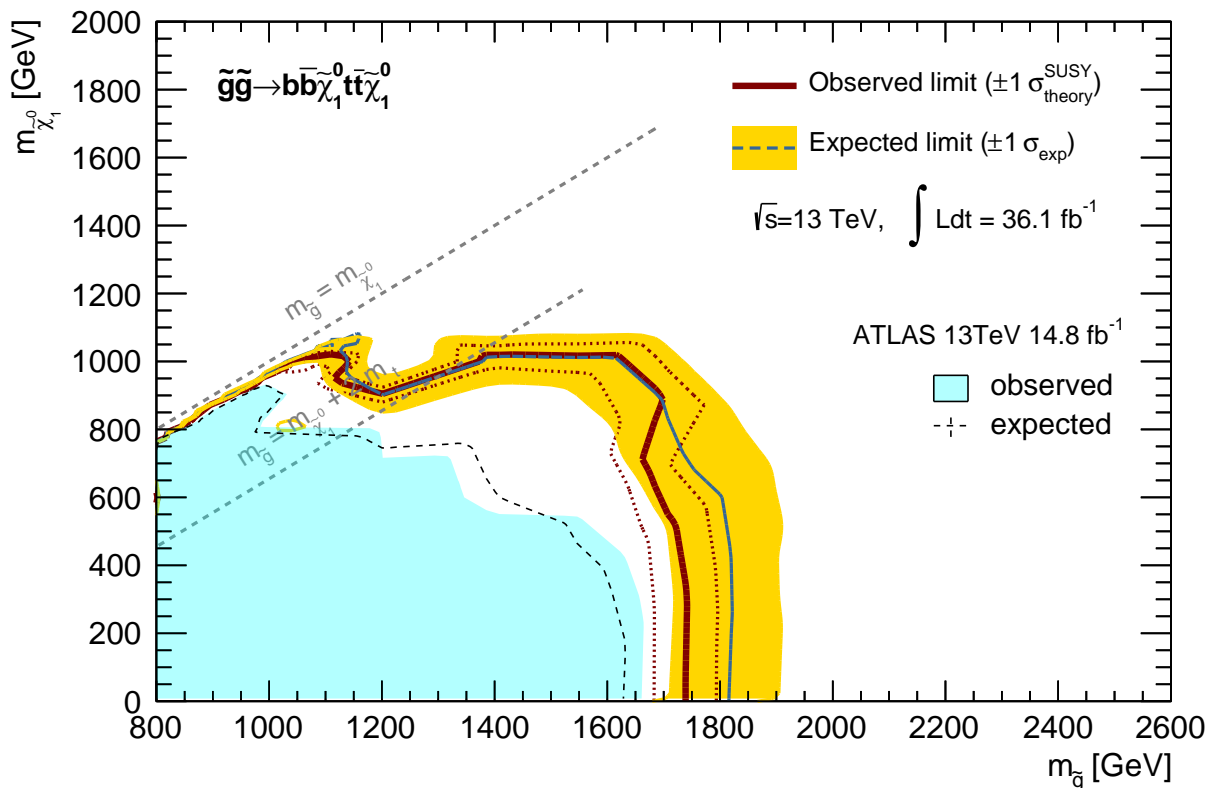


Figure 193: Exclusion limit (95% CL) on the benchmark model **BBN1BTC1** for the grids (a)  $x=1/2$ , (b)  $m_{\tilde{\chi}_1^0} = 60$  GeV, (c)  $\Delta m(\tilde{\chi}_1^\pm, \tilde{\chi}_1^0) = 20$  GeV, (d)  $\Delta m(\tilde{\chi}_1^\pm, \tilde{\chi}_1^0) = 30$  GeV.

## BBN1BTC1



(a)

Figure 194: Exclusion limit (95% CL) on the benchmark model **BBN1TTN1**.

**BBN1TTN1**

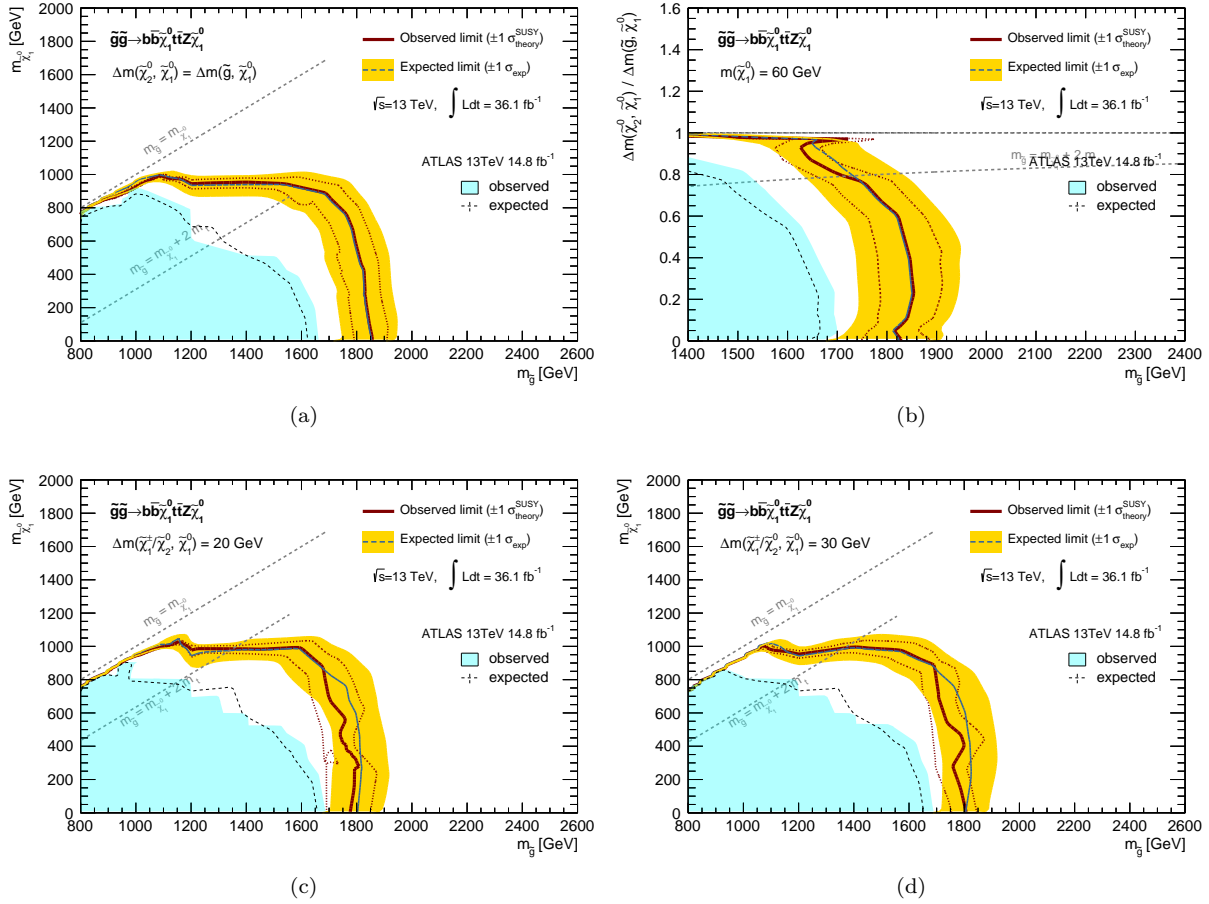
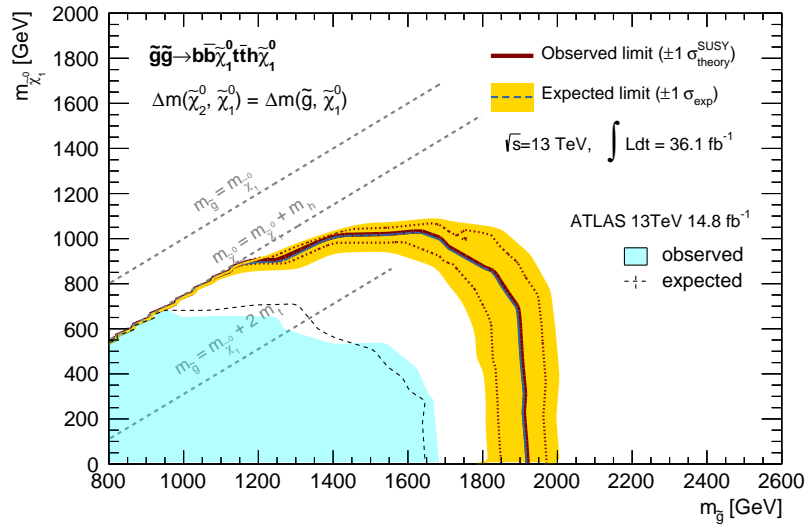
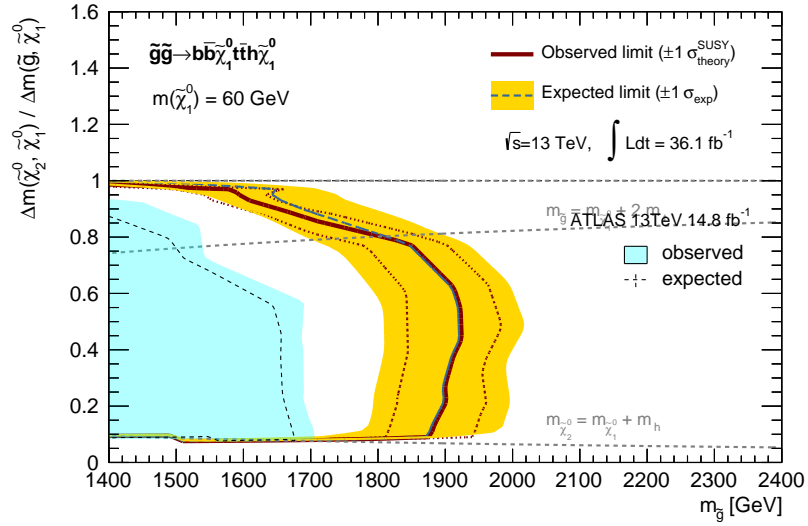


Figure 195: Exclusion limit (95% CL) on the benchmark model **BBN1TTN2Z** for the grids (a)  $x=1/2$ , (b)  $m_{\tilde{\chi}_1^0} = 60 \text{ GeV}$ , (c)  $\Delta m(\tilde{\chi}_1^\pm, \tilde{\chi}_1^0) = 20 \text{ GeV}$ , (d)  $\Delta m(\tilde{\chi}_1^\pm, \tilde{\chi}_1^0) = 30 \text{ GeV}$ .

## BBN1TTN2Z



(a)



(b)

Figure 196: Exclusion limit (95% CL) on the benchmark model **BBN1TTN2H** for the grids (a)  $x=1/2$ , (b)  $m_{\tilde{\chi}_1^0} = 60$  GeV.

## BBN1TTN2H

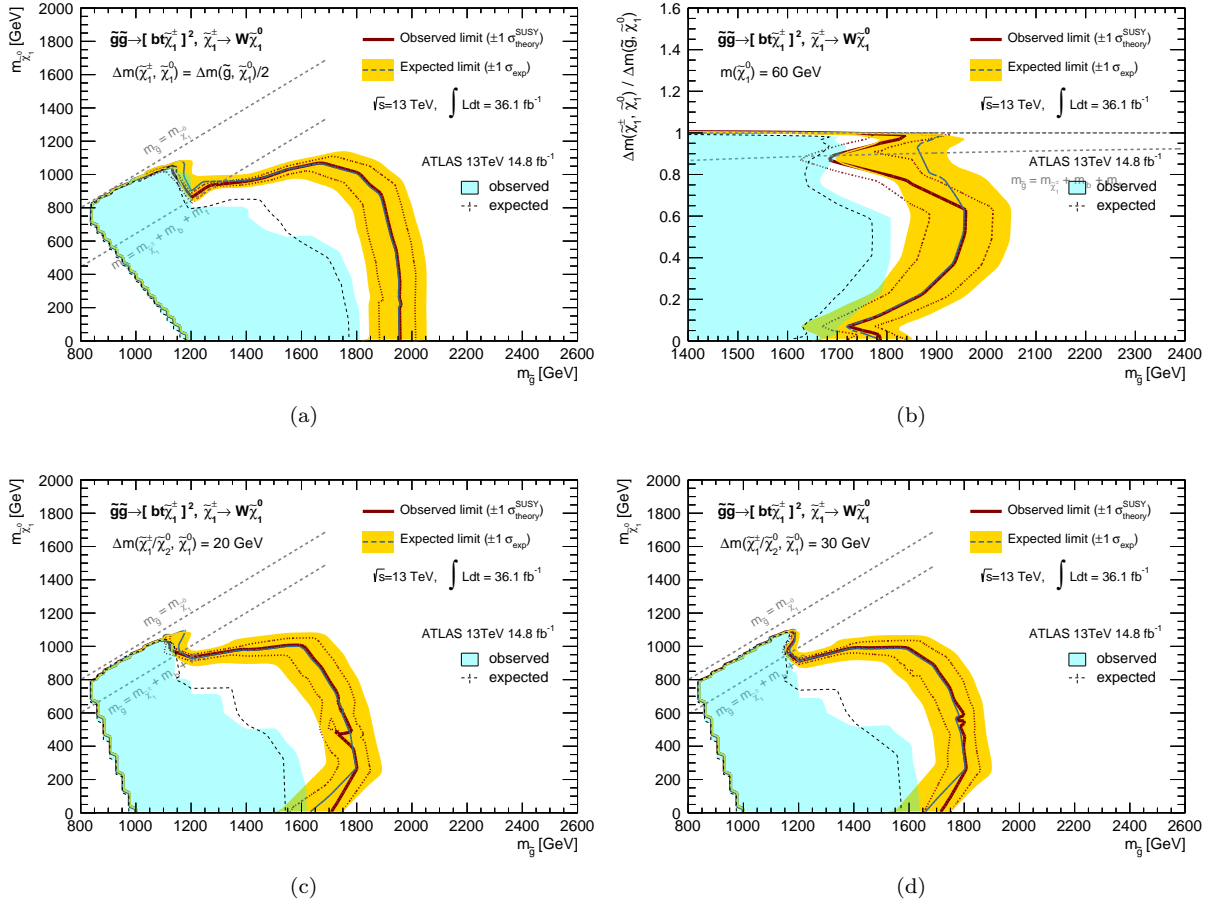


Figure 197: Exclusion limit (95% CL) on the benchmark model **symBTC1** for the grids (a)  $x=1/2$ , (b)  $m_{\tilde{\chi}_1^0} = 60$  GeV, (c)  $\Delta m(\tilde{\chi}_1^\pm, \tilde{\chi}_1^0) = 20$  GeV, (d)  $\Delta m(\tilde{\chi}_1^\pm, \tilde{\chi}_1^0) = 30$  GeV.

**symBTC1**

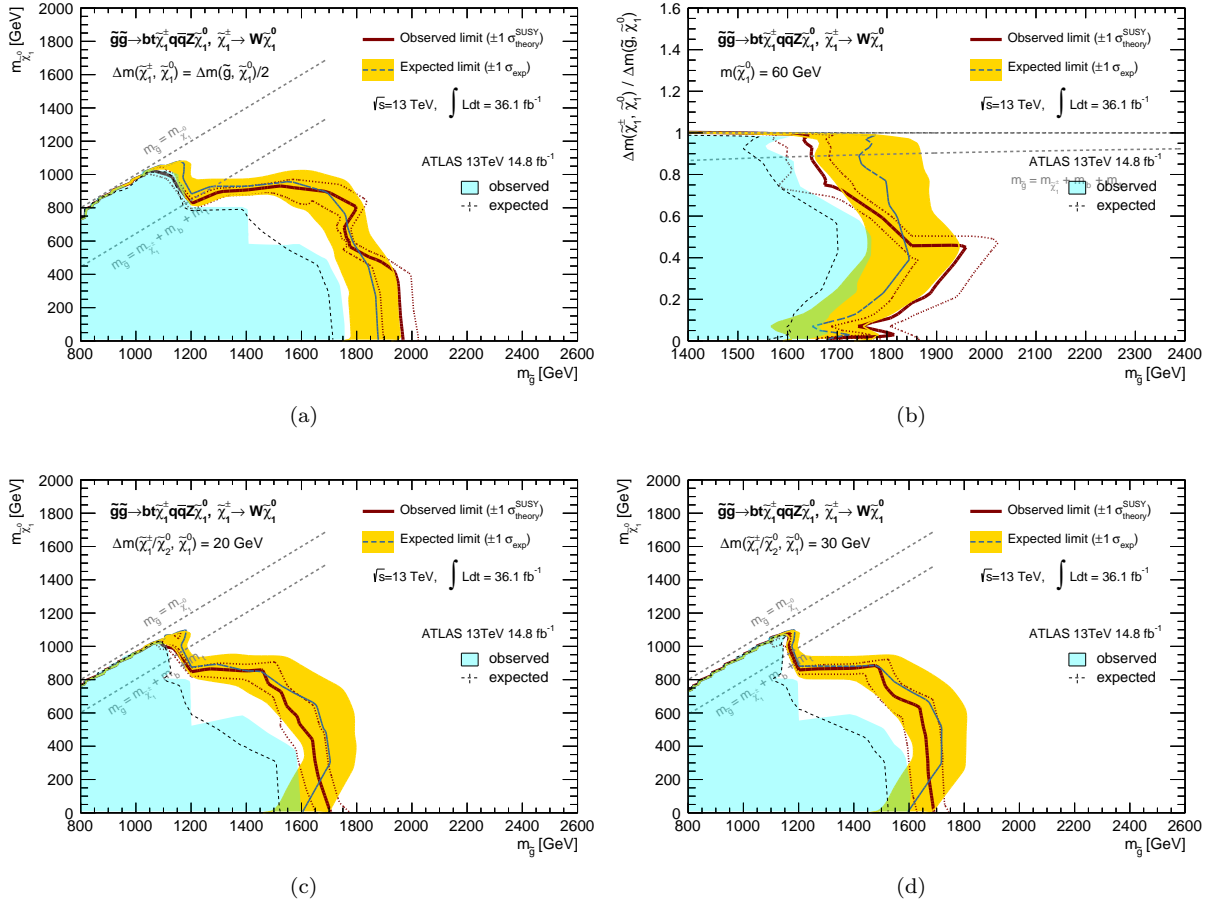


Figure 198: Exclusion limit (95% CL) on the benchmark model **BTC1QQN2Z** for the grids (a)  $x=1/2$ , (b)  $m_{\tilde{\chi}_1^0} = 60$  GeV, (c)  $\Delta m(\tilde{\chi}_1^\pm, \tilde{\chi}_1^0) = 20$  GeV, (d)  $\Delta m(\tilde{\chi}_1^\pm, \tilde{\chi}_1^0) = 30$  GeV.

## BTC1QQN2Z

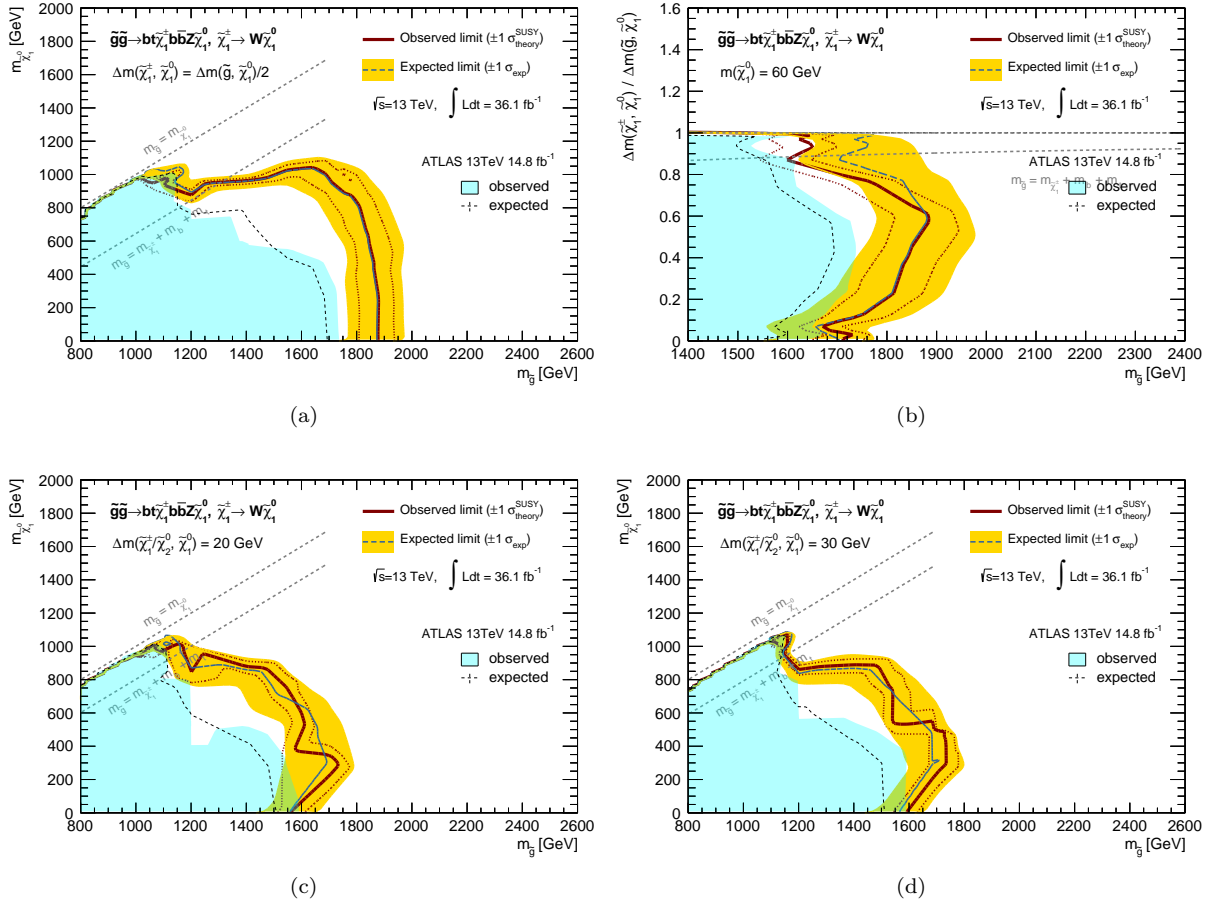


Figure 199: Exclusion limit (95% CL) on the benchmark model **BTC1BBN2Z** for the grids (a)  $x=1/2$ , (b)  $m_{\tilde{\chi}_1^0} = 60$  GeV, (c)  $\Delta m(\tilde{\chi}_1^\pm, \tilde{\chi}_1^0) = 20$  GeV, (d)  $\Delta m(\tilde{\chi}_1^\pm, \tilde{\chi}_1^0) = 30$  GeV.

## BTC1BBN2Z

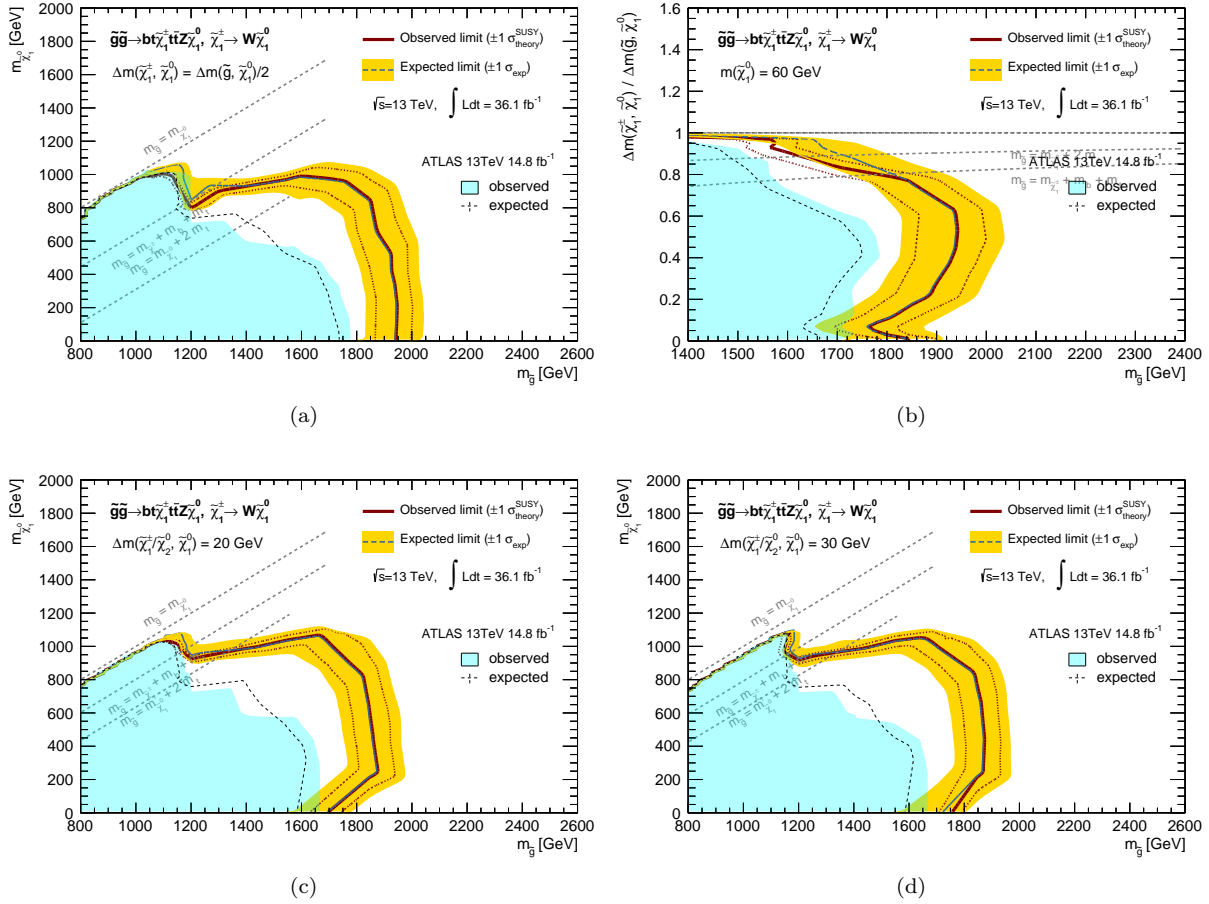
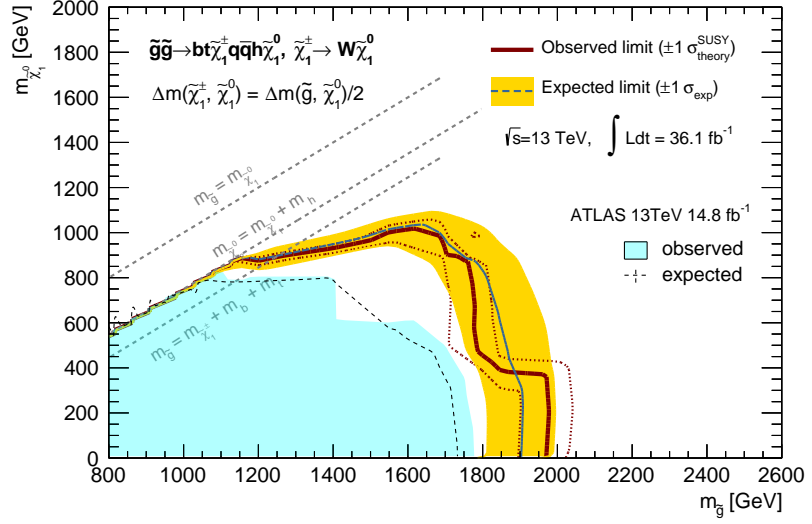
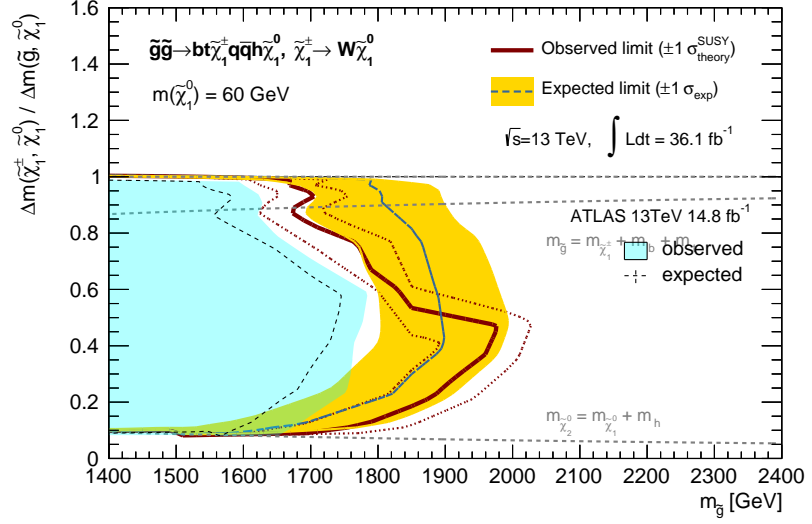


Figure 200: Exclusion limit (95% CL) on the benchmark model **BTC1TTN2Z** for the grids (a)  $x=1/2$ , (b)  $m_{\tilde{\chi}_1^0} = 60$  GeV, (c)  $\Delta m(\tilde{\chi}_1^\pm, \tilde{\chi}_1^0) = 20$  GeV, (d)  $\Delta m(\tilde{\chi}_1^\pm, \tilde{\chi}_1^0) = 30$  GeV.

## BTC1TTN2Z



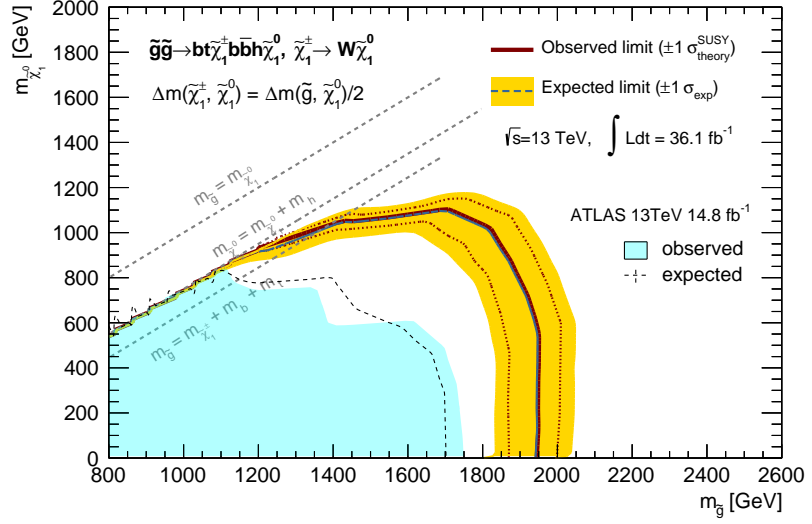
(a)



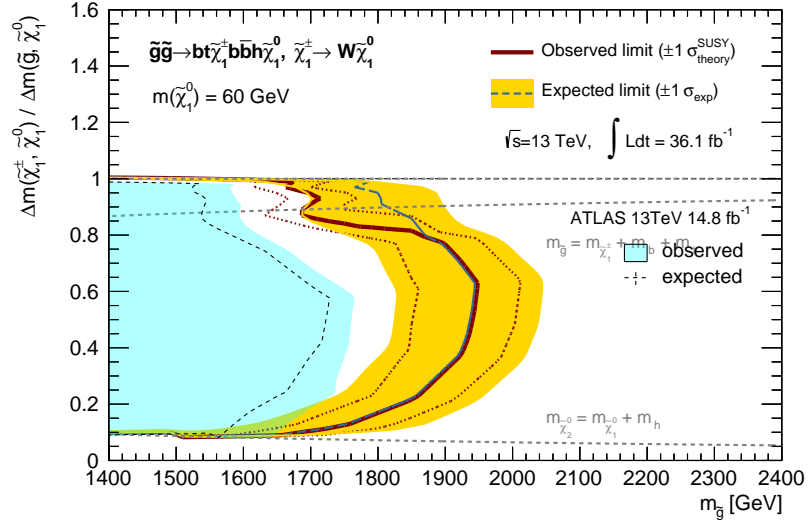
(b)

Figure 201: Exclusion limit (95% CL) on the benchmark model **BTC1QQN2H** for the grids (a)  $x=1/2$ , (b)  $m_{\tilde{\chi}_1^0} = 60$  GeV.

## BTC1QQN2H



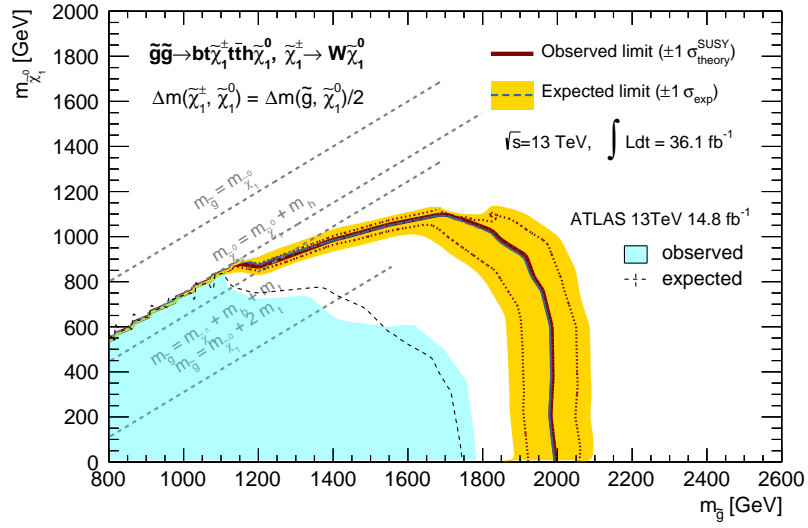
(a)



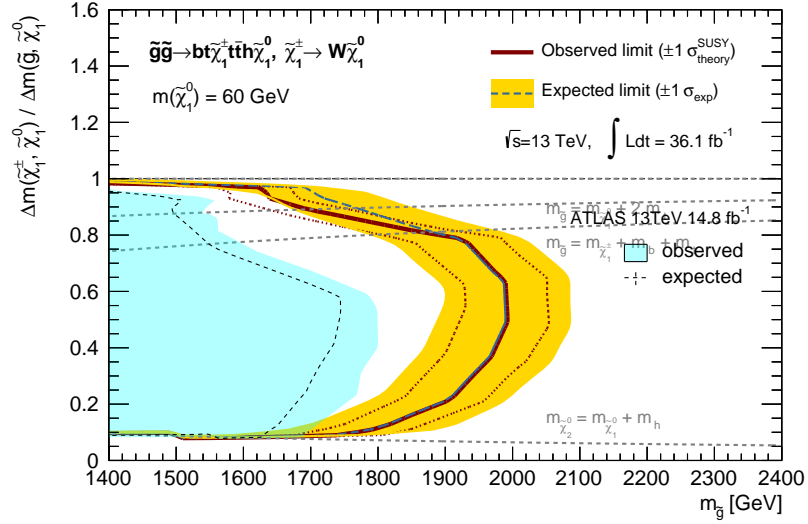
(b)

Figure 202: Exclusion limit (95% CL) on the benchmark model **BTC1BBN2H** for the grids (a)  $x=1/2$ , (b)  $m_{\tilde{\chi}_1^0} = 60$  GeV.

### BTC1BBN2H



(a)



(b)

Figure 203: Exclusion limit (95% CL) on the benchmark model **BTC1TTN2H** for the grids (a)  $x=1/2$ , (b)  $m_{\tilde{\chi}_1^0} = 60$  GeV.

### BTC1TTN2H

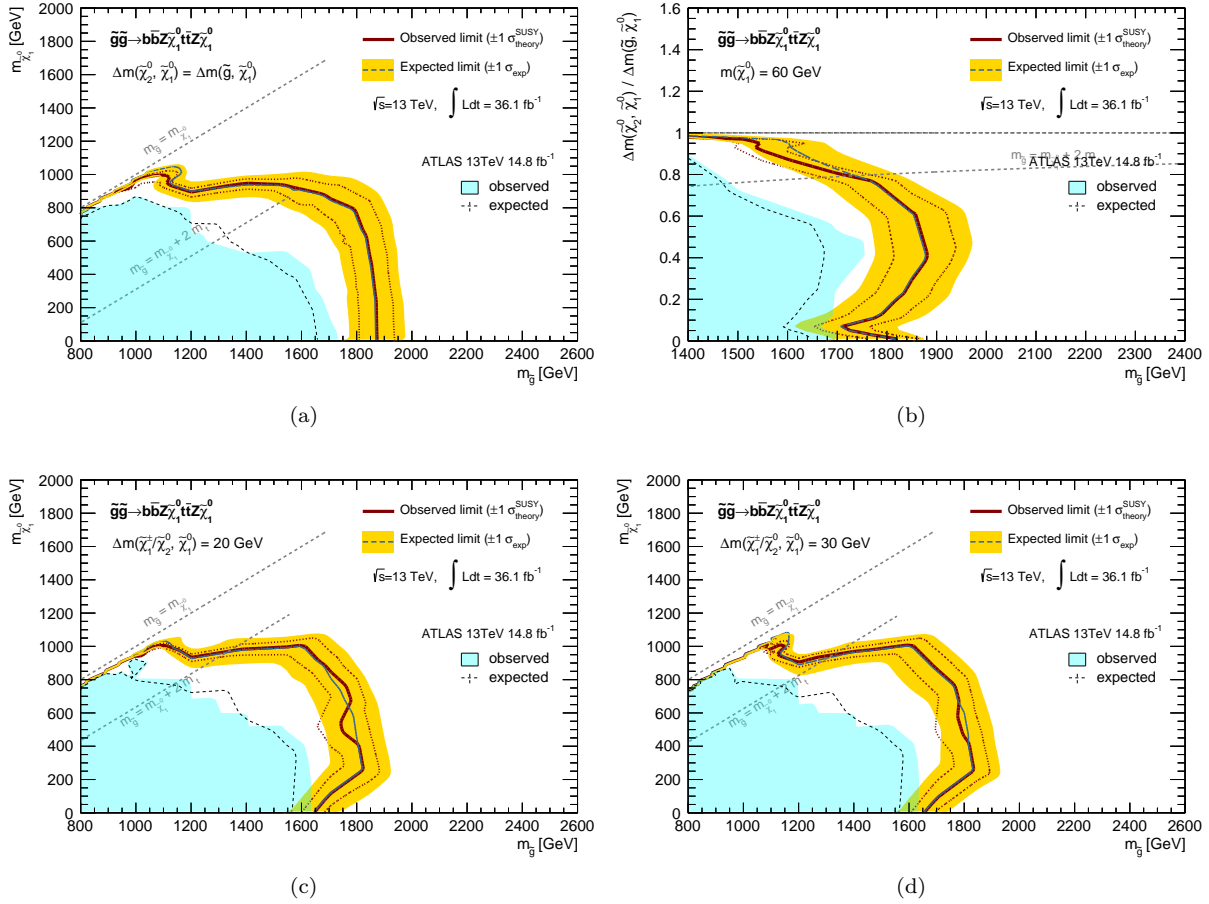
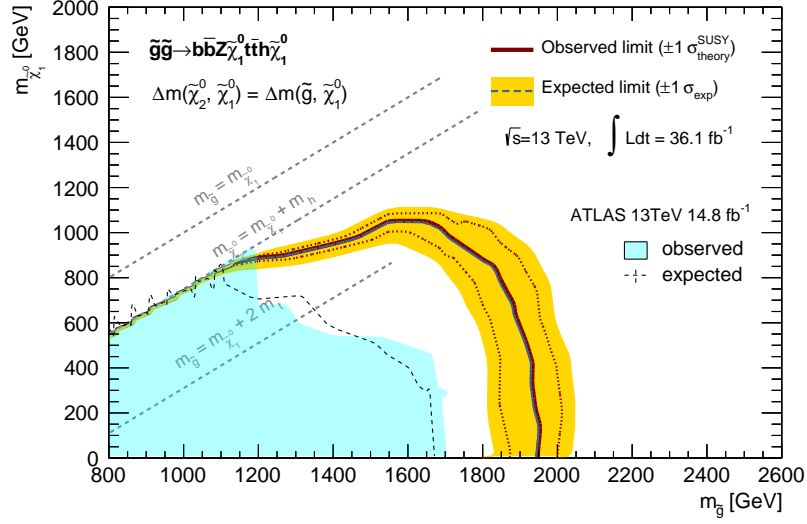
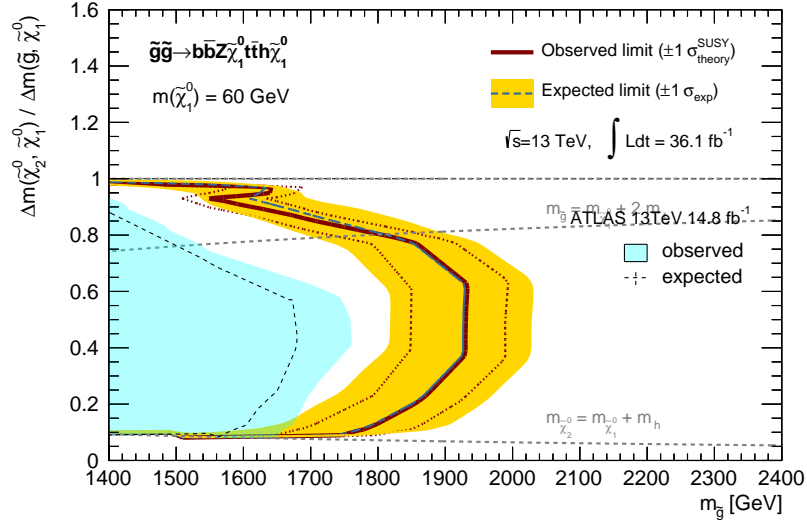


Figure 204: Exclusion limit (95% CL) on the benchmark model **BBN2ZTTN2Z** for the grids (a)  $x=1/2$ , (b)  $m_{\tilde{\chi}_1^0} = 60 \text{ GeV}$ , (c)  $\Delta m(\tilde{\chi}_1^\pm, \tilde{\chi}_1^0) = 20 \text{ GeV}$ , (d)  $\Delta m(\tilde{\chi}_1^\pm, \tilde{\chi}_1^0) = 30 \text{ GeV}$ .

## BBN2ZTTN2Z



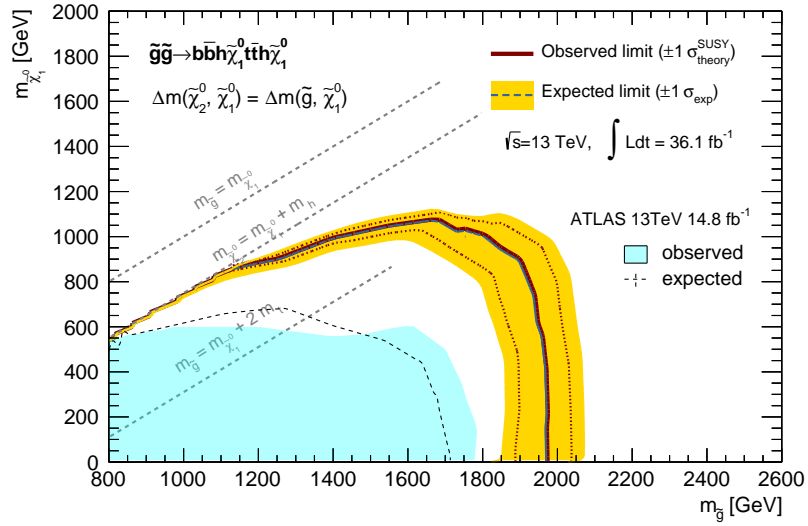
(a)



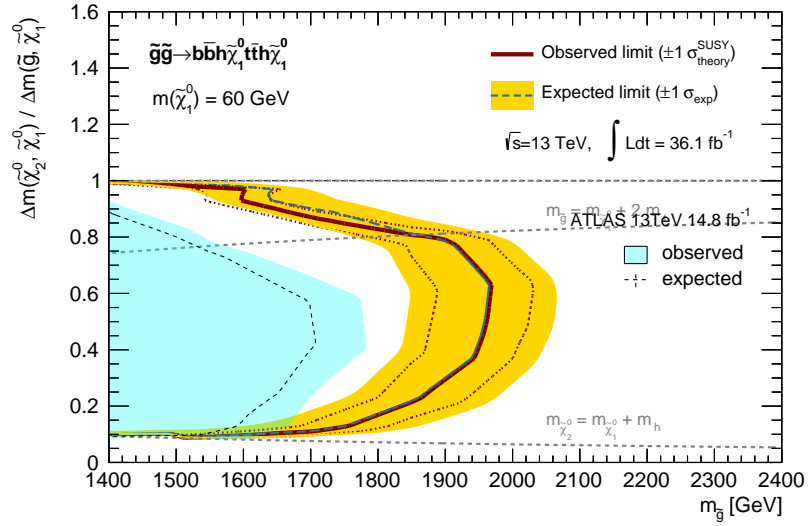
(b)

Figure 205: Exclusion limit (95% CL) on the benchmark model **BBN2ZTTN2H** for the grids (a)  $x=1/2$ , (b)  $m_{\tilde{\chi}_1^0} = 60$  GeV.

## BBN2ZTTN2H



(a)



(b)

Figure 206: Exclusion limit (95% CL) on the benchmark model **BBN2HTTN2H** for the grids (a)  $x=1/2$ , (b)  $m_{\tilde{\chi}_1^0} = 60$  GeV.

## BBN2HTTN2H

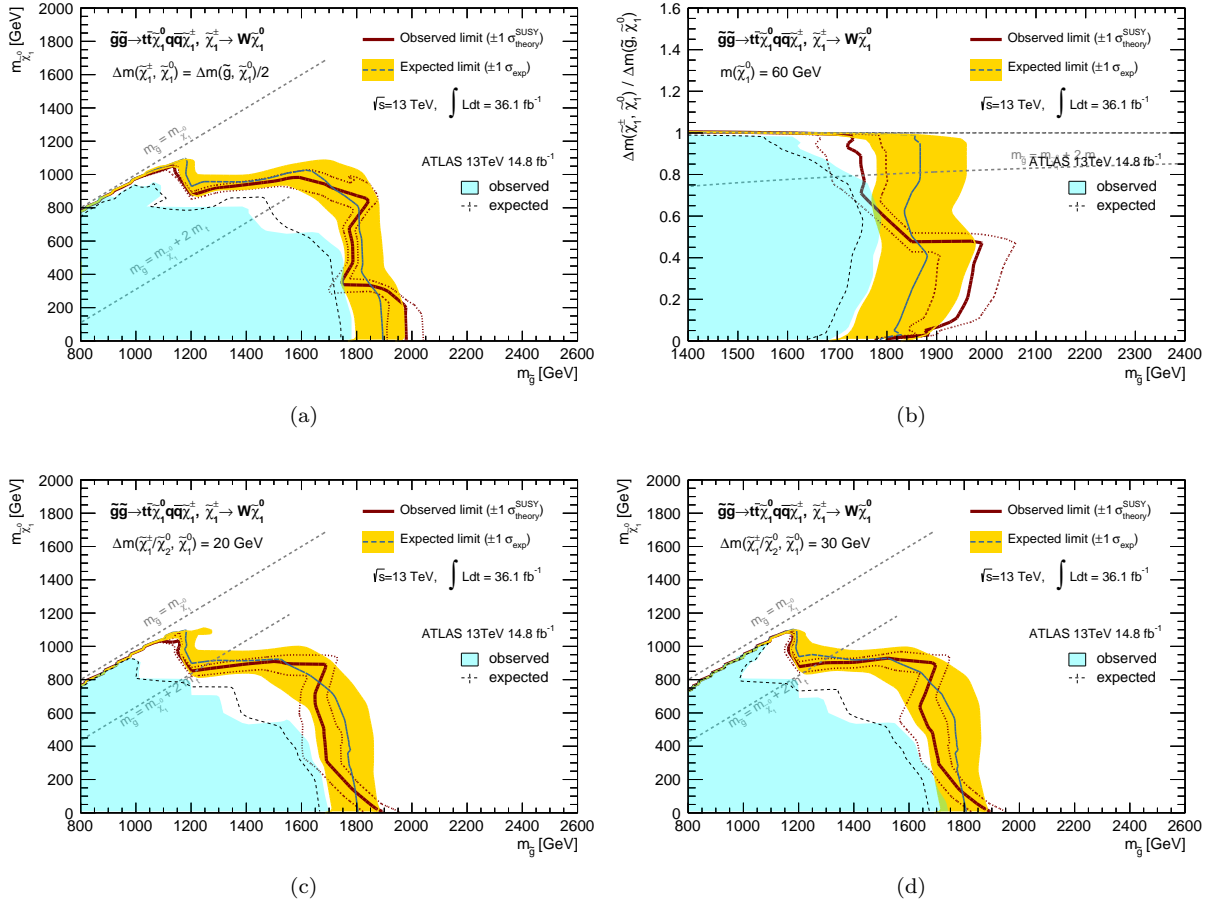


Figure 207: Exclusion limit (95% CL) on the benchmark model **TTN1QQC1** for the grids (a)  $x=1/2$ , (b)  $m_{\tilde{\chi}_1^0} = 60$  GeV, (c)  $\Delta m(\tilde{\chi}_1^\pm, \tilde{\chi}_1^0) = 20$  GeV, (d)  $\Delta m(\tilde{\chi}_1^\pm, \tilde{\chi}_1^0) = 30$  GeV.

## TTN1QQC1

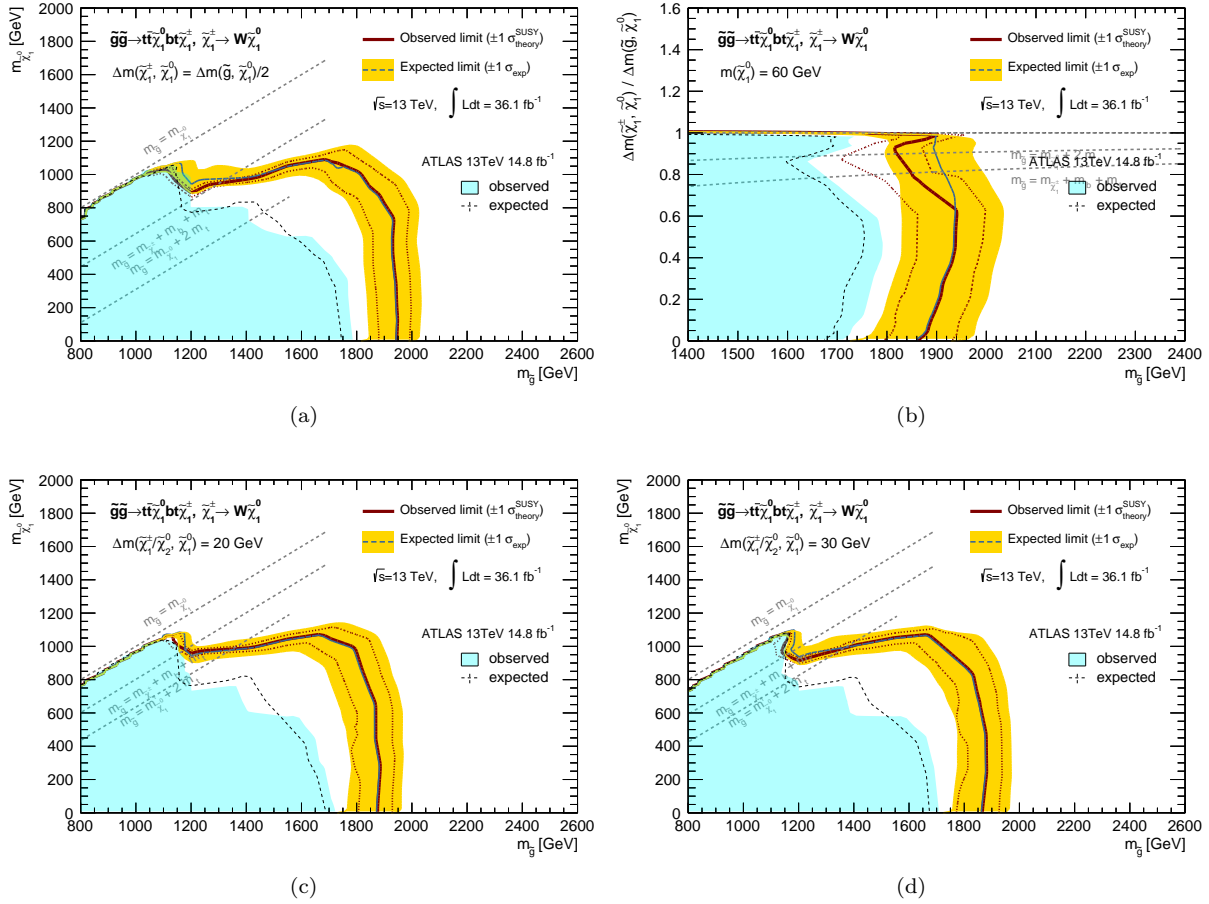


Figure 208: Exclusion limit (95% CL) on the benchmark model **TTN1BTC1** for the grids (a)  $x=1/2$ , (b)  $m_{\tilde{\chi}_1^0} = 60$  GeV, (c)  $\Delta m(\tilde{\chi}_1^\pm, \tilde{\chi}_1^0) = 20$  GeV, (d)  $\Delta m(\tilde{\chi}_1^\pm, \tilde{\chi}_1^0) = 30$  GeV.

**TTN1BTC1**

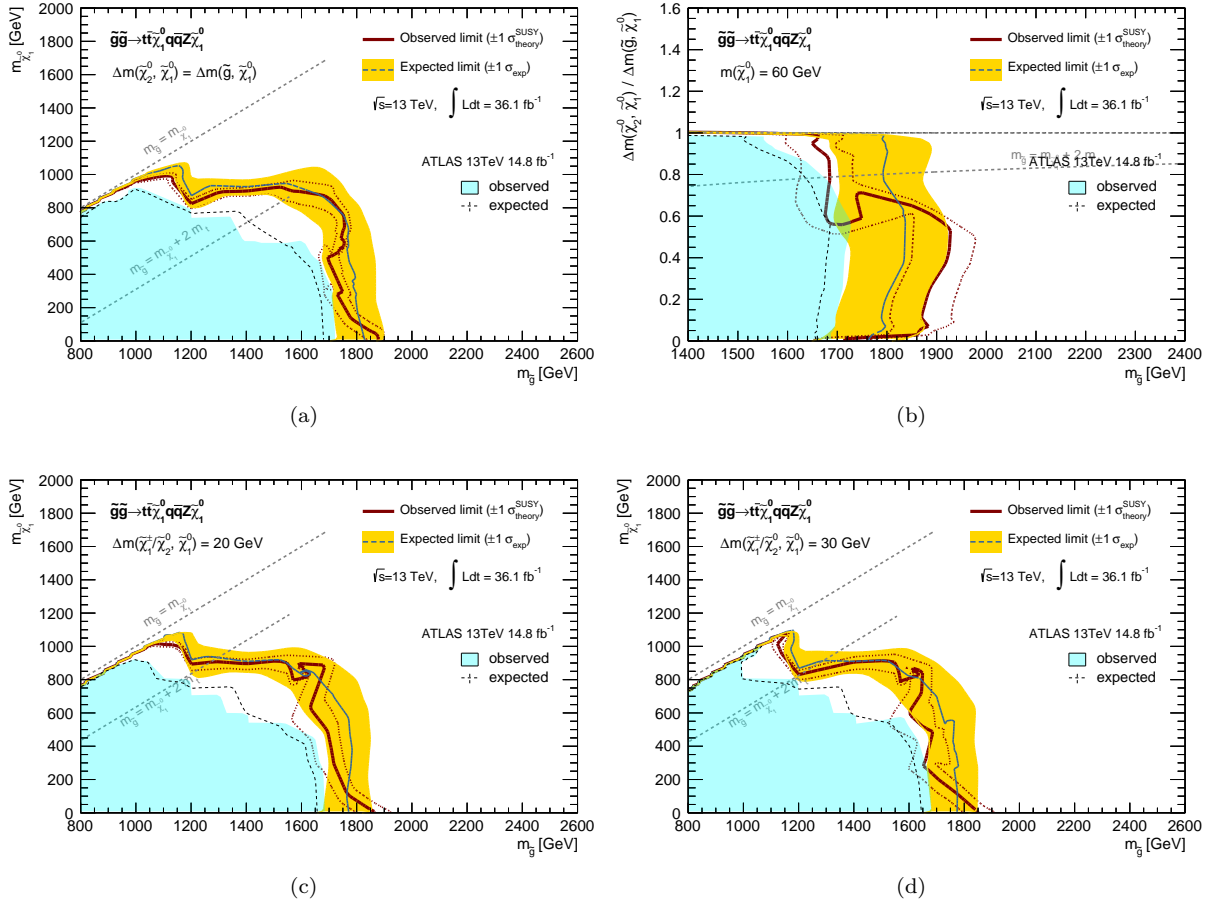


Figure 209: Exclusion limit (95% CL) on the benchmark model **TTN1QQN2Z** for the grids (a)  $x=1/2$ , (b)  $m_{\tilde{\chi}_1^0} = 60$  GeV, (c)  $\Delta m(\tilde{\chi}_1^\pm, \tilde{\chi}_1^0) = 20$  GeV, (d)  $\Delta m(\tilde{\chi}_1^\pm, \tilde{\chi}_1^0) = 30$  GeV.

## TTN1QQN2Z

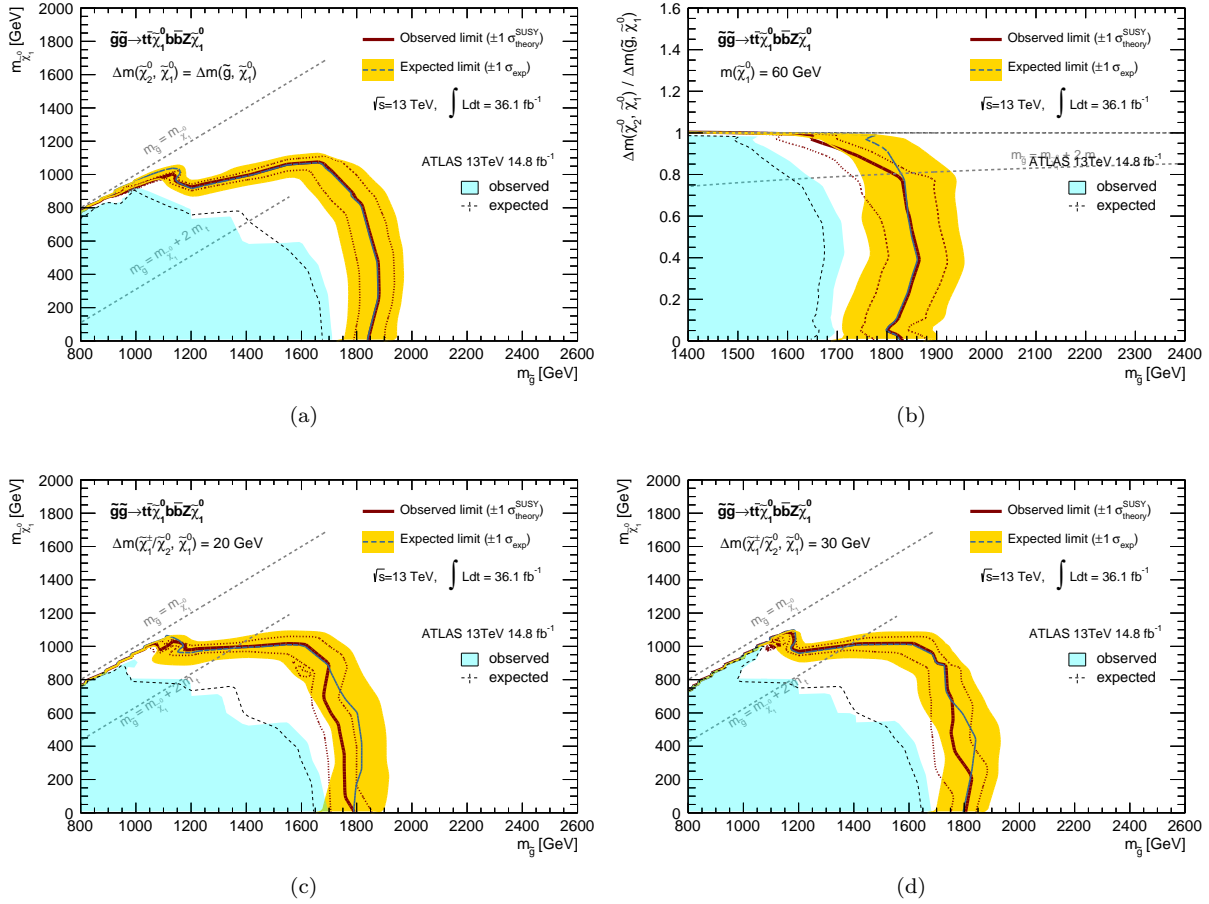


Figure 210: Exclusion limit (95% CL) on the benchmark model **TTN1BBN2Z** for the grids (a)  $x=1/2$ , (b)  $m_{\tilde{\chi}_1^0} = 60 \text{ GeV}$ , (c)  $\Delta m(\tilde{\chi}_1^\pm, \tilde{\chi}_1^0) = 20 \text{ GeV}$ , (d)  $\Delta m(\tilde{\chi}_1^\pm, \tilde{\chi}_1^0) = 30 \text{ GeV}$ .

## TTN1BBN2Z

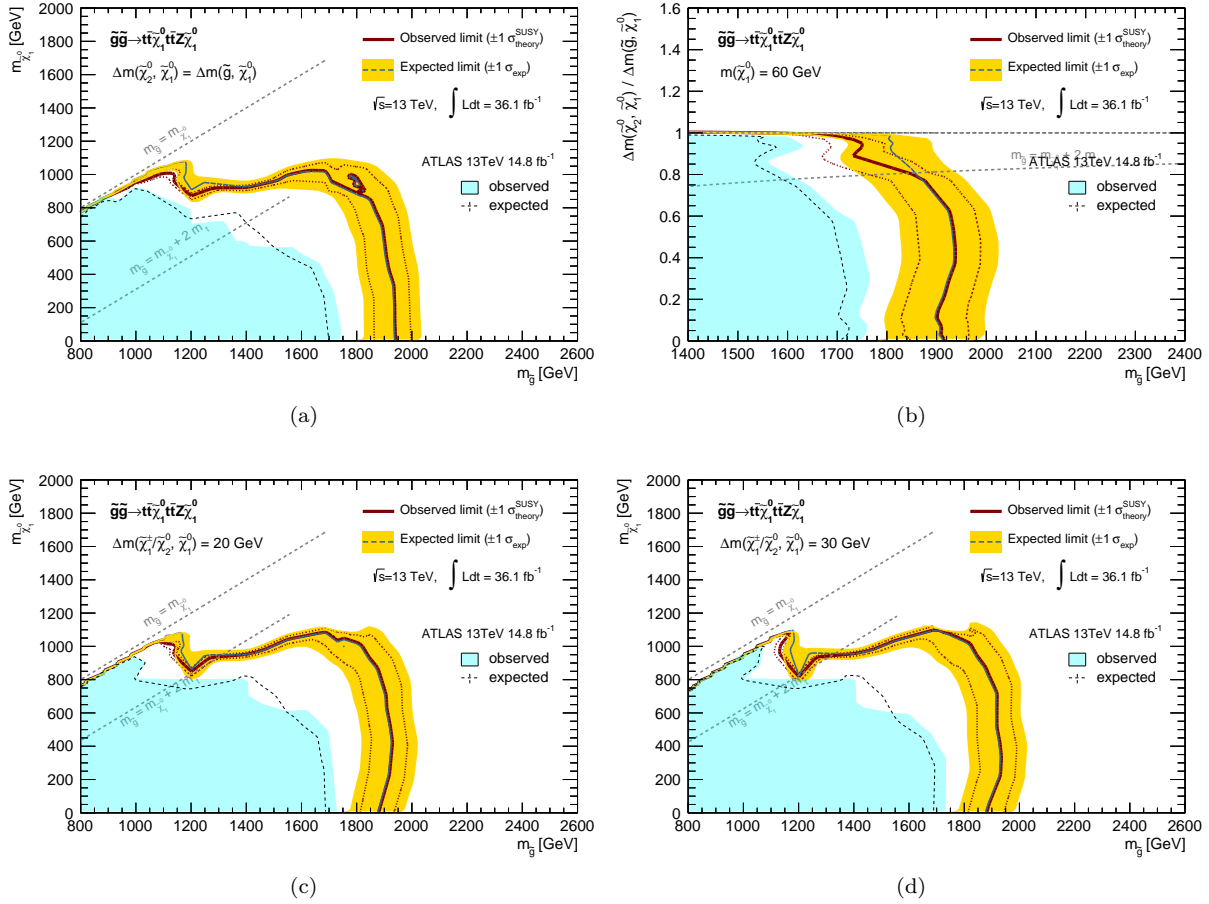
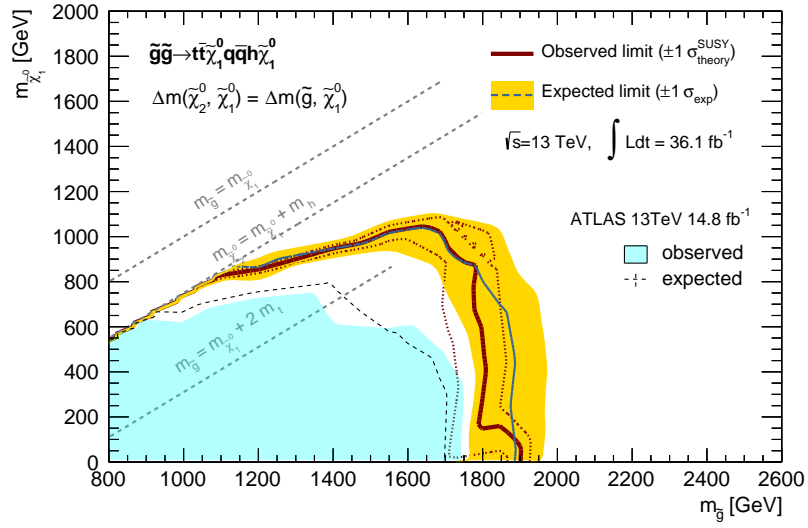
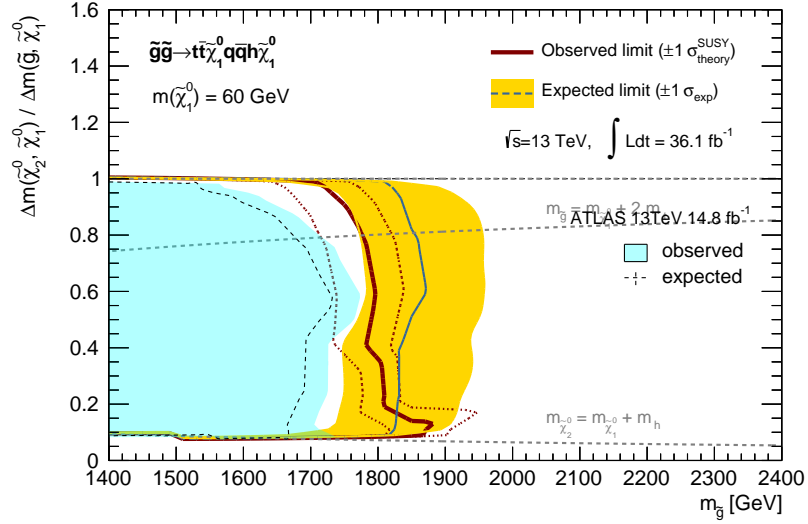


Figure 211: Exclusion limit (95% CL) on the benchmark model **TTN1TTN2Z** for the grids (a)  $x=1/2$ , (b)  $m_{\tilde{\chi}_1^0} = 60$  GeV, (c)  $\Delta m(\tilde{\chi}_1^\pm, \tilde{\chi}_1^0) = 20$  GeV, (d)  $\Delta m(\tilde{\chi}_1^\pm, \tilde{\chi}_1^0) = 30$  GeV.

**TTN1TTN2Z**



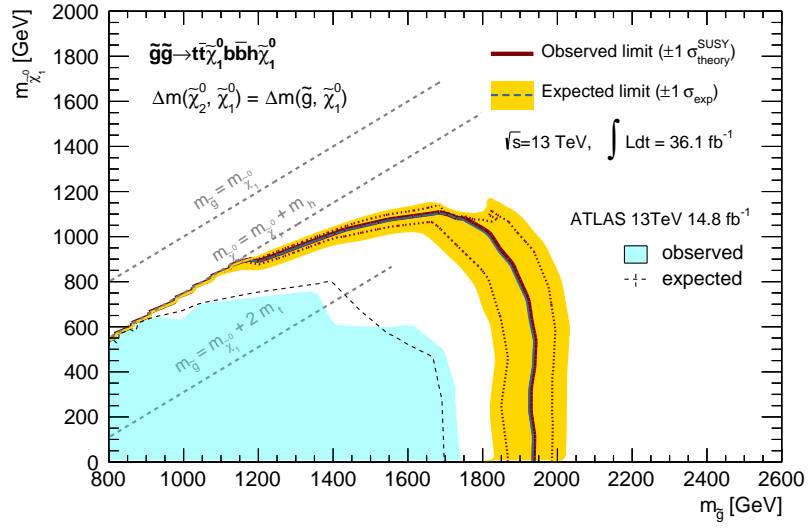
(a)



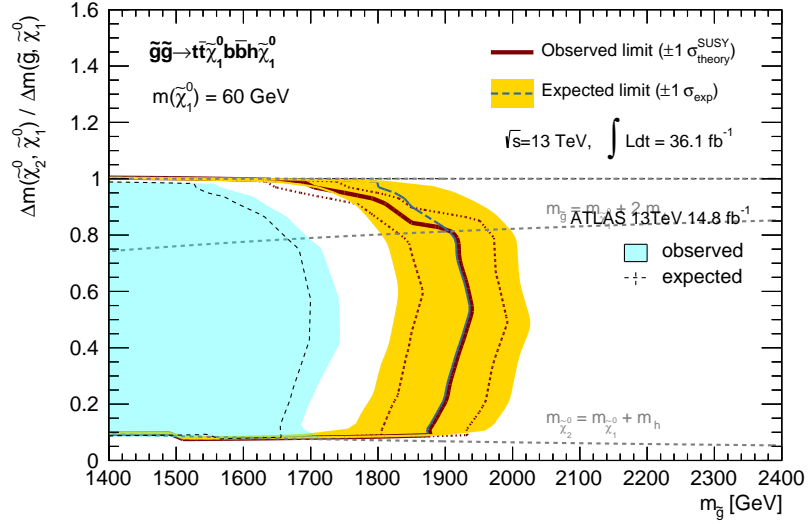
(b)

Figure 212: Exclusion limit (95% CL) on the benchmark model **TTN1QQN2H** for the grids (a)  $x=1/2$ , (b)  $m_{\tilde{\chi}_1^0} = 60$  GeV.

### TTN1QQN2H



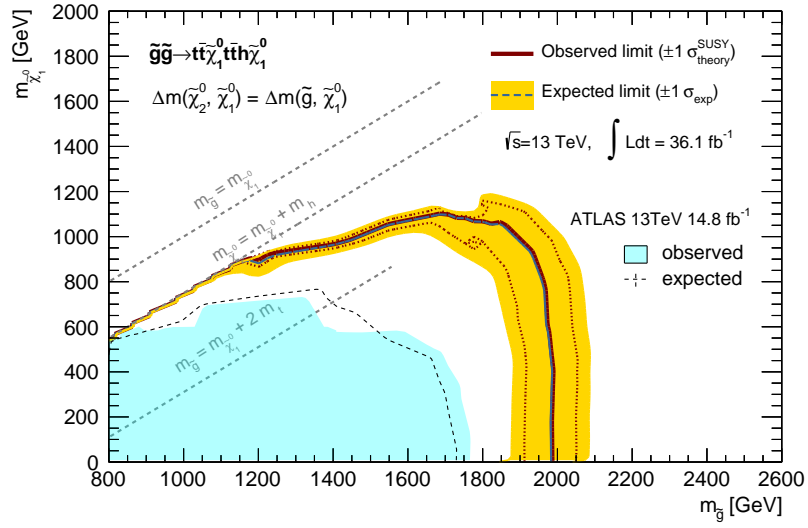
(a)



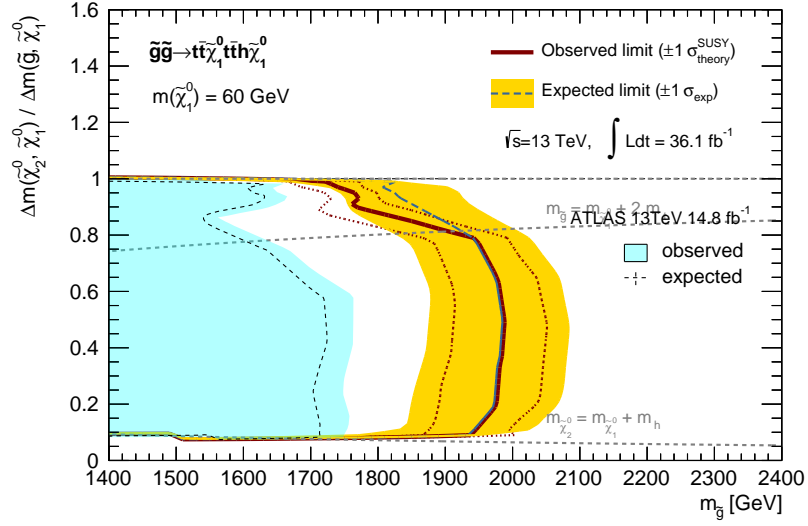
(b)

Figure 213: Exclusion limit (95% CL) on the benchmark model **TTN1BBN2H** for the grids (a)  $x=1/2$ , (b)  $m_{\tilde{\chi}_1^0} = 60$  GeV.

### TTN1BBN2H



(a)



(b)

Figure 214: Exclusion limit (95% CL) on the benchmark model **TTN1TTN2H** for the grids (a)  $x=1/2$ , (b)  $m_{\tilde{\chi}_1^0} = 60$  GeV.

**TTN1TTN2H**

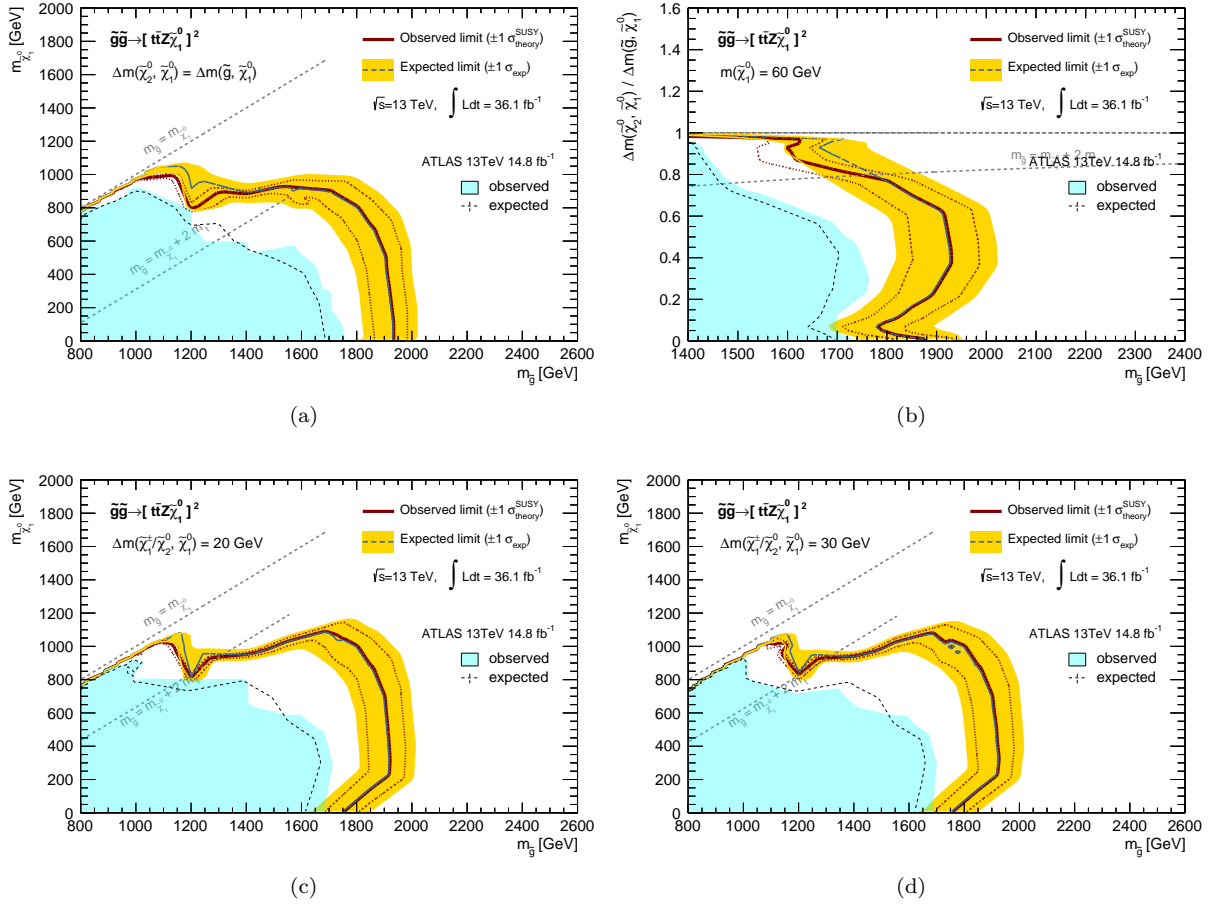
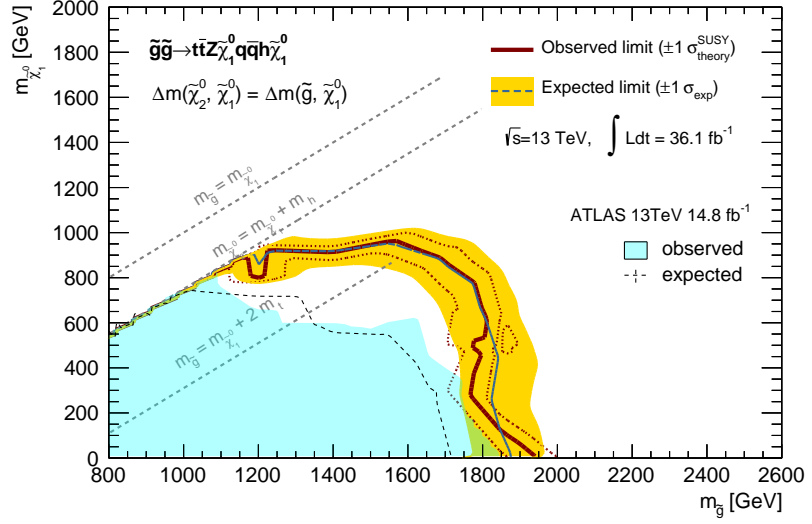
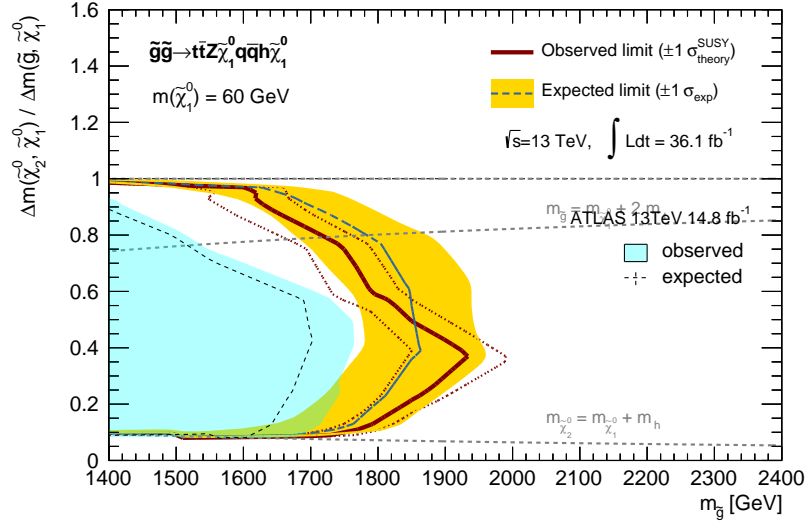


Figure 215: Exclusion limit (95% CL) on the benchmark model **symTTN2Z** for the grids (a)  $x=1/2$ , (b)  $m_{\tilde{\chi}_1^0} = 60$  GeV, (c)  $\Delta m(\tilde{\chi}_1^\pm, \tilde{\chi}_1^0) = 20$  GeV, (d)  $\Delta m(\tilde{\chi}_1^\pm, \tilde{\chi}_1^0) = 30$  GeV.

**symTTN2Z**



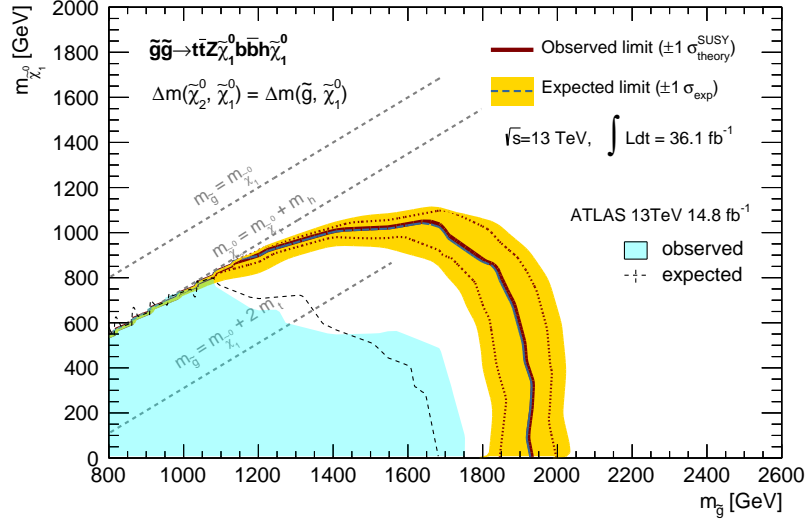
(a)



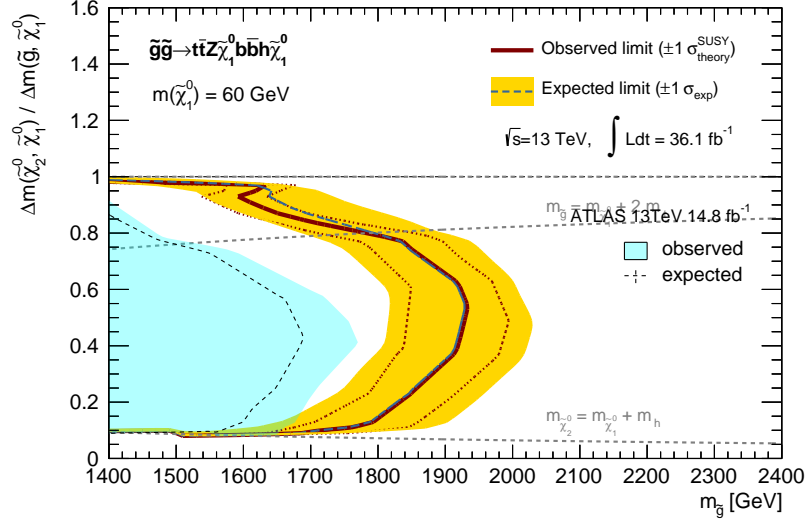
(b)

Figure 216: Exclusion limit (95% CL) on the benchmark model **TTN2ZQQN2H** for the grids (a)  $x=1/2$ , (b)  $m_{\tilde{\chi}_1^0} = 60$  GeV.

### TTN2ZQQN2H



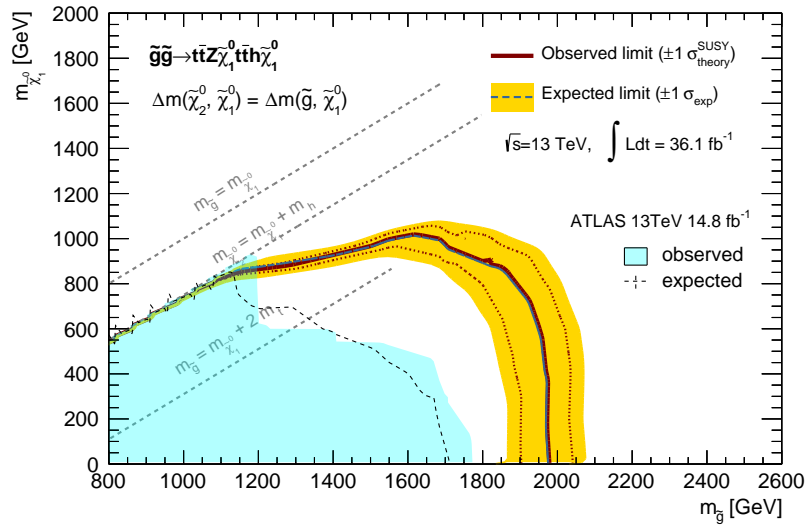
(a)



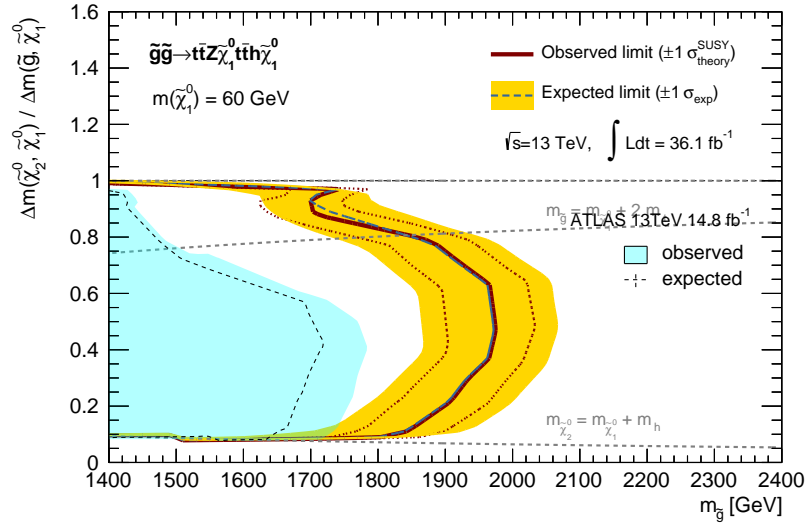
(b)

Figure 217: Exclusion limit (95% CL) on the benchmark model **TTN2ZBBN2H** for the grids (a)  $x=1/2$ , (b)  $m_{\tilde{\chi}_1^0} = 60$  GeV.

## TTN2ZBBN2H



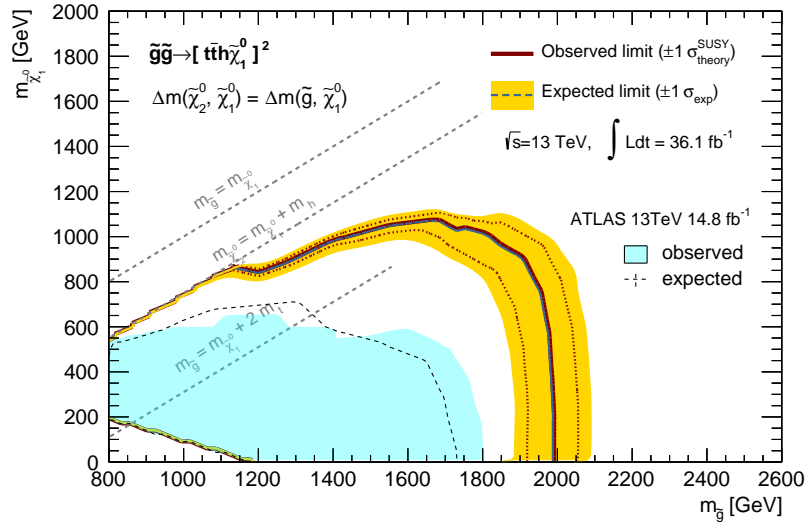
(a)



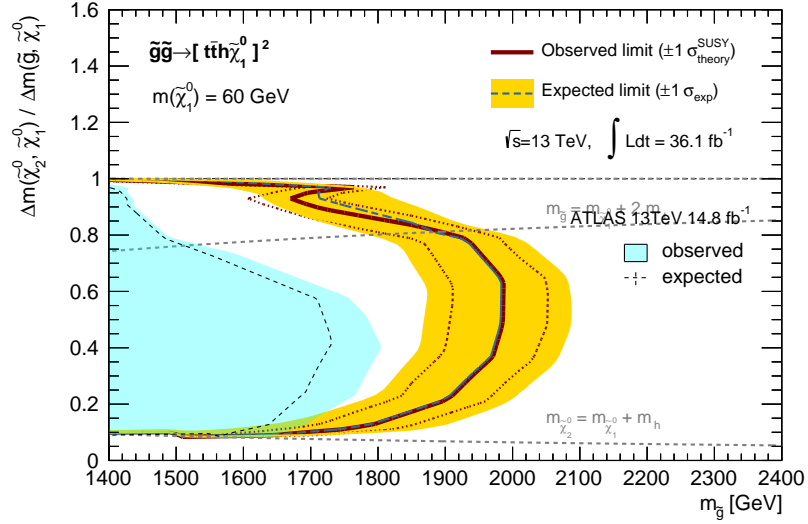
(b)

Figure 218: Exclusion limit (95% CL) on the benchmark model **TTN2ZTTN2H** for the grids (a)  $x=1/2$ , (b)  $m_{\tilde{\chi}_1^0} = 60$  GeV.

### TTN2ZTTN2H



(a)



(b)

Figure 219: Exclusion limit (95% CL) on the benchmark model **symTTN2H** for the grids (a)  $x=1/2$ , (b)  $m_{\tilde{\chi}_1^0} = 60$  GeV.

**symTTN2H**

## References

- [1] Michael Peskin and David V. Schröder. An introduction to Quantum Filed Theory. Westview Press, Boulder, CO, 1995.
- [2] Francis Halzen and Alan. D. Martin. Quarks & Leptons: An Introductory Course in Modern Particle Physics. Wiley; 1st edition, 1984.
- [3] François Englert and Robert Brout. Broken symmetry and the mass of gauge vector mesons. *Physical Review Letters*, 13(9):321, 1964.
- [4] Peter W Higgs. Broken symmetries, massless particles and gauge fields. *Physics Letters*, 12(2):132–133, 1964.
- [5] J. C. Ward. An Identity in Quantum Electrodynamics. *Physical Review*, 78(2):182–182, 1950.
- [6] Y. Takahashi. On the generalized ward identity. *Il Nuovo Cimento*, 6(2):371–375, 1957.
- [7] G. 'tHooft and M. Veltman. Regulariation and Renormalization of Gauge Fields. *Nuclear Physics B*, 44:189–213, 1972.
- [8] Sheldon L Glashow. Partial-symmetries of weak interactions. *Nuclear Physics*, 22(4):579–588, 1961.
- [9] Steven Weinberg. A model of leptons. *Physical review letters*, 19(21):1264, 1967.
- [10] Abdus Salam and John Clive Ward. Electromagnetic and weak interactions. *Physics Letters*, 13(2):168–171, 1964.
- [11] Tsung-Dao Lee and Chen-Ning Yang. Question of parity conservation in weak interactions. *Physical Review*, 104(1):254, 1956.
- [12] Chien-Shiung Wu, Ernest Ambler, RW Hayward, DD Hoppes, and R P1 Hudson. Experimental test of parity conservation in beta decay. *Physical review*, 105(4):1413, 1957.
- [13] Makoto Kobayashi and Toshihide Maskawa. CP-Violation in the Renormalizable Theory of Weak Interaction. *Progress of Theoretical Physics*, 49(2):652–657, 1973.
- [14] ATLAS Collaboration. Observation of a new particle in the search for the Standard Model Higgs boson with the ATLAS detector at the LHC. *Physics Letters, Section B: Nuclear, Elementary Particle and High-Energy Physics*, 716(1):1–29, 2012.
- [15] CMS Collaboration. Observation of a new boson at a mass of 125 GeV with the CMS experiment at the LHC. *Physics Letters, Section B: Nuclear, Elementary Particle and High-Energy Physics*, 716(1):30–61, 2012.
- [16] Vera C Rubin and W Kent Ford Jr. Rotation of the andromeda nebula from a spectroscopic survey of emission regions. *The Astrophysical Journal*, 159:379, 1970.
- [17] Vera C Rubin, W Kent Ford Jr, and Norbert Thonnard. Rotational properties of 21 sc galaxies with a large range of luminosities and radii, from ngc 4605/r= 4kpc/to ugc 2885/r= 122 kpc. *The Astrophysical Journal*, 238:471–487, 1980.

- [18] Prateek Agrawal, Francis-Yan Cyr-Racine, Lisa Randall, and Jakub Scholtz. Make dark matter charged again. *Journal of Cosmology and Astroparticle Physics*, 5(22), 2017.
- [19] C. L. Bennett, D. Larson, J. L. Weiland, N. Jarosik, G. Hinshaw, N. Odegard, K. M. Smith, R. S. Hill, B. Gold, M. Halpern, E. Komatsu, M. R. Nolta, L. Page, D. N. Spergel, E. Wollack, J. Dunkley, A. Kogut, M. Limon, S. S. Meyer, G. S. Tucker, and E. L. Wright. Nine-Year Wilkinson Microwave Anisotropy Probe (WMAP) Observations: Final Maps and Results. *The Astrophysical Journal Supplement Series*, 208(20), 2012.
- [20] Planck Collaboration. Astrophysics Special feature Planck 2015 results. *Astronomy & Astrophysics*, 594(A13), 2016.
- [21] Stephen P. Martin. A Supersymmetry Primer. *Adv. Ser. Direct. High Energy Phys*, 21(515), 1997.
- [22] GF Giudice and R Rattazzi. Theories with gauge mediated supersymmetry breaking, *phys. rept.* 322 (1999) 419–499. arXiv preprint hep-ph/9801271, 89.
- [23] Gian F Giudice, Riccardo Rattazzi, Markus A Luty, and Hitoshi Murayama. Gaugino mass without singlets. *Journal of High Energy Physics*, 1998(12):027, 1999.
- [24] Lisa Randall and Raman Sundrum. Out of this world supersymmetry breaking. *Nuclear Physics B*, 557(1-2):79–118, 1999.
- [25] Julius Wess and Jonathan Bagger. *Supersymmetry and supergravity*. Princeton university press, 1992.
- [26] H Nishino, S Clark, K Abe, Y Hayato, T Iida, M Ikeda, J Kameda, K Kobayashi, Y Koshio, M Miura, et al. Search for proton decay via  $p \rightarrow e^+ \pi_0$  and  $p \rightarrow \mu^+ \pi_0$  in a large water cherenkov detector. *Physical Review Letters*, 102(14):141801, 2009.
- [27] Lawrence J Hall, David Pinner, and Joshua T Ruderman. A natural susy higgs near 125 gev. *Journal of High Energy Physics*, 2012(4):131, 2012.
- [28] N. Arkani-Hamed, A. Delgado, and G.F. Giudice. The Well-Tempered Neutralino. *Nuclear Physics B*, 741(1-2):108–130, 2006.
- [29] Howard Baer, Tadas Krupovnickas, Azar Mustafayev, Eun-Kyung Park, Stefano Profumo, and Xerxes Tata. Exploring the BWCA (Bino-Wino Co-Accretion) Scenario for Neutralino Dark Matter. *Journal of High Energy Physics*, 2005(11), 2005.
- [30] Joseph Bramante, Nishita Desai, Patrick Fox, Adam Martin, Bryan Ostdiek, and Tilman Plehn. Towards the final word on neutralino dark matter. *Physical Review D*, 93(6), 2016.
- [31] ATLAS Collaboration. Summary plots from the ATLAS Supersymmetry physics group. <https://atlas.web.cern.ch/Atlas/GROUPS/PHYSICS/CombinedSummaryPlots/SUSY/index.html>, 2017.
- [32] CMS Collaboration. CMS Supersymmetry Physics Results. <https://twiki.cern.ch/twiki/bin/view/CMSPublic/PhysicsResultsSUSY>, 2017.
- [33] ATLAS Collaboration. Search for electroweak production of supersymmetric particles in the two and three lepton final state at  $\sqrt{s} = 13$  TeV with the ATLAS detector. CONF-SUSY, 2017-039, 2017.

- [34] CMS Collaboration. Search for electroweak production of charginos and neutralinos in multilepton final states in pp collision data at  $\sqrt{s} = 13$  TeV. CMS PAS SUS, 16-039, 2017.
- [35] ATLAS Collaboration. Search for long-lived charginos based on a  $\sqrt{s} = 13$  TeV with the ATLAS detector. ATLAS-CONF, 2017-017, 2017.
- [36] CMS Collaboration. Search for disappearing tracks in proton-proton collisions at  $\sqrt{s} = 8$  TeV. Journal of High Energy Physics, 2015(96), 2015.
- [37] LEP2 SUSY Working Group. Combined LEP Chargino Results, up to 208 GeV for low DM. [http://lepsusy.web.cern.ch/lepsusy/www/inoslowdmsummer02/charginolowdm\\_pub.html](http://lepsusy.web.cern.ch/lepsusy/www/inoslowdmsummer02/charginolowdm_pub.html), 2002.
- [38] Wim Beenakker, R Höpker, Michael Spira, and PM Zerwas. Squark and gluino production at hadron colliders. Nuclear Physics B, 492(1-2):51–103, 1997.
- [39] C. Patrignani et al. (Particle Data Group). Review of Particle Physics. Chinese Physics C, 40(10):100001, 2016.
- [40] ATLAS Collaboration. The simulation principle and performance of the ATLAS fast calorimeter simulation FastCaloSim. ATL-PHYS-PUB-2010-013, 2010.
- [41] Lyndon Evans and Philip Bryant. LHC Machine. Journal of Instrumentation, 3(08):S08001, 2008.
- [42] ATLAS Collaboration. The ATLAS Experiment at the CERN Large Hadron Collider. J. Instrum., 3:S08003, 2008.
- [43] CMS Collaboration. The CMS experiment at the CERN LHC. J. Instrum., 3(S08004):285, 2008.
- [44] ALICE Collaboration. The ALICE experiment at the CERN LHC. J. Instrum., 3(S08002), 2008.
- [45] ATLAS Collaboration. The LHCb Detector at the LHC. Journal of Instrumentation, 3(08):S08005–S08005, 2008.
- [46] CERN. CERN Media Archive Photo. <https://mediastream.cern.ch/MediaArchive/Photo/Public/2008/0812015/0812015/A4-at-144-dpi.jpg>.
- [47] ATLAS Collaboration. ATLAS Data Preparation Summary 2016. <https://atlas.web.cern.ch/Atlas/GROUPS/DATAPREPARATION/DataSummary/2016/>.
- [48] ATLAS Collaboration. ATLAS Luminosity Public Results Run2. <https://twiki.cern.ch/twiki/bin/view/AtlasPublic/LuminosityPublicResultsRun2>.
- [49] ATLAS Collaboration. ATLAS detector and physics performance: Technical Design Report, 1. Technical report, CERN, 1999.
- [50] ATLAS Collaboration. Studies of the performance of the ATLAS detector using cosmic-ray muons. Eur. Phys. J. C, 71(1593), 2011.
- [51] ATLAS Collaboration. ATLAS TRT Public Result. <https://twiki.cern.ch/twiki/bin/view/AtlasPublic/TRTPublicResults>
- [52] ATLAS Collaboration. Liquid Argon Technical Design Report, CERN-LHCC-96-041. Technical report, CERN, 1996.

- [53] ATLAS Collaboration. Tile Calorimeter Technical Design Report, CERNLHCC-96-042. Technical report, CERN, 1996.
- [54] Simon van der Meer. Calibration of the Effective Beam Height in the ISR. Technical report, CERN, 1968.
- [55] ATLAS Collaboration. Improved luminosity determination in pp collisions at  $\sqrt{s} = 7$  TeV using the ATLAS detector at the LHC. *Eur. Phys. J. C*, 73(8):2–39, 2013.
- [56] ATLAS Collaboration. Performance of the ATLAS Trigger System in 2015. *Eur. Phys. J. C*, 77(317), 2017.
- [57] ATLAS Collaboration. ATLAS Trigger operation public results. <https://twiki.cern.ch/twiki/bin/view/AtlasPublic/TriggerOperationPublicResults>.
- [58] ATLAS Collaboration. The Optimization of ATLAS Track Reconstruction in Dense Environments. ATL-PHYS-PUB, 2015-006, 2015.
- [59] Azriel Osenfeld and John Pfaltz L. Sequential Operations in Digital Picture Processing. *Journal of the ACM*, 13(4):471–494, 1966.
- [60] ATLAS Collaboration. A neural network clustering algorithm for the ATLAS silicon pixel detector. *J. Instrum.*, 9(P09009), 2014.
- [61] Giuseppe Cerati, Peter Elmer, and Steven Lantz. Advances in tracking and trigger concepts. In International Conference on Computing in High Energy and Nuclear Physics, 2008.
- [62] ATLAS Collaboration. Performance of primary vertex reconstruction in proton-proton collisions at  $\sqrt{s} = 7$  TeV in the ATLAS experiment. ATLAS-CONF, 2010-069, 2010.
- [63] ATLAS Collaboration. Performance of the ATLAS Inner Detector Track and Vertex Reconstruction in the High Pile-Up LHC Environment. ATLAS-CONF, 2012-042, 2012.
- [64] Wolfgang Waltenberger, Rudolf Frühwirth, and Pascal Vanlaer. Adaptive vertex fitting. *J. Phys. G: Nucl. Part. Phys.*, 34:343–356, 2007.
- [65] ATLAS Collaboration. Topological cell clustering in the ATLAS calorimeters and its performance in LHC Run1. CERN-PH-EP, 2015-304, 2016.
- [66] ATLAS Collaboration. Electron efficiency measurements with the ATLAS detector using the 2015 LHC proton-proton collision data. ATLAS-CONF, 2016-024, 2016.
- [67] ATLAS Collaboration. Improved electron reconstruction in ATLAS using the Gaussian Sum Filter-based model for bremsstrahlung. ATLAS-CONF, 2012-047, 2012.
- [68] ATLAS Collaboration. Electron and photon energy calibration with the ATLAS detector using LHC Run 1 data. *Eur. Phys. J. C*, 74(3071), 2013.
- [69] Nencki Neyman and E. S. Pearson. On the Problem of the most Efficient Tests of Statistical Hypotheses. *Philosophical Transactions of the Royal Society of London Series A*, 231(289), 1933.

- [70] ATLAS Collaboration. Electron and photon energy calibration with the ATLAS detector using data collected in 2015 at  $\sqrt{s} = 13$  TeV. ATLAS-PHYS-PUB, 2016-015, 2016.
- [71] ATLAS Collaboration. Measurement of the muon reconstruction performance of the Measurement of the muon reconstruction performance of the ATLAS detector using 2011 and 2012 LHC proton – proton collision data. CERN-PH-EP, 2014-151, 2014.
- [72] ATLAS Collaboration. Muon reconstruction performance of the ATLAS detector in proton–proton collision data at  $\sqrt{s} = 13$  TeV. Eur. Phys. J. C, 76(292), 2016.
- [73] Matteo Cacciari, Gavin P. Salam, and Gregory Soyez. The anti- $k_t$  jet clustering algorithm. Journal of High Energy Physics, 2008(63), 2008.
- [74] ATLAS Collaboration. Jet energy scale measurements and their systematic uncertainties in proton–proton collisions at  $\sqrt{s} = 13$  TeV with the ATLAS detector. ATLAS-PHYS-PUB, 2015-015, 2017.
- [75] ATLAS Collaboration. Jet energy measurement and its systematic uncertainty in proton–proton collisions at  $\sqrt{s} = 7$  TeV with the ATLAS detector. Eur. Phys. J. C, 75(17), 2015.
- [76] Matteo Cacciari and Gavin P Salam. Pileup subtraction using jet areas. Physics Letters B, 659(1-2):119–126, 2007.
- [77] Gavin P Salam. Towards Jetography. Eur. Phys. J. C, 67(3-4):637–686, 2010.
- [78] ATLAS Collaboration. Jet energy measurement with the ATLAS detector in proton-proton collisions at  $\sqrt{s} = 7$  TeV. Eur. Phys. J. C, 73(2304), 2013.
- [79] ATLAS Collaboration. Expected performance of the ATLAS b-tagging algorithms in Run-2. ATL-PHYS-PUB, 2015-022, 2015.
- [80] ATLAS Collaboration. Optimisation of the ATLAS b-tagging performance for the 2016 LHC Run. ATL-PHYS-PUB, 2016-012, 2016.
- [81] ATLAS Collaboration. Performance of b-jet identification in the ATLAS experiment. Journal of Instrumentation, 11(04):P04008–P04008, 2016.
- [82] ATLAS Collaboration. Commissioning of the ATLAS high-performance b-tagging algorithms in the 7 TeV collision data. Europhysics Conference on High Energy Physics, 2011.
- [83] Giovanni Pauletta, Franco Simonetto, and Mariusz Witek. A new inclusive secondary vertex algorithm for b-jet tagging in ATLAS. International Conference on Computing in High Energy and Nuclear Physics, 2008.
- [84] ATLAS Collaboration. Tagging and suppression of pileup jets with the ATLAS detector. ATLAS-CONF, 2014-018, 2014.
- [85] C. W. Miller, A. Schwartzman, and D. Su. Jet-Vertex Association Algorithm. ATL-COM-PHYS, 2008-008, 2008.
- [86] ATLAS Collaboration. Performance of missing transverse momentum reconstruction with the ATLAS detector in the first proton-proton collisions at  $\sqrt{s} = 13$  TeV. ATL-PHYS-PUB, 2015-027(July), 2015.

- [87] ATLAS Collaboration. Missing Transverse Momentum Distribution and Performance in 2016 data. <https://atlas.web.cern.ch/Atlas/GROUPS/PHYSICS/PLOTS/JETM-2016-008/>, 2016.
- [88] Andy Buckley, Jonathan Butterworth, Stefan Gieseke, David Grellscheid, Stefan Höche, Hendrik Hoeth, Frank Krauss, Leif Lönnblad, Emily Nurse, Peter Richardson, Steffen Schumann, Michael H. Seymour, Sjöstrand Torbjörn, Peter Skands, and Webber Bryan. General-purpose event generators for LHC physics. *Physics Reports*, 504(5):145–233, 2011.
- [89] Peter Skands. QCD for Collider Physics. CERN-TH, 2011-080, 2011.
- [90] Constantia Alexandrou. Parton Distribution Functions from Lattice QCD. *Few-Body Systems*, 57(8):621–626, 2016.
- [91] Jon Butterworth, Stefano Carrazza, Amanda Cooper-Sarkar, Albert De Roeck, Joël Feltesse, Stefano Forte, Jun Gao, Sasha Glazov, Joey Huston, Zahari Kassabov, Ronan McNulty, Andreas Morsch, Pavel Nadolsky, Voica Radescu, Juan Rojo, and Robert Thorne. PDF4LHC recommendations for Run II. *J. Phys. G: Nucl. Part. Phys.*, 43(023001), 2016.
- [92] Richard D. Ball, Valerio Bertone, Stefano Carrazza, Christopher S. Deans, Luigi Del Debbio, Stefano Forte, Alberto Guffanti, Nathan P. Hartland, José I. Latorre, Juan Rojo, and Maria Ubiali. Parton distributions for the LHC run II. *Journal of High Energy Physics*, 2015(40), 2015.
- [93] Sayipjamal Dulat, Tie Jiun Hou, Jun Gao, Marco Guzzi, Joey Huston, Pavel Nadolsky, Jon Pumplin, Carl Schmidt, Daniel Stump, and C. P. Yuan. New parton distribution functions from a global analysis of quantum chromodynamics. *Physical Review D*, 93(033006), 2016.
- [94] A. D. Martin, W. J. Stirling, R. S. Thorne, and G. Watt. Heavy-quark mass dependence in global PDF analyses and 3- and 4-flavour parton distributions. *Eur. Phys. J. C*, 70(1):51–72, 2010.
- [95] Y. L. Dokshitzer. Calculation of the Structure Functions for Deep Inelastic Scattering and e+ e- Annihilation by Perturbation Theory in Quantum Chromodynamics. *Sov. Phys. JETP*, 46(641), 1977.
- [96] V. N. Gribov Lipatov and L. N. Deep inelastic e-p scattering in perturbation theory. *Sov. J. Nucl. Phys.*, 15(Yad. Fiz. 15, 781):438, 1972.
- [97] G. Altarelli and G. Parisi. Asymptotic freedom in parton language. *Nuclear Physics B*, 126(2):298–318, 1977.
- [98] V. V. Sudakov. Vertex parts at very high-energies in quantum electrodynamics. *Sov. Phys. JETP*, 3(65), 1965.
- [99] S. Catani, F. Krauss, R. Kuhn, and B. R. Webber. QCD Matrix Elements + Parton Showers. *Journal of High Energy Physics*, 2001(63), 2001.
- [100] M.Worek J. Alwall, S. Höche, F. Krauss, N. Lavesson, L. Lönnblad, F.Maltoni, M.L.Mangano, M.Moretti, C.G. Papadopoulos, F. Piccinini, S. Schumann, M. Treccani, J.Winter. Comparative study of various algorithms for the merging of parton showers and matrix elements in hadronic collisions. *Eur. Phys. J. C*, 53:473–500, 2008.
- [101] B. Andersson, G. Gustafson, G. Ingelman, and T. Sjöstrand. Parton fragmentation and string dynamics. *Physics Reports*, 97(2-3):31–145, 1983.

- [102] J. Alwall, R. Frederix, S. Frixione, V. Hirschi, F. Maltoni, O. Mattelaer, H. S. Shao, T. Stelzer, P. Torrielli, and M. Zaro. The automated computation of tree-level and next-to-leading order differential cross sections, and their matching to parton shower simulations. *JHEP*, 07:079, 2014.
- [103] Torbjorn Sjöstrand, Stephen Mrenna, and Peter Z. Skands. A Brief Introduction to PYTHIA 8.1. *Comput.Phys.Commun.*, 178:852–867, 2008.
- [104] T. Gleisberg, Stefan. Höche, F. Krauss, M. Schönherr, S. Schumann, et al. Event generation with SHERPA 1.1. *JHEP*, 02:007, 2009.
- [105] Richard D. Ball et al. Parton distributions for the LHC Run II. *JHEP*, 04:040, 2015.
- [106] Simone Alioli, Paolo Nason, Carlo Oleari, and Emanuele Re. A general framework for implementing NLO calculations in shower Monte Carlo programs: the POWHEG BOX. *JHEP*, 06:043, 2010.
- [107] Hung-Liang Lai, Marco Guzzi, Joey Huston, Zhao Li, Pavel M. Nadolsky, Jon Pumplin, and C. P. Yuan. New parton distributions for collider physics. *Phys. Rev.*, D82:074024, 2010.
- [108] Torbjorn Sjöstrand, Stephen Mrenna, and Peter Z. Skands. PYTHIA 6.4 Physics and Manual. *JHEP*, 05:026, 2006.
- [109] W. Beenakker, R. Hopker, M. Spira, and P.M. Zerwas. Squark and gluino production at hadron colliders. *Nucl. Phys. B*, 492:51–103, 1997.
- [110] A. Kulesza and L. Motyka. Threshold resummation for squark-antisquark and gluino-pair production at the LHC. *Phys. Rev. Lett.*, 102:111802, 2009.
- [111] A. Kulesza and L. Motyka. Soft gluon resummation for the production of gluino-gluino and squark-antisquark pairs at the LHC. *Phys. Rev. D*, 80:095004, 2009.
- [112] Wim Beenakker et al. Soft-gluon resummation for squark and gluino hadroproduction. *JHEP*, 12:041, 2009.
- [113] W. Beenakker et al. Squark and gluino hadroproduction. *Int. J. Mod. Phys. A*, 26:2637–2664, 2011.
- [114] Ryan Gavin, Ye Li, Frank Petriello, and Seth Quackenbush. FEWZ 2.0: A code for hadronic Z production at next-to-next-to-leading order. *Comput. Phys. Commun.*, 182:2388–2403, 2011.
- [115] Michal Czakon and Alexander Mitov. Top++: A Program for the Calculation of the Top-Pair Cross-Section at Hadron Colliders. *Comput. Phys. Commun.*, 185:2930, 2014.
- [116] Nikolaos Kidonakis. Two-loop soft anomalous dimensions for single top quark associated production with a W- or H-. *Phys.Rev. D*, 82:054018, 2010.
- [117] P. Kant, O. M. Kind, T. Kintscher, T. Lohse, T. Martini, S. Mölbitz, P. Rieck, and P. Uwer. HATHOR for single top-quark production: Updated predictions and uncertainty estimates for single top-quark production in hadronic collisions. *Comput. Phys. Commun.*, 191:74–89, 2015.
- [118] ATLAS Collaboration. Multi-Boson Simulation for 13 TeV ATLAS Analyses. ATL-PHYS-PUB-2016-002, 2016.

- [119] Achilleas Lazopoulos, Thomas McElmurry, Kirill Melnikov, and Frank Petriello. Next-to-leading order QCD corrections to  $t\bar{t}Z$  production at the LHC. *Phys. Lett.*, B666:62–65, 2008.
- [120] John M. Campbell and R. Keith Ellis.  $t\bar{t}W^{+-}$  production and decay at NLO. *JHEP*, 07:052, 2012.
- [121] Tanju Gleisberg and Stefan Höche. Comix, a new matrix element generator. *JHEP*, 12:039, 2008.
- [122] Fabio Caccioli, Philipp Maierhofer, and Stefano Pozzorini. Scattering Amplitudes with Open Loops. *Phys. Rev. Lett.*, 108:111601, 2012.
- [123] Steffen Schumann and Frank Krauss. A Parton shower algorithm based on Catani-Seymour dipole factorisation. *JHEP*, 03:038, 2008.
- [124] Stefan Höche, Frank Krauss, Marek Schönherr, and Frank Siegert. QCD matrix elements + parton showers: The NLO case. *JHEP*, 04:027, 2013.
- [125] ATLAS Collaboration. Comparison of Monte Carlo generator predictions for gap fraction and jet multiplicity observables in  $t\bar{t}$  events. ATL-PHYS-PUB, 2014-005, 2010.
- [126] L. Lönnblad and S. Prestel. Matching Tree-Level Matrix Elements with Interleaved Showers. *JHEP*, 03:019, 2012.
- [127] Christoph Borschensky, Michael Krämer, Anna Kulesza, Michelangelo Mangano, Sanjay Padhi, Tilman Plehn, and Xavier Portell. Squark and gluino production cross sections in pp collisions at  $\sqrt{s} = 13, 14, 33$  and 100 TeV. *Eur. Phys. J. C*, 74:3174, 2014.
- [128] ATLAS Collaboration. Summary of ATLAS Pythia 8 tunes. ATL-PHYS-PUB-2012-003, 2012.
- [129] ATLAS Collaboration. The ATLAS Simulation Infrastructure. *Eur. Phys. J. C*, 70:823–874, 2010.
- [130] S. Agostinelli et al. GEANT4: A Simulation toolkit. *Nucl. Instrum. Meth. A*, 506:250–303, 2003.
- [131] ATLAS Collaboration. Selection of jets produced in 13 TeV proton-proton collisions with the ATLAS detector. ATLAS-CONF, 2015-029, 2015.
- [132] J M Campbell, M A Cullen, and E W N Glover. Four jet event shapes in electron-positron annihilation. *Eur. Phys. J. C*, 9(2):245–265, 1999.
- [133] Michael L. Graesser and Jessie Shelton. Hunting mixed top squark decays. *Physical Review Letters*, 111(121802), 2013.
- [134] Stanisław Jadach, Johann H. Kühn, and Zbigniew Was. TAUOLA - a library of Monte Carlo programs to simulate decays of polarized tau leptons. *Computer Physics Communications*, 64(2):275–299, 1991.
- [135] P. Golonka, B. Kersevan, T. Pierzchała, E. Richter-Was, Z. Was, and M. Worek. The tauola-photos-F environment for the TAUOLA and PHOTOS packages, release II. *Computer Physics Communications*, 174(10):818–835, 2006.
- [136] N. Davidson, G. Nanava, T. Przedziński, E. Richter-Was, and Z. Was. Universal interface of TAUOLA: Technical and physics documentation. *Computer Physics Communications*, 183(3):821–843, 2012.

- [137] ATLAS Collaboration. Measurement of the inclusive  $W\pm$  and  $Z/\gamma^*$  cross sections in the  $e$  and  $\mu$  decay channels in  $pp$  collisions at  $\sqrt{s} = 7$  TeV with the ATLAS detector. *Physical Review D*, 85(7):072004, 2012.
- [138] J.M. Butterworth; E. Dobson; U. Klein; B.R. Mellado Garcia; T. Nunnemann; J. Qian; D. Rebuzzi; R.Tanaka;. Single Boson and Diboson Production Cross Sections. ATL-COM-PHYS, 2010-695, 2010.
- [139] F James and M Roos. MINUIT A SYSTEM FOR FUNCTION MINIMIZATION AND ANALYSIS LONG WRITE-UP I . Introduction A large class of problems in many different fields of research can be reduced to the problem of finding the smallest value taken on by a function of one or more variable. *Computer Physics Communications*, 10:343–367, 1975.
- [140] M Baak, G J Besjes, D Côté, A Koutsman, J Lorenz, and D Short. HistFitter software framework for statistical data analysis. *Eur. Phys. J. C*, 75(153), 2015.
- [141] K. Cranmer, George Lewis, Lorenzo Moneta, Akira Shibata, and Wouter Verkerke. HistFactory; A tool for creating statistical models for use with RooFit and RooStats. Technical report, 2012.
- [142] Wouter Verkerke and David Kirkby. The RooFit toolkit for data modeling. Technical report, 2016.
- [143] Abraham Wald. Tests of Statistical Hypotheses Concerning Several Parameters When the Number of Observations is Large. American Mathematical Society,, 54(3):426–482, 2017.
- [144] Glen Cowan, Kyle Cranmer, Eilam Gross, and Ofer Vitells. Asymptotic formulae for likelihood-based tests of new physics. *Eur. Phys. J. C*, 71(1554), 2011.
- [145] ATLAS Collaboration. Search for squarks and gluinos in events with an isolated lepton, jets and missing transverse momentum at  $\sqrt{s} = 13$  TeV with the ATLAS detector. 38th International Conference On High Energy Physics 2016, ATL-COM-PH, 2016.
- [146] ATLAS Collaboration. Search for pair production of gluinos decaying via top or bottom squarks in events with b-jets and large missing transverse momentum in  $p p$  collisions at  $\sqrt{s} = 13$  TeV with the ATLAS detector. 38th International Conference On High Energy Physics 2016, ATLAS-CONF, 2016.
- [147] ATLAS Collaboration. Search for gluinos in events with an isolated lepton, jets and missing transverse momentum at  $\sqrt{s} = 13$  Te V with the ATLAS detector. *Eur. Phys. J. C*, 76(10), 2016.